Crystallography Reports, Vol. 45, No. 5, 2000, pp. 705–708. Translated from Kristallografiya, Vol. 45, No. 5, 2000, pp. 775–778.

DIFFRACTION AND SCATTERING OF X-RAYS AND SYNCHROTRON RADIATION

Laue Diffraction of X-rays in GaAs at the Zero Value of the Real Part of the Structure Factor for Quasiforbidden Reflections

L. I. Datsenko and V. P. Klad'ko

Institute of Physics of Semiconductors, National Academy of Sciences of Ukraine, pr. Nauki 45, Kiev 28, 252650 Ukraine

e-mail: datsenko@radius.semicond.kiev.ua

Received October 28, 1998; in final form, February 18, 1999

Abstract—Specific features of the Laue diffraction of X-rays are considered for quasiforbidden reflections within the wavelength range between the *K*-absorption edges of Ga and As in a GaAs crystal. It is established that scattering for the 200 reflection is of the dynamical nature in the wavelength range where the real part of the structure factor F_{r200} is zero and diffraction is determined by the imaginary part of the atomic form factor $f''(\omega)$ alone. It is shown that the position of the minimum of the function $R_i = f(\lambda)$ is sensitive to the crystal nonstoichiometry predicted by the numerical calculations within the theory taking into account both the real and the imaginary parts of the structure factor. © *2000 MAIK "Nauka/Interperiodica".*

INTRODUCTION

The study of X-ray scattering at the wavelengths close to those of the *K*-absorption edge of Ga in GaAs crystals with the use of quasiforbidden Laue reflections has experimentally confirmed the dynamical character of the interaction between the X-ray radiation and the crystal lattice (Pendellösung intensity oscillations) and allowed the determination of some parameters of structural perfection of the samples such as the static Debye–Waller factor *L*, coefficient of intensity reduction due to diffuse scattering μ_{ds}, and the nonstoichiometry parameter [1–3]. Earlier [4, 5], it was shown that the intensity of the diffraction maximum in the vicinity of the *K*-absorption edge of the material should be described by the formulas of the dynamical theory of scattering, which takes into account the contributions of both real and imaginary parts of the atomic scattering function into the crystal polarizability χ. In the studies of X-ray diffraction for quasiforbidden reflections, of special interest is the situation where the real part of the structure factor for the *h*th reflection with due regard for the corrections for the atomic scattering function for anomalous dispersion, $f_0(\mathbf{h}) + f'(\omega)$, equals zero. The modified theory of X-ray scattering for this case established the existence of the Pendellösung fringes of intensity oscillations on the rocking curve for the Laue-diffraction [6]. It was also established that Pendellösung fringes are described by the imaginary part of the atomic scattering function alone. In the case of Bragg diffraction, narrow rocking curves were observed. The situation where $f_0(\mathbf{h}) + f'(\omega) = 0$ was observed experimentally in the measurements of integrated intensities in the vicinity of the *K*-absorption edge of Ge [7]. An attempt to use this wavelength range to control the nonstoichiometry parameter of crystals in the Bragg diffraction geometry was made in [8, 9], where the authors assumed that X-ray scattering is of purely kinematical character, i.e., that the total integrated reflectivity of a crystal consists of two components—those of coherent and diffuse scattering—and, according to [10], is independent of the structure defects [10].

Below, we describe the study of X-ray scattering for quasiforbidden reflections in real GaAs crystals in the case where the real part of the structure factor vanishes. We also investigated the effect of structure defects and crystal nonstoichiometry on the behavior of integrated intensities of the diffraction maxima in this wavelength range.

THEORETICAL CONSIDERATION

As is well known, the atomic scattering factor has the form

$$f = f_0(\mathbf{h}) + f'(\omega) + i f''(\omega), \qquad (1)$$

where $f_0(\mathbf{h})$ is the normal value of the atomic scattering factor for the *h* reflection, and $f'(\omega)$ and $f''(\omega)$ the frequency-dependent real and imaginary corrections to $f_0(\mathbf{h})$ caused by anomalous dispersion. These corrections are especially important in the vicinity of the *K*-absorption edges of the crystal components. It is seen from (1) that the condition $f_0(\mathbf{h}) + f'(\omega) = 0$ is fulfilled for reflections with large absolute values of the diffraction vector (since $f_0(\mathbf{h})$ decreases with an increase of $\mathbf{h}$) in the vicinity of the *K*-edge, where the corrections $f'(\omega)$ are especially pronounced. The case where the

1063-7745/00/4505-0705$20.00

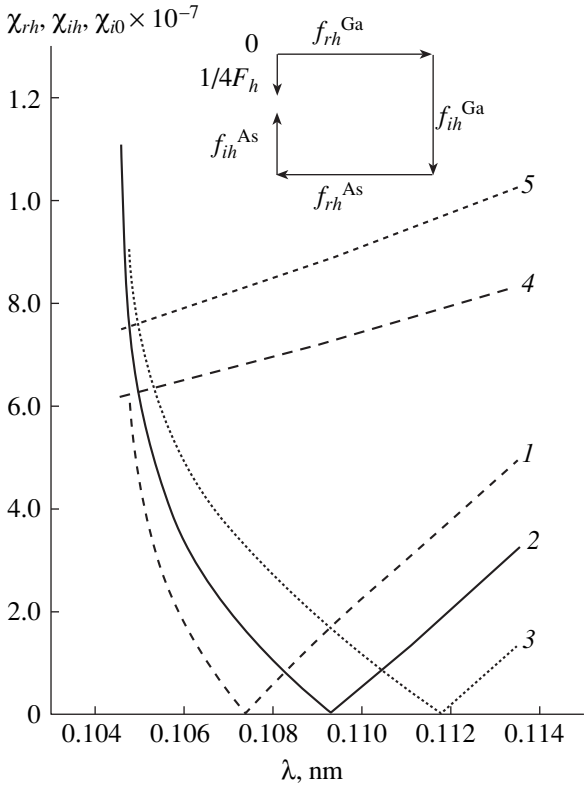

Fig. 1. Energy dependence of the real (curves *1–3*) and imaginary (curve *4*) parts of the Fourier coefficient of GaAs polarizability for crystals with various nonstoichiometries ($c_{Ga} - c_{As}$): (*1*) –0.03, (*2*) 0, (*3*) 0.03, (*5*) the value of χ_{i0}. 200 reflection. In the inset: the vector diagram of the contributions of the real and the imaginary parts of atomic Ga and As form factors to the structure factor of the quasiforbidden 200 reflection.

structure factor F_h is determined by the imaginary part of f alone was considered for a Ge crystal [7]. The situation where $F_{rh} \longrightarrow 0$ can readily be obtained for binary crystals, e.g., GaAs, by using the quasiforbidden 200 reflection and the wavelength range between the K-absorption edges of the crystal components ($F_{rh} \sim [c_{Ga}(f_{Ga} + f'_{Ga}) - c_{As}(f_{As} + f'_{As})] \longrightarrow 0$, where c_{Ga} and c_{As} are the atomic concentrations of Ga and As, respectively). For the reflections of the $h + k + l = 4n + 2$ type with $n = 0, 1, \ldots$ the atoms in the sphalerite-type lattice scatter the X-ray radiation in the counterphase. In this wavelength range, the imaginary part of the atomic scattering function, $f''(\omega)$, has quite a large value because of the jump in absorption at the K-absorption edge of gallium ($f''(\omega) \geq f_0(\mathbf{h}) + f'(\omega)$). Figure 1 shows the vector diagram of the structure factor of the 200 reflection for the wavelength $\lambda = 0.1093$ nm which shows that the resulting value, $1/4F_h$, is imaginary. Figure 1 also shows energy dependence of the Fourier coefficients of polarizability, $\chi_{rh} = -(e^2/mc^2)(\lambda^2/\pi V)F_{rh}$ and $\chi_{ih} = -(e^2/mc^2)(\lambda^2/\pi V)F_{ih}$, for the quasiforbidden 200 reflection in GaAs in the above indicated wavelength range. Here e^2/mc^2 is the classical radius of an electron, λ is the X-ray wavelength, and V is the unit-cell volume of the crystal, and $F_{ih} \sim f''(\omega)$. The dispersion corrections to the atomic form factor $f'(\omega)$ and $f''(\omega)$ were calculated by the method described in [11] with due regard for the oscillator strengths taken from [12]. It is seen that for the wavelength close to 0.109 nm, we have $\chi_{ih} \gg \chi_{rh}$. The integrated reflectivity of an ideal crystal for this case can be calculated by the formula of the modified theory [13] as

$$R_i = (\gamma_h/\gamma_0)^{1/2}(|\chi_h|/\sin 2\vartheta)\int R_i^y dy,$$

$$R_i^y = \exp(-\mu t')(1 - 2p\sin\delta) \qquad (2)$$

$$\times [\sin^2((t/\Lambda)\mathrm{Re}M^{1/2}) + \sinh^2((t/\Lambda)\mathrm{Im}M^{1/2})],$$

where t is the crystal thickness; $t' = t\cos\vartheta\sin\beta/\gamma_0\gamma_h$; $\Lambda = \lambda(\gamma_0\gamma_h)^{1/2}/\pi|\chi_h|$ is the extinction length; γ_0 and γ_h are the directional cosines of the incident and reflected X-ray beams, respectively; ϑ is the Bragg angle; and β is the angle formed by the crystal surface and the reflecting planes. An important parameter entering (2) is the quantity M dependent on both χ_{rh} and χ_{ih}. All the remaining symbols correspond to those used in [13]. The influence of defects on the reflectivity can be estimated by the Molodkin formula [14], which takes into account the contribution of diffuse scattering from structure imperfections. To confirm the validity of these formulas for quasiforbidden reflections, we compared the reflectivities calculated by (2) and by formulas for an ideal crystal [15] with due regard for the contributions that come to χ_h from both real and imaginary components. The satisfactory agreement of these values allowed the numerical evaluation of the effect of structural imperfections on the reflectivity for quasiforbidden reflections at various values of the static Debye–Waller factors L for the case where $\chi_{rh} = 0$.

EXPERIMENTAL

The integrated intensities of the symmetric 200 Laue reflections were measured on a single-crystal spectrometer by the method suggested in [16] with the use of a standard perfect silicon crystal. The parameters of the X-ray tube (20 kV, 35 mA) provided the elimination of the parasitic effect of a harmonics multiple of $n\lambda/2$. We used a 35-μm-thick (100)-oriented GaAs sample with the dislocation density ~10^3 cm^{-2}. Special precautions were taken to avoid the elastic strains during sample positioning on a crystal holder. The energy resolution of the setup was characterized by the width of the spectral window $\Delta\omega$:

$$\Delta\omega = \omega\cot\vartheta\Delta\vartheta, \qquad (3)$$

where ϑ is the Bragg angle, ω is the frequency of the X-ray radiation, and $\Delta\vartheta$ is the angular range of simultaneously recorded diffracted waves. With due regard

for the widths of two exit slits (50 μm), the resolution was 35 eV.

Since the integrated intensities of 200 Laue reflections in this wavelength range were close to the background intensity ($k_f = i_f/i_d = 2.0$, where i_f and i_d are the pulse densities in the intensity measurements of the background and the diffracted-beam intensity), the 1% measurement accuracy was attained by collecting the necessary number of pulses and multiple energy passages. The statistical error in the measurements of integrated intensities against the background was determined as

$$\varepsilon(i_d) = \frac{1}{\sqrt{i_d T}}\sqrt{1 + 2k_f}, \qquad (4)$$

where T is the time of measuring the integrated intensity. In our case, $k_f = 2.0$, $\varepsilon \approx 0.01$, and the measurement time at each point for the normal law of error distribution ranged within 40–200 s (depending on the wavelength).

RESULTS AND DISCUSSION

Experimental points and the R_i curves calculated as functions of X-ray wavelength by (2) for crystals *1* (nonstoichiometric), *2* (ideal stoichiometric) at $\chi_{ih} = 0$, and *3* (ideal at $\chi_{ih} \neq 0$) are shown in Fig. 2. One can see that all the curves have the minima, with the extremum point *E* on the experimental curve being more clearly pronounced than the point *T* on the theoretical curve *3*. In the vicinity of the wavelengths where $\chi_{rh} = 0$, the experimental reflectivity R_i has the nonzero values and is determined by the value of χ_{ih}. The contribution of χ_{ih} to X-ray diffraction for the quasiforbidden 200 reflection is quite considerable in the whole wavelength range studied (Fig. 1) with the role of the real part χ_h being important only in the vicinity of the *K*-absorption edge of As ($\lambda_K^{As} = 0.1045$ nm). Therefore, neglecting the imaginary part ($\chi_{ih} \longrightarrow 0$) in the calculation of the parameters $b = \sqrt{2}\,|\chi_{ih}|/|\chi_{rh}|$ and $p = |\chi_{ih}||\chi_{rh}|/|\chi_h|^2$ determining M in (2) results in considerable discrepancies between the theory and the experiment in this wavelength range (see inset in Fig. 2 and curve *2*) everywhere except in the wavelength close to the *K*-absorption edge of As where the term of χ_{rh} becomes important. This fact shows that X-ray scattering at the point $\chi_{rh} = 0$ is described by the imaginary part of the structure factor alone. The positions of the reflectivity minima $R_i = f(\lambda)$ (both calculated and experimental) also seem to depend on the sample nonstoichiometry. Therefore, the positions of these minima slightly differ from the position of the point, where $\chi_{rh} = 0$.

In order to interpret the above discrepancies between the experimental and calculated integrated reflectivity for an ideal (stoichiometric) crystal (curve *3*), we studied the effect of nonstoichiometry on

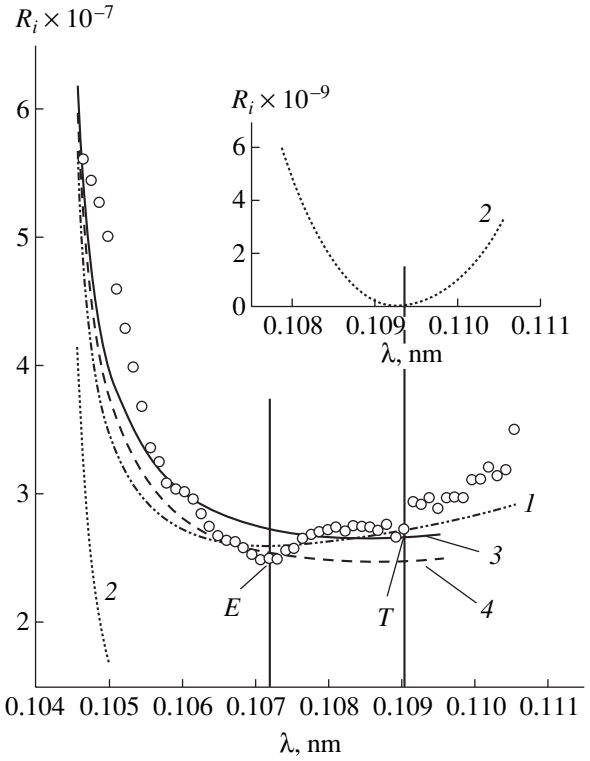

Fig. 2. Experimental reflectivity (dots) and reflectivity calculated by formula (2) as functions of the X-ray wavelength for a 35 μm-thick GaAs specimen; 200 reflection; (*1*) a nonstoichiometric crystal; (*2*) an ideal stoichiometric crystal with $\chi_{ih} = 0$; (*3*) an ideal stoichiometric crystal with $\chi_{ih} \neq 0$; (*4*) a real stoichiometric crystal with $\chi_{ih} \neq 0$, $L = 0.01$, and $\mu_{DS} = 30$ cm^{-1}. In the inset: curve *2* in the vicinity of the wavelength at which the reflectivity value calculated without the allowance for the contribution of χ_{ih} into diffraction is less by several orders of magnitude than its experimental value.

the energy position of the point $\chi_{rh} = 0$ and the run of $R_i = f(\lambda)$. The results of such calculations for the real part of the structure factor F_{rh} are shown in Fig. 1. The analysis of these data shows that the position of $F_{rh} = 0$ is sensitive to the variations in the chemical composition of the crystal. Indeed, calculated curve *1* in Fig. 2 with due regard for possible nonstoichiometry at the level $c_{Ga} - c_{As} = 0.01$ satisfactorily agrees with the experimental dependence $R_i = f(\lambda)$ and the position of its minimum. The variations in the component concentration at a level of 10^{17} cm^{-3} do not noticeably change the energy position of the structure factor minimum at the given width of the spectral window. The position of the reflectivity minimum is even less sensitive to such small variations in the chemical composition of the crystal.

One more interesting fact established in the wavelength range studied is the effect of various structural defects on reflectivity. This problem is especially important because of obvious discrepancies between the theory (even with due regard for possible nonsto-

ichiometry) and the experiment in the wavelength range close to the *K*-absorption edge of As atoms (Fig. 2). The calculation of this effect at various values of the static Debye–Waller factors *L* and the coefficient of energy losses due to diffuse scattering μ_{DS} is illustrated by Fig. 2 (curve *4*). In the calculations, the values of the parameters *L* and μ_{DS} were assumed to be independent of the scattering parameters λ and χ_h. The calculations show that reflectivity is slightly sensitive to the variations in the parameter *L* but is strongly dependent on the coefficient μ_{DS}. This can be explained by the fact that a decrease in $\chi\exp(-L)$ cannot be compensated with an increase in reflectivity due to the diffuse-scattering component. Unlike the case of nonstoichiometry, structural defects described by the parameters *L* and μ_{DS} considerably influence the energy position of the minimum Laue intensity. This fact is very important for the separation of the effects caused by various factors on reflectivity of quasiforbidden reflections. The effect of λ on μ_{DS} and, thus, also on reflectivity of the quasiforbidden reflection in this wavelength range will be studied separately.

CONCLUSIONS

Thus, the study of X-ray dynamical scattering for the quasiforbidden 200 reflection for gallium arsenide crystals provided the establishment of the following facts.

In the wavelength range between the *K*-absorption edges of Ga and As, there is a weak reflectivity minimum (revealed experimentally), which is explained by the zero value of the real part of the structure factor in this range.

The experimental reflectivity values for quasiforbidden reflections cannot be adequately described by the scattering theory not taking into account the imaginary part of the Fourier coefficient of polarizability. The reflectivity at the wavelengths at which $\chi_{rh} \longrightarrow 0$ is described by the imaginary part of the atomic formfactor alone.

The position of the minimum on the energy dependence of reflectivity for the quasiforbidden reflection in this wavelength range is sensitive to crystal nonstoichiometry, but is independent of the parameters *L* and μ_{DS} of the structural perfection of the crystal.

REFERENCES

1. V. P. Klad'ko, L. I. Datsenko, I. I. Tkach, *et al.*, Metallofiz. Noveĭshie Tekhnol. **21** (3), 3 (1999).
2. L. I. Datsenko, V. P. Klad'ko, V. M. Mel'nik, and V. F. Machulin, Metallofiz. Noveĭshie Tekhnol. **21** (8), 46 (1999).
3. L. I. Datsenko, V. P. Klad'ko, V. F. Machulin, and V. M. Mel'nik, Poverkhnost', No. 12 (1999) (in press).
4. M. Laue, *Röntgenstrahlinterferenzen* (Akad. Verlag, Leipzig, 1960).
5. E. Zielinska-Rohosinska, Acta Phys. Pol. **27**, 587 (1965).
6. T. Fukamachi and T. Kawamura, Acta Crystallogr., Sect. A: Fundam. Crystallogr. **49**, 384 (1993).
7. T. Fukamachi, R. Negishi, M. Yoshizawa, *et al.*, Acta Crystallogr., Sect. A: Fundam. Cryslallogr. **49**, 573 (1993).
8. V. P. Klad'ko, Metallofiz. Noveĭshie Tekhnol. **20** (1), 3 (1988).
9. G. Cockerton, G. S. Green, and B. K. Tanner, Mater. Soc. Res. Symp. Proc. **138**, 65 (1989).
10. M. A. Krivoglaz, *Theory of X-Ray and Thermal Neutron Scattering by Real Crystals* (Nauka, Moscow, 1967; Plenum Press, New York, 1969).
11. T. Fukamachi, S. Hosoya, T. Kawamura, and M. Okunuko, *X-ray Intensity Measurements on Large Crystals by Energy-Dispersive Diffractometry,* Preprint No. 760 (Institute for Solid State Physics, University of Tokyo, Tokyo, 1976).
12. D. T. Cromer, Acta Crystallogr. **18** (10), 17 (1965).
13. Z. Zhao, J. Han, S. Zhou, *et al.*, Physica B (Amsterdam) **216**, 96 (1995).
14. L. I. Datsenko, V. B. Molodkin, and M. E. Osinovskiĭ, *Dynamic X-ray Scattering by Real Crystals* (Naukova Dumka, Kiev, 1988).
15. Z. G. Pinsker, *X-ray Crystal Optics* (Nauka, Moscow, 1982).
16. L. I. Datsenko, Ukr. Fiz. Zh. (Russ. Ed.) **24**, 577 (1979).

Translated by L. Man

Crystallography Reports, Vol. 45, No. 5, 2000, pp. 709–713. Translated from Kristallografiya, Vol. 45, No. 5, 2000, pp. 779–783.

THEORY OF CRYSTAL STRUCTURES

Geometrical Laws in Inorganic Chemistry

S. V. Borisov

Institute of Inorganic Chemistry, Siberian Division, Russian Academy of Sciences, pr. Akademika Lavrent'eva 3, Novosibirsk, 630090 Russia

e-mail: borisov@che.nsk.su

Received November 2, 1998

Abstract—On the basis of an original interpretation of the crystal state, it is shown that most of the structural types are determined by a small set of planar nets densely filled with the heaviest atoms of the structure. These nets are combined into atomic sublattices (matrices of the structure types) by the operations of (pseudo)symmetry, thus reducing the number of the degrees of freedom in the structure, which, in turn, provides structure stability. It is shown on examples of heavy-cation oxides, fluorides, and sulfides that the number of the types of such matrices (*F*-, *I*-, etc.) is limited. Each type is characterized by a certain structure-determining complex of mutually intersecting crystallographic planes parallel to the most densely filled atomic nets. Most of the atomic nets considered in crystal chemistry are, in fact, various sections of the sublattices–matrices formed by a limited number of densely filled atomic nets. © *2000 MAIK "Nauka/Interperiodica".*

Today, the determination of the crystal structure presents no difficulty. Therefore, much more effort and attention is now given to interpreting the results obtained in structural studies. These are, first and foremost, the characteristics of atomic coordination, valence angles, bond lengths, and the scheme of most important chemical interactions. However, we believe that all these characteristics should be considered in stereochemistry rather than in crystal chemistry because, with small variations, they describe atomic interactions not only in crystals but also in liquids and in the amorphous state.

Among numerous crystallochemical studies, we mention the following problems here: the application of the principles of close packing conjugated with the space-group symmetry [1]; a large cycle of studies aimed at revealing regular and semiregular infinite atomic nets in inorganic and intermetallic structures also used in the systematization and classification of crystal structures [2–4], and the attempts of *a priori* modeling of the crystalline state proceeding from the given atomic composition.

Taking into account that, according to P. Curie, symmetry is the state of a compound, one can consider the crystalline state as a type of the spatial organization of atomic ensembles. This state seems to be the best studied in comparison with the symmetric quasicrystalline or fractal states. However, even for this case, it is impossible to predict all the facts, e.g., the number and variety of planar atomic nets encountered in crystal structures, despite the fact that it follows from the principle of close packings underlying crystal chemistry that the number of such nets should be limited. Geometry in nature is always a spatial manifestation of interacting forces. We believe that the problem is that there is no commonly accepted concept of which forces provide the conservation of an ideal long-range order in crystals experimentally confirmed by diffraction from the coherently scattering blocks with dimensions of tens of thousands of angstroms.

Our concept of the crystalline state as an atomic ensemble in which the atoms are ordered due to mutually correlated system of plane elastic standing waves of various orientations parallel to the (*hkl*) planes of the crystal was best formulated in 1992 [5] and since then has been confirmed by a large number of real structures [6]. The objective consequence of the validity of our concept should be the presence in the structures of planes densely filled with the heaviest atoms or by highly charged ions with the interatomic distances close to the shortest interatomic contacts. To confirm our concept, we examined ionic compounds with heavy cations (fluorides, oxides, and sulfides) where the effect of light anions on the systems of plane elastic standing waves can be neglected. Therefore, densely filled atomic nets were sought only for cations. It is shown that it is in these atomic nets that the strongest chemical bonds between the structure atoms are concentrated. In the first approximation, the parallel densely-filled nets can be considered as rigid two-dimensional objects related to one another by elastic forces. Such interactions are those between the atoms from various nets–layers averaged over the interaction area. These atomic networks with concentrating heavy cations were revealed in the majority of the simple and complicated structures of molybdenum, tungsten, niobium, and tantalum oxides, in heavy-metal fluorides, and in some other structures. As was to be expected from the estimated shortest interatomic distances (~3.5–4.5 Å), the

1063-7745/00/4505-0709$20.00

interplanar spacings (d_{hkl}) for the crystallographic planes parallel to these nets range within 2.5–3.5 Å [7].

We developed a special algorithm and wrote the complex of programs for crystallochemical analysis of similarity in planar atomic nets, CAS-PAN [8], which provide the determination of the relative densities of filling of the parallel atomic nets with atoms of certain kinds (ρ_n) for the systems of crystallographic planes within the given d_{hkl} range. In other words, for each (*hkl*) plane, we calculated the degree of order (coherence) of atoms along the normal to the given plane. The relative density ρ of plane filling is normalized to unity. At $\rho = 1$, the centers of all the atoms lie exactly in the planes of the (*hkl*) family. The calculation is similar to that of the unit structural factor because the deviations (δ) of the atoms from the plane are taken into account by the weighting function $\cos(2\pi\delta/d_{hkl})$, whereas the position of the net with respect to the coordinate origin is determined by the phase (sign) of the structure factor. The existence in the structure of one plane with the ρ-value close to unity signifies the existence of pseudoperiodicity along the normal to this plane, with the pseudoperiod being equal to d_{hkl}. If there are two or more such planes, then the pseudoperiodicity exists along two or three noncoplanar directions which indicates that there exists a two- or three-dimensional sublattice within the unit cell. The translations of this sublattice can readily be calculated by the rules suggested in [9]. The volume of the corresponding subcell is a certain rational fraction of the total unit-cell volume of the crystal V_0 equal to V_0/Δ, where Δ is the determinant of the matrix composed of the indices of the densely filled ($h_1k_1l_1$), ($h_2k_2l_2$), and ($h_3k_3l_3$) planes. In order to reveal the sublattices in the structures described by highly symmetric space groups, it is not necessary to consider three different densely filled planes. Thus, even one plane with the indices of the general type in the orthorhombic system determines the subcell. Since $\rho_{(hkl)} = \rho_{(-hkl)} = \rho_{(h-kl)}$, we arrive at three noncoplanar families of planes whose intersection points determine the atomic sublattice of the structure.

We analyzed the symmetry of the cationic sublattices of the above indicated classes of inorganic compounds. It was shown that more than 40% of these sublattices can be reduced to the pseudocubic face-centered (the *F*-type) and about 30%, to the pseudocubic body-centered (the *I*-type) sublattices. The most densely filled cationic nets in the *F*-type sublattice are parallel to the (111), ($\bar{1}11$), and ($1\bar{1}1$) planes (the indices are indicated for the cationic sublattice). Therefore, the crystallographic planes of the {111} family are, in fact, a structure-forming complex of the *F*-type. The indices of the planes parallel to all the other cationic nets are obtained as the linear combinations of the indices of three planes chosen to be the major planes of this family. The next family (in the order of a decrease in d_{hkl}) is {200}. If cations form a regular most densely filled trigonal net (3^6 in the Schläfli symbols [4]), then the net in the planes parallel to {200} is square, (4^4). In the *I*-type sublattice, the structure-forming complex consists of six planes of the {110} family, any three planes of this family can be chosen as the main ones. The indices of all the remaining planes parallel to any cationic nets of the *I*-type sublattices are obtained as the linear combinations of these three main planes. The atomic planes parallel to the planes of the {110} family are trigonal, but the triangles are not equilateral but isosceles with the sides a and $a\sqrt{3}/2$ and the apex angle ~71°. Similar to the *F*-type, the {200} faces of the cubic *I*-sublattice are characterized by square atomic nets, 4^4. It is well known that a continuous transition between the *F*- and *I*-types is possible via the uniform linear deformation of the space [10].

The widespread occurrence of the *F*- and *I*-type cationic sublattices and, therefore, the stability of the structures with such heavy-cation arrangement can be explained by a considerable effect of (pseudo)symmetry operations on the thermodynamic stability. In the *F*-type, the (pseudo)symmetry makes four cationic nets equivalent, namely, those parallel to the (111), ($\bar{1}11$), ($1\bar{1}1$), and ($11\bar{1}$) nets, whereas in a less dense I-type structures, six cationic nets parallel to the structure-forming {110} family of planes are equivalent to one another. Similar (pseudo)symmetry relationships are also known for all the remaining densely filled atomic nets.

The third most often encountered cationic lattice in heavy-cation fluorides and oxides is the cationic sublattice of the β-K_2UF_6 structure type consisting of alternating hexagonal nets 6^3 of K cations and enlarged 3^6 nets of U cations. Bringing these two neighboring nets into coincidence, one can see that the U cations occupy the empty centers of the K-hexagons in such a way that the projection onto the (001) plane yields the densely filled net 3^6 (Fig. 1). The stability of this structure type in terms of our concept can be interpreted in such a way. The one-layer packing of the equal spheres or the *AA*-packing in the close-packing notation would possess a high symmetry [1]. Of course, its space-packing coefficient is rather low and, as a consequence, the coordination number of each sphere is also very low (c.n. = 6 + 2). However, if some of these spheres are displaced by a half-interplanar spacing with preservation of its high (hexagonal) symmetry, the coordination numbers become close to 12. Thus, the coordination number for U atoms is equal to 12(K) + 2(U) and for K atoms, 5(K) + 6(U). It should be noted that one third of all the sites in the K-net are vacant, whereas in the U-net, two thirds of the sites are vacant. The structure-forming complex of the crystallographic planes for this structure type is: {001} + {110}. Parallel to the (001) plane, the densely filled cationic net is split into two sublevels (Fig. 1), whereas parallel to the planes of the {110} family, the nets with the maximum density are

located (Fig. 2a). The nets derived from the main cationic nets are parallel to the faces of the {011} hexagonal bipyramid (Fig. 2b) and are the second densely filled planes. Each of the cationic nets considered above (Figs. 1, 2) was used in the earlier crystallochemical studies, however, the authors did not realize that these nets were, in fact, different sections of the same atomic configuration.

The phenomenon of splitting of a densely filled planar net into two planes complementing each other is not the only example. Detailed consideration showed that the well-known β-W structure (cubic structure type *A*15, according to the *Structure Bericht* classification [11]), can also be considered as a split slightly deformed trigonal net. It is seen from Fig. 3 that, parallel to the coordinate plane *xy*, the $6363 + 3^26^2$ nets, in which the hexagon (with two sides equal to $a/2$ and four sides equal to $a\sqrt{5}/2$) is inscribed into the square, alternate with square nets centering these hexagons and are displaced with respect to the first nets by a quarter-translation along the *z*-axis. Both nets are repeated with a 90°-rotation about this axis at each 0.5 period along the *z*-axis. The structure is cubic and, therefore, the same should also take place along the *x*- and *y*-axes. The coordination number of one independent atom is 12; its coordination polyhedron is a distorted icosahedron; the coordination number of another independent atom is 12 + 2; its coordination polyhedron is a bicapped hexagonal antiprism with the centered bases. On the whole, this structure shows that the hexagonal and cubic motifs are consistent with the close-packing principle.

A large number of various splittings of the trigonal net into two levels was also encountered in the analysis of the heavy-atom sulfides possessing mirror-reflection planes spaced by ~2 Å (the period along the normal to these planes equals ~4 Å). If the cationic and anionic radii exceed 1 Å, the centers of these atoms can be located in the structure only on the mirror reflection planes. This is an example of the unique situation of absolute ordering of atoms by a family of mirror reflection planes. The higher mass of a sulfur anion (in comparison with the mass of oxygen and fluorine) results in the fact that the degree of spatial order of anions in many structures approaches the degree of the cationic order, although the planes providing such ordering for anions and cations are different, as was to be expected from different numbers of cations and anions in the unit cell.

All the sulfide structures with such systems of mirror reflection planes had the *AA'*-type cationic sublattice (where the prime indicates splitting). Unlike splitting in the β-K_2UF_6-type, splitting of the basal plane into two planes occurs according to the parity principle—the numbers of occupied and vacant sites in each plane are equal [12, 13].

The above types of cationic sublattices, which can be called the matrices of the corresponding structural

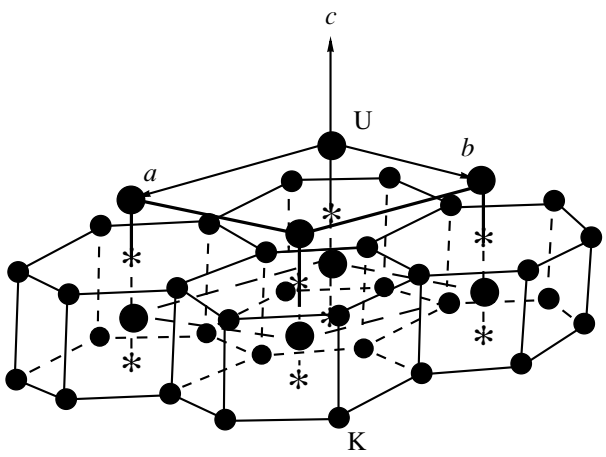

Fig. 1. Cationic sublattice–matrix for the structure type β-K_2UF_6, which illustrates the principle of splitting of a densely filled atomic net 3^6 into the hexagonal 6^3 net (K) and an enlarged 3^6 net (U). Asterisks show U atoms projected onto the K-net. The nets are parallel to the {001} planes of the structure-forming complex.

types, form the basis of most structures analyzed in our study. In some cases, we also encountered some other sublattices–matrices, namely, those with four-layer close packing of the *ABAC*-type ($NH_4Er_3F_{10}$ and $Na_2Ta_2O_{11}$), with two-layer close packing of the *AB*-type (BiPbOF and YF_3), with one-layer *AA*-type packing ($AgPdZr_2F_{11}$), with primitive cubic lattice ($CsWO_2F_4$), etc. In some cases, we failed to identify the cationic sublattice–matrix with any of the known types, despite the fact that the atomic net had a characteristic form providing the comparison of structures with one another. Thus, the net in which two adjacent rows of squares alternate with two rows of rhombuses is characteristic of the alluaudite structure type $Na_2Fe_3(PO_4)_3$ characteristic of crystallization of double molybdates and tungstanates of various compositions [14].

Thus, the large volume of the structural data analyzed led us to the following conclusions.

The phenomenon of ordering (coherence) of the heavy-atom positions in the subsystem of crystallographic planes with the formation of the structure-type basis is revealed. These subsystems, called the structure-forming complexes of crystallographic planes, provide the most intense diffraction reflections, i.e., in accordance with [15], give the main information about the structure.

The most densely filled nets of the structure are parallel to the planes of the structure-forming complex and are related by the (pseudo)symmetry elements into atomic (most often cationic) sublattices–matrices of the corresponding structure types, which possess clearly pronounced (pseudo)symmetry of supergroups. The symmetry of these supergroups for the matrices is not always ideal, but the deviations from the ideal matrix are insignificant. Therefore, there exists a certain lim-

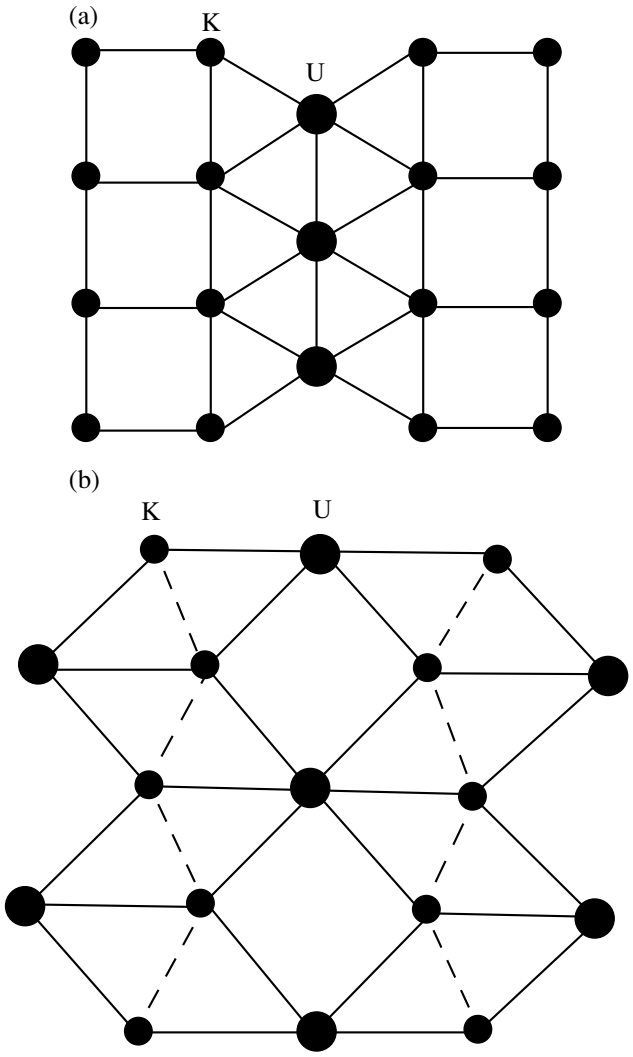

Fig. 2. Densely filled planes of the cationic sublattice–matrix β-K_2UF_6: (a) the most densely filled atomic net of squares and rhombuses parallel to the planes of the {110} structure-forming complex; (b) the second densely filled atomic net parallel to the {011} faces of the hexagonal bipyramid.

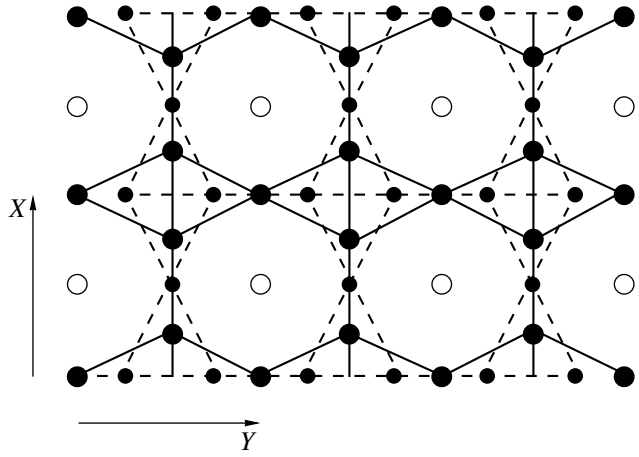

Fig. 3. Scheme of splitting of the 3^6 net in the β-W structure type. Four atomic nets located along the *Z*-axis are shown: nets of hexagons and rhombuses $6363 + 3^26^2$ at the level $z = 0$ (solid lines and large filled circles), square nets 4^4 at the levels $z = 1/4$ and $3/4$ (empty circles), and the net similar to the first net but rotated by 90° at the level of $z = 1/2$ (dashed lines and small filled circles).

ited range of the parameters of atomic (cationic) sublattices–matrices (the so-called range of structure-type stability) within which this structure type can be formed depending on the composition and the external conditions.

The planar atomic nets usually considered in classical inorganic crystal chemistry are, in fact, various sections of a small number of atomic (cationic) sublattices–matrices of different types consisting of densely filled nets ordered by structure-forming complexes of crystallographic planes in accordance with the (pseudo)symmetry of the supergroups.

Thus, we believe that it is necessary to consider not only the traditional crystallochemical principle of close packing (providing only the minimum information on the crystal structure), but also the principle of the maximum possible (pseudo)symmetry. In terms of mathematics, the energy gain due to an increase in the symmetry is explained by a decrease of the number of degrees of freedom. In the first approximation, the number of degrees of freedom coincides with the number of independent coordinate parameters of the basis atoms. Some interesting examples of the relation between the structure stability and symmetry were considered elsewhere [16].

ACKNOWLEDGMENTS

This study was supported by the Russian Foundation for Basic Research, project nos. 93-03-5991 and 96-03-33010.

REFERENCES

1. N. V. Belov, *Structure of Ionic Crystals and Metal Phases* (Akad. Nauk SSSR, Moscow, 1947), p. 238.
2. A. F. Wells, *Structural Inorganic Chemistry* (Clarendon, Oxford, 1984; Mir, Moscow, 1987), Vol. 1, p. 408.
3. P. I. Kripyakevich, *Structure Types of Intermetallic Compounds* (Nauka, Moscow, 1977), p. 288.
4. W. B. Pearson, *Crystal Chemistry and Physics of Metals and Alloys* (Wiley, New York, 1972; Mir, Moscow, 1977), Chap. 1.
5. S. V. Borisov, Zh. Strukt. Khim. **34** (5), 116 (1992).
6. S. V. Borisov, Zh. Strukt. Khim. **37** (5), 907 (1996).
7. S. V. Borisov and R. F. Klevtsova, Kristallografiya **32** (1), 113 (1987) [Sov. Phys. Crystallogr. **32** (1), 62 (1987)].

8. N. A. Bliznyuk and S. V. Borisov, Zh. Strukt. Khim. **34** (2), 145 (1992).
9. S. V. Borisov, Zh. Strukt. Khim. **27** (3), 164 (1986).
10. S. V. Borisov, N. A. Bliznyuk, and E. S. Kuklina, Zh. Strukt. Khim. **35** (3), 3 (1994).
11. I. Narai-Sabo, *Inorganic Crystallochemistry* (Hungary Academy of Sciences, Budapest, 1969).
12. S. V. Borisov, N. V. Podberezskaya, S. A. Magarill, and N. V. Pervukhina, Zh. Strukt. Khim. **38** (5), 908 (1997).
13. S. V. Borisov, N. V. Podberezskaya, N. V. Pervukhina, and S. A. Magarill, Z. Kristallogr. **213**, 253 (1998).
14. R. F. Klevtsova, S. V. Borisov, N. A. Bliznyuk, *et al.*, Zh. Strukt. Khim. **32** (6), 127 (1991).
15. B. K. Vaĭnshteĭn and R. L. Kayushina, Kristallografiya **11** (4), 526 (1966) [Sov. Phys. Crystallogr. **11** (4), 468 (1966)].
16. S. V. Borisov, Zh. Strukt. Khim. **38**, 1156 (1995).

Translated by L. Man

Crystallography Reports, Vol. 45, No. 5, 2000, pp. 714–717. Translated from Kristallografiya, Vol. 45, No. 5, 2000, pp. 784–787.

Inversion of X-ray Transform in Spaces of Odd Dimensions

Ya. A. Ilyushin and O. A. Terekhova

Moscow State University, Vorob'evy gory, Moscow, 119899 Russia

e-mail: asi@phys.msu.su

Received October 20, 1998

Abstract—The problem of reconstruction of an unknown function from the spatial synthesis of its projections onto the spaces of odd dimensions has been considered. The explicit formulas for such reconstruction are obtained for the spaces with dimension up to 11. © *2000 MAIK "Nauka/Interperiodica".*

In recent years, we have seen evidence of an ever increasing interest in X-ray transforms in spaces of various dimensions [1–7] and, first of all, in three-dimensional space. To a large extent, this interest is explained by the development of tomographic studies of objects of the most diverse natures and the ever increasing use of scanners providing this type of integral transform. As compared to the two- and three-dimensional Radon transforms, widely used in most medical tomographs, the use of X-ray transform results in the necessity of processing a much larger volume of information. The limited power of today's computers hinders the use of X-ray transforms in medical practice.

The X-ray transform converts the function determined on R_n into a set of its integrals along various possible straight lines belonging to the space R_n. In two dimensional space, this transform coincides with the Radon transform. In the general case, the X-ray transform maps the space of functions determined on R_n into the space of functions determined on $R_{(n-1)^2}$. Thus, the dimension of the space of the experimental results obtained exceeds the dimension of the space of the initial data, i.e., the volume of information generated by the X-ray transform is somewhat excessive. On the other hand, the volume of these data is usually too large. This is especially true for the tomographic problems solved in the spaces of a dimension exceeding three, more and more often encountered in practice [4]. Thus, the algorithms used for processing the data of the X-ray transform should necessarily be written with due regard for the above facts.

One of the possible approaches to the solution of such problems is the method of spatial synthesis of projections [1, 4, 5, 7] (back projection and summation). The method was first used in X-ray diffraction analysis at the beginning of the twentieth century [8]. The back projection and summation in two-dimensional space can be performed with the use of a rather simple photosummation apparatus. There are some tomographic apparatus that can directly perform such summation without explicit representation of any information on the projection. In some practical situations, this approach proved to be the only one possible [4].

One can show that the operator of back projection and summation is an adjoint operator of the X-ray transform. Therefore, the sum of the back projections belongs to the same space of the functions as the initial object and is related to it by a certain self-adjoint operator. Thus, the problem of the reconstruction of the initial function is reduced to the solution of a linear integral equation with the symmetric self-adjoint kernel in this space. Then, the transition to the spatial synthesis of projections allows one to considerably reduce the volume of the data that require further processing. For three-dimensional space, the solution of the problem of function reconstruction from the data of the back projection and summation was considered in [7]. Below, we study the spaces of arbitrary dimensions.

As was shown in [7], the synthesis of the projections $\Sigma(\mathbf{r})$ in three-dimensional space is related to the initial function $f(\mathbf{r})$ by the transform

$$f(\mathbf{r}) * \frac{1}{r^2} = \Sigma(\mathbf{r}), \tag{1}$$

where the asterisk denotes the operation of convolution. The solution of this equation has the form

$$f(\mathbf{r}) = -\frac{1}{4\pi^4}\Delta\left(\Sigma(\mathbf{r}) * \frac{1}{r^2}\right). \tag{2}$$

Consider the spatial synthesis for space of an arbitrary dimension R_n. We assume that all the projections along all the directions are known. Then, choosing the coordinate origin at a certain point R_n and introducing the spherical coordinates $(r, \boldsymbol{\omega})$, where $\boldsymbol{\omega}$ denotes the direction on the unit sphere Ω_n in the n-dimensional space, we obtain the integral of the unknown function $f(\mathbf{r})$ along a certain direction $\boldsymbol{\omega}$ passing through the chosen point $\int_0^\infty f(r, \boldsymbol{\omega})dr$. The sum of such integrals

1063-7745/00/4505-0714$20.00

(projections) is equal to

$$\Sigma(\mathbf{r}) = \int_{\Omega_n}\int_0^\infty f(r, \boldsymbol{\omega})dr d\Omega = f(\mathbf{r}) * \frac{1}{r^{n-1}}, \qquad (3)$$

where integration is performed over all possible directions on the sphere Ω_n.

When deriving formula (2), we used the relationship for the three-dimensional space, $\Delta(1/r) = -4\pi\delta(r)$. In the space of an arbitrary dimension n, this relationship acquires the following form [9]:

$$\Delta\left(\frac{1}{r^{n-2}}\right) = -(n-2)\Omega_n\delta(\mathbf{r}), \quad n \geq 3, \qquad (4)$$

where Δ is the Laplacian in the n-dimensional space.

Now, consider the convolution $r^{-m} * r^{-k}$, which is the uniform function of degree $n - m - k$, i.e., has the form $\text{const}\, r^{n-m-k}$. Indeed,

$$\begin{aligned} r^{-m} * r^{-k} &= \int_{R_n} \frac{d^n\mathbf{r}'}{|\mathbf{r}'|^m|\mathbf{r} - \mathbf{r}'|^k} \\ &= \frac{1}{r^{m+k-n}}\int_{R_n} \frac{d^n(\mathbf{r}'/r)}{|(\mathbf{r}'/r)|^m|(\mathbf{r}'/r) - (\mathbf{r}/r)|^k}. \end{aligned} \qquad (5)$$

One can readily show that this integral converges if $k \leq n - 1$ at $m + k > n$. Now, obtain the convolutions of both sides of equation (3) with the function $r^{-(n-1)}$:

$$\begin{aligned} \Sigma(\mathbf{r}) * \frac{1}{r^{n-1}} &= f(\mathbf{r}) * \frac{1}{r^{n-1}} * \frac{1}{r^{n-1}} \\ &= \text{const}\, f(\mathbf{r}) * \frac{1}{r^{n-2}}. \end{aligned} \qquad (6)$$

Applying the Laplacian to both sides of (6), we arrive at function $f(\mathbf{r})$ sought on the right-hand side within the accuracy of a certain constant factor.

The transforms of a more general form were studied in [2, 3]. They map the functions defined on space R_n ($1 \leq m < n$) onto the family of integrals over all possible m-dimensional subspaces R_n ($1 \leq m < n$). In particular, at $m = 1$, we arrive at the X-ray transform proper, and at $m = n - 1$, at the Radon transform. The back projection and summation for such transforms yields the convolution of the initial function with $r^{-(n-m)}$ within an accuracy of a certain constant factor. In the formal way, we can write the formula of type (2) for an arbitrary m as

$$f(\mathbf{r}) = -\text{const}\Delta\left(\Sigma(\mathbf{r}) * \frac{1}{r^k}\right).$$

In this case, the exponent k should be such that the differentiation would result in delta function (4). The exponent is determined from the condition $m + k - n = n - 2$, i.e., $k = 2n - 2 - m$. However, for all the m except of $m = n - 1$, the convolution integral $r^{-m} * r^{-k}$ is divergent. If $m = n - 2$, the initial function can be reconstructed by direct differentiation of the spatial synthesis of the projections:

$$f(\mathbf{r}) = -\text{const}\Delta\Sigma(\mathbf{r}).$$

Now consider the possible approaches to the calculation of the convolutions $\frac{1}{r^{n-1}} * \frac{1}{r^{n-1}}$ in the spaces of arbitrary dimension n. The denominator of the integrand in (5) goes to zero at two points of the space R_n. Let us choose the coordinate origin on the line L connecting these two points and located equidistantly from both. Introduce the coordinate z on this line. In the space $R_n \backslash L$ complementing this line to the space R_n, introduce the system of spherical coordinates (r', $\boldsymbol{\omega}$), where $\boldsymbol{\omega}$ is a certain direction on the $(n-1)$-dimensional sphere. Then the convolution integral can be written as

$$\begin{aligned} &r^{-(n-1)} * r^{-(n-1)} \\ &= \int_{\Omega_{n-1}} d\Omega \int_{-\infty}^{+\infty}\int_0^\infty \frac{r'^{n-2}dr'dz}{\sqrt{((z-(r/2))^2 + r'^2)((z+(r/2))^2 + r'^2)}^{n-1}}. \end{aligned} \qquad (7)$$

The expression under the integral sign is independent of the angular variables. Therefore, integration over the angular part of the variables reduces to the multiplication by the area of the unit sphere Ω_{n-1}. The area of a sphere of unit radius in the n-dimensional space is equal to [9]

$$\Omega_n = 2\frac{\pi^{n/2}}{\Gamma(n/2)}.$$

Since the convolution is uniform, the dependence on r can be taken outside the integral sign. As a result, we arrive at the following expression for the convolution:

$$\begin{aligned} &r^{-(n-1)} * r^{-(n-1)} \\ &= \frac{2^{n-2}\Omega_{n-1}}{r^{n-2}}\int_{-\infty}^{+\infty}\int_0^\infty \frac{\rho^{n-2}d\rho d\zeta}{\sqrt{((\zeta-1)^2 + \rho^2)((\zeta+1)^2 + \rho^2)}^{n-1}}. \end{aligned} \qquad (8)$$

Since the integrand is an even function of ζ, integration with respect to ζ can be performed over the domain of positive ζ values. Changing the variables, $t = \rho^2$, we reduce the integral in (8) to the form

$$\begin{aligned} &r^{-(n-1)} * r^{-(n-1)} \\ &= \frac{2^{n-2}\Omega_{n-1}}{r^{n-2}}\int_0^{+\infty}\int_0^\infty \frac{t^{(n-3)/2}dtd\zeta}{\sqrt{((\zeta-1)^2 + t)((\zeta+1)^2 + t)}^{n-1}}. \end{aligned} \qquad (9)$$

At even values of n, integration with respect to dt leads to the elliptic integrals that cannot be expressed in terms of elementary functions. Consider the odd n and

assume that $2m = n - 1$. Then the integral with respect to dt entering (9) can be written in the form

$$\int_0^\infty \frac{t^{m-1}dt}{(((\zeta-1)^2+t)^m((\zeta+1)^2+t)^m}. \quad (10)$$

Such integrals are calculated by the recurrence formulas [10]

$$\begin{aligned} F_{n,m} &= RF_{n-1,m} + RF_{n-2,m}, \\ F_{1,m} &= R + RF_{0,m}, \\ F_{0,m} &= R + RF_{0,m-1}, \quad m \geq 2, \\ F_{0,1} &= \frac{1}{a\sqrt{D}} \ln\left|\frac{p}{q}\right|, \end{aligned} \quad (11)$$

where $F_{n,m} = \int_0^\infty \frac{x^n dx}{(ax^2+bx+c)^m}$, $D = b^2 - 4ac$, p and q are the roots of a squared trinomial, $R = R(a, b, c, D)$ are the rational expressions of the coefficients of this trinomial, with the denominators having the form $a^i c^j D^k$, where i, j, and k are certain integers.

For integral (10), we have: $a = 1$, $b = 2(1 + \zeta^2)$, $c = (1 - \zeta^2)^2$, $D = (4\zeta)^2$, $p = (1 + \zeta)^2$, and $q = (1 - \zeta)^2$. Relationships (11) provide the general expression for integral (10) in the form $R_1 + R_2 \frac{1}{4\zeta} \ln\left|\frac{1+\zeta}{1-\zeta}\right|$. Now, we can integrate this expression with respect to ζ. The integral of the rational expression R_1 can be written in terms of the elementary function. Consider the integral of the second term

$$\int_0^\infty R_2 \frac{1}{4\zeta} \ln\left|\frac{1+\zeta}{1-\zeta}\right| d\zeta = \int_0^\infty R_2 \frac{1}{8\zeta^2} \ln\left|\frac{1+\zeta}{1-\zeta}\right| d\zeta^2.$$

This integral can also be represented in the form

$$\int_0^\infty R(\zeta^2, 1+\zeta^2) \ln\left|\frac{1+\zeta}{1-\zeta}\right| d\zeta^2, \quad (12)$$

where $R(\zeta^2, 1 + \zeta^2)$ is the rational function of its arguments, and the denominator has the form $(\zeta^2)^i(1 - \zeta^2)^j$. Using the theorem on decomposition of rational fractions into elementary ones, we can represent this function in the form

$$R(\zeta^2, 1+\zeta^2) = \sum_i \frac{A_i}{(\zeta^2)^i} + \sum_j \frac{B_j}{(1-\zeta^2)^j}. \quad (13)$$

Substituting (13) into (12), we arrive at the expression for (12) in the form

$$\int_0^\infty \left\{ \sum_i \frac{A_i}{(\zeta^2)^i} + \sum_j \frac{B_j}{(1-\zeta^2)^j} \right\} \ln\left|\frac{1+\zeta}{1-\zeta}\right| d\zeta^2,$$

where A_i and B_j are certain constants. Now, integrating all the terms of the above expression, we can express them via elementary functions by integrating them by parts, except for

$$\int_0^\infty \ln\left|\frac{1+\zeta}{1-\zeta}\right| \frac{d\zeta^2}{\zeta^2} \text{ and } \int_0^\infty \ln\left|\frac{1+\zeta}{1-\zeta}\right| \frac{d\zeta^2}{(1-\zeta^2)}. \quad (14)$$

The first of these integrals is equal to [10]

$$\int_0^\infty \ln\left|\frac{1+\zeta}{1-\zeta}\right| \frac{d\zeta^2}{\zeta^2} = 2\int_0^\infty \ln\left|\frac{1+\zeta}{1-\zeta}\right| \frac{d\zeta}{\zeta} = 4\int_0^1 \ln\left|\frac{1+\zeta}{1-\zeta}\right| \frac{d\zeta}{\zeta} = \pi^2.$$

Using the substitution $x = \zeta^{-1}$, we can reduce the second of these integrals (14) to the first one. In practice, integrals (10) have the form

$$\frac{1}{\zeta^{2(m-1)}} \left\{ P_{m-2}(\zeta^2) + P_{m-1}(\zeta^2) \frac{1}{\zeta} \ln\left|\frac{1+\zeta}{1-\zeta}\right| \right\},$$

where $P_k(\cdot)$ are certain polynomials of degree k. Therefore, the convolution $r^{-(n-1)} * r^{-(n-1)}$ in the space of an odd dimension can be calculated in terms of elementary functions. Thus, in the spaces of odd dimensions, the solution of the problem of inverse X-ray transform by the method of back projection and summation has the form

$$f(\mathbf{r}) = \frac{\Delta\left(\Sigma(\mathbf{r}) * \frac{1}{r^{n-1}}\right)}{2^{n-2}(n-2)\Omega_n\Omega_{n-1}\int_0^\infty\int_0^\infty \frac{t^{m-1}dt}{(((\zeta-1)^2+t)((\zeta+1)^2+t))^m} d\zeta}, \quad (15)$$

where $\Sigma(\mathbf{r})$ is the spatial synthesis of the projections. The values of the double integral entering (15) for m = 2–5 are equal to $\pi^2/32$, $3\pi^2/512$, $5\pi^2/4096$, and $35\pi^2/131072$ (calculated by the MATH KERNEL 3.0 package of programs). The inversion of the X-ray transform by formula (15) for the spaces of dimensions 5, 7,

9, and 11 yields

$$f(\mathbf{r}) = -\frac{1}{4\pi^6}\Delta\left(\Sigma(\mathbf{r}) * \frac{1}{r^4}\right), \quad n = 5,$$

$$f(\mathbf{r}) = -\frac{1}{\pi^8}\Delta\left(\Sigma(\mathbf{r}) * \frac{1}{r^6}\right), \quad n = 7,$$

$$f(\mathbf{r}) = -\frac{9}{\pi^{10}}\Delta\left(\Sigma(\mathbf{r}) * \frac{1}{r^8}\right), \quad n = 9,$$

$$f(\mathbf{r}) = -\frac{144}{\pi^{12}}\Delta\left(\Sigma(\mathbf{r}) * \frac{1}{r^{10}}\right), \quad n = 11.$$

The above relationships can be written in the operator form as

$$\Delta \cdot \Sigma \cdot \Sigma = \Delta \cdot \Sigma^2 = \text{const}I, \tag{16}$$

where I is the identity operator and Σ is the operator of the back projecting and summation. Formula (16) provides the study of the eigenfunctions of the spatial synthesis of projections in terms of the eigenfunctions of the Laplace operator, which are well studied, at least for the three-dimensional space.

REFERENCES

1. B. K. Vaĭnshteĭn and A. M. Mikhaĭlov, Kristallografiya **17** (2), 258 (1972) [Sov. Phys. Crystallogr. **17** (2), 217 (1972)].
2. D. C. Solmon, J. Math. Anal. Appl. **56**, 61 (1976).
3. F. Natterer, *The Mathematics of Computerized Tomography* (Wiley, New York, 1986; Mir, Moscow, 1990).
4. V. V. Pikalov and N. G. Preobrazhenskiĭ, *Reconstructive Tomography in Gas Dynamics and Plasma Physics* (Nauka, Novosibirsk, 1987).
5. G. G. Levin and G. N. Vishnyakov, *Optic Tomography* (Radio i Svyaz', Moscow, 1987).
6. M. Defrise, R. Clack, and D. Townsend, J. Opt. Soc. Am. A **10**, 869 (1993).
7. Ya. A. Ilyushin, Kristallografiya **42** (2), 364 (1997) [Crystallogr. Rep. **42** (2), 323 (1997)].
8. E. Bocage, French Patent No. 536, 464 (Paris, France, 1921).
9. I. M. Gel'fand and G. E. Shilov, *Generalized Functions* (Fizmatgiz, Moscow, 1958).
10. I. S. Gradshteyn and I. M. Ryzhik, *Tables of Integrals, Series, and Products* (Nauka, Moscow, 1971; Academic, New York, 1980).

Translated by L. Man

Crystallography Reports, Vol. 45, No. 5, 2000, pp. 718–720. Translated from Kristallografiya, Vol. 45, No. 5, 2000, pp. 788–790.

STRUCTURES OF INORGANIC COMPOUNDS

X-ray Diffraction Study of $Ca_{0.88}Gd_{0.12}F_{2.12}$ Single Crystals with a Modified Fluorite Structure

N. B. Grigor'eva, B. A. Maksimov, and B. P. Sobolev

Shubnikov Institute of Crystallography, Russian Academy of Sciences, Leninskiĭ pr. 59, Moscow, 117333 Russia

Received December 28, 1998

Abstract—The characteristic structural features of a single crystal of the anion-excessive fluorite phase $Ca_{0.88}Gd_{0.12}F_{2.12}$ have been studied by X-ray diffraction analysis (MoK_α radiation), sp. gr. *Fm*3*m*, $Z = 4$, $a = 5.5000(4)$ Å. The structure was refined in the anharmonic approximation of thermal atomic vibrations to $R_w = 0.0047$. A total of 78 independent structure amplitudes were measured; 14 parameters were refined; $\sin\theta/\lambda \le 1.13$ Å^{-1}. In the structure under study, the replacement of the divalent Ca^{2+} cations by the trivalent Gd^{3+} cations in the position 4*a* (0, 0, 0) resulted in the statistical distribution of the fluorine atoms over three positions of the sp. gr. *Fm*3*m*. Thus, the fluorine atoms occupy the position 8*c* (1/4, 1/4, 1/4), the main position in the fluorite structure type, and the position 32*f* (*v*, *v*, *v*) with $v = 0.417(1)$ on threefold symmetry axes. In addition, some fluorine atoms are shifted from the main 8*c* position along the threefold symmetry axis to the position 32*f* (*w*, *w*, *w*) with $w = 0.313(2)$. © *2000 MAIK "Nauka/Interperiodica".*

This work continues the studies of anion-excessive fluorite phases $Ca_{1-x}R_xF_{2+x}$, where R^{3+} are rare-earth (RE) elements from La to Lu and Y [1–3]. Interest in the crystal structures of the nonstoichiometric phases stems from the fact that the change of the type of the introduced R^{3+} cation usually changes the type of structural defects in the fluorite CaF_2 crystal structure [4]. The crystallochemical scheme of these changes and the main types of structural defects caused by the introduction of the R^{3+} cations and additional fluoride anions into the matrix of fluorite were described in [5].

In this work, the results of the structure determination of the $Ca_{0.88}Gd_{0.12}F_{2.12}$ solid solution are discussed. The structure of a single crystal of this composition was studied for the first time. The ratio between the ionic radii of the trivalent and divalent cations in the crystal under study is 0.98 and lies in the range $0.9 < r(Cd^{3+}): r(Ca^{2+}) < 1.02$. According to [5], this value gives grounds to expect that the fluorine atoms occupy two additional positions on two- and threefold symmetry axes in the vicinity of the centers of the cubic cavities in the fluorite structure. The high concentration of the introduced rare-earth Gd^{3+} cations (12 mol %) made it possible to determine the positions of interstitial fluorine atoms and the occupancies of the additional positions in the $Ca_{1-x}Gd_xF_{2+x}$ solid solution.

Single crystals were grown by the Stockbarger technique in graphite crucibles under conditions, which virtually excluded the compensation of an excessive charge of Gd^{3+} by oxygen (at the Shubnikov Institute of Crystallography of the Russian Academy of Sciences). The nominal composition (based on the charge) corresponds to the formula $Ca_{0.88}Gd_{0.12}F_{2.12}$ [6].

X-ray diffraction data were collected from a single-crystalline spherical sample 0.35(1) mm in diameter on a four-circle automated CAD-4 diffractometer (λMoK_α radiation; $\lambda = 0.7107$ Å; graphite monochromator, $\omega/2\theta$ scanning technique) at room temperature. Diffraction patterns showed no deviations from the symmetry of the fluorite structure (sp. gr. *Fm*3*m*). A total of 2104 reflections with $I_{hkl} > 3\sigma(I_{hkl})$ were measured within the complete sphere of the reciprocal space ($\sin\theta/\lambda \le 1.13$ Å^{-1}). The cubic unit-cell parameter a is 5.5000(4) Å. Upon averaging, the set consisted of 78 independent reflections (the R_{int} factor for equivalent reflections $|F_{hkl}|$ was 0.0149).

The intensities were converted to the moduli of structure amplitudes with due regard for the Lorentz and polarization factors. A correction for absorption by the spherical sample was applied. For this composition, the absorption coefficient μ for MoK_α radiation was 76.94 cm^{-1} [7].

The structure was refined by the full-matrix least-squares method with the use of the fourth-order Gram–Charlier expansion into series for the anharmonicity of thermal atomic vibrations with allowance for a correction for isotropic extinction (the Becker–Coppens approximation, type 1, the Lorentz distribution). All the computations were carried out using the PROMETHEUS program package [8]. The structure of the solid solution under study was refined with the use of the scattering curves for ions with due regard for dispersion corrections [7].

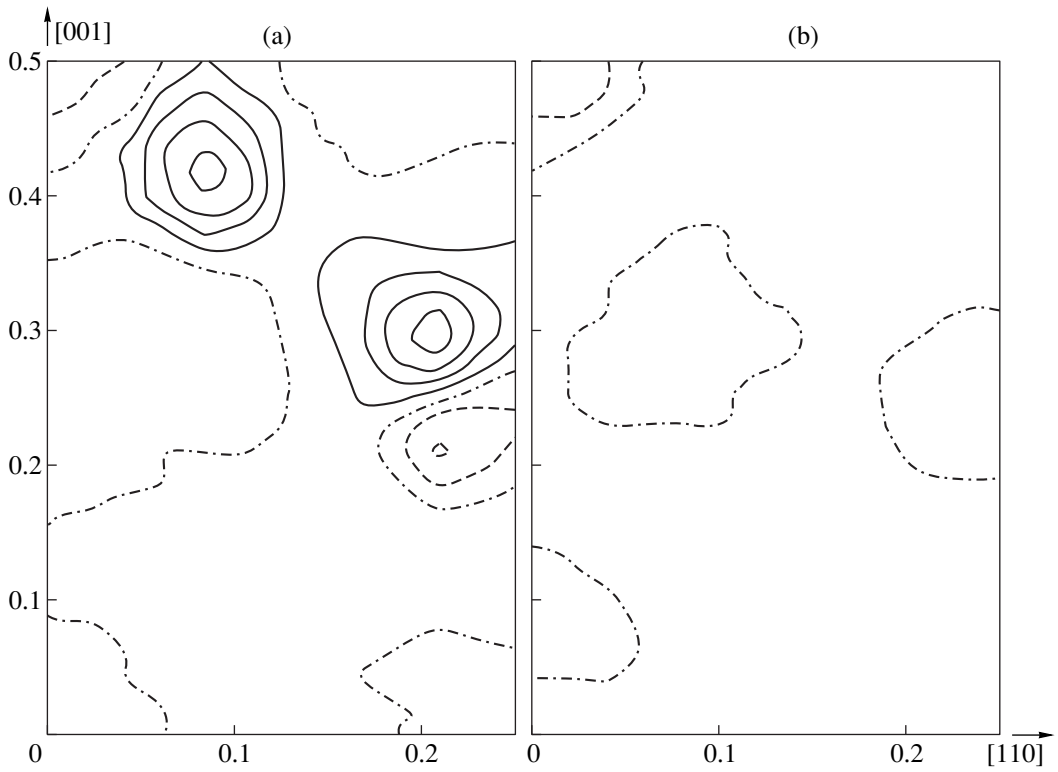

Difference electron density maps in the plane $x - y = 0$ calculated (a) after the refinement of model **Ia** and (b) after the refinement of model **IIa**. The positive and negative contours are shown by solid and dashed lines, respectively; the zero contour is shown as a dash-and-dot line. The maps are contoured at intervals of 0.1 e/A^3. The network of coordinates is given in fractions of the parameters unit-cell.

At the initial stage of the structure refinement, the following characteristics were determined: the coefficient of reduction of $|F_{hkl}|$ to the absolute scale, the isotropic extinction parameter, and the isotropic thermal parameters of the cations and fluoride anions located in the main position of the fluorite crystal structure, namely, in 8*c* (1/4, 1/4, 1/4). To decrease the correlation, the preliminary refinement of the extinction parameter and the occupancies of the ionic positions was performed with the use of reflections in the near (low-order) region of the reciprocal space up to $\sin\theta/\lambda < 0.7$ Å^{-1}.

The thermal parameters of the ions were refined on the reflections in the far region of the reciprocal space ($\sin\theta/\lambda > 0.5$ Å^{-1}). The coefficient of reduction to the absolute scale was refined based on a total number of reflections. In the course of the refinement, the errors of all the parameters were monitored and three-dimensional difference electron density maps were analyzed.

The results of the refinement of model **I** (with the cations located in the position 4*a* (0, 0, 0) and the fluoride anions, in the main position of the fluorite structure—8*c* (1/4, 1/4, 1/4); isotropic thermal atomic vibrations) are given in the table. It was established that the main position occupied by the fluorine atoms had vacancies; the occupancy of the position q_{F_0} is 1.876(8) (hereinafter, the occupancies are given per formula unit).

To determine the positions of additional fluorine atoms, the subsequent refinement of this model was performed in the anharmonic approximation of thermal vibrations of the cations using the fourth-order Gram–Charlier expansion into series. The results the refinement of this model (**Ia**) are listed in the table.

For the structure under consideration, the most informative section of the difference electron-density map is that lying in the plane $x - y = 0$. The difference electron-density map for model **Ia** is shown in the figure. The character of the electron density distribution shows that the fluorine atoms are located on threefold symmetry axes in the vicinity of the cubic cavities in the fluorite structure (the F" position) and that some fluorine atoms are shifted from the main position 8*c* along the threefold symmetry axes toward the centers of the cubic cavities and occupy the so-called relaxed positions F'''. The coordinates of these additional fluorine positions were revealed from the difference electron-density map: F" – 32*f* (*v*, *v*, *v*) with $v = 0.42$ and F''' – 32*f* (*w*, *w*, *w*) with $w = 0.30$ for F" and F''', respectively.

At the following stage, the structural parameters of $Ca_{0.88}Gd_{0.12}F_{2.12}$ were refined within the framework of model **IIa** containing fluorine atoms in the positions F"

Results of the structure refinement of different models of $Ca_{0.88}Gd_{0.12}F_{2.12}$

Parameters of the refinement; *R* factors	Model		
	I	**Ia**	**IIa**
R_w	0.0140	0.0129	0.0047
R	0.0112	0.0105	0.0044
Ca, Gd:			
B_{iso}, Å^2	0.712(2)	–	–
B_{11}, Å^2		0.00638(1)	0.00626(1)
D^*_{1111}, Å^2		0.00055(3)	0.00053(1)
D^*_{1122}, Å^2		0.00014(1)	0.000143(6)
F_0: q	1.876(8)	1.860(7)	1.841(3)
B_{iso}, Å^2	1.005(8)	1.014(8)	–
B_{11}, Å^2			0.00817(2)
C^{**}_{123}, Å^2			0.0015(1)
F": q			0.140(7)
v			0.417(1)
B_{iso}, Å^2			1.6(1)
F"': q			0.139(6)
w			0.313(2)
B_{iso}, Å^2			2.8(3)
Sum of q_F	1.876	1.860	2.12

* Coefficients are multiplied by 10^4.
** Coefficients are multiplied by 10^3.

and F"'. The refinement was carried out in the anharmonic approximation of thermal vibrations of cations (the fourth-order Gram–Charlier expansion into series) and the fluorine atoms in the main position 8*c* (the third-order Gram–Charlier expansion into series). The thermal vibrations of the fluorine atoms in the positions F" and F"' were refined isotropically. At the initial stage of the refinement within the framework of model **IIa**, the distribution of the fluorine atoms over positions was revealed using step-by-step scanning of their occupancies. Once the reliable occupancies of all positions of the fluorine atoms have been determined, we proceeded to the final stage of the refinement, where their positional parameters were refined in the same way as other structural parameters. A total of 11 parameters were refined based on 78 independent structure amplitudes.

The refinement of model **IIa** was performed to the reliability factors $R_w = 0.0047$ and $R = 0.0044$ (table). The difference electron density synthesis calculated at the final stage of the refinement is shown in the figure. The total occupancy of all the fluorine positions is 2.12, which corresponds to the condition of electricneutrality of the unit cell. The difference electron density maps, the standard deviations of the parameters refined, and the *R* factors confirm the validity of the chosen model.

The X-ray structure study of a single crystal of the $Ca_{0.88}Gd_{0.12}F_{2.12}$ ($r(Gd^{3+}) : r(Ca^{2+}) = 0.98$) solid solution demonstrated that the replacement of some divalent Ca^{2+} by trivalent Gd^{3+} cations in the position 4*a* of the sp. gr. *Fm*3*m* leads to the following changes in the anionic sublattice of the crystal. (1) Formation of vacancies in the main fluorine position 8*c*; (2) location of interstitial fluorine atoms mainly in the position 32*f* (v, v, v) with $v = 0.420(3)$ on threefold symmetry axes; (3) location of some fluorine atoms in the vicinity of the so-called relaxed position 32*f* (w, w, w) with $w = 0.315(2)$. The assumption on possible location of a number of fluorine atoms on twofold symmetry axes has not been confirmed.

ACKNOWLEDGMENTS

We thank A.A. Bystrova for preparing samples for X-ray study. This work was supported by the Russian Foundation for Basic Research, project no. 96-03-32250.

REFERENCES

1. V. B. Aleksandrov and L. S. Garashina, Dokl. Akad. Nauk SSSR **189**, 307 (1969) [Sov. Phys. Dokl. **14**, 1040 (1970)].
2. N. B. Grigor'eva, L. P. Otroshchenko, B. A. Maksimov, *et al.*, Kristallografiya **41** (1), 60 (1996) [Crystallogr. Rep. **41** (1), 45 (1996)].
3. N. B. Grigor'eva, L. P. Otroshchenko, B. A. Maksimov, *et al.*, Kristallografiya **41** (4), 644 (1996) [Crystallogr. Rep. **41** (4), 607 (1996)].
4. L. H. Ahrens, Geochim. Cosmochim. Acta **2** (3), 155 (1952).
5. B. A. Maksimov, L. A. Muradyan, and V. I. Simonov, in *Crystallography and Crystal Chemistry* (Nauka, Moscow, 1986), p. 215.
6. *Multicomponent Crystals Based on Heavy-Metal Fluorides for Radiation Detector*, Ed. by B. P. Sobolev (Inst. d'Estudis Catalans, Barselona, 1994).
7. *International Table for Crystallography*, Ed. by T. Hahn (Kluwer, Dordrecht, 1992).
8. U. H. Zucker, E. Perenthaler, W. F. Kuhs, *et al.*, J. Appl. Crystallogr. **16**, 358 (1983).

Translated by T. Safonova

Crystallography Reports, Vol. 45, No. 5, 2000, pp. 721–722. Translated from Kristallografiya, Vol. 45, No. 5, 2000, pp. 791–792.

STRUCTURES OF INORGANIC COMPOUNDS

Growth of $Er_2(SO_4)_3 \cdot 8H_2O$ Crystals and Study of Their Structure and Properties

L. V. Soboleva*, A. Pietraszko, L. F. Kirpichnikova*, and L. A. Shuvalov***

** Shubnikov Institute of Crystallography, Russian Academy of Sciences, Leninskiĭ pr. 59, Moscow, 117333 Russia*

*** Institute of Low Temperatures and Structure Research, Polish Academy of Sciences, Ocolna 2, Wroclaw, 50-950 Poland*

Received May 31, 1999

Abstract—New crystals of the composition $Er_2(SO_4)_3 \cdot 8H_2O$ have been synthesized by the method similar to that used for synthesis of $(CH_3)_2NH_2Al(SO_4)_2 \cdot 6H_2O$. The synthesized crystals were studied by the X-ray diffraction method. The crystals are monoclinic ($C2/c$) and contain no $(CH_3)_2NH_2$ ions. It is established that, contrary to DMAAS crystals, $Er_2(SO_4)_3 \cdot 8H_2O$ crystals undergo no phase transitions and possess neither ferroelectric nor ferroelastic properties. © *2000 MAIK "Nauka/Interperiodica".*

The discovery of ferroelectric and ferroelastic properties in $(CH_3)_2NH_2Al(SO_4)_2 \cdot 6H_2O$ (DMAAS) crystals [1] gave an impetus to growth and study other crystals of this family. DMAAS crystals, being the first representative of a new family of ferroics, possess the structure that can be considered as a new structure type among the large family of double phosphate crystal hydrates [2, 3]. In the present study, we made an attempt to substitute aluminium by a trivalent RE metal—erbium.

We assumed that dimethylammonium erbium sulfate crystals can be synthesized by the method similar to that used in the synthesis of DMAAS, i.e., grown by the chemical reaction between dimethylamine and erbium sulfate dissolved in the stoichiometric ratio in 30% sulfuric acid aqueous solution. The mother solution was prepared from dimethylamine (33%), $Er_2(SO_4)_3 \cdot 6H_2O$ obtained by dehydration of water-insoluble $Er_2(SO_4)_3$, and 30% H_2SO_4 solution (d = 1.22 g/cm^3). First, we dissolved $Er_2(SO_4)_3$ in water under constant stirring, then added sulfuric acid and heated the solution up to 55°C, and finally, added dimethylamine. The solution prepared was filtered and cooled from 45 to 23°C. As a result of spontaneous crystallization, transparent pink crystals were obtained.

The structural studies were performed on 0.22 × 0.22 × 0.23 mm-large samples on an automatic KUMA-KM4 diffractometer (MoK_α radiation, graphite monochromator, 9661 reflections with $I > 4\sigma(I)$). The calculations were performed by the SHELXTL program to the reliability factor R = 0.0155.

Dielectric measurements were performed by the low-frequency bridge method on samples oriented normally to the twofold axis and the [101]-direction, i.e., close to the P_S direction in DMAAS crystals. The polarization-optical measurements were made with the use of a VTO-232 M videosystem, the differential scanning calorimetry (DSC) measurements were made on a Netsch DSC-200 apparatus.

The X-ray diffraction studies showed that the crystals grown could be described by the chemical formula $Er_2(SO_4)_3 \cdot 8H_2O$, which was also confirmed by the chemical analysis. The monoclinic crystals belong to sp. gr. $C2/c$. The unit-cell parameters determined at 300 K are: a = 13.438(3); b = 6.6660(10); and c = 18.203(4) Å; β = 101.90°; V = 1595.5(6) Å^3; Z = 4. The X-ray density equals 3.192 g/cm^3; the density measured by the pycnometric method is 3.016 g/cm^3. The

Atomic coordinates and the parameters of atomic thermal vibrations (B_{eq}) in $Er_2(SO_4)_3 \cdot 8H_2O$ crystals

Atom	x	y	z	U_{eq}
Er(1)	3339(1)	4798(1)	1079(1)	9(1)
O(1)	1583(1)	5164(1)	450(1)	16(1)
O(2)	4594(1)	2691(1)	641(1)	16(1)
O(3)	4837(1)	6633(2)	1391(1)	29(1)
O(4)	2444(1)	5146(2)	2019(1)	25(1)
S(1)	5000	1805(1)	2500	10(1)
O(5)	5348(1)	540(2)	1932(1)	17(1)
O(6)	4155(1)	3074(2)	2122(1)	22(1)
S(2)	2804(1)	5263(1)	9108(1)	9(1)
O(7)	3508(1)	5720(1)	–162(1)	15(1)
O(8)	2623(1)	1726(1)	828(1)	19(1)
O(9)	3022(1)	8246(1)	1022(1)	15(1)
O(10)	3375(1)	5346(2)	8510(1)	19(1)

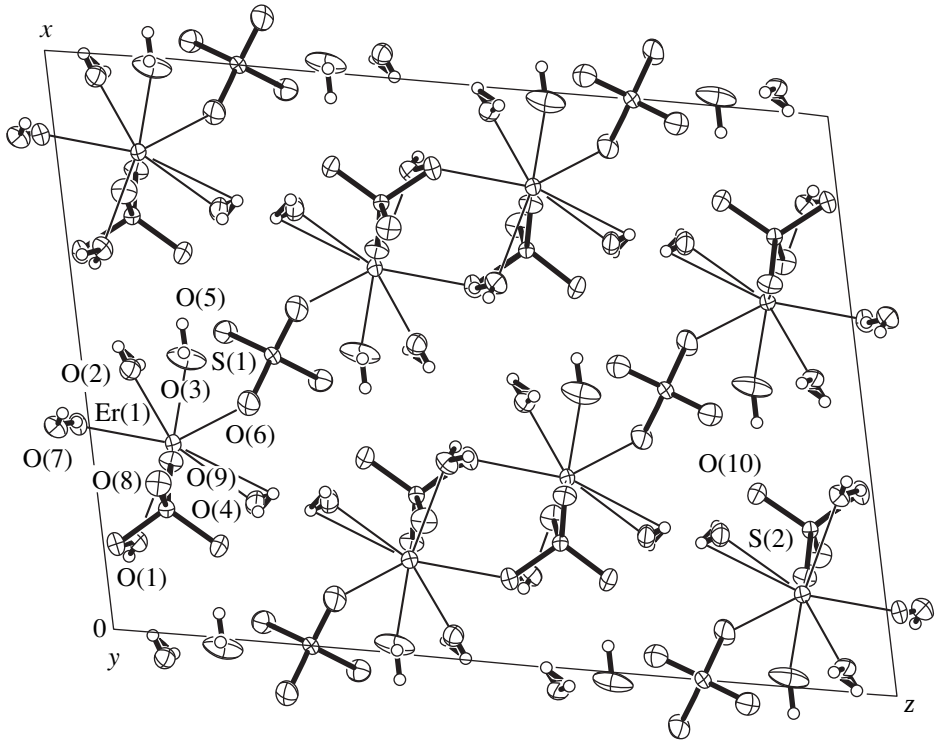

$Er_2(SO_4)_3 \cdot 8H_2O$ structure projected onto the (101) plane.

atomic coordinates and the parameters of atomic thermal vibrations are listed in table.

The crystal structure of the synthesized crystals (see figure) reminds us of the DMAAS structure, but with the positions which are occupied by the $(CH_3)_2NH_2$ ions in the DMAAS structure being filled with water molecules, which completely excludes the presence of dimethylammonium ions in the $Er_2(SO_4)_3 \cdot 8H_2O$ structure.

The dielectric, optic, and DSC measurements of the crystals grown in the temperature range from 190°C to the melting point showed that they undergo no phase transitions and have neither ferroelectric nor ferroelastic properties which indirectly confirmed the assumption about the crucial part played by dimethylammonium ions in appearance of ferroelectricity in DMAAS crystals.

ACKNOWLEDGMENTS

This study was supported by the Russian Foundation for basic Research, project no. 97-02-16372a.

REFERENCES

1. L. F. Kirpichnikova, L. A. Shuvalov, N. R. Ivanov, *et al.*, Ferroelectrics **96**, 313 (1989).
2. L. F. Kirpichnikova, G. A. Kiosse, B. Hilczer, *et al.*, Kristallografiya **42** (6), 1076 (1997) [Crystallogr. Rep. **42**, 1000 (1997)].
3. V. M. Petruševski, Acta Crystallogr., Sect. B: Struct. Sci. **50**, 625 (1994).

Translated by L. Man

Crystallography Reports, Vol. 45, No. 5, 2000, pp. 723–727. Translated from Kristallografiya, Vol. 45, No. 5, 2000, pp. 793–797.

STRUCTURES OF INORGANIC COMPOUNDS

Crystal Structure of Urusovite $Cu[AlAsO_5]$: a New Type of a Tetrahedral Aluminoarsenate Polyanion

S. V. Krivovichev, A. V. Molchanov, and S. K. Filatov

St. Petersburg State University, Universitetskaya nab. 7/9, St. Petersburg, 199034 Russia

e-mail: filatov@mail.ru

Received June 15, 1999

Abstract—The crystal structure of the new mineral urusovite $Cu[AlAsO_5]$ has been determined (monoclinic system, sp. gr. $P2_1/c$, $a = 7.335(1)$ Å, $b = 10.255(1)$ Å, $c = 5.599(1)$ Å, $\beta = 99.79(1)°$, $V = 415.0(1)$ Å^3, $Z = 4$). The structure is solved by direct methods and refined to $R = 0.048$ ($wR = 0.103$). The structure is built by open-branched $\{uB, {}^{2}_{\infty}\}[AlAsO_5]^{2-}$ layers parallel to the (100) plane. The layers consist of two-link chains of ${}^{1}_{\infty}[Al_2O_6]$ tetrahedra, which are parallel to the *z*-axis and are connected through the $[AsO_4]$-groups. The sharing-edges $[CuO_5]$ tetragonal pyramids link the aluminoarsenate layers to form a three-dimensional framework. The established layer is the second example of an tetrahedral aluminoarsenate polyanion. © *2000 MAIK "Nauka/Interperiodica".*

INTRODUCTION

Polyanions consisting of various tetrahedra belong to one of the most abundant types of mixed anionic radicals [1]. However, aluminoarsenate structures formed by condensation of the $[Al^{+3}O_4]$ and $[As^{+5}O_4]$-tetrahedra are very rarely observed in compounds of this type. The well-known and, apparently, the only representative of this group is the exhalative mineral alarsite $AlAsO_4$ [2], recently discovered in fumaroles of the Bol'shoi Tolbachinskiĭ fissure eruption (BTFE, the Kamchatka peninsula). Alarsite belongs to the structural-type of berlinite, $AlPO_4$. This mineral is a close analogue of quartz and has a framework structure built by vertex-sharing $[Al^{+3}O_4]$ and $[As^{+5}O_4]$ tetrahedra [3–5]. In this work, we report the results of the crystal structure determination of the new mineral urusovite $Cu[AlAsO_5]$ discovered in fumaroles of BTFE and named after the well-known scientist working in the field of crystal chemistry, Corresponding Member of the Russian Academy of Sciences V.S. Urusov. (Urusovite was recognized as a new mineral type by the Commission on New Minerals and Mineral Names of the International Mineralogical Association on March 5, 1999).

EXPERIMENTAL

Urusovite crystals, $Cu[AlAsO_5]$, chosen for our study were elongated transparent pale-green plates with vitreous luster. X-ray study by the Laue and Weissenberg methods showed that the crystals are monoclinic, the sp. gr. $P2_1/c$. The detailed description of data collection and the results of determination of the unit-cell parameters and structure refinement are given in Table 1.

The structure was solved by direct methods. The positions of the copper and arsenic atoms were determined. The remaining atoms were located using successive approximations of difference Fourier syntheses. The initial processing of X-ray intensities and the choice of the structural model were performed using the AREN program package [6]. The structure was refined by the least-squares method to the *R* factor of 0.048 ($wR = 0.103$) by the SHELXL93 program package [7]. The absorption corrections were introduced using the DIFABS program [8].

The atomic coordinates and thermal parameters are listed in Table 2. The local valence balance calculated by the method suggested by Brown [9, 10] (the bond valences were calculated with the use of parameters taken from [10]) is given in Table 3.

RESULTS AND DISCUSSION

All atoms in the crystal structure of urusovite $Cu[AlAsO_5]$ occupy the general positions. The calculation of the local valence balance (Table 3) demonstrated that the sum of the valence bond stresses at each atom is equal (within the admissible error) to the formal valences corresponding to the chemical formula of the compound.

One crystallographically independent copper atom is coordinated by five oxygen atoms, forming a tetragonal pyramid. Four oxygen atoms located in the base of the pyramid are at distances of 1.960–1.975 Å from the copped atom, whereas the oxygen atom occupying the

1063-7745/00/4505-0723$20.00 © 2000 MAIK "Nauka/Interperiodica"

Table 1. Crystallochemical characteristics of urusovite and the details of X-ray data collection and structure refinement

Chemical formula	$Cu[AlAsO_5]$
System	Monoclinic
Sp. gr., Z	$P2_1/c$, 4
Unit-cell parameters	a = 7.335(1) Å
	b = 10.255(1) Å
	c = 5.599(1) Å
	β = 99.79(1)°
	V = 415.0(1) Å
d_{calc}, g/cm^3	3.93
Radiation	MoK_α(λ = 0.71069 Å)
Diffractometer, scanning mode	Syntex $P2_1$; ω–2θ
Number of independent reflections	1333
Number of observed reflections	1134 [$I > 2\sigma(I)$]
Ranges of indices	$-13 \le h \le 12$; $0 \le k \le 18$; $0 \le l \le 10$
$2\theta_{min}$–$2\theta_{max}$	2.8–40.0
μ, mm^{-1}	13.292
$R(F)$	0.048
$wR(F)$	0.103
S	0.977
Weighting scheme	$w = 1/[\sigma^2(F_0^2) + (0.0606P)^2]$, where $P = (F_0^2 + 2F_c^2)/3$
$\delta\rho_{min}$, $\delta\rho_{max}$	$-1.305 \le \delta\rho \le 1.417$ eÅ^3

Table 2. Atomic coordinates and thermal parameters (Å^2) in the crystal structure of urusovite

Atom	x	y	z	U_{eq}^*	Atom	x	y	z	U_{eq}^*
Cu	0.4618(1)	0.14033(8)	0.9095(1)	0.0102(2)	O(2)	0.9041(7)	0.1996(5)	0.3745(8)	0.0123(9)
Al	0.1455(3)	0.1770(2)	0.4355(4)	0.0080(4)	O(3)	0.5707(7)	0.1946(5)	0.5470(9)	0.0110(9)
As	0.7257(1)	0.10839(6)	0.4261(1)	0.0082(1)	O(4)	0.2354(7)	0.2223(5)	0.7328(8)	0.0101(9)
O(1)	0.6231(8)	0.0407(4)	0.1596(8)	0.013(1)	O(5)	0.1984(8)	0.0136(5)	0.3844(9)	0.013(1)

* $U_{eq} = (1/3)\Sigma_i\Sigma_j U_{ij} a_i^* a_j^* a_i a_j$.

Table 3. Local valence balance in the crystal structure of urusovite according to [9, 10]

	O(1)		O(2)	O(3)		O(4)		O(5)	Σ
Cu	0.47	0.45		0.45	0.15	0.45			1.97
Al			0.74			0.78	0.77	0.75	3.04
As	1.19		1.29	1.30				1.29	5.07
Σ	2.11		2.03	1.90		2.00		2.04	

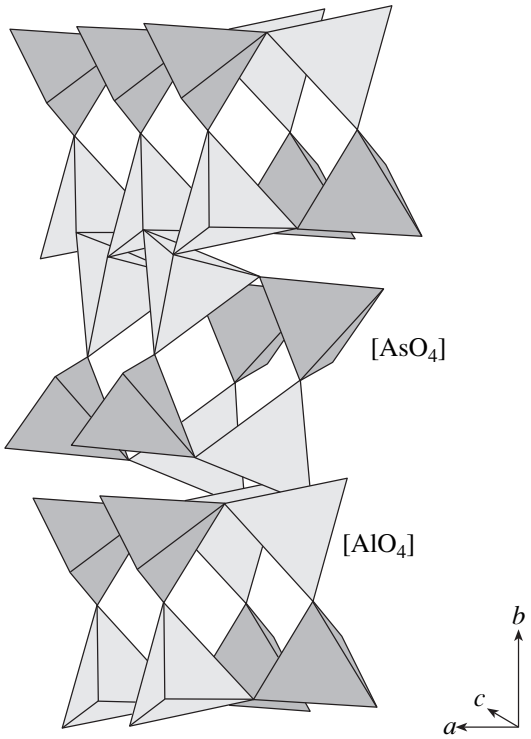

Fig. 1. Open-branched $\{uB^2_\infty\}$ $[AlAsO_5]^{2-}$ layer of tetrahedra in the urusovite structure (side view).

vertex is located at a distance of 2.370 Å. This coordination of the copper atom is typical of oxygen compounds [11, 12].

The coordination polyhedra of the aluminum and arsenic atoms are tetrahedra formed by oxygen atoms with the following average bond lengths and bond angles: Al–O, 1.751 Å; O–Al–O 109.5°; As–O 1.679 Å; and O–As–O 109.4°.

The crystal structure of urusovite consists of the $^2_\infty[AlAsO_5]^{2-}$ tetrahedral layers parallel to the (100) plane (Fig. 1). The layers are built by two-link tetrahedral $^1_\infty[Al_2O_6]$ chains parallel the *z*-axis and linked to the $[AsO_4]$ groups through the bridging O(2) and O(5) vertices. Two oxygen atoms (O(1) and O(3)) of the arsenate groups are terminal. In the $^1_\infty[Al_2O_6]$ chains, the $[AlO_4]$-tetrahedra are linked together via the O(4) atoms. Within the framework of the silicate classification developed by Liebau [13], the mixed aluminoarsenate tetrahedral layer thus formed can be described as an open-branched layer. The major structural unit of this layer is a two-membered aluminate chain branching because of attachment of arsenate "branches." A similar structure of the aluminosilicate layer $^2_\infty[Si_3AlO_{10}]$ was also observed in prehnite [14, 15]. This layer consists of two-link aluminosilicate

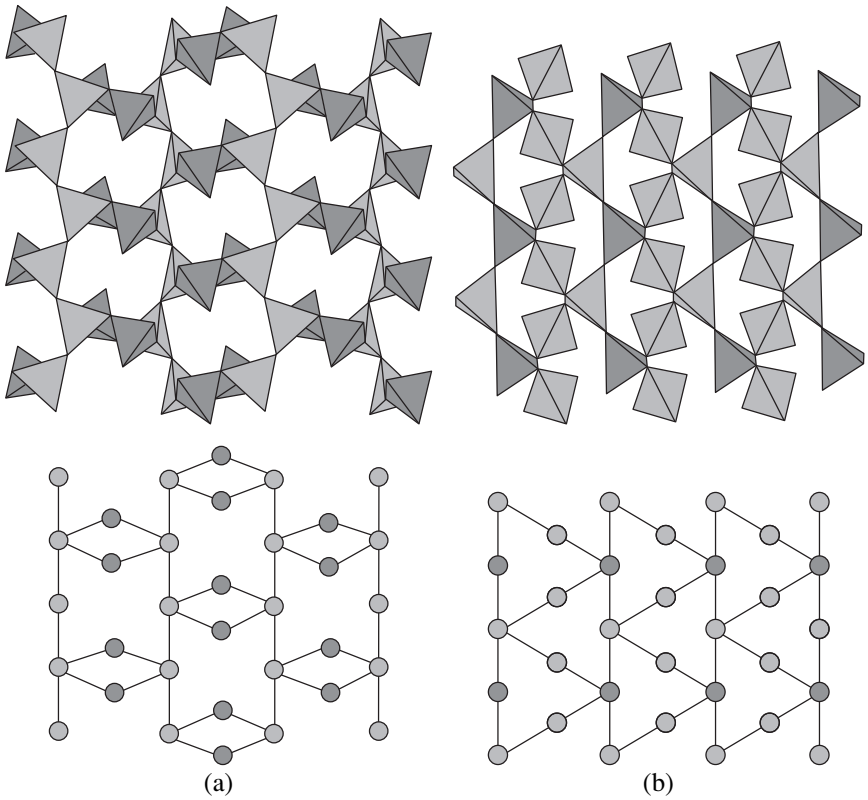

Fig. 2. Structure of the open-branched $\{uB^2_\infty\}$ $[AlAsO_5]^{2-}$ layers of tetrahedra in (a) urusovite and (b) prehnite and the corresponding topological diagrams (tetrahedra are indicated by circles).

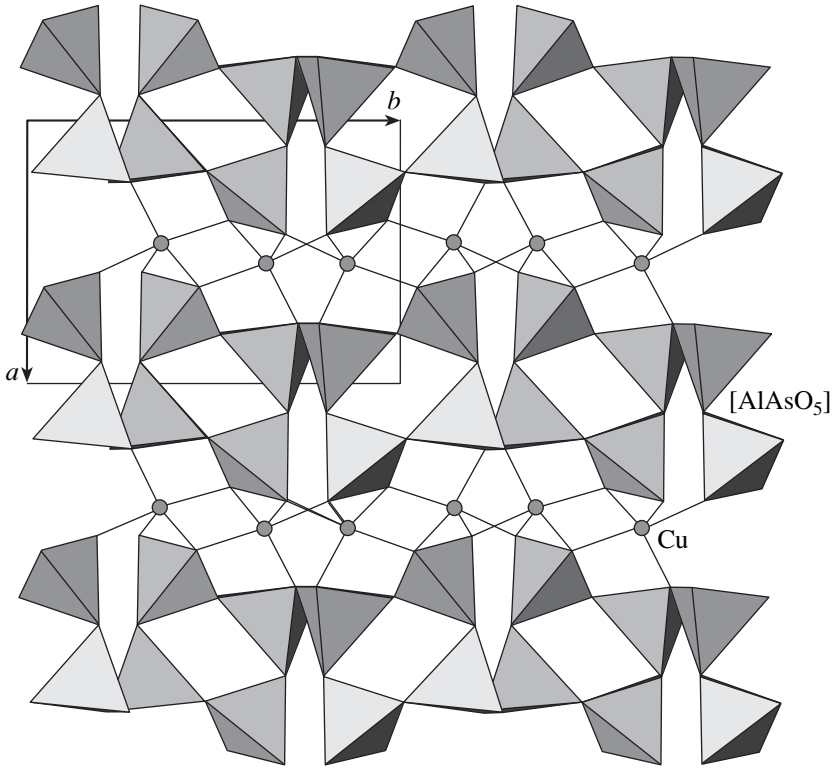

Fig. 3. Crystal structure of urusovite projected onto the *xy* plane.

chains connected via single [SiO_4]-tetrahedra playing the role of "branches." However, the topology of the structure of the layered polyanion in prehnite is essentially different from that of the mineral under study. The structures of the layers of the minearls under consideration and their topological diagrams are shown in Fig. 2. The aluminosilicate layer in prehnite can be represented as a layer consisting of six-membered rings, whereas the aluminoarsenate layer in urusovite consists of four- and eight-membered rings. In the latter case, the four-membered rings are not directly linked to each other, i.e., they share no tetrahedra. No analogous tetrahedral layers were revealed in the known crystal structures, which indicates that we observed a new type of tetrahedral layers in the mineral under consideration.

As is seen from Table 3, the bridging O(2) and O(5) atoms, "connecting" the aluminate and arsenate tetrahedra, are completely valence-saturated, whereas the O(1), O(3), and O(4) coordinated with the copper atoms are not. The tetragonal [CuO_5]-pyramids are linked in pairs by shared O(1)–O(1) edges (Fig. 3). These pairs are responsible for linking of aluminoarsenate layers into a three-dimensional structure. The O(1)–Cu–O(1) bond angle resting on the shared O(1)–O(1) edge is shortened to 77.4°.

As was mentioned above, the crystal structure of urusovite is the second example of the tetrahedral polyanion formed by condensation of the [AsO_4] and [AlO_4] tetrahedra. Note that the change of trivalent aluminum by a divalent cation results a substantially wider variety of mixed anions. As an example, we refer to a series of compounds with the [ZnO_4]- and [AsO_4]-tetrahedra, which are linked by bridging vertices into layered and framework structures [16–20].

ACKNOWLEDGMENTS

We are grateful to L. P. Vergasova for providing a single crystal for X-ray diffraction study and I. I. Bannovaya and V. S. Fundamenskiĭ for their help in X-ray data collection.

This study was supported by the Russian Foundation for Basic Research (project no. 96-05-65576) and the Program "Russian Universities."

REFERENCES

1. P. A. Sandomirskiĭ and N. V. Belov (Nauka, Moscow, 1984).
2. L. P. Vergasov, T. F. Semenova, S. K. Filatov, *et al.*, Dokl. Akad. Nauk **338** (4), 501 (1994).
3. A. Goiffon, G. Bayle, R. Astier, *et al*., Rev. Chim. Miner. **20**, 338 (1983).
4. O. Baumgartner, M. Behmer, and A. Preisinger, Z. Kristallogr. **187**, 125 (1989).
5. H. Sowa, Z. Kristallogr. **194**, 291 (1991).
6. V. I. Andrianov, Kristallografiya **32**, 228 (1987) [Sov. Crystallogr. Rep. **32**, 130 (1987)].

7. G. M. Sheldrick, *SHELXTL 93: Program for the Refinement of Crystal Structures* (Univ. of Göttingen, Germany, 1993).
8. N. V. Walker and D. Stewart, Acta Crystallogr. Sect. A: Found. Crystallogr. **39**, 158 (1983).
9. I. D. Brown, in *Structure and Bonding in Crystals*, Ed. by M. O'Keefe and A. Navrotsy (Academic, New York, 1981), Vol. 2, pp. 1–30.
10. N. E. Brese and M. O'Keefe, Acta Crystallogr., Sect. B: Struct. Sci. **47**, 192 (1991).
11. P. C. Burns and F. C. Hawthorne, Can. Mineral. **33**, 889 (1995).
12. R. K. Eby and F. C. Hawthorne, Acta Crystallogr., Sect. B: Struct. Sci. **49**, 28 (1993).
13. F. Liebau, *Structural Chemistry of Silicates: Structure, Bonding and Classification* (Springer-Verlag, New York, 1985; Mir, Moscow, 1988).
14. J. J. Papike and T. Zoltai, Am. Mineral. **52**, 974 (1967).
15. T. B. Zunic, S. Scavnicar, and G. Molin, Eur. J. Mineral. **2**, 731 (1990).
16. I. E. Grey, I. C. Madsen, D. J. Jones, *et al*., J. Solid State Chem. **82**, 52 (1989).
17. M. Andratschke, K.-J. Range, and U. Klement, Z. Naturforsch. B **48**, 965 (1993).
18. T. M. Nenoff, W. T. A. Harrison, G. D. Stucky, *et al*., Zeolites **13**, 506 (1993).
19. T. M. Nenoff, W. T. A. Harrison, T. E. Gier, *et al*., Inorg. Chem. **33**, 2472 (1994).
20. X. Bu, T. E. Gier, and G. D. Stucky, Chem. Commun., 2271 (1997).

Translated by T. Safonova

Crystallography Reports, Vol. 45, No. 5, 2000, pp. 728–733. Translated from Kristallografiya, Vol. 45, No. 5, 2000, pp. 798–803.

STRUCTURES OF INORGANIC COMPOUNDS

Crystal Structures of Double Vanadates, $Ca_9R(VO_4)_7$. III. R = Nd, Sm, Gd, or Ce

A. A. Belik*, V. A. Morozov*, S. V. Grechkin*, S. S. Khasanov, and B. I. Lazoryak***

** Department of Chemistry, Moscow State University, Vorob'evy gory, Moscow, 117234 Russia*

e-mail: belik@tech.chem.msu.ru

*** Institute of Solid-State Physics, Russian Academy of Sciences, Chernogolovka, Moscow oblast, 142432 Russia*

Received July 29, 1998; in final form, June 23, 1999

Abstract—The crystal structures of $Ca_9R(VO_4)_7$ (R = Nd (**I**), Sm (**II**), or Gd (**III**)) were studied by the Rietveld method. The compounds are isostructural to $Ca_3(VO_4)_2$ and are crystallized in the trigonal system (sp. gr. $R3c$, $Z = 6$). The unit-cell parameters are as follows: for **I**, a = 10.8720(5) Å, c = 38.121(1) Å; for **II**, a = 10.8652(5) Å, c = 38.098(1) Å; and for **III**, a = 10.8631(5) Å, c = 38.072(1) Å. In the structures of **I** and **II**, the $M(1)$, $M(2)$, and $M(3)$ positions are statistically occupied by the rare-earth cations and calcium anions. In the structure of **III**, the Gd^{3+} cations occupy the $M(1)$ and $M(2)$ positions. The distributions of the R^{3+} cations over the positions are characteristic of each structure. The composition of the cerium-containing compound $Ca_{9.81}Ce_{0.42}(VO_4)_7$ (a = 10.8552(5) Å, c = 38.037(1) Å) was refined and its crystal structure was solved from the X-ray powder data. In this compound, cerium atoms are in the oxidation states +3 and +4. © *2000 MAIK "Nauka/Interperiodica".*

INTRODUCTION

This work was undertaken as part of the structural studies of the $Ca_9R(VO_4)_7$ compounds (R = REE or Y) and the analysis of the distributions of the R^{3+} cations over the positions in the initial $Ca_3(VO_4)_2$ structure [1]. The $Ca_3(VO_4)_2$ structure has five cationic positions, namely, three 18-fold positions, $M(1)$, $M(2)$, and $M(3)$ (with the coordination numbers are 7, 8, and 8), with the average $\langle M\text{–O}\rangle$ distances 2.44, 2.53, and 2.57 Å, respectively, the octahedral sixfold position, $M(5)$, with $\langle M\text{–O}\rangle$ = 2.30 Å, and the sixfold $M(4)$ position (half-occupied in $Ca_3(VO_4)_2$). The positions of the latter type form the $M(4)O_{15}$ cavity elongated in the z direction [2, 3].

The $Ca_9R(VO_4)_7$ compounds (R = REE or Y) are divided into two groups according to the character of the variations in the unit-cell parameters [4]. The compounds containing R = La–Eu belong to the first group, and the compounds containing R = Tb–Lu or Y, to the second one. The compound with R = Gd is shared by both groups. Sstructural studies of the $Ca_9R(VO_4)_7$ compounds (R = REE or Y) from the first group (R = La, Pr, or Eu [5]) demonstrated that R^{3+} and calciuim cations statistically occupy the $M(1)$, $M(2)$, and $M(3)$ positions. In the compounds of the second group (R = Tb, Dy, Ho, or Y [6]), R^{3+} and calcium cations statistically occupy the $M(1)$, $M(2)$, and $M(5)$ positions. The distribution of R^{3+} cations over the above-mentioned positions is characteristic of each $Ca_9R(VO_4)_7$ compound.

In this work, we studied the structures of $Ca_9R(VO_4)_7$ compounds, where R = Nd (**I**), Sm (**II**), or Gd (**III**) and the structure of cerium-containing compound (**IV**).

EXPERIMENTAL

Compounds **I**–**IV** were synthesized from stoichiometric mixtures of V_2O_5, $CaCO_3$, and oxides of the corresponding elements (R_2O_3 or CeO_3) by a solid-phase procedure (40–140 h, 1173–1273 K) preceded by 15 h-annealing at 873 K [4].

X-ray diffraction powder patterns were obtained on a SIEMENS D500 diffractometer ($CuK_{\alpha 1}$ radiation, λ = 1.54060 Å, a SiO_2 monochromator for the primary beam, a Ni filter, the 2θ scanning range 10°–110°, the scan step $\Delta(2\theta) = 0.01°$, the Bragg–Brentano focusing) equipped with a BRAUN position-sensitive detector (the efficient exposure time per step was ~20–30 min) at 297 K. The structures were refined by the Rietveld method [7] with the use of the RIETAN-94 program [8, 9]. The main details of X-ray data collection and the results of the structure refinement for **I**–**IV** are given in Table 1.

The X-ray phase analysis of **I**–**III** demonstrated that they were one-phase samples. The sample of **IV** contained the admixture phase CeO_2 and an unknown phase characterized by the most intense lines with d =

Table 1. Details of X-ray diffraction studies and the results of structure refinement of $Ca_9R(VO_4)_7$ (R = Nd (**I**), Sm (**I**), Sm (**II**), or Gd (**III**)) and compound **IV**

	Compound			
	I	**II**	**III**	**IV**
Space group	*R*3*c*	*R*3*c*	*R*3*c*	*R*3*c*
	$Z = 6$	$Z = 6$	$Z = 6$	$Z = 6$
I_{max}, pulses	15213	17539	23308	27074
Unit-cell parameters, Å:				
a	10.8720(5)	10.8652(5)	10.8631(5)	10.8552(5)
c	38.121(1)	38.098(1)	38.072(1)	38.037(1)
V	3902.2	3894.9	3890.8	3881.6
Number of reflections	552	551	549	548 + 12*
Number of parameters used**	18 + 54	17 + 54	17 + 54	19 + 63
Reliability factors***				
R_{WP}, R_P	5.93; 4.21	3.36; 2.64	2.99; 2.31	3.98; 3.03
R_I, R_F	4.82; 2.51	3.41; 1.55	3.23; 1.58	4.06; 2.80
				2.80*; 1.84*
S	2.12	1.38	1.40	1.56
(*D*–*W*)*d*	0.50	1.09	1.04	0.86

* For CeO_2.

** The first number in the column indicates the total number of the background and profile parameters, the scale factor, the unit-cell parameters, and the zero shift; the second number indicates the total number of the positional and thermal parameters and occupancies.

*** Calculated by the formulas reported in [8].

Table 2. Occupancies of the *M*(1)–*M*(5) positions in the structures of $Ca_9R(VO_4)_7$ (R = Nd (**I**), Sm (**II**), or Gd (**III**)) and compound **IV**

Position		Compound; radius of R^{3+}_{VIII}, Å			
		I, 1.12	**II**, 1.09	**III**, 1.06	**IV**, 1.14
M(1)	n_{Ca}	0.87(1)	0.851(5)	0.826(5)	0.941(5)
	m_R	0.13(1)	0.149(5)	0.174(5)	0.059(5)
	Number of R^{3+} cations	2.3(2)	2.7(1)	3.1(1)	1.1(1)
	$n_{f\text{–Ca}}$	1.18(1)	1.257(6)	1.273(7)	1.117(6)
M(2)	n_{Ca}	0.91(1)	0.886(5)	0.841(5)	0.985(5)
	m_R	0.09(1)	0.114(5)	0.159(5)	0.015(5)
	Number of R^{3+} cations	1.6(2)	2.0(1)	2.9(1)	0.3(1)
	$n_{f\text{–Ca}}$	1.14(1)	1.192(7)	1.212(8)	1.036(6)
M(3)	n_{Ca}	0.89(1)	0.930(5)	1.0	0.936(5)
	m_R	0.11(1)	0.070(5)	0.0	0.064(5)
	Number of R^{3+} cations	2.0(2)	1.3(1)	0.0	1.1(1)
	$n_{f\text{–Ca}}$	1.22(1)	1.113(6)	1.007(5)	1.125(6)
M(4)	$n_{f\text{–Ca}}$	0.02(1)	–0.016(9)	0.023(9)	0.226(9)
M(5)	$n_{f\text{–Ca}}$	0.98(1)	1.006(8)	1.034(8)	1.003(7)

Note: n_{Ca} and m_R are the occupancies of the position by the calcium and R^{3+} cations; $n_{f\text{–Ca}}$ is the occupancy of the position calculated with the use of the *f* curves for the Ca^{2+} cations.

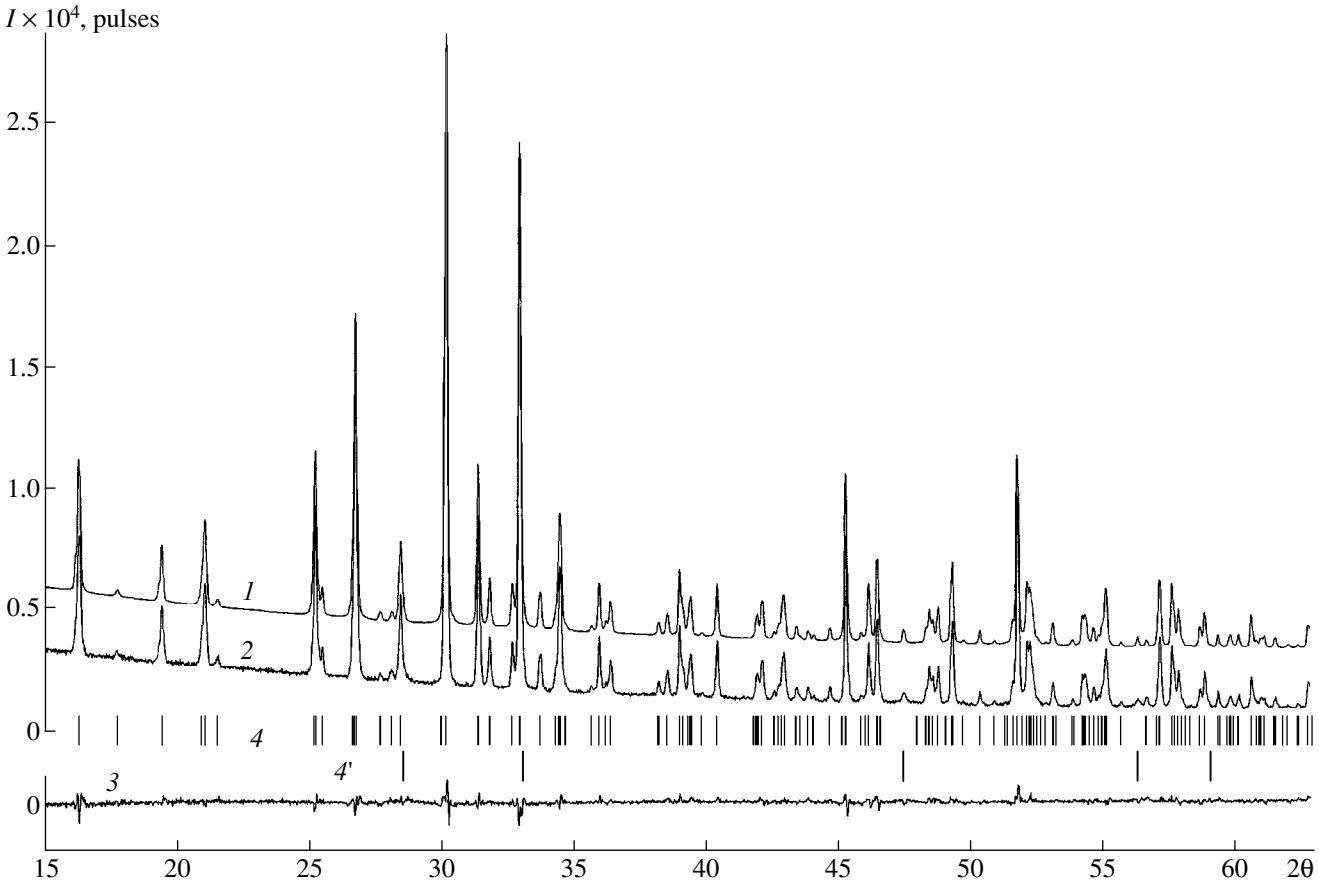

Fragments of the (*1*) calculated, (*2*) experimental, and (*3*) difference X-ray diffraction patterns for sample **IV** synthesized at 1473 K (*4* and *4*' are X-ray diffraction diagrams for $Ca_{9.81}Ce_{0.42}(VO_4)_7$ and CeO_2, respectively). The calculated X-ray diffraction pattern is shifted with respect to the experimental pattern by 2500 pulses.

3.60 and 1.853 Å. An increase in the annealing temperature from 1173 to 1273 K led to a decrease in the relative intensities of peaks of CeO_2 and the unidentified phase. Annealing at 1473 resulted in the formation of a sample containing CeO_2 and a phase isostructural to $Ca_3(VO_4)_2$. The full-profile refinement of the structure of this sample was performed simultaneously for both phases. The structural parameters of CeO_2 [10] were not refined. It should be noted that the synthesis from $Ca_3(VO_4)_2$ and $CeVO_4$ starting materials provided the phase composition analogous to that obtained in the synthesis from V_2O_5, $CaCO_3$, and CeO_2.

The structures were refined with the use of the *f* curves for Ca^{2+}, R^{3+}, V, and O^-. The peak profiles were described using the modified pseudo-Voigt function (Mod-TCH pV [8]). The background profile was described by a fifth-degree polynomial. The occupancies of the vanadium and oxygen positions were not refined. For a more detailed description of the experimental X-ray pattern from sample **I**, we specified the texture modeled by the March–Dollase function with the [001] texture vector.

The starting model for structure refinement was the structure of $Ca_3(VO_4)_2$ [1]. At the first stage, the *f* curve for Ca^{2+} was used for all the cationic positions and all the parameters of the chosen model were refined. The analysis of the occupancies demonstrated (Table 2, $n_{f\text{-}Ca}$) that the R^{3+} cations are distributed over the *M*(1), *M*(2), and *M*(3) positions in the structures of **I**, **II**, and **IV** and over the *M*(1) and *M*(2) positions in the structure of **III**. The occupancy of the *M*(4) position is close to zero in the structures of **I**–**III** and is ~0.2 in the structure of **IV**. The occupancy of the *M*(5) position is close to unity (Table 2). At the second stage, the distributions of the R^{3+} cations over the *M*(1), *M*(2), and *M*(3) positions in the structures of **I**, **II**, and **IV** and over the *M*(1) and *M*(2) positions in the structure of **III** were refined with due regard of their multiplicities ($n_{Ca} + m_R = 1$). The *f* curve for Ca^{2+} cations was used for the *M*(5) position. The *M*(4) position in the structures of **I**–**III** remained vacant. The refinement of all the model parameters gave 5.7, 6.0, 5.1, and 2.5 R^{3+} cations per unit cell for compounds **I**–**IV**, respectively. It is well known that the position occupancies correlate with the thermal parameters. Taking into account the stoichiom-

Table 3. Structural parameters for the $Ca_9R(VO_4)_7$ compounds (R = Nd (**I**), Sm (**II**), or Gd (**III**)) and compound **IV**

Atom	R^{3+}	x	y	z	B_{iso}	Atom	R^{3+}	x	y	z	B_{iso}	Atom	R^{3+}	x	y	z	B_{iso}
$M(1)$**	**I**	0.7293(5)	0.8594(7)	0.4304(3)	0.1(1)	V(3)	**I**	0.6495(6)	0.8488(7)	0.0316(3)	0.5*	O(24)	**I**	0.488(2)	0.750(3)	0.1232(6)	1.0*
	II	0.7270(3)	0.8596(4)	0.4307(3)	0.1(1)		**II**	0.6499(4)	0.8459(4)	0.0319(3)	0.5(1)		**II**	0.493(1)	0.749(2)	0.1222(4)	0.5*
	III	0.7253(4)	0.8585(4)	0.4303(2)	0.9(1)		**III**	0.6536(5)	0.8472(4)	0.0317(2)	0.53(9)		**III**	0.497(1)	0.752(1)	0.1253(4)	0.5*
	IV	0.7240(4)	0.8603(4)	0.4305(2)	0.6(1)		**IV**	0.6490(3)	0.8486(3)	0.0316(2)	0.71(8)		**IV**	0.499(1)	0.752(1)	0.1269(3)	1.2(2)
$M(2)$**	**I**	0.6146(6)	0.8211(7)	0.2333(3)	0.5(1)	O(11)	**I**	0	0	0.3137(7)	1.0*	O(31)	**I**	0.603(2)	0.959(2)	0.0482(7)	1.0*
	II	0.6150(4)	0.8231(4)	0.2338(3)	0.5(1)		**II**	0	0	0.3129(5)	0.5*		**II**	0.592(1)	0.950(1)	0.0459(5)	0.5*
	III	0.6128(3)	0.8232(4)	0.2333(2)	0.4(1)		**III**	0	0	0.3129(5)	0.5*		**III**	0.590(1)	0.955(1)	0.0463(4)	0.5*
	IV	0.6136(3)	0.8243(4)	0.2335(2)	0.4(1)		**IV**	0	0	0.3127(4)	0.5*		**IV**	0.590(1)	0.9536(9)	0.0461(3)	0.3(2)
$M(3)$**	**I**	0.1181(5)	0.2626(4)	0.3228(3)	1.4(1)	O(12)	**I**	0.020(2)	0.859(2)	0.2563(6)	1.0*	O(32)	**I**	0.559(2)	0.674(2)	0.0527(6)	1.0*
	II	0.1212(4)	0.2668(3)	0.3246(3)	1.18(9)		**II**	0.013(1)	0.858(1)	0.2572(4)	0.5*		**II**	0.563(1)	0.682(1)	0.0511(4)	0.5*
	III	0.1242(4)	0.2700(3)	0.3249(2)	0.61(8)		**III**	0.017(1)	0.8661(9)	0.2576(4)	0.5*		**III**	0.569(1)	0.688(1)	0.0516(4)	0.5*
	IV	0.1196(3)	0.2663(2)	0.3244(2)	1.3(1)		**IV**	0.014(1)	0.8603(8)	0.2565(3)	0.3(2)		**IV**	0.552(1)	0.680(1)	0.0510(3)	0.3(2)
Ca(5)	**I**	0	0	0	0.8(2)	O(21)	**I**	0.712(2)	0.907(2)	0.1789(6)	1.0*	O(33)	**I**	0.833(2)	0.920(3)	0.0439(7)	1.0*
	II	0	0	0	0.8(1)		**II**	0.706(1)	0.904(1)	0.1786(4)	0.5*		**II**	0.826(1)	0.924(2)	0.0432(5)	0.5*
	III	0	0	0	0.2(1)		**III**	0.706(1)	0.909(1)	0.1770(4)	0.5*		**III**	0.825(1)	0.920(2)	0.0495(4)	0.5*
	IV	0	0	0	0.27(9)		**IV**	0.726(1)	0.916(1)	0.1766(4)	3.4(3)		**IV**	0.8241(8)	0.921(1)	0.0468(3)	0.4(2)
V(1)	**I**	0	0	0.2558(3)	0.5*	O(22)	**I**	0.764(3)	0.757(2)	0.1201(6)	1.0*	O(34)	**I**	0.620(2)	0.832(2)	0.9868(5)	1.0*
	II	0	0	0.2669(3)	1.0(1)		**II**	0.771(1)	0.760(1)	0.1242(5)	0.5*		**II**	0.628(1)	0.827(1)	0.9892(4)	0.5*
	III	0	0	0.2661(2)	0.3(1)		**III**	0.763(1)	0.756(1)	0.1250(4)	0.5*		**III**	0.6353(9)	0.823(1)	0.9904(3)	0.5*
	IV	0	0	0.2666(2)	0.7(1)		**IV**	0.757(1)	0.757(1)	0.1243(3)	1.5(3)		**IV**	0.6263(9)	0.825(1)	0.9879(3)	1.3(2)
V(2)	**I**	0.6827(4)	0.8556(7)	0.1333(3)	0.5*	O(23)	**I**	0.722(3)	0.027(2)	0.1117(6)	1.0*	Ca(4)	**IV**	0	0	0.1809(7)	2.5*
	II	0.6798(3)	0.8553(4)	0.1335(3)	0.45(9)		**II**	0.726(1)	0.019(1)	0.1144(4)	0.5*						
	III	0.6827(3)	0.8569(4)	0.1332(2)	0.43(9)		**III**	0.730(1)	0.028(1)	0.1135(4)	0.5*						
	IV	0.6843(3)	0.8569(3)	0.1334(2)	0.82(8)		**IV**	0.713(1)	0.015(1)	0.1112(3)	0.5*						

* Fixed B_{iso}.

** The $M(1)$, $M(2)$, and $M(3)$ positions are occupied by the Ca^{2+} and R^{3+} ions in the ratios given in Table 2. The occupancy of the Ca(5) position is 1. The oxygen atoms are numbered as follows: the first and the second numbers correspond to the numbers of the vanadium and oxygen atoms in the tetrahedron, respectively.

etry and the fact that **I**–**III** are one-phase substances, the total number of the R^{3+} cations per unit cell was fixed to be 6 in the subsequent refinement. The R^{3+} cations are distributed over the positions in the structures of **I**–**IV** (n_{Ca}, m_R) as is indicated in Table 2.

Figure shows the experimental, the calculated, and the difference X-ray diffraction patterns for sample **IV**. The atomic coordinates and thermal parameters for compounds **I**–**IV** are listed in Table 3.

RESULTS AND DISCUSSION

The crystallochemical formula of $Ca_3(VO_4)_2$ ($Z = 21$) can be written as $Ca_{18}(1)Ca_{18}(2)Ca_{18}(3)Ca_3(4)\square_3(4)Ca_6(5)(VO_4)_{42}$ ($Z = 1$) or, taking into account that the $M(1)$, $M(2)$, and $M(3)$ positions have sizes and environments, as $Ca_{54}(1,2,3)Ca_3(4)\square_3(4)Ca_6(5)(VO_4)_{42}$ ($Z = 1$) [11]. In the case of the replacement $3Ca^{2+} \longrightarrow 2R^{3+} + \square$, the existence region of the $Ca_{54-2x}R_{2x}(1,2,3)Ca_{3-x}(4)\square_{3+x}(4)Ca_6(5)(VO_4)_{42}$ solid solutions lies within $0 \le x \le 3$. The formation of the vacant $M(4)$ position determines the boundary of the existence of solid solutions ($x = 3$). In the case of the replacement $2Ca^{2+} \longrightarrow R^{4+} + \square$, the range of existence of solid solutions $Ca_{54-x}R_x(1,2,3)Ca_{3-x}(4)\square_{3+x}(4)Ca_6(5)(VO_4)_{42}$ is $0 \le x \le 3$.

Under the conditions of the synthesis performed, we also obtained sample **IV** consisting of more than one phase. The unit-cell parameters of a phase isostructural to $Ca_3(VO_4)_2$ ($a = 10.8552(5)$ Å; $c = 38.037(1)$ Å) are substantially smaller than those for the $Ca_9R(VO_4)_7$ compounds containing the R^{3+} cations with similar radii (for R = La; $a = 10.8987(5)$ Å, $c = 38.147(1)$ Å; for R = Pr, $a = 10.8808(7)$ Å, $c = 38.135(1)$ Å [5]) and are closer to those of pure $Ca_3(VO_4)_2$ ($a = 10.809(1)$ Å, $c = 38.028(9)$ Å [1]). X-ray diffraction analysis shows that the $M(4)$ position in the structure of **IV** is partly occupied by Ca^{2+} cations ($n = 0.226(9)$) and that the number of cerium cations (2.5) is substantially less than 6. These data indicate that compound **IV** is an intermediate solid solution. The value of x (1.6) can be calculated from the occupancy of the $M(4)$ position. The number of cerium cations lies in the range from x to $2x$. Therefore, X-ray diffraction analysis demonstrated that the cerium cations in compound **IV** have two oxidation states (+3 and +4). Under the conditions of the synthesis performed in this work, cerium cations partly stabilized in the trivalent state. Some cerium atoms in the structure of **IV** exist in the tetravalent state, a sample of composition $Ca_9Ce^{3+}(VO_4)_7$ is not formed and, thus, sample **IV** has more than one phase. The phase is isostructural to $Ca_3(VO_4)_2$ and its composition can be written as $Ca_{9.81}Ce^{4+}_{0.12}\,Ce^{3+}_{0.30}\,(VO_4)_7$. Whitlockite-like phosphate compounds containing tetravalent cerium atoms can readily be prepared under the same conditions as $Ca_{19}Ce(PO_4)_{14}$ [12] and $Ca_8MgCe(PO_4)_6(SiO_4)$ [13]. It should be noted that the whitlockite-like matrix stabilizes cations in unusual oxidation states. Thus, the attempts to synthesize a compound of composition $Ca_9Co^{3+}(PO_4)_7$ in air at 1273 and 1473 K led to partial stabilization of Co^{3+} with the formation of $Ca_{9.28}Co^{2+}_{0.98}\,Co^{3+}_{0.16}\,(PO_4)_7$ and $Ca_{9.07}Co^{2+}_{0.35}\,Co^{3+}_{0.72}\,(PO_4)_7$ compounds, respectively.

Cerium cations are distributed over the $M(1)$, $M(2)$, and $M(3)$ positions in the ratio of $M(1) : M(2) : M(3) = 2.5 : 0.7 : 2.8$, which is consistent with the distributions of the La^{3+} and Pr^{3+} cations in the first group ($M(1) : M(2) : M(3) = 1.6 : 0.4 : 4.0$ and $2.1 : 1.7 : 2.2$, respectively [5]).

The distribution of the R^{3+} cations over the $M(1)$, $M(2)$, and $M(3)$ positions is inherent in compounds **I**–**III**. This situation was also observed for other $Ca_9R(VO_4)_7$ compounds (R = REE or Y) [5, 6]. For all the compounds from the first group (R = La–Eu), the number of the R^{3+} cations occupying the $M(3)$ positions decreases monotonically with a decrease in the radius of the R^{3+} cation (from four cations per unit cell for R = La to 0.8 cations per unit cell for R = Eu [5]). In the $Ca_9Gd(VO_4)_7$ compound, the $M(3)$ position is occupied by calcium cations alone and, correspondingly, the occupancies of the $M(1)$ and $M(2)$ positions by the R^{3+} cations increase. The distributions of the R cations (R = La–Eu) in compounds of the first group were discussed in [5] and will be considered in detail for the whole series of rare-earth cations in the next publication.

Compound **III** separates the $Ca_9R(VO_4)_7$ series (R = REE or Y) into two groups. Therefore, it is quite possible that a small number of Gd^{3+} cations can occupy the $M(3)$ and $M(5)$ positions. However, this fact is difficult to reliably establish from the X-ray powder data because of the correlation with thermal parameters. Apparently, this correlation is also responsible for the fact that the number of the Gd^{3+} cations per unit cell equals 5.1 in the refinement of the number of the R^{3+} cations in the $M(1)$ and $M(2)$ positions without the use of an additional constraint that the number of the R^{3+} cations per unit cell equals 6. However, it should be noted that the latter fact may be associated with the conditions of the sample preparation for X-ray diffraction study. For example, sample of **I** showed the texture which we failed to adequately model. For the sample of **I**, the experimental and the calculated X-ray diffraction patterns show rather poor agreement, and the reliability factors are substantially higher than those obtained for the other $Ca_9R(VO_4)_7$ compounds (Table 1; [5, 6]). However, these facts did not prevent the determination of the distributions of Nd^{3+} cations over the $M(1)$–$M(3)$ positions. This distribution corresponds to the data observed for the compounds of the first group.

ACKNOWLEDGMENTS

This work was supported by the Russian Foundation for Basic Research, project no. 97-03-33224a.

REFERENCES

1. R. Gopal and C. Calvo, Z. Kristallogr. **137**, 67 (1973).
2. V. A. Morozov, I. A. Presnyakov, A. A. Belik, *et al.*, Kristallografiya **42** (5), 825 (1997) [Crystallogr. Rep. **42** (5), 758 (1997)].
3. N. Khan, V. A. Morozov, S. S. Khasanov, and B. I. Lazoryak, Mater. Res. Bull. **32**, 1211 (1997).
4. B. I. Lazoryak, L. O. Dmitrienko, and S. V. Grechkin, Zh. Neorg. Khim. **35**, 1095 (1990).
5. A. A. Belik, V. A. Morozov, S. S. Khasanov, and B. I. Lazoryak, Kristallografiya **42** (5), 818 (1997) [Crystallogr. Rep. **42** (5), 751 (1997)].
6. A. A. Belik, V. A. Morozov, R. N. Kotov, *et al.*, Kristallografiya **45** (6) (2000) [Crystallogr. Rep. **45** (6) (2000)].
7. H. M. Reitveld, Acta Crystallogr. **22**, 151 (1967).
8. F. Izumi, *The Rietveld Method*, Ed. by R. A. Young (Oxford Univ. Press, New York, 1993), Chap. 13.
9. Y.-I. Kim and F. Izumi, J. Ceram. Soc. Jpn. **102**, 401 (1994).
10. H. J. Whitfield, D. Roman, and A. R. Palmer, J. Inorg. Nucl. Chem. **28**, 2817 (1966).
11. B. I. Lazoryak, Usp. Khim. **65**, 307 (1996).
12. B. I. Lazoryak, R. N. Kotov, and S. S. Khasanov, Zh. Neorg. Khim. **41**, 1281 (1996).
13. R. N. Kotov, V. A. Morozov, S. S. Khasanov, and B. I. Lazoryak, Kristallografiya **42** (6), 1027 (1997) [Crystallogr. Rep. **42** (6), 951 (1997)].
14. A. A. Belik, V. A. Morozov, S. S. Khasanov, and B. I. Lazoryak, Mater. Res. Bull. **33**, 987 (1998).

Translated by T. Safonova

Crystallography Reports, Vol. 45, No. 5, 2000, pp. 734–738. Translated from Kristallografiya, Vol. 45, No. 5, 2000, pp. 804–808.

STRUCTURES OF INORGANIC COMPOUNDS

Synthesis, X-ray and Neutron Diffraction and Mössbauer Studies of $SrFeO_x$ Crystals

A. A. Bush*, V. A. Sarin, D. G. Georgiev**, and V. M. Cherepanov*****

** Institute of Informatics, Moscow State Institute of Radio Engineering, Electronics, and Automatics (Technical University), pr. Vernadskogo 78, Moscow, 117454 Russia*

e-mail: bush@cc.nifhi.ac.ru

*** Joint Institute for Nuclear Research, Dubna, Moscow oblast, Moscow, 141980 Russia*

**** Russian Research Center Kurchatov Institute, pl. Kurchatova 1, Moscow, 123182 Russia*

Received January 15, 1999

Abstract—Tetragonal single crystals of the nonstoichiometric strontium ferrate with the lattice parameters a = 3.8525(3) and c = 3.8781 (3) Å have been synthesized for the first time by the method of floating-zone melting in the $SrFeO_x$ system. The neutron diffraction patterns of the crystals showed weak additional reflections indicating the formation of the superstructure with double spacing along the [*hh*0] direction. The Mössbauer spectra of the crystals were obtained and measured in the temperature range 80–300 K. It was established that below the temperature T_N = 232(1) K, the crystals are in the magnetically ordered state with 3/5 of iron ions being in the trivalent state and all the remaining iron ions in the tetravalent state. This leads to the crystal composition $SrFeO_{2.71}$. The electric resistivity of the crystals equal to 100 Ω cm at room temperature drastically decreases at temperatures exceeding 470 K. © *2000 MAIK "Nauka/Interperiodica".*

INTRODUCTION

Crystals of the composition $SrFeO_x$ are of great interest as a promising material for the search of new weakly anisotropic ferromagnetics with high temperatures of magnetic transition and susceptibility and also because of their possible use as high-temperature oxygen-selective membranes for various physicochemical processes [1–5].

The oxygen-nonstoichiometric phase $SrFeO_x$ with an anion-deficient perovskite structure has two types of iron cations—Fe^{3+} and Fe^{4+} [1–17]. Depending on the conditions of crystal synthesis, the Fe^{4+}/Fe^{3+} ratio can range from 0 to infinity, which provides the change of the oxygen content x in the formula unit of this phase from 2.5 to 3.0. These variations considerably influence the structure and the properties of this phase, in particular, the character of ordering of oxygen vacancies, the type of the magnetic structure, conductivity, etc. [6–17].

At x = 2.5, the crystal lattice has an orthorhombic structure with the unit-cell volume $V \approx \sqrt{2}\,a_p \times 4a_p \times \sqrt{2}\,a_p$ (where a_p = 3.9 Å is the unit-cell parameter of the perovskite unit cell). In this form of strontium ferrate, all the iron ions are in the Fe^{3+} state, the oxygen vacancies are ordered. Thus, this ferrate is a stoichiometric compound with 100% occupancy of the positions in the brownmillerite-type (Ca_2FeAlO_5) structure [6, 7, 9–16]. The phase with x = 2.97–3.0 has only Fe^{4+} cations and is characterized by the cubic unit cell with the parameter $a \approx a_p$ [7, 8, 12, 13, 15, 16].

The data on the compositions, symmetries, and dimensions of the unit cells of the intermediate forms of $SrFeO_x$ [12–17] are somewhat inconsistent. The most systematic studies of the $SrFeO_x$ system made by the methods of nuclear gamma-resonance and X-ray phase analysis [15, 16] led to the conclusion that at x = 2.87, a tetragonal phase with $V \approx 2\sqrt{2}\,a_p \times 2\sqrt{2}\,a_p \times 2a_p$ is formed, whereas at x = 2.68–2.73, an orthorhombic one with $V \approx 2\sqrt{2}\,a_p \times 2a_p \times \sqrt{2}\,a_p$. All the remaining compositions with x ranging from 2.5 to 3.0 are considered as the mixtures of the phases with various oxygen contents. It is also established [15, 16] that, with an increase of the temperature, all the nonstoichiometric $SrFeO_x$ phases are transformed into the cubic phase, with the transitions temperature decreasing from 830°C at x = 2.5 to 250°C at x = 2.86.

It is rather difficult to synthesize single-phase samples of the intermediate ferrates with the tetragonal symmetry [15, 16], which is explained by nonstability of formation of the highest oxidation state of iron, Fe^{4+}, at the temperature of the phase formation. This also explains the ambiguous interpretation of the known results. Some additional difficulties are associated with the presence of weak superstructural reflections on the corresponding diffraction patterns, ordering of oxygen vacancies, and also with magnetic, charge, or orbital ordering of ions with varying valence. It is rather difficult to record such reflections in conventional X-ray diffraction experiments on polycrystals. In this case, it

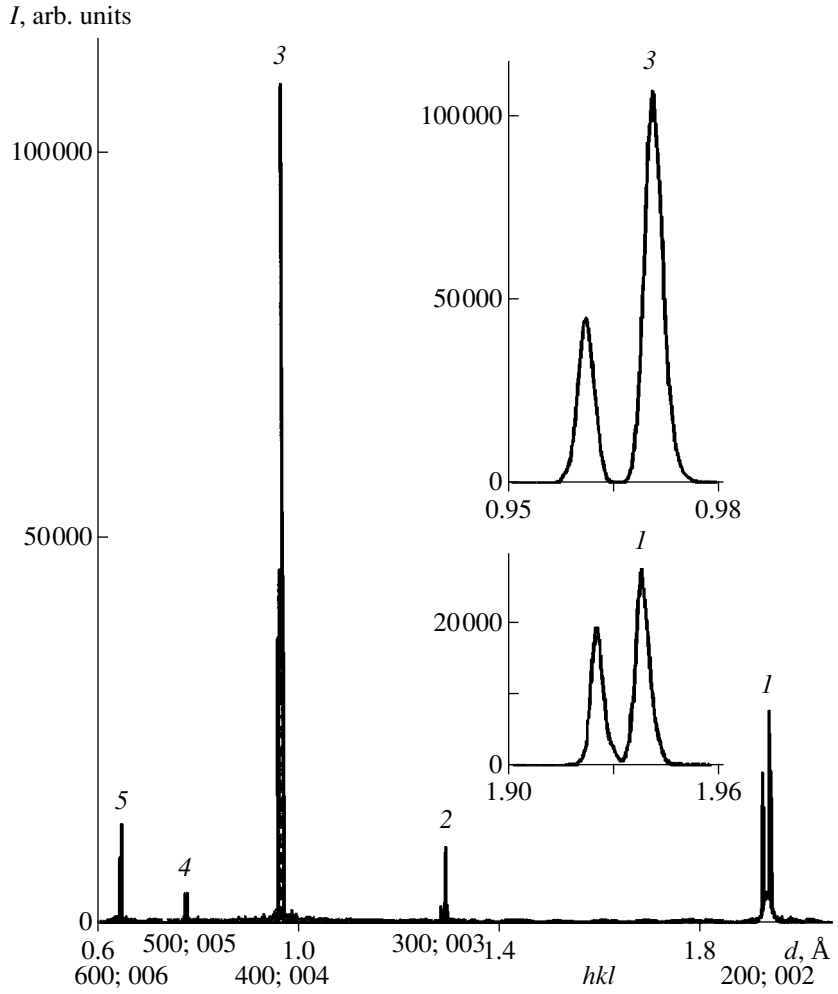

Fig. 1. High-resolution neutron diffraction pattern along the [*h*00] direction from a $SrFeO_x$ crystal at room temperature.

is more expedient to perform the neutron diffraction studies of the corresponding single crystals.

The present investigation was undertaken with the aim to grow and study single crystals of nonstoichiometric strontium ferrate because all the known studies of this phase were performed on polycrystal samples.

SYNTHESIS OF CRYSTALS

The crystals were synthesized by the methods of ceramic technology and floating-zone melting with optical heating on an URN-2-3P setup [18]. The starting materials were Fe_2O_3 and strontium carbonate $SrCO_3$ of the grade "pure for the analysis."

First, the ceramic rods 8 mm in diameter and 90 mm in length were synthesized from the charge of the composition $2SrO \cdot Fe_2O_3$ at 1300°C. The zone recrystallization of these rods was performed at the linear velocities 3, 9, and 33 mm/h. During floating-zone melting, the rod and a seed sample were rotated in opposite directions with an angular velocity of 30–60 rev/min. Upon the passage of the melt zone and crystallization, the crystal was transferred to the zone of post-growth annealing with a temperature of 1400°C and was cooled in the furnace for several hours to room temperature. During crystallization, no component volatility was observed against the mirror background. In all the cases, synthesis was performed in the air atmosphere.

As a result, black mirror-smooth cylindrical single-crystal boules (6 mm in diameter and 30 mm in length) were grown at low growth rates (3–9 mm/h) on preliminarily grown small crystalline seeds. The microscopy and X-ray diffraction studies showed that the boules grown at a rate of 33 mm/h were intergrowth of millimeter-large crystals. The single crystals obtained showed no clearly pronounced cleavages.

X-RAY AND NEUTRON DIFFRACTION STUDIES

In order to control the phase composition of the boules, determine the crystallographic characteristics and the structure of the specimens, the methods of the

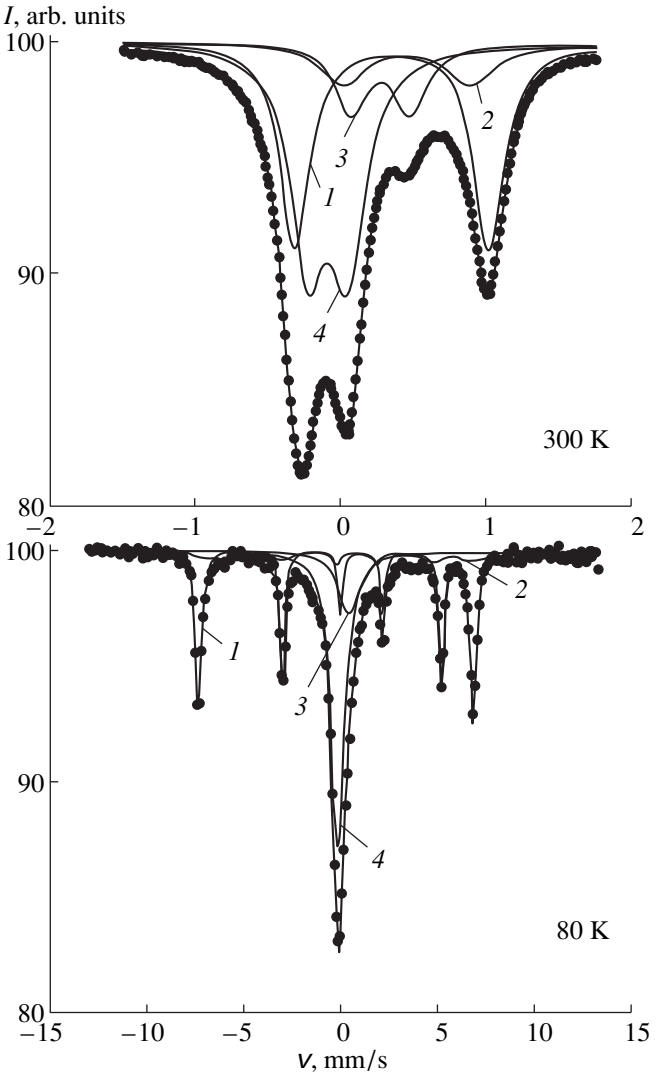

Fig. 2. Mössbauer spectra of a $SrFeO_x$ crystal at room temperature and 80 K (the numbers at the curves of the subspectra coincide with the ordinal numbers of cations in table).

X-ray and neutron diffraction were used. X-ray diffraction measurements were made on a DRON-3 diffractometer (CuK_α radiation) on powder samples. Neutron diffraction studies of single crystals were performed by the time-of-flight technique on a SNIM-2 setup for single crystals and a high-resolution Fourier-diffractometer of the pulsed IBR-2 reactor (JINR, Dubna) [19].

The diffraction pattern from finely ground powders of the crystals corresponded to the phase with the perovskite structure and the unit-cell parameter of a pseudocubic unit cell a_p = 3.9 Å. The reflection splitting indicated the tetragonal distortion of the cubic lattice. The diffraction pattern containing no additional reflection was indexed on the basis of the tetragonal unit cell with the parameters $a = b$ = 3.851(5) and c = 3.870(5) Å.

The pseudocubic perovskite unit cell was also confirmed by the neutron diffraction patterns of the corresponding single crystals taken along the [*h*00], [*hh*0], and [*hhh*] directions. High-resolution neutron diffraction patterns obtained along the [*h*00] directions on a Fourier-diffractometer showed splitting of diffraction reflections into two components corresponding to the [*h*00] and [00*l*] directions of the pseudocubic axes of the crystal (Fig. 1).

Splitting of reflections is caused by twinning which, in turn, seems to be caused by the phase transition accompanied by lowering of the symmetry from cubic to tetragonal during post-growth cooling of the crystals. Upon this phase transitions, one of the cubic axes (a_1, a_2, or a_3) is transformed into the *c*-axis of the tetragonal unit cell. The transformation occurs along different axes in different regions of the crystal. The character of twinning allowed us to obtain the lattice parameters *a* and *c* from only one high-resolution spectrum.

The lattice parameters determined, $a = b$ = 3.8525(3) and c = 3.8781(3) Å, correspond to the composition $SrFeO_{2.78}$ [7]. The absence of systematic reflection extinctions indicate the sp. gr. *P*4*mm*. No reflections from other phases were revealed. The unit-cell dimensions determined using various orders of the *h*00 and 00*l* reflections were almost independent on the reflection order which, according to [20], indicates the absence of stacking faults in the crystal lattice.

The diffraction pattern obtained along the [*hh*0] direction had weak superstructural reflections of the $h + 1/2$, $h + 1/2$, 0 type. Since the temperature of magnetic ordering for the crystals is lower than room temperature, the presence of these reflections is explained by the formation of a superstructure along the [*hh*0] direction. In this connection, the true unit cell of the crystals should have the dimensions $a = b = \sqrt{2}\,a_p$ = 5.4483(4) and c = 3.8781(3) Å.

MÖSSBAUER MEASUREMENTS

The Mössbauer spectra of the crystals were measured in the absorption geometry in the temperature range 80–300 K on a standard spectrometer based on a NOKIA LP4900B multichannel analyzer operating in the mode of constant acceleration of the motion of a ^{57}Co(Rh) source with an activity of about 10 mCi. Polycrystal samples for measurements were prepared by grinding single crystals in ethyl alcohol with the subsequent deposition of the suspension onto the aluminum foil and addition of the BF-2 glue up to the attainment of the surface density of 40 mg/cm^2. The spectra obtained were processed by the least squares method using SPECTR and DISTRI programs for the Lorentzian line shape [21].

First consider the Mössbauer spectrum of the crystal obtained at room temperature (Fig. 2) which, in this case, is higher than the Néel point. Several lines of var-

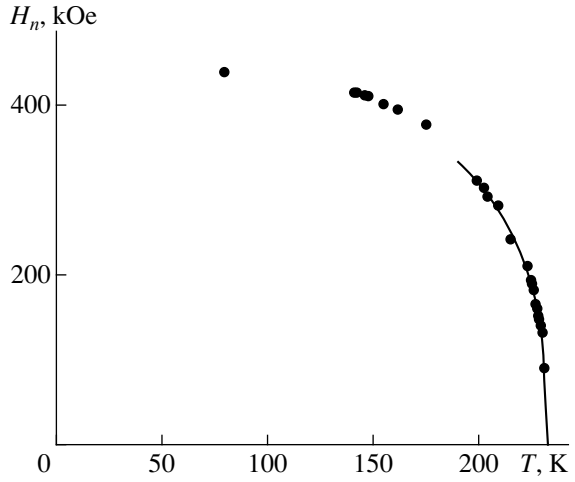

Fig. 3. Temperature dependence of the effective magnetic field at ^{57}Fe nuclei in the $SrFeO_x$ crystals according to the Mössbauer spectra (solid line indicates the experimental dependence $H_n = H_0(1 - T/T_N)^{\beta}$ at $\beta = 0.31$).

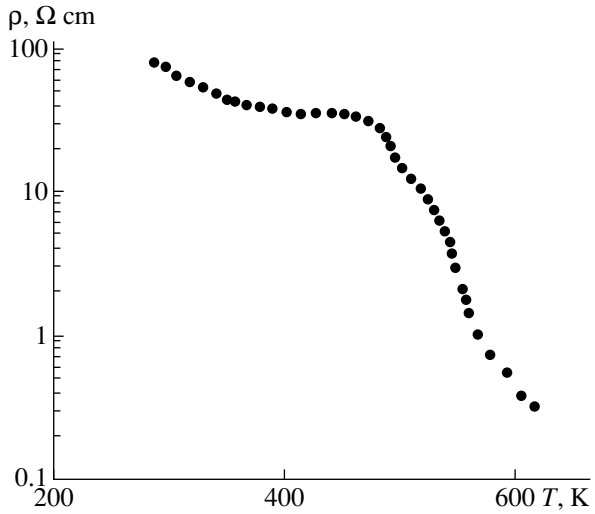

Fig. 4. Temperature dependence of electric resistivity of a $SrFeO_x$ crystal.

ious intensities indicate that the spectrum is, in fact, a superposition of several subspectra. The analysis shows that the minimum number of doublets necessary for the adequate description of the structure and therefore, also the number of various types of the positions for iron ions equals four. Earlier, similar spectra were observed from polycrystals obtained by solid-state synthesis [15, 16].

The parameters of isomer shirt and hyperfine quadrupole splitting of doublets are given in table. The model used for spectrum processing agrees with the measurements at $T = 80$ K (Fig. 2 and table) with due regard for the fact that two doublets corresponding to trivalent iron with the maximum isomeric shift and quadrupole splitting are transformed into sextets, which indicates the attainment of a magnetic order in the system.

In this case, the values of quadrupole splitting in doublets *1* and *2* and sextets *1* and *2* are very close, which is possible only if the direction of the easy-magnetization axis coincides with the axis of the electric-field gradient tensor (EFG) at iron nuclei. Moreover, with a decrease of the temperature, the linewidth of two remaining doublets (corresponding to trivalent iron coordinated with four oxygen atoms and tetravalent iron) noticeably increases. This, in turn, indicates a considerable decrease of the frequency of fluctuations of their magnetic moments due to weak magnetization effect of magnetically ordered sublattices. The total intensities of the subspectra of tri- and tetravalent iron at room and liquid-nitrogen temperatures are also close to one another (within the measurement error). Under the assumption that the probabilities of the Mössbauer effect for various iron positions in the lattice are equal, the ratio of the areas of doublets of tri- and tetravalent iron allows us to write the composition as $SrFeO_{2.71}$. It seems that this composition is more accurate than the composition determined from the unit-cell parameters. One has to also bear in mind that the concentration dependences of the unit-cell parameters given by various authors are obviously inconsistent.

We also studied the temperature dependences of the Mössbauer spectra in the temperature range 80–300 K (Fig. 3) and determined the temperature of the magnetic phase transition, $T_N = 232(1)$ K, and the value of the critical sublattice-magnetization index $\beta = 0.31(1)$ in the temperature range $0.01 > (1 - T/T_N) > 0.001$ characteristic of Ising-type magnetics with pronounced

Isomer shifts (*IS*) with respect to metal iron, quadrupole splitting (*QS*), linewidths (*LW*) (mm/s), relative areas of partial spectra (Å), and the effective magnetic fields H_n (kOe) at ^{57}Fe for various positions of iron ions in the $SrFeO_x$ lattice at 300 and 80 K

Fe ion	300				80				
	IS	*QS*	*LW*	*A*	*IS*	*QS*	*LW*	H_n	*A*
(3+)-1	0.36	1.34	0.25	35	0.48	−1.35	0.32	442	35
(3+)-2	0.45	0.87	0.37	11	0.56	−0.72	0.40	418	11
(3+)-3	0.28	0.41	0.27	12	0.41	0.40	1.17		13
(4+)-4	−0.08	0.27	0.29	42	−0.07	0.26	0.89		41

uniaxial anisotropy. It should also be noted that, contrary to the data [15], both systems of magnetic sextets "collapse" at the same temperature, which indicates the phase homogeneity of the specimen studied.

ELECTRIC CONDUCTIVITY

Using an E7-15 apparatus for measuring emittance, we determined the temperature dependence of electric conductivity ρ of $SrFeO_{2.7}$ crystals at a frequency of 1 kHz. At room temperature, $\rho \approx 100\ \Omega$ cm; above 470 K, it drastically decreases (Fig. 4), which can be explained by the phase transition into the high-temperature cubic phase at this temperature [15, 16].

Thus, using the method of floating-zone melting, we manage to grow, for the first time, the single crystals of nonstoichiometric strontium ferrate of the composition $SrFeO_x$. We also studied the grown crystals by the X-ray and neutron diffraction and the gamma resonance methods. The set of neutron diffraction reflections was used for the complete structure determination of the synthesized strontium ferrate phase.

ACKNOWLEDGMENTS

The authors are grateful to A. M. Balagurov for his help in collecting high-resolution neutron diffraction data and fruitful discussions of the results.

The study was supported by the Russian Foundation for Basic Research, project no. 99-02-17186.

REFERENCES

1. G. A. Smolenskiĭ, V. A. Bokov, V. A. Isupov, N. N. Kraĭnik, R. E. Pasynkov, and M. S. Shur, *Ferro- and Antiferroelectrics* (Nauka, Leningrad, 1971).
2. K. S. Aleksandrov and B. V. Beznosikov, *Perovskite-like Crystals* (Nauka, Sib. Predpriyatie Ross. Akad. Nauk, 1997), p. 27.
3. U. Bakachandran, J. T. Dusek, S. M. Sweeney, *et al.*, Am. Ceram. Soc. Bull. **74**, 71 (1995).
4. Y. S. Liu and Y. Zeng, J. Catal. **164**, 220 (1996).
5. U. Balachandran, J. T. Dusek, P. S. Maiya, *et al.*, Catal. Today **36**, 265 (1997).
6. P. K. Gallagher, J. B. MacChesney, and D. N. E. Buchanan, J. Chem. Phys. **41**, 2429 (1964).
7. J. B. MacChesney, R. C. Sherwood, and J. F. Potter, J. Chem. Phys. **43**, 1907 (1965).
8. T. Takeda, Y. Yamaguchi, and H. Watanabe, J. Phys. Soc. Jpn. **23**, 967 (1972).
9. T. Takeda, Y. Yamaguchi, Y. Watanabe, *et al.*, J. Phys. Soc. Jpn. **26**, 320 (1969).
10. C. Greaves, A. J. Jacobson, B. C. Tofield, and B. E. F. Fender, Acta Crystallogr., Sect. B: Struct. Crystallogr. Cryst. Chem. **31**, 641 (1975).
11. M. Harder and H. Mueller-Buschbaum, Z. Anorg. Allg. Chem. **464**, 169 (1980).
12. B. C. Tofield, C. Greaves, and B. E. F. Fender, Mater. Res. Bull. **10**, 737 (1975).
13. J.-C. Granier, N. Ea, M. Pouchard, and P. Hagenmuller, J. Solid State Chem. **58**, 243 (1985).
14. T. C. Gibb, J. Chem. Soc. Dalton Trans., 1455 (1985).
15. Y. Takeda, K. Kanno, T. Takada, *et al.*, J. Solid State Chem. **63**, 237 (1986).
16. M. Takano, T. Okita, M. Nakayama, *et al.*, J. Solid State Chem. **73**, 140 (1988).
17. T. I. Vetrova, Tszi Shishan', and A. V. Vishnyakov, Zh. Fiz. Khim. **72**, 253 (1998).
18. A. M. Balbashov, S. K. Egorov, *et al.*, J. Crystal. Growth **52**, 498 (1981).
19. D. Georgiev, V. V. Nietz, T. B. Petukhova, *et al.*, J. Neutron Res. **5**, 109 (1997).
20. V. I. Iveronova and G. P. Revkevich, *Theory of X-ray Scattering* (Mosk. Gos. Univ., Moscow, 1978, 2nd ed.), Chap. 7.
21. V. I. Nikolaev and V. S. Rusakov, *Mössbauer Studies of Ferrites* (Mosk. Gos. Univ., Moscow, 1985).

Translated by L. Man

Crystallography Reports, Vol. 45, No. 5, 2000, pp. 739–743. Translated from Kristallografiya, Vol. 45, No. 5, 2000, pp. 809–813.

STRUCTURES OF INORGANIC COMPOUNDS

Structure and Properties of Niobium-Doped Potassium Titanyl Phosphate Crystals

T. Yu. Losevskaya*, O. A. Alekseeva, V. K. Yanovskiĭ*, V. I. Voronkova*, N. I. Sorokina**, V. I. Simonov**, S. Yu. Stefanovich***, S. A. Ivanov***, S. Eriksson****, and S. A. Zverkov*******

** Moscow State University, Vorob'evy gory, Moscow, 119899 Russia*

*** Shubnikov Institute of Crystallography, Russian Academy of Sciences, Leninskiĭ pr. 59, Moscow, 117333 Russia*

**** Karpov Institute of Physical Chemistry, Vorontsovo pole 10, Moscow, 103064 Russia*

***** Götteborg University, Sweden*

****** Institute of Solid-State Physics, Russian Academy of Sciences, Chernogolovka, Moscow oblast, 142432 Russia*

Received November 18, 1999

Abstract—A series of potassium titanyl phosphate crystals, $KTiOPO_4$, with various concentrations of niobium dopant has been grown, and some of their physical properties and structural characteristics have been studied. The incorporation of a small amount of niobium results in considerable changes in the electrical conductivity of KTP : Nb crystals and the temperature of the ferroelectric phase transition. Thus, the presence of 3–4 at. % of niobium results in an increase of conductivity by more than an order of magnitude, whereas T_C decreases from 930 to 620°C. The X-ray diffraction study of the crystals has been performed at room temperature; the neutron diffraction analysis was made at temperatures of 20, 330, and 730°C. It was revealed that two crystallographically independent positions are statistically (by 90%) occupied by potassium cations, which results in the concentration of potassium atoms in the structure higher than it was expected from the condition of preservation of crystal electroneutrality. At high niobium concentrations, the monoclinic compound of the composition $K_2TiNb_2P_2O_3$ is formed. © *2000 MAIK "Nauka/Interperiodica".*

INTRODUCTION

Potassium titanyl phosphate of the composition $KTiOPO_4$ (KTP) and some other crystals of this family and solid solutions on their basis are among the best optical materials and therefore are actively studied. Of great importance are also ferroelectric phase transitions and high ionic conductivity inherent in these crystals. All these properties are rather sensitive to the compositional variations associated with heterovalent substitutions over the wide compositional ranges. The structural characteristics and the properties of KTP-based solid solutions and other compounds of this family are studied by substituting potassium by sodium, rubidium, cesium, thallium, and NH_4; tetravalent titanium by germanium, lead, and other elements, and also phosphorus by antimony [1, 2]. In particular, a number of publications [3–7] are devoted to KTP crystals with tetravalent titanium partly substituted by pentavalent niobium and tantalum. It was shown that such substitution results in the formation of additional vacancies in the K(1) and K(2) positions [3] or only in the K(1) positions [6], with niobium being located mainly in the Ti(1) positions. It should be emphasized that the number of vacancies in the potassium sublattice is higher than it could be expected from the condition of preservation of electroneutrality of the crystals without changes in the valence of other ions [3]. At the same time, the data on the physical properties of KTP : Nb crystals are rather scarce. However, it is known [4] that the substitution of titanium by niobium is accompanied by a considerable increase in birefringence [4]. Moreover, niobium-doped KTP crystals showed drastic jumps in electric conductivity, which amounted to up to three orders of magnitude in the temperature range from 200 up to 250°C [7].

We grew a series of KTP : Nb single crystals with various niobium concentrations and studied the main physical properties and the atomic structures of some of the synthesized crystals by the X-ray and neutron diffraction methods.

SYNTHESIS OF CRYSTALS AND THEIR PHYSICAL PROPERTIES

The $KTiOPO_4$ crystals with a different concentration of niobium dopant were synthesized by the method of spontaneous crystallization from flux in the quaternary K_2O–TiO_2–Nb_2O_5–P_2O system. The melt contained 40 mol % K_2O, 27 mol % P_2O_5, and 33 mol % (TiO_2 + Nb_2O_5). The ratio of the latter two components ranged from 32 : 1 to 13 : 20 (Table 1). The starting mixtures prepared from the corresponding high-purity grade reagents were heated in 50-ml platinum crucibles up to 1100°C; then, in order to provide the mixture

Table 1. Concentration of niobium in the starting melt and grown KTP : Nb crystals and their characteristics

Experiment	Nb/(Nb + Ti), at. %		Crystal composition	Extinction in polarized light	T_m, °C
	melt	crystals			
1	5.9	0.2	$KTi_{0.98}Nb_{0.02}OPO_4$	Direct	1128
2	11.4	2.1	$KTi_{0.95}Nb_{0.02}OPO_4$		1152
3	16.7	3.1	$KTi_{0.95}Nb_{0.03}OPO_4$		1160
4	46.5	11.3	$K_{0.96}Ti_{0.86}Nb_{0.11}OPO_4$		1120
5	66.6	66.6	$K_{2.18}Ti_{1.00}Nb_2P_2O_{13}$	Oblique	1096
6	75.5	71.4	$K_{2.02}Ti_{0.82}Nb_{2.05}P_{1.95}O_{13}$		1080

homogenization, the melts were kept at this temperature for 20 h and then cooled to 850°C at a rate of 1 deg/h. The remaining melt was poured out, and the crystals grown at the crucible walls were washed off from the remained solvent with hot water. Some characteristics of the crystals obtained and the results of their chemical analysis are indicated in Table 1. Usually, the 5–10-mm-long crystals had the shape characteristic of KTP crystals with only one difference: doping with niobium made them somewhat flattened; the {110} faces were often absent. The crystals grown in the last experiments (Table 1) had the same faces but were more isometric than most of other crystals and showed oblique extinction in the polarized light. With an increase of the niobium content, the crystal quality considerably deteriorated, which was also observed earlier [5]. The grown crystals were of light violet color, which disappeared upon an additional 30-min-annealing of the crystals in air at 300–600°C.

The behavior of the crystals grown during heating was studied by the differential thermal analysis with the use of a *Thermoflex* scanning microcalorimeter. The chemical composition of the crystal was determined with the aid of a *Cameca SX-50* microanalyzer. The temperature dependences of the dielectric constant and conductivity were measured with the aid of a *Tesla* BM 431E bridge at a frequency of 1 MHz in the temperature range from room temperature to 800°C. The temperature dependence of the intensity of the second-harmonic generation of the laser radiation was studied by the method similar to that suggested by Kurtz [8]. The chemical compositions of the crystals grown in experiments 5 and 6 were close to $K_2TiNb_2P_2O_{13}$ and, despite their morphological similarity to KTP, these were crystals of quite a different compound. The X-ray diffrac-

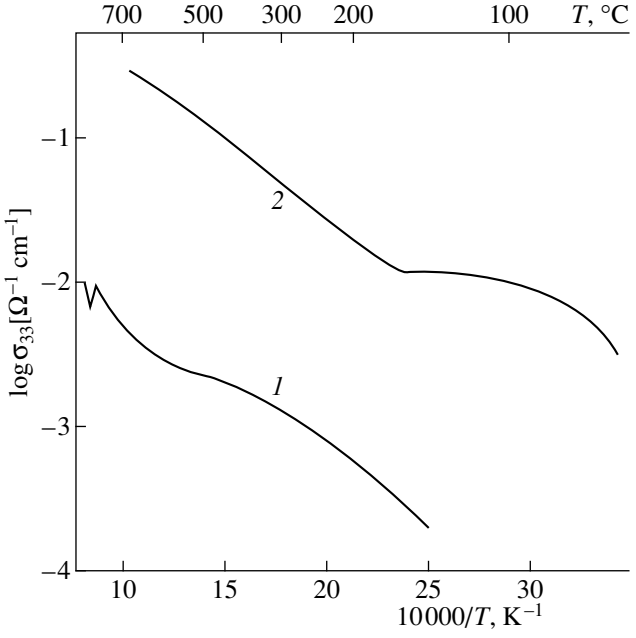

Fig. 1. Temperature dependence of conductivity of (*1*) undoped KTP crystals and (*2*) KTP crystals with 3 at. % Nb.

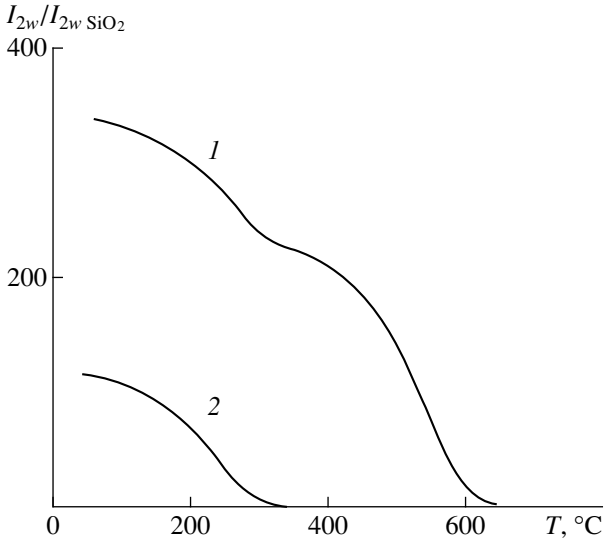

Fig. 2. Temperature dependence of the intensity of the second-harmonic generation during laser irradiation of KTP crystals doped with (*1*) 3 and (*2*) 11 at. % Nb.

Table 2. Experimental conditions and crystallographic data for $K_{0.90}(K_{0.06})Ti_{0.96}Nb_{0.04}OPO_4$ single crystals

Parameter	Data
Chemical composition	$K_{0.90}Ti_{0.96}Nb_{0.04}OPO_4$
Specimen diameter, mm	0.105(1)
μ, cm^{-1}	32.16
Diffractometer	Enraf-Nonius CAD-4F
Radiation	MoK_α
Monochromator	Graphite
Scan	$\omega/2\theta$
Sp. gr.	$Pna2_1$
Unit-cell parameters *a*, *b*, *c*, Å	12.814(2), 6.408(1), 10.587(2)
Range of *h*, *k*, *l*	$-25 \le h \le 25$; $-12 \le k \le 12$; $0 \le l \le 21$
Total number of measured reflections	10052
Total number of independent reflections	2699, $\lvert F\rvert \ge 3\sigma_{\lvert F\rvert}$
$R_{av}(\lvert F\rvert)$	0.010
Structure type	$KTiOPO_4$
Programs used	PROMETEUS, AREN
Weighting scheme	$1/\sigma^2$
Number of refined parameters	147
Reliability factors R/R_w	0.028/0.022

Table 3. Atomic coordinates, occupancies *q* of positions, and equivalent isotropic thermal parameters B_{eq} (Å^2) in the $K_{0.90}(K_{0.06})Ti_{0.96}Nb_{0.04}OPO_4$ structure

Atom	*x*/*a*	*y*/*b*	*z*/*c*	*q*	B_{eq}
Ti(1)	0.3725(1)	0.4999(1)	0	0.920(2)	0.44(1)
Nb(1)	0.3725(1)	0.4999(1)	0	0.080	0.44(1)
Ti(2)	0.2472(1)	0.2673(1)	0.2504(1)	1.000	0.50(1)
P(1)	0.4983(1)	0.3370(1)	0.2587(1)	1.000	0.45(2)
P(2)	0.1815(1)	0.5016(2)	0.5108(1)	1.000	0.47(2)
K(1)	0.1049(1)	0.6968(1)	0.0664(1)	0.891(3)	1.80(3)
K(2)	0.3788(1)	0.7814(1)	0.3103(1)	0.901(3)	1.73(2)
O(1)	0.4858(2)	0.4851(5)	0.1480(3)	1.000	0.79(5)
O(2)	0.5100(2)	0.4678(5)	0.3811(2)	1.000	0.77(7)
O(3)	0.4004(2)	0.2008(4)	0.2791(3)	1.000	0.67(5)
O(4)	0.5939(2)	0.1937(4)	0.2401(2)	1.000	0.63(8)
O(5)	0.1120(2)	0.3112(4)	0.5396(3)	1.000	0.65(7)
O(6)	0.1122(2)	0.6923(4)	0.4861(3)	1.000	0.82(9)
O(7)	0.2530(2)	0.5401(4)	0.6267(3)	1.000	0.78(6)
O(8)	0.2535(2)	0.4615(5)	0.3972(3)	1.000	0.76(5)
O(9)	0.2238(2)	0.0408(5)	0.3882(3)	1.000	0.70(7)
O(10)	0.2246(2)	−0.0356(4)	0.6413(3)	1.000	0.72(8)

tion analysis of theses single crystals showed that their unit cell is monoclinic with the unit cell parameters *a* = 13.7864(7); *b* = 6.4078(3); *c* = 16.9384(7) Å; β = 96.844(4)° and *a* = 13.804(7); *b* = 6.413(1); and *c* = 16.918(9) Å; β = 97.03(1)° (for crystals synthesized in experiments 5 and 6, respectively). The structural characteristics and the physical properties of these crystals will be the subject of another publication.

Table 4. Symmetry and unit-cell parameters of KTP crystals with 3 at. % Nb at three different temperatures

	20°C	330°C	730°C
Sp. gr.	$Pna2_1$	$Pna2_1$	*Pnan*
Unit-cell parameters, Å:			
a	12.8059 ± 0.0011	12.8594 ± 0.0015	12.9190 ± 0.0016
b	6.4041 ± 0.0005	6.4332 ± 0.0006	6.4690 ± 0.0006
c	10.5829 ± 0.0007	10.5760 ± 0.0009	10.5521 ± 0.0009

Conductivity of KTP : Nb crystals are very sensitive to the niobium concentration. Incorporation of only 3 at. % of niobium increased the conductivity by more than an order of magnitude in comparison with the conductivity of undoped ("pure") KTP crystals up to a value of 5×10^{-2} Ω^{-1} $1cm^{-1}$ at 300°C (Fig. 1). In this case, the temperature of the ferroelectric phase transition was considerably lower. Figure 2 shows the temperature dependences of the intensity of the second-harmonic generation upon laser irradiation of crystals containing 3 and 11 at. % Nb. It is seen that T_C of such crystals decreases down to 650 and 320°C in comparison the temperature of 930°C observed in pure (undoped) KTP crystals.

STRUCTURAL DATA

The atomic structure of KTP : Nb crystals was studied by X-ray diffraction analysis at room temperature and by neutron diffraction analysis at 20, 330, and 730°C. Upon preliminary study, a crystal grown in experiment 3 was chosen for the detailed X-ray diffraction analysis. The experimental conditions and the crystallographic data obtained are listed in Table 2. The unit-cell parameters of the orthorhombic crystals were refined over 25 reflections in the least-squares procedure.

It was natural to use as the starting model for the structure refinement the atomic coordinates of pure $KTiOPO_4$ crystals. The least-squares refinement was performed in the full-matrix approximation. At the first stage, it was assumed that Nb atoms substitute titanium in both Ti(1) and Ti(2) positions.

We checked all the three models of allowance for extinction admissible in the PROMETEUS package of programs. The best results were obtained for model 2, which took into account the dimensions of the blocks of mosaics in the crystals. The atomic thermal vibrations were refined in the anisotropic approximation. The occupancies of the crystallographically independent positions with potassium cations were determined as 0.89 for K(1) and 0.90 for K(2), whereas the occupancies with titanium and niobium were $Ti_{0.92} + Nb_{0.08}$ for the Ti(1) positions and $Ti_{1.00}$ for the Ti(2) positions, which led to the chemical formula for the specimen close to $K_{0.90}Ti_{0.96}Nb_{0.04}OP_4$. The refinement of the Ti(1) and Ti(2) occupancies was performed under the assumption that each of these positions is fully (by 100%) occupied by titanium and niobium atoms. The coordinates of the basis atoms in the structure, the occupancies *q* of the crystallographic positions by various atoms, and the equivalent isotropic factors of atomic thermal vibrations, B_{eq}, are listed in Table 3.

It is seen that the occupancy of the positions with potassium cations is lower than could be expected from partial substitution of tetravalent titanium cations only by pentavalent niobium cations [3]. One of possible explanation of this fact can be the formation of new additional positions for potassium atoms in the structure. However, the final answer can be given only after the study of this crystal by the methods of the X-ray diffraction analysis at 15 K. The neutron diffraction analysis of KTP : Nb crystal was performed on crushed crystals grown in experiment 3 (Table 1) at three temperatures—room, 330, and 730°C—on an R2 reactor (Studsvik, Sweden). A two-circle diffractometer with the analyzer consisting of a set of 35 ^{3}He-detectors was used. The intensity readings of all the detectors were statistically averaged and summed up. The monochromator consisted of a system of two parallel (220)-oriented copper crystals. The wavelength was 1.470 Å, with the neutron flux on the specimen being 10^6 cm^{-2} s^{-1}. We studied a 5 g-specimen in a vanadium container. The absorption corrections were introduced during data processing. The scan step of 0.08° provided scanning in the range of 2θ angles from 4° up to 140°. The data obtained were refined by the Rietveld method using the FULLPROF program.

The check of possible space groups during structure refinement (the polar group $Pna2_1$ and the nonpolar group *Pnan*) showed that, in full accordance with the experiments on the second-harmonic generation (Fig. 2), the crystals are described by the noncentrosymmetric sp. gr. $Pna2_1$ at 20 and 330°C, and by the centrosymmetric sp. gr. *Pnan* at 730°C (Table 4). With an increase of the temperature, the *a* and *b* parameters also increase, whereas the *c* parameter decreases, which is consistent with the data for the KTP and $RbTiOPO_4$ (RTP) crystals obtained earlier [9, 10].

Thus, the composition of the crystals at room temperature corresponds to the formula $K_{0.94}Ti_{0.97}Nb_{0.03}OPO_4$. In this case as well, the concen-

tration of potassium vacancies is higher than it could be expected from the conditions of conservation of electroneutrality.

ACKNOWLEDGMENTS

This study was supported by the program *Universities of Russia*, project no. 5017, the Russian Foundation for Basic research, project no. 00-02-16059, and the Program for Leading Scientific School, project no. 00-15-96633.

REFERENCES

1. G. D. Stuchky, M. L. F. Phillips, and T. E. Gier, Chem. Mater. **1**, 492 (1989).
2. M. T. Anderson, M. L. F. Phillips, M. B. Sinclair, and G. D. Stucky, Chem. Mater. **8**, 298 (1996).
3. P. A. Thomas and B. E. Watts, Solid State Commun. **73**, 97 (1990).
4. L. T. Cheng, L. K. Cheng, R. L. Harlow, and J. D. Bierlein, Appl. Phys. Lett. **64**, 155 (1994).
5. J. Wei, J. Wang, Y. Liu, *et al.*, Chin. Phys. Lett. **13**, 203 (1996).
6. G. Moorthy, F. J. Kumar, C. Subramanian, *et al.*, Mater. Lett. **36**, 266 (1998).
7. T. Yu. Losevskaya, E. P. Kharitonova, V. I. Voronkova, *et al.*, Kristallografiya **44** (1), 95 (1999) [Crystallogr. Rep. **44**, 90 (1999)].
8. S. K. Kurtz and T. T. Perry, J. Appl. Phys. **39** (8), 3798 (1968).
9. P. Delarue, C. Lecomte, M. Jannin, *et al.*, J. Phys.: Condens. Matter **11**, 4123 (1999).
10. P. Delarue, C. Lecomte, M. Jannin, *et al.*, Phys. Rev. B **58** (9), 5287 (1998).

Translated by L. Man

Crystallography Reports, Vol. 45, No. 5, 2000, pp. 744–753. Translated from Kristallografiya, Vol. 45, No. 5, 2000, pp. 814–823.

STRUCTURES OF INORGANIC COMPOUNDS

$Na_{0.5}Pb_2[B_5O_9]Cl(OH)_{0.5}$, a New Polar Variety of Hilgardite Containing Na^+ Cations in the Cavities of the Framework. The *OD*-Family of the 5: 2△ + 3◸ Pentaborates: Hilgardites, Heidornite, Probertite, and Ulexite

E. L. Belokoneva, T. A. Korchemkina, O. V. Dimitrova, and S. Yu. Stefanovich

Moscow State University, Vorob'evy gory, 119899 Russia

e-mail: elbel@geol.msu.ru

Received July 28, 1999

Abstract—A new orthorhombic polar variety of Pb-hilgardite containing Na^+ and $HOCl^{2-}$ ions in the cavities of the framework has been prepared by hydrothermal synthesis. A correlation between the structural features and nonlinear-optical properties of the crystals is discussed. Similar to the hexaborate group, pentaborates with different degrees of condensation of the boron–oxygen radical are characterized by close structural similarity, which is described within the *OD* theory with distinguishing structural units (blocks or modules) of different dimensionality—bricks, rods, and layers. Consideration of the variants of their connection allows us to describe the diversity of the pentaborate family including hypothetical structures. *© 2000 MAIK "Nauka/Interperiodica".*

INTRODUCTION

Lead borates are of interest to material-science researchers, because compounds with nonlinear-optical properties have been found in this class [1, 2]. Earlier, we prepared a new nonpolar modification of Pb-hilgardite and determined its single-crystal structure [3]. Concurrently, a powder of a polar phase was obtained. According to the test for the second harmonic generation, this phase exhibited nonliner-optical properties, and its X-ray diffraction pattern indicated probable structural similarity to the natural polar hilgardite [3]. In the present work, we performed the directed synthesis of the polar modification, determined the conditions of its formation, prepared single crystals, solved the crystal structure, and established the correlations between the structure and properties. The specific structural features of the hilgardite *OD*-family described in [3] were considered in more detail, and the family was extended by addition of the structures of other pentaborates.

EXPERIMENTAL

Lead borates in the $PbO–B_2O_3–H_2O$ system were prepared by the hydrothermal synthesis in standard autoclaves lined with fluoroplastic. As is known, the conditions of formation of natural polar hilgardites correspond to the chloride "brines" [4, 5]. In order to obtain their analogues, alkali metal chlorides, bromides, and iodides were added to the carbonate solution. The batch consisted of the oxide mixture. The synthesis proceeded at T = 250°C and P = 30–300 atm for 20 days. Colorless transparent crystals were obtained. In most experiments, they had a shape of either small prisms or thin needles. The crystals were small, up to fine-grained powder. Only in one experiment, prismatic crystals up to $0.6 \times 0.1 \times 0.1$ mm in size were obtained; one of them was chosen for crystal structure determination.

The compounds synthesized were tested for the second harmonic generation (SHG) with an YAG : Nd pulsed laser operating in a reflecting mode [2, 6]. The intensity of the second-harmonic signal $I_{2\omega}$ was within 80–300 SiO_2 units (powder α-quartz as a standard), which indicated the absence of the center of symmetry and a high optical nonlinearity of the substances synthesized. Crystals of natural polar hilgardite (space group *Aa*) were earlier tested for SHG with a Nd–glass laser [4]. The intensity of their signal was comparable to that of quartz, indicating their weak nonlinear-optical activity. The synthetic variety of hilgardite prepared in this work exhibits much more pronounced nonlinear-optical properties.

The powder X-ray diffraction diagnostics was performed on a DRON-UM1 diffractometer (Co radiation; 40 kV; 25 mA; 0.05°-step scans; exposure, 2 s per point). The identical X-ray diffraction patterns of the crystals obtained in different experiments indicated that all of them corresponded to the same modification of synthetic hilgardite. However, its X-ray spectrum was simpler than that of the Pb-hilgardite studied earlier in [3].

Unit cell parameters characteristic of the hilgardite family were chosen from a set of vectors of the reciprocal and direct lattices that was obtained by a routine

procedure on a Syntex $P\bar{1}$ diffractometer. The parameters were refined using 15 large-angle reflections. Two longer translation vectors (a = 11.51 Å and b = 11.45 Å) were perpendicular to the planes of symmetry in the oscillating-crystal X-ray photographs that were obtained on the diffractometer. These vectors were much closer in length than the corresponding vectors in all the hilgardites reported. This suggests that we deal with the orthorhombic polar variety of hilgardite with space group *Pnn*2. Its structure (the first in the hilgardite family) was determined in [7], refined in [8], and considered as a member of the *OD*-family in [3]. Earlier, an attempt to determine the structure of this polar Pb-hilgardite variety was undertaken for thin-needle crystals, which have a similar X-ray diffraction pattern. Heavy Pb atoms were located and refined; however, the complete structure determination failed. Our study showed that single crystals of this group of polar compounds are characterized by twinning due to pseudosymmetry. Pseudotetragonality of hilgardites ($a \approx b$) was noted in [7]. In the crystal under study, the pseudosymmetry is more pronounced than in other compounds, since the difference in the lengths of the axes is only 0.06 Å. This results in a relative simplicity of the X-ray diffraction pattern of the orthorhombic pseudotetragonal phase in comparison with the pattern of the monoclinic phase studied earlier. We also found pseudohexagonality of the *a*-axis (a = 11.51 Å): in the (100) plane, two pseudotranslation vectors that are equal in length to the *c* parameter ($c \cong 6.6$ Å) and form angles of 60° with the *c*-axis are observed.

The crystal data and data collection parameters are listed in Table 1. The intensities were processed and converted into F^2_{hkl} with the PROFIT program [9]. All further calculations were performed with the CSD program package. Analysis of systematic absences (*h*0*l*: $h + l = 2n$ and 0*kl*: $k + l = 2n$) confirmed the presence of two *n* planes and space group *Pnn*2, the same as in the earlier-studied $Ca_2B_5O_9Br$ [7] and $Eu_2B_5O_9Br$ [8]. The refinement of the starting atomic coordinates found in [7, 8] was unsuccessful. Analysis of the Patterson map P_{uvw} revealed two Pb atoms at the general positions. Their refinement led to R_{hkl} = ~0.17. A series of difference electron-density syntheses revealed first the atoms with a higher scattering power, i.e., the Cl atoms at the special positions on the 2 axes inside the channels of the framework, and then the atoms of the boron–oxygen radical. Analysis of the structure determined shows that it is similar to the structures studied earlier [7, 8] and transforms into the Eu-borate structure [8] upon shift of the origin by 1/2 along the *a*-axis and the following interchange of axes: $a_{Eu} \longrightarrow b_{Pb}$, $b_{Eu} \longrightarrow -a_{Pb}$, and $c_{Eu} \longrightarrow -c_{Pb}$ (the longer of the two axes close in length is changed for the shorter one). The symmetry of the atomic arrangement is close to space group $P\bar{4}n2$ with the inversion axes $\bar{4}$ (the special point lies at z = 0.405) instead of the 2 axes. In this structure, the tetragonal pseudosymmetry is more pronounced than that in Eu- and Ca-borates because of the higher scattering power of Pb atoms. The hexagonal pseudosymmetry, which was revealed by the vector analysis, is due to the formation of the hexagonal networks of Pb(1) atoms at the 1/4 and 3/4 levels of the *a*-axis (the *bc* projection in Fig. 1b).

Table 1. Crystal data, data collection, and refinement parameters

Space group	*P n n* 2
a, Å	11.51(1)
b, Å	11.45(4)
c, Å	6.563(4)
V, Å^3	865(4)
d_{calcd}, g/cm^3	5.20(3)
μ, cm^{-1}	388.4
Crystal size, mm	$0.19 \times 0.10 \times 0.05$
Diffractometer	Sintex $P\bar{1}$
Radiation	MoK_α, 0.71069
Scan mode	2θ–θ
Scan speed	4 deg/min
2θ and sinθ/λ, Å^{-1}(max)	92.35°, 1.015
No. of measured reflections	1429
Criterion for observed rflections	$F_{hkl} > 4.00\sigma(F)$
Weighting scheme	$1/[\sigma(F)^2 + 0.0050F^2]$
No. of atomic positions	20
R, R_w	0.0695, 0.0792
Scale factor (K)	0.723(3)
S	1.080

It has been noted that pentaborates in hilgardites have zeolite-like structures [4, 5]. Unlike all the hilgardites studied earlier, the new polar variety exhibits a radically different population of the structural channels. Upon location of all atoms of the framework, the electron-density peaks inside the channels were analyzed. Based on the crystal-chemical role in the structure and the results of the refinement of the thermal factors, three of the peaks were identified with the Cl(1) anion on the 2 axis, the Cl(2) anion at a half-occupied general position, and the O atom of the OH group on the 2 axis. There was one more high peak of the electron density on the 2 axis in the channel. Based on its height, anionic environment, and interatomic distances, as well as the composition of the batch, it was identified

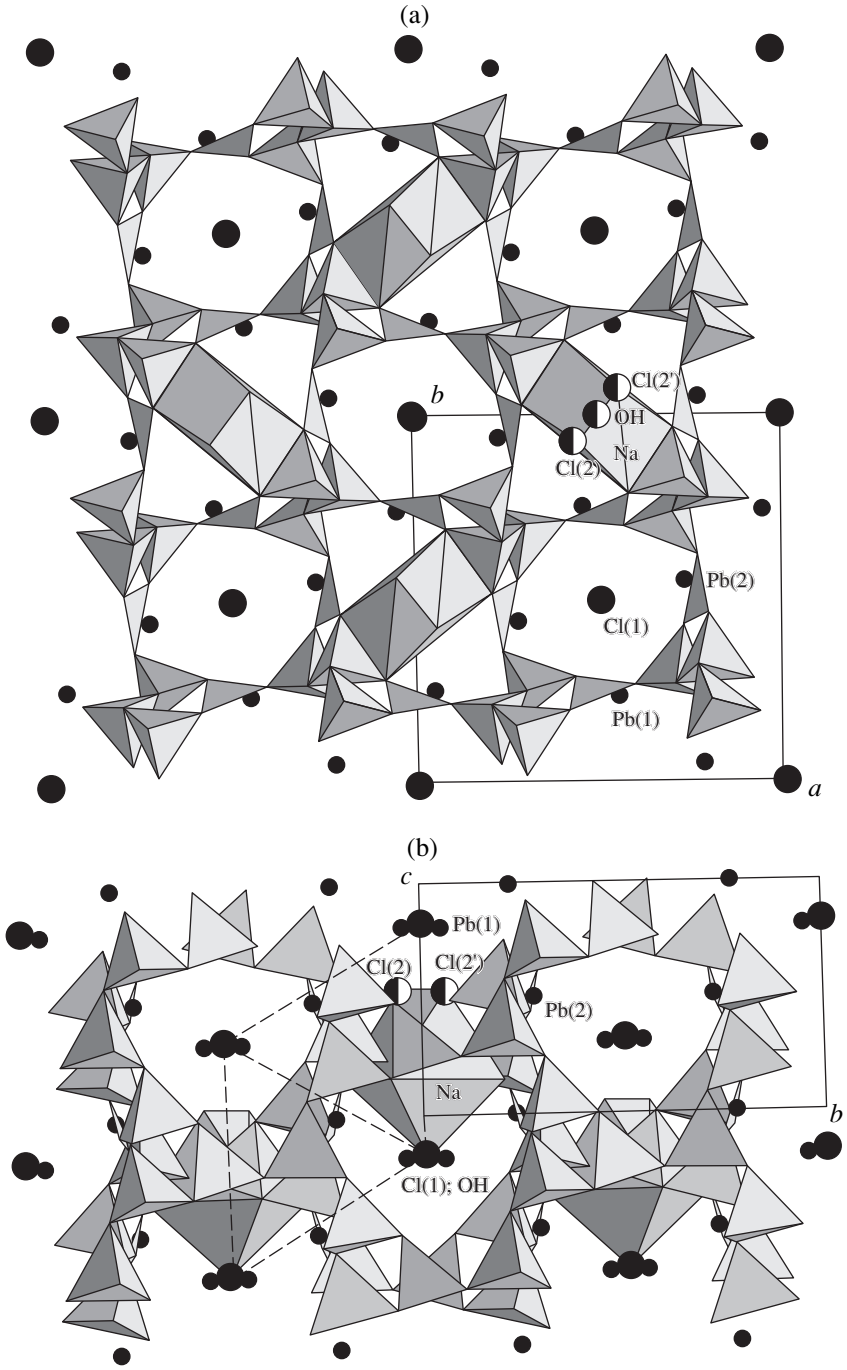

Fig. 1. Projections of the crystal structure of $Na_{0.5}Pb_2[B_5O_9]Cl(OH)_{0.5}$ onto the (a) *ab* and (b) *bc* planes. The Pb and Cl atoms and the OH group are shown by the circles. The B and Na atoms are represented by polyhedra. The half-closed circles of the Cl(2) atoms indicate that the position is occupied by half.

with the Na atom. The X-ray microanalysis (Camebax SX-50) confirmed the presence of sodium and chlorine atoms in the crystals.

The high double pseudosymmetry interfered in the refinement of even the positional parameters. Indeed, the coordinates of the O(8) and O(9) atoms were obtained from the high-resolution (0.13 Å) difference syntheses. The Pb and Na atoms were refined in the anisotropic approximation of thermal vibrations, and the rest of the atoms were refined isotropically. The data were corrected for anomalous dispersion. Strong absorption and its pronounced anisotropy motivated the correction of the data at the final stage with the DIFABS program [10]. The final indices of refinement (S = 1.08) are given in Table 1, and the atomic coordinates are listed in Table 2.

DESCRIPTION OF THE $Na_{0.5}Pb_2[B_5O_9]Cl(OH)_{0.5}$ STRUCTURE

In the structure of Na,Pb-hilgardite, the boron atoms have a tetrahedral or a trigonal coordination. The interatomic B–O distances have the normal values: in the B(1) and B(3) triangles, the distances lie in the range 1.34–1.43 Å; and in the B(2), B(4), and B(5) tetrahedra, the distances are within 1.43–1.53 Å. In the structure, we can distinguish the polar $[B_5O_{11}]^{7-}$ chains, which condense first into the $[B_5O_{10}]^{12-}$ layers and then into the $[B_5O_9]^{3-}$ framework. The framework of the structure is identical with that in the Ca- and Eu-borates. It is polar along the *c*-axis: all the tetrahedra point toward the same direction of this axis (Fig. 1a).

The arrangement of Pb atoms follows the fourfold inversion pseudosymmetry. In the *ab* projection (Fig. 1a), the Pb atoms approach the walls of intersecting channels, and, in the *bc* projection (Fig. 1b), they are located at the centers of the channels. The Pb atoms have nine- and ten-vertex coordination polyhedra. The polyhedron of the Pb(1) atom consists of the O(2), O(3), O(4), O(5), O(6), O(7), O(8), Cl(1), and Cl(2) atoms (the interatomic distances vary between 2.49 and 3.37 Å), and the polyhedron of the Pb(2) atom includes the O(1), O(2), O(3), O(4), O(7), O(8), O(9), Cl(1), and Cl(2) atoms and the OH group (the distances are within 2.43–3.01 Å). There is an asymmetry in the arrangement of the bonds with respect to the polar axis, which differs from a more symmetric bond arrangement in the centrosymmetrical Pb-hilgardite.

In distinction to lead, the Na atoms are located at the centers of the channels in the *ab* projection and approach their walls in the *bc* projection. The coordination polyhedron of the sodium atom is a distorted octahedron with the twofold rotation symmetry (Figs. 1a, 1b). Its square section is formed by the O atoms at the Na–O distances of 2.38 and 2.54 Å. The apices are formed by the OH group (2.38 Å) and the Cl(2) atom [the Na–Cl(2) distance is 2.58 Å] at the general position. Two Cl(2) positions related by the twofold rotation axis are closely spaced [the Cl(2)–Cl(2') distance is 2.08 Å], so that actually they are occupied statistically (the site multiplicity is 1/2). The $HOCl^{2-}$ groups with the O–Cl distance of 2.10 Å are distinguished in the structure above and below the Na-polyhedra. These groups consist of the OH groups and the Cl(2) atoms and are directed along the *c*-axis. The upper part of each framework cavity (Fig. 1b) is occupied by the Na^+ ions, and the lower part contains the $HOCl^{2-}$ group. The HOCl molecule was described in the literature [11]; it exists only in a solution and has the O–Cl distance of 1.70 Å. The charges are distributed over the channel as follows. The positive charge of the Na atom is predominantly compensated by the charge of the closely spaced OH group, which additionally coordinates the Pb atom. The negative charges of the Cl atoms in the channels are compensated by the Na and Pb cations. For the structure under study that contains heavy Pb atoms and shows strong absorption and pseudosymmetry, we have made no attempts to locate the position of the H atom. Our structural results corroborate the zeolite-like type of the hilgardite structures; in particular, in the new variety, the Na^+ ions and acid $HOCl^{2-}$ groups are trapped in the cavities. The direct ion exchange in hilgardites is observed for the first time. The framework of the structure and the population of the cavities are polar along the *c*-axis, which results in a pronounced optical nonlinearity of the crystals. Piezoelectric and nonlinear-optical properties of natural hilgardite [4] were associated with the polarity of the framework only along the *a*- and *c*-axes, because it is nonpolar along the unique *b*-axis.

Table 2. Atomic coordinates and thermal parameters in the structure of $Na_{0.5}Pb_2[B_5O_9]Cl(OH)_{0.5}$

Atom	*x*/*a*	*y*/*b*	*z*/*c*	B^*_{eq}/B_{iso}
Pb(1)	0.0561(1)	0.2252(6)	0	1.54(2)
Pb(2)	0.7577(1)	0.5461(1)	0.3125(3)	1.08(2)
O(1)	0.205(2)	0.068(2)	0.491(4)	0.8(3)
O(2)	0.296(2)	0.084(2)	0.161(4)	0.9(3)
O(3)	0.782(2)	0.203(2)	0.573(3)	0.5(3)
O(4)	0.334(2)	0.236(2)	0.417(4)	0.5(3)
O(5)	0.473(2)	0.205(2)	0.158(3)	0.8(3)
O(6)	0.938(2)	0.226(2)	0.318(4)	0.8(2)
O(7)	0.242(2)	0.204(2)	0.747(3)	0.1(1)
O(8)	0.6320	0.2330	0.9350	1.1(1)
O(9)	0.7786	0.0929	0.252	0.7(3)
O(10)	0.2739(7)	0.002(2)	0.6061(7)	1.4(2)
B(1)	0.2447	0.0170	0.3170	0.8(3)
B(2)	0.808(2)	0.200(2)	0.349(4)	0.1(1)
B(3)	0.515(2)	0.240(2)	0.978(4)	0.2(2)
B(4)	0.234(2)	0.194(2)	0.520(5)	0.3(3)
B(5)	0.343(2)	0.205(2)	0.199(5)	0.2(2)
Cl(1)	0	0	0.831(4)	3.9(4)
Cl(2)**	0.571(2)	0.056(2)	0.545(5)	3.8(5)
OH	0.5	0	0.822(7)	1.9(5)
Na	0.5	0	0.185(4)	1.2(4)

* $B_{eq} = 1/3[B_{11}a^{*2}a^2 + ... 2B_{23}b^*c^*bc\cos\alpha]$.
** Site occupancy is 0.5.

STRUCTURES OF HILGARDITES, HEIDORNITE, PROBERTITE, AND ULEXITE AS MEMBERS OF THE COMMON *OD*-FAMILY WITH BUILDING BLOCKS (MODULES) OF DIFFERENT DIMENSIONALITY

Ghose and Wan [4] considered the genesis of hilgardite and pointed out a series of pentaborate structures.

In these structures, the pentaborate group (polyanion) consisting of two triangles and three tetrahedra 5: (2△ + 3◪) polymerizes with water release to form the structures containing radicals with different degrees of condensation: the isolated $[B_5O_6(OH)_6]^{3-}$ group in the structure of ulexite $NaCa[B_5O_6(OH)_6]$, the $[B_5O_7(OH)_4]^{3-}$ chain in probertite $NaCa[B_5O_7(OH)_4]$, the $[B_5O_8(OH)_2]^{3-}$ layer in heidornite $Na_2Ca_3[B_5O_8(OH)_2]Cl(SO_4)_2$, and the $[B_5O_9]^{3-}$ framework in hilgardite $Ca_2[B_5O_9]Cl \cdot H_2O$. The condensation is accompanied by a decrease in the number of the hydroxyl groups in terminal (unshared) vertices of the B triangles and tetrahedra in these structures. It was concluded that at high temperatures, hilgardite is formed with a higher probability than ulexite [4].

The structural features of the hexaborate group, which includes macallisterite, aristarainite, strontioginorite (ginorite and volkovite), tunellite (nobleite), strontioborite, and the new Pb-borate, were determined in [12]. All the structures are based on the same building blocks: nondimensional isolated groups (according to [13], bricks), which condense into one-dimensional chains (rods [13]) and two-dimensional layers. All of them belong to the same structural *OD*-family and are characterized by the groupoids of symmetry of different ranks. Here, we analyze the structural features of the pentaborate group within the same approach as we used earlier for hexaborates.

Diversity of the hilgardite structures containing two-dimensional blocks (layers) based on the OD-groupoids of symmetry. As shown in [3], natural monoclinic hilgardite [4], synthetic orthorhombic phases [7, 8], and the new Pb-hilgardite [3] are polytypes and belong to the same *OD*-family. The diversity of structures in this family is due to the condensation of identical $[B_5O_{10}]^{5-}$ layers of symmetry *n* (λ-*PO*) into a framework through the association of their constituent polar $[B_5O_{11}]^{7-}$ chains (related by the *n* plane) into a layer (Figs. 1, 2). Each two layers are interrelated by one of the three σ-*PO* operations: centers of symmetry $\bar{1}$ [3], the *a* planes [4], or 2 axes [7, 8, and this work]. This family is described by the *OD*-groupoid of symmetry

$$\begin{matrix} P\ \ 11\ \ (n) & \lambda\text{-}PO, \\ \{1\ \ 1\ \ (\bar{1}\|a\|2)\} & \sigma\text{-}PO. \end{matrix} \qquad (1)$$

According to [13], each structure characterized by a single σ-*PO* ($\bar{1}$, 2, or *a* [3]) is a polytype with the maximum degree of order (the *MDO* polytype). Different periodic sequences of σ-*PO* operations result in peri-

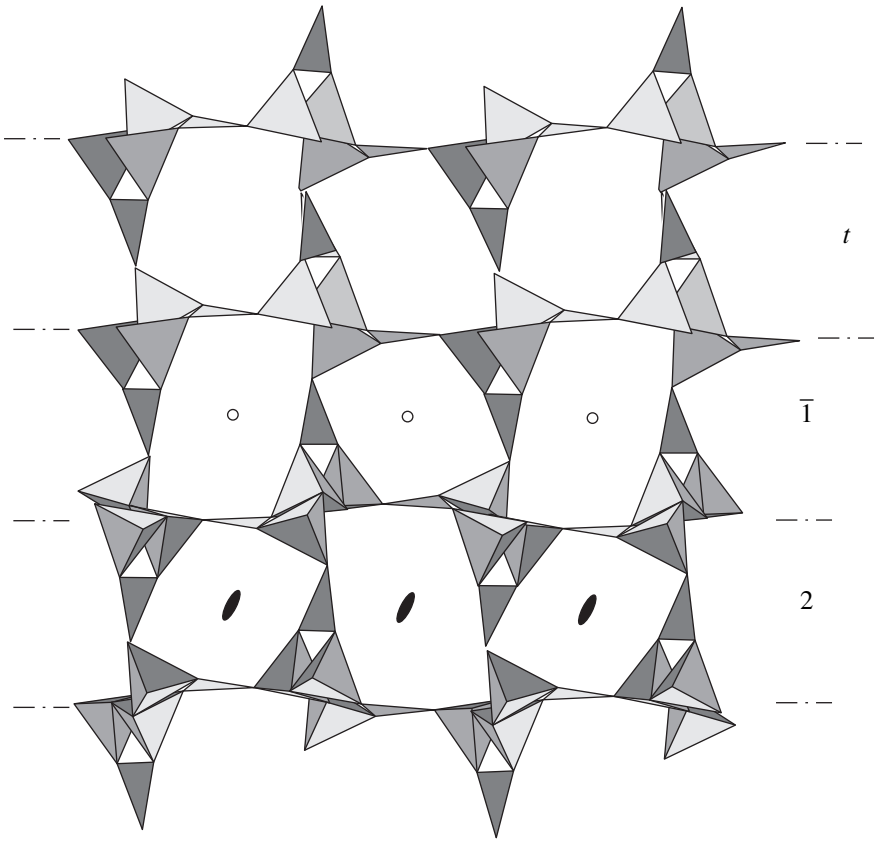

Fig. 2. Patterns of arrangement of the nonpolar layers with symmetry *n*, related by the λ-*PO* operations (translation *t*, center of symmetry $\bar{1}$, and axis 2).

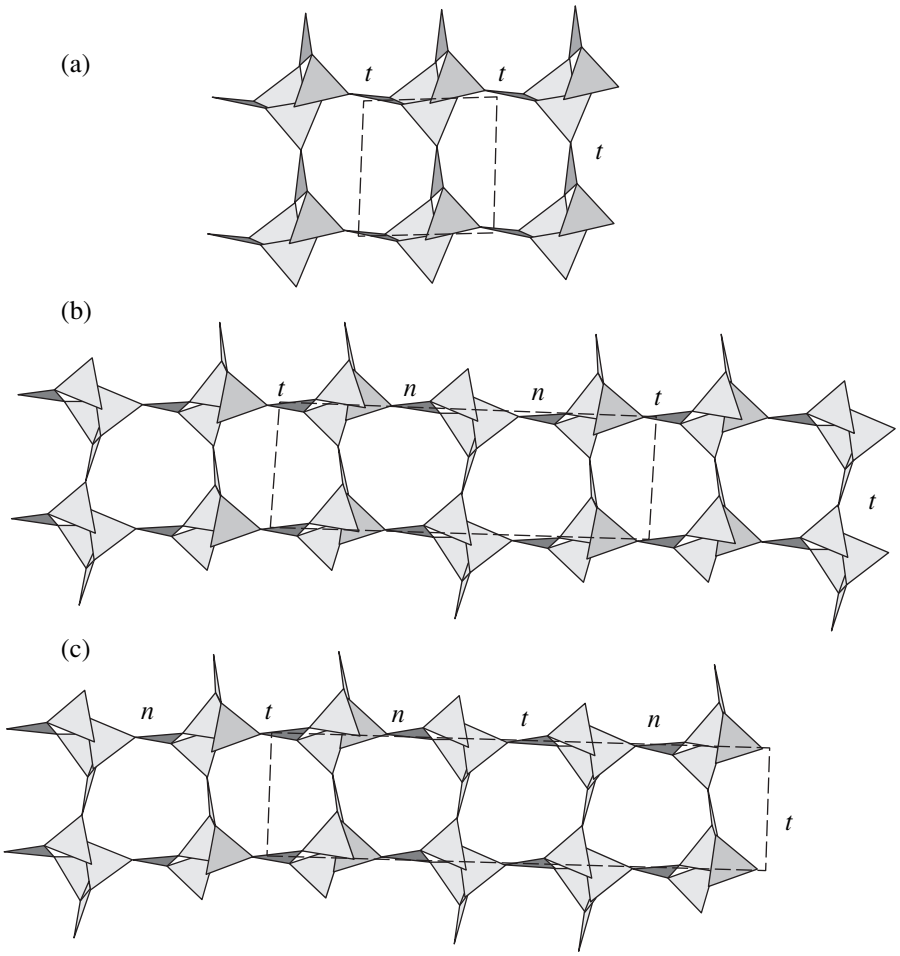

Fig. 3. Arrangement of the polar layers related by translation *t*. The sequence of operations in the layer: (a) *t*, *t*; (b) *t*, *n*, *n*, *t*; and (c) *n*, *t*, *n*, *t*.

odic structures. Figure 2 shows the alternation of the *n*-symmetry layers related by the twofold axes 2, centers of symmetry $\bar{1}$, and translation *t*. One can derive different hypothetical structures (including the structures with very long periods, that is, a low degree of order) and determine their unit cell parameters and space groups.

Depending on the characteristics of the polarity of the layer and the type of its repetition, three classification categories were proposed for the *OD*-structures in [13]: (**I**) the nonplanar λ-ρ layer is repeated by a nonpolar symmetry operation σ-ρ, (**II**) the polar λ-τ layer is repeated by a polar operation σ-τ, and (**III**) the polar λ-τ layer is repeated by a nonpolar operation σ-ρ. The *OD*-groupoid (1) describes the *MDO* polytypes and periodic structures belonging to category **I**.

Two triclinic hilgardites included in the *OD*-family considered [3] consist of the polar λ-τ layers of symmetry 1. This polarity results from the repetition of the chains in the layer by translations *t* in the triclinic hilgardite or the *n*, *n*, *t* sequence of symmetry operations in parahilgardite. The structural character of the layers dictates only the σ-τ character of their arrangement along the axis of alternation. Figure 3 shows three polytypes corresponding to (a, b) two natural triclinic hilgardites and (c) a hypothetical one, in which the alternation of the chains in the layer follows the *n*, *t*, *n*, *t* sequence of operations. The in-layer translation parameter is ~5.7 Å for the first polytype, ~5.7 Å × 3 for parahilgardite, and ~5.7 Å × 4 for the hypothetical structure. The probability of the existence of the last structure is low, since it has a larger parameter. In addition to the σ-τ operation *t*, the σ-τ operation 2*t* perpendicular to the layer is possible. In this case, the period along the layer is ~5.7 Å, and in the direction of the layer repetition, it is ~5.7 Å × 2 (Fig. 4a), that is, twice as long as the usual translation (Fig. 3a). The same is true for two other polytypes, which are characterized by the *n*, *n*, *t* and *n*, *t*, *n*, *t* sequences of operations. All these polytypes belong to category **II**. The *OD*-groupoid for this category of the *OD*-family under consideration can be

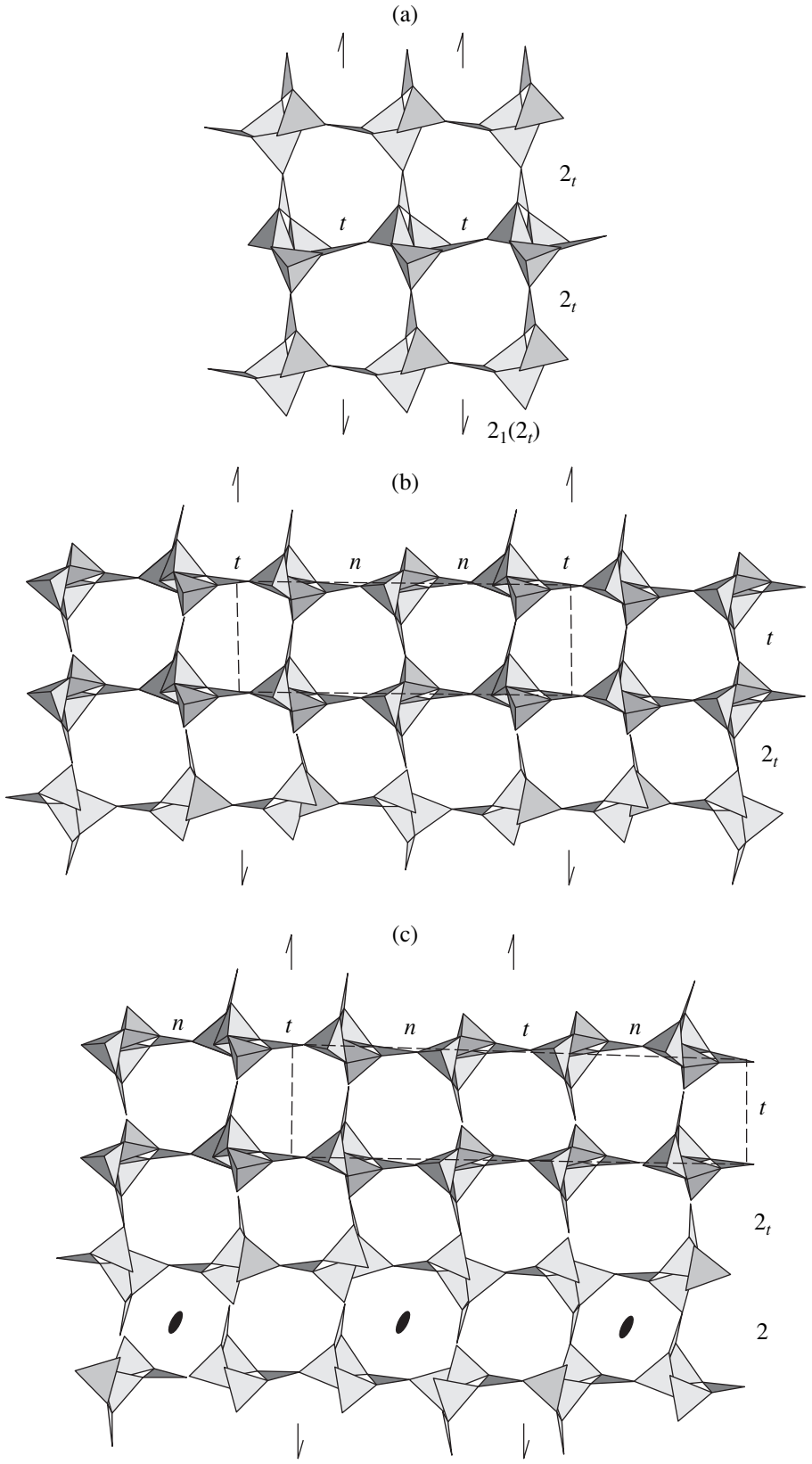

Fig. 4. Connection of the same three layers as in Fig. 3 by other possible symmetry operations: (a) 2_t; (b) $2_{t,}\ t$; and (c) 2, 2_t, t.

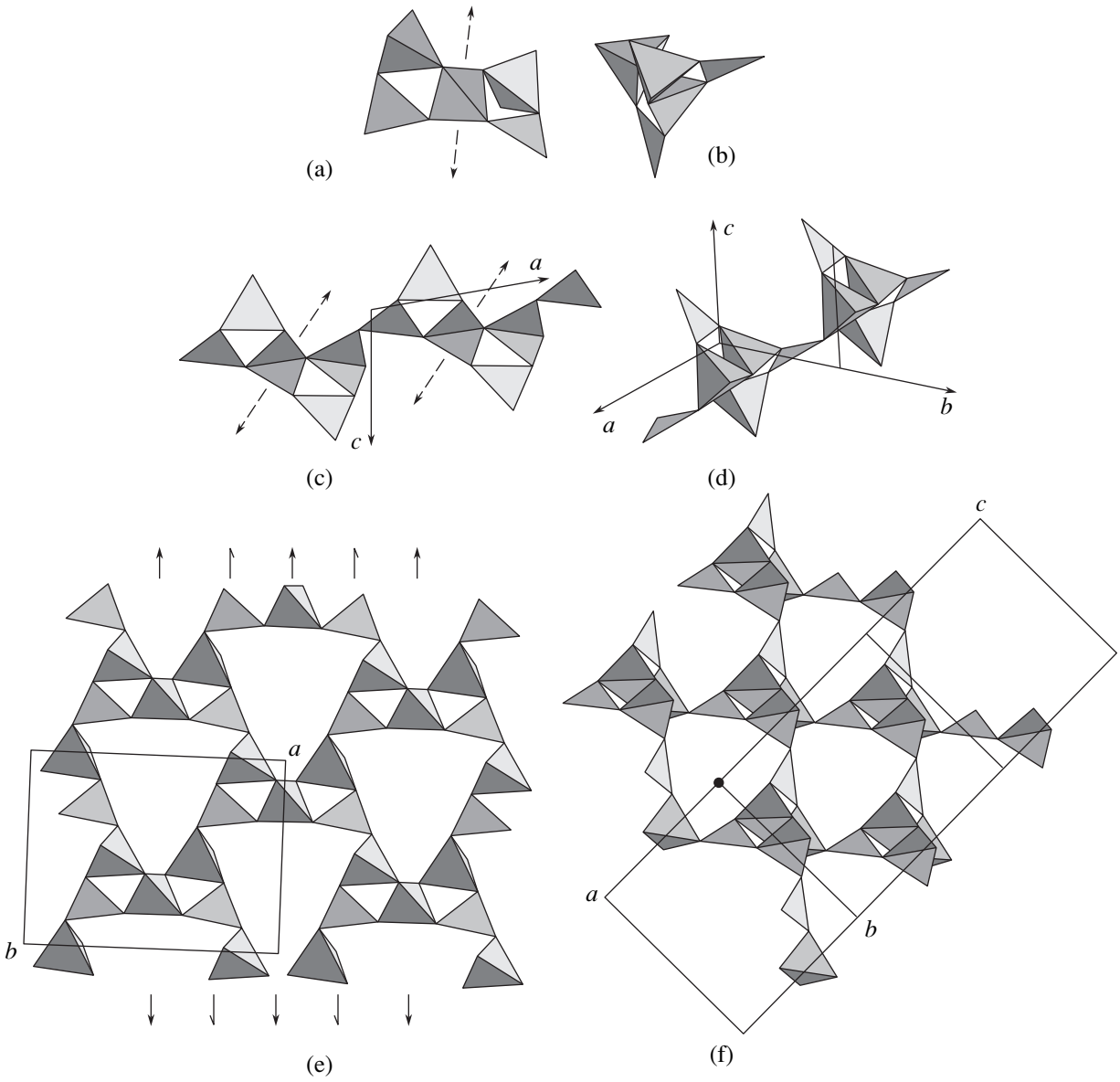

Fig. 5. Two views of common blocks (modules) with different degrees of condensation and periodicity for three minerals: (a, b) ulexite, (c, d) probertite, and (e, f) heidornite.

represented as

$$\begin{aligned} &P\ \ 11\ \ (1)\quad \lambda\text{-}PO, \\ &\{1\ \ 1\ \ (t\|2_t)\}\qquad \sigma\text{-}PO. \end{aligned} \tag{2}$$

Note that if a pair of chains is considered as a structural unit, the layer characterized by the *n*, *t*, *n*, *t* sequence of operations takes on the λ-ρ character, and the diversity of structures on its base can be obtained by the *OD*-groupoid (1) but with the occurrence of the σ-ρ operations in every two channels (Fig. 4b).

The parameters of the hilgardite phases, whose structures are unknown but can be predicted from the symmetry-group analysis, were reported in [7]. The monoclinic phase with the parameters a = 11.35 Å, b = 11.12 Å, c = 6.20 Å, and β = 90° is natural hilgardite [4]. The triclinic phase with the parameters a = 11.24 Å, b = 22.28 Å, c = 6.20 Å, α = 90°, β = 90°, and γ = 90° most likely is a polytype, in which the chains are related in the λ-τ layer by the *n*, *n*, *t*, *t* sequence of symmetry operations, which results in a period of ~22 Å, and the layers are repeated by the σ-τ operation 2_t, which results in a period of ~11 Å (a fragment of Fig. 4c) and a polar triclinic structure. In an alternative variant of the structure, the chains follow the *nn* sequence of operations to form the λ-layer with a period of ~11 Å, and the repetition of layers follows a sequence, in which four independent layers are related by any combination of symmetry elements (for example, as in Fig. 2), which corresponds to a period of ~22 Å. Such a structure has a low degree of order.

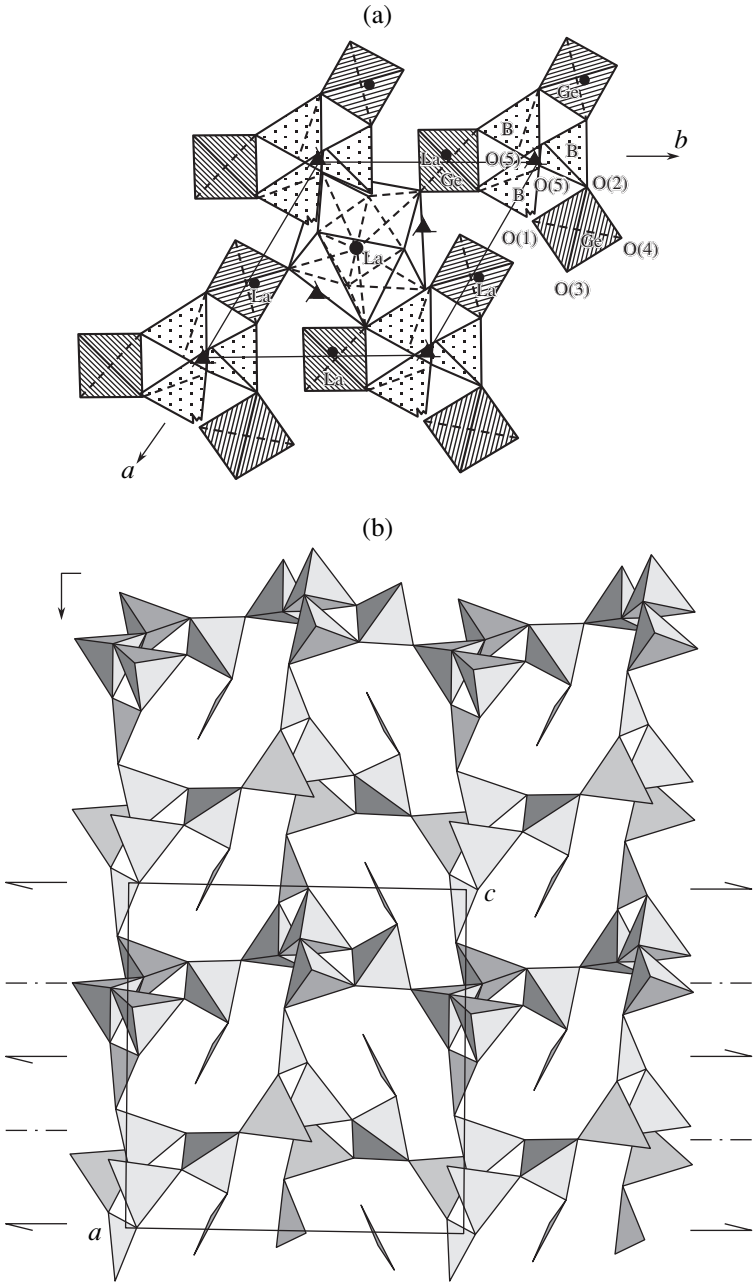

Fig. 6. Structures with tetrahedral "framing" of helical B–O chains: (a) stillwellite (three tetrahedra per translation unit) and (b) CaB_2O_4 (a tetrahedron and a triangle per translation unit).

Structural unity of pentaborates described within the symmetry-group analysis by identical blocks or modules with different degrees of condensation: from the bricks (nondimensional blocks) to the rods (one-dimensional blocks) and layers (two-dimensional blocks). Figures 5a and 5b show two views of the boron–oxygen pentaradical 5: $2\triangle + 3\boxslash$ $[B_5P_6(OH)_6]^{3-}$. It contains six OH groups at the unshared vertices, and its symmetry is described by a 2 pseudoaxis. In fact, it is a fragment of the helical chain that forms hilgardite layers. This radical can be considered a nondimensional block (brick), i.e., an elementary building block of the common pentaborate family. In the structure of propertite, these blocks condense to form a radical with the one-dimensional periodicity (the 2 pseudoaxes are retained), i.e., a chain with the formula $[B_5O_7(OH)_4]^{3-}$ (Fig. 5c). A view of the structure along the direction close to the body diagonal of the unit cell (Fig. 5d) shows that the chain is a fragment of the hilgardite layer. It is characterized by the one-dimensional periodicity with condensation of the nondimensional blocks in a "horizontal" direction. In the structure of

heidornite, the $[B_5O_8(OH)_2]^{3-}$ layer (Figs. 5e, 5f) has the *C*2 symmetry, that is, the 2 pseudoaxes become true axes. This layer is a "horizontal" fragment of the hilgardite framework. The type of the block repetition here is the two-dimensional variant of that in the polar triclinic hilgardite (λ-τ-*t* and σ-τ-*t*).

Thus, in the pentaborate family (6.*E* according to the Strunz terminology [14]), as well as in the hexaborate family, a number of minerals show close structural similarity, because they consist of identical blocks (modules) condensed to different degree. These are a nondimensional block in ulexite (*6.EA.15*), a one-dimensional periodical block in probertite (*6.EB.15*), a two-dimensional periodical block in heidornite (*6.EC.15*), whose symmetry differs from that of hilgardites, and, finally, a three-dimensionally condensed block in the hilgardite group (*6.ED.05*). This similarity allows us to include them in the *OD*-family, which is described by two groupoids of the same rank [(1) and (2)] and one groupoid with a lower rank [3]. Up to now, the structures containing isolated chains with the one-dimensional periodicity in the "vertical" direction, which have been described in [3, 4], are unknown. The structure of mineral stillwellite is characterized by isolated helical chains of B-tetrahedra. These chains are framed by three tetrahedra per translation unit, not two triangles as in hilgardites (Fig. 6a). The chains in stillwellite and hilgardite were compared in [3]. The hybrid chains were found in the high-pressure phase of CaB_2O_4 [15]: the translation unit of a helical chain consisting of B-tetrahedra is linked with a triangle and a tetrahedron with an additional terminal B-triangle (Fig. 6b). Similar to hilgardite, the chains are linked into the layer of the *n* symmetry. This means that the family becomes wider due to the possible existence of the structures characterized by combinations of these types of layers.

CONCLUSION

A directed search for the crystals exhibiting nonlinear-optical properties led us to the synthesis of a new polar variety of Pb-hilgardite. Application of the *OD*-theory of symmetry-group analysis allowed the systematization of the known structures of hilgardites within the common family and the prediction of possible polytypes, which can exist in nature along with the reported compounds or be synthesized for the material-science purposes. Most structures considered are polar; therefore, they are candidates for nonlinear-optical studies. The group of pentaborates, similar to hexaborates, is characterized by a "genetic" unity of structures, since they are built of identical nondimensional blocks (modules), which form one-dimensional, two-dimensional, and three-dimensional anionic radicals that correspond to different degrees of condensation and periodicity.

ACKNOWLEDGMENTS

The authors are grateful to I.S. Bryzgalov for the determination of the crystal composition.

This work was supported by the Russian Foundation for Basic Research, project no. 98-03-32719a.

REFERENCES

1. D. L. Corker and A. M. Glazer, Acta Crystallogr., Sect. B: Struct. Sci. **52**, 260 (1996).
2. R. K. Rastsvetaeva, A. V. Arakcheeva, D. Yu. Pushcharovsky, *et al.*, Z. Kristallogr. **213**, 1 (1998).
3. E. L. Belokoneva, O. V. Dimitrova, T. A. Korchemkina, and S. Yu. Stefanovich, Kristallografiya **43**, 864 (1998) [Crystallogr. Rep. **43**, 810 (1998)].
4. S. Ghose and C. Wan, Am. Mineral. **64**, 187 (1979).
5. Sh. Wan and S. Ghose, Am. Mineral. **68**, 604 (1983).
6. S. Yu. Stefanovich, in *Proceedings of the 2nd International Conference "Real Structure and Properties of Acentrical Crystals," Aleksandrov, VNIISIMS, 1995*, p. 48.
7. D. J. Lloyd, A. Levasseur, and C. Fouassier, J. Solid State Chem. **6**, 179 (1973).
8. K.-I. Machida, G.-Y. Adachi, *et al.*, Inorg. Chem. **19**, 3807 (1980).
9. V. A. Strel'tsov and V. E. Zavodnik, Kristallografiya **34**, 1369 (1989) [Sov. Phys. Crystallogr. **34**, 824 (1989)].
10. N. Walker and D. Stuart, Acta Crystallogr., Sect. A: Found. Crystallogr. **39**, 158 (1983).
11. A. Wells, *Structural Inorganic Chemistry* (Clarendon Press, Oxford, 1984; Mir, Moscow, 1987), Vol. 2, p. 79.
12. E. L. Belokoneva, T. A. Korchemkina, and O. V. Dimitrova, Zh. Neorg. Khim. **44**, 955 (1999).
13. K. Dornberger-Schiff, Abh. Dtsch. Akad. Wiss. Berlin **3**, 1 (1964).
14. H. Strunz, Eur. J. Mineral. **9**, 225 (1997).
15. M. Marezio, J. P. Remeika, and P. D. Dernier, Acta Crystallogr., Sect. B: Strutc. Crystallogr. Cryst. Chem. **25**, 955 (1969).

Translated by I. Polyakova

Crystallography Reports, Vol. 45, No. 5, 2000, pp. 754–758. Translated from Kristallografiya, Vol. 45, No. 5, 2000, pp. 824–829.

STRUCTURES OF INORGANIC COMPOUNDS

Refinement of the Crystal Structure of Sanidine-Like Feldspar

N. A. Yamnova*, A. P. Khomyakov, and I. V. Zlykhenskaya***

**Faculty of Geology, Moscow State University,*
Vorob'evy gory, Moscow, 119899 Russia
e-mail: elbel@geol.msu.ru
***Institute of Mineralogy, Geochemistry, and Crystal Chemistry of Rare Elements,*
ul. Veresaeva 15, Moscow, 121327 Russia

Received November 16, 1998

Abstract—The crystal structure of sanidine-like feldspar of the composition $KAlSi_3O_8$ from the Khibiny alkaline massif (the Kola Peninsula) has been refined (X-ray diffraction analysis; automated Syntex $P\bar{1}$ diffractometer; $2\theta : \theta$ scanning technique; 2320 reflections; $R_{(hkl)} = 0.0409$; anisotropic refinement; AREN program package). The data obtained for $KAlSi_3O_8$ are: $a = 8.615(9)$, $b = 13.030(7)$, $c = 7.200(5)$ Å, $\alpha = 89.99(5)°$, $\beta = 116.01(6)°$, $\gamma = 89.98(7)°$, $Z = 4$, sp. gr. $C\bar{1}$. Microtwinning revealed in the crystal structure of the mineral explains the simultaneous existence of two structural-optical types in one sample—"high" and "low" sanidines.

INTRODUCTION

Below, we describe the study of unusual low-temperature potash feldspar crystals possessing the optical properties characteristic of sanidine and orthoclase, which were found in quarry taluses of the Koashva apatite deposit of the Khibiny alkaline massif (the Kola Peninsula). The crystals were found in solution cavities of pegmatitic rocks along with crystals of natrolite, labuntsovite, and carbonate-apatite. These crystals form both druses on cavity walls and well-faceted individual crystals overgrown on the aegirine needles in the central region of the cavities. High-temperature mineral complexes comprising the major vein-stone of the pegmatitic rocks are represented by nepheline, micrlocline-type cancellated potash feldspar, alkaline amphibole, aegirine-diopside, eudialyte, lamprophyllite, murmanite, and pectolite. The chemical composition of the crystals in question was studied on a Superprobe-733 X-ray microanalyzer by G.N. Nechelyustov (Fedorov All-Russia Institute of Mineral Resources). The analysis showed that the composition of the mineral averaged over six grains is Na_2O, 0.03; K_2O, 16.64; Rb_2O, 0.17; SrO, 0.10; Fe_2O_3, 0.03; Al_2O_3, 18.33; SiO_2, 64.53 wt %; the sum is 99.83 wt %. The chemical composition (with respect to eight O atoms) corresponds to the empiric formula $(K_{0.986}Rb_{0.005}Na_{0.003}Sr_{0.003})Al_{1.003}(Si_{2.997}Fe_{0.001})O_8$ or, in the simplified form, to $K_{0.99}(Rb, Na, Sr)_{0.01}AlSi_3O_8$, which is close to the theoretical composition $KAlSi_3O_8$.

Perfect water-clear transparent or slightly turbid crystals of the feldspar under study have the following morphological characteristics: the combination of the {010}, {001}, {110} forms, and {111}, a noticeable elongation in the [001] direction, and a slight flattening along the [010] direction. The relative crystals sizes along the coordinate *a*-, *b*-, and *c*- axes approximately correspond to the 3 : 2 : 5 ratio. These data were obtained in crystal optics studies by the immersion and Fedorov methods, which also revealed the crystal inhomogeneity. In the polarized light, all the crystals, had the sectorial structure or the "sand glass structure" with sequential extinction of different growth pyramids. Each crystal showed three types of optically distinguishable pyramids, with the bases being parallel to the (100) (type *A*), (010) (type *B*), and (001) (type *C*) coordinate planes. The subindividuals of all the three types have the same parallel crystallographic orientations. Their optical orientations are characterized by the following distinguishing features. In the subindividuals of type *B*, the plane of optical axes is perpendicular to the (010) plane whereas in the subindividuals *A* and *C*, the planes of the optical axes are parallel to (010) plane. Within the accuracy of the immersion method, both structural-optical types have equal refractive indices: $n_p = 1.520(2)$, $n_m = 1.525(2)$, and $n_g = 1.526(2)$. Both types are negative optically biaxial crystals with the angle between the optical axes noticeably varying from one grain to another: the $2V$ values for the subindividuals of types *A* and *C* vary from 10°–12° to 45°, and the $2V$ values for type *B*, vary within 40°–50°. According to the crystal optics data for soda-potash feldspars [1], the above facts allows one to relate these subindividuals to two different mineral types—"high sanidine" (types *A* and *C*) and "low sanidine" or "high orthoclase" (type *B*), which should also differ in the degree of Si,Al-ordering in the crystal structure. The simultaneous

Table 1. Main details of X-ray diffraction experiment

Crystal dimensions, mm	$0.250 \times 0.150 \times 0.125$
Diffractometer	Syntex $P\bar{1}$
Radiation	Mo$K\alpha$
Monochromator	Graphite
Sp. gr.	$C\bar{1}$
Unit-cell parameters, Å, deg	a = 8.615(9), α = 89.99(5)
	b = 13.030(7), β = 116.01(6)
	c = 7.200(5), γ = 89.98(7)
	V = 726.4(1)
Number of formula units, Z	4
Scanning technique	$2\theta : \theta$
Maximum $\sin\theta/\lambda$	1.076
Scanning rate	6–24 deg/min
Number of measured reflections with $I > 1.96\sigma(I)$	2320
Program package	AREN
Reliability factors R_{hkl}:	
isotropic refinement	0.1022
anisotropic refinement	0.0415
with allowance for the refined twinning coefficients	0.0409
Weighting scheme used in the least-squares procedure	$w = 1/(A + F + BF^2)$
	$A = 2F_{min}$, $B = 2/F_{max}$

presence of two modifications of potash feldspar (orthoclase) with different degrees of Si,Al-ordering, of which one single crystal is of considerable interest, because it was crystallized absolutely synchronously and under precisely the same physicochemical conditions. The only difference was slightly different growth rates along different directions. In accordance with the crystal morphology, the growth rate was minimum along the *b*-axis moderate along the *a*-axis and maximal along the *c*-axis. Evidently, even such a small difference in the growth rates was sufficient for the formation of the structure of a relatively ordered "low" sanidine by subindividuals of type *B* which crystallized very slowly. The subindividuals of types *A* and *C*, which crystallized at a higher rates, provided the formation of the structure of completely disordered "high" sanidine. This crystal inhomogeneity also manifested itself in the X-ray diffraction patterns. Thus, although no split spots typical of twin crystals were observed on the Laue diffraction patterns, the spots present on these patterns were diffuse and were elongated, which indicate possible microtwinning in the structure. We undertook our study to confirm microtwinning and refine the distribution of Si and Al atoms over the crystal structure.

EXPERIMENTAL AND STRUCTURE REFINEMENT

We chose a single crystal with a prismatic habitus for X-ray diffraction study. The linear dimensions of the crystal, the parameters of a (pseudo)monoclinic unit cell determined by the Laue and oscillation methods and refined on an automated Synthex $P\bar{1}$ diffractometer, and the major characteristics of X-ray diffraction study are given in Table 1. Despite substantially broadened the reflections, they were not split, and X-ray data were collected at large scan angles. The intensities were converted into $|F_{hkl}|$, and all the subsequent calculations were made by the AREN program package [2].

The observed systematic absences of the *hkl* reflections not satisfying the condition $h + k = 2n$, indicated three possible space groups, namely, *C*2/*m*, *Cm*, and *C*2. At the first stage of the structure refinement within these space groups, the X-ray data were averaged to obtain 1338 reflections. We used as the initial model the structure reported in [3] and assumed that all the Al atoms are uniformly (disordered) distributed over the tetrahedral (*T*) positions. According to [4, 5], the degree of Si,Al-ordering, i.e., the concentration of Al in two (*T*1 and *T*2) and four (*T*1(*o*), *T*1(*m*), *T*2(*o*), and *T*2(*m*))

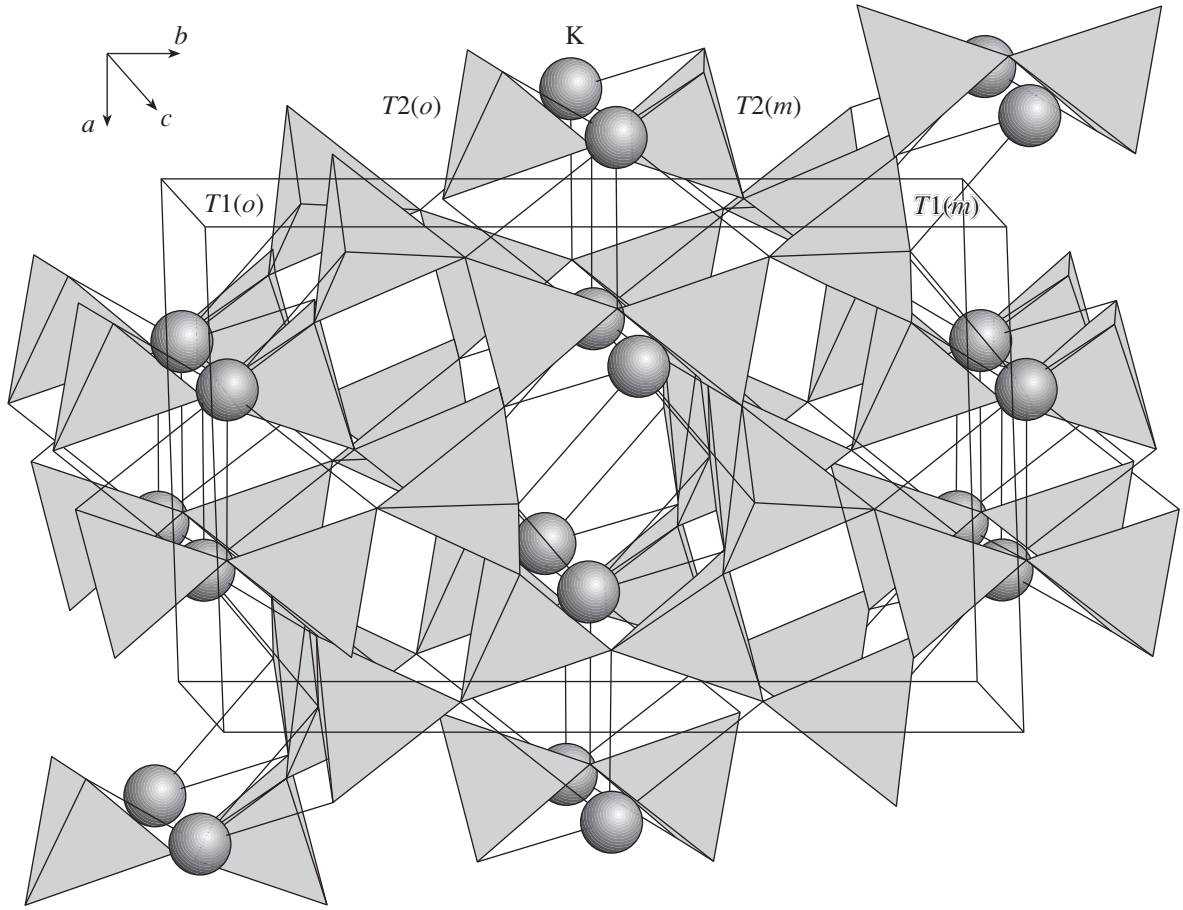

Fig. 1. Crystal structure of sanidine-like feldspar (axonometric projection).

crystallographically nonequivalent positions of the monoclinic and triclinic feldspar modifications, respectively, determines the structural state of the sample and is described as $2t1 = t1o + t1m$, where $t1o$ and $t1m$ are fractions of Al atoms in the corresponding tetrahedral positions. In completely disordered feldspars, Al atoms are statistically distributed over all the crystallographically nonequivalent tetrahedral positions, whereas the process of ordering is accompanied by an increase of the fraction of Al atoms in the positions $T1$ or $T1(o)$ and $T1(m)$. For different structure types, the following ordering ranges were assumed: "the highest" ($2t1 = 0.50$), "high" ($0.50 < 2t1 < 0.60$), "intermediate" ($0.60 < 2t1 < 0.67$), and "low" ($0.67 < 2t1 < 0.75$). It should be stipulated that this model is rather conventional and does not cover all the relationships which can exist in real structures. It is reasonable to expect that the *T*–O interatomic distances in the tetrahedra should increase with an increase of the fraction of Al atoms in the tetrahedral positions. The analysis of the average *T*–O distances in the structure models refined within three monoclinic space groups provided the calculation of possible mixed atomic scattering curves and the refinement of the models in the isotropic and anisotropic approximations by the full-matrix least-squares method neglecting absorption ($\mu r_{max} = 0.17$). The final reliability factors are 0.096, 0.097, and 0.059 for the space groups $C2/m$, Cm, and $C2$, respectively. In all three groups, the thermal parameters (B_{iso}) for oxygen atoms occupying special positions (on twofold rotation axes and in symmetry planes) appeared to be either considerably underestimated (compared to the B_{iso} values for other oxygen atoms) or close to zero. Therefore, it was suggested that the symmetry lowered to triclinic and that all oxygen atoms being displaced to the general positions. The isotropic and anisotropic refinement of the triclinic structure model on the basis of the initial experimental data set within the space group $C\bar{1}$ gave the reliability factors $R = 0.102$ and $R = 0.042$, respectively. The final coordinates of the basis atoms are given in Table 2. The distribution of Al atoms over all four crystallographically nonequivalent positions was calculated by the equations proposed in [4] and taking into account the average *T*–O distances in the tetrahedra $T1(o) = 1.659$ Å, $T1(m) = 1.652$ Å, $T2(o) = 1.631$ Å, and $T2(m) = 1.635$ Å). According to [5], the sample under study can be classified as a "low" sanidine ($2t1 = 0.68$), but existing in the range at the boundary with "intermediate" sanidines.

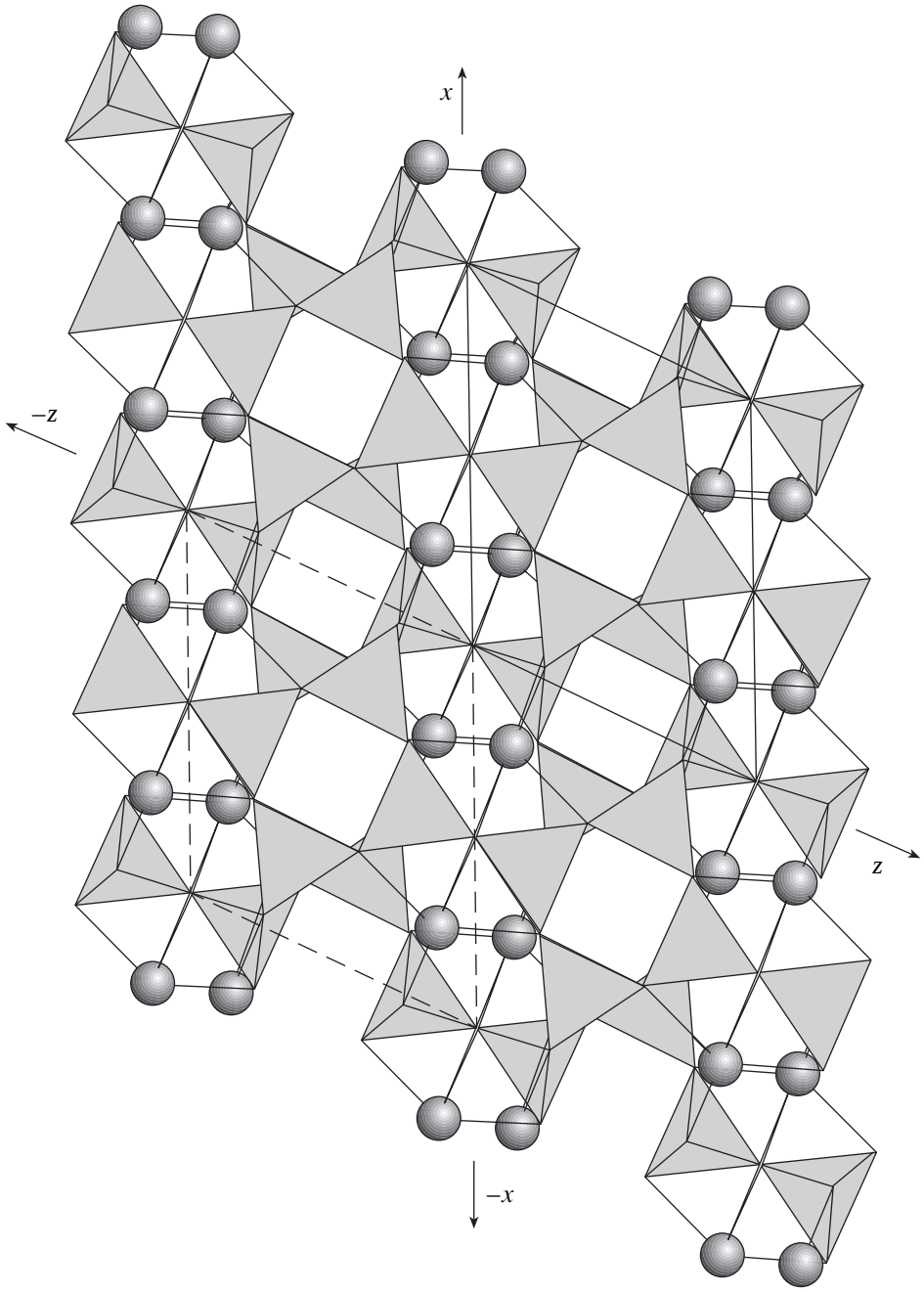

Fig. 2. Crystal structure of sanidine-like feldspar projected onto the *xz* plane. The coordinate axes of the unit cells of the possible twin components are shown. The unit cells of components **I** and **II** are indicated by solid and dashed lines, respectively.

The crystal structure of the feldspar under study (Fig. 1) consists of the framework of silicon–oxygen tetrahedra. The large cavities of this framework are occupied by atoms with large ionic radii (K, Na, Ca, Rb, Ba, and Sr). In monoclinic modifications, the oxygen atoms form four regular point systems denoted by O*A*, O*B*, O*C*, and O*D*. The O*A* atoms occupy special positions and are located on twofold rotation axes (O*A*1) or in mirror planes (O*A*2), whereas the remaining atoms (O*B*, O*C*, and O*D*) occupy general positions. In triclinic modifications, the O*A* positions become general ones, while each of the remaining three positions is split into two independent ones. The nonuniform distribution of Al atoms over four crystallographically nonequivalent tetrahedral positions (Table 2) corresponds to the triclinic symmetry of the crystal. However, the crystal retains also the monoclinic pseudosymmetry, namely, the differences in the coordinates of the pairs of the atoms related by the pseudoelements of symmetry (twofold rotation axes and mirror planes)

Table 2. Coordinates of the basis atoms and individual thermal parameters

Atom	*x/a*	*y/b*	*z/c*	B_{eq}, Å^2
K	0.2858(1)	–0.0006(2)	0.1380(1)	2.17(3)
*T*1(*o*)	0.0096(1)	0.1856(1)	0.2238(1)	0.93(1)
*T*1(*m*)	0.0099(1)	0.8148(1)	0.2240(1)	0.95(1)
*T*2(*o*)	0.7108(1)	0.1183(1)	0.3443(1)	0.93(1)
*T*2(*m*)	0.7104(1)	0.8821(1)	0.3447(1)	0.92(1)
O*A*(1)	–0.000(1)	0.1466(1)	–0.002(1)	1.64(8)
O*A*(2)	0.6399(2)	0.0001(5)	0.2848(3)	1.71(7)
O*B*(*o*)	0.8273(4)	0.1475(2)	0.2262(4)	1.95(7)
O*B*(*m*)	0.8297(4)	0.8521(2)	0.2283(5)	2.05(8)
O*C*(*o*)	0.0365(3)	0.3113(2)	0.2584(4)	1.56(8)
O*C*(*m*)	0.0355(3)	0.6887(2)	0.2592(4)	1.59(7)
O*D*(*o*)	0.1791(3)	0.1264(2)	0.4044(4)	1.64(8)
O*D*(*m*)	0.1798(3)	0.8735(2)	0.4064(4)	1.68(8)

Note: *T*1(*o*) = 0.63Si + 0.37Al; *T*1(*m*) = 0.69Si + 0.31Al; *T*2(*o*) = 0.85Si + 0.15Al; *T*2(*m*) = 0.82Si + 0.18Al.

are either within the standard deviations or are close to these values. This indicates possible microtwinning in the crystal, with two twinning components being related as $a_{\mathbf{I}} = -a_{\mathbf{II}}$, $b_{\mathbf{I}} = b_{\mathbf{II}}$, and $c_{\mathbf{I}} = -c_{\mathbf{II}}$, where *a*, *b*, and *c* are the unit vectors of components **I** and **II**, respectively (Fig. 2). At the final stage, the triclinic model of the structure was refined with due regard for microtwinning. The twinning coefficients (*K*) (the contributions of both components) were refined simultaneously with the model by the full-matrix least-squares method. The final reliability factor was $R = 0.0409$ and the final values of the coefficients were $K_{\mathbf{I}} = 0.61(3)$ and $K_{\mathbf{II}} = 0.39(3)$.

RESULTS AND DISCUSSION

The refinement of the feldspar crystal structure confirmed microtwinning in the sample under study. The triclinic symmetry and the structural state (the degree of Si,Al-ordering) characterize each component of the twin as a relatively ordered "low" sanidine. However, one cannot exclude the possible tendency of disordering in the averaged monoclinic structure. Microtwinning may be associated with the inhomogeneity of the crystals mentioned above. However, the existence of two different orientations of two structural-optical types [of high sanidine with the plane of the optical axes parallel to (010) and low sanidine with the plane of the optical axes normal to (010)] remains unclear. This can be microtwinning, but occurring by another low: the twin components should differ both in the orientation and the unit-cell metrics. It is not inconceivable that this type of twinning is really present in the crystal under study where the second twin component is related to the initial one as $a_2 = a_1$, $b_2 = -b_1$, $c_2 = -(a_1 + c_1)$, where *a*, *b*, and *c* are the unit vectors of the first and the second twin components). In this case, the twin components have different orientations and unit-cell metrics. The structure models of both components can be refined using the X-ray diffraction data set collected in a special way, where the contributions of all component to the diffraction pattern are separated.

In conclusion, we should like to emphasize that the ambiguous results obtained in the refinement of the soda-potash feldspar structures [6] are explained by the microtwinning. Similar to the situation in our study, different degrees of ordering in four *T* subpositions typical of the triclinic feldspars were observed in a number of samples studied in [6], although the symmetry (the geometry of the atomic arrangement) remains monoclinic.

ACKNOWLEDGMENTS

We are grateful to E. L. Belokoneva for her help in collection of the X-ray data and A. V. Arakcheeva for valuable advice.

REFERENCES

1. A. S. Marfunin, Vestn. Mosk. Univ., Ser. 4: Geol., No. 11, 65 (1988).
2. V. I. Andrianov, Kristallografiya **32** (1), 228 (1987) [Sov. Phys. Crystallogr. **32**, 130 (1987)].
3. I. M. Marsiĭ, N. I. Organova, and I. V. Rozhdestvenskaya, Zap. Vses. Mineral. O–va **127** (2), 85 (1993).
4. G. V. Smith, *Feldspars Minerals* (Springer-Verlag, Berlin, 1974), Vol. 1.
5. É. É. Senderov, *Processes of Ordering of Aluminosilicates* (Nauka, Moscow, 1990).
6. A. D. Negro, R. D. Pieri, and S. Quareni, Acta Crystallogr., Sect. B: Struct. Crystallogr. Crysl. Chem. **34**, 2699 (1978).

Translated by T. Safonova

Crystallography Reports, Vol. 45, No. 5, 2000, pp. 759–761. Translated from Kristallografiya, Vol. 45, No. 5, 2000, pp. 830–832.

STRUCTURES OF INORGANIC COMPOUNDS

Refined Crystal Structure of Kuzmenkoite

R. K. Rastsvetaeva*, N. V. Chukanov, and I. V. Pekov*****

** Shubnikov Institute of Crystallography, Russian Academy of Sciences, Leninskiĭ pr. 59, Moscow, 117333 Russia*

*** Institute of Chemical Physics in Chernogolovka, Russian Academy of Sciences, Chernogolovka, Moscow oblast, 142432 Russia*

**** Faculty of Geology, Moscow State University, Vorob'evy gory, Moscow, 119899 Russia*

Received December 30, 1999

Abstract—The structure of the mineral kuzmenkoite found in the Lovozero massif (the Kola Peninsula) was reinvestigated by the X-ray diffraction analysis. This mineral belongs to the labuntsovite family and differs from other members of this family by the absence of Na atoms, a high Mn content, and the new type of filling framework channels because of the replacement of Na atoms by H_2O molecules and H_3O groups. It was found that the disorder of atoms in the channels leads to lowering of the symmetry to *Cm*. *© 2000 MAIK "Nauka/Interperiodica".*

Kuzmenkoite is a mineral of the labuntsovite family. Recently, representatives of this family have attracted the attention of researchers because of their ion-exchange properties. The mineral was found in the near-contact zone of the Lovozero alkaline massif and was structurally studied by Golovina *et al.* [1] in the centrosymmetric sp. gr. *C*2/*m* typical of labuntsovites. However, the cited work did not give a detailed picture of the cation distribution in the structure channels. Using the analogy with other minerals of this family, e.g., vuoriyarvite [2, 3] and the oxonium mineral [4] from the Khibiny massif, one can associate a high degree of decationization of the sample with probable lowering of the symmetry. Our reinvestigation of the mineral in the sp. gr. *Cm* showed a number of additional statistically occupied and split positions. We also refined the occupancies of a number of positions using the mixed atomic scattering curves.

The principal characteristics of the crystal and the details of the X-ray diffraction study are indicated in Table 1. The coordinates of the basis atoms are listed in Table 2. The compositions of the positions and selected interatomic distances are given in Table 3.

The structure of kuzmenkoite (figure) is characterized by a mixed framework consisting of "deformable" chains of Ti(Nb)-octahedra linked via four-membered rings of Si-tetrahedra characteristic of labuntsovites and nenadkevichites. The channels along the coordinate axes are filled with small and large cations and water molecules. The structure of kuzmenkoite is characterized by a high Mn-content and an almost complete absence of Na atoms (which are replaced by oxonium ions and water molecules). The crystallochemical formula of the mineral provides a rather low value or the *R*-factor (3.4%) and is in good agreement with the data of the local X-ray spectral analysis ($Z = 1$): $\{K_{3.2}(H_3O)_{1.5}Na_{0.35}Ba_{0.1}[Mn_{1.12}Nb_{0.28}] \cdot 8.5H_2O\}$ $\{[(Ti_{3.2}Fe^{3+}_{0.8})(Ti_{3.6}Nb_{0.4})](OH_{7.6}O_{0.4})(Si_4O_{12})_4\}$.

Because of the mineral decationization, about half of the cations (out of 10–12 cations, usually present in labuntsovites and nenadkevichites) are retained in the structure channels (the first braces). At the same time, two peaks were localized in the vicinity of the Na posi-

Table 1. Structural data and details of X-ray diffraction experiment

Unit-cell parameters, Å, deg	$a = 14.369(3)$
	$b = 13.906(3)$
	$c = 7.812(1)$
	$\beta = 117.09(2)$
Unit-cell volume, Å^3	1389.7
Sp. gr., *Z*	*Cm*, 4
Radiation; λ, Å	MoK_α, 0.70926
Calculated density, g/cm^3	2.6
Crystal dimensions, mm	$0.2 \times 0.15 \times 0.05$
Diffractometer	KM-4
$\sin\theta/\lambda$	<0.98
Ranges of index variations for measured reflections	$-26 < h < 25$, $0 < k < 21$, $0 < l < 8$
Total number of reflections	3269
Number of independent reflections	1167 $\lvert F\rvert > 4\sigma(F)$
R-factor upon anisotropic refinement	0.034
Extinction parameter	0.0000156
Program used in calculation	AREN [5]

1063-7745/00/4505-0759$20.00 © 2000 MAIK "Nauka/Interperiodica"

Table 2. Coordinates, equivalent thermal parameters (B_{eq}), multiplicities (Q), and occupancies (q) of the atomic positions in the kuzmenkoite structure

Atom	*x*/*a*	*y*/*b*	*z*/*c*	B_{eq}, Å^2	*Q*	*q*
Si(1)	0.1830(1)	0.3892(1)	0.7538(2)	0.43(7)	4	1
Si(2)	0.8170(1)	0.6109(1)	0.2476(3)	1.16(7)	4	1
Si(3)	0.2932(1)	0.3906(1)	0.1963(2)	0.63(7)	4	1
Si(4)	0.7064(1)	0.6099(1)	0.8027(2)	0.83(7)	4	1
M(1)	0.0000(1)	0.2301(1)	0.5000(1)	1.22(2)	4	1
M(2)	0.2510(3)	0.2511(3)	0.5028(6)	1.02(2)	4	1
Mn	–0.0024(5)	0	0.5017(9)	1.25(3)	2	0.70(1)
K(1)	0.0945(7)	0	0.336(2)	3.5(1)	2	0.30(1)
K(2)	0.5725(4)	0.0393(5)	0.2865(7)	3.6(2)	4	0.41(1)
K(3)	0.4275(6)	0.0543(7)	0.731(1)	3.3(1)	4	0.30(1)
K(4)	0.518(1)	0.112(2)	0.027(6)	5.0(7)	4	0.06(1)
H_3O	0.497(2)	0.346(1)	0.011(3)	5.1(4)	4	0.65(1)
O(1)	0.0835(4)	0.3221(3)	0.6918(8)	1.5(2)	4	1
O(2)	0.2399(3)	0.3717(3)	0.6203(6)	0.9(2)	4	1
O(3)	0.7696(4)	0.6790(4)	0.7304(8)	1.5(2)	4	1
O(4)	0.4176(2)	0.3791(3)	0.3275(6)	0.5(2)	4	1
O(5)	0.3563(5)	0	0.2724(9)	0.7(3)	2	1
O(6)	0.2665(3)	0.3723(3)	0.9740(7)	1.2(2)	4	1
O(7)	0.2409(5)	0	0.786(1)	1.3(3)	2	1
O(8)	0.9193(3)	0.6794(4)	0.3107(7)	1.1(2)	4	1
O(9)	0.7617(4)	0.6288(3)	0.3832(8)	1.3(2)	4	1
O(10)	0.2264(3)	0.3192(3)	0.2621(7)	0.8(2)	4	1
O(11)	0.5816(4)	0.6204(4)	0.6710(8)	1.8(2)	4	1
O(12)	0.1411(6)	0.5	0.7335(9)	2.2(3)	2	1
O(13)	0.7324(4)	0.6303(4)	0.0244(7)	1.5(2)	4	1
O(14)	0.2578(5)	0.5	0.2123(9)	1.3(3)	2	1
OH(1)	0.0999(3)	0.2306(3)	0.6059(6)	0.9(2)	4	1
OH(2)	0.0994(3)	0.7722(4)	0.3918(7)	1.3(2)	4	1
H_2O(1)	0.896(1)	0	0.656(2)	2.7(2)	2	0.80(2)
H_2O(2)	0.491(1)	0.139(2)	–0.048(2)	9.3(3)	4	0.50(1)
H_2O(3)	0.977(1)	0.162(1)	0.980(2)	1.7(4)	4	0.35(1)
H_2O(4)	0.085(1)	0	0.333(2)	3.1(3)	2	0.70(1)
H_2O(5)	0.531(2)	0.119(2)	0.129(4)	1.6(8)	4	0.20(2)

Table 3. Characteristics of the coordination polyhedra in the kuzmenkoite structure

Position	Composition	Coordination number	Cation–anion distances		
			minimum	maximum	average
Si(1)	4 Si	4	1.587(5)	1.635(3)	1.609
Si(2)	4 Si	4	1.607(7)	1.631(4)	1.622
Si(3)	4 Si	4	1.613(3)	1.626(2)	1.619
Si(4)	4 Si	4	1.592(7)	1.629(3)	1.615
M(1)	3.6Ti + 0.4Nb	6	1.884(4)	2.018(4)	1.96
M(2)	3.2Ti + 0.8Fe	6	1.930(6)	1.988(7)	1.96
Mn	1.12Mn + 0.28Nb	6	2.14(1)	2.28(2)	2.17
K(1)	0.54K + 0.06Ba	11	2.88(1)	3.37(1)	3.13
K(2)	1.64K	9	2.46(2)	3.32(1)	2.97
K(3)	0.84K + 0.36Na	9	2.85(1)	3.33(1)	3.03
K(4)	0.24K	9	2.87(1)	3.44(1)	3.26
H_3O	1.3H_3O + 1.3H_2O	11	2.84(2)	3.57(2)	3.19

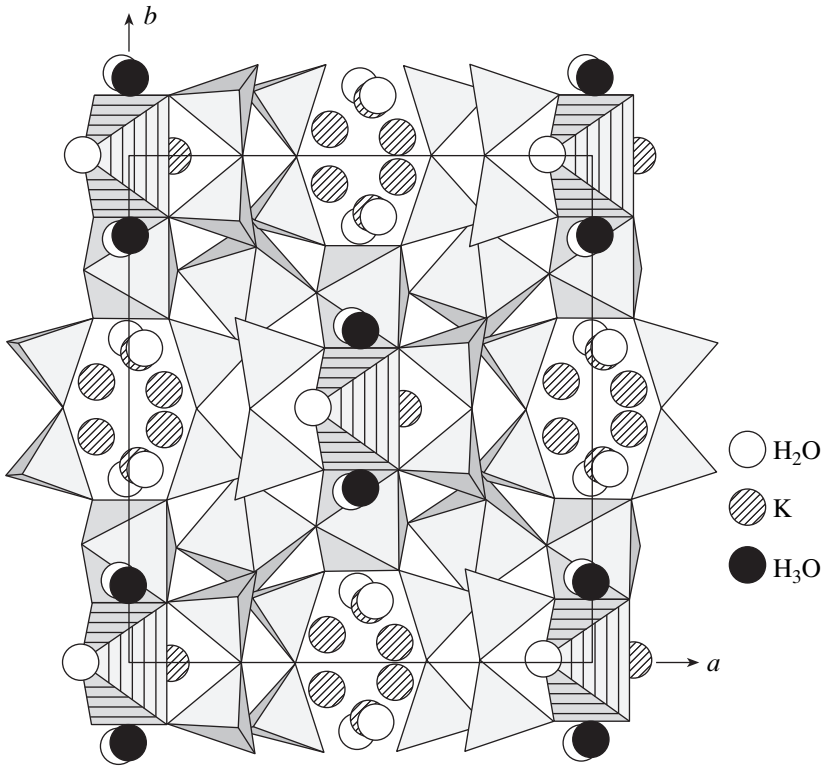

Kuzmenkoite structure projected onto the (001) plane. The Mn-octahedra are hatched with solid lines. Cations, water molecules, and H_3O groups are indicated by circles of different types.

tion on the electron-density maps. These peaks were identified with the positions partly occupied by oxygen. We assumed that one of these peaks corresponds to an H_2O molecule, whereas the second one spaced by ~0.3 Å from the first peak corresponds to the oxonium group. The presence of oxonium ions in this position has also been indicated in [4]. In the structure under consideration, the presence of these ions is explained by a low cation content.

The structure of this mineral is also highly disordered. Thus, all the positions within the channels are split spaced by shortened distances from one another, and only partly occupied. Different occupancies of the positions (related by a twofold rotation pseudoaxis) indicate a lowered symmetry.

ACKNOWLEDGMENTS

We are grateful to N. I. Golovina for providing the experimental data.

This work was supported by the Russian Foundation for Basic Research, project no. 99-05-65035.

REFERENCES

1. N. I. Golovina, G. V. Shilov, N. V. Chukanov, and I. V. Pekov, Dokl. Akad. Nauk **362** (3), 350 (1998).
2. R. K. Rastsvetaeva, R. A. Tamazyan, D. Yu. Pushcharovskiĭ, *et al.*, Kristallografiya **39** (6), 994 (1994) [Crystallogr. Rep. **39**, 908 (1994)].
3. R. K. Rastsvetaeva, R. A. Tamazyan, D. Yu. Pushcharovsky, and T. N. Nadeshina, Eur. J. Mineral. **6**, 503 (1994).
4. R. K. Rastsvetaeva, N. I. Organova, I. V. Rozhdestvenskaya, *et al.*, Dokl. Akad. Nauk **371** (3), 336 (2000).
5. V. I. Andrianov, Kristallografiya **32** (1), 228 (1987) [Sov. Phys. Crystallogr. **32**, 130 (1987)].

Translated by T. Safonova

Crystallography Reports, Vol. 45, No. 5, 2000, pp. 762–770. Translated from Kristallografiya, Vol. 45, No. 5, 2000, pp. 833–841.

STRUCTURE OF COORDINATION COMPOUNDS

Complexes in the Ni^{2+}–Imidazole–*R*N$(CH_2COO^-)_2$ Systems. The Crystal Structures of Tris(imidazole)iminodiacetatonickel(II) Monohydrate, Hexa(imidazole)nickel(II) Bis(*N*-Methyliminodiacetato)nickelate(II) Hexahydrate, and Tetra(aqua)bis(imidazole)nickel(II) Bis(*N*-Benzyliminodiacetato)nickelate(II)

I. N. Polyakova*, A. L. Poznyak, and V. S. Sergienko***

** Kurnakov Institute of General and Inorganic Chemistry, Russian Academy of Sciences, Leninskiĭ pr. 31, Moscow, 117907 Russia*

*** Institute of Molecular and Atomic Physics, Belarussian Academy of Sciences, pr. F. Skoriny 70, Minsk, 220072 Belarus*

Received September 21, 1998

Abstract—Crystals of different compositions, namely, [Ni(*Ida*)(*Im*)$_3$] · H_2O (**I**), [Ni(*Im*)$_6$][Ni(*Mida*)$_2$] · $6H_2O$ (**II**), and [Ni(*Im*)$_2$(H_2O)$_4$][Ni(*Bida*)$_2$] (**III**), have been precipitated from aqueous solutions of the Ni^{2+}–Lig^{2-}–*Im* systems, where Lig^{2-} is *Ida*, *Mida*, and *Bida*, respectively. The crystal structures of **I**–**III** are determined by X-ray diffraction analysis (R = 0.0307, 0.0348, and 0.0302 for 3061, 4706, and 2882 reflections, respectively). Crystals **I** are built of monomeric mixed-ligand complexes and molecules of crystallization water, which are interlinked by hydrogen bonds into a three-dimensional framework. In **II** and **III**, the ligands Lig^{2-} and *Im* form charged complexes separately. In **II**, the cationic and anionic layers of the complexes alternate along the *c*-axis. Numerous hydrogen bonds involving molecules of crystallization water link the layers into a three-dimensional framework. In **III**, the cationic and anionic complexes, which serve as proton donors and acceptors, respectively, are bound into layers parallel to the *xy* plane. © *2000 MAIK "Nauka/Interperiodica".*

INTRODUCTION

In the octahedral complexes of Ni^{2+} with the Ni : *Lig* ratio equal to 1 : 1, the tridentate ligands based on iminodiacetic acid (H_2*Ida*) populate the coordination sphere only by half. The metal coordination can be completed in different ways. For example, crystals of [Ni(*Mida*)(D_2O)$_3$] · D_2O [1], which contain the monomeric complexes, were obtained from a D_2O solution of Ni^{2+} and methyliminodiacetic acid (H_2*Mida*). The related ligand H_2*Mipa*, which differs from H_2*Mida* by the elongation of an acetate arm to the propionate arm, forms the dimeric complexes [Ni_2(*Mipa*)$_2$(H_2O)$_4$] · $2H_2O$ [2].

Continuing the studies of the 1 : 1 complexes of nickel with the ligands of the diacetate series, we prepared compounds with H_2*Ida* and H_2*Bida* (benzyliminodiacetic acid); however, we failed to grow their single crystals. Assuming that these compounds have polymeric structures, we decided to prevent polymerization by the addition of a competing ligand, namely, imidazole (*Im*), to the systems. We expected that the Ni^{2+}–Lig^{2-}–*Im* systems could yield the monomeric mixed-ligand [Ni(*Lig*)(*Im*)$_3$] complexes similar to the [Ni(*Asp*)(*Im*)$_3$] complex with aspartic acid [3]. H_2*Ida*, H_2*Bida*, and H_2*Mida* were used as the main ligand H_2*Lig*.

EXPERIMENTAL

Synthesis. The acid H_2*Bida* was synthesized by the reaction of benzylamine with chloroacetate ions according to the standard procedure described in [4]. Equimolar amounts of Ni$(CH_3CO_2)_2$ · $4H_2O$ and the acid (H_2*Ida* or H_2*Bida*) were dissolved in water, and $NaHCO_3$ was added to neutral reaction. Concentration of these solutions resulted in powder precipitates of the complexes, which were arbitrarily denoted as Ni(*Ida*) and Ni(*Bida*). The starting complex with *Mida* was prepared according to [1].

Weighed portions of Ni(*Ida*) (0.7 g), Ni(*Bida*) (1.1 g), and Ni(*Mida*) (0.8 g) were added to solutions of imidazole (0.6 g) in water (20 ml). The bluish-green complexes gradually dissolved giving blue solutions. These solutions were allowed to evaporate at room temperature. After a few weeks, the crystals with different tints of blue precipitated from all the solutions. The composition and structure of the crystals were deter-

Table 1. Main crystal data, data collection, and refinement parameters for compounds **I**–**III**

Parameter	**I**	**II**	**III**
Formula	$C_{13}H_{19}N_7NiO_5$	$C_{14}H_{25}N_7NiO_7$	$C_{14}H_{19}N_3NiO_6$
Molecular weight	412.06	462.12	384.03
Space group	$P2_1/n$	$P\bar{1}$	$P\bar{1}$
a, Å	8.126(2)	9.746(2)	7.040(1)
b, Å	26.083(5)	13.465(3)	10.058(2)
c, Å	8.595(2)	15.839(3)	12.555(3)
α, deg	90	83.65(2)	69.89(3)
β, deg	109.27(2)	82.99(1)	74.86(2)
γ, deg	90	85.04(2)	87.76(2)
V, Å^3	1719.6(8)	2044.8(7)	804.5(5)
Z	4	4	2
ρ_{calcd}, g/cm^3	1.592	1.501	1.585
Crystal size, mm	$0.07 \times 0.49 \times 0.74$	$0.18 \times 0.21 \times 0.39$	$0.05 \times 0.14 \times 0.35$
μ_{Mo}, mm^{-1}	1.17	1.00	1.24
θ_{max}, deg	28	26	30
No. of measured reflections	4083	7149	4221
No. of observed reflections [$I > 2\sigma(I)$]	3061	4706	2882
R	0.0307	0.0348	0.0302
wR	0.0328	0.0354	0.0334
GOOF	1.0359	1.2423	0.7221
$\Delta\rho_{min}$ and $\Delta\rho_{max}$, e/Å^3	−0.28; 0.32	−0.31; 0.41	−0.41; 0.33

mined by X-ray diffraction analysis: [Ni(*Ida*)(*Im*)$_3$] · H_2O (**I**), [Ni(*Im*)$_6$][Ni(*Mida*)$_2$] · 6H_2O (**II**), and [Ni(*Im*)$_2$(H_2O)$_4$][Ni(*Bida*)$_2$] (**III**).

X-ray diffraction study. Main crystal data and characteristics of the experiment and refinement for **I**–**III** are summarized in Table 1. The sets of the **I** (*hkl*) intensities for crystals **I**–**III** were obtained on a CAD4 automated diffractometer (λMoK_α, graphite monochromator, ω scan mode).

The structures were solved by the direct method (SHELXS86 [5]). All H atoms in structures **I** and **III** and most of the H atoms in **II** were located from difference Fourier synthesis. In structures **I** and **III**, all the non-hydrogen atoms were refined in the anisotropic approximation, and all H atoms were refined isotropically. The coordinates of the H(1*A*), H(1*B*), H(3*B*), and H(5*C*) atoms in structure **II** were calculated. Apparently, these H atoms could not be located at reasonable positions because of the increased thermal vibrations of the C atoms, to which they are attached. It is probable that the C(1) atom is in fact disordered over two unresolved positions. The oxygen atom of a water molecule in structure **II** is disordered over four closely spaced positions O(6*w*), O(7*w*), O(8*w*), and O(9*w*) with the 0.5, 0.25, 0.125, and 0.125 occupancies, respectively. The positions of the H atoms in these water molecules were not found. In structure **II**, the non-hydrogen atoms, other than O(7*w*), O(8*w*), and O(9*w*) were refined anisotropically. The O(7*w*), O(8*w*), and O(9*w*), and H atoms were refined isotropically. The U_{iso} parameters for the H(2*w*3), H(2*w*4), and H(2*w*5) atoms, as well as for the calculated atoms, are fixed by the values of 0.01 Å^2 larger than U_{eq} of the atoms to which they are attached. The H(1*A*) and H(1*B*) atoms were refined as riding atoms. The refinement of structures **I**–**III** was performed with the SHELX76 program [6]. In **I** and **II**, the data were corrected for absorption with the DIFABS program [7].

The atomic coordinates and parameters of thermal vibrations in structures **I**–**III** are listed in Table 2, and the geometric parameters of the hydrogen bonds are given in Table 3.

DESCRIPTION OF THE STRUCTURES

[Ni(*Ida*)(*Im*)$_3$] · H_2O (I). The structure is built of discrete mixed-ligand complexes [Ni(*Ida*)(*Im*)$_3$] (Fig. 1) and molecules of crystallization water. A distorted octahedral coordination of the Ni(1) atom is formed by the N(1), O(1), and O(3) atoms of the Ida^{2-} ligand and the N(2), N(4), and N(6) atoms of the *Im*(1), *Im*(2), and *Im*(3) molecules, respectively. The complex has a facial structure. The conformations of both five-membered chelate rings are N(1)-envelopes [the aver-

Table 2. Atomic coordinates and parameters of thermal vibrations U_{eq} (for H atoms, U_{iso}) in structures **I**–**III**

Atom	*x*	*y*	*z*	U_{eq}/U_{iso}, Å^2	Atom	*x*	*y*	*z*	U_{eq}/U_{iso}, Å^2
		I					**II**		
Ni(1)	0.73882(4)	0.12884(1)	0.15094(4)	0.0233(1)	Ni(1)	0	0	0	0.0432(3)
O(1)	1.0067(2)	0.1345(1)	0.2697(2)	0.0299(6)	Ni(2)	0	0	0.5	0.0290(2)
O(2)	1.2319(3)	0.0937(1)	0.4434(3)	0.0500(8)	Ni(3)	0.5	0.5	0.5	0.0351(2)
O(3)	0.7947(3)	0.1037(1)	−0.0558(2)	0.0335(7)	Ni(4)	0.5	0.5	0	0.0303(2)
O(4)	0.7827(4)	0.0343(1)	−0.2067(3)	0.071(1)	O(1)	0.0191(4)	−0.1204(3)	0.0890(2)	0.060(1)
N(1)	0.7923(3)	0.0508(1)	0.2135(3)	0.0303(8)	O(2)	0.1355(4)	−0.1820(3)	0.1961(2)	0.081(2)
N(2)	0.4693(3)	0.1207(1)	0.0340(3)	0.0316(8)	O(3)	0.1699(3)	−0.0583(3)	−0.0769(2)	0.058(1)
N(3)	0.1876(3)	0.1206(1)	−0.0076(4)	0.047(1)	O(4)	0.3808(4)	−0.0215(3)	−0.1253(3)	0.098(2)
N(4)	0.7081(3)	0.1506(1)	0.3762(3)	0.0303(7)	O(5)	0.3874(3)	0.4591(2)	−0.0904(2)	0.044(1)
N(5)	0.7432(3)	0.1477(1)	0.6398(3)	0.0391(9)	O(6)	0.3377(4)	0.3241(3)	−0.1462(2)	0.066(1)
N(6)	0.7405(3)	0.2033(1)	0.0661(3)	0.0296(8)	O(7)	0.3522(3)	0.4414(2)	0.0939(2)	0.044(1)
N(7)	0.6584(4)	0.2793(1)	−0.0371(4)	0.045(1)	O(8)	0.3287(3)	0.3110(2)	0.1921(2)	0.057(1)
C(1)	0.9696(4)	0.0471(1)	0.3326(4)	0.037(1)	N(1)	0.1563(4)	0.0509(3)	0.0594(2)	0.041(1)
C(2)	1.0790(4)	0.0949(1)	0.3506(3)	0.0294(9)	N(2)	0.0995(3)	0.0441(2)	0.5997(2)	0.036(1)
C(3)	0.7672(5)	0.0227(1)	0.0593(4)	0.043(1)	N(3)	0.2022(5)	0.0365(4)	0.7153(3)	0.066(2)
C(4)	0.7837(4)	0.0553(1)	−0.0792(4)	0.036(1)	N(4)	0.0346(3)	0.1420(2)	0.4257(2)	0.033(1)
C(5)	0.3473(4)	0.1207(1)	0.1046(4)	0.038(1)	N(5)	0.1190(4)	0.2554(3)	0.3277(3)	0.047(1)
C(6)	0.2069(4)	0.1204(1)	−0.1591(5)	0.053(1)	N(6)	−0.1914(3)	0.0572(2)	0.5585(2)	0.035(1)
C(7)	0.3791(4)	0.1203(1)	−0.1323(4)	0.044(1)	N(7)	−0.3513(4)	0.1052(3)	0.6578(3)	0.047(1)
C(8)	0.7122(4)	0.1203(1)	0.5010(4)	0.038(1)	N(8)	0.5339(4)	0.3585(3)	0.4502(2)	0.041(1)
C(9)	0.7585(4)	0.1974(1)	0.6028(4)	0.045(1)	N(9)	0.5949(5)	0.2523(3)	0.3541(3)	0.055(2)
C(10)	0.7360(4)	0.1991(1)	0.4402(4)	0.037(1)	N(10)	0.6084(4)	0.4479(3)	0.6071(2)	0.042(1)
C(11)	0.6080(4)	0.2340(1)	0.0040(5)	0.048(1)	N(11)	0.7227(5)	0.3467(4)	0.6988(3)	0.067(2)
C(12)	0.8319(4)	0.2779(1)	−0.0005(4)	0.042(1)	N(12)	0.3111(4)	0.4537(3)	0.5701(2)	0.044(1)
C(13)	0.8822(4)	0.2308(1)	0.0627(4)	0.040(1)	N(13)	0.1579(5)	0.3977(4)	0.6729(4)	0.065(2)
O(1*w*)	0.5962(4)	−0.0076(1)	0.3782(4)	0.057(1)	N(14)	0.5783(3)	0.3509(2)	0.0069(2)	0.034(1)
H(1N)	0.726(4)	0.038(1)	0.250(4)	0.030(8)	C(1)	0.1818(9)	−0.0217(5)	0.1296(4)	0.124(4)
H(3N)	0.086(6)	0.121(2)	0.002(5)	0.08(1)	C(2)	0.1061(5)	−0.1153(4)	0.1393(3)	0.054(2)
H(5N)	0.754(5)	0.135(1)	0.730(5)	0.06(1)	C(3)	0.2716(7)	0.0571(6)	−0.0069(5)	0.085(3)
H(7N)	0.595(5)	0.301(2)	−0.087(5)	0.07(1)	C(4)	0.2751(6)	−0.0156(3)	−0.0731(3)	0.053(2)
H(1*A*)	0.965(4)	0.040(1)	0.447(4)	0.048(9)	C(5)	0.1251(8)	0.1515(7)	0.0874(7)	0.102(4)
H(1*B*)	1.025(4)	0.020(1)	0.305(4)	0.046(9)	C(6)	0.1365(5)	−0.0141(4)	0.6661(3)	0.047(2)
H(3*A*)	0.839(4)	−0.006(1)	0.075(4)	0.05(1)	C(7)	0.2051(6)	0.1323(4)	0.6796(4)	0.061(2)
H(3*B*)	0.652(5)	0.010(1)	0.024(5)	0.06(1)	C(8)	0.1425(5)	0.1368(4)	0.6085(3)	0.044(2)
H(5)	0.370(4)	0.120(1)	0.213(4)	0.046(9)	C(9)	0.1326(4)	0.1608(3)	0.3623(3)	0.039(1)
H(6)	0.112(6)	0.119(2)	−0.257(5)	0.08(1)	C(10)	0.0065(5)	0.3012(4)	0.3704(3)	0.055(2)
H(7)	0.439(4)	0.120(1)	−0.208(4)	0.05(1)	C(11)	−0.0444(5)	0.2309(3)	0.4305(3)	0.049(2)
H(8)	0.699(4)	0.085(1)	0.499(4)	0.05(1)	C(12)	−0.2153(5)	0.0922(3)	0.6333(3)	0.040(1)
H(9)	0.783(5)	0.222(1)	0.677(4)	0.06(1)	C(13)	−0.4181(5)	0.0760(4)	0.5963(3)	0.057(2)
H(10)	0.733(4)	0.228(1)	0.376(4)	0.042(9)	C(14)	−0.3203(5)	0.0478(4)	0.5351(3)	0.053(2)
H(11)	0.491(5)	0.224(1)	−0.013(4)	0.06(1)	C(15)	0.6218(5)	0.3364(4)	0.3842(3)	0.048(2)
H(12)	0.894(4)	0.305(1)	−0.014(4)	0.05(1)	C(16)	0.4823(6)	0.2174(4)	0.4037(4)	0.061(2)
H(13)	0.997(4)	0.215(1)	0.106(4)	0.046(9)	C(17)	0.4457(5)	0.2823(3)	0.4617(3)	0.052(2)
H(1*w*)	0.640(6)	−0.033(2)	0.433(5)	0.07(1)	C(18)	0.6597(5)	0.3551(4)	0.6271(3)	0.048(2)
H(2*w*)	0.498(5)	−0.014(2)	0.366(5)	0.06(1)	C(19)	0.7103(7)	0.4422(4)	0.7244(4)	0.061(2)

Table 2. (Contd.)

Atom	*x*	*y*	*z*	U_{eq}/U_{iso}, Å^2	Atom	*x*	*y*	*z*	U_{eq}/U_{iso}, Å^2
C(20)	0.6413(6)	0.5005(4)	0.6688(3)	0.057(2)	H(20)	0.616(4)	0.568(3)	0.675(3)	0.05(1)
C(21)	0.2899(6)	0.4202(4)	0.6513(3)	0.054(2)	H(21)	0.359(5)	0.410(3)	0.688(3)	0.05(1)
C(22)	0.0916(6)	0.4169(4)	0.6029(4)	0.070(2)	H(22)	0.001(6)	0.405(4)	0.600(4)	0.10(2)
C(23)	0.1854(5)	0.4514(4)	0.5398(4)	0.058(2)	H(23)	0.178(5)	0.472(4)	0.478(3)	0.07(2)
C(24)	0.5106(7)	0.3020(4)	–0.0540(4)	0.057(2)	H(24*A*)	0.473(6)	0.246(5)	–0.025(4)	0.10(2)
C(25)	0.4037(4)	0.3678(3)	–0.1002(3)	0.041(1)	H(24*B*)	0.578(6)	0.273(5)	–0.095(4)	0.10(2)
C(26)	0.5329(5)	0.3120(3)	0.0958(3)	0.041(1)	H(26*A*)	0.535(4)	0.237(3)	0.101(3)	0.05(1)
C(27)	0.3922(4)	0.3578(3)	0.1298(3)	0.038(1)	H(26*B*)	0.598(5)	0.332(3)	0.129(3)	0.05(1)
C(28)	0.7310(5)	0.3350(4)	–0.0108(4)	0.050(2)	H(28*A*)	0.761(5)	0.257(4)	–0.004(3)	0.06(1)
O(1*w*)	–0.2086(4)	0.2018(3)	0.2098(2)	0.063(1)	H(28*B*)	0.771(5)	0.369(4)	0.032(3)	0.06(2)
O(2*w*)	–0.5198(5)	0.1550(4)	–0.2014(3)	0.076(2)	H(28*C*)	0.749(5)	0.356(4)	–0.065(4)	0.08(2)
O(3*w*)	0.8072(5)	0.4103(3)	0.1896(3)	0.074(2)	H(1*w*1)	–0.199(6)	0.261(4)	0.197(4)	0.08(2)
O(4*w*)	0.0450(5)	0.3332(4)	0.8401(3)	0.086(2)	H(2*w*1)	–0.202(8)	0.165(6)	0.167(5)	0.15(3)
O(5*w*)	–0.5845(5)	0.1098(3)	0.2398(3)	0.095(2)	H(1*w*2)	–0.543(6)	0.107(4)	–0.179(3)	0.07(2)
O(6*w*)*	0.0728(7)	0.4770(6)	0.1741(6)	0.075(3)	H(2*w*2)	–0.573(5)	0.212(4)	–0.189(3)	0.07(2)
O(7*w*)*	0.057(2)	0.477(1)	0.112(1)	0.084(5)	H(1*w*3)	0.762(7)	0.463(5)	0.164(4)	0.11(2)
O(8*w*)*	0.056(3)	0.453(2)	0.074(2)	0.076(8)	H(2*w*3)	0.914(5)	0.416(3)	0.175(3)	0.086***
O(9*w*)*	0.084(4)	0.418(3)	0.003(3)	0.12(1)	H(1*w*4)	0.005(7)	0.274(5)	0.834(4)	0.11(2)
H(3N)	0.225(5)	0.015(4)	0.757(3)	0.06(2)	H(2*w*4)	0.094(7)	0.322(6)	0.871(5)	0.096***
H(5N)	0.164(5)	0.277(4)	0.290(3)	0.06(2)	H(1*w*5)	–0.607(6)	0.191(5)	0.219(4)	0.10(2)
H(7N)	–0.391(5)	0.125(3)	0.706(3)	0.06(1)	H(2*w*5)	–0.510(6)	0.079(4)	0.195(4)	0.104***
H(9N)	0.634(6)	0.226(4)	0.313(4)	0.09(2)			**III**		
H(11N)	0.773(6)	0.286(5)	0.730(4)	0.11(2)	Ni(1)	0.5	0.5	0	0.0227(2)
H(13N)	0.136(6)	0.383(4)	0.716(3)	0.07(2)	Ni(2)	0	0	0	0.0249(2)
H(1*A*)**	0.150	0.011	0.180	0.140***	O(1)	0.6893(3)	0.6819(2)	–0.0656(2)	0.0317(8)
H(1*B*)**	0.280	–0.038	0.130	0.140***	O(2)	0.7321(3)	0.8965(2)	–0.2040(2)	0.0414(9)
H(3*A*)	0.344(7)	0.030(5)	0.024(4)	0.10(3)	O(3)	0.7136(3)	0.3884(2)	–0.0740(2)	0.0317(7)
H(3*B*)	0.267(6)	0.133(5)	–0.029(4)	0.100***	O(4)	0.7943(3)	0.3243(2)	–0.2326(2)	0.0348(8)
H(5*A*)	0.206(6)	0.173(4)	0.110(4)	0.09(2)	N(1)	0.4610(3)	0.5850(2)	–0.1695(2)	0.0232(8)
H(5*B*)	0.072(8)	0.192(5)	0.057(5)	0.12(3)	N(2)	–0.2098(4)	–0.0816(3)	0.1584(2)	0.0328(9)
H(5*C*)	0.059(7)	0.136(5)	0.134(4)	0.110***	N(3)	–0.4862(5)	–0.1863(3)	0.2819(3)	0.046(1)
H(6)	0.126(5)	–0.083(4)	0.676(3)	0.06(2)	C(1)	0.4871(4)	0.7394(3)	–0.2002(3)	0.027(1)
H(7)	0.241(5)	0.180(4)	0.704(3)	0.07(2)	C(2)	0.6515(4)	0.7765(3)	–0.1541(2)	0.028(1)
H(8)	0.126(5)	0.194(3)	0.570(3)	0.06(1)	C(3)	0.6219(4)	0.5335(3)	–0.2459(3)	0.028(1)
H(9)	0.202(4)	0.114(3)	0.343(3)	0.05(1)	C(4)	0.7164(4)	0.4039(3)	–0.1789(2)	0.0255(9)
H(10)	–0.025(4)	0.370(3)	0.357(3)	0.05(1)	C(5)	0.2619(4)	0.5396(3)	–0.1705(3)	0.028(1)
H(11)	–0.111(5)	0.240(3)	0.472(3)	0.05(1)	C(6)	0.2061(4)	0.6043(3)	–0.2854(2)	0.029(1)
H(12)	–0.148(4)	0.114(3)	0.664(3)	0.04(1)	C(7)	0.2271(5)	0.5314(4)	–0.3630(3)	0.041(1)
H(13)	–0.509(6)	0.085(4)	0.599(3)	0.08(2)	C(8)	0.1730(5)	0.5908(5)	–0.4674(3)	0.053(2)
H(14)	–0.325(4)	0.022(3)	0.485(3)	0.04(1)	C(9)	0.0954(5)	0.7200(5)	–0.4938(3)	0.057(2)
H(15)	0.692(4)	0.371(3)	0.359(3)	0.05(1)	C(10)	0.0709(6)	0.7939(5)	–0.4176(4)	0.055(2)
H(16)	0.445(5)	0.160(4)	0.395(3)	0.06(1)	C(11)	0.1257(5)	0.7354(4)	–0.3130(3)	0.039(1)
H(17)	0.380(4)	0.280(3)	0.508(3)	0.04(1)	C(12)	–0.3806(5)	–0.1422(4)	0.1703(3)	0.039(1)
H(18)	0.650(4)	0.300(3)	0.596(3)	0.05(1)	C(13)	–0.3813(6)	–0.1507(4)	0.3460(3)	0.052(2)
H(19)	0.738(7)	0.452(5)	0.756(4)	0.09(3)	C(14)	–0.2107(6)	–0.0872(4)	0.2692(3)	0.043(1)

Table 2. (Contd.)

Atom	*x*	*y*	*z*	U_{eq}/U_{iso}, Å^2	Atom	*x*	*y*	*z*	U_{eq}/U_{iso}, Å^2
O(1*w*)	−0.0129(4)	0.2000(2)	0.0232(2)	0.0352(9)	H(10)	0.022(6)	0.887(4)	−0.435(4)	0.07(1)
O(2*w*)	−0.2195(3)	0.0556(2)	−0.0826(2)	0.0327(8)	H(11)	0.110(5)	0.785(4)	−0.262(3)	0.05(1)
H(1*A*)	0.520(4)	0.788(3)	−0.285(3)	0.033(8)	H(3)	−0.592(6)	−0.225(5)	0.309(4)	0.07(1)
H(1*B*)	0.368(4)	0.773(3)	−0.162(3)	0.027(8)	H(12)	−0.428(5)	−0.155(4)	0.106(3)	0.06(1)
H(3*A*)	0.730(5)	0.610(4)	−0.289(3)	0.037(9)	H(13)	−0.420(6)	−0.171(4)	0.425(4)	0.07(1)
H(3*B*)	0.582(5)	0.515(3)	−0.304(3)	0.037(9)	H(14)	−0.108(5)	−0.049(4)	0.282(3)	0.04(1)
H(5*A*)	0.163(4)	0.561(3)	−0.106(3)	0.027(8)	H(1*w*1)	0.074(6)	0.241(4)	0.032(3)	0.05(1)
H(5*B*)	0.254(4)	0.439(3)	−0.149(3)	0.025(7)	H(2*w*1)	−0.065(7)	0.252(5)	−0.010(4)	0.07(2)
H(7)	0.273(5)	0.441(5)	−0.343(3)	0.04(1)	H(1*w*2)	−0.201(6)	0.148(4)	−0.133(3)	0.05(1)
H(8)	0.185(5)	0.541(4)	−0.517(3)	0.05(1)	H(2*w*2)	−0.234(5)	0.008(4)	−0.120(3)	0.05(1)
H(9)	0.065(6)	0.759(4)	−0.562(4)	0.07(1)					

* Site occupancies for the O(6*w*), O(7*w*), O(8*w*), and O(9*w*) atoms are 0.5, 0.25, 0.125, and 0.125, respectively. The O(7*w*), O(8*w*), and O(9*w*) atoms are refined isotropically.
** Refined as a riding atom.
*** U_{iso} is fixed in the refinement.

age atomic deviations (Δ_{av}) from the Ni(1)C(1)C(2)O(1) and Ni(1)C(3)C(4)O(3) planes are 0.029 and 0.042 Å, respectively; and the deviations of the N(1) atom from these planes are 0.260 and 0.447 Å, respectively]. The plane of the *Im*(1) molecule and the basal Ni(1)O(1)O(3)N(2)N(4) plane forms an angle of 17.5°. The *Im*(2) and *Im*(3) planes are almost perpendicular to each other (92.8°) and to the basal plane (96.8° and 87.3°) and form angles of 97.2° and 69.9°, respectively, with the *Im*(1) plane. All potentially donor H atoms are involved in the O–H··O and N–H··O hydrogen bonds, which interlink the complexes and water molecules into a three-dimensional framework.

$[Ni(Im)_6][Ni(Mida)_2] \cdot 6H_2O$ (II). The structure is built of the anionic complexes $[Ni(Mida)_2]^{2-}$, the cationic complexes $[Ni(Im)_6]^{2+}$, and molecules of crystallization water. The structures of the complexes and the atomic numbering are shown in Fig. 2. All the complexes are centrosymmetric. The symmetry-independent complexes having the same composition are close in structure but slightly differ in geometric parameters. In the $[Ni(Mipa)_2]^{2-}$ complexes, the Ni atoms are coordinated by the tridentate (N + 2O) ligands, which close two five-membered chelate rings. In both independent complexes, one of the chelate rings is flattened [Δ_{av} for the Ni(1)N(1)C(1)C(2)O(1) and Ni(4)N(14)C(24)C(25)O(5) planes are 0.019 and 0.018 Å, respectively], and the other ring has the N-envelope conformation [Δ_{av} = 0.033 Å for Ni(1)C(3)C(4)O(3) and 0.014 Å for Ni(4)C(26)C(27)O(7); and the deviations of the N(1) and N(14) atoms from these planes are 0.523 and 0.598 Å, respectively]. In the $[Ni(2)(Im)_6]^{2+}$ cation, the imidazole molecules N(2)C(6)N(3)C(7)C(8), N(4)C(9)N(5)C(10)C(11), and N(6)C(12)N(7)C(13)C(14) [*Im*(1)–*Im*(3)] are located in approximately mutually perpendicular planes; the dihedral angles *Im*(1)/*Im*(2), *Im*(1)/*Im*(3), and *Im*(2)/*Im*(3) are 83.4°, 91.1°, and 89.0°, respectively. In the $[Ni(3)(Im)_6]^{2+}$ cation, the planes of the molecules N(8)C(15)N(9)C(16)C(17) [*Im*(4)] and N(12)C(21)N(13)C(22)C(23) [*Im*(6)] form a dihedral angle of 113.7°. The plane of the N(10)C(18)N(11)C(19)C(20) [*Im*(5)] molecule is approximately perpendicular to the above two planes: *Im*(5)/*Im*(4) is 83.5° and *Im*(5)/*Im*(6) is 95.9°. In the crystal, the cationic and anionic layers of the complexes alternate along the *c*-axis. An extensive hydrogen-bond system interlinks the complexes and water molecules into a three-dimensional framework.

$[Ni(Im)_2(H_2O)_4][Ni(Bida)_2]$ (III). The structure is built of centrosymmetric anionic $[Ni(Bida)_2]^{2-}$ and cationic $[Ni(Im)_2(H_2O)_4]^{2+}$ complexes (Fig. 3). The $Bida^{2-}$ ligand coordinates the Ni(1) atom by the N(1), O(1), and O(3) atoms by closing two glycinate chelate rings. The Ni(1)N(1)C(1)C(2)O(1) and Ni(1)N(1)C(3)C(4)O(3) rings adopt the N(1)-envelope conformations [for the Ni(1), C(1), C(2), and O(1) atoms, Δ_{av} = 0.012 Å; the N(1) atom deviates from this plane by 0.648 Å] and C(3),C(4)-*gauche* conformation [the C(3) and C(4) atoms deviate from the Ni(1)N(1)O(3) plane by 0.185 and –0.146 Å, respectively]. In the hydrated cation $[Ni(Im)_2(H_2O)_4]^{2+}$, the plane of the imidazole molecule N(2)C(12)N(3)C(13)C(14) is approximately perpendicular (88.8°) to the basal Ni(2)O(1*w*)O(2*w*) plane of the octahedron and divides the O(1*w*)'Ni(2)O(2*w*) quadrant of the octahedron into unequal parts: the torsion angles O(1*w*)'–Ni(2)–N(2)–C(12) and O(2*w*)–Ni(2)–N(2)–C(12) are 57.7° and 33.4°, respectively. The hydrogen bonds, in which the cations serve as pro-

Table 3. Geometric characteristics of hydrogen bonds in structures **I**–**III**

D–H···*A*	Symmetry operation	*D*···*A*, Å	*D*–H, Å	H···*A*, Å	*DHA* angle, deg
		I			
N(1)–H(1N)···O(1*w*)	*x*, *y*, *z*	2.891(4)	0.79(3)	2.12(3)	166(3)
N(3)–H(3N)···O(3)	*x* – 1, *y*, *z*	3.113(4)	0.85(5)	2.30(5)	160(4)
N(5)–H(5N)···O(3)	*x*, *y*, *z* + 1	2.760(3)	0.82(4)	1.94(4)	177(4)
N(7)–H(7N)···O(1)	–0.5 + *x*, 0.5 – *y*, –0.5 + *z*	2.824(3)	0.79(4)	2.07(4)	160(4)
O(1*w*)–H(1*w*)···O(2)	2 – *x*, –*y*, 1 – *z*	2.816(4)	0.81(4)	2.01(4)	174(4)
O(1*w*)–H(2*w*)···O(4)	1 – *x*, –*y*, –*z*	3.023(5)	0.79(5)	2.30(4)	153(4)
		II*			
N(3)–H(3N)···O(4)	*x*, *y*, 1 + *z*	3.228(7)	0.74(5)	2.53(5)	159(5)
N(5)–H(5N)···O(8)	*x*, *y*, *z*	2.861(5)	0.75(5)	2.13(5)	166(5)
N(7)–H(7N)···O(2*w*)	*x*, *y*, 1 + *z*	2.714(6)	0.87(5)	1.87(5)	164(5)
N(9)–H(9N)···O(1*w*)	1 + *x*, *y*, *z*	2.898(6)	0.82(6)	2.13(6)	157(6)
N(11)–H(11N)···O(2)	1 – *x*, –*y*, 1 – *z*	2.969(6)	1.03(6)	1.95(6)	172(5)
N(13)–H(13N)···O(4*w*)	*x*, *y*, *z*	2.814(7)	0.70(5)	2.12(5)	173(6)
O(1*w*)–H(1*w*1)···O(3*w*)	*x* – 1, *y*, *z*	2.807(6)	0.81(6)	2.01(6)	169(6)
O(1*w*)–H(2*w*1)···O(3)	–*x*, –*y*, –*z*	2.980(5)	0.88(8)	2.11(8)	171(7)
O(2*w*)–H(1*w*2)···O(4)	*x* – 1, *y*, *z*	2.742(6)	0.74(6)	2.00(6)	175(6)
O(2*w*)–H(2*w*2)···O(6)	*x* – 1, *y*, *z*	2.735(6)	0.92(5)	1.83(5)	169(5)
O(3*w*)–H(1*w*3)···O(5)	1 – *x*, 1 – *y*, –*z*	2.949(5)	0.88(5)	2.12(6)	157(6)
O(3*w*)–H(2*w*3)···O(6*w*)	1 + *x*, *y*, *z*	2.786(8)	1.05(5)	1.81(5)	154(4)
O(4*w*)–H(1*w*4)···O(2)	–*x*, –*y*, 1 – *z*	2.948(6)	0.94(7)	2.06(7)	159(6)
O(4*w*)–H(1*w*4)···O(1)	–*x*, –*y*, 1 – *z*	3.048(6)	0.94(7)	2.30(7)	137(5)
O(4*w*)–H(2*w*4)···O(6)	*x*, *y*, 1 + *z*	2.879(6)	0.72(7)	2.36(7)	131(7)
O(5*w*)–H(1*w*5)···O(8)	*x* – 1, *y*, *z*	2.817(5)	1.12(6)	1.71(6)	170(5)
O(5*w*)–H(2*w*5)···O(4)	–*x*, –*y*, –*z*	2.799(6)	1.04(6)	1.76(6)	177(5)
		III			
N(3)–H(3)···O(4)	–*x*, –*y*, –*z*	2.923(4)	0.78(5)	2.34(5)	132(4)
O(1*w*)–H(1*w*1)···O(1)	1 – *x*, 1 – *y*, –*z*	2.858(3)	0.81(4)	2.06(4)	172(4)
O(1*w*)–H(2*w*1)···O(3)	*x* – 1, *y*, *z*	2.852(3)	0.71(5)	2.16(5)	166(5)
O(2*w*)–H(1*w*2)···O(4)	*x* – 1, *y*, *z*	2.699(3)	0.92(4)	1.79(4)	171(4)
O(2*w*)–H(2*w*2)···O(2)	*x* – 1, *y* – 1, *z*	2.645(3)	0.80(4)	1.84(4)	179(4)

* The contacts of water molecules in poorly populated positions O(7*w*), O(8*w*), and O(9*w*) are not included in the table. Molecule O(6*w*) with the occupancy $\mu = 0.5$ has short contacts with the atoms O(7) (*x*, *y*, *z*) and O(4*w*) (–*x*, 1 – *y*, 1 – *z*), whose lengths [2.885(8) and 2.708(9) Å] and directions [the O(7)–O(6*w*)–O(4*w*) angle is 117.9°] indicate possible hydrogen bonds.

ton donors and the anions are proton acceptors, link the structural units into layers parallel to the *xy* plane.

RESULTS AND DISCUSSION

The expected mixed-ligand $[Ni(Lig)(Im)_3]$ complexes were obtained only for $Lig^{2-} = Ida$ (structure **I**). In two other systems, the ligands form separate complexes—the cationic complexes $[Ni(Im)_6]^{2+}$ in **II** and $[Ni(Im)_2(H_2O)_4]^{2+}$ in **III** and the anionic complexes $[Ni(Lig)_2]^{2-}$ in both structures. In the literature, we find many structures of mixed-ligand complexes of Ni^{2+} with imidazole and organic ligands and a unique structure of $[Ni(Im)_4 \cdot (H_2O)_2] \cdot 2L$ [8], which consists of free saccharin anions (L^-) and di(aqua)imidazole complexes. As far as we know, there are no examples of compounds in which imidazole and the "main" ligand coordinate nickel separately.

The geometric characteristics of the complexes and ligands in structures **I**–**III** are normal. Complex **I** is close in structure to $[Ni(Asp)(Im)_3]$ (**IV**) [3], $[Ni(Mida)(D_2O)_3]$ [1], and $[Ni(Ida)(H_2O)_3]$ (the last complex is involved in the compound

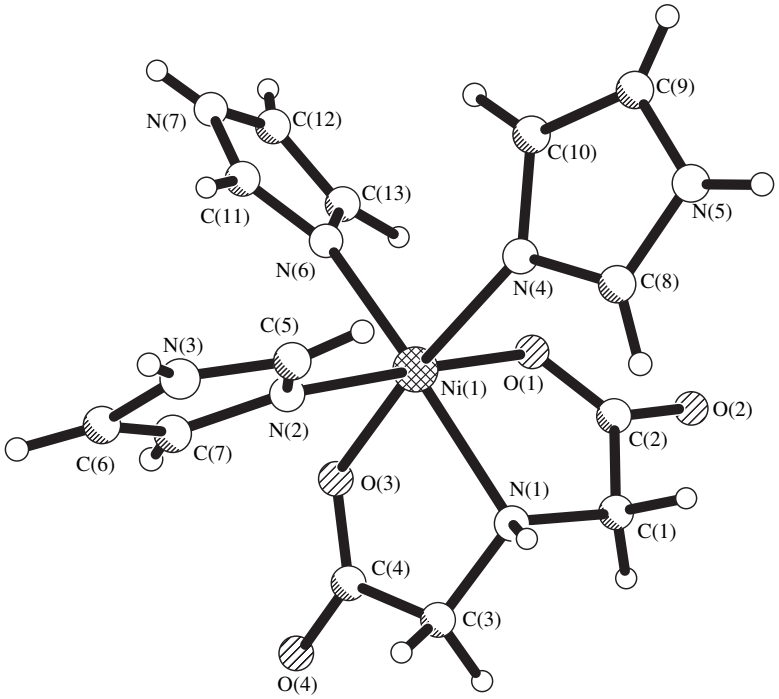

Fig. 1. Structure of the [Ni(*Ida*)(*Im*)$_3$] complex in compound **I**.

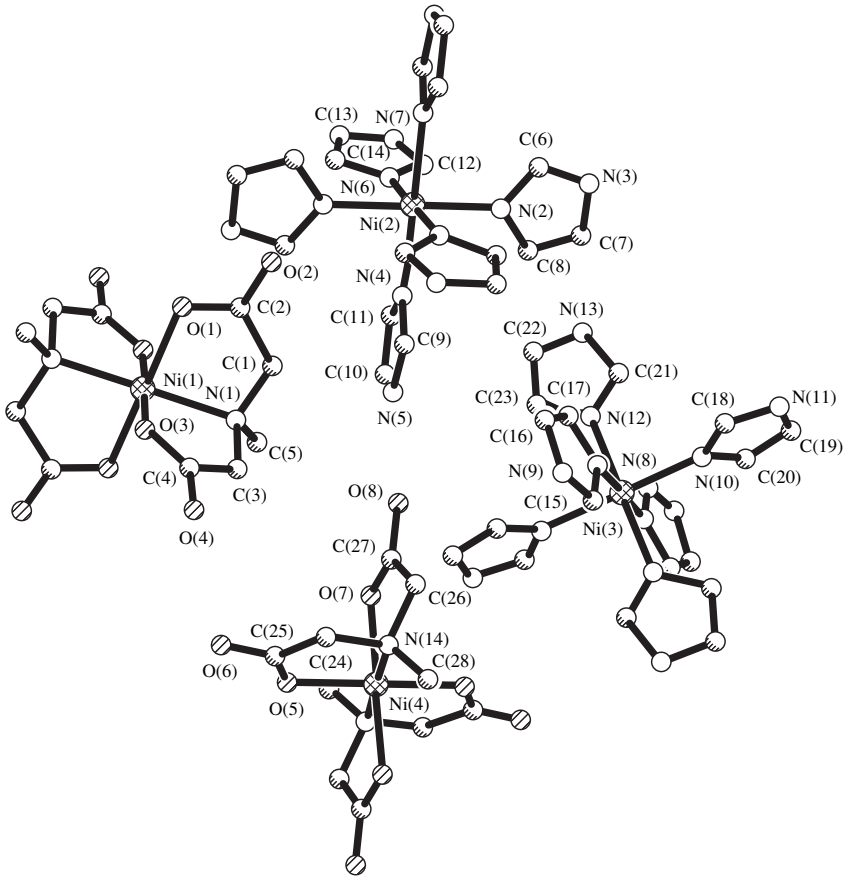

Fig. 2. Structures of anionic [Ni(*Mida*)$_2$]$^{2-}$ and cationic and [Ni(*Im*)$_6$]$^{2+}$ complexes in compound **II**. The hydrogen atoms are omitted.

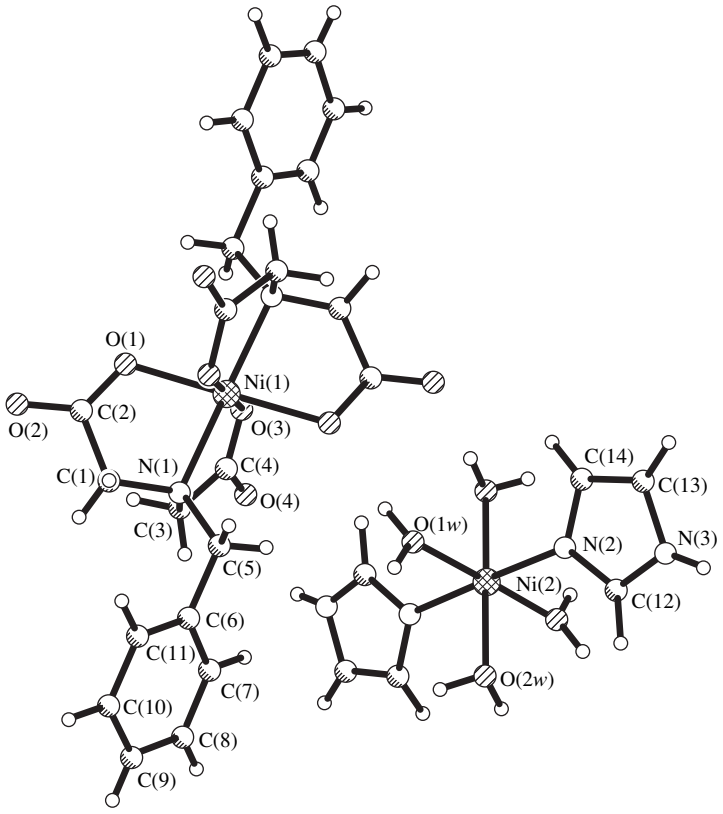

Fig. 3. Structures of anionic $[Ni(Bida)_2]^{2-}$ and cationic $[Ni(Im)_2(H_2O)_4]^{2+}$ complexes in compound **III**.

$K_2[Ni(Ida)_2][Ni(Ida)(H_2O)_3] \cdot 3H_2O$ (**V**) [9]). Similar to **I**, all the three complexes form facial isomers. The O–Ni–O angles lie in range from 86.4° to 92.8°. The bonds between the Ni atom and the *Ida* ligand in **I** [Ni–N, 2.113(2) Å; Ni–O, 2.080(2) and 2.082(2) Å] are slightly longer than those in the triaquacomplex of structure **V** [2.064(4), 2.045(4), and 2.052(3) Å, respectively]. The lengths of the Ni–N bonds with the imidazole molecules in structures **I** and **IV** have close values (av. 2.095 and 2.102 Å, respectively). The dihedral angles between the planes of the *Im* rings in **I** and two independent complexes **IV** have different values. The common feature of these complexes is the short distance between the plane of one of the *Im* rings and the basal NiO_2N_2 plane of the octahedron (the corresponding dihedral angles are 17.5° in **I** and 9.8° and 16.6° in **IV**).

In **II** and **III**, the $[Ni(Lig)_2]^{2-}$ complexes have the *trans* structure similar to almost all the known 1 : 2 complexes of nickel with the ligands of the iminodiacetate series, namely, $Cs_2[Ni(Ida)_2] \cdot 4H_2O$ (**VI**) [10], $Li_2[Ni(Ida)_2] \cdot 4H_2O$ (**VII**) [10, 11], and $Na_2[Ni(Heida)_2] \cdot 4H_2O$ (**VIII**) [12], where H_2Heida is hydroxyethyliminodiacetic acid. There is the only example of the *cis*-$[Ni(Ida)_2]^{2-}$ complex: this anion is a part of the abovementioned compound **V** [9].

The coordination octahedra (2N + 4O) in all the *trans* complexes are close in geometry. The Ni–N bond lengths in the complexes of *Ida* [2.091(2) Å in **VI** and 2.079(2) Å in **VII**], *Mida* [2.081(3) and 2.085(3) Å in **II**], and *Bida* [2.090(2) Å in **III**] are almost identical. In the *Heida* complex, the Ni–N bond is slightly elongated [2.108(3) Å [11]]. In two independent *Mida* complexes and the *Bida* complex, the Ni–O distances differ significantly and fall outside the narrow range of bond lengths (2.042–2.065 Å) observed in the *Ida* and *Heida* compounds [2.039(3), 2.083(3) and 2.054(3), 2.079(3) Å in **II**; 2.059(2), 2.093(2) Å in **III**]. Note that, in complexes **II** and **III**, as well as in **IV**, in which the Ni–O bond lengths are nonequivalent, the long Ni–O bond is included in the more puckered ring with the *N*-envelope conformation. In these rings, the endochelate angles are decreased to the largest degree [81.8(1)° and 81.7(1)° in **II**; 80.62(8)° in **III**].

A retrieval from the Cambridge Structural Database revealed several compounds of the $[Ni(Im)_6]^{2+}$ cationic complex with inorganic anions, namely, Cl^- [13], ClO_4^- [14], NO_3^- [15], BF_4^- [16], and SO_4^{2-} [17]. In the nitrate [15], the cation occupies a high-symmetry position (threefold rotation axis), which provides identical relative rotations of all the *Im* rings (106.4°). In the

remaining compounds,[1] similar to **II**, the $[Ni(Im)_6]^{2+}$ complexes are located at the centers of inversion, and the dihedral angles between the planes of the *Im* rings deviate from the ideal position to different degrees under the effect of hydrogen bonds and molecular packing.

The Cambridge Database contains a single example of a nickel complex with *Im* and H_2O molecules: it is the $[Ni(Im)_4(H_2O)_2]^{2+}$ cation (**IX**) in the compound with the saccharin anion [8]. In this centrosymmetric cation, the planes of two independent *Im* molecules form an angle of 88.7°.

In the $[Ni(Im)_6]^{2+}$ complexes with inorganic anions, the Ni–N bond lengths fall within a very narrow range (2.122–2.134 Å). Compound **II** expands this range in both directions (2.102–2.162 Å). In diaquacomplex **IX**, the Ni–N bond lengths are close the lower bound of the range [2.093(3) and 2.113(3) Å], and in tetraaqua-complex **III**, the Ni–N bond is noticeably shorter [2.061(3) Å].

Thus, crystals of different compositions precipitate under the same conditions from aqueous solutions of the Ni^{2+}–Lig^{2-}–*Im* systems, where Lig^{2-} is *Ida*, *Mida*, or *Bida*. Structures **II** and **III** are the first examples of the Ni^{2+} compounds, in which the competing ligands form separate complexes. Structure **II** provides the first example of a compound between the $[Ni(Im)_6]^{2+}$ cation and an anionic complex formed by an organic ligand. In structure **III**, the $[Ni(Im)_2(H_2O)_4]^{2+}$ cationic complex was first revealed and described.

ACKNOWLEDGMENTS

We are grateful to the Russian Foundation for Basic Research (project no. 96-07-89187) for financially supporting the license to use the Cambridge Structural Database, which was widely employed for the analysis of the structural results obtained in this work. The study was supported in part by the Belarussian Republican Foundation for Basic Research (project no. F96-92).

[1] The structure of $[Ni(Im)_6]SO_4 \cdot 6H_2O$ [17] is not determined. Judging from the unit-cell dimensions and symmetry, the $[Ni(Im)_6]^{2+}$ cation occupies either position $\bar{3}$ in space group $P6_3/m$ or position 3 in space group $P6_3$.

REFERENCES

1. M. R. Wagner and D. B. Beach, Acta Crystallogr., Sect. C: Cryst. Struct. Commun. **41**, 669 (1985).
2. A. S. Antsyshkina, G. G. Sadikov, V. S. Sergienko, and A. L. Poznyak, Zh. Neorg. Khim. **42**, 238 (1997).
3. L. P. Battaglia, A. B. Corradi, L. Antolini, *et al.*, J. Am. Chem. Soc. **104**, 2407 (1982).
4. N. M. Dyatlova, V. Ya. Temkina, and K. I. Popov, in *Complexones and Metal Complexonates* (Khimiya, Moscow, 1988), p. 14.
5. G. M. Sheldrick, Acta Crystallogr., Sect. A: Found. Crystallogr. **46**, 467 (1990).
6. G. M. Sheldrick, *SHELX76: Program for Crystal Structure Determination* (Univ. of Cambridge, Cambridge, 1976).
7. N. Walker and D. Stuart, Acta Crystallogr., Sect. A: Found. Crystallogr. **39**, 158 (1983).
8. Yu. Zhang, J. Li, W. Lin, *et al.*, J. Crystallogr. Spectrosc. Res. **22**, 433 (1992).
9. V. M. Agre, T. F. Sysoeva, V. K. Trunov, *et al.*, Zh. Strukt. Khim. **25**, 141 (1984).
10. N. J. Mammano, D. H. Templeton, and A. Zalkin, Acta Crystallogr., Sect. B: Struct. Crystallogr. Cryst. Chem. **33**, 1251 (1977).
11. F. G. Kramarenko, T. N. Polynova, M. A. Poraĭ-Koshits, *et al.*, Zh. Strukt. Khim. **15**, 161 (1974).
12. I. N. Polyakova, T. N. Polynova, and M. A. Poraĭ-Koshits, Koord. Khim. **8**, 1268 (1982).
13. J. P. Konopelski, C. W. Reimann, C. R. Hubbard, *et al.*, Acta Crystallogr., Sect. B: Struct. Crystallogr. Cryst. Chem. **32**, 2911 (1976).
14. G. J. M. Ivarsson and W. Forsling, Acta Crystallogr., Sect. B: Struct. Crystallogr. Cryst. Chem. **35**, 1896 (1979).
15. A. J. Finney, M. A. Hitchman, C. L. Raston, *et al.*, Aust. J. Chem. **34**, 2113 (1981).
16. A. D. van Ingen Schenau, Acta Crystallogr., Sect. B: Struct. Crystallogr. Cryst. Chem. **31**, 2736 (1975).
17. N. D. Phung, J.-C. Tedenac, and M. Maurin, J. Inorg. Nucl. Chem. **38**, 2316 (1976).

Translated by I. Polyakova

Crystallography Reports, Vol. 45, No. 5, 2000, pp. 771–774. Translated from Kristallografiya, Vol. 45, No. 5, 2000, pp. 842–845.

STRUCTURE OF ORGANIC COMPOUNDS

Crystal and Molecular Structures of Potassium Cobalt Hydrogen Phthalate $K_2[Co(H_2O)_6](C_8H_5O_4)_4 \cdot 4H_2O$ and Mechanism of Co^{2+} Impurity Trapping in KAP Crystals

N. G. Furmanova, T. A. Eremina, T. M. Okhrimenko, and V. A. Kuznetsov

Shubnikov Institute of Crystallography, Russian Academy of Sciences, Leninskiĭ pr. 59, Moscow, 11733 Russia

e-mail: furm@rsa.crystal.msk.su

Received November 3, 1998

Abstract—The single-crystal X-ray diffraction analysis of $K_2[Co(H_2O)_6](C_8H_5O_4)_4 \cdot 4H_2O$ has been carried out. The $K_2[Co(H_2O)_6](C_8H_5O_4)_4 \cdot 4H_2O$ single crystals are obtained in attempting to grow the KAP crystals with the maximum possible content of Co^{2+} impurity cations. The crystals are isostructural to the earlier-studied similar crystals with Ni(II). The structure is formed by double layers of biphthalate anions and the Co^{2+} and K^+ cations in between. The Co^{2+} cations are coordinated only by water molecules, whereas the coordination of the K^+ cations involves both the biphthalate anions and water molecules. A detailed crystal chemical analysis, together with the data on the growth kinetics of KAP crystals in the presence of Co^{2+} and the mass-spectrometric data obtained earlier for the KAP crystals, leads to the conclusion that the Co^{2+} impurity cations should be located in the form of the $[Co(H_2O)_6]^{2+}$ cationic complexes in the interblock layers of the KAP crystals. © *2000 MAIK "Nauka/Interperiodica".*

INTRODUCTION

Earlier, we investigated how the impurities of trivalent and bivalent cations affect the crystallization kinetics and defect structure of the KAP crystals and found that the Co^{2+} impurity in a solution even at low concentrations (~10^{-5} mol %) brings about a drastic deterioration of the crystal quality, namely, the splitting of crystals along the (010) cleavage planes, a sharp increase in the amount of gas–liquid inclusions, and, eventually, the turbidity of crystals. No similar phenomena are observed for other impurities (for example, Fe^{3+} and Cr_3+) at comparable concentrations. This suggests a specific character of the incorporation of Co^{2+} impurities into the KAP structure, which should be accompanied by a strong deformation of the structure. As follows from our crystal chemical analysis of the KAP structure [1], the conditions for the incorporation of the Co^{2+} ions into the K^+ positions are extremely unfavorable due to a large difference between the radii of K^+ (1.33 Å) and Co^{2+} (0.78 Å) ions. The KAP structure have no holes that can be occupied by the impurity cations, as is the case in KDP crystals [2].

In order to elucidate the mechanism of incorporating Co^{2+} into the KAP structure, the KAP crystals were grown from a solution highly enriched with Co^{2+} (~1 mol %) by its evaporation at room temperature. As a result, we obtained crystals (morphologically identical and without visible defects) of two types: almost colorless and light-rose crystals (without intermediate variants). The preliminary X-ray structure investigation revealed that the colorless crystals are the KAP crystals, and the unit cell parameters of the light-rose samples differ from those of the KAP crystals. To determine the composition and structure of the light-rose crystals, we carried out their complete X-ray diffraction analysis.

EXPERIMENTAL

A single crystal $0.5 \times 0.5 \times 0.2$ mm in size was chosen for the investigation. A set of experimental intensities of diffraction reflections was obtained by Yu.L. Slovokhotov at room temperature on a Siemens diffractometer (MoK_α radiation, $\theta/2\theta$ scan mode, $\theta \le 27°$) at the Center of X-ray Structure Investigations (Nesmeyanov Institute of Organoelement Compounds, Russian Academy of Sciences). A total of 5824 reflections were measured, of which 5057 reflections were unique and 3428 reflections were observed with $I > 2\sigma(I)$. Crystals are monoclinic, a = 10.4344(9) Å, b = 6.8553(6) Å, c = 29.446(4) Å, and β = 98.065(8)°. According to the absences, the structure is uniquely assigned to the space group $P2_1/c$.

At the first stage, the structure was solved under the assumption of the $KCo(C_8H_5O_4)_3$ composition with the use of the AREN software package [3]. The direct method in the automatic mode failed. A decrease in the permissible probability of sign determination down to 0.8 resulted in the E-synthesis with R = 0.227 for 199 reflections. The phase correction [4] led to R = 0.257 for 3428 reflections with $F > 4\sigma(F)$; the electron den-

Atomic coordinates and equivalent [isotropic for O(4), O(4'), and all H] thermal parameters U_{eq}/U_{iso} (Å^2)

Atom	*x*	*y*	*z*	U_{eq}/U_{iso}
Co	0.5	0.5	0.5	0.0264(1)
K	0.79135(9)	0.0539(1)	0.47368(3)	0.0582(2)
O(1)	0.3768(2)	0.2619(3)	0.47764(8)	0.0352(4)
O(2)	0.3608(2)	0.7034(3)	0.47159(8)	0.0389(4)
O(3)	0.4148(3)	0.5055(4)	0.55869(8)	0.0542(6)
O(4)	0.924(1)	0.005(1)	0.5560(3)	0.087(3)
O(4')	0.8581(7)	−0.0001(8)	0.5687(2)	0.064(2)
O(5)	0.9662(6)	−0.2758(8)	0.4912(2)	0.095(2)
O(5')	0.863(2)	−0.386(3)	0.4753(6)	0.107(8)
O(6)	1.0226(2)	−0.3464(4)	0.39389(9)	0.0534(6)
O(7)	1.1760(2)	−0.5372(4)	0.42835(9)	0.0556(6)
O(8)	0.8816(2)	−0.7300(4)	0.40230(8)	0.0609(7)
O(9)	0.7578(2)	−0.7842(4)	0.33562(8)	0.0442(5)
O(10)	0.5884(2)	0.1702(3)	0.38971(9)	0.0529(6)
O(11)	0.4682(2)	−0.0176(3)	0.42649(8)	0.0509(6)
O(12)	0.7424(2)	−0.2121(4)	0.40397(8)	0.0539(6)
O(13)	0.8157(2)	−0.2887(4)	0.33915(8)	0.0460(6)
C(1)	1.0869(2)	−0.6151(4)	0.3519(4)	0.0326(6)
C(2)	0.9788(3)	−0.7262(4)	0.33418(9)	0.0320(6)
C(3)	0.9770(3)	−0.8268(5)	0.2933(1)	0.0414(7)
C(4)	1.0809(4)	−0.8155(5)	0.2690(1)	0.0525(9)
C(5)	1.1872(4)	−0.7054(6)	0.2862(1)	0.0574(9)
C(6)	1.1914(3)	−0.6084(5)	0.3272(1)	0.0459(8)
C(7)	1.0944(2)	−0.4940(4)	0.3946(1)	0.0361(6)
C(8)	0.8683(3)	−0.7453(4)	0.3611(1)	0.0355(6)
C(9)	0.4975(2)	−0.1102(4)	0.35120(9)	0.0302(6)
C(10)	0.5936(2)	−0.2228(4)	0.33520(9)	0.0297(5)
C(11)	0.5646(3)	−0.3299(4)	0.2949(1)	0.0384(6)
C(12)	0.4428(4)	−0.3223(5)	0.2700(1)	0.0466(8)
C(13)	0.3484(3)	−0.2103(5)	0.2853(1)	0.0489(8)
C(14)	0.3744(3)	−0.1079(4)	0.3259(1)	0.0403(7)
C(15)	0.5213(2)	0.0204(4)	0.3926(1)	0.0327(6)
C(16)	0.7248(3)	−0.2378(4)	0.3626(1)	0.332(6)
H(1O1)	0.411(4)	0.179(7)	0.462(1)	0.07(1)
H(2O1)	0.321(4)	0.296(6)	0.462(1)	0.06(1)
H(1O2)	0.393(4)	0.776(7)	0.451(2)	0.07(1)
H(2O2)	0.301(4)	0.650(6)	0.456(1)	0.06(1)
H(1O3)	0.422(4)	0.610(7)	0.576(1)	0.07(1)
H(2O3)	0.372(4)	0.434(6)	0.568(1)	0.06(1)
H(O9)	0.703(4)	−0.798(6)	0.355(1)	0.06(1)
H(O13)	0.884(5)	−0.304(7)	0.359(2)	0.08(2)
H(C3)	0.902(4)	−0.909(6)	0.281(1)	0.06(1)
H(C4)	1.085(4)	−0.878(6)	0.242(1)	0.06(1)
H(C5)	1.258(4)	−0.697(7)	0.268(2)	0.08(1)
H(C6)	1.265(4)	−0.540(6)	0.340(1)	0.06(1)
H(C11)	0.630(4)	−0.409(6)	0.285(1)	0.06(1)
H(C12)	0.421(4)	−0.384(6)	0.243(1)	0.06(1)
H(C13)	0.268(4)	−0.212(5)	0.269(1)	0.05(1)
H(C14)	0.311(3)	−0.042(5)	0.337(1)	0.05(1)

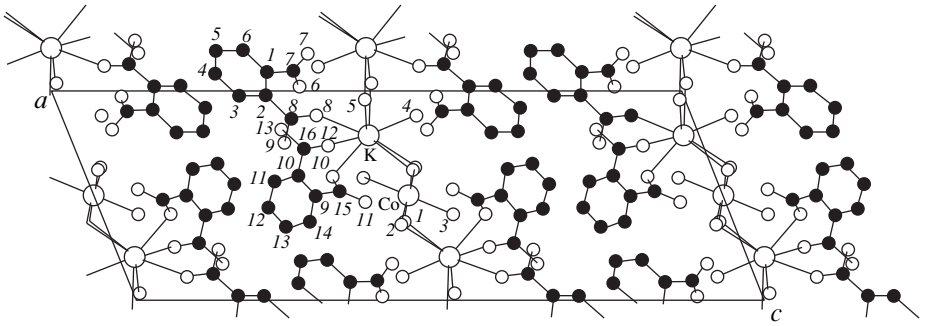

Projection of the $K_2[Co(H_2O)_6](C_8H_5O_4)_4 \cdot 4H_2O$ structure onto the *ac* plane. The hydrogen atoms and the splitting of the O(4) and O(5) positions are omitted. Numbering of O (open circles) and C (filled circles) atoms matches that given in the table.

sity synthesis made it possible to reveal the Co atom at the center of symmetry and the K atom, two biphthalate anions, and five water molecules in general positions. Therefore, the studied compound has the formula $K_2[Co(H_2O)_6](C_8H_5O_4)_4 \cdot 4H_2O$ (**I**), and the crystals are isostructural to the previously studied similar crystals with Ni(II) (**II**) [5].[1] For the above formula unit, $Z = 2$ and $d_{calcd} = 1.557$ g/cm^3.

Structure **I** was refined first in the isotropic approximation and then in the anisotropic approximation according to the SHELXL93 software package [7]. At this stage, the hydrogen atoms, except for the atoms of water molecules involving the O(4) and O(5) atoms (with increased thermal parameters), were located from the difference synthesis. The second position of the O(5) atom [hereafter, O(5')] was determined from the subsequent difference synthesis. In the course of the refinement, the position O(4) was also split [O(4) and O(4')]. The refinement of this model in the anisotropic approximation for the non-hydrogen atoms [except the O(4) and O(4') atoms] and in the isotropic approximation for these oxygen atoms and hydrogen atoms led to $R1 = 0.0481$ for 3428 reflections with $F > 4\sigma(F)$ and 0.0953 for all 5057 reflection (352 refined parameters); $wR2 = 0.1347$ and $S = 1.048$ for 5013 reflections used in the least-squares procedure; and $(\Delta/\sigma)_{max} = 0.003$, $\rho_{max} = 0.59$ e/Å^3, and $\rho_{min} = -0.43$ e/Å^3.

The site occupancies of the O(5) and O(5') atoms are equal to 0.77(1) and 0.23(1), respectively. These values are somewhat different from the occupancies for compound **II** (0.67 and 0.33, respectively) [5]. The site occupancies of the O(4) and O(4') atoms in crystal **I** are approximately identical [0.48(1) and 0.52(1)]. In structure **II**, the corresponding position is not split, but the O(4) atom has the increased parameter $B_{eq} = 13.2(2)$ Å^2. The atomic coordinates and thermal parameters in structure **I** are listed in the table.

[1] The data for this structure and the structures of cobalt hydrogen phthalates (see below) were obtained using the Cambridge Structural Database [6].

RESULTS AND DISCUSSION

Similar to hydrogen phthalates of alkali metals (K, Rb, and Cs) [8], cobalt hydrogen phthalate hexahydrate [9, 10], and a number of other metal hydrogen phthalates [11], compound **I** has a layered structure (figure). In **I**, the double layers of biphthalate anions are aligned parallel to the (001) plane. In these layers, the anions are joined into chains parallel to [100] by the hydrogen bonds between the carboxyl group of one anion and the carboxylate group of another anion. The cations are located between the anion layers. Note that the cation layer in structure **I** can be considered as consisting of chains of similar cations that are aligned parallel to [100] and alternate along [010]. The Co^{2+} cation is coordinated only by water molecules forming its octahedral environment. The Co–O distances (2.125, 2.052, and 2.100 Å) are close to those determined in [9, 10] (2.047–2.150 Å). The K^+ cations are coordinated by the O atoms of both the anions and the water molecules (K–O, 2.639–3.244 Å). They are alternately adjacent to one of the neighboring anion layer and are coordinated by the water molecules of the second layer. Thus, compared to the pure KAP crystal, in which each K^+ cation is in contact with both layers, the anion layers in the mixed crystal are separated: the thickness of a cation–anion "stack" is $(c/2)\sin\beta = 14.578$ Å in crystal **I** and $b = 13.330$ Å in the KAP crystal [12].

It is worth noting that, in compound **I** and the aforementioned cobalt hydrogen phthalate hexahydrates [9, 10], the Co^{2+} cation is coordinated only by the water molecules. One more modification of cobalt hydrogen phthalate also crystallizes in the form of hexahydrate [13]. Unlike the other polymorphic forms [9, 10], this structure does not contain well-defined layers, and the strong intramolecular hydrogen bond between the carboxyl and carboxylate groups is realized in the biphthalate anion. However, in this structure cobalt occurs in the form of the $[Co(H_2O)_6]^{2+}$ cationic complex as well.

The above results and the crystal chemical analysis of the KAP structure suggest with a high degree of confidence that, most probably, the Co^{2+} impurity cations are imbedded into the interblock layers in the form of

the hydrated complexes $[Co(H_2)_6]^{2+}$. The KAP crystals exhibit a perfect cleavage along the (010) pinacoid face, which corresponds to the layer plane. Earlier [14], it was experimentally demonstrated that monomolecular water interlayers are arranged along these planes in the crystals. These interlayers are interpreted as regions of the surface adsorption film, which is "immured" in the course of crystal growth [15].

These findings and the structural features of the (010) face [12] confirm a high hydration activity of the (010) surface during the crystal growth. This most likely promotes the adsorption of Co^{2+} on the (010) surface either immediately in the form of the $[Co(H_2O)_6]^{2+}$ complex or in the form of isolated Co^{2+} ion followed by the formation of the hydrated complex at the surface. During the growth, the complexes are immured in the interblock layers, which should be attended by a strong deformation of local regions in the crystalline matrix, i.e., by a considerable separation of the anion layers (by more than 1 Å).

The data obtained enable us to make the following inferences confirmed experimentally:

(i) The strong lattice deformations prevent the incorporation of the Co^{2+} impurity into the structure, and, hence, the trapping coefficient for Co^{2+} in the KAP crystals should be small, which is characteristic of bivalent cation impurities in these crystals [16]. Actually, we failed to obtain the KAP crystals containing more than $\sim 10^{-3}$ mol % Co^{2+}, and, according to our estimates, the trapping coefficient for Co^{2+} does not exceed $\sim 10^{-3}$.

(ii) A substantial change in the *b* parameter in local regions upon incorporation of Co^{2+} even in small amounts should result in the cracking of crystals owing to the well-known phenomenon of the heterometry [17]. As mentioned above, this is observed at a cobalt content of more than $\sim 10^{-5}$ mol %.

ACKNOWLEDGMENTS

This work was supported by the Russian Foundation for Basic Research, project nos. 96-03-34141, 96-07-80187, and 97-03-33783.

REFERENCES

1. G. B. Bokiĭ, *Crystal Chemistry* (Nauka, Moscow, 1971).
2. T. A. Eremina, V. A. Kuznetsov, T. M. Okhrimenko, and N. G. Furmanova, Kristallografiya **41**, 717 (1996) [Crystallogr. Rep. **41**, 680 (1996)].
3. V. I. Andrianov, Kristallografiya **32**, 228 (1987) [Sov. Phys. Crystallogr. **32**, 130 (1987)].
4. V. I. Andrianov, T. A. Shibanova, and V. I. Simonov, Kristallografiya **32**, 41 (1987) [Sov. Phys. Crystallogr. **32**, 20 (1987)].
5. M. B. Cingi, A. M. M. Lanfredi, and A. Tiripicchio, Acta Crystallogr., Sect. C: Cryst. Struct. Commun. **40**, 56 (1984).
6. F. H. Allen, S. A. Bellard, M. D. Brice, *et al.*, Acta Crystallogr., Sect. B: Struct. Crystallogr. Cryst. Chem. **35**, 2331 (1979).
7. G. M. Sheldrick, *SHELXL93: Program for the Refinement of Crystal Structures* (Univ. of Göttingen, Göttingen, 1993).
8. N. I. Sorokina, V. N. Molchanov, T. N. Turskaya, *et al.*, Kristallografiya **34**, 112 (1989) [Sov. Phys. Crystallogr. **34**, 64 (1989)].
9. G. Adiwidjaja, E. Rossmanith, and H. Kuppers, Acta Crystallogr., Sect. B: Struct. Crystallogr. Cryst. Chem. **34**, 3079 (1978).
10. B. M. Kariuki and W. Jones, Acta Crystallogr., Sect. C: Cryst. Struct. Commun. **49**, 2100 (1993).
11. B. M. Kariuki and W. Jones, Mol. Cryst. Liq. Cryst. **211**, 233 (1992).
12. T. A. Eremina, N. G. Furmanova, L. F. Malakhova, *et al.*, Kristallografiya **38**, 236 (1993) [Crystallogr. Rep. **38**, 554 (1993)].
13. H. Kuppers, Z. Kristallogr. **192**, 97 (1990).
14. O. F. Pozdnyakov, B. P. Redkov, A. S. Smirnov, *et al.*, Kristallografiya **33**, 994 (1988) [Sov. Phys. Crystallogr. **33**, 588 (1988)].
15. T. M. Okhrimenko, V. A. Kuznetsov, O. F. Pozdnyakov, and V. P. Redkov, Kristallografiya **42**, 541 (1997) [Crystallogr. Rep. **42**, 494 (1997)].
16. M. H. J. Hottenhuis and C. B. Lucasius, J. Cryst. Growth **91**, 623 (1988).
17. A. A. Shternberg, Kristallografiya **7**, 114 (1962) [Sov. Phys. Crystallogr. **7**, 92 (1962)].

Translated by O. Borovik-Romanova

Crystallography Reports, Vol. 45, No. 5, 2000, pp. 775–777. Translated from Kristallografiya, Vol. 45, No. 5, 2000, pp. 846–849.

STRUCTURE OF ORGANIC COMPOUNDS

Crystal and Molecular Structures of 4-*N*-Morpholino-7-Phenyl-1,3-Isobenzofurandione

A. S. Lyakhov*, L. S. Ivashkevich*, G. K. Zhavnerko, T. A. Kuchuk**, O. L. Sadovskiĭ**, and A. A. Govorova*****

** Research Institute of Physicochemical Problems, Belarussian State University, Leningradskaya ul. 14, Minsk, 220080 Belarus*

*** Institute of Physicoorganic Chemistry, Belarussian Academy of Sciences, Minsk, 220072 Belarus*

**** Institute of Bioorganic Chemistry, Belarussian Academy of Sciences, Zhodinskaya ul. 5/2, Minsk, 220141 Belarus*

e-mail: lyakhov@fhp.bsu.unibel.by

Received December 30, 1998

Abstract—The crystal and molecular structures of 4-*N*-morpholino-7-phenyl-1,3-isobenzofurandione have been determined by X-ray diffraction analysis (Nicolet *R*3*m* automated diffractometer, MoK_α radiation, graphite monochromator, θ/2θ scan mode). It is found that the compound crystallizes in the orthorhombic system, space group *Pbca*. The unit cell parameters are as follows: $a = 7.773(2)$ Å, $b = 14.652(3)$ Å, $c = 25.614(5)$ Å, and $Z = 8$. The structure is solved by the direct method and refined to $R1 = 0.0504$ [$I > 2\sigma(I)$]. The conformational and geometric characteristics of the studied compound and the molecular packing in the crystal are discussed. © *2000 MAIK "Nauka/Interperiodica".*

INTRODUCTION

In recent years, considerable interest has been expressed by researchers in the crystal structure of 4-*N*-morpholino-7-phenyl-1,3-isobenzofurandione because this compound is very promising in the preparation of thin organic films by the thermal vacuum evaporation technique [1]. As a rule, organic vacuum-evaporated films have an amorphous or polycrystalline structure. However, the production of epitaxial ordered films is an urgent problem. The epitaxial oriented organic films were grown on the high-energy surfaces of ionic crystals (see, for example, [2, 3]). Of special interest is the problem concerning the formation of "quasi-epitaxial" films on different-type surfaces (with mismatched crystal structures of a growing layer and the substrate, on modifying single-layer coatings, etc.) [4–6]. It is believed that the *structure* of evaporated organic compound plays a decisive role in the quasi-epitaxial growth. In this respect, investigations into the crystal and molecular structures of evaporated compounds are of crucial importance.

The structural studies make it possible to reveal the main regularities in the oriented growth of films and to elucidate the *compound structure–substrate structure–film properties* correlations.

The purpose of this work was to determine the molecular and crystal structures of 4-*N*-morpholino-7-phenyl-1,3-isobenzofurandione

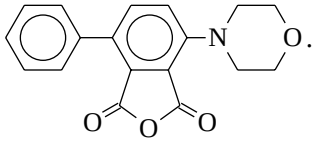

EXPERIMENTAL

4-*N*-Morpholino-7-phenyl-1,3-isobenzofurandione was synthesized according to the procedure described in [7]. The compound was further purified by extractive crystallization from toluene. Single crystals were obtained by crystallization of the compound from ethyl alcohol at room temperature. A prismatic single crystal $0.9 \times 0.6 \times 0.4$ mm in size was chosen for the X-ray diffraction analysis.

A three-dimensional set of X-ray diffraction data was collected on a Nicolet *R*3*m* automated four-circle diffractometer (MoK_α radiation, graphite monochromator, θ/2θ scan mode, $2\theta_{max} = 55°$). The structure of 4-*N*-morpholino-7-phenyl-1,3-isobenzofurandione was solved by the direct method. The hydrogen atoms were located from the difference Fourier synthesis. The refinement was performed by the full-matrix least-squares method with allowance made for anisotropic thermal vibrations of non-hydrogen atoms. The hydrogen atoms were refined in the isotropic approximation. All the calculations were carried out with the SHELX97 (PC Version) software package [8–10]. The crystal data and least-squares refinement parameters of the structure are presented in Table 1. The atomic coordinates and isotropic equivalent thermal parameters are listed in Table 2.

RESULTS AND DISCUSSION

Figure 1 demonstrates the molecular structure of 4-*N*-morpholino-7-phenyl-1,3-isobenzofurandione. The morpholine substituent adopts a typical chair confor-

1063-7745/00/4505-0775$20.00 © 2000 MAIK "Nauka/Interperiodica"

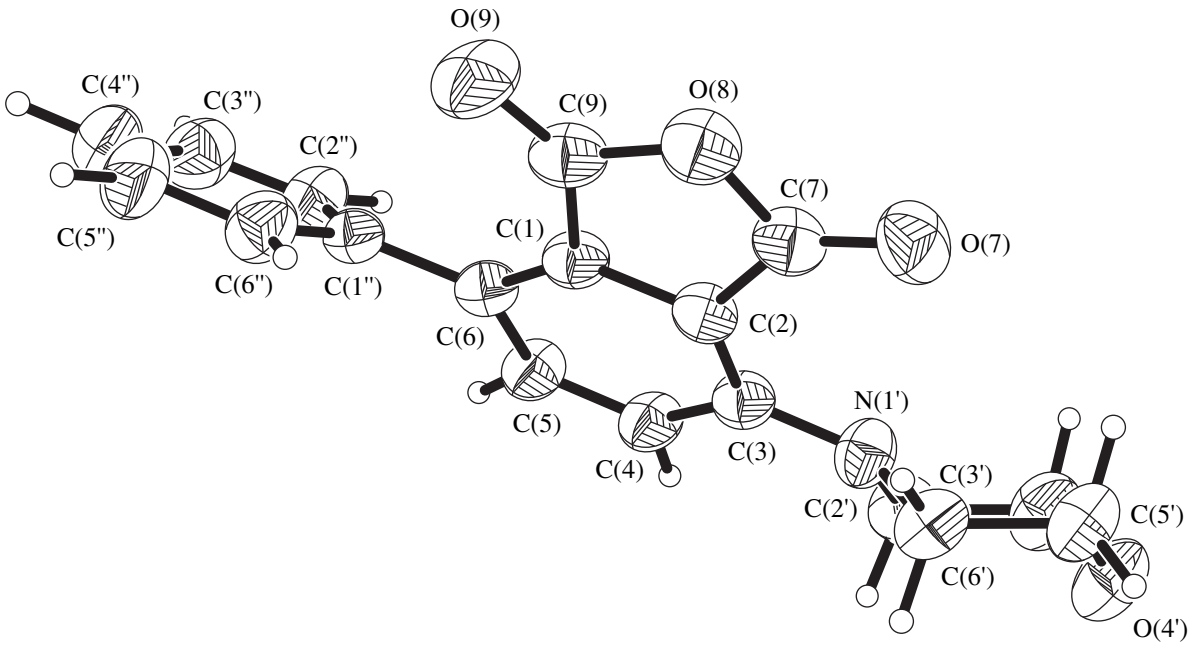

Fig. 1. Molecular structure of 4-*N*-morpholino-7-phenyl-1,3-isobenzofurandione.

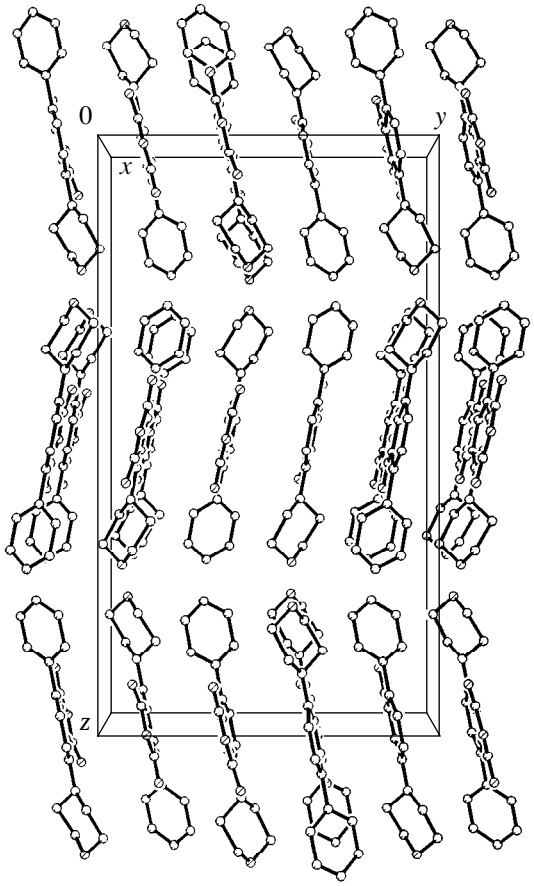

Fig. 2. Molecular packing in the structure of 4-*N*-morpholino-7-phenyl-1,3-isobenzofurandione.

mation. The C(2'), C(3'), C(5'), and C(6') atoms form the planar part of the morpholine ring. Their mean deviation from the root-mean-square plane is equal to 0.008 Å. The folding angles of the N and O corners are 51.4(1)° and 53.2(2)°, respectively. The phenyl substituent is planar: the mean deviation of the atoms in the phenyl ring from the root-mean-square plane is equal to 0.004 Å. The bond lengths and bond angles in the aforementioned rings are not significantly different from those usually observed in similar systems [11]. The phenyl ring of the isobenzofurandione fragment is also planar; however, the mean deviation of the atoms from the root-mean-square plane is somewhat larger (0.01 Å). The angle between the planes of the phenyl substituent and the phenyl ring of isobenzofurandione is equal to 43.82(8)°. The planar part of the morpholine ring is rotated through an angle of 38.5(1)° with respect to the plane of the phenyl ring of isobenzofurandione. The structure of the isobenzofurandione fragment in 4-*N*-morpholino-7-phenyl-1,3-isobenzofurandione differs only slightly from the structure of isobenzofurandione [12] and its methyl derivative [13]. A decrease in the bond angles (by ~2°) at the atoms of the phenyl ring with substituents is associated with the electron-donating character of these substituents, which follows from analysis of the data available in the literature [14].

The molecular packing in the structure is shown in Fig. 2. As can be seen the 4-*N*-morpholino-7-phenyl-1,3-isobenzofurandione molecules form the layers aligned parallel to the *ab* plane of the unit cell. In this case, the molecules in the layer are arranged such that the planes of the isobenzofurandione fragments are parallel and the orientation of adjacent molecules can be

Table 1. Crystal data and least-squares refinement parameters for the structure of 4-*N*-morpholino-7-phenyl-1,3-isobenzofurandione

Empirical formula	$C_{18}H_{15}NO_4$
Molecular weight	309.31
Temperature	293(2) K
Crystal system	Orthorhombic
Space group	*Pbca*
Unit cell parameters	a = 7.773(2) Å
	b = 14.652(3) Å
	c = 25.614(5) Å
Volume	2917.2(11) Å^3
Z	8
Density	1.409 g/cm^3
μ	1.00 cm^{-1}
No. of measured reflections:	
total/unique	3019/2728 [$R_{(int)}$ = 0.0538]
Refinement technique	Full-matrix least-squares method on F^2
Goodness-of-fit on F^2	1.026
R [$I > 2\sigma(I)$]	$R1$ = 0.0504, $wR2$ = 0.1370
R (for all reflections)	$R1$ = 0.0590, $wR2$ = 0.1476
Extinction coefficient	0.0033(8)

Table 2. Atomic coordinates ($\times 10^4$) and equivalent isotropic thermal parameters (Å$^2 \times 10^3$) in the structure of 4-*N*-morpholino-7-phenyl-1,3-isobenzofurandione

Atom	*x*/*a*	*y*/*b*	*z*/*c*	U_{eq}
C(1)	4989(2)	1430(1)	284(1)	39(1)
C(2)	4896(2)	1236(1)	−252(1)	40(1)
C(3)	6377(2)	1069(1)	−553(1)	41(1)
C(4)	7934(2)	1067(1)	−269(1)	45(1)
C(5)	7993(2)	1246(1)	260(1)	46(1)
C(6)	6524(2)	1445(1)	560(1)	41(1)
C(7)	3073(2)	1119(1)	−387(1)	47(1)
C(9)	3190(2)	1493(1)	478(1)	47(1)
O(7)	2349(2)	883(1)	−776(1)	61(1)
O(8)	2111(2)	1304(1)	60(1)	55(1)
O(9)	2591(2)	1647(1)	895(1)	64(1)
N(1')	6316(2)	890(1)	−1081(1)	47(1)
C(2')	7817(3)	500(2)	−1345(1)	54(1)
C(3')	7228(4)	32(2)	−1841(1)	67(1)
O(4')	6319(2)	626(1)	−2178(1)	72(1)
C(5')	4846(3)	977(2)	−1917(1)	63(1)
C(6')	5355(3)	1498(2)	−1433(1)	53(1)
C(1")	6703(2)	1632(1)	1128(1)	42(1)
C(2")	7809(3)	1102(2)	1431(1)	53(1)
C(3")	7998(3)	1281(2)	1958(1)	64(1)
C(4")	7116(3)	1986(2)	2191(1)	68(1)
C(5")	6044(3)	2519(2)	1892(1)	67(1)
C(6")	5832(3)	2345(2)	1368(1)	55(1)

referred to as "antiparallel." No short contacts are observed in the structure, and therefore, the molecular packing is determined by the van der Waals interactions.

The crystal data obtained in the present work made it possible to evaluate the orientation of the 4-*N*-morpholino-7-phenyl-1,3-isobenzofurandione molecules in the thermally evaporated film and to examine the growth of plane-oriented films on different-type substrates under various evaporation conditions [6].

ACKNOWLEDGMENTS

This work was supported by the Russian Foundation for Basic Research, project no. 96-07-89187. We also acknowledge the support of this Foundation in the payment of the license to use the Cambridge Structural Database in analyzing the results obtained in this work.

REFERENCES

1. G. K. Zhavnerko, T. A. Kuchuk, and V. E. Agabekov, Thin Solid Films **286** (1–2), 227 (1996).
2. K. Matsushige, T. Hamano, T. Horiuchi, and J. B. Mullin, J. Cryst. Growth **146** (1–4), 641 (1995).
3. S. Hayashi, H. Yanagi, and M. Ashida, Mol. Cryst. Liq. Cryst. **216** (8), 135 (1992).
4. S. R. Forrest, P. E. Burrows, E. I. Haskal, and F. F. So, Phys. Rev. B **49** (16), 11309 (1994).
5. R. Schlesser, T. Dietrich, Z. Sitar, *et al.*, J. Appl. Phys. **78** (8), 4943 (1995).
6. G. K. Zhavnerko, V. E. Agabekov, T. A. Kuchuk, *et al.*, Zh. Fiz. Khim. **72** (8), 1427 (1998).
7. I. G. Tishchenko, O. G. Kulinkovich, and N. V. Masalov, Zh. Org. Khim. **18** (5), 991 (1982).
8. G. M. Sheldrick, *SHELX97: Program for the Solution and Refinement of Crystal Structures* (Univ. of Göttingen, Göttingen, Germany, 1997).
9. G. M. Sheldrick, Acta Crystallogr., Sect. A: Found. Crystallogr. **46**, 467 (1990).
10. G. M. Sheldrick, Z. Dauter, K. S. Wilson, *et al.*, Acta Crystallogr., Sect. D: Biol. Crystallogr. **49**, 18 (1993).
11. F. H. Allen and O. Kennard, Chem. Design Automat. News **8** (1), 31 (1993).
12. R. B. Bates and R. S. Cutler, Acta Crystallogr., Sect. B: Struct. Crystallogr. Cryst. Chem. **33**, 893 (1977).
13. G. Bocelli and A. Captoni, Acta Crystallogr., Sect. C: Cryst. Struct. Commun. **51**, 265 (1995).
14. *Accurate Molecular Structures: Their Determination and Importance*, Ed. by A. Domenicano and I. Hargittai (Oxford Univ. Press, Oxford, 1992; Mir, Moscow, 1997).

Translated by O. Borovik-Romanova

Crystallography Reports, Vol. 45, No. 5, 2000, pp. 778–781. Translated from Kristallografiya, Vol. 45, No. 5, 2000, pp. 850–853.

STRUCTURE OF ORGANIC COMPOUNDS

Synthesis and IR and NMR Spectroscopic Studies of Amino Derivatives of Oxo-, Thio-, and Selenopyrazole. Crystal and Molecular Structure of 1-Phenyl-3-Methyl-4-Methylene-(*N*-8-Aminoquinoline)-5-Oxopyrazole

A. S. Antsyshkina*, G. G. Sadikov*, A. I. Uraev, O. Yu. Korshunov**, A. L. Nivorozhkin**, and A. D. Garnovskiĭ****

** Kurnakov Institute of General and Inorganic Chemistry, Russian Academy of Sciences, Leninskiĭ pr. 31, Moscow, 117907 Russia*

*** Research Institute of Physical and Organic Chemistry, Rostov State University, Rostov-on-Don, 344090 Russia*

e-mail: asants@ionchran.rinet.ru

Received November 19, 1998; in final form, September 20, 1999

Abstract—Three compounds of the pyrazole series—*o*-oxo, thio, and seleno derivatives—have been synthesized and characterized by IR and NMR spectroscopy. The crystal structure of the oxo derivative is determined (Syntex $P2_1$ diffractometer, MoK_α radiation, graphite monochromator, $\theta/2\theta$ scan mode, $2\theta_{max} = 57°$, direct method, anisotropic–isotropic (H) least-squares refinement for 2015 reflections, $R = 0.043$, $wR2 = 0.1084$). The crystals are monoclinic, $a = 7.543(1)$ Å, $b = 7.850(2)$ Å, $c = 27.909(6)$ Å, $\beta = 93.79(3)°$, $Z = 2$, and space group $P2_1/c$. It is found that the *o*-hydroxyazomethine derivatives of the pyrazolone series exist in the crystal as 4-aminomethylene-5-oxo tautomers. The proton is localized at the exocyclic N atom. It lies in the plane of the main molecular fragment and participates in the intramolecular bifurcate N–H···O(N) hydrogen bond, which closes the six-membered and five-membered H-rings, respectively. *© 2000 MAIK "Nauka/Interperiodica".*

INTRODUCTION

Molecules of *o*-hydroxy(chalcogen)azomethine derivatives of the pyrazole series have attracted steady interest due to their tendency to tautomeric transformations [1–14] and the capacity to form metallochelate complexes [15–17].

According to the data of IR and NMR (^{1}H and ^{13}C) spectroscopy, compounds of this type exist in solutions of different organic solvents as an equilibrium of the (a)–(d) tautomers with the prevailing aminomethylene form (c):

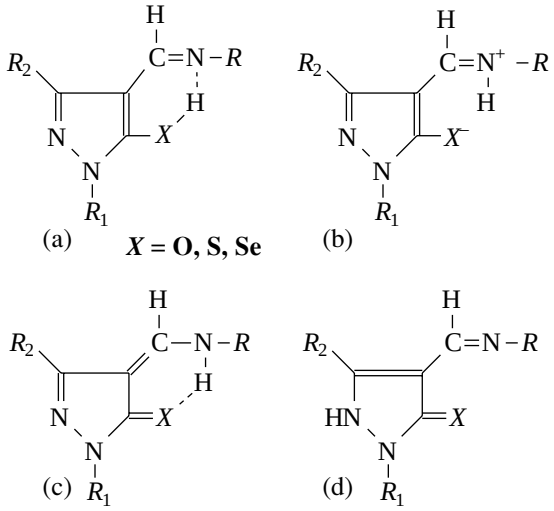

Up to now, the structure of the only compound of this type has been reported, namely, the compound with R = *cyclo*-C_6H_{11}, R_1 = *iso-Pr*, and R_2 = *Me* [18].

In order to establish correlations between the structures of molecules in solutions and in the crystalline state and to characterize hydrogen bonds, which are of considerable importance in the structures of these compounds, we determined the crystal structure of a 4-methylene-5-oxopyrazole derivative containing the 8-aminoquinoline substituent in the methylene fragment (**I**)

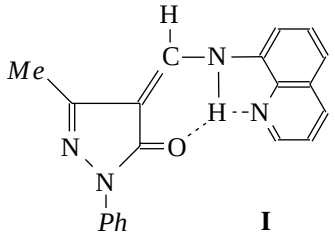

I

EXPERIMENTAL

Synthesis. An ethanol solution of 8-aminoquinoline (0.01 mol, 1.44 g) was added to an ethanol solution of 1-phenyl-3-methyl-4-formyl-5-hydroxypyrazole (0.01 mol, 2.06 g) prepared by the procedure described in [19, 20]. The mixture was heated for 10–15 min in a water bath. The yellow precipitate was filtered off,

washed with ethanol and ether, and recrystallized from a solution in isopropanol. The yield of compound **I** was 70%.

For $C_{20}H_{16}N_{40}$ anal. calcd. (%): C, 73.17; H, 4.89; N, 17.07.

Found (%): C, 72.8; H, 4.02; N, 16.95.

Crystals suitable for X-ray structure analysis were obtained by slow evaporation of a solution of the substance in isopropanol.

Amino derivatives of 5-thio- and 5-selenopyrazoles were prepared by the procedure described in [21].

IR and NMR studies. The IR spectra of the samples prepared as suspensions in Vaseline were recorded on a Specord 75-IR spectrophotometer. The ^{1}H NMR spectra of the compounds prepared as solutions in $CDCl_3$ were measured on a Varian UNITY-300 spectrometer. For 1-phenyl-3-methyl-4-methylene-(*N*-8-aminoquinoline)-5-oxopyrazole: ^{1}H NMR (δ, ppm, $CDCl_3$) 2.4 (s, 3H, CH_3), 7.1–9.0 (m, 11H, C_6H_5, =CH–NH=, C_9H_6N), 12.8–13.0 (br s, 1H).[1] For 1-phenyl-3-methyl-4-methylene-(*N*-8-aminoquinoline)-5-thiopyrazole: ^{1}H NMR (δ, ppm, $CDCl_3$) 2.35 (s, 2H, CH_3), 7.2–9.0 (m, 11H, C_6H_5, C_9H_6N), 8.5 (d, 1H, =CH–NH=, ^3J = 12 Hz), 15.2 (d, 1H, =NH–CH=, ^3J = 12 Hz). For 1-phenyl-3-methyl-4-methylene-(*N*-8-aminoquinoline)-5-selenopyrazole: ^{1}H NMR (δ, ppm, $CDCl_3$) 2.42 (s, 3H, CH_3), 7.0–9.1 (m, 11H, C_6H_5, C_9H_6N), 8.84 (d, 1H, =CH–NH=, ^3J = 12 Hz), 15.6 (d, 1H, =NH–CH=, ^3J = 12 Hz).

X-ray structure analysis. Crystals **I** are monoclinic. The unit cell parameters are as follows: a = 7.453(1) Å, b = 7.850(2) Å, c = 27.909(6) Å, β = 93.79(3)°, V = 1629.3(6) Å^3, M = 328.37, F(000) = 688, d_{calcd} = 1.339 g/cm^3, $\mu_{(Mo)}$ = 0.09 mm^{-1}, Z = 4, and space group $P2_1/n$.

The data set was collected on a Syntex $P2_1$ automated diffractometer (λMoK_α, graphite monochromator, θ/2θ scan mode, $2\theta_{max}$ = 57°). The structure was solved by the direct method using 2023 observed reflections with $I > 2\sigma(I)$. The hydrogen atoms were located from difference F syntheses. The structure was refined in the anisotropic (isotropic for H atoms) approximation by the full-matrix least-squares procedure to R = 0.0438 (0.0470 for all reflections), $wR2$ = 0.1084, and $GOOF$ = 0.85 for 2015 reflections and 291 parameters. The atomic coordinates are listed in the table.

The calculations were performed with the SHELXL93 software package [22] on an IBM Pentium 75 personal computer.

[1] Abbreviations: ppm—part per million, s—singlet, m—multiplet, br s—broad signal, d—doublet.

Fractional atomic coordinates and thermal parameters U_{eq} or U_{iso} for compound I

Atom	X	Y	Z	U_{iso}/U_{eq}, Å^2
O(1)	0.3694(4)	0.1255(4)	0.4110(1)	0.0932(9)
N(1)	0.1806(4)	0.1628(4)	0.5390(1)	0.0774(8)
N(2)	0.4944(5)	0.2572(4)	0.5036(1)	0.0782(8)
N(3)	0.5961(5)	0.1683(4)	0.3575(1)	0.0811(9)
N(4)	0.7713(5)	0.2342(4)	0.3605(1)	0.0835(9)
C(1)	0.1116(7)	0.2096(6)	0.6351(2)	0.089(1)
C(2)	–0.0121(7)	0.1363(6)	0.6042(2)	0.090(1)
C(3)	0.0289(6)	0.1149(5)	0.5563(2)	0.085(1)
C(4)	0.3053(5)	0.2358(4)	0.5699(1)	0.0709(9)
C(5)	0.2780(6)	0.2627(5)	0.6195(1)	0.078(1)
C(6)	0.4135(7)	0.3397(6)	0.6491(2)	0.090(1)
C(7)	0.5685(7)	0.3907(6)	0.6310(2)	0.095(1)
C(8)	0.5975(6)	0.3660(6)	0.5824(2)	0.086(1)
C(9)	0.4719(5)	0.2888(5)	0.5524(1)	0.0746(9)
C(10)	0.6396(6)	0.2914(5)	0.4803(2)	0.076(1)
C(11)	0.6553(5)	0.2554(5)	0.4328(1)	0.076(1)
C(12)	0.5189(6)	0.1753(5)	0.4016(2)	0.078(1)
C(13)	0.8063(5)	0.2862(5)	0.4040(2)	0.079(1)
C(14)	0.9814(7)	0.3633(7)	0.4199(2)	0.094(1)
C(15)	0.5303(7)	0.0881(5)	0.3147(2)	0.084(1)
C(16)	0.6478(9)	0.0498(6)	0.2798(2)	0.098(1)
C(17)	0.588(1)	–0.0351(7)	0.2390(2)	0.112(2)
C(18)	0.415(1)	–0.0839(8)	0.2322(2)	0.120(2)
C(19)	0.296(1)	–0.0438(9)	0.2661(2)	0.120(2)
C(20)	0.3523(8)	0.0423(7)	0.3073(2)	0.099(1)
H	0.405(5)	0.209(4)	0.487(1)	0.052(9)
H(1)	0.078(7)	0.225(6)	0.665(2)	0.10(1)
H(2)	–0.117(6)	0.099(6)	0.615(2)	0.09(1)
H(3)	–0.053(5)	0.065(5)	0.535(1)	0.07(1)
H(6)	0.398(6)	0.354(6)	0.680(2)	0.10(1)
H(7)	0.658(6)	0.453(6)	0.651(2)	0.09(1)
H(8)	0.708(6)	0.405(5)	0.571(1)	0.08(1)
H(10)	0.742(5)	0.335(4)	0.499(1)	0.063(9)
H(16)	0.766(7)	0.076(6)	0.285(2)	0.09(1)
H(17)	0.670(8)	–0.068(8)	0.221(2)	0.12(2)
H(18)	0.361(8)	–0.145(7)	0.205(2)	0.12(2)
H(19)	0.175(7)	–0.060(6)	0.262(2)	0.09(1)
H(20)	0.264(7)	0.078(6)	0.326(2)	0.10(1)
H(142)	0.958(8)	0.491(8)	0.431(2)	0.13(2)
H(141)	1.046(8)	0.297(8)	0.446(2)	0.13(2)
H(143)	1.051(9)	0.388(8)	0.399(2)	0.12(2)

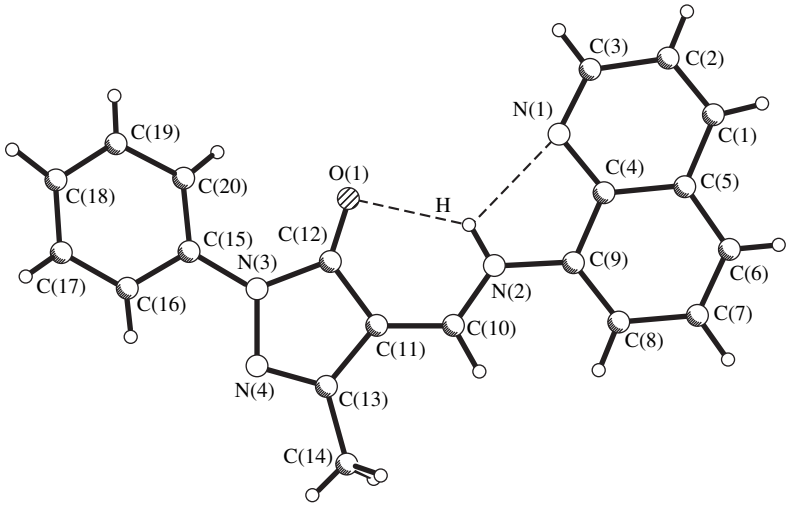

Fig. 1. A general view of molecule **I**.

RESULTS AND DISCUSSION

In $CDCl_3$ solutions, the aminomethylene derivatives of 5-thio- and 5-selenopyrazoles (prepared by condensation of 5-thio- and 5-selenopyrazole aldehyde, respectively) and 8-aminoquinoline have an enamine structure with the strong NH···*X* hydrogen bond. This structure is confirmed by the doublet signals of the NH-group protons (δ = 13–15 ppm) with $^3J_{=NH-CH=}$ = 12 Hz. The ^{1}H NMR spectrum of the oxygen derivative differs essentially from the spectra of the S and Se analogues. A broad diffuse signal is observed in the range 12–13 ppm. This signal can be assigned to the proton of the NH group, which is involved in a rapid exchange.

The IR spectrum of the crystalline sample of **I** exhibits absorption bands at 1673 (the C=O group) and 1633 (the N–H bending vibrations) cm^{-1}. This eliminates form (a) (see Introduction) from consideration but allows no choice among the remaining tautomers. Form (c) was chosen based on the data of the X-ray structure analysis.

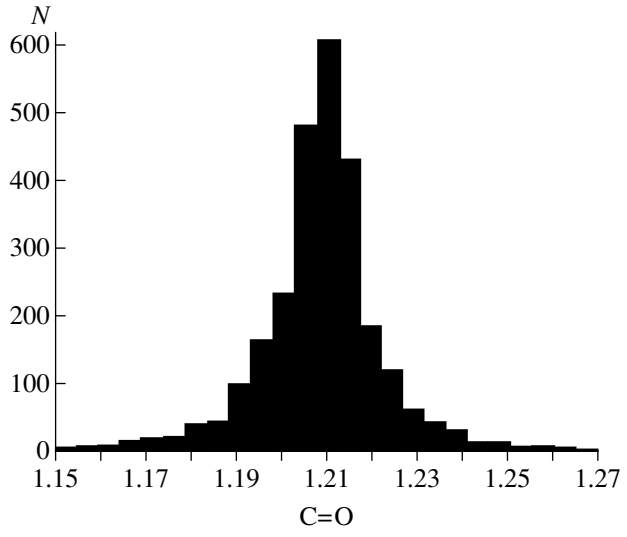

Fig. 2. A histogram of the C=O bond lengths according to the CSDB data.

A general view of molecule **I** is shown in Fig. 1. The phenyl ring C(15)–C(16)–C(17)–C(18)–C(19)–C(20) forms a dihedral angle of 16.6° with the remaining part of the molecule, which is planar within ~0.03 Å. In the crystal, molecule **I** has an aminomethylene structure that corresponds to tautomer (c). The proton is localized at the exocyclic nitrogen atom N(2) and lies in the plane of the main molecular fragment. It participates in a bifurcate intramolecular hydrogen bond, which closes the conjugated six-membered and five-membered H-rings. The hydrogen bonds are characterized by the following parameters: N(2)–H, 0.87(3) Å; H···O(1), 2.21(3) Å; N(2)···O(1), 2.881(4) Å; H···N(1), 2.32(3) Å; and N(2)···O(1), 2.702(4) Å. The endocyclic angles N(2)–H–O(1) and N(2)–H–N(1) are equal to 133° and 107° respectively; and the exocyclic angle N(1)–H–O(1) is 121°.

The bond lengths in the O=C–C=C–NH–C– fragment indicate that tautomer (c) prevails in the crystal: C=O, 1.226(3) Å; C–C, 1.440(6) Å; C=C, 1.366(6) Å; and C–N, 1.327(6) Å (for planar C_{sp2} and N_{sp2} configurations, the corresponding distances are 1.209, 1.445, 1.369, and 1.339 Å, respectively [23, 24]). This means that, in the crystal, these compounds are characterized by the aminomethylene structure, as is the case in the solutions [1–15]. A substantial lengthening of the C=O bond relative to the mean value of 1.209 Å, which was obtained for 2679 compounds in the CSDB retrieval (see the histogram in Fig. 2), can be due to the participation of the oxygen atom in the hydrogen bond and a certain contribution of the zwitterion structure (b).

Similar to **I**, the uncoordinated molecule **II** (X = S, R = *cyclo*-C_6H_{11}, R_1 = *iso-Pr*, and R_2 = *Me*) [18] has an aminothione structure. However, the contribution of the zwitterion form to molecule **II** increases, which results in a pyramidalization of the N atom (in the S=C–C=C–NH–C– fragment, the H atom deviates by 0.44 Å from the mean plane passing through the other atoms of the fragment).

In crystal **I**, the molecules related by inversion centers stack along the *y*-axis. No short intermolecular contacts are observed and the molecules are linked by van der Waals interactions.

ACKNOWLEDGMENTS

This work was supported by the Russian Foundation for Basic Research, project no. 97-03-33479a. We also acknowledge the support of this Foundation in the payment of the license to use the Cambridge Structural Database (project no. 96-07-89187) and the aid of A. V. Churakov in the work with the Cambridge Database.

REFERENCES

1. L. N. Kurkovskaya, N. N. Shapet'ko, I. Ya. Kvitko, *et al.*, Zh. Org. Khim. **9** (4), 821 (1973).
2. L. N. Kurkovskaya, N. N. Shapet'ko, I. Ya. Kvitko, *et al.*, Zh. Org. Khim. **10** (10), 2210 (1974).
3. L. N. Kurkovskaya, N. N. Shapet'ko, N. V. Sokolova, *et al.*, Zh. Org. Khim. **11** (5), 1091 (1975).
4. L. N. Kurkovskaya, N. N. Shapet'ko, E. D. Samartseva, *et al.*, Zh. Org. Khim. **11** (8), 1734 (1975).
5. A. Maguestiau, Y. van Haverbeke, and J. C. Vanovervelt, Bull. Soc. Chim. Belg. **84** (7), 741 (1975).
6. Y. van Haverbeke, A. Maguestiau, R. N. Muller, *et al.*, Bull. Soc. Chim. Belg. **84** (8/9), 845 (1975).
7. J. Elguero, C. Marzin, A. R. Katrizky, and P. Linda, Adv. Heterocycl. Chem., Suppl. **1**, 336 (1976).
8. W. Freyer, Pract. Chem. **320** (1), 17 (1978).
9. W. Freyer, Pract. Chem. **320** (4), 508 (1978).
10. W. Freyer, Pract. Chem. **320** (4), 521 (1978).
11. W. Freyer and R. Radeglia, Monatsch. Chem. **109** (7), 1093 (1978).
12. V. A. Bren' and V. I. Minkin, Izv. Vyssh. Uchebn. Zaved., Khim. Khim. Tekhnol. **25** (6), 663 (1982).
13. V. P. Litvinov, A. F. Vaĭsburg, and V. Yu. Mortikov, Khim. Geterotsikl. Soedin., No. 1, 5 (1992).
14. V. P. Litvinov, A. F. Vaisburg, and V. Yu. Mortikov, Sulfur Rep. **11** (3), 321 (1992).
15. A. D. Garnovskiĭ, A. L. Nivorozhkin, and V. L. Minkin, Coord. Chem. Rev. **126** (1), 1 (1993).
16. A. L. Nivorozhkin, A. I. Uraev, A. S. Burlov, and A. D. Garnovskiĭ, Zh. Ross. Khim. O–va im. D. I. Mendeleeva **40** (4/5), 162 (1996).
17. S. Mandal, G. Das, R. Singh, *et al.*, Coord. Chem. Rev. **160** (2), 191 (1997).
18. T. G. Takhirov, O. A. D'yachenko, D. B. Tagiev, *et al.*, Koord. Khim. **17** (6), 817 (1991).
19. B. A. Poraĭ-Koshits and I. Ya. Kvitko, Zh. Obshch. Khim. **32** (12), 4050 (1962).
20. B. A. Poraĭ-Koshits and I. Ya. Kvitko, Zh. Obshch. Khim. **34** (9), 2999 (1964).
21. A. I. Uraev, V. P. Kurbatov, and A. D. Garnovskiĭ, Koord. Khim. **23** (2), 159 (1997).
22. G. M. Sheldrick, *SHELXL93: Program for the Refinement of Crystal Structures* (Univ. of Göttingen, Göttingen, Germany, 1993).
23. F. N. Allen, O. Kennard, D. G. Watson, *et al.*, J. Chem. Soc., Perkin Trans. 2, 1 (1987).
24. F. N. Allen and O. Kennard, Chem. Design Automat. News **8**, 1 (1993); Cambridge Structural Database System, Version 5.15, November, 1997.

Translated by I. Polyakova

Crystallography Reports, Vol. 45, No. 5, 2000, pp. 782–784. Translated from Kristallografiya, Vol. 45, No. 5, 2000, pp. 854–856.

STRUCTURE OF ORGANIC COMPOUNDS

Crystal Structure of 4-Phenyl-3,5-Dioxacyclohexyl-1,1'-Cyclopentane-2',3''-(1,5,8,11-Tetraoxacyclotridecane)

S. T. Malinovskiĭ*, N. G. Luk'yanenko, and O. T. Mel'nik****

** Institute of Chemistry, Academy of Sciences of Moldova, Academiei 3, Chisinau, 20-28 Moldova*

*** Bogatskiĭ Physicochemical Institute, National Academy of Sciences of Ukraine, Chernomorskaya doroga 86, Odessa, 270080 Ukraine*

Received December 7, 1998; in final form, March 26, 1999

Abstract—The structure of the title compound is determined by X-ray diffraction (DAR-UMB diffractometer, θ–θ/2θ scan mode, MoK_α radiation, direct method). The crystal is monoclinic, a = 24.582(6) Å, b = 22.812(8) Å, c = 8.647(3) Å, γ = 60.64(2)°, ρ_{calcd} = 1.232 g/cm^3 space group $A2/a$, and Z = 8 for $C_{22}H_{32}O_6$. The molecule consists of four fragments: 13-crown-4 (*A*), 1,3-dioxane (*B*), a five-membered ring (*C*) acting as a bridge between fragments *A* and *B*, and a phenyl ring (*D*). Introduction of the bulky ring *C* as a bridge into the molecule results in significant deviations (up to ±0.014 Å) of the ether O atoms from planarity. The conformation of the macrocyclic fragment is [3433] according to the Dale notation. The C–H···O 1,4-interactions, which are energetically favorable occur in the propylene part of 13-crown-4: the C(2)···O(5) and C(4)···O(1) distances are 2.82 Å. The molecules in the structure form planar networks parallel to the *xy* plane. The intermolecular contacts correspond to the van der Waals interactions. © *2000 MAIK "Nauka/Interperiodica".*

INTRODUCTION

A unique property of the binuclear crown ethers is their ability to form with a high selectivity different complexes with metal cations [1]. Owing to the specific structure, these crown ethers can form sandwich complexes exhibiting a bis(crown ether) effect [2, 3], which manifests itself as a cooperative effect of two unsaturated rings on the complexing ion. The selectivity of bis(crown ether) molecules and stability of their complexes are significantly higher than those of their monocyclic analogues. The structural readiness of such a molecule to form complexes is primarily determined by the properties of the bridges between polyether rings [4]:

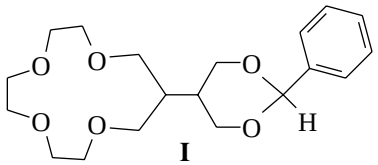

I

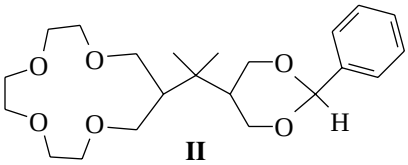

II

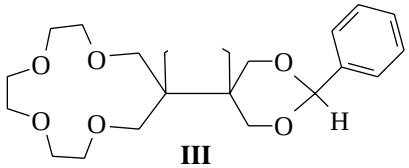

III

Earlier [5, 6], we considered the effect of the bridge between the polyether rings on the conformation of the macrocyclic 13-crown-4 ligand and the configuration of the molecule as a whole in compounds **I** and **II**. Continuing these studies, we report the X-ray crystal structure of 4-phenyl-3,5-dioxacyclohexyl-1,1'-cyclopentane-2',3''-(1,5,8,11-tetraoxacyclotridecane) **III**. In this compound, two polyether fragments (we arbitrarily consider that dioxacyclohexyl is a polyether ring) are bridged by a bulky five-membered ring.

EXPERIMENTAL

A colorless single crystal of compound **III** with a prismatic habit and linear dimensions of 0.2 × 0.3 × 0.5 mm was chosen for the X-ray diffraction analysis. The crystal is monoclinic. The unit cell parameters are as follows: a = 24.582(6) Å, b = 22.812(8) Å, c = 8.647(3) Å, γ = 60.64(2)°, ρ_{calcd} = 1.232 g/cm^3 space group $A2/a$, and Z = 8 for the $C_{22}H_{32}O_6$ formula unit.

The experimental data were obtained on a DAR-UMB diffractometer (MoK_α radiation, θ–θ/2θ scan mode). A set of 1247 reflections with $I(hkl) \geq 3\sigma(I)$ was used for structure determination and refinement. The structure was solved by the direct method using the SHELXS86 software package [7]. The non-hydrogen atoms were refined in the anisotropic approximation, and the hydrogen atoms were not refined. In the macrocyclic part of the molecule, the C(7) and C(12) atoms are statistically disordered over two positions each with the occupancy ratio ~0.65 : 0.35. The structure was refined to R = 0.062. The atomic coordinates and equiv-

1063-7745/00/4505-0782$20.00 © 2000 MAIK "Nauka/Interperiodica"

Atomic coordinates ($\times 10^4$) and equivalent thermal parameters ($Å^2 \times 10^3$) in the structure of $C_{22}H_{32}O_6$

Atom	*x*/*a*	*y*/*b*	*z*/*c*	U_{eq}	Atom	*x*/*a*	*y*/*b*	*z*/*c*	U_{eq}
O(1)	−1682(3)	2404(4)	6134(9)	39(1)	C(14)	−0649(6)	0964(5)	8702(15)	72(1)
C(2)	−1497(5)	1837(6)	7030(10)	47(1)	C(15)	0043(6)	0535(6)	8520(17)	68(1)
C(3)	−0848(4)	1597(5)	7700(13)	51(1)	C(16)	0263(5)	0888(6)	7372(16)	49(1)
C(4)	−0864(5)	2159(5)	8647(14)	64(1)	C(17)	−0321(4)	1366(5)	6435(13)	52(1)
O(5)	−1305(3)	2322(4)	9864(10)	47(1)	C(18)	−0237(5)	1912(5)	5701(14)	63(1)
C(6)	−1367(6)	2832(9)	10972(19)	50(1)	O(19)	0241(3)	1655(3)	4562(9)	71(1)
C(7)	−1750(8)	3539(7)	10146(20)	46(1)	C(20)	0124(5)	1307(5)	3387(14)	63(1)
C(7*)	−1981(20)	3360(24)	11324(62)	76(1)	O(21)	0068(3)	0767(4)	4001(10)	59(1)
O(8)	−2393(5)	3666(6)	10014(13)	39(1)	C(22)	−0444(5)	1001(6)	5115(15)	69(1)
C(9)	−2724(9)	4260(8)	9185(23)	43(1)	C(23)	0667(4)	1040(5)	2281(13)	65(1)
C(10)	−3030(6)	4139(9)	7867(28)	52(1)	C(24)	0690(5)	1502(6)	1259(14)	71(1)
O(11)	−2582(5)	3806(5)	6704(14)	48(1)	C(25)	1193(5)	1272(6)	0266(15)	69(1)
C(12)	−2560(10)	3400(12)	5431(10)	54(1)	C(26)	1659(5)	0608(6)	0277(14)	75(1)
C(12*)	−1239(11)	3230(16)	6820(45)	81(1)	C(27)	1622(5)	0184(6)	1280(74)	74(1)
C(13)	−2334(6)	2741(7)	5761(22)	61(1)	C(28)	1132(5)	0392(5)	2278(16)	69(1)

alent thermal parameters with the estimated standard deviations are listed in the table.

RESULTS AND DISCUSSION

The structure of molecule **III** is shown in the figure. The molecule consists of four fragments: 13-crown-4 (*A*), 1,3-dioxane (*B*), a five-membered ring (*C*) acting as a bridge, and a phenyl ring (*D*).

Similar to molecules **I** and **II**, molecule **III** as a whole is nonplanar. The bulky five-membered ring, which performs a bridging function, is responsible for the rotation of fragment *A* relative to *B* by an angle of 83.3° and for the significant deviation of the ether oxygen atoms of the macrocyclic part of the molecule from planarity (±0.14 Å). In the corresponding fragments of molecules **I** and **II**, the ether oxygen atoms are coplanar within ±0.013 Å. The macrocyclic 13-crown-4 fragments of molecules **III** with different positions of the disordered atoms—C(7) and C(7*), C(12) and C(12*)—adopt different conformations. As in **I** and **II**, the ring in molecule **III** that contains the C(7) and C(12) atoms has a quadrangular conformation with one "genuine" corner and three "pseudocorners." However, all three conformations differ from one another. According to the Dale notation, they are represented as [3334] in **I**, [3343] **II**, and [3433] **III**. The conformation of the macrocyclic ligand that contains atoms at the statistically disordered positions C(7*) and C(12*) is radically different: it is quinquangular [31117] with three genuine corners and two pseudocorners.

In **III**, the configuration of the molecule as a whole changes significantly. Indeed, the torsion angle across the C(4)–C(3)–C(17)–C(22) bridge is –158.9°, whereas in the structures studied earlier [5, 6], this angle is no larger than 54°. The torsion angles in the

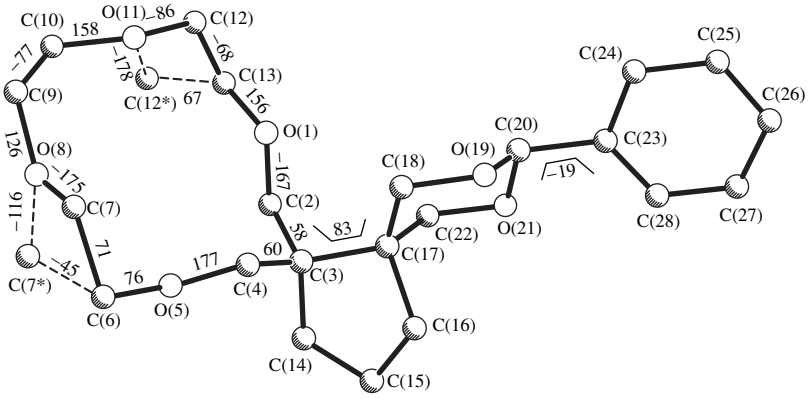

Structure of molecule **III**.

studied ring are shown in the figure. The C–H··O 1,4-interactions, which are energetically favorable, occur in the propylene part of 13-crown-4: the C(2)··O(5) and C(4)··O(1) distances are 2.82 Å.

Two positions of the disordered atoms—C(7) and C(7*), C(12) and C(12*)—are spaced at 1.325 and 1.399 Å, respectively. The disordering leads to the distortion of the endocyclic angles and interatomic distances: the C(12)–C(13) bond length is 1.353 Å and the O(8)–C(7)–C(6) angle is 106.3°. Insignificant distortions of the endocyclic angles are also due to the destabilizing interactions O(1)··O(11), O(5)··O(8), and O(8)··O(11), which are characteristic of quadrangular molecules; the corresponding interatomic distances are 2.90, 2.92, and 2.89 Å. For the most part, the bond lengths and angles in the molecule agree with the available data [5, 6] and correspond to the hybrid state of atoms.

The dioxane fragment has a typical chair conformation. The C(17) and C(20) atoms deviate from the mean C(18)C(19)O(21)O(22) plane by –0.64 and 0.70 Å, respectively. The phenyl ring is planar; its carbon atoms are coplanar within 0.002 Å. The bridging five-membered ring *C* is essentially nonplanar. Its conformation can be described as an envelope: the deviations of the C(3), C(14), C(15), C(16), and C(17) atoms from the mean plane are 0.20, –0.08, –0.06, 0.19, and –0.23 Å, respectively. Ring *B* is rotated relative to *D* by 48.6°. Apparently, this rotation is also caused by the electrostatic interaction between atoms: the O(21)··C(28) contact is 2.76 Å.

The intermolecular distances in the crystal correspond to the van der Waals contacts. Thus, comparison with the earlier-studied analogues **I** and **II** shows that introduction of the bridging five-membered ring into molecule **III** resulted in the changes in the conformation of the 13-membered ring and the configuration of the molecule as a whole.

REFERENCES

1. M. Hiraoka, *Crown Compounds* (Kodansha, Tokyo, 1982; Mir, Moscow, 1986).
2. F. Jong and D. N. Reinhoudt, in *Stability and Reactivity of Crown-Ether Complexes* (Academic, London, 1981).
3. K. Kimura, T. Maeda, and T. Shono, J. Electroanal. Chem. **95**, 91 (1979).
4. K. Kimura and T. Tsuchida, Talanta **27** (10), 801 (1980).
5. S. T. Malinovskiĭ, Yu. A. Simonov, and N. G. Luk'yanenko, Izv. Akad. Nauk Mold. SSR, Ser. Fiz.-Tekh. Mat. Nauk, No. 1, 29 (1988).
6. S. T. Malinovskiĭ, Yu. A. Simonov, N. G. Luk'yanenko, and O. T. Mel'nik, Zh. Strukt. Khim. **32** (3), 136 (1991).
7. G. M. Sheldrick, *SHELXS86: Crystallographic Computing 3* (Oxford Univ. Press, Oxford, 1986), p. 175.
8. J. Dale, Acta Chem. Scand. **27** (6), 1115 (1973).

Translated by I. Polyakova

Crystallography Reports, Vol. 45, No. 5, 2000, pp. 785–788. From Kristallografiya, Vol. 45, No. 5, 2000, pp. 857–860.

STRUCTURE OF ORGANIC COMPOUNDS

Crystal Structure of 5α-Cholest-6-One[1]

Rajnikant*[2], V. K. Gupta*, Jamal Firoz, Shafiullah**, and R. Gupta***

** X-ray Crystallography Laboratory, Department of Physics, University of Jammu, Jammu Tawi, 180006 India*

e-mail: rajni_kant_verma@hotmail.com

*** Steroid Research Laboratory, Department of Chemistry, Aligarh Muslim University, Aligarh, 202002 India*

Received October 4, 1999; in final form, January 26, 2000

Abstract—The crystal and molecular structure of the steroid 5α-cholest-6-one has been determined by X-ray diffraction analysis. The compound crystallizes in space group $P2_1$ with the unit cell parameters a = 10.575(1) Å, b = 7.698(1) Å, c = 15.284(2) Å, β = 99.34(1)°, V = 1227.72 Å^3, Z = 2, and R = 0.054 for 1634 observed reflections. The six-membered rings (*A*, *B*, and *C*) have the chair conformations, whereas the five-membered ring *D* is intermediate between 13β-envelope and 13β–14α half-chair. All the rings of the steroid skeleton are *trans* connected. The molecules are linked together by the intermolecular C–H···O hydrogen bonds.

The structure analysis of the title compound has been undertaken as a part of our systematic crystallographic investigations on steroids [1–6].

EXPERIMENTAL

Synthesis. The synthesis of 5α-cholest-6-one was accomplished by dissolving 6-nitrocholest-5-ene (6.0 g) in acetic acid (200 ml); then a Zn dust (12.0 g) was added to the solution in small portions. The suspension was heated under refluxing for 3 h, and water (12 ml) was added. The solution was filtered off and then was washed with warm acetic acid. Water (a few milliliters) was added to the filtrate until the turbidity developed, and it was allowed to stand overnight at room temperature. The crystalline material thus obtained was filtered under suction and washed thoroughly with water in order to remove the zinc acetate. The organic solid was dried in air and then recrystallized from methanol to yield 5α-cholest-6-one (3.6 g). The chemical structure as shown in Fig. 1 has been assigned on the basis of IR, UV, NMR and mass spectroscopic data [7].

Structure analysis. Transparent platelike crystals of 5α-cholest-6-one (melting point is 368 K) were grown in a single crystalline form from methanol by employing slow evaporation technique at room temperature. Three-dimensional intensity data were collected on an Enraf–Nonius CAD4 diffractometer (CuK_α radiation). The unit cell parameters were refined by the least-squares procedure. The data were corrected for Lorentz and polarization factors, but no absorption or extinction corrections were made.

The structure has been determined by direct methods using the SHELXS86 software package [8] and refined according to the SHELXL93 software package [9]. All the positions of hydrogen atoms were calculated geometrically with U_{iso}(H) = 1.2 U_{eq} (parent atom). A riding-atom model was used in their refinement (C–H = 0.96 Å). The final refinement cycle converged R = 0.054, $wR(F^2)$ = 0.166, and S = 1.013. Atomic scattering factors were taken from the International Tables for Crystallography (1992, Vol. C: Tables 4.2.6.8 and 6.1.1.4). The crystallographic data are summarized in Table 1.

RESULTS AND DISCUSSION

The fractional coordinates and equivalent isotropic temperature factors for non-hydrogen atoms are presented in Table 2. Endocyclic torsion angles for different rings of the molecule are listed in Table 3. A general view of the molecule and the atomic numbering scheme are shown in Fig. 2 [10].

The observed bond lengths and angles are in good agreement with the corresponding values obtained in case of 5-ene steroidal molecules [11]. Ring *A* has a

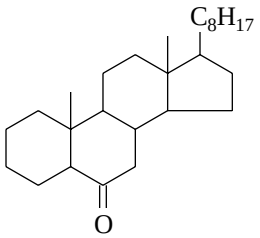

Fig. 1. Chemical structure of 5α-cholest-6-one.

[1] This article was submitted by the authors in English.

[2] Author for correspondence.

Table 1. Crystal data and experimental details

Crystal habit	White transparent plate
Chemical formula	$C_{27}H_{46}O$
Molecular weight	386.66
Unit cell parameters	$a = 10.575(1)$ $b = 7.698(1)$
	$c = 15.284(2)$Å $\beta = 99.34(1)°$
Unit cell volume	1227.72 Å^3
Crystal system	Monoclinic
Space group	$P2_1$
Density (calculated)	1.046 mg m^{-3}
No. of molecules per unit cell, Z	2
Radiation	CuK_α
Wavelength, λ	1.5418Å
Absorption coefficient, μ	0.45 mm^{-1}
$F(000)$	432
Crystal size	$0.40 \times 0.20 \times 0.10$ mm
Refinement of unit cell	25 reflections, $7.1° < \theta < 25.7°$
θ range for entire data collection	$2° < \theta < 60°$
No. of measured reflections	1970
No. of unique reflections	1863
No. of observed reflections	1634 [$F_0 > 4\sigma(F_0)$]
No. of parameters refined	254
Final R-factor	0.054
wR	0.166
Weighting scheme	$1/[\sigma^2(F_0^2) + (0.1283P)^2 + 0.11P]$, where $P = [F_0^2 + 2F_c^2]/3$
Final residual electron density	$-0.15 < \Delta\rho < 0.32$ eÅ^{-3}
$(\Delta/\sigma)_{max}$ in the final cycle	0.048 (for U_{11} atom C(27))
Flack parameter X	0.13

Table 2. Atomic coordinates and equivalent isotropic thermal parameters (Å^2)

Atom	x	y	z	U^*_{eq}	Atom	x	y	z	U^*_{eq}
C(1)	0.6019(4)	−0.0616(7)	0.1805(3)	0.080(2)	C(13)	0.2841(3)	0.1000(5)	0.4101(2)	0.057(1)
C(2)	0.6649(5)	−0.0591(9)	0.0972(3)	0.098(2)	C(18)	0.1520(3)	0.0863(6)	0.3514(2)	0.072(1)
C(3)	0.7382(5)	0.1091(11)	0.0929(4)	0.115(2)	C(14)	0.3604(3)	0.2598(5)	0.3859(2)	0.056(1)
C(4)	0.6513(5)	0.2636(9)	0.0931(3)	0.101(2)	C(15)	0.2907(4)	0.4148(5)	0.4183(3)	0.069(1)
C(5)	0.5870(4)	0.2623(7)	0.1757(3)	0.073(1)	C(16)	0.2434(4)	0.3482(6)	0.5015(3)	0.071(1)
C(6)	0.5045(4)	0.4179(6)	0.1839(3)	0.077(2)	C(17)	0.2693(3)	0.1474(5)	0.5063(2)	0.059(1)
O(6)	0.4795(4)	0.5245(5)	0.1267(2)	0.117(2)	C(20)	0.1694(3)	0.0509(5)	0.5523(2)	0.064(1)
C(7)	0.4531(4)	0.4281(5)	0.2689(3)	0.071(1)	C(21)	0.1878(4)	−0.1469(6)	0.5536(3)	0.079(2)
C(8)	0.3871(3)	0.2586(5)	0.2921(2)	0.058(1)	C(22)	0.1721(3)	0.1201(7)	0.6460(2)	0.074(1)
C(9)	0.4704(3)	0.0983(5)	0.2795(2)	0.056(1)	C(23)	0.0609(4)	0.0706(8)	0.6912(3)	0.084(2)
C(10)	0.5113(4)	0.0924(6)	0.1865(2)	0.064(1)	C(24)	0.0610(5)	0.1639(8)	0.7776(3)	0.095(2)
C(19)	0.3948(4)	0.0784(7)	0.1130(3)	0.079(2)	C(25)	−0.0583(6)	0.1396(12)	0.8215(4)	0.121(3)
C(11)	0.4050(4)	−0.0666(5)	0.3058(3)	0.071(1)	C(26)	−0.0655(9)	−0.0432(13)	0.8544(5)	0.162(4)
C(12)	0.3665(4)	−0.0590(5)	0.3977(3)	0.066(1)	C(27)	−0.0577(9)	0.2715(16)	0.8952(5)	0.183(5)

* $U_{eq} = (1/3)\Sigma_i\Sigma_j U_{ij} a_i^* a_j^* a_i a_j$.

Table 3. Endocyclic torsion angles (deg) (e.s.d.'s in parentheses)

C(2)–C(1)–C(10)–C(5)	–53.2(5)	C(14)–C(8)–C(9)–C(11)	54.5(4)
C(10)–C(1)–C(2)–C(3)	57.3(6)	C(8)–C(9)–C(10)–C(5)	58.6(4)
C(1)–C(2)–C(3)–C(4)	–58.1(6)	C(8)–C(9)–C(11)–C(12)	–52.2(4)
C(2)–C(3)–C(4)–C(5)	57.8(6)	C(9)–C(11)–C(12)–C(13)	53.7(4)
C(3)–C(4)–C(5)–C(10)	–56.1(6)	C(11)–C(12)–C(13)–C(14)	–53.8(4)
C(4)–C(5)–C(10)–C(1)	52.5(5)	C(12)–C(13)–C(14)–C(8)	60.4(4)
C(6)–C(5)–C(10)–C(9)	–59.4(4)	C(14)–C(13)–C(17)–C(16)	39.3(3)
C(10)–C(5)–C(6)–C(7)	57.5(5)	C(17)–C(13)–C(14)–C(15)	–45.8(3)
C(5)–C(6)–C(7)–C(8)	–50.7(5)	C(13)–C(14)–C(15)–C(16)	33.9(4)
C(6)–C(7)–C(8)–C(9)	46.6(4)	C(14)–C(15)–C(16)–C(17)	–8.5(4)
C(7)–C(8)–C(9)–C(10)	–52.4(4)	C(15)–C(16)–C(17)–C(13)	–19.7(4)
C(9)–C(8)–C(14)–C(13)	–62.0(4)		

symmetrical chair conformation with all asymmetry parameters below 5.10 [12]. The mirror symmetry is dominant, with the asymmetry parameters ΔC_s[C(3)] = 0.82, ΔC_s[C(5)] = 3.40, and ΔC_2[C(2)–C(3)] = 2.08. Ring *B* adopts a chair conformation with the best rotational axis bisecting C(5)–C(10) and C(7)–C(8) and the asymmetry parameter ΔC_2[C(5)–C(10)] = 1.43. The best mirror plane passes through C(7) and C(10) with ΔC_s(C(7)–C(10)) = 3.80. Ring *C* is also in a chair conformation with the best rotational axis bisecting C(8)–C(14) and C(11)–C(12) bonds; ΔC_2(C(8)–C(14)) = 4.32. The best mirror plane passes through C(11) and C(14) with ΔC_s(C(11)–C(14)) = 1.32. The conformation of ring *D* is intermediate between 13β-envelope [ΔC_s(C(13)) = 11.04] and 13β-14α half-chair [ΔC_2(C(13)–C(14)) = 8.79] with the phase angle of pseudorotation Δ = 13.43 and the maximum angle of torsion φ = –46.1° [13].

The following two intermolecular hydrogen bonds have been observed in the unit cell packing, which appear to be responsible for the stability of the crystal structure:

X–H···Y	H···Y(Å)	X···Y(Å)	X–H···Y(°)
C(1)–H(1)B···O6$^{(i)}$	2.584(6)	3.487(6)	154.9(5)
C(2)–H(2)B···O6$^{(i)}$	2.720(6)	3.572(5)	146.9(5)

Symmetry codes: (*i*) *x*, –1 + *y*, *z* (*ii*) 1 – *x*, –1/2 + *y*, –*z*.

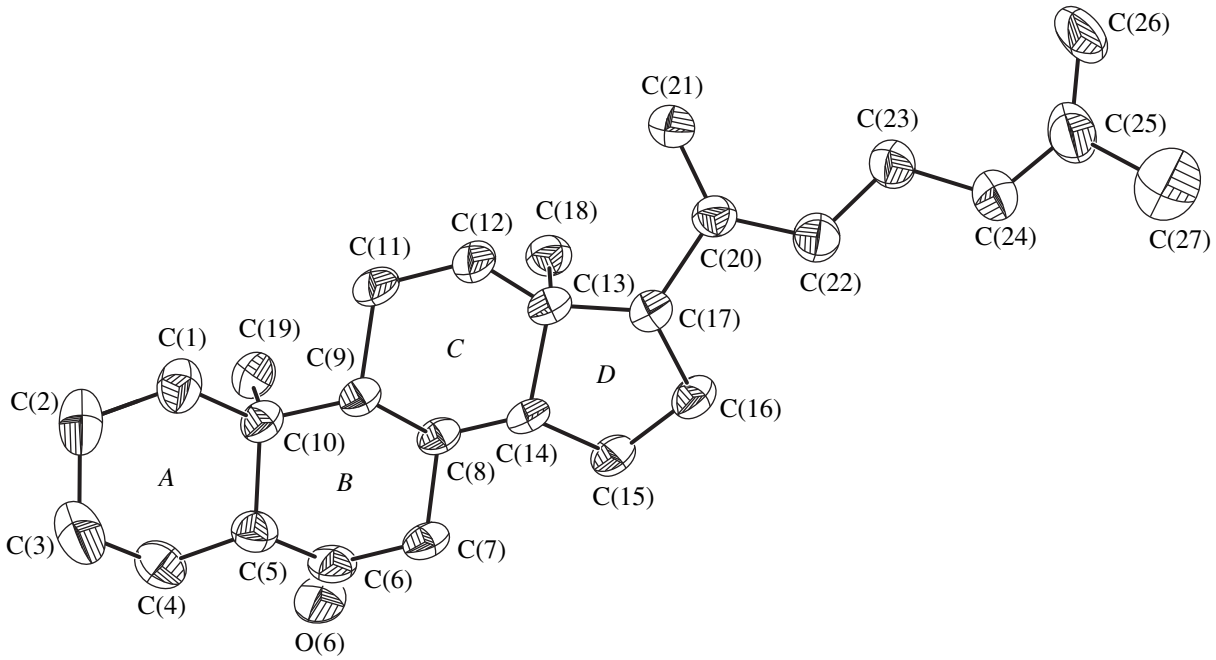

Fig. 2. A general view of the molecule with atomic numbering scheme and thermal ellipsoids at 50% probability.

ACKNOWLEDGMENTS

Rajnikant is thankful to the Head of the Regional Sophisticated Instrumentation Center of the Indian Institute of Technology (Chennai) for extending data collection facility. He also acknowledges the financial support received under DSA Program of the University Grants Commission of the Government of India, project no. F530/1/DSA/95(SAP-I).

REFERENCES

1. V. K. Gupta, Rajnikant, K. N. Goswami, and K. K. Bhutani, Cryst. Res. Technol. **29**, 77 (1994).
2. V. K. Gupta, K. N. Goswami, K. K. Bhutani, and R. M. Vaid, Mol. Mater. **4**, 303 (1994).
3. V. K. Gupta, Rajnikant, K. N. Goswami, *et al.*, Acta Crystallogr., Sect. C: Cryst. Struct. Commun. **50**, 798 (1994).
4. A. Singh, V. K. Gupta, Rajnikant, and K. N. Goswami, Cryst. Res. Technol. **29**, 837 (1994).
5. A. Singh, V. K. Gupta, Rajnikant, *et al.*, Mol. Mater. **4**, 295 (1994).
6. A. Singh, V. K. Gupta, K. N. Goswami, *et al.*, Mol. Mater. **6**, 53 (1996).
7. J. Firoz, Ph. D. Thesis (Aligarh Muslim University, Aligarh, India, 1998).
8. G. M. Sheldrick, *SHELXS86: Program for the Solution of Crystal Structures* (Univ. of Göttingen, Germany, 1986).
9. G. M. Sheldrick, *SHELXL93: Program for the Refinement of Crystal Structures* (Univ. of Göttingen, Germany, 1993).
10. C. K. Johnson, ORTEPII: *A Fortran Thermal Ellipsoid Plot Program for Crystal Structure Illustrations*, Report No. ORNL-5138 (Oak Ridge National Laboratory, Tennessee, 1976).
11. J. F. Griffin, W. L. Duax, and G. M. Weeks, *Atlas of Steroid Structure* (Plenum, New York, 1984), Vol. 2, p. 21.
12. W. L. Duax, C. M. Weeks, and D. C. Rohrer, in *Topics in Stereochemistry*, Ed. by E. L. Eliel and N. Allinger (Wiley, New York, 1976), Vol. 9, p. 271.
13. C. Altona, H. J. Geise, and C. Romers, Tetrahedron **24**, 13 (1998).

Crystallography Reports, Vol. 45, No. 5, 2000, pp. 789–791. Translated from Kristallografiya, Vol. 45, No. 5, 2000, pp. 861–863.

STRUCTURE OF ORGANIC COMPOUNDS

Crystal and Molecular Structures of 11,12-Epoxydrim-8(9)-en-11β-ol-7-one

V. Kh. Kravtsov*, Yu. A. Simonov*, E. K. Gorinchoĭ, M. N. Koltsa**, and P. F. Vlad****

** Institute of Applied Physics, Academy of Sciences of Moldova, Academiei 5, Chisinau, 20-28 Moldova*

e-mail: simonov.xray@phys.asm.md

*** Institute of Chemistry, Academy of Sciences of Moldova, Academiei 3, Chisinau, 20-28 Moldova*

Received May 25, 1999

Abstract—The crystal structure of 11,12-epoxydrim-8(9)-en-11β-ol-7-one is determined by X-ray diffraction. The crystal data for the $C_{15}H_{22}O_3$ composition are as follows: a = 6.646(1) Å, b = 7.242(1) Å, c = 7.635(2) Å, α = 84.34(3)°, β = 84.50(3)°, γ = 69.84(3)°, space group $P1$, and Z = 1. The structure is solved by the direct method and refined in the anisotropic approximation to R = 0.043 and R_w = 0.110. The stereochemical formula of the compound is determined. It is shown that the hydroxyl group at the C(11) atom is situated at the β position. In the crystal, the molecules related by the translation along the **a–b** direction of the unit cell are linked into infinite chains by intermolecular hydrogen bonds between the hydrohyl group and the carbonyl oxygen atom [O–H···O, 2.867(4) Å].© *2000 MAIK "Nauka/Interperiodica".*

INTRODUCTION

Recently, we reported an efficient procedure of synthesis [1] and determined the crystal structure [2] of 11,12-dihydroxydrim-8(9)-en-7-one (**I**), a well-known sesquiterpenoid, which is used in the preparation of important natural compounds exhibiting biological activity [3]. We also studied some of its chemical transformations, in particular, the reactions of its oxidation by manganese dioxide under normal conditions or by a small excess of pyridinium chlorochromate. Mixtures of two products were obtained. The major product was found to be the well-known 7-ketoisodrimenin (**II**) [4], and the minor product, according to the spectral data, was identified with ketol **III**, which has not yet been described.

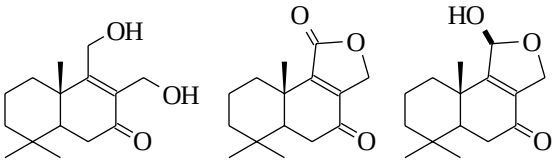

(**I**) (**II**) (**III**)

For conclusive identification of the latter compound, we determined its crystal structure by X-ray diffraction analysis.

EXPERIMENTAL

Single crystals of **III** were obtained by recrystallization of the substance from an acetonitrile solution. Colorless triclinic crystals have a prismatic habit. A sample, 0.30 × 0.35 × 0.65 mm in size μ(MoK_α) = 0.83 cm^{-1}, was chosen for X-ray structure analysis. The experimental data were collected on a DAR-UMB automated inclined diffractometer using MoK_α radiation (graphite monochromator) at room temperature. The unit cell parameters were refined using 15 reflections measured in the θ range from 10.7° to 14.2°. The unit cell parameters are a = 6.646(1) Å, b = 7.242(1) Å, c = 7.635(2) Å, α = 84.34(3)°, β = 84.50(3)°, γ = 69.84(3)°, V = 342.5(1) Å^3, d_{calcd} = 1.214 g/cm^3, noncentrosymmetric space group $P1$, Z = 1 for the $C_{15}H_{22}O_3$ composition, and structural class $P1(1)$. The diffractometric experimental data were obtained by the ω–θ/2θ scan mode in the θ range 2.69°–26.53°. A total of 1074 reflections with $I \geq 2\sigma(I)$ were collected, of which 1069 reflections were unique (R_{int} = 0.035).

The structure was solved by the direct method using the SHELXS86 program [5]. The E-synthesis revealed all the non-hydrogen atoms. Their positional and anisotropic thermal parameters were refined by the full-matrix least-squares procedure using the SHELXL93 program [6]. All the hydrogen atoms were located from the difference synthesis calculated at this stage. The geometry of the CH_3 and OH groups observed in the difference Fourier synthesis was idealized and refined by the least-squares procedure. The remaining hydrogen atoms were assigned to the calculated ideal positions; in the refinement, they were rigidly bound to the corresponding carbon atoms. The isotropic thermal parameters of the hydrogen atoms in the CH_3 and OH groups were taken to be 1.5 times greater than the equivalent isotropic thermal parameters U_{eq} of the non-hydrogen atoms bonded to these hydrogen atoms. For the rest of the hydrogen atoms, U_{iso} was taken equal to $1.2U_{eq}$ of the corresponding atom. The final discrepancy factors were R = 0.043, R_w = 0.110, and S = 1.14.

Atomic coordinates ($\times 10^4$) and equivalent thermal parameters ($\times 10^3$)

Atom	*x*	*y*	*z*	U_{eq}, Å^2	Atom	*x*	*y*	*z*	U_{eq}, Å^2
O(1)	4828(4)	974(4)	7993(4)	54(1)	C(7)	2080(5)	6457(5)	7040(4)	33(1)
O(2)	526(4)	7201(4)	8088(3)	44(1)	C(8)	3466(6)	4332(5)	7205(4)	34(1)
O(3)	8193(4)	1355(4)	7898(4)	52(1)	C(9)	5350(5)	3595(5)	6275(4)	32(1)
C(1)	7572(7)	3367(6)	3410(5)	54(1)	C(10)	6215(5)	4760(5)	4865(4)	35(1)
C(2)	8129(9)	4529(8)	1799(6)	67(1)	C(11)	6479(6)	1442(5)	6934(5)	41(1)
C(3)	6079(8)	6023(7)	1063(5)	58(1)	C(12)	3081(6)	2784(6)	8485(5)	45(1)
C(4)	4578(6)	7535(6)	2367(4)	42(1)	C(13)	5545(8)	9126(7)	2663(6)	58(1)
C(5)	4193(5)	6343(5)	4086(4)	34(1)	C(14)	2421(7)	8597(7)	1558(6)	60(1)
C(6)	2721(6)	7646(5)	5519(5)	41(1)	C(15)	7653(6)	5625(6)	5763(6)	51(1)

The weighting scheme used was $w = 1/[\sigma^2(F_0^2) + (0.0741P)^2 + 0.07P]$, where $P = (\max(F_0^2, 0) + 2F_c^2)/3$. The minimum and maximum residual densities at the zero synthesis were –0.169 and 0.151 e Å^{-3}, respectively. The atomic coordinates and equivalent isotropic thermal parameters are listed in the table.

RESULTS AND DISCUSSION

The X-ray structure analysis revealed that the crystalline product studied is 11,12-epoxydrim-8(9)-en-11β-ol-7-one, which corresponds to compound **III**. Its molecular structure and atomic numbering are shown in the figure. In **III**, similar to its precursor **I** [2], the cyclohexane fragment *A* has a chair conformation, and ring *B* adopts a half-chair conformation (figure). The conformations of these fragments were quantitatively estimated by calculation of the puckering parameters [7, 8]. Ring *A* is characterized by the parameters θ = 5.7(5)°, φ = 30(5)°, and *Q* = 0.544(5). For ring *B*, these parameters are as follows: θ = 60.6(4)°, φ = –9.6(4)°, and *Q* = 0.526(4). We also calculated the puckering parameters for compound **I** [θ = 3.3(6)°, φ = 27(10)°, and *Q* = 0.538(6) for ring *A*; and θ = 53.2(5)°, φ = 3.9(4)°, and *Q* = 0.497(4) for ring *B*]. Close values of these parameters for the studied compound **III** and its precursor **I** indicate that the formation of the heterocyclic five-membered ring *C* (instead of the seven-membered ring closed by the intramolecular hydrogen bond in compound **I**) results in no distinct conformational changes of rings *A* and *B*. Ring *C* is characterized by the puckering parameters φ = 100(1)° and *q*2 = 0.171(4), which correspond to the conformation intermediate between the twisted form (φ = 90°) and the envelope (φ = 108°).

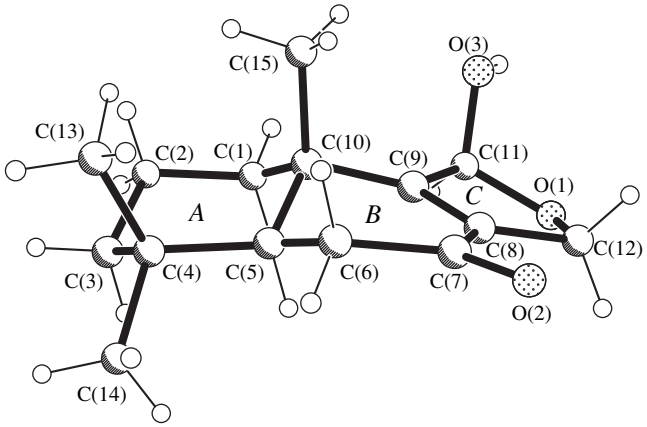

Molecular structure of 11,12-epoxydrim-8(9)-en-11β-ol-7-one.

In the cyclohexane fragment *A*, the mean C–C and C–*Me* bond lengths are 1.549 and 1.541 Å, respectively; the mean endocyclic angle is 112.1°, and the exocyclic angles at the C(4) and C(10) atoms fall in the range from 106.8° to 114.2°. A slight variation in the bond angles is determined by the steric factors in the rigid part of the molecule, in particular, by the short contact between two axial methyl groups [C(13)⋯C(15), is 3.316 Å]. The bond lengths in ring *B* are close to the corresponding distances in **I** [2]; however, the C(8)–C(9) double bond is shorter than that in compound **I** [1.342(5) and 1.385(6) Å, respectively], which indicates a larger degree of the double-bond character. The O(1)–C(11) and O(1)–C(12) bond lengths [1.416(4) and 1.473(5) Å, respectively] indicate a pronounced asymmetry of ring *C*. In related compounds with close molecular skeletons [9, 10], the corresponding bonds lie in the range 1.415–1.453 Å (the structure parameters for the compounds cited were obtained using the Cambridge Structural Database [11]). The lengths of the C(sp^2)–C(sp^3) single bonds in ring *C* also differ noticeably [C(8)–C(12), 1.487(5) Å and C(9)–C(11), 1.536(5) Å]. Apparently, this asymmetry can be associated with the effect of the C(7)–O(2) double bond of the carbonyl group [1.241(4) Å].

In the crystal structure, the molecules related by the translation along the **a–b** direction are linked by the intermolecular O(11)–H⋯O(7) hydrogen bond [O⋯O, 2.867(4) Å; H⋯O, 2.04 Å; and O–H⋯O, 174°] into infinite chains P_c1, which are typical of space group *P*1

[12]. These chains are linked only by van der Waals interactions.

ACKNOWLEDGMENTS

The synthesis of the crystals studied in this work was supported by INTAS, grant no. 96-1109.

REFERENCES

1. P. F. Vlad, D. P. Popa, E. C. Gorincioi, G. N. Mironov, and M. N. Coltsa, *Book of Abstracts of International Conference on Natural Products and Physiologically Active Substances* (Novosibirsk, 1998), p. 184.
2. V. Kh. Kravtsov, E. K. Gorinchoĭ, G. N. Mironov, *et al.*, Kristallografiya **45** (2), 289 (2000) [Crystallogr. Rep. **45**, 258 (2000)].
3. T. Nakata, H. Akita, T. Naito, and T. Oishi, Chem. Pharm. Bull. (Tokio) **28**, 2172 (1980).
4. H. H. Appel, J. D. Connolly, K. H. Overton, and R. P. M. Bond, J. Chem. Soc., 4685 (1960).
5. G. M. Sheldrick, *SHELXS86: Program for the Solution of Crystal Structures* (Univ. of Göttingen, Germany, 1986).
6. G. M. Sheldrick, *SHELXL93: Program for the Refinement of Crystal Structures* (Univ. of Göttingen, Germany, 1993).
7. D. Cremer and J. A. Pople, J. Am. Chem. Soc. **97**, 1354 (1975).
8. M. Nardelli, J. Appl. Crystallogr. **28**, 659 (1995).
9. M. Pulici, F. Sugawara, H. Koshino, *et al.*, J. Nat. Prod. **59**, 47 (1996).
10. T. Tozyo, F. Yasuda, H. Nakai, and H. Tada, J. Chem. Soc., Perkin Trans. 1, No. 14, 1858 (1992).
11. F. N. Allen and O. Kennard, Chem. Design Automat. News **8**, 131 (1993).
12. P. M. Zorky and O. N. Zorkaya, Zh. Strukt. Khim. **39**, 126 (1998).

Translated by I. Polyakova

Crystallography Reports, Vol. 45, No. 5, 2000, pp. 792–798. Translated from Kristallografiya, Vol. 45, No. 5, 2000, pp. 864–870.

CRYSTALLOCHEMISTRY

Perovskite-Like Crystals of the Ruddlesden–Popper Series[1]

B. V. Beznosikov and K. S. Aleksandrov

Institute of Physics, Siberian Division, Russian Academy of Sciences, Akademgorodok, Krasnoyarsk, 660036 Russia

e-mail: dir@iph.krasnoyarsk.su

Received August 10, 1998

Abstract—The layer perovskite-like structures of the so-called Ruddlesden–Popper phases have been analyzed in terms of crystal chemistry. The geometrical boundaries of the existence ranges of these compounds with multilayer stacks are determined and new phases of this type are predicted. The possible variants of related structures are also considered. © *2000 MAIK "Nauka/Interperiodica".*

INTRODUCTION

The analysis of the structural data [2–4] shows that all the variety of the well-known perovskite-like structures can be represented as combinations of four series of stacks formed by layers of octahedra, pyramids, and squares and twenty variants of the intermediate block layers. Thus, using the principle of combination of such stacks and block layers, one can obtain several hundreds of hypothetical tetragonal phases and consider the conditions of their formation in the concrete crystals of various chemical compositions.

We begin the analysis with the family of the phases in which the intermediate block layer is denoted as *R*1 [2], which can be represented by an element of the NaCl-type structure. Such structures are usually named after their first researchers [5, 6] the Ruddlesden–Popper (RP) phases. Earlier [7–10], we performed the crystallochemical analysis of one-layer (or the K_2MgF_4- or K_2NiF_4-type) structures and predicted new phases of this type. The present study is aimed to predict new multilayer structures of such type.[1]

STRUCTURAL CHARACTERISTICS OF RUDDLESDEN–POPPER PHASES

The general formula of the Ruddlesden–Popper phases can be written as $A_{n-1}A'_2B_nX_{3n+1}$, where *A*, *A*', and *B* are cations, *X* is an anion, and *n* is the number of the layers of octahedra in the perovskite-like stack. The hypothetical tetragonal phases and possible related structures are shown in Fig. 1. There exist stoichiometric compounds with *n* = 1–3. The *A* cations are characterized by cuboctahedral anionic coordination with the coordination number c.n. = 12 and are included into the perovskite-like stack. The *A*' cations (c.n. = 9) are located at the stack boundaries with an intermediate block layer. The *B* cations are located inside the anionic octahedra, pyramids, and squares.

These phases are the "closest successors" of the perovskite structure. Therefore, numerous crystal lattices with the stacks containing octahedra show some perovskite features (Figs. 1a–1d), whereas those with the anion-deficient compositions, show some Ruddlesden–Popper phase features (Figs. 1e–1i).

Five hypothetical phases shown in Figs.1e–1i are the combinations of the perovskite-like stacks of type B with the block layer *R*1 [2], of them three types of the structures were found in real compounds with the compositions $AA'_2B_2X_6$, $A_2A'_2B_3X_8$, and $A_3A'_2B_4X_{12}$. As far as we know, no representatives of the four-layer hypothetical phases of the compositions $A_3A'_2B_4X_{10}$ and $A_3A'_2B_4X_{11}$ have been found.

In one-layer RP-phases, the *A* cations occupy one crystallographic position at the boundary between the perovskite-like stack and the block layer. Therefore, the general formula of the compounds with *n* = 1 can be written in a more convenient form as A'_2BX_4 or A_2BX_4.

The most symmetric tetragonal RP-phases (sp. gr. *I*4/*mmm*) contain two formula units per unit cell (*Z* = 2). The coordination formula of one-layer compounds is written as $A_2^{IX}B^{VI}X_4$. Some compositions are characterized by less symmetric structures. In some crystals, where the cation size R_B exceeds the size of the anionic vacancy ($R_B > 0.41R_X$), the decrease of the temperature can give rise to the rotational structural phase transitions. However, the number of such crystals is still rather small.

The sites of layer contacts in the K_2MgF_4-type structures and their multilayer analogues are square networks with *A*, *A*', and *X* anions at the lattice sites, which are displaced with respect to one another by a

[1] A more detailed consideration of the results obtained is given in our preprint [1], which can be sent to all those interested by requesting to the following address: Institute of Physics, Siberian Division, Russian Academy of Sciences, Akademgorodok, Krasnoyarsk, 660036 Russia.

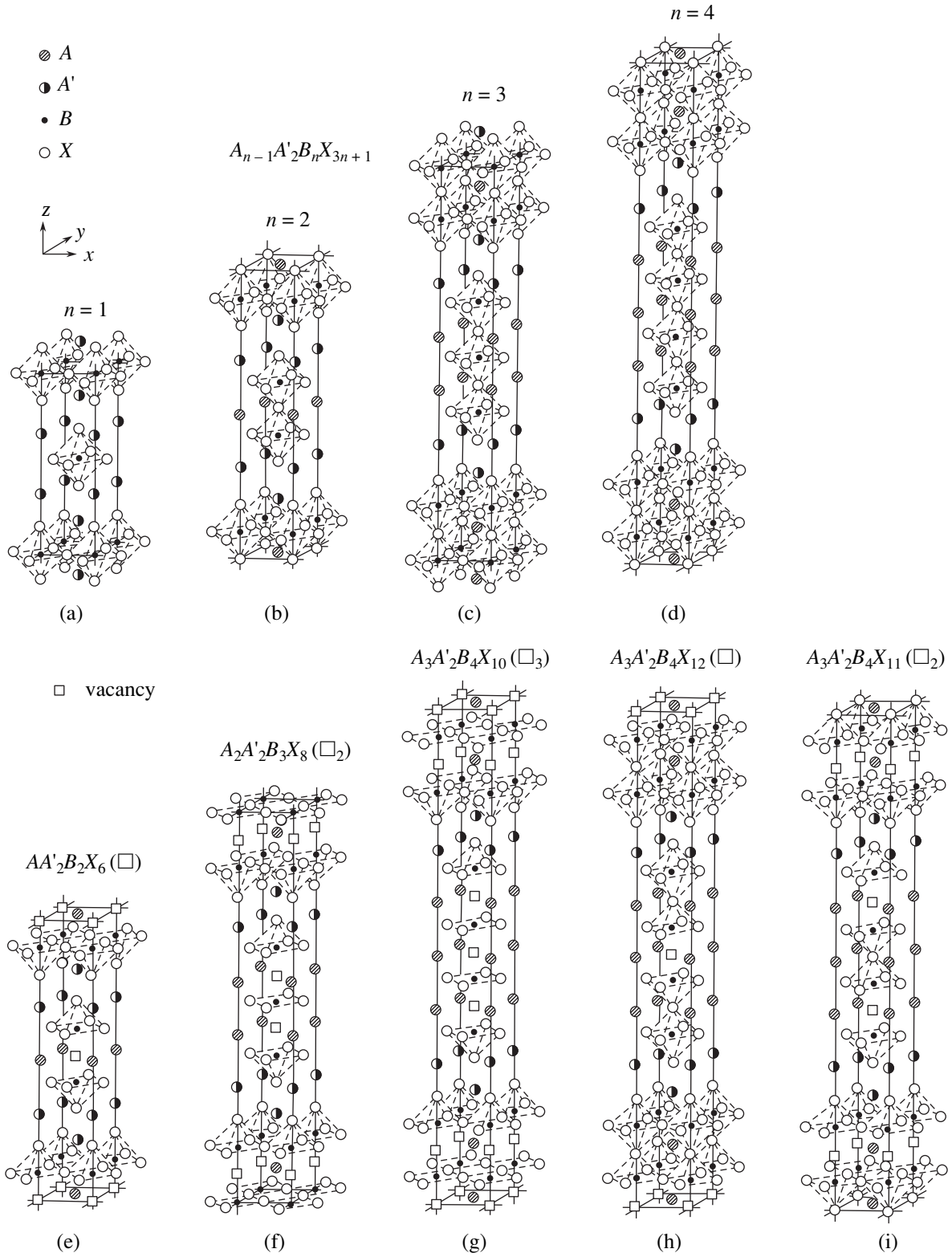

Fig. 1. (a–d) Ruddlesden–Popper phases and (e–i) possible related tetragonal structures.

half-diagonal of the unit cell. These stacks always have matching dimensions, which, probably, can explain the widespread occurrence of one-layer RP-phases. There exists a variant of the K_2MgF_4 antiphase, the Na_4OI_2 structure [11], where the stack is formed according to the antiperovskite principle ($IONa_3$).

In order to establish the laws of RP-phase formation, we used the bond strengths calculated by the Fesenko method [12]. The bond length in a crystal is compared with the sum of ionic radii with due regard for the cation coordination. If the calculated ratio exceeds unity, the bond is extended, if it is less than unity, it is shortened.

The calculation of bond lengths and strengths for a nine-vertex polyhedron showed that most of the tetragonal phases can "solve their internal problems" not only with the aid of rotation of octahedra, but also with the aid of their deformation. The octahedron deformation within certain limits does not change the total symmetry of the crystal lattice.

There exist some Nd_2CuO_4-type structures (sp. gr. $I4/mmm$, $Z = 2$) [13] well known for cuprates. In these compounds, copper is located in the anionic squares. The *A*-cations are usually trivalent and form an interlayer as in the CaF_2-type structures.

Thus, the Ruddlesden–Popper phases in oxides are most probable if the cation valence is $A = 1+$ or $2+$. If the cation valence is equal to $3+$ or exceeds $3+$, the structure of the Nd_2CuO_4 type with the square coordination of the *B* cations is formed.

Two-layer structures differ from the one-layer structures in the following. The *A* cation in A_2BX_4 has the c.n. = 9 and has only one position for all the *A* cations, whereas in $A_3B_2X_7$, the *A* cation has two different positions in the unit cell—one with the $\text{c.n.}_{A'} = 9$ (i.e., the same as in the one-layer unit cell) filled with cations located at the boundary between the stack and the block layer, whereas the second position with the coordination number $\text{c.n.}_A = 12$ is located in the perovskite-like stack. This signifies that in such structures, the positions with coordination number c.n._A can be filled only with larger cations and that the structure can contain two different *A*-cations. Therefore, the general formula of the two-layer compound should be written as $AA'_2B_2X_7 = [A^{\text{XII}}A_2^{\text{IX}}B_2^{\text{VI}}X_7]$. In the one-layer structures, the anions can fill two crystallographic positions with $(\text{c.n.})_X = 6$, but with different sets of surrounding cations. In the two-layer structures, there are three anionic positions with six surrounding cations, but their sets are also different. This provides the prerequisites for the formation of these structures in crystals with mixed anions, e.g., oxyhalides, or in crystals with a deficiency in anions.

At $n = 3$, *A*-cations also have two possible positions with c.n. = 12 and 9. The coordination formula has the form $[A_2^{\text{XII}}A_2^{\text{IX}}B_3^{\text{VI}}X_{10}]$. *B*-cations have two octahedral positions and the anions have four positions, so there exist wider possibilities for composition variation.

The RP phases are formed if the *A* positions are occupied with larger cations. This signifies that these cations should again have the valences $1+$ and $2+$.

RANGES OF EXISTENCE OF THE RUDDLESDEN–POPPER-PHASES

The geometrical limits of existence of the *K*-type structures depend on the cationic coordination. They were established in our earlier study [9] as $0.41R_X \le R_B \le 0.73R_X$ and $R_A \le 0.73R_X$. All the known compounds with such a structure exist within these ranges. However, in oxides, the Sr_2PbO_4-type structures also exist in the same composition range [14, 15], with their isolated octahedra forming no stacks at all. Therefore, it was necessary to refine the existence ranges of one-layer structures and determine the existence ranges for multilayer RP-phases. With this aim, we calculated bond strengths for the compositions $A_{n+1}^{2+}B_n^{4+}O_{3n+1}^{2-}$ and the unit-cell parameters, and also the lengths and strengths of the bonds for hypothetical compounds with different combinations of the cationic *A* and *B* radii using the formulas obtained for such compositions by averaging the structural data [16] and modifying them in a way to take into account the multilayer nature of the phases under consideration. We used the values of the free parameters for the atomic coordinates determined for the compositions $Sr_{n-1}Ti_nO_{3n+1}$. The formulas for the unit-cell parameters of the tetragonal phases are:

$$a = 0.166 \times 2R_A^{\text{IX}} + 1.705R_B + 2.418 \ (n = 1),$$

$$a = 0.166(R_A^{\text{XII}} + R_A^{\text{IX}}) + 1.705R_B + 2.418 \ (n = 2, 3).$$

The *a* parameters for $n = 1$–3 have close values and are almost independent of the number of perovskite-like stacks:

$$c = 2.158(R_A^{\text{XII}} + R_A^{\text{IX}}) + 0.396R_B + 6.752 + 2(n-1) \times a,$$

where R_A and R_B are the Shannon cationic radii [17]. The Roman superscripts of *A* and *B* ions show their coordination.

The formation of the RP-phases was assumed to be possible if the bond lengths *A–X* and *B–X* were elongated or shortened by not more than 10%.

Proceeding from the number of the known RP-phases, it seemed that two- and also three-layered structures should be less common. The range of phase existence should decrease with an increase of the number of layers in the structure.

However, analysis showed that the existence ranges of RP phases with $n = 1$–3 almost coincide (within the accuracy of the calculation) (Fig. 2). With an increase of the cationic radii, the existence range of these phases becomes narrower and then is tampered at the hypothetical point with the approximate coordinates $R_A = 4$ and $R_B = 2.5$ Å.

According to the minimum cationic radius *B*, the range of the structure existence is written as $R_B > 0.50$ Å, which is close to the boundary of existence of

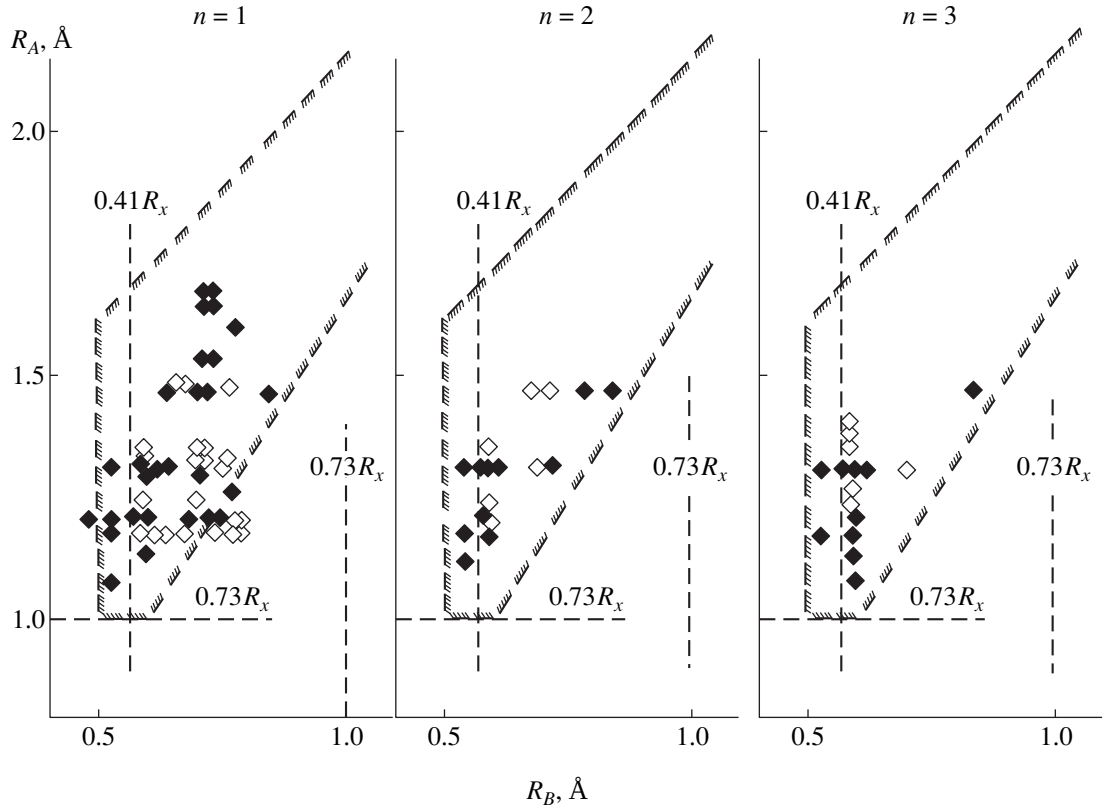

Fig. 2. (◆) Known and (◇) predicted Ruddlesden–Popper phases and possible ranges of their existence.

Sn oxygen octahedron. The approximate existence range for oxides can be written as $1.6R_B < R_A < 1.24R_B + 0.9$ Å. The values of the ionic radii F^- and O^{2-} are close and therefore, the existence ranges of the fluoride-based RP-phases should be approximately the same.

Although the geometric ranges of the phase existence are independent of the number of layers in the stack, the structures become less strong with an increase in n, and their formation can be limited because of the following. In the K_2MgF_4-type structures, the intermediate block layer stabilizes the octahedral part of the stack, which is similar to an increase of the number cubic densely filled layers AX_3 in halide polytypes, ABX_3, under high pressures. With an increase of the number of layers in these stacks, the stabilizing effect of the block layer is diminished. Therefore, the number of layers in stacks would also be limited. Numerous perovskite-like oxides ABX_3 possess cubic lattices at high temperatures, and distorted lattices at room temperature. This "heredity" can also affect the stack stability. Thus, some constraints are imposed on the formation of multilayer RD-phases.

Since the existence ranges of RP phases with n = 1–3 coincide, two important conclusions can be drawn:

1. In the composition providing no formation of one-layer structures or in the compositions where no such structures can be predicted, no multilayer structures can form. This considerably reduces the number of possible compositions.

2. The formation of the compounds with n = 3 is the most probable for the compositions, where the compound with n = 1, 2 are known.

PREDICTION OF NEW COMPOUNDS

The following cations are appropriate for synthesis of new oxides: A^{2+} = Ba, Sr, and Ca, then A^{2+} = Nd, Sm, Eu, and Dy and B^{4+} = Cr, V, Fe, Sn, Ru, and Zr.

The probable compositions are: $Sr_4Cr_3O_{10}$, $Ca_4V_3O_{10}$, $Ca_3V_2O_7$, $Sr_4Ru_3O_{10}$, $Eu_4Ti_3O_{10}$, and $Sm_4Ti_3O_{10}$ (see table). Since the compounds $K_2Gd_2Ti_3O_{10}$ and $K_2La_2Ti_3O_{10}$ exist [18], one can expect the formation of a three-layer structure within the compositions with intermediate RE cations, namely, $K_2Pr_2Ti_3O_{10}$, $K_2Eu_2Ti_3O_{10}$, and $K_2Ce_2Ti_3O_{10}$. The size of Bi-cation is comparable with the sizes of RE cations, and, therefore, the synthesis of $K_2Bi_2Ti_3O_{10}$ is possible. The structure of the $Na_2Nd_2Ti_3O_{10}$ compound is solved up to the determination of atomic coordinates [19]. In this structure, Nd is surrounded with 12 anions, whereas Na is surrounded with 9 anions. Therefore, the formula of this compound should rather

Predicted Ruddlesden–Popper Phases with the composition $(ABX_3)_nAX$, n = 1–3

B^{4+}-oxides

A^{2+}	Ti	Zr	Cr	Mn	V	Fe	Sn	Pb	Hf	Tb	Rh	Ru
Ba		12**3**					12**3**	123	1**23**	**123**		1**23**
Sr	123	123	12**3**	123	123	123	12**3**		1**23**	**123**	1**23**	12**3**
Ca	**1**'2'3'			123	**123**							
Nd	**123**	**123**			**123**	**123**			**123**	**123**		
Sm	**123**	**123**			**123**	**123**			**123**			
Eu	12**3**	1**23**			**123**	**123**			**123**			
Dy	**123**				**123**	**123**			**123**			

B^{2+}-fluorides

A^+	Ni	Co	Fe	V	Mn	Ti	Cu	Cr	Zn	Cd	Hg	Mg
Cs			**12**3	**123**	1**23**	**123**	1**23**	**123**		**123**	1**23**	**12**3
Rb	1**23**	1**23**	1**23**	**123**	12**3**	**123**	1**23**	**123**	1**23**	12**3**	1**23**	1**23**
Tl	1**23**	1**23**	1**23**	**123**	**123**	**123**	1**23**	**123**	1**23**	**123**		1**23**
NH_4	1**23**	**123**	**123**	**123**	**123**	**123**	**123**	**123**	1**23**	**123**		1**23**
K	12**3**	12**3**	123	**123**	12**3**		12**3**		12**3**			1**23**

B^{2+}-chlorides

A^+	Ni	Co	Fe	V	Mn	Ti	Cu	Cr	Zn	Cd	Hg	Yb	Mg	Ca
Cs					1**23**	**123**		1**23**		1**23**		1**23**		12**3**
Rb				1**23**	12**3**	**123**		1**23**		123	**123**		1**23**	2
Tl				**123**	**123**	**123**		**123**						
NH_4				**123**		**123**		**123**						
K					1**23**	1**23**							1**23**	

Notation

Compounds	Known	Predicted	Composition
n = 1	1	**1**	A_2BX_4
n = 2	2	**2**	$A_3B_2X_7$
n = 3	3	**3**	$A_4B_3X_{10}$
	1', 2', 3'	**1'**	Distorted phases
	RD-phases are low probable		

be written as $Nd_2Na_2Ti_3O_{10}$. The size of the A_2^{XII}-cation in this compound can still be increased and, therefore, it might be possible to synthesize the compounds $Pr_2Na_2Ti_3O_{10}$, $Ce_2Na_2Ti_3O_{10}$, $La_2Na_2Ti_3O_{10}$, and $Bi_2Na_2Ti_3O_{10}$.

In the compositions $A_2A'_2B_3X_{10}^{2-}$ with the odd valence of B-cations (3+ or 5+), only nonstoichiometric compounds can be synthesized. The stoichiometric compositions can be formed only by cations with the even valence. The most often encountered compositions are formed by B-cations with valence 4+. Theoretically, the cations with the valence 2+ (B^{2+}) can form the composition $A_2^{3+}A_2^{4+}B_3^{2+}X_{10}^{2-}$, but, in practice, it is hardly probable, because it is difficult to find the cations with such valences that would simultaneously satisfy the geometric conditions for the existence of this structure type.

Since Bi is often present in many layer structures (especially in the Aurivillius phases), the new compounds of the $Bi_2^{3+}M^{2+}O_4$ type with M^{2+} = Ni, Co, Fe, V, Mn, Ti, Cr, Zn, Mg, Cd, and Ca are of great interest from the standpoint of their physical properties. One can expect the formation of the K_2MgF_4-type structures in these compounds.

However, the synthesis of new compounds and especially the growth of single crystals from melts encounter some specific difficulties. The compounds with such structures (even one-layer compounds) melted

incongruently, and, therefore, no such structures (especially of two- and three-layered structures) were revealed in the studies of the phase diagrams of the multicomponent compositions of many of these phases. They were synthesized only recently by solid-phase synthesis at high temperatures and, sometimes, also under high pressures.

Is the synthesis of RP phases with $n > 3$ possible at all? For simple compositions, it is hardly probable. In the compositions with complicated combinations of cations, such structures are possible.

Is it possible to synthesize the compound of the composition Ca_2TiO_4? We know the compounds $Ca_3Ti_2O_7$ (sp. gr. $Ccm2_1$) and $Ca_4Ti_3O_{10}$ (sp. gr. *Pcab*). Even at room temperature, their structures have the characteristic orthorhombic distortion, more pronounced for the two-layer structure than for the three-layer one. This signifies that the one-layer Ca_2TiO_4 compound can also be distorted or it can exist only at elevated temperatures.

RELATED STRUCTURES

Numerous compounds show some similarity to the RP-phases. Structurally, the compounds closest to the RP-phases are oxyhalides [20] containing no anionic vacancies at all. However, since the cation–halogen bond in octahedron is much weaker than the corresponding bond with oxygen, the cation is displaced from the octahedron center, and acquires the coordination number five (the coordination polyhedron is four-faced pyramid).

In one-layer oxyhalides of the compositions $Ca_2CuO_2Cl_2$ and $Ca_2CuO_2Br_2$ [21], the copper coordination can still be considered as octahedral, because the elongation of the copper–halogen bond does not exceed 10% (in $Ca_2CuO_2Cl_2$, it equals 7.7%, and in $Ca_2CuO_2Br_2$ 9.6%). In oxychlorides of the compositions $Ba_3In_2O_5Cl_2$ [22] and $Ba_3Tl_2O_5Cl_2$ [23], despite their structural similarity to two-layer RP-phases, the cation displacement in the octahedron is much more pronounced. In the first compound, the metal–halogen bond is elongated by 17.6%, in the second, by 30%. The coordination numbers of In^{3+} and Tl^{3+} ions are equal to five. Comparing these structures with their prototype, $Sr_3Ti_2O_7$, we see that despite the same structure type, the *B*-cations in these structures have different coordinations.

A similar situation is also characteristic of the $Nd_2Na_2Ti_3O_{10}$ [19, 24] structure. Titanium atoms of the outer octahedral layers are displaced by 0.4 Å toward block layers. This increases the coordination number of Ti^{4+} up to five (the four-faced pyramid). The bond to the sixth anion of the octahedron is elongated by 17.3%. Assuming the titanium coordination to be (5 + 1), we can relate this structure to the RP-phases with $n = 3$. These structures have the following characteristic features:

In oxyhalides, the coordination of the central cation in the outer octahedral layers in the stacks increases to five, and the cation itself is displaced toward the stack.

At different valences of cations in the *A* positions, the *B* cation is displaced toward the block layer.

The $La_2Sr_4Cu_2Ti_2O_{13}$ structure [25], which is the closest to the RP-phases with $n = 2$, acquires some vacancies. The lattice has about 30% of disordered anionic vacancies located at the centers of the stacks. This signifies that the stack has up to 30% of semioctahedra. Thus, the bonds inside the stack are weakened due to formation of such vacancies.

A bright example of the anion-deficient structures are the Sr_2CuO_3 and Ca_2CuO_3 crystals with the formal copper valence 2+. The structure has no octahedra anymore; they are degenerated into squares. The tetragonal $Sr_2CuO_{3+\delta}$ crystal is a closer analogue of the K_2MgF_4 structure, but its basal planes formed by the octahedral layers contain oxygen vacancies ($g = 1/2$). The structures of the compounds $LnSr_5Ni_3O_8$ (Ln = Y, Dy, Ho, Er, and Tm) [26] are close to the Sr_2CuO_3-type, nickel has the formal valence 1+ and is coordinated with a square of oxygen atoms.

Among the related RP-phases, one can find the compounds with the number of perovskite-like layers exceeding three. An example here is the $Ba_2CaGd_2Ti_2Cu_2O_{12}$ structure [27].

The ion sizes in all the known nonstoichiometric compounds range within the limits R_A = (1.05–1.47) and R_B = (0.58–0.80) Å. Therefore, similar to the stoichiometric phases, all the nonstoichiometric compounds exist within the range shown in Fig. 2 in the R_B–R_A coordinates. Proceeding from this fact and knowing the cationic dimensions [17] for each concrete chemical composition, one can change these cations in the *A* and *B* positions and, thus, synthesize new crystals. It is also possible to synthesize the A_2BO_3 compounds using the cations A^{2+} = Ba, Sr, Nd, Sm, Eu and B^{2+} = Ni, Co, Fe, V, Cr, Mn, Cu. Within the compositions $A_3^{2+}B_2^{3+}O_{7\pm\delta}$, one can synthesize the compounds $Ba_3Tl_2O_{7\pm\delta}$ and $Sr_3In_2O_{7\pm\delta}$.

CONCLUSION

The existence ranges of all the tetragonal Ruddlesden–Popper phases with n = 1–3 in the R_B–R_A coordinates are the same.

With an increase of R_A and R_B, the existence ranges become narrower and are tapered at the hypothetical point with the coordinates $R_A = 4$ and $R_B = 2.5$ Å (for oxides and fluorides).

The calculation of bond strengths shows that the similar tapering of the cubic phases is also characteristic of perovskites. The existence range of cubic fluo-

rides–perovskites in the R_B–R_A coordinates almost coincides with the existence range of the corresponding RP phases.

The apical anion in the octahedron of all the tetragonal phases is strongly sterically hindered, which can give rise to the formation of rotational RP-phases at lower temperatures. However, four anions of their octahedra lying in the layer plane cannot be displaced, which seems to explain the fact that only a small number of rotational RP-phases is known in these systems.

The stoichiometric (with respect to anion) RP phases can be formed only at n = 1–3, however the related nonstoichiometric phases can have a larger number of perovskite-like layers.

The prediction of one-layered RP phases showed that the possible number of such phases can attain about 2400. Since the existence ranges of two- and three-layer phases coincide with the existence range of one-layer ones, one can predict the synthesis of a quite a large number of new crystals with n = 2, 3.

ACKNOWLEDGMENTS

This study was supported by the Russian Foundation for Basic Research, projects nos. 96-02-16542a and 96-15-96700, and the Krasnoyarsk Regional Science Foundation.

REFERENCES

1. B. V. Beznosikov and K. S. Aleksandrov, Preprint No. 786F, IF SO RAN (Institute of Physics, Siberian Division, Russian Academy of Sciences, Krasnoyarsk, 1998).
2. K. S. Aleksandrov and B. V. Beznosikov, *Perovskite-like crystals* (Nauka, Novosibirsk, 1997).
3. K. S. Aleksandrov and B. V. Beznosikov, Kristallografiya **42** (4), 613 (1997) [Crystallogr. Rep. **42** (4), 556 (1997)].
4. K. S. Aleksandrov and B. V. Beznosikov, Fiz. Tverd. Tela (St. Petersburg) **39**, 785 (1997) [Phys. Solid State **39**, 695 (1997)].
5. S. N. Ruddlesden and P. Popper, Acta Crystallogr. **10**, 538 (1957).
6. S. N. Ruddlesden and P. Popper, Acta Crystallogr. **11**, 54 (1958).
7. K. S. Aleksandrov, B. V. Beznosikov, and S. V. Misyul', Kristallografiya **32** (4), 937 (1987) [Sov. Phys. Crystallogr. **32** (4), 551 (1987)].
8. B. V. Beznosikov and K. S. Aleksandrov, in *Proceedings of the II International Conference "Real Structure and Properties of Acentric Crystals," 1995* (VNIISIMS, Aleksandrov, 1995), p. 79.
9. B. V. Beznosikov and K. S. Aleksandrov, Kristallografiya **30** (3), 509 (1985) [Sov. Phys. Crystallogr. **30** (3), 295 (1985)]; Kristallografiya **30** (5), 919 (1985) [Sov. Phys. Crystallogr. **30** (5), 533 (1985)].
10. B. V. Beznosikov, Kristallografiya **38** (5), 139 (1993) [Crystallogr. Rep. **38** (5), 657 (1993)].
11. H. Sabrowsky, K. Hippler, S. Sitta, *et al.*, Acta Crystallogr., Sect. C: Cryst. Struct. Commun. **46**, 367 (1990).
12. E. G. Fesenko, *Perovskite Family and Ferroelectricity* (Atomizdat, Moscow, 1972).
13. Hk. Müller-Buschbaum and W. Wollschläger, Z. Anorg. Allg. Chem. **414**, 76 (1975).
14. M. Trömel, Naturwissenschaften **54**, 17 (1967).
15. M. Trömel, Naturwissenschaften **52**, 492 (1965).
16. B. V. Beznosikov, Kristallografiya **38** (2), 189 (1993) [Crystallogr. Rep. **38** (2), 234 (1993)].
17. R. D. Shannon, Acta Crystallogr., Sect. A: Cryst. Phys., Diffr., Theor. Gen. Crystallogr. **32**, 751 (1976).
18. J. Gopalakrishnan and V. Bhat, Inorg. Chem. **26**, 4299 (1987).
19. M. Richard, L. Brohan, and M. Tournoux, J. Solid State Chem. **112**, 345 (1994).
20. N. V. Anshukova, A. I. Golovashkin, L. I. Ivanova, and A. P. Rusakov, Usp. Fiz. Nauk **167**, 887 (1997) [Phys. Usp. **40**, 843 (1997)].
21. B. Grande and Hk. Müller-Buschbaum, Z. Anorg. Allg. Chem. **429**, 88 (1977).
22. W. Gutau and Hk. Müller-Buschbaum, Z. Anorg. Allg. Chem. **584**, 125 (1990).
23. F. Letouze, C. Martin, D. Pelloquin, *et al.*, Mater. Res. Bull. **31**, 773 (1996).
24. J. S. Kim, H. Kawaji, M. Itoh, *et al.*, Mater. Res. Bull. **27**, 1193 (1992).
25. R. Li, Mater. Res. Bull. **31**, 539 (1996).
26. M. James and P. Attfield, Physica C (Amsterdam) **235–240**, 751 (1994).
27. Li Rukang, Dong Chen, and Yang Li, Physica C (Amsterdam) **247**, 62 (1995).

Translated by L. Man

Crystallography Reports, Vol. 45, No. 5, 2000, pp. 799–803. Translated from Kristallografiya, Vol. 45, No. 5, 2000, pp. 871–875.

CRYSTALLOCHEMISTRY

Crystallochemical Model of Ion-Transport Percolation in Nonstoichiometric $M_{1-x}R_xF_{2+x}$ Phases with the Defect CaF_2-type Structure

N. I. Sorokin

Shubnikov Institute of Crystallography, Russian Academy of Sciences, Leninskiĭ pr. 59, Moscow, 117333 Russia
e-mail: sorokin1@mail.ru

Received April 6, 1998; in final form, June 7, 1999

Abstract—A crystallochemical model of ion-transport percolation in $M_{1-x}R_xF_{2+x}$ (M = Ca, Sr, Ba; R = RE) solid solutions with the "defect" CaF_2-type structure has been suggested. Within this model, the percolation thresholds in $M_{1-x}R_xF_{2+x}$ crystals with tetrahedral R_4F_{26}- and octahedral R_6F_{37}-clusters are considered, whose existence is highly probable in these disordered fluorite phases. It is established that the calculated percolation thresholds x_c = 2.8 mol % for *nnn* (next nearest neighbors) $[(R_6F_{37})_{M_6F_{32}}–F_i]$ and x_c = 4.7 mol % for *nn* (nearest neighbor) $[(R_4F_{26})_{M_6F_{32}}–F_i]$ are in satisfactory accord with the experimental percolation thresholds determined from the conductometric data. © *2000 MAIK "Nauka/Interperiodica".*

INTRODUCTION

Single crystal $M_{1-x}R_xF_{2+x}$ solid solutions (**I**) (M = Ca, Sr, Ba; R = RE) with the defect CaF_2-type structure are model objects for studying ionic transfer in superionic conductors with impurity-type electric conductivity. The form of the concentration dependence of the anionic conductivity of these solid solutions [1–4] indicates the percolation nature of ionic transport resulting in high conductivity values. The nature of high anionic conductivity in nonstoichiometric crystals **I** is associated with the formation of mobile interstitial fluoride ions (the current carriers $(F_i)^-_{mobl}$) and a reduction of the potential-barrier height for their migration in comparison with that in the fluorite matrix, which, in turn, results in a higher carrier mobility).

Numerous studies of electrophysical properties of these compounds [1–6] show that some solid solutions of type **I** have "defect" regions with high conductivity. In this case, with an increase of the impurity-component (RF_3) concentration, the defect regions with high conductivity start merging and, upon the attainment of the critical concentration x_c (the so-called percolation threshold), form a percolation channel for fast fluoride transport.

The percolation threshold x_c is well exhibited on the concentration dependence of conductivity, where the defect phase shows a much higher conductivity than the matrix. The percolation threshold x_c is determined by the type of the defect structure (composition and, therefore, the dimensions and the structure of point-defect complexes). It was shown [7] that x_c can be determined from the experimental conductivity data within the framework of the two-level percolation model. It was also established [8] that for $Sr_{1-x}Er_xF_{2+x}$, $Ba_{1-x}La_xF_{2+x}$, and $Ba_{1-x}Lu_xF_{2+x}$ solid solutions, the percolation threshold $x^{(1)}_{c,\,exp}$ = 2–3 mol %, whereas for the $Sr_{1-x}La_xF_{2+x}$, $Sr_{1-x}Ce_xF_{2+x}$, and $Ca_{1-x}Gd_xF_{2+x}$ solid solutions, it has the value $x^{(2)}_{c,\,exp}$ = 7–8 mol %.

Earlier [4], we described the percolation anionic transport in the $M_{1-x}R_xF_{2+x}$ solid solutions **I** within the model of conducting spheres of equal radii in a continuous dielectric medium, which provided the evaluation of the defect-region (conducting sphere) radius proceeding from the experimental values of the percolation threshold $x_{c,\,exp}$. At the same time, the model of conducting spheres takes into account the crystal (lattice) structure of nonstoichiometric phases **I** only partly.

Below, we suggest another model of anionic-transport percolation in crystals **I** with the CaF_2 structure based on crystallochemical data on the defect structure of these solid solutions.

CRYSTALLOCHEMICAL LATTICE MODEL OF FLUORIDE-ION TRANSPORT PERCOLATION IN NONSTOICHIOMETRIC $M_{1-x}R_xF_{2+x}$ CRYSTALS

The percolation theory studies the nets of resistors (or nets of local conductivities) with some randomly removed elements [9–11]. The normalized conductivity G of these nets is characterized by a rigorous concentration dependence in the vicinity of the percolation

1063-7745/00/4505-0799$20.00

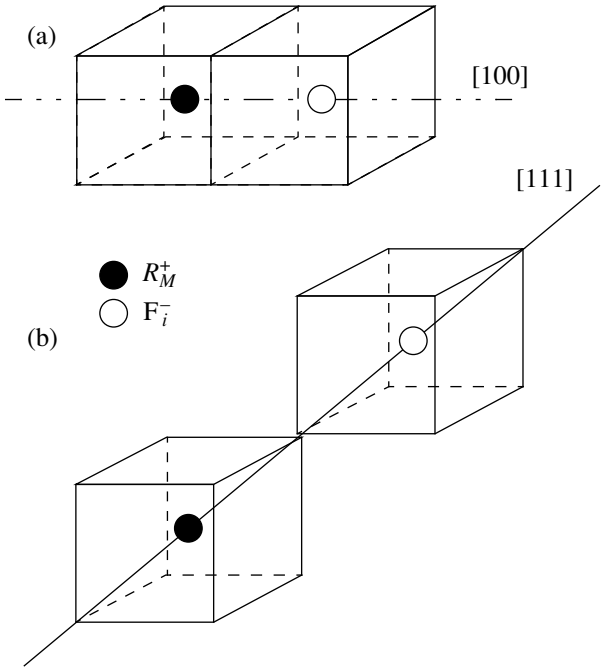

Fig. 1. Type of $[R_M–F_i]$-dipoles in the fluorite-type MF_2 : R^{3+} crystals (a) *nn*-dipole, (b) *nnn*-dipole.

threshold $G \propto (x - x_c)^{\alpha}$, where the value of the parameter α is determined only by the system dimensionality (1*D*, 2*D*, or 3*D*). Outside the region close to the percolation threshold, the properties of various percolation models are well described within the framework of the theory of an effective medium. In the model of "percolation over points," some lattice points are removed. The absence of a point denotes that no ionic current can flow along any of the bonds connecting this empty point with other nearest points. The percolation probability $P^{(V)}$ in this model is determined by the ratio of the total allowed volume (volume of the conducting phase) to the total volume of the system, $P^{(V)} = V_{cond}/V_{total}$. The corresponding theoretical calculations [9–11] show that the probability of percolation in a face-centered cubic model at the percolation threshold $x = x_c$ equals $P_c^{(V)} = 14.7\%$.

A fluorite-type structure can be represented as a structure built by F_8 cubes of volumes $a^3/8$ (where a is the unit-cell parameter) filled with cations in a chessboard like manner. In an ideal CaF_2 unit cell, four F_8-cubes are filled with cations and four F_8-cubes corresponding to the so-called interstitial anionic position are empty (the so-called interstitial F_8^{int}-cubes). In the case of isomorphous introduction of RE trifluorides into the MF_2 matrix, some additional (superstoichiometric) interstitial fluoride ions $(F_i)^-_{dop}$ are formed, which are located in F_8^{int}-cubes. The $(F_i)^-_{dop}$ defects can exist in both delocalized (free) and localized (bound) states. In the delocalized state, the impurity or doping $(F_i)^-_{dop}$ anions are the major anionic carriers $(F_i)^-_{mobl}$. In the localized state, with an increase of the RE ion concentration in crystals **I**, first the pair complexes of the point defects are formed (dipoles, the number of rare-earth ions $S = 1$) and then, more complicated point-defect complexes of various configuration are formed (clusters, $S \geq 2$).

The F_8 cubes containing cations in structures **I** take no active part in the anionic transport and therefore are ignored in the further consideration. The centers of gravity of the remaining F_8^{int}-cubes obey the law of the face-centered cubic lattice and their number is equal to the total number of cations. The set of interstitial F_8^{int}-cubes can be considered as a face-centered cubic lattice in which an individual F_8^{int}-cube can be considered as a lattice pseudopoint.

Consider the position 4*b* of the centers of F_8^{int}-cubes in the sp. gr. $Fm\bar{3}m$ as the crystallographic positions for anionic carriers $(F_i)^-_{mobl}$. The distance between the sites of the position 4*b* equals $a/\sqrt{2}$. Prior to calculations, assume that (i) $(F_i)^-_{mobl}$ defects not reached the percolation barrier are in the bound state with a positively charged center (a rare earth ion in a dipole or a charged cluster) in a (quasi)dipole complex; (ii) no thermal dissociation of $(F_i)^-_{mobl}$ defects from (quasi)dipole complexes occur, and (iii) there are two possible positions for a bound $(F_i)^-_{mobl}$ defect in the vicinity of the positively-charged center: (a) in the first coordination sphere, the *nn* (nearest neighbor) position, and (b) in the second coordination sphere, the *nnn* (next nearest neighbor) position.

A decrease of the potential barrier for the bound defects $(F_i)^-_{mobl}$ indicates that the interstitial $(F_i)^-_{mobl}$ ion is located in a conducting defect cube F_8^{cond}. The F_8^{cond}-cubes (conducting pseudopoints) are favorable for ionic transport and can be considered as those taking part in the formation of percolation–conductivity channels. Inside clusters, a considerable rearrangement of the fluoride sublattice occurs. Strongly distorted internal F_8^{cl}-cubes in the clusters do not participate in ionic transport (forbidden pseudopoints). At the same time, similar to dipoles, some conducting defect F_8^{cond}-cubes are formed in the vicinity of clusters, which favor ionic transport. With an increase of the RE concentration, the number of conducting points increases, which, finally, results in the formation of a 3*D* percolation channel.

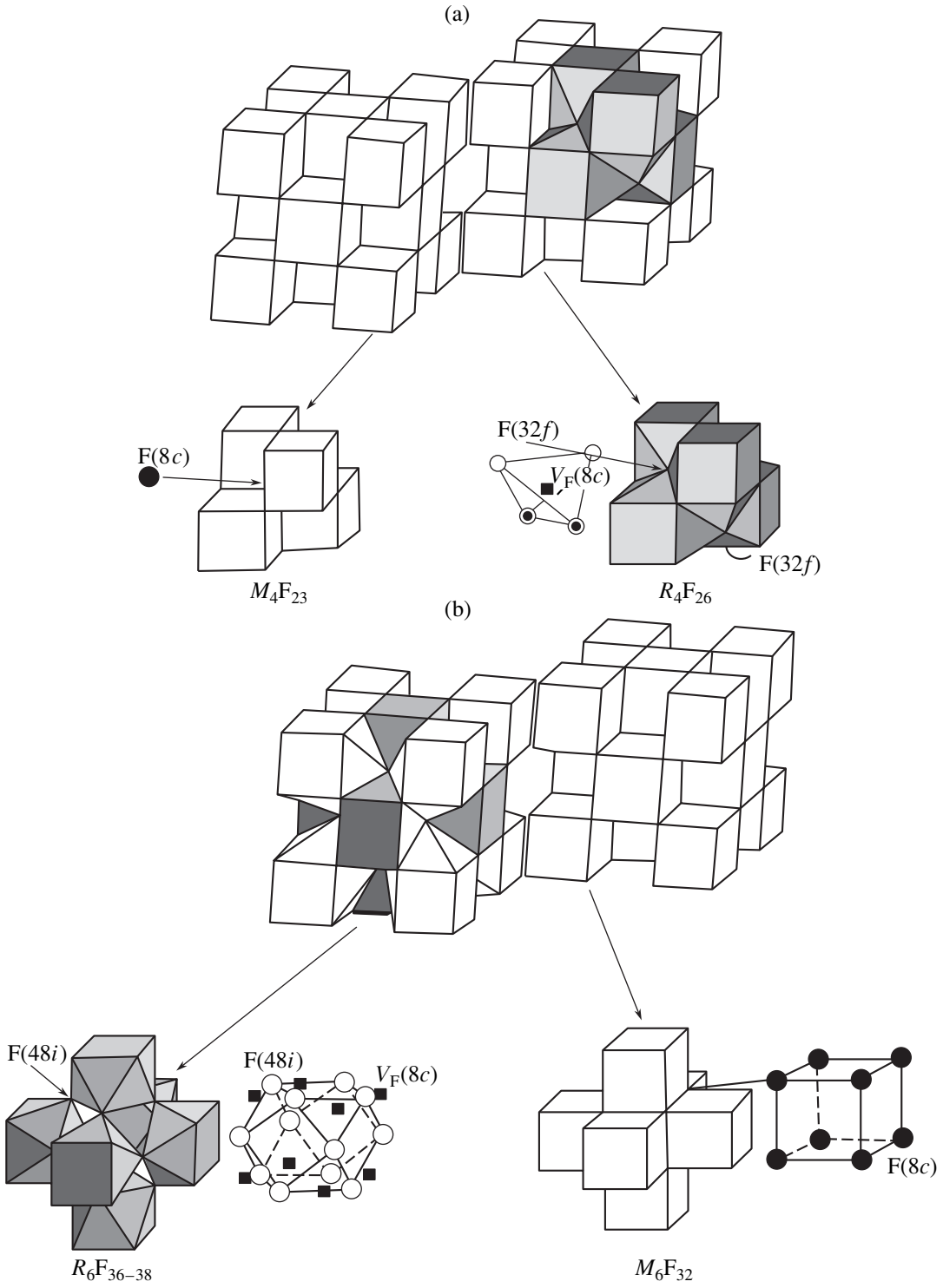

Fig. 2. Types of clusters in the fluorite-type $M_{1-x}R_xF_{2+x}$ solid solutions (a) R_4F_{26}-cluster and (b) R_6F_{36-38}-cluster.

To construct the models providing the interpretation of the electric properties of solid solutions **I** in the whole range of RF_3 concentrations, one has to know the location of RE-dopant and additional fluoride ions compensating the excessive positive charge in the crystal lattice. These data can be obtained by studying the defect structure of crystals **I**.

In lightly-doped $MF_2 : R^{3+}$ crystals, the simplest associates of $[R_M–F_i]$-defects of two types are formed

Calculation of ion-transport percolation thresholds in fluorite-type $M_{1-x}R_xF_{2+x}$ solid solutions

Type of structural defect	S	Number of pseudopoints per 1R		$P^{(V)}$	x_c, mol %	$x_{c,\,\mathrm{exp}}$, mol %
		conducting	forbidden			
nn-dipole [R_M–F_i]	1	6	–	$6x$	2.5	
nn-quasidipole [$(R_4F_{26})_{M_4F_{23}}$–F_i]	4	12/4	4/4	$3x/(1-x)$	4.7	7–8
nnn-quasidipole [$(R_4F_{26})_{M_4F_{23}}$–F_i]	4	12 + 28/4	4/4	$10x/(1-x)$	1.4	
nnn-dipole [R_M–F_i]	1	6 + 8	–	$14x$	1.1	
nn-quasidipole [$(R_6F_{37})_{M_6F_{32}}$–F_i]	6	6/6	13/6	$6x/(6-13x)$	11.1	2–3
nnn-quasidipole [$(R_6F_{37})_{M_6F_{32}}$–F_i]	6	6 + 24/6	13/6	$30x/(6-13x)$	2.8	

(Fig. 1). If the charge-compensating interstitial $(F_i)^-_{dop}$-anion is located in the first coordination sphere of a RE-cation, the so-called *nn*-dipole is formed, whereas if such an anion is located in the second coordination sphere, and *nnn*-dipole is formed. The symmetry of the *nn*-[R_M–F_i] dipole is 4*mm* (C_{4v}) and that of the *nnn*-[R_M–F_i] – 3*m* dipole, 3*m* (C_{3v}). The introduction of RE ions into the CaF_2 matrix mainly results in the formation of *nn*-dipoles; if they are introduced into the BaF_2 matrix, the *nnn*-dipoles are formed. Finally, the change of the RE along the lanthanoid series from La to Lu in the SrF_2 matrix results in the transition from the *nn* to the *nnn*-dipoles [12, 13].

For the *nn*-dipole ($S = 1$) in the first coordination sphere, the number of conducting F_8^{cond} pseudopoints is 6, i.e., there are no forbidden pseudopoints F_8^{cl} at all. The percolation threshold $x_c = P_c^{(V)}/6 = 2.5$ mol %. For an *nnn*-dipole with due regard for the second coordination sphere, the number of conducting F_8^{cond} pseudopoints increases by eight in comparison with that for an *nn*-dipole. This results in the formation of a lower percolation threshold $x_c = P_c^{(V)}/14 = 1.1$ mol %.

Since the values of the experimental percolation thresholds $x_{c,\,\mathrm{exp}}^{(1)}$ and $x_{c,\,\mathrm{exp}}^{(2)}$ exceed 1 mol %, the clusters should play an important role in the process of ion-transport percolation. Using the structural data on the defects in the fluorine sublattice (the coordinates of the interstitial fluoride ions, their number, and the number of fluoride vacancies in the main 8*c* positions), various authors suggest several cluster models for strongly nonstoichiometric crystals **I**. Some types of possible structural clusters were considered in [14–18]. The known structural data and the theoretically calculated energies of cluster formation [14–18] indicate that nonstoichiometric crystals **I** are characterized by block isomorphism and that the most probable clusters are octahedral and tetrahedral R_6F_{36-38}-clusters of type R_4F_{26} substituting structural fluorite M_6F_{32}- and M_4F_{23}-fragments, respectively (Fig. 2).

In the R_4F_{26}-type clusters, four interstitial fluoride ions occupy the position 32*f* (*vvv*) with $v \approx 0.37$ on threefold axes and form one fluoride vacancy. In the R_6F_{36-38}-type clusters, twelve interstitial fluoride ions are located on twofold symmetry axes at cuboctahedron vertices in the positions 48*i* with the coordinates (0.5*uu*) with $u \approx 0.41$ and form eight vacancies in the main fluorine position 8*c*. In the vicinity of the cluster center (position 4*b*), there are also eight equivalent 32*f* positions in which fluoride anions can occupy either two sites related by the center of inversion (R_6F_{38}-type cluster) or one site (R_6F_{37}-type cluster) or do not occupy any of these sites (R_6F_{36}-type cluster).

The first coordination sphere of the R_4F_{26} cluster includes twelve conducting F_8^{cond} pseudopoints. Inside the R_4F_{26}-cluster, there are four F_8^{cl}-cubes forbidden for ion motion. For an *nn*-quasidipole [$(R_4F_{26})_{M_4F_{23}}$–F_i]-complex, the percolation threshold equals $x_c = P_c^{(V)}/(3 + P_c^{(V)}) = 4.7$ mol %. The percolation thresholds for two other cases are given in table.

The analysis of conductometric and structural data [4, 12–14] shows that the experimental percolation threshold $x_{c,\,\mathrm{exp}}^{(1)} = 2$–3 mol % is observed only in the fluorite-type solid solutions **I**, in which the key role is played by fluoride ions in the position 48*i*, *nnn*-dipoles (in the diluted region), and octahedral R_6F_{37}-type clusters (in the concentrated region). The percolation threshold $x_{c,\,\mathrm{exp}}^{(1)} = 7$–8 mol % is observed in those solid solutions, where the interstitial ions occupy the position 32*f*, *nn*-dipoles, and tetrahedral R_4F_{26}-clusters. This indicates that in the first case, the *nnn*-[$(R_6F_{37})_{M_6F_{32}}$–F_i] complexes participate in the percolation ionic transport, whereas in the second case, the *nn*-

$[(R_4F_{26})_{M_4F_{23}}–F_i]$ complexes participate in percolation. Table shows the satisfactory agreement between the experimental values $x_{c,\,\mathrm{exp}}^{(1)}$ = 2–3 mol % and $x_{c,\,\mathrm{exp}}^{(2)}$ = 7–8 mol % in the $M_{1-x}R_xF_{2+x}$ (M = Ca, Sr, Ba) solid solutions **I** and the percolation thresholds calculated within the framework of the percolation model for quasidipole *nnn*-$[(R_6F_{37})_{M_6F_{32}}–F_i]$ complexes (x_c = 2.8 mol %) and the *nn*-$[(R_4F_{26})_{M_4F_{23}}–F_i]$ complexes (x_c = 4.7 mol %).

ACKNOWLEDGMENTS

The authors is grateful to B.P. Sobolev and P.P. Fedorov for valuable remarks.

REFERENCES

1. K. E. D. Wapenaar, J. L. van Koesveld, and J. Schoonman, Solid State Ionics **2**, 145 (1981).
2. P. P. Fedorov, T. M. Turkina, B. P. Sobolev, *et al.*, Solid State Ionics **6**, 331 (1982).
3. H. W. den Hartog and J. C. Langevoort, Phys. Rev. B **24**, 3547 (1981).
4. A. K. Ivanov-Shitz, N. I. Sorokin, P. P. Fedorov, and B. P. Sobolev, Solid State Ionics **31**, 253 (1989).
5. J. M. Reau and J. Grannec, in *Inorganic Solid Fluorides (Chemistry and Physics)*, Ed. by P. Hagenmuller (Academic Press, New York, 1985), p. 423.
6. J. Schoonman, in *High Conductivity Solid Ionic Conductors: Recent Trends and Application*, Ed. by T. Takahashi (World Scientific, Singapore, 1989), p. 366.
7. N. I. Sorokin, Kristallografiya **38** (1), 245 (1993) [Crystallogr. Rep. **38**, 132 (1993)].
8. N. I. Sorokin, in *Proceedings of Res. Soc. Fall Meet. Symposium on Solid State Ionics. Abstr., Boston, 1995*, p. 160.
9. S. Kirkpatrick, Nov. Fiz. Tverd. Tela, No. 7, 249 (1977) [Rev. Mod. Phys. **45**, 57 (1973)].
10. H. Sher and R. Zallen, J. Chem. Phys. **53**, 3759 (1970).
11. F. Lux, J. Mater. Sci. **28**, 285 (1993).
12. I. V. Murin and W. Gunsser, Solid State Ionics **53–56**, 837 (1992).
13. P. Dorenbos and H. W den Hartog, Phys. Rev. B **31**, 3932 (1985).
14. L. A. Muradyan, B. A. Maksimov, and V. I. Simonov, Koord. Khim. **12**, 1398 (1986).
15. J. M. Reau and P. Hagenmuller, Appl. Phys. A **49**, 3 (1989).
16. P. P. Fedorov, Bull. Soc. Catalana Cienc. Fis. **12** (2), 349 (1991).
17. J. Corish, C. R. A. Catlow, P. W. M. Jacobs, and S. H. Ong, Phys. Rev. B **25**, 6425 (1982).
18. P. J. Bendal, C. R. A. Catlow, J. Corish, and P. W. M. Jacobs, J. Solid State Chem. **51**, 159 (1984).

Translated by L. Man

Crystallography Reports, Vol. 45, No. 5, 2000, pp. 804–807. Translated from Kristallografiya, Vol. 45, No. 5, 2000, pp. 876–880.

LATTICE DYNAMICS

Modeling of the Lattice Dynamics and Elastic Properties of the $Sn_2P_2S_6$ Ferroelectric

A. A. Grabar, R. M. Evich, and Yu. M. Vysochanskiĭ

Institute of Solid State Physics and Chemistry, Uzhgorod State University, Pidhirna 46, Uzhgorod, 88000 Ukraine

e-mail: grabar@iss.univ.uzhgorod.ua

Received October 29, 1998; in final form, April 12, 1999

Abstract—The lattice-dynamics calculations for the paraelectric phase of the $Sn_2P_2S_6$ ferroelectric are performed within the model of rigid ions. The model parameters were chosen by fitting the calculated phonon spectra to the known data on inelastic neutron scattering. The dispersion curves obtained were then used for calculating the orientational dependences of sound velocity and the variation of the phonon frequencies under the hydrostatic compression. The data obtained are in good agreement with the experimental results. *© 2000 MAIK "Nauka/Interperiodica".*

Instability of a crystal lattice with respect to some of the degrees of freedom causes structural transitions, in particular, ferroelectric phase transitions. In order to understand the mechanism of phase transitions and their changes under the effect of various external factors or the variations in the chemical composition, one has to know the law of phonon dispersion within the whole Brillouin zone and also the nature of the interaction between the branches of the phonon spectrum. Therefore, the construction of the appropriate model of lattice dynamics is an important stage in the study of phase transitions in every specific case.

Ferroelectrics of the $Sn_2P_2S_6$ family are attractive objects for studying a relationship between structural characteristics and the nature of the phase transition studied [1]. These are a proper uniaxial ferroelectric in which a phase transition occurs with the change in the point-symmetry, $2/m \longrightarrow m$, but without unit-cell multiplication and takes place with the a soft-mode condensation in the center of the Brillouin zone. The compound $Sn_2P_2S_6$ is characterized by a second-order phase transition at 337 K. The compound $Sn_2P_2Se_6$ is characterized by a second-order phase transitions from the paraelectric to the incommensurate phase followed by a first-order phase transition from the incommensurate to the ferroelectric phase. In the $Sn_2P_2(Se_xS_{1-x})_6$ solid solutions, an increase in the selenium content x above 0.28 results in the split of the line of phase transitions and the appearance of the Lifshitz point on the phase diagram [3]. The split of the line of phase-transitions is also observed under the hydrostatic compression [4].

One of possible causes of the formation of an incommensurate phase during the variation of the chemical composition or pressure may be an increase of the linear interactions between optical and acoustical phonons, resulting in condensation of the superposition of these excitations at the nonzero value of the wave vector. In the simplest case, this situation can be described by the model of coupled oscillators characterized by linear interactions [5, 6]. However, the detailed analysis requires the allowance for dispersion of phonon excitation over the whole Brillouin zone. This information can be obtained from inelastic neutron scattering data. At the same time, the construction of a dynamical model consistent with the experimental data allows one to study the above phenomena in more detail.

Lattice dynamics of the $Sn_2P_2S(Se)_6$ crystals was studied in [7, 8]. However, the experimental data were restricted to phonon frequencies at the center of the Brillouin zone and the velocities of the sonic wave. Unfortunately, the first data on inelastic neutron scattering [9] and some additional data (atomic coordinates at various temperatures [10], compressibility [11]) were obtained only recently. This makes it possible to refine the parameters of the model. Below, we present the phonon spectra of the paraelectric $Sn_2P_2S_6$ phase calculated with regard of new experimental data, and the results obtained in modeling of its elastic properties.

The calculations were performed within the approximation of rigid ions by using the DISPR program [12] specially modified for the $Sn_2P_2S_6$ structure. We used the conventional procedure for constructing the dynamical matrix [13] and its diagonalization by the Jacobi method. We calculated the eigenvalues (squared frequencies) and eigenvectors of phonon excitations for different wave vectors in the Brillouin zone. We used the approximation in which the crystal structure is represented by tin cations and molecular P_2S_6 anions considered are vibrational units with six (translational and

1063-7745/00/4505-0804$20.00

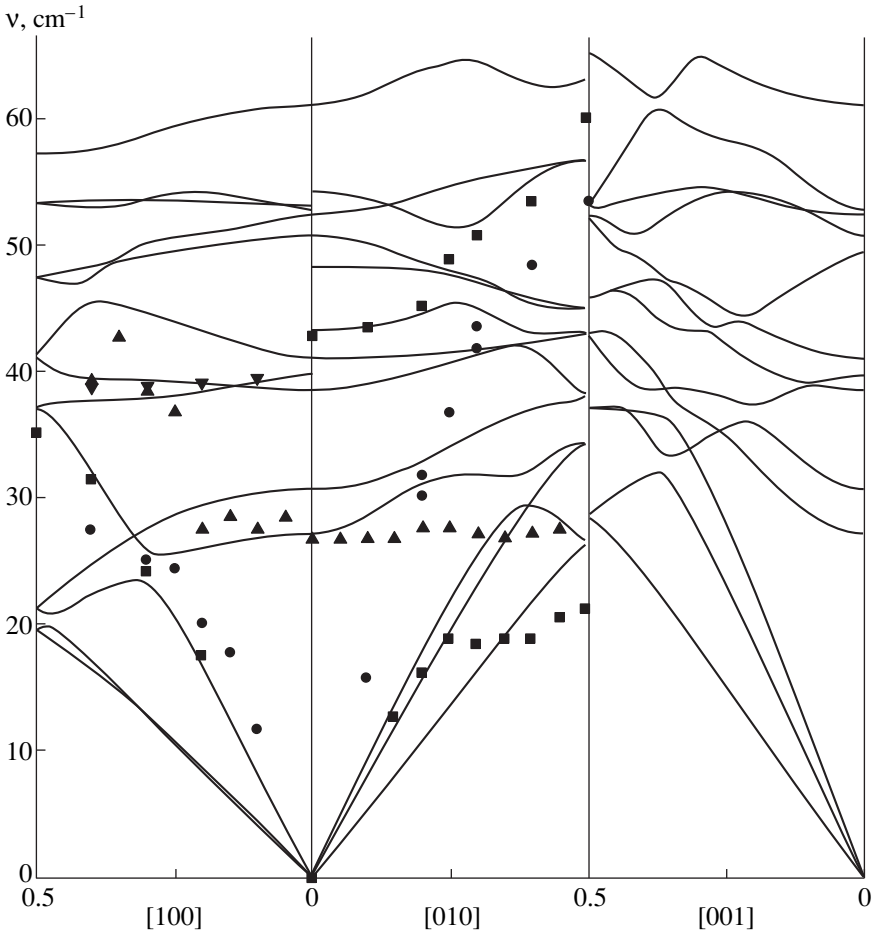

Fig. 1. Dispersion phonon branches for the paraelectric phase of the ferroelectric $Sn_2P_2S_6$. Experimental data on inelastic neutron scattering are shown by dots [9].

vibration) degrees of freedom. Since $Sn_2P_2S_6$ has two formula units in the unit cell, the dimension of the complex dynamical matrix is 24×24. The internal degrees of freedom of an ethane-like molecular complex P_2S_6 were ignored, and therefore, only the "external" vibrations were calculated. The above approximation was chosen because of the gap between the upper frequency limit of the "external" vibrations (150 cm^{-1}) and the lower frequency limit of the internal vibrations of the anion. The latter range from 180 cm^{-1} (deformation vibration) to 580 cm^{-1} (P–S valence vibrations) [14, 15].

The potential of atomic interaction includes the Coulomb and the short-range (Born–Mayer) components in the form:

$$V(r) = (e^2/4\pi\varepsilon_0)(Z(Kk)Z(K'k')/r) + A\exp\{-Br/[R(Kk) + R(K'k')]\}, \quad (1)$$

where r is the interatomic distance, $Z(Kk)$ and $R(Kk)$ are effective charge and the radius of the K atom in the kth cell, e is the electron charge, ε_0 is the dielectric constant, and A and B are the empirical constants equal to 18.22 and 12.364 eV, respectively [12]. The calculation of the short-range potential was restricted to the first coordination polyhedron, the Coulomb sums were calculated the Ewald method within the distances equal to two lattice constants.

Thus, the model parameters are, in fact, the effective charges Z and the effective radii R of tin, phosphorus, and sulfur atoms. With due regard for the condition of total electrical neutrality, $Z(Sn) + Z(P) + 3Z(S) = 0$, the total number of independent parameters reduces to five. Of course, this approximation is rather crude, however, it is sufficient for the qualitative agreement between the theory and the experiment and can be taken as the first approximation for further calculations.

In our previous papers [7, 8], we used the following set of parameters: $Z(Sn) = 1.20$; $Z(P) = 0.60$; $Z(S) = -0.60$; $R(Sn) = 2.45$ Å; $R(P) = 1.08$ Å; and $R(S) = 1.40$ Å. The new refined parameters were chosen in a way to achieve the best possible agreement for the phonon frequencies in the center of the Brillouin zone and for the shape of the phonon dispersion curves.

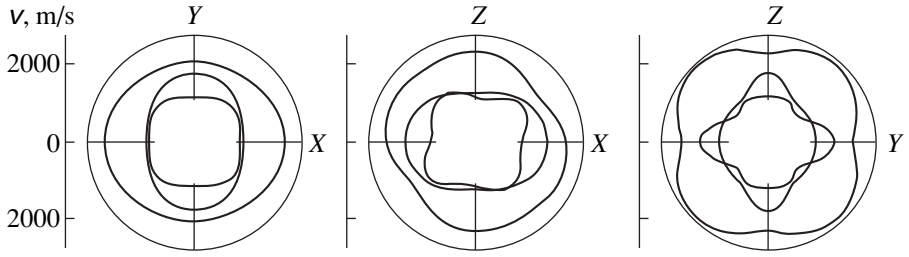

Fig. 2. Orientational dependences of the sonic velocity in a $Sn_2P_2S_6$ crystal calculated in the model of rigid ions.

Figure 1 shows the low-frequency part of the phonon dispersion curves calculated for the paraelectric $Sn_2P_2S_6$ phase and the experimental data on inelastic neutron scattering (dots) taken from [9]. The curves correspond to the following set of parameters: $Z(Sn) = 1.40$; $Z(P) = 0.34$; $Z(S) = -0.58$; $R(Sn) = 2.40$ Å; $R(P) = 1.08$ Å; $R(S) = 1.40$ Å. On the whole, the agreement between the calculated optic and acoustic phonon branches and the experimental points is rather good. However, the experimental points are obtained only for most intense low-frequency modes and the wave vectors directed along two crystallophysical axes. There are no experimental data for the [001]-direction. The upper boundary of the external frequencies (not shown in Fig. 1) corresponds to the frequency 140 cm^{-1}, which is close to the experimental value. The number of the branches calculated within the interval shown in Fig. 1 exceeds the number of the experimental curves in [9], which is explained by a rather poor resolution of experimental spectra of neutron scattering. The points shown in Fig. 1 correspond to the most intense peaks.

Lowering the soft-mode frequency can be modeled by changing the parameters of potential (1). In this case, the low optical vibration mode can be made unstable at the stable acoustic degrees of freedom by varying the long-range potential (decreasing of the effective charge of tin and an increase of the effective charge) of phosphorus or else, by decreasing the short-range potential. For instance, the change in the effective parameters up to the values $Z(Sn) = 1.19$; $Z(P) = 0.46$; $Z(S) = -0.55$; $R(Sn) = 2.12$ Å; $R(P) = 1.08$ Å; and $R(S) = 1.53$ Å decreases the frequency of the low optical mode down to 16 cm^{-1}. The further change of the effective parameters lead to negative values of acoustic frequencies. It should be noted that in experimental studies of Raman spectra, the condensation of the soft mode was also observed up to frequencies of 10–15 cm^{-1}; at higher frequencies, the anharmonic interactions stabilized the soft optical mode [16]. The value of the lowest optical frequency is approximately equal to the applicability limit of our model.

The slope of acoustical branches at the center of Brillouin zone is used to calculate the phase velocity of sonic waves propagating along the corresponding wave vector. The wave polarization is determined from the eigenvector of the acoustic phonon. Similar calculations for different directions of the Brillouin zone provide the determination of all the components of the elasticity tensor and orientation dependences (wave fronts) of sonic waves. The results obtained for three perpendicular crystallophysical planes are shown in Fig. 2. On the average, the calculated phase velocities of the acoustic excitations are less by 40% than the experimental values obtained from the sonic velocity at the frequency of about 30 MHz. In particular, the longitudinal (along the [010]-direction) sonic velocity in the paraelectric phase is 3.1×10^3 m/s [2]. At the same time, the agreement between the calculated slope of the longitudinal acoustic branch and the value obtained from neutron scattering is better and does not exceed 20% (see Fig. 1). Within the framework of the model used, we failed to achieve better correspondence for sonic velocities without a noticeable deterioration of consistency with the dispersion in the optical branches. Nevertheless, in view of the absence of more reliable experimental data, the results of our calculation (Fig. 2) can be used for modeling the processes depending on the anisotropy of elastic properties.

One of the criteria showing the adequacy of the model interaction potential is its applicability in simulation of hydrostatic compression by varying interatomic distances. Using the experimental data on the linear compressibility of $Sn_2P_2S_6$ crystals in the paraelectric phase [11], one can calculate the effective pressure in terms of model deformations and then compare the results obtained with the experiment. The effect of compression on the phonon frequencies in the Raman spectra was studied earlier [17]. It was found that the "external" frequencies linearly depend on the pressure, with the baric derivatines being 1–3 cm^{-1}/kbar. The relative change in the internal frequencies is several times less, which can be explained by a more pronounced rigidity intramolecular covalent P–P and P–S bonds. When modeling the effect of compression on phonon spectra, we used two models of deformation: a uniform model, when only the lattice constants were varied, and a more realistic model of an incompressible P_2S_6 anion. In the first model, we calculated the changes in the crystal-lattice parameters *a*, *b*, and *c* for the given pressure from the known values of the linear compressibilities from [11]. Then, new values of phonon frequencies changed because of reduced inter-

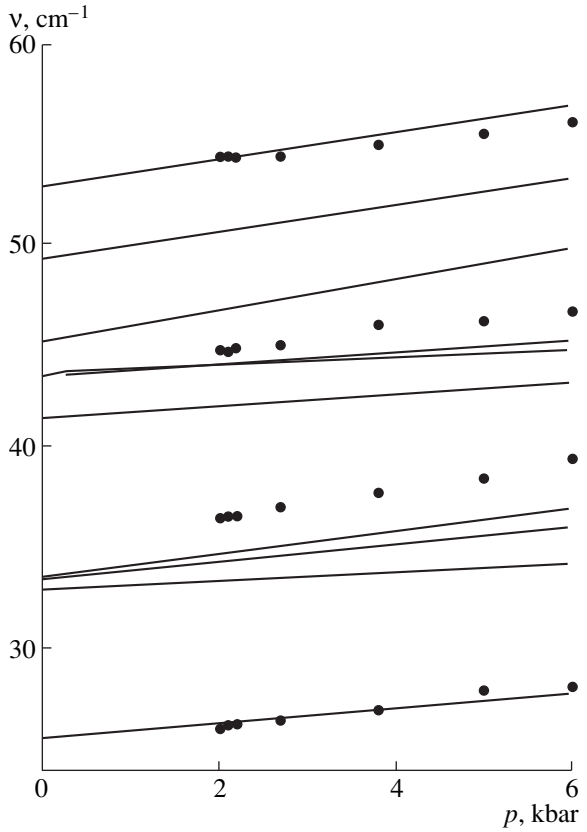

Fig. 3. Modeling of hydrostatic compression of $Sn_2P_2S_6$ crystals as a function of the optical-phonon frequencies at the center of the Brillouin zone. Dots indicate the frequencies of the Raman spectra measured as functions of pressure [17].

atomic distances in potential (1), were calculated. In the second model, anions were treated as incompressible—the initial dimensions of P_2S_6 complexes in the deformed unit cell were restored with respect to their centers-of-mass. As was to be expected, the second model gave the better results that were consistent with those from [17]. The phonon frequencies at the center of the Brillouin zone calculated as function of pressure are shown in Fig. 3 together with the corresponding experimental data from [17].

Thus, the results obtained on the lattice dynamics of the $Sn_2P_2S_6$ crystal within the model of rigid ions are consistent with the experimental data on neutron scattering. This model can be used for refining the experimental data on neutron scattering, calculating the phonon density of states and anisotropy of elastic properties. The model can be further developed for calculating phonon spectra of other related compounds.

ACKNOWLEDGMENTS

This study was supported by the INCO-COPERNICUS program, project ERBIC 15 CT 970712.

REFERENCES

1. Yu. M. Vysochanskiĭ and V. Yu. Slivka, *Ferroelectrics of the $Sn_2P_2S_6$ Family. Properties in the Vicinity of the Lifshitz Point* (Oriana-Nova, Lviv, 1994).
2. A. V. Gomonnaĭ, A. A. Grabar, Yu. M. Vysochanskiĭ, *et al.*, Fiz. Tverd. Tela (Leningrad) **23**, 3602 (1981) [Sov. Phys. Solid State **23**, 2093 (1981)].
3. Yu. M. Vysochanskiĭ and V. Yu. Slivka, Usp. Fiz. Nauk **162** (2), 139 (1992) [Sov. Phys. Usp. **35**, 123 (1992)].
4. Yu. I. Tyagur and E. I. Gerzanich, Kristallografiya **29** (5), 957 (1984) [Sov. Phys. Crystallogr. **29** (5), 563 (1984)].
5. V. Dvorak, Phys. Rev. **167**, 525 (1968).
6. A. P. Levanyuk and D. G. Sannikov, Fiz. Tverd. Tela (Leningrad) **18**, 1927 (1976) [Sov. Phys. Solid State **18**, 1122 (1976)].
7. A. A. Grabar, Yu. M. Vysochanskiĭ, and V. Yu. Slivka, Fiz. Tverd. Tela (Leningrad) **26**, 3469 (1984) [Sov. Phys. Solid State **26**, 2087 (1984)].
8. V. M. Rizak, Yu. M. Vysochanskiĭ, A. A. Grabar, and V. Yu. Slivka, Fiz. Tverd. Tela (Leningrad) **31** (7), 154 (1989) [Sov. Phys. Solid State **31**, 1185 (1989)].
9. S. W. H. Eijt, R. Currat, J. E. Lorenzo, *et al.*, Eur. Phys. J. B **5**, 169 (1998).
10. B. Scott, M. Pressprich, R. D. Willett, and D. A. Cleary, J. Solid State Chem. **96**, 294 (1992).
11. V. S. Shusta, P. P. Guranich, E. I. Gerzanich, *et al.*, Ukr. Fiz. Zh. (Russ. Ed.) **40**, 959 (1995).
12. S. L. Chaplot, Govt. India Atom. Energy Commis. (Rept.), No. 972, 1 (1978).
13. M. Born and Huang Kun, *Dynamical Theory of Crystal Lattices* (Oxford Univ. Press, Oxford, 1954; Inostrannaya Literatura, Moscow, 1958).
14. Yu. M. Vysochanskiĭ, V. Yu. Slivka, Yu. V. Voroshilov, *et al.*, Fiz. Tverd. Tela (Leningrad) **21**, 211 (1979) [Sov. Phys. Solid State **21**, 123 (1979)].
15. A. V. Gomonnaĭ, Yu. M. Vysochanskiĭ, M. I. Gurzan, and V. Yu. Slivka, Fiz. Tverd. Tela (Leningrad) **25**, 1454 (1983) [Sov. Phys. Solid State **25**, 835 (1983)].
16. A. A. Bokoteĭ, Yu. M. Vysochanskiĭ, V. M. Rizak, *et al.*, Ukr. Fiz. Zh. (Russ. Ed.) **42**, 55 (1997).
17. A. A. Grabar, Yu. M. Vysochanskiĭ, N. N. Mel'nik, *et al.*, Fiz. Tverd. Tela (Leningrad) **26**, 65 (1984) [Sov. Phys. Solid State **26**, 36 (1984)].

Translated by M. Savrov

Crystallography Reports, Vol. 45, No. 5, 2000, pp. 808–810. From Kristallografiya, Vol. 45, No. 5, 2000, pp. 881–883.

On Existence of One-Partial Bulk Waves in Semi-infinite Piezoelectric Media[1]

A. L. Shuvalov* and A. Radowicz**

** Shubnikov Institute of Crystallography, Russian Academy of Sciences, Leninskiĭ pr. 59, Moscow, 117333 Russia*

*** Kielce Technological University, Al. Tysiacialecia Panstva Polskiego, Kielce, 25-314 Poland*

Received October 30, 1998

Abstract—The conditions for the existence of one-partial bulk waves satisfying the boundary conditions on a mechanically free surface of a semi-infinite piezoelectric medium have been analyzed. In purely elastic media, similar wave solutions are known to exist along the propagation directions **m** which form lines on the sphere $\mathbf{m} \cdot \mathbf{m} = 1$, passing through all the available degeneracy points (acoustic axes). It is shown that in a triclinic piezoelectric half-space with a metallized surface, one-partial bulk waves may exist solely along isolated propagation orientations, whereas for a nonmetallized surface, such waves can exist only if an additional condition for the material constants of the medium is fulfilled. It is also shown that the one-partial bulk solution may not exist along an arbitrary acoustic axis in a piezoelectric. These conclusions are valid in the general case of unrestricted anisotropy, i.e., they do not take into account the material symmetry. In addition, the orientations providing the propagation of one-partial bulk waves because of the existing symmetry are specified for piezoelectric media of various symmetry classes. © *2000 MAIK "Nauka/Interperiodica".*

An important role in the theory of surface acoustic waves is played by the so-called exceptional waves, which are bulk (homogeneous) modes satisfying the boundary condition of a free surface [1, 2]. The conditions for the existence of such waves in a purely elastic medium have been analyzed in [3]. It was established that the wave normals **m** of the exceptional waves in arbitrarily anisotropic elastic media form lines on the sphere $\mathbf{m} \cdot \mathbf{m} = 1$ and that the acoustic axes ensure the propagation of the exceptional waves. It seems expedient to study how these properties change in the case of one-partial bulk modes in a piezoelectric half-space with a mechanically free metallized or nonmetallized surface.

Consider a piezoelectric medium with the density ρ, elastic coefficients c_{ijkl}, piezoelectric constants e_{ijk}, and dielectric permittivity ε_{ij}. In the quasistatic approximation, the propagation of plane acoustoelectric waves $\sim e^{i(k_\alpha \mathbf{m} \cdot \mathbf{r} - \omega t)}$ ($\alpha = 1, 2, 3$) is described by the modified Christoffel equation

$$\left(m_i c_{ijkl} m_l - \frac{m_i e_{ijl} m_l m_i e_{ikl} m_l}{m_i \varepsilon_{il} m_l}\right) A_{\alpha k} = \rho v_\alpha^2 A_{\alpha j}, \quad \alpha = 1, 2, 3, \tag{1}$$

where $\mathbf{A}_\alpha$ is the polarization vector of elastic displacements and $v_\alpha = \omega/k_\alpha$ is the phase velocity. The mechanical stresses, the induced electric potential, and induction are

$$\sigma_{ij}^{(\alpha)} = ik_\alpha \left[c_{ijkl} m_l A_{\alpha k} + \frac{1}{m_i \varepsilon_{il} m_l} (m_i e_{ikl} m_l A_{\alpha k}) m_l e_{lij} \right], \tag{2}$$

$$\varphi_\alpha = m_i e_{ikl} m_l A_{\alpha k}, \tag{3}$$

$$D_{\alpha i} = ik_\alpha \left[e_{ikl} m_l - \frac{1}{m_i \varepsilon_{il} m_l} \varepsilon_{ij} m_j m_j e_{jkl} m_l \right] A_{\alpha k}. \tag{4}$$

The bulk mode described by the above equations meets the boundary conditions on a metallized surface with the normal **n**, provided that $\sigma_{ij}^{(\alpha)} n_j = 0$ and $\varphi_\alpha = 0$. Hence, the directions of propagation **m** of these bulk modes, each satisfying the boundary conditions on a family of parallel planes with the normal **n** dependent on **m**, are set by the system of equations

$$\det[\sigma_{ij}^{(\alpha)}] = 0, \quad \varphi_a = 0. \tag{5}$$

Since $\mathbf{m} \cdot (\boldsymbol{\sigma}^{(\alpha)} \mathbf{n})$ is proportional to $ik_\alpha \mathbf{A}_\alpha \cdot \mathbf{n}$, the condition of a traction-free surface restricts the orientation of the polarization vector to the boundary plane, as in the case of a purely elastic medium. With due regard for (2) and (3), the solutions of system (5) can exist in a tri-

[1] This article was submitted by the authors in English.

clinic piezoelectric medium only for isolated points on the sphere $\mathbf{m} \cdot \mathbf{m} = 1$; these points are the intersections of the lines L_1 of the propagation directions of the exceptional waves in the absence of piezoelectricity [3] with the lines L_2 of the propagation directions which provide zero of the electric potential. It is readily seen from (3) and (1) that the equality $\varphi_\alpha = 0$ is the necessary and sufficient condition for the phase velocity to be independent of the piezoelectric coupling [4]. The lines L_2 necessarily exist for the wave branches $\alpha = 1, 2$ containing degeneracy along the stable (conical-type) acoustic axis, because it is always possible to choose the polarization vectors $\mathbf{A}_\alpha$ in these branches in such a way that they would be odd in $\mathbf{m}$ and that any two inversion-equivalent points $\mathbf{m}$ and $-\mathbf{m}$ could be connected by a continuous path without sign reversal in $\mathbf{A}_\alpha$ [3]. However, this does not guarantee the existence of solutions of system (5), because the lines L_1 and L_2 may not form the large circumferences on the sphere $\mathbf{m} \cdot \mathbf{m} = 1$ and thus do not necessarily intersect one another.

The bulk mode on a nonmetallized surface of a piezoelectric medium, which is in contact with vacuum, should satisfy the boundary conditions $\sigma_{ij}^{(\alpha)} n_j = 0$, $\varphi_\alpha = \varphi_v$, $\mathbf{D}_\alpha \cdot \mathbf{n} = \mathbf{D}_v \cdot \mathbf{n}$. Here, the amplitudes of the potential and induction of the accompanying electric field obey the relationship $\mathbf{D}_v \cdot \mathbf{n} = ik_v\varphi_v$, whence it follows that $\mathbf{D}_\alpha \cdot \mathbf{n} = ik_v\varphi_\alpha$. Since the amplitudes $\mathbf{D}_\alpha$, φ_α are real, the wave normals $\mathbf{m}$ of the bulk modes meeting the boundary conditions on the nonmetallized planes with the normal $\mathbf{n} = \mathbf{n}(\mathbf{m})$ are given by the system of equations

$$\begin{aligned} \det[\sigma_{ij}^{(\alpha)}] &= 0, \\ \varphi_\alpha &= 0, \\ \mathbf{D}_\alpha \cdot \mathbf{n} &= 0, \end{aligned} \tag{6}$$

which complement equations (5) with the condition $\sigma_{ij}^{(\alpha)} n_j = 0$. Thus, the sought manifold of solutions $n_i l_{ikl} m_l A_{\alpha k} = 0$ for bulk waves on the nonmetallized surfaces is enclosed into that defined by (5) for the metallized surfaces. In accordance with (5), generally (i.e., in the absence of any symmetry), only the isolated propagation directions $\mathbf{m}$ can exist for the bulk modes, which satisfy the boundary conditions on the metallized surfaces with normals $\mathbf{n}$ identified for the given $\mathbf{m}$. Hence, the bulk modes in a triclinic piezoelectric medium with nonmetallized surface can exist only because of an appropriate coincidence of material constants.

The symmetry essentially facilitates the fulfillment of the conditions for the existence of the one-partial bulk wave solutions in piezoelectric semi-infinite media. For instance, the SH mode travelling in the symmetry plane $\mathbf{m}$ in a piezoelectric medium satisfies the boundary conditions on a mechanically free surface with the normal $\mathbf{n} \in m$ both in the presence and in the absence of metal coating (as well as in the case of a purely elastic medium).

In the case of degenerate bulk modes propagating along acoustic axes $\mathbf{m}_0$, the arbitrariness of orientation of their polarization vector is an additional factor which could promote the fulfillment of the boundary conditions. According to [3], the degenerate-mode polarization $\mathbf{A}_\alpha$ can always adjust its orientation in such a way which provides zero traction on the family of parallel planes with the normal $\mathbf{n}$ orthogonal to $\mathbf{A}_\alpha$. For an acoustic axis with a generic nonsymmetrical direction $\mathbf{m}_0$ (conical-type degeneracy), there are three orientations of the polarization vector, which satisfy condition [5] for traction-free surface and which usually are not orthogonal to the vector $\mathbf{e}_0$ with components $e_{0k} = m_{0i}e_{ikl}m_{0l}$, hence, they do not turn the potential $\varphi_\alpha = \mathbf{e}_0 \cdot \mathbf{A}_\alpha$ into zero. Thus, these degenerate bulk modes do not satisfy the boundary conditions on a traction-free surface (metallized or, all the more, nonmetallized) of a piezoelectric medium, contrary to the case of purely elastic media. In the particular case of the conical-type acoustical axis $\mathbf{m}_0$ parallel to the threefold axis, the vector $\mathbf{e}_0$ is parallel to $\mathbf{m}_0$, whereas the degenerate modes are transversely polarized and therefore provide the equality $\varphi_\alpha = 0$. Therefore, there exist three orientations of $\mathbf{A}_\alpha$ obeying the boundary conditions on the traction-free metallized surface with the normal $\mathbf{n}$ orthogonal to $\mathbf{A}_\alpha$ (but not to $\mathbf{m}_0$). In piezoelectric crystals of the classes $3m$, $\bar{4}3m$, 23 the boundary conditions on these surfaces are satisfied also in case of no metal coating, which is due to the presence of the symmetry planes (the symmetry of the involved equations is implied, which is provided by the intersection of the symmetry groups of the tensors c_{ijkl} and e_{ijk}, so it is the symmetry $\bar{4}3m$ for crystals of the 23 class).

As regards to the degenerate transverse modes propagating along fourfold axes $\mathbf{m}_0$ of rotational and inversion symmetry (tangential-type degeneracy), any orientation of their polarization vector $\mathbf{A}_\alpha$ provides the vanishing potential $\varphi_\alpha = 0$ and keeps the planes with the normal $\mathbf{n} = \mathbf{m}_0 \times \mathbf{A}_\alpha$ free of traction, thus satisfying the boundary conditions for a metallized surface on these planes. Calculating the induction vectors $\mathbf{D}_\alpha \cdot \mathbf{n} = 0$ associated with the degenerate modes by (4) (see Table 1 in [6]) and taking a scalar product with $\mathbf{n} = \mathbf{m}_0 \times \mathbf{A}_\alpha$, we see that the boundary conditions on the nonmetallized surface orthogonal to $\mathbf{n}$ are satisfied for any orientation of the polarization vector $\mathbf{A}_\alpha$ of the transverse modes propagating along the main symmetry axis in piezoelectrics of classes $6mm$, $\bar{6}m2$, $\bar{6}$, and $4mm$; for two orientations of $\mathbf{A}_\alpha$ (orthogonal to symmetry planes in the intersection of the symmetry groups of the tensors c_{ijkl} and e_{ijk}) in case of the classes $\bar{4}3m$, 23, $\bar{4}2m$, and $\bar{4}$; but these boundary conditions are not fulfilled

for an arbitrary orientation of $\mathbf{A}_\alpha$ in the case of the classes 622, 6, 422, and 4.

ACKNOWLEDGMENTS

This study was supported by the Russian Foundation for Basic Research, project 97-02-16338.

REFERENCES

1. J. Lothe and D. M. Barnett, J. Appl. Phys. **47**, 428 (1976).
2. J. Lothe and D. M. Barnett, J. Appl. Phys. **47**, 1799 (1976).
3. V. I. Al'shits and J. Lothe, Kristallografiya **24** (6), 1123 (1979) [Sov. Phys. Crystallogr. **24**, 644 (1979)].
4. V. I. Al'shits, A. V. Sarychev, and A. L. Shuvalov, Fiz. Tverd. Tela (Leningrad) **28**, 1890 (1986) [Sov. Phys. Solid State **28**, 1052 (1986)].
5. V. I. Al'shits, V. N. Lyubimov, and A. L. Shuvalov, Kristallografiya **32** (4), 828 (1987) [Sov. Phys. Crystallogr. **32**, 487 (1987)].
6. V. I. Al'shits, V. N. Lyubimov, A. V. Sarychev, and A. L. Shuvalov, Zh. Éksp. Teor. Fiz. **93**, 723 (1987) [Sov. Phys. JETP **66**, 408 (1987)].

Crystallography Reports, Vol. 45, No. 5, 2000, pp. 811–815. Translated from Kristallografiya, Vol. 45, No. 5, 2000, pp. 884–887.

PHASE TRANSITIONS

Specific Features of the Temperature Dependence of the Low- and Infralow-Frequency Spectra of Complex Permittivity ε* for the Polar Phase of Diglycine Nitrate Crystals

A. V. Shil'nikov*, V. A. Fedorikhin*, E. G. Nadolinskaya*, S. V. Rodin, and L. A. Fedotova***

** Volgograd State Academy of Architecture and Civil Engineering, Volgograd, 400074 Russia*

*** Minsk Institute of Radio Engineering, Minsk, 220726 Belarus*

Received October 5, 1998

Abstract—The low- and infralow-frequency (ε*) spectra have been studied for the polar phase of diglycine nitrate crystals of different history (slowly cooled and heated above the Curie point T_c). The specific features of the spectra are discussed in terms of point defect "freezing" and interaction with domain walls. *© 2000 MAIK "Nauka/Interperiodica".*

Dielectric properties of the polar phase of diglycine nitrate crystals have been studied in detail in [1–4]. However, the lowest frequency of the field applied did not exceed 20 or 30 Hz. At the same time, it is well known [5] that many of the ferroelectric crystals exhibit the dispersion of ε* in the infralow-frequency range associated with the reversible motion of domain walls. The present study was undertaken to check whether diglycine nitrate crystals also behave in the same way. As is well known, these crystals undergo a phase transition at a rather low temperature (T_c ~ 205–206 K) and have a structure close to that of triglycine sulfate. In such studies of dielectric and other macroscopic properties of ferroelectrics, it is important to also take into account the history of the crystals studied.

The preparation of specimens and the procedure of measuring the complex permittivity ε* were, in principle, the same as described in [6]. The measurements were performed on the specimens slowly cooled from room temperature to the boiling point of nitrogen and

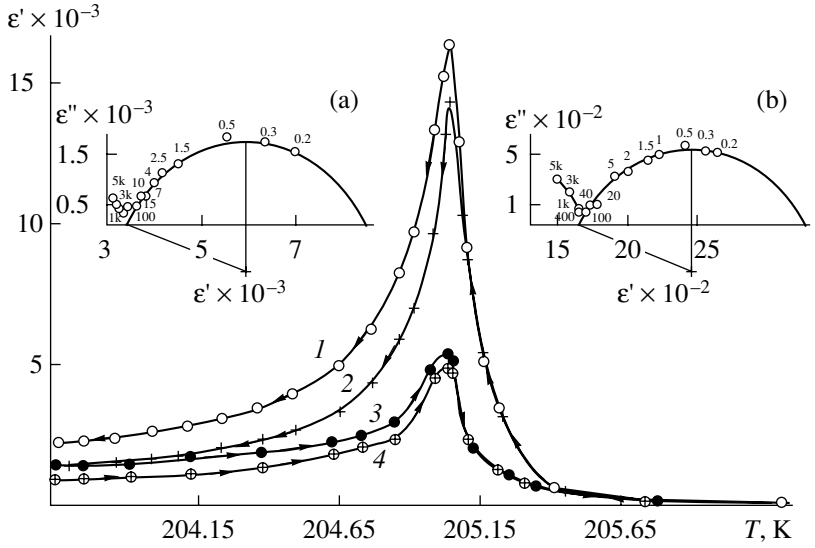

Fig. 1. Variation of the real part ε' of the complex permittivity with temperature for diglycine nitrate specimens having different history: (*1*, *2*) crystal cooling (*3*, *4*) crystal heating. The measurement frequency is (*1*, *3*) 1 Hz and (*2*, *4*) 1 kHz. The insets show the dielectric spectra of the polar phase of diglycine nitrate (204.63 K) measured during (a) cooling and (b) heating; numbers indicate frequencies in hertzs or kilohertzs (k).

1063-7745/00/4505-0811$20.00 © 2000 MAIK "Nauka/Interperiodica"

Main parameters of phase transitions in diglycine nitrate crystals of different history

Parameters	ε'_{max}, 1 kHz	ε'_{max}, 1 Hz	ε''_{max}, 1 kHz	ε''_{max}, 1 Hz	C_p, K paraelectric phase, 1 kHz, 1 Hz	C_f, K ferroelectric phase		T_0, K, from $1/\varepsilon' = f(T)$	U_1 (eV), LF	U_2 (eV), LF
						1 kHz	1 Hz			
Mode:										
cooling	14333	16299	368	2581	231	1900	3125	205.06	0.1–0.3	0.8
heating	4700	5076	159	512	206	1374	2529	205.06	–	0.8–1.1

then slowly heated to room temperature. The specimens were thermostated at each temperature point, at which the complete ε^* spectrum ($\nu = 0.1$–10^4 Hz) was recorded. In contrast to [6], the specimens were not irradiated, the maximum rate of the temperature variation did not exceed 1–2 K/h, and the time of keeping the specimen at each temperature was not shorter than 0.5 h.

Figure 1 shows the variation of the real part ε' of the complex permittivity ε^* recorded during cooling and subsequent heating of a specimen at field frequencies of 1 and 10^3 Hz. In the temperature range corresponding to the polar and partly nonpolar (close to T_C) phases, all the $\varepsilon'(T)$ values obtained during cooling (upon specimen "annealing" at room temperature) are much higher than the corresponding values obtained during heating (upon slow cooling of the specimen to the boiling temperature of nitrogen). The dispersion depth $\Delta\varepsilon = \varepsilon_s - \varepsilon_\infty$ also markedly decreased, as is evident from both the Cole–Cole plots (Figs. 1a, 1b) and the ε' values measured at frequencies of 1 Hz and 1 kHz (Fig. 1, table). Here, ε_s and ε_∞ are the low- and high-frequency limits of the ε^* dispersion.

Comparing Figs. 1a and 1b we see that heating of a preliminarily cooled specimen results not only in a decrease of $\Delta\varepsilon$, but also of ε_∞, ε_s, and ε''_{max}. At the same time, the relaxation frequency of polarization ν_r in the infralow-frequency range of the ε^* dispersion increased. Tabulated data show a certain decrease in the Curie–Weiss constant (C_p) of the paraelectric phase of the specimen upon its cooling and subsequent heating followed by the transition from the polar to the nonpolar phase.

Figure 2 shows the Cole–Cole plots and the dependence of $\tan\delta$ on the logarithm of the frequency of the field applied at 202 K. Two ranges of the ε^* dispersion are determined—the low-frequency (LF) range with the relaxation frequency $\nu_r \sim 150$ Hz and the infralow-frequency (ILF) range with $\nu_{r2} \sim 0.3$ Hz. In some temperature ranges, both ν_r frequencies obey the Arrhenius equation [5] with the most probable activation energies of polarization, whose values depend on the specimen history and lie within the ranges $U_1 \sim 0.1$–0.3 and $U_2 \sim 0.8$–1.1 eV (see table). (Note that the low-frequency range of the ε^* dispersion was first described in [1] and later in [2].) It should be emphasized that our previous studies [7] showed that the reversible dependences of the dispersion depths $\Delta\varepsilon$, relaxation frequencies ν_r, and other parameters of the ε^* dispersion in both above

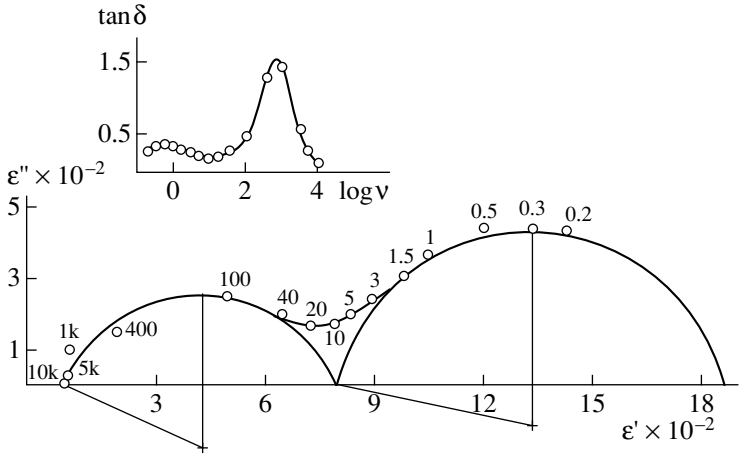

Fig. 2. Dielectric spectrum of the polar phase of diglycine nitrate measured during heating at $T = 201.97$ K. The inset shows the tangent of dielectric losses as a function of frequency measured under the same conditions; numbers indicate frequencies in hertzs or kilohertzs (k).

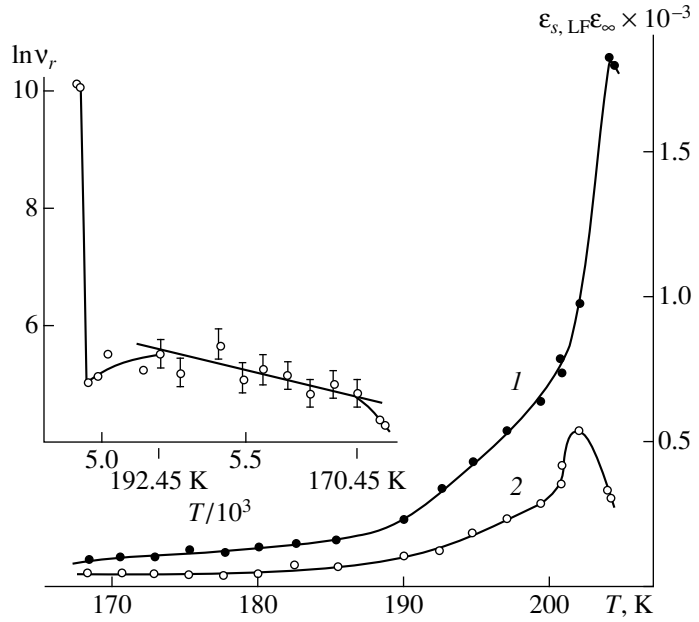

Fig. 3. Temperature dependences of the limits of (*1*) the low-frequency dispersion ε_s and (*2*) high-frequency dispersion ε_∞ of diglycine nitrate measured during cooling. The inset shows the logarithm of the relaxation frequency of polarization as a function of the reciprocal temperature (the Arrhenius dependence) measured during cooling. The activation energy of polarization $U = 0.1$ eV.

ranges were similar to their field evolution and confirmed their domain nature.

Figures 3 and 4 show the temperature dependences of the low- and high-frequency limits (ε_s and ε_∞) of the low- and infralow-frequency ranges, of the ε^* dispersion for different directions of the temperature variations. The inset in Fig. 3 shows the variation in $\ln\nu_{r1}(1/T)$ with $1/T$ and Fig. 4 also shows the $\Delta\varepsilon_1(T)$ curve for the low-frequency range obtained in the heating mode.

The comparison of the $\varepsilon_s(T)$ curves for the low-frequency range and the $\varepsilon_\infty(T)$ curves for the infralow-frequency range in the same temperature range, show their different run (in Fig. 2, ε_sLF = ε_∞ILF corresponds to the contact point of two half-circles at the given T). In general, this result can also be obtained from the analysis of the curves in Fig. 1. It is also worth noting that the $\varepsilon_s(T)$ curve for the low-frequency range of the ε^* dispersion obtained during cooling (Fig. 3) attains a maximum in the vicinity of T_C, whereas the corresponding $\varepsilon_\infty(T)$ curve for the infralow-frequency range obtained during heating asymptotically approaches $\varepsilon_s(T)$ in the infralow-frequency range at T_C (Fig. 4). Note also that, similar to the corresponding curves $\varepsilon_s(T)$ and $\varepsilon_\infty(T)$ recorded during (Fig. 3), the $\Delta\varepsilon_1(T)$ curve in the low-frequency range obtained during heating goes up very slowly at low temperatures (Figs. 3, 4) and attains the maximum in the vicinity of T_C (Fig. 4). Apparently, this indicates that the mechanisms of the low- and infralow-frequency ε^* dispersion have different natures.

A decrease in ε', ε''_{max}, $\Delta\varepsilon$, ε_∞, and ε_s and an increase in ν_{r2} for the infralow-frequency ε^* dispersion upon cooling and subsequent heating of the crystal (Fig. 1) can be explained by a small contribution of the domain walls to ε^* because of their lower domain-wall concentration due to the effect of a field on their "soft" part. This field arises from the pyrroelectric charge that appears under the changes in P_s with temperature [8]. A similar behavior of the above parameters was also observed for the Seignette salt crystals upon their partial polarization and aging [9]. However, we can assume that, in addition to the possible decrease in the domain wall concentration, an essential role in the change ε^* dispersion parameters during deep cooling and subsequent heating of a diglycine nitrate crystal is played by "frozen" point defects and, possibly, also linear defects interacting with domain walls at the points of their equilibrium. This increases their stiffness and, finally, results in the above increase in ν_r and the decrease in ε_∞, ε_s, and $\Delta\varepsilon$ [10].

The considerable effect of the "frozen" ("strong") defects is confirmed by several factors. These are (1) different values of the ε_sLF and ε_∞ILF at the same temperatures for specimens having different history (Figs. 3, 4); (2) a decrease in the ε'_{max} and ε''_{max} values at a point close to T_C in the transition from the polar to

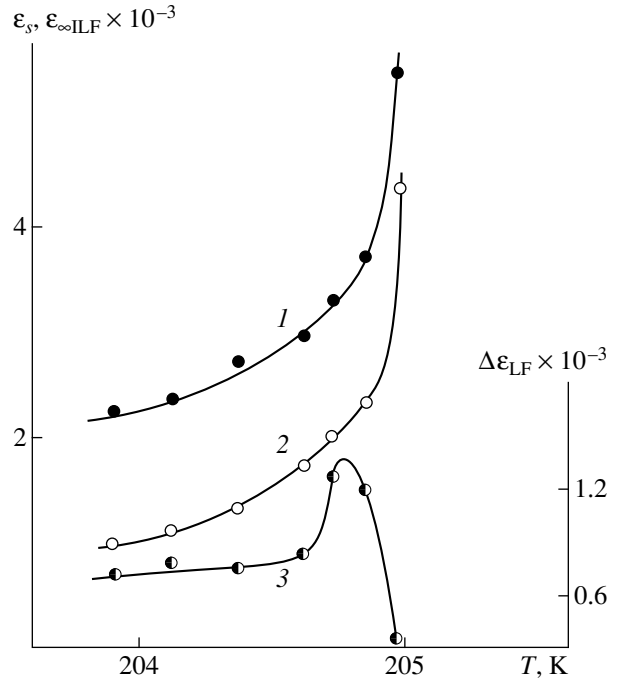

Fig. 4. Temperature dependences of the limits of (*1*) the low-frequency dispersion ε_s and (*2*) high-frequency dispersion ε_∞ of the infralow-frequency range of dispersion and (*3*) low-frequency depth of dispersion $\Delta\varepsilon$ for diglycine nitrate measured during heating.

the nonpolar phase (Fig. 1, table); and (3) a decrease in the Curie–Weiss constant C_p (table) upon this transition. Note that the latter factor was observed, e.g., for γ-irradiated diglycine nitrate [4] and triglycine sulfate crystals [11].

The difference in the activation energies U (table) and the thermal behavior of the parameters of the low- and infralow-frequency ε* dispersions (Figs. 3, 4), and different domain nature of both ranges of ε*-dispersion (the types of reversible dependences of $\Delta\varepsilon$ and ν_r [7]) indicate different "structures" of relaxors providing a certain contribution to ε*. In the case of infralow-frequency dispersion, we deal, in our opinion, with the sideward reversible motion of 180°-domain walls. This conclusion is drawn from the values of ν_{r2}, U_2, and $\Delta\varepsilon_2$ characteristic of such domain-walls contribution to ε* [5, 8–10]. We assume that in the case of low-frequency dispersion, the relaxors are nuclei of new domains formed on the domain-wall and crystal surfaces. This assumption is confirmed not only by the values of U_1 (relatively low at such low temperatures, Fig. 3 and table), ν_{r1}, and $\Delta\varepsilon_1$ (Fig. 2), but also by the type of the thermal behavior of $\Delta\varepsilon_2$ at low frequencies (Fig. 4). Indeed, as is seen from Figs. 3 and 4, the $\Delta\varepsilon_2$ values only slightly change at low frequencies over a wide temperature range. This indicates that the relaxors are "rigid" and that their number is approximately constant [5, 8–10]. The curve $\Delta\varepsilon_2$LF attains the maximum in the vicinity of T_C and then goes to zero at T_C. The curve $\Delta\varepsilon_1$ILF (attributed to the domain-wall oscillations and proportional to their concentration), also goes to zero at this point (Fig. 4).

Similar to [4, 10, 12], a considerable contribution to the Curie–Weiss constant in the polar phase (C_f) comes from the reversible motion of domain walls (table).

CONCLUSIONS

The infralow-frequency range of the ε* dispersion found in a diglycine nitrate crystal is associated with the sideward motion of 180°-domain walls.

The existence of the low-frequency range of the ε* dispersion observed earlier [1, 2] is confirmed. The existence of this range is attributed to thermally-activated nucleation at the domain-wall surfaces and crystal surfaces.

It is shown that the dielectric properties of the polar phase and the parameters of phase transition are essentially dependent on the direction and sequence (cooling from the nonpolar phase or heating from the polar phase) of ε* measurements. The changes in the dielectric properties and the parameters of the phase transition are attributed to the existence of "frozen" defects.

ACKNOWLEDGMENTS

This study is dedicated to the 75th birthday of Professor L. A. Shuvalov.

The main results were reported on the XIV All-Russia Conference on Physics of Ferroelectrics (Ivanovo, September 19–23, 1995).

This work was supported by the Russian Foundation for Basic Research (project no. 98-02-16146) and the Competition Center of the Ministry of Education of the Russian Federation.

REFERENCES

1. V. V. Bondarenko, V. M. Varikash, S. A. Gridnev, and L. A. Shuvalov, Izv. Akad. Nauk SSSR, Ser. Fiz. **47**, 825 (1983).
2. I. P. Igoshin, Author's Abstract of Candidate's Dissertation (Shubnikov Institute of Crystallography, Russian Academy of Sciences, Moscow, 1986).
3. I. P. Igoshin, Fiz. Tverd. Tela (Leningrad) **26**, 985 (1984) [Sov. Phys. Solid State **26**, 602 (1984)].
4. I. P. Igoshin, V. V. Gladkiĭ, and V. A. Kirikov, Fiz. Tverd. Tela (Leningrad) **26**, 3688 (1984) [Sov. Phys. Solid State **26**, 2220 (1984)].
5. A. V. Shil'nikov, Izv. Akad. Nauk SSSR, Ser. Fiz. **51**, 1726 (1987).
6. A. V. Shil'nikov, E. G. Nadolinskaya, V. A. Fedorikhin, and S. V. Rodin, Kristallografiya **39** (1), 84 (1994) [Crystallogr. Rep. **39** (1), 74 (1994)].

7. A. V. Shil'nikov, E. G. Nadolinskaya, V. A. Fedorikhin, and L. A. Fedotova, in *Proceedings of the International Seminar on "Relaxation Phenomena in Solids," 1996* (Voronezh. Politekh. Inst., Voronezh, 1996), Chap. I, p. 176.
8. A. V. Shil'nikov, É. S. Popov, S. V. Gorin, *et al.*, in *Physics of Dielectrics and Semiconductors. Collection of Articles of Higher Schools* (Volgograd. Politekh. Inst., Volgograd, 1981), p. 74.
9. A. V. Shil'nikov, É. S. Popov, S. L. Rapoport, and L. A. Shuvalov, Kristallografiya **15** (6), 1176 (1970) [Sov. Phys. Crystallogr. **15** (6), 1027 (1970)].
10. A. V. Shil'nikov, N. M. Galiyarova, S. V. Gorin, *et al.*, Izv. Akad. Nauk SSSR, Ser. Fiz. **47**, 820 (1983).
11. Cz. Pawlaczyk and G. Luther, Fiz. Dielektr. Radiospektrosk. **8**, 32 (1976).
12. A. V. Shil'nikov, N. M. Galiyarova, E. G. Nadolinskaya, *et al.*, Kristallografiya **31** (2), 326 (1986) [Sov. Phys. Crystallogr. **31** (2), 192 (1986)].

Translated by I. Polyakova

Crystallography Reports, Vol. 45, No. 5, 2000, pp. 816–820. Translated from Kristallografiya, Vol. 45, No. 5, 2000, pp. 888–892.

PHASE TRANSITIONS

Growth, Structure, and Properties of Ferroelectric–Ferroelastic–Superionic $K_3Nb_3B_2O_{12}$ and $K_{3-x}Na_xNb_3B_2O_{12}$ Crystals

V. I. Voronkova*, E. P. Kharitonova*, V. K. Yanovskiĭ*, S. Yu. Stefanovich, A. V. Mosunov**, and N. I. Sorokina**

** Moscow State University, Vorob'evy gory, Moscow, 119899 Russia*

*** Karpov Physicochemical Research Institute, Russian State Scientific Center, ul. Vorontsovo pole 10, Moscow, 103064 Russia*

Received July 22, 1998

Abstract—The potassium niobate-borate $K_3Nb_3B_2O_{12}$ (KNB) crystals and their solid solutions with partial substitution of potassium by sodium (KNB : Na) are grown from flux and their physical properties are studied. The specific feature of the crystals grown is a complicated polymorphism and the unique combination of ferroelectric and ferroelastic properties with superionic conductivity with respect to potassium ions. © *2000 MAIK "Nauka/Interperiodica".*

INTRODUCTION

At present, $K_3Nb_3B_2O_{12}$(KNB) crystals attract ever growing attention as new promising ferroelectrics. However, the data on their structure and properties are still contradictory. The first data on the existence of the $K_3M_3B_2O_{12}$ compound (where M = Nb and Ta) were reported in [1]. It was shown that both compounds have the tunnel-type crystal structure described by the sp. gr. $P31m$. As shown in [2], the $K_3Ta_3B_2O_{12}$ crystals are described by the sp. gr. $P\bar{6}2m$ and show a high piezoelectric activity, whereas the $K_3Nb_3B_2O_{12}$ crystals are low piezoelectrically active. In [3–6] it was reported that KNB crystals demonstrate a complicated polymorphism with several successive ferroelectric and ferroelastic phase transitions in the temperature interval from –60 to 505°C. It is shown that above 505°C, KNB crystals have a hexagonal structure described by the sp. gr. $P\bar{6}2m$. The ferroelectric nature of the phase transitions in KNB crystals follows from the data obtained in our earlier study [7]. We also emphasized an anomalously high value of ionic conductivity of these crystals. In the present paper we performed the detailed analysis of polymorphism and the nature of the electric conductivity of the nominally pure $K_3Nb_3B_2O_{12}$ crystals and the crystals with the partial substitution of K by Na.

EXPERIMENTAL

KNB and $K_{3-x}Na_xNb_3B_2O_{12}$ (KNB : Na) single crystals were grown from the flux the K_2O–Na_2O–NB_2O_5–B_2O_3 system. The best results were obtained for the following compositions of the starting charge: 41 mol % of $K_2O(K_2CO_3)$, 24 mol % of Nb_2O_5, and 35 mol % B_2O_3 for pure KNB; 31 mol % K_2O (K_2CO_3), 10 mol % Na_2O (Na_2CO_3), 24 mol % Nb_2O_5, and 35 mol % B_2O_3 for KNB : Na (composition 1); and 26 mol % $K_2O(K_2CO_3)$, 15 mol % $Na_2O(Na_2CO_3)$, 24 mol % Nb_2O_5 and 35 mol % B_2O_3 for KNB : Na (composition 2). The mixtures of the above components were calcined at 600°C, placed into 50 ml platinum crucibles, heated to 1000°C, and treated for 24 h at this temperature and then were cooled to 900–860°C at a rate of 0.5°C/h. The remaining melt was poured out, and the crystals grown on the crucible walls were cooled down to room temperature in the furnace.

The crystals were studied by X-ray diffraction analysis (CAD-4 and Dron-2.0 diffractometers, MoK_α and CuK_α radiations). The density was measured by the method of hydrostatic weighing. The crystal morphology was examined on a ZRG-3 (optical goniometer). The domain structure was studied in a polarization microscope with a heating table in the temperature range from room temperature to 550°C. The refractive indices were determined by the Chaulnes method. The temperature variations of the intensity of the second harmonic generation under laser irradiation were studied by the method described in [8]. Dielectric constant and electric conductivity were measured on samples with gold and silver electrodes at the frequencies from 100 Hz to 1 MHz in the temperature range from liquid nitrogen to 900°C with the use of P-5083, E7-12, and Tesla BM-431E bridges.

1063-7745/00/4505-0816$20.00 © 2000 MAIK "Nauka/Interperiodica"

RESULTS AND DISCUSSION

Crystals

The grown KNB and KNB : Na crystals are colorless hexagonal prisms about 10 mm in size with the prismatic $\{10\bar{1}0\}$ (the most developed) and $\{11\bar{2}0\}$ faces, and bipyramidal $\{10\bar{1}1\}$ and pinacoidal {0001} faces (in hexagonal setting with the lattice parameters a = 8.76 Å and c = 3.79 Å). All the crystals consist of small twin domains. According to X-ray data, their real atomic structure at room temperature is orthorombic (pseudohexagonal), which is consistent with data [5]. The parameters of an ortorombic unit cell, the densities, and some other characteristics of the crystals are given in table.

The chemical composition of KNB : Na crystals grown from the melts of the two types mentioned above was determined using their unit-cell parameters and densities. Their compositions can be described by the formulas $K_{2.7}Na_{0.3}Nb_3B_2O_{12}$ (the melt of composition 1) and $K_{2.2}Na_{0.8}Nb_3B_2O_{12}$ (the melt of composition 2). In this connection, it should be emphasized that according to the data of an independent study of ceramic samples obtained by the two-stage calcination at 500 and 800°C with the subsequent sample quenching, the existence range of solid solutions in the $K_{3-x}Na_xNb_3B_2O_{12}$ system is limited, and the ultimate rate of substitution potassium by sodium under the above conditions equals x = 0.9. The sodium content in the crystals grown from the melt of composition 2 is close to this limiting level.

Phase Transitions

The temperature dependences of dielectric constants, the electric conductivity measurements, the generation of the second harmonic under the laser irradiation, and the rearrangements of a domain structure (all these aspects will be discussed later) show that the KNB and KNB : Na crystals undergo a number of phase transitions which may be schematically represented in a following way (the transition temperatures during heating of KNB crystals are given on the centigrade scale)

$$\varphi \xrightarrow[-97]{} \phi \xrightarrow[-85]{} \varepsilon \xrightarrow[115]{} \delta \xrightarrow[417]{} \gamma \xrightarrow[477]{} \beta \xrightarrow[510]{} \alpha.$$

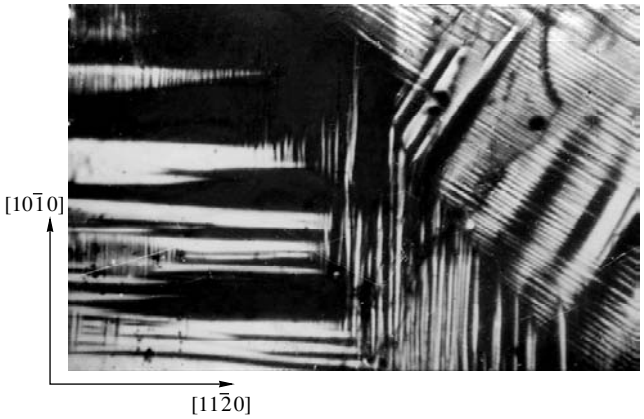

Fig. 1. Domain structure of $K_3Nb_3B_2O_{12}$ crystals at 120°C. Polarized light, magnification ×50.

The error in determination of the temperatures of phase transitions with due regard of the scatter in the values for different samples is ±5 K. We also observed a pronounced hysteresis (40 K) for the $\gamma \rightleftharpoons \beta$ transition and (20 K), for $\delta \rightleftharpoons \gamma$ transition during heating and cooling of the crystals at a rate of 2 K/min. This provides the identification of these transitions with first-order phase transitions. For the remaining transitions, the hysteresis ranged from 1 K ($\varphi \rightleftharpoons \phi$) to 8 K ($\beta \rightleftharpoons \alpha$) and therefore these transitions are close to second order phase transitions.

The temperatures of the $\delta \rightleftharpoons \gamma$, $\gamma \rightleftharpoons \beta$, and $\beta \rightleftharpoons \alpha$ transitions are close to the temperatures determined earlier in [4] by the method of scanning calorimetry, but the data indicated in [4] for other phase transitions (–60, 140, and 142°C) considerably differ from those obtained in the present work.

For KNB : Na crystals, the scheme of the phase transitions is almost the same. The temperature of $\beta \rightleftharpoons \alpha$ transition is also the same or slightly higher, but the

Some data for $K_{3-x}Na_xNb_3B_2O_{12}$ crystals

Crystals	$K_3Nb_3B_2O_{12}$	$K_{2.7}Na_{0.3}Nb_3B_2O_{12}$	$K_{2.2}Na_{0.8}Nb_3B_2O_{12}$
a, Å	17.436	17.422	17.394
b, Å	15.239	15.225	15.213
c, Å	3.973	3.962	3.959
V, Å^3	1055.7	1050.9	1047.6
ρ_{cal}, g/cm^3	3.834	3.821	3.782
ρ_{exp}, g/cm^3	3.80(1)	3.79(3)	3.75(1)
ε_c(20°C)	130	65	46
σ_c(300°C), Ω^{-1} cm^{-1}	1.1×10^{-4}	1.3×10^{-4}	1.1×10^{-4}
n_c	1.96	2.02	2.03

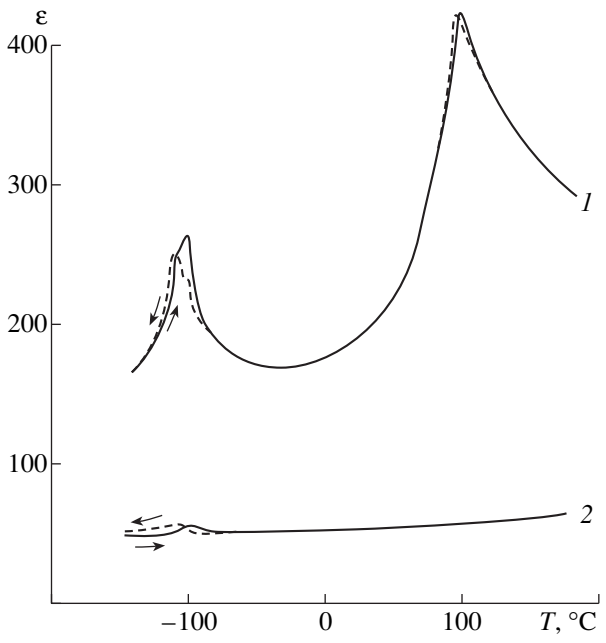

Fig. 2. (*1*) Dielectric constant ε_c and (*2*) ε_b of $K_3Nb_3B_2O_{12}$ crystals in the low temperature range at the frequency of 10 kHz during heating (solid line) and cooling (broken line).

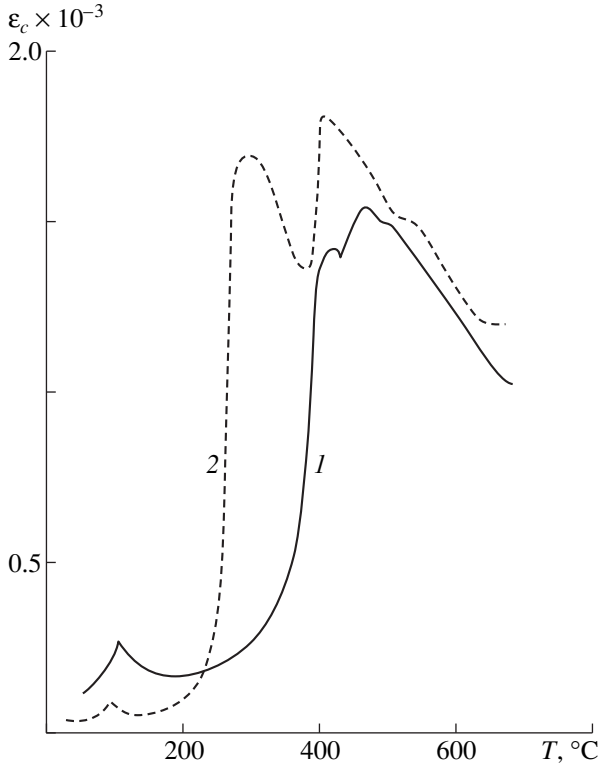

Fig. 3. Dielectric constant ε_c of (*1*) $K_3Nb_3B_2O_{12}$ and (*2*) $K_{2.2}Na_{0.8}Nb_3B_2O_{12}$ crystals at a frequency of 1 MHz in the high-temperature range.

temperatures of other transitions are lower by 20–50 K depending on the sodium content.

Domain Structure

The KNB and KNB : Na crystals at room temperature consist of numerous small domains with the walls parallel to the $\{10\bar{1}0\}$ and $\{11\bar{2}0\}$ pseudohexagonal planes (Fig. 1). This configuration of domain walls remains unchanged during heating, but the pattern contrast gradually deteriorates and finally vanishes in the range of 400–460°C. The $\varepsilon \rightleftharpoons \delta \rightleftharpoons \gamma$ transitions are accompanied by a jump-like reorientation of the optical axes and the changes in the interference color of domains, with their wall positions being unchanged.

It is found that at room temperature, domain walls can easily move under the action of an external mechanical loading. This confirms the ferroelectric nature of domains formed in low-temperature phase transitions. Thus, the stress acting along the $[10\bar{1}0]$-direction completely eliminates the domain wall of the first type, while the walls of the $\{11\bar{2}0\}$-type survive.

Dielectric Constant

The typical results of the measurements of the dielectric constant ε_c and ε_b for one of the KNB crystals in the temperature range from –150 to 200°C are illustrated by Fig. 2. The ε_c values for KNB and $K_{2.2}Na_{0.8}Nb_3B_2O_{12}$ at higher temperatures are shown in Fig. 3. The anomalies of dielectric constant typical of ferroelectric and antiferroelecric transitions are observed. These anomalies are especially pronounced in the $\delta \rightleftharpoons \gamma$, $\gamma \rightleftharpoons \beta$, and $\beta \rightleftharpoons \alpha$ transitions. They were measured in an electric field applied along the *c*-axis. With the field applied normally to the *c*-axis, these anomalies are feebly marked or absent.

Generation of the Second Optical Harmonic

The temperature dependence of the intensity of second optical harmonic generation under the laser irradiation of KNB crystals was studied by a powder technique in the temperature range of 20–750°C, The crystals were preliminarily ground, and the fraction with 3–5 μm-large grains was selected for further measurements. In the whole temperature range studied, the intensity of the second harmonic remained almost constant being equal to 8–9 units of $I_{2\omega}$ of the quartz standard and showed no pronounced anomalies during phase transitions (Fig. 4). The second-harmonic signal for these crystals is almost two orders of magnitude lower than those in the well-known niobate-type ferroelectrics, such as $LiNbO_3$ or $Ba_2NaNb_5O_{15}$. The generation of a second harmonic for the KNB crystals in the high-temperature range is consistent with the noncen-

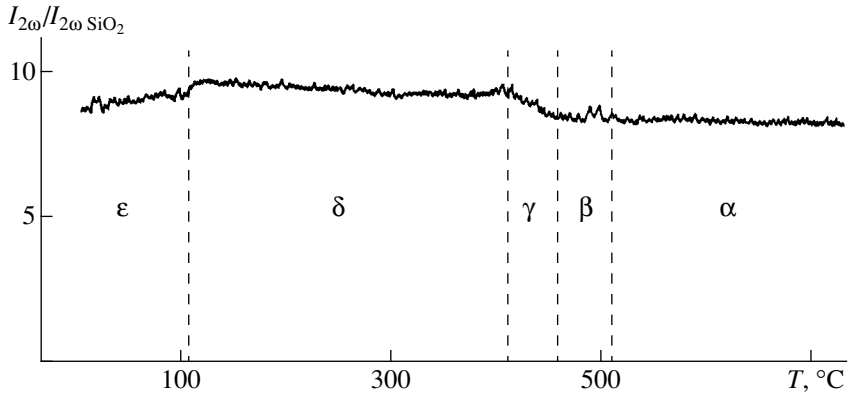

Fig. 4. Temperature dependence of the intensity of the second optical-harmonic generation (in the $I_{2\omega}$ units of the quartz standard) during cooling of ground $K_3Nb_3B_2O_{12}$ crystals. The stability ranges of various phases of this compound are shown.

tosymmetric sp. gr. $P\bar{6}2m$ determined from the X-ray data for the high-temperature phase [6].

Elecrtric Conductivity

The temperature and frequency measurements of the electric conductivity of the KNB and KNB : Na crystals agree with an idea of the ionic origin of conductivity (Fig. 5). Conductivity at a frequency of 1 MHz measured along the *c*-axis for KNB in the stability range of the hexagonal α phase at 600°C is $3 \times 10^{-4}\ \Omega^{-1}\ cm^{-1}$ with the activation energy being 0.59 eV. Conductivity measured normally to the *c*-axis is equal to $7 \times 10^{-4}\ \Omega^{-1}\ cm^{-1}$, with the activation energy being 0.43 eV. These values are close to the conductivity with respect to potassium ions for the best solid electrolytes [9]. With lowering of the temperature to the point of the $\alpha \rightleftharpoons \beta$ transition, the deviation from the Arrhenius

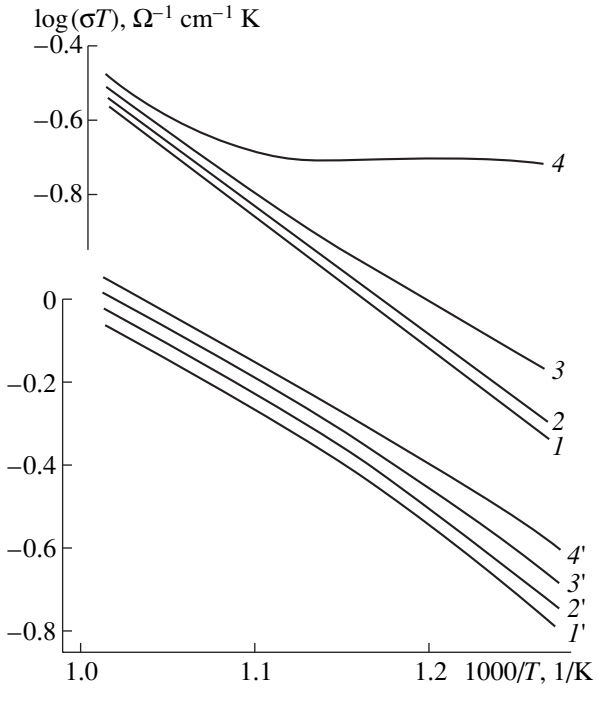

Fig. 5. (Curves *1*–*4*) electric conductivity of $K_3Nb_3B_2O_{12}$ crystals in the stability range of the hexagonal phase at various frequencies along the *c*-axis and (curves *1*'–*4*') normally to this direction. Curves *1*, *1*' correspond to a frequency of 1 kHz; curves *2*, *2*', to 10 kHz; curves *3*, *3*', to 100 kHz; curves *4*, *4*', to 1000 kHz.

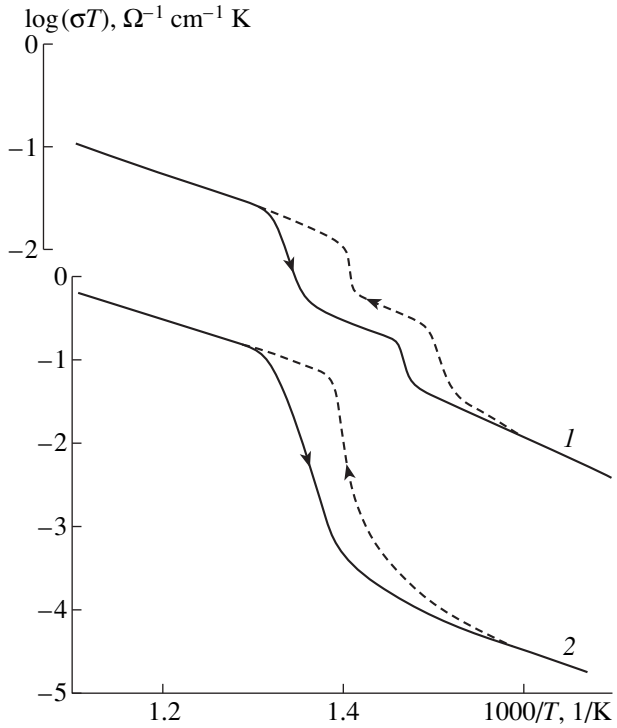

Fig. 6. Temperature dependence of the electric conductivity of the $K_3Nb_3B_2O_{12}$ crystal in the range of the $\alpha \rightleftharpoons \beta$ and $\beta \rightleftharpoons \gamma$ phase transitions measured at a frequency of 10 kHz (*1*) along and (*2*) perpendicular to the pseudohexagonal *c*-axis during heating (solid line) and cooling (broken line).

low becomes more pronounced at a frequency of 1 MHz along the *c*-axis. With an approach to this transition, the relaxation processes make essentially larger contribution to the imaginary part of the dielectric constant. The same samples display the jumps in the electric conductivity (by 1–3 orders of magnitude) in the range of phase transitions $\alpha \rightleftharpoons \beta$, $\beta \rightleftharpoons \gamma$, which is typical of superionics (Fig. 6).

CONCLUSION

The KNB and KNB: Na crystals studied are characterized by complicated polymorphism and show a variety of dramatic features characteristic of active dielectrics. At present, it is impossible to give a complete and unambiguous description of all the experimental data obtained. However, it is possible to assume that the high temperature $\alpha \rightleftharpoons \beta$ and $\beta \rightleftharpoons \gamma$ transitions accompanied by the formation of strong anomalies in the dielectric constant along the *c*-axis are of the antiferro- and ferroelectric origin and give rise to spontaneous polarization along the [0001]-direction. As was mentioned above, the structure of the α phase is a hexagonal and is described by the sp. gr. $P\bar{6}2m$ [3–6]. The absence of pronounced anomalies in the dielectric constant measured along the direction normal to the *c*-axis indicates that the same polarization direction is retained in the low-temperature δ, ε, ϕ, and φ phases. The domain formation in these phases can be observed in the polarized light and is caused by the ferroelastic transitions accompanied by a further lowering of the symmetry. For example, the ε phase stable at room temperature, according to [5, 7], is an orthorombic phase. The spontaneous polarization can be estimated by comparing the data on nonlinear optical susceptibility of these crystals with the corresponding data for the paraelectric phase α [8, 10]. The spontaneous polarization does not exceed 1.5 $\mu C/cm^2$, a typical value of pseudoproper ("weak") ferroelectrics, whose properties are determined by several interacting mechanisms of polar ordering [11]. For KNB crystals, the dipole formation in the subsystem of niobium–oxygen octahedra can be considered as one of such mechanisms, whereas the change of ordering in the potassium sublattice, as another mechanism.

In the low temperature range, two closely located transitions (at –85 and –97°C) are observed, in contrast to [4], where only one transition was found. The shape and the unusual behavior of the anomalies in the dielectric constants observed during the heating–cooling cycles for such transitions lead to an assumption that the ϕ phase, stable in the above temperature range, is an incommensurate phase.

ACKNOWLEDGMENTS

This work was supported by the Russian Foundation for Basic Research, project no. 98-03-32719a.

REFERENCES

1. J. Choisnet, D. Groult, B. Raveau, and M. Gasperin, Acta Crystallogr., Sect. B: Struct. Crystallogr. Cryst. Chem. **33**, 1841 (1977).
2. S. C. Abrahams, L. E. Zyontz, J. L. Bernstein, *et al.*, J. Chem. Phys. **75**, 5456 (1981).
3. P. Becker, J. Schneider, and L. Bohaty, Z. Kristallogr., Suppl. **7**, 14 (1993).
4. P. Becker and L. Bohaty, Z. Kristallogr., Suppl. **9**, 28 (1995).
5. P. Becker, P. Held, and L. Bohaty, Z. Kristallogr. **211**, 449 (1996).
6. P. Becker, L. Bohaty, and J. Schneider, Kristallografiya **42** (2), 250 (1997) [Crystallogr. Rep. **42** (2), 213 (1997)].
7. V. I. Voronkova, V. K. Yanovskiĭ, I. N. Leont'eva, *et al.*, Kristallografiya **41** (5), 879 (1996) [Crystallogr. Rep. **41** (5), 837 (1996)].
8. S. Yu. Stefanovich, in *Proceedings of the 2th International Conference Real Structure and Properties of Acentric Crystals, VNIISIMS, Aleksandrov, 1995*, p. 48.
9. V. B. Kalinin and S. Yu. Stefanovich, Itogi Nauki Tekh., Ser. Khim. Tverd. Tela 3 (1992).
10. S. K. Kurtz and T. T. Perry, J. Appl. Phys. **39**, 3798 (1968).
11. M. E. Lines and A. M. Glass, *Principles and Applications of Ferroelectrics and Related Materials* (Oxford Univ. Press, Oxford, 1977; Mir, Moscow, 1981).

Translated by A. Zalesskiĭ

Crystallography Reports, Vol. 45, No. 5, 2000, pp. 821–826. Translated from Kristallografiya, Vol. 45, No. 5, 2000, pp. 893–898.

REAL CRYSTAL STRUCTURE

Effect of Thermal Annealing Conditions on the Microdefect Formation in Undoped GaAs Single Crystals Grown by Czochralski Method

V. T. Bublik*, M. I. Voronova*, A. V. Markov, and K. D. Shcherbachev***

** Moscow State Institute of Steel and Alloys (Technological University), Leninskiĭ pr. 4, Moscow, 117936 Russia*

*** Institute for Chemical Problems of Microelectronics, B. Tolmachevskiĭ per. 5, Moscow, 109017 Russia*

Received October 26, 1998

Abstract—The effect of thermal annealing conditions on the microdefect formation in undoped GaAs single crystals grown by the Czochralski method has been studied by X-ray diffraction and metallographic analyses. It is found that the standard heat treatments performed with the aim to relieve elastic stresses and to increase the homogeneity of wafers substantially affect microdefects formed in the crystal. Upon annealing, the microdefects in ingots and wafers exhibit different behavior. Prolonged annealing leads to an increase in the sizes of large microdefects but does not suppress the formation of small-sized microdefects. The latter defects are formed at $T < 950$°C upon cooling from the annealing temperature, and their number strongly depends on the density of dislocations, which serve as sinks for intrinsic point defects. *© 2000 MAIK "Nauka/Interperiodica".*

INTRODUCTION

At present, the heat treatment is an obligatory stage of technology for producing single crystals and wafers of undoped semi-insulating gallium arsenide GaAs. As a rule, the grown ingots are annealed at the temperature T_{an} = 850–950°C for 1–10 h followed by a slow cooling (standard annealing). Originally, these annealing conditions were worked out to remove the residual elastic stresses in an ingot with the aim of achieving the mechanical strength required for its cutting into wafers. Subsequently, it was found that the annealing at T_{an} results in a considerably more uniform distribution of the concentration of the main deep centers *EL*2 (deep electron traps, according to the universally accepted classification). As a consequence, the distribution of electrophysical characteristics over the cross-section of the ingot becomes more uniform [1]. However, after the standard annealing, the crystals still possess a substantial microinhomogeneity, which is associated with a nonuniform distribution of intrinsic point defects and can be revealed, for example, by the photoluminescence technique. Usually, the microinhomogeneity observed correlates with the dislocation arrangement. In order to decrease the degree of microinhomogeneity, it was proposed to anneal materials first at T_{an} = 1100–1150°C and, then, at T_{an} = 850–950°C. The second annealing is necessary for the recovery of the *EL*2 centers "destroyed" at temperatures above ~1100°C. The two-stage annealing was employed for the treatment of ingots [2] and wafers [3] of undoped GaAs. Compared to the standard annealing, the two-stage annealing brings about a decrease in the microinhomogeneity. A further optimization of conditions for the heat treatment of semi-insulating GaAs requires detailed information on the structural changes occurring with the point defects and their associates—microdefects. However, an amount of the currently available data concerning this problem is extremely small. In this respect, the purpose of the present work was to study how the heat treatment conditions used in the technology affect the formation of microdefects in the undoped GaAs crystals.

EXPERIMENTAL

The investigations were carried out with 1.2–1.5-mm-thick wafers cut from a bottom part of undoped semi-insulating GaAs ingots 40 mm in diameter. The ingots were grown in the [100] direction from the melt of equiatomic composition by the Czochralski method. We studied the samples of five types with different "thermal history" (table).

The ingots and wafers were annealed in sealed silica tubes in an arsenic vapor atmosphere at a pressure of 10^5 Pa. Prior to heat treatments nos. 3–5, the wafers were ground and chemically polished for the removal of disturbed layer and the cleaning of the surface. The dislocation structure of the samples was inspected using the selective chemical etching with an AB etchant [4]. The wafers were etched prior to and after the annealing. The cross-sectional cleavages of wafers (without any preliminary treatment) and their surfaces after elimination of a layer about 10 μm deep by chemical polishing were etched after the annealing. These wafers were used for X-ray measurements, which were

1063-7745/00/4505-0821$20.00 © 2000 MAIK "Nauka/Interperiodica"

Heat treatment conditions for the studied samples of GaAs

Heat treatment no.	Heat treatment conditions											
	first stage				second stage				third stage			
	sample type	T_{an}, °C	time t, h	cooling conditions	sample type	T_{an}, °C	time t, h	cooling conditions	sample type	T_{an}, °C	time t, h	cooling conditions
1	I	950	5	1	–	–	–	–	–	–	–	–
2	I	950	140	1	–	–	–	–	–	–	–	–
3	I	950	5	1	W	950	5	1	–	–	–	–
4	I	950	5	1	W	1150	5	2	–	–	–	–
5	I	950	5	1	W	1150	5	2	W	950	5	1

Designations: 1—slow cooling (in a furnace at a rate of $v \sim 100$ K/h), 2—rapid cooling (quenching in air), I—ingot, and W—wafer (cut from the corresponding ingot).

performed in regions located along the wafer diameter. The lattice spacings were measured accurate to within 10^{-6} nm (by using the Bond method [5]) in the center of scattering regions, in which the distribution of the diffuse X-ray scattering intensity was explored.

The diffuse X-ray scattering was investigated on a triple-crystal X-ray diffractometer with quasi-nondispersion (n, $-m$, n) arrangement. Perfect Ge single crystals were used as a monochromator and an analyzer, and GaAs served as the samples (Cu$K_{\alpha 1}$ radiation; X-ray tube power, 1.2 kW). In order to obtain the intensity distribution in the neighborhood of the reciprocal lattice point [[400]], we constructed the sections in the directions perpendicular (the $\mathbf{q}_x$ direction) and parallel (the $\mathbf{q}_z$ direction) to the reciprocal lattice vector (sections q_x and q_z, respectively). The theoretical rocking curves for the coherent scattering from a perfect GaAs crystal were calculated along the q_x and q_z sections. These curves were subtracted from the experimental curves for the purpose of separating the incoherent (diffuse) scattering component.

The intensity measured along the q_z section is the integral over the q_y. As a result, the diffuse X-ray scattering intensity recorded varies proportionally to q^{-3} rather than to q^{-4} [6]. Analysis of the q_z sections is described, for example, in [7]. The distribution of the diffuse X-ray scattering intensity J along this direction is most sensitive to the deformation sign. Maxima of the function $Jq^3 = f(q)$ are shifted toward the negative q_z values (angles are less than the Bragg angle) for vacancy microdefects and toward the positive q_z values for "interstitial" microdefects. When the crystal contains the microdefects of both (vacancy and interstitial) types, the maxima of intensity are observed on both sides of the point $\mathbf{q}_z = 0$ [8]. Moreover, the scattering toward the $\mathbf{q}_z$ direction is determined by microdefects with the displacement field of any symmetry, including spherical symmetry, which does not contribute to the scattering toward the $\mathbf{q}_x$ direction [9].

The crystal perfection and the features in the dislocation structure of GaAs under consideration were examined by the single-crystal X-ray topography (CuK_α radiation) with the (531) reflection, which ensures the maximum contrast of the dislocation image for the GaAs(001) crystal surface [10].

RESULTS AND DISCUSSION

Results of Metallographic Investigation

The selective chemical etching patterns of the samples cut from the ingot subjected to the standard annealing (heat treatment no. 1) are typical of the undoped GaAs crystals. The dislocation density has a characteristic W-shaped distribution over the wafer diameter with a mean dislocation density of $(2–4) \times 10^4$ cm^{-2}. The microdistribution of dislocations exhibits a cellular structure with a cell size of 200–600 μm. The etch pits produced by etch removal of As precipitates [11] formed on the dislocations upon postcrystallization cooling of the ingot are located along the dislocation trails.

The annealing of the ingot at T = 950°C for 140 h (heat treatment no. 2) does not lead to considerable changes in the macrodistribution and microdistribution of the dislocations and the morphology of their trails. The same holds true upon selective etching of the surface of the wafer, which, apart from the standard annealing, was subjected to an additional annealing at 950°C (heat treatment no. 3). No changes in the etching pattern in depth are observed upon selective etching of the cross-sectional cleavages of this wafer.

For the wafer quenched from 1150°C (heat treatment no. 4), the macrodistribution and microdistribution of the dislocations do not change in character, but the etch pits that are located along the dislocation trails and correspond to the As precipitates disappear in the etching pattern. This result confirms the data obtained earlier in [2] and, most likely, indicates that the annealing brings about the dissolution of the precipitates, and

the cooling rate upon quenching is high enough to prevent the repeat formation of rather large-sized particles revealed by the etching. No any features in the etching pattern are observed for the cleavage of the quenched wafer.

However, the two-stage annealing (heat treatment no. 5) leads to a sharp increase in the dislocation density, which varies in the range 10^5–10^6 cm^{-2} along the diameter. The microdistribution of the dislocations loses its cellular structure and becomes close to uniform. The absence of clear-cut slip bands suggests that the dislocations are formed in the sample at temperatures above 1100°C. This is also supported by the absence of differences in the morphology of trails of the "growth" and newly formed dislocations. It seems likely that the dislocations are formed at the first instant of quenching. Upon subsequent annealing, the state of point defects changes at a high dislocation density.

The etch pits associated with the As precipitates are observed along the dislocation etch trails; however, their linear density and sizes are substantially less than those in the initial sample. It is evident that the high density of sinks at the second annealing stage prevents the As precipitation. In the cross-section of the wafer, there are the regions adjacent to the surface with a length of about 100 μm, in which the relief of the dislocation etch trails substantially differs from that in the wafer bulk. The presence of these regions demonstrates that the composition of point defects in near-surface regions changes as a result of interaction with a tube atmosphere. Taking into consideration the diffusion character of an increase in the size of the near-surface regions, it can be assumed that they are predominantly formed at the high-temperature stage of annealing, and the changes in the defect composition (which provide a way of revealing these regions) occur at the next stage. Consequently, both for this sample and for the sample after heat treatment no. 4, the results obtained in the metallographic and X-ray diffraction investigations refer to the heat-treated material whose defect composition changed owing to the interaction with the environment.

Results of X-ray Diffraction Investigation

The lattice spacings measured for all the studied samples are larger than that for the GaAs crystal of stoichiometric composition ($a_{\text{stoich}} = 0.565365 \pm 1 \times 10^{-6}$ nm [12]). It is known that the elastic stresses caused by dislocations can produce a different effect on the lattice spacing at different points [13]. However, in the studied samples (wafers and their parts after the cleavage), the lattice spacing is almost constant throughout the cross-section. This gives grounds to believe that the annealings lead to the relaxation of elastic stresses even in the wafers with dislocations induced by quenching stresses (upon heat treatment no. 5), and the lattice spacing depends only on the concentration of intrinsic point defects. An increase in the lattice spacing indicates an excess of interstitial arsenic in all the samples [14], which means that the crystals were grown with a deviation from the stoichiometry toward an As excess. The amount of nonassociated interstitial arsenic resulting in an increase in the lattice spacing can be evaluated from the relationship

$$\frac{\Delta a}{a} = \frac{\Delta r}{r}\frac{N}{N_0}, \quad (1)$$

where $\Delta a/a$ is the relative change in the lattice spacing, $\Delta r/r$ is the difference between the radii of tetragonal pore and interstitial arsenic (determined from the increase in the lattice spacing in GaAs crystals with the excess of arsenic [14]), N is the number of As interstitial atoms per 1 cm^3 (which caused the change in the lattice spacing), and N_0 is the number of atoms per 1 cm^3 in GaAs.

For different crystals, the lattice spacing increases by $(2–7) \times 10^{-6}$ nm. By assuming that the change in the lattice spacing is equal to 5×10^{-6} nm, and $\Delta r/r$ for the As interstitial atoms is 0.3 [14], we obtain $N \approx 2 \times 10^{18}$ cm^{-3}. According to [15], the maximum solubility of excess arsenic in GaAs is equal to $\sim 1 \times 10^{19}$ cm^{-3}. Therefore, the supersaturation observed in the samples is considerably less than the limiting value. The As precipitates, which are revealed by the metallographic analysis along the dislocation lines and dissolve at 1150°C, are formed from thermally nonequilibrium, mobile As interstitial atoms due to a decrease in the equilibrium arsenic concentration upon cooling the crystal. At $T = 950$°C, these precipitates already exist. It is clear that they are unrelated to the precipitation of excess arsenic upon passing through the homogeneity region boundary during the cooling of the crystal.

As follows from the metallographic and X-ray diffraction investigations, the crystals consist of sufficiently perfect fragments separated by two-dimensional dislocation walls. The scattering patterns (averaged over the crystal volume) obtained by the diffuse X-ray scattering technique reflect the structural changes of point defects within the fragments. The narrowest rocking curve is observed for the sample subjected to heat treatment no. 2, even though no metallographically radical distinction in the dislocation density is found for this sample. In the topogram, the image of walls is fogged by large-sized microdefects, which occur throughout the bulk and create an almost uniform background.

Figure 1a displays the distributions of the diffuse X-ray scattering intensity along the q_z section of the crystal after heat treatment no. 1 for regions with different dislocation densities (curves *1–3*). The oscillations in the intensity distribution are observed on both sides of the point $q_z = 0$. This indicates that the scattering regions contain microdefects of the vacancy and interstitial types. Their number and sizes differ in the regions with different dislocation densities.

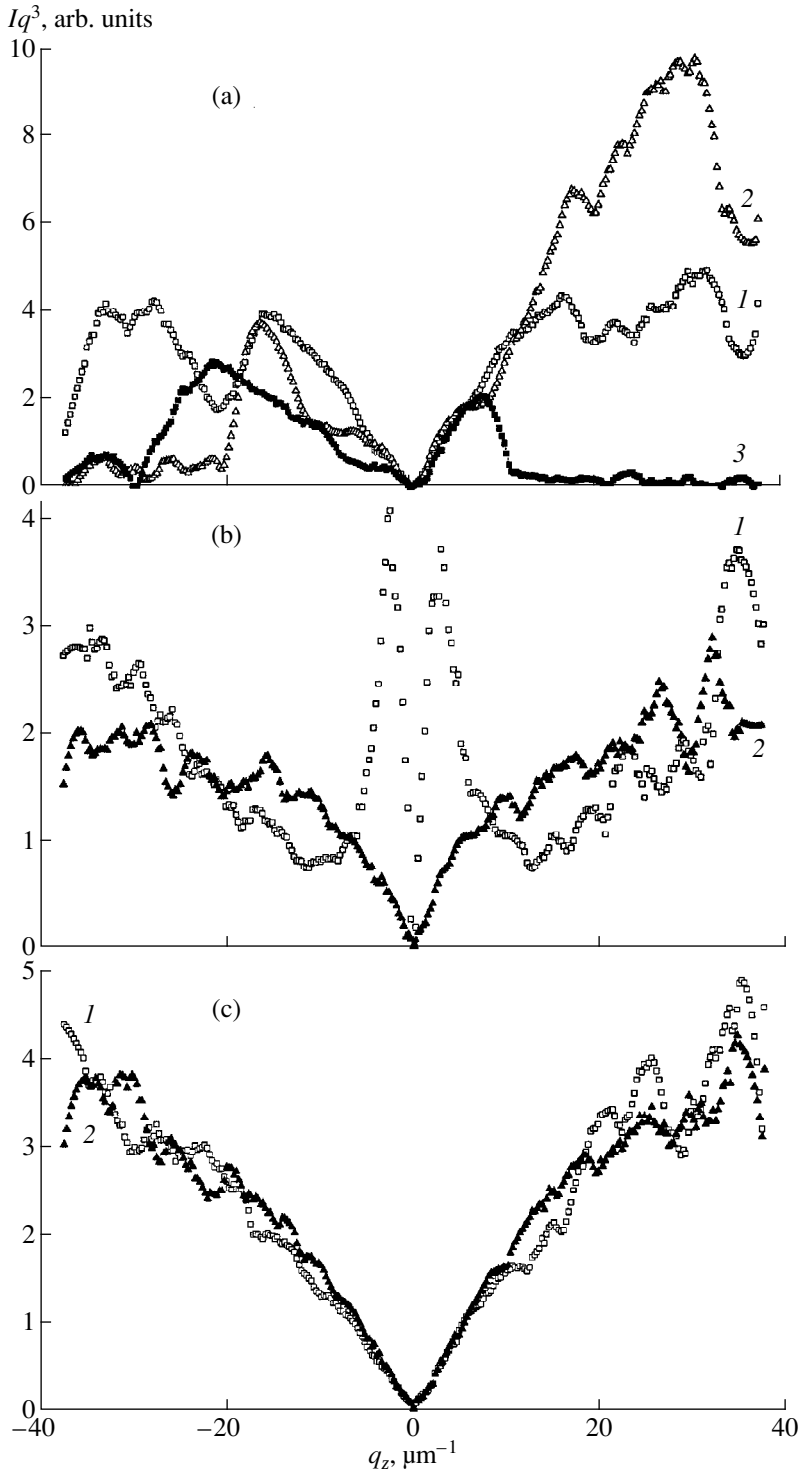

Fig. 1. Distributions of the reduced diffuse X-ray scattering intensity Jq_z^3 along the direction $q_z \parallel [100]$ near the [[400]] point for undoped GaAs after heat treatment (a) no. 1 (an increase in the curve number corresponds to the increase in the distance between the measuring point and the wafer center), (b) (*1*) no. 2, (*2*) no. 3, and (c) (*1*) no. 4, and (*2*) no. 5.

The following characteristic feature is found at $q_z > 0$. The curves describing the scattering from regions with different dislocation densities almost coincide up to the inflection point at $q_z \sim 8$ μm^{-1}. Evidently, the largest fraction of the interstitial microdefects is virtually identical in all the regions irrespective of the dislocation density. This suggests that these microdefects are formed in the crystal upon decomposition of the solu-

tion of thermal intrinsic point defects prior to the generation of a large number of sinks in the form of dislocations.

The dislocation cell structure in the GaAs single crystals grown by Czochralski method is formed in the temperature range $1100°C < T < T_m$ [16]. Since the nonconservative motion of dislocations is determined by the inflow of intrinsic point defects, it is clear that large-sized microdefects are formed at temperatures above the cooling stage when the dislocation density in isolated regions becomes sufficiently high.

As regards the scattering at $q_z > 8\ \mu m^{-1}$, there is a correlation between the dislocation density and the scattering intensity. The scattering intensity and, correspondingly, the microdefect density are higher in the region with the minimum dislocation density (Fig. 1a, curve *2*). By contrast, the scattering intensity at $q_z > 8\ \mu m^{-1}$ is minimum for the region with the maximum dislocation density (Fig. 1a, curve *3*). It is evident that the number of small-sized interstitial microdefects sharply decreases with an increase in the dislocation density. Likely, the small-sized interstitial microdefects are formed at lower temperatures when the dislocation sinks play a considerable role in the transformation of intrinsic point defects upon cooling. This can be explained by the overlapping between the temperature ranges of forming the dislocation walls (fragment boundaries) and the small-sized interstitial microdefects.

It should be noted that there is no simple correlation between the dislocation density and the scattering intensity at $q_z < 0$, i.e., between the dislocation density and the sizes and number of vacancy microdefects. It can be only seen that the function Jq^3 at small $q_z < 0$ increases substantially more slowly than at $q_z > 0$. This suggests a considerably smaller number of large-sized vacancy microdefects.

The experimental data on the diffuse X-ray scattering intensity for the crystals after heat treatments nos. 2 and 3 are compared in Fig. 1b. The prolonged homogenizing annealing (heat treatment no. 2) leads to a considerable change in the distribution of the diffuse X-ray scattering intensity as compared to the preceding case (Fig. 1b, curve *1*). A strong scattering is observed on both sides of the point $q_z = 0$ at $|q_z| < 5\ \mu m^{-1}$. The change in the pattern of diffuse scattering indicates a substantial increase in the sizes of both vacancy and interstitial microdefects. An increase in q_z (at $|q_z| > 10\ \mu m^{-1}$) results in a certain increase in the function Jq^3, which implies that the diffuse X-ray scattering intensity decreases more slowly than q^{-3}. This can be explained by the fact that the scattering is contributed by small-sized microdefects, for which the scattering is not described by the asymptotic dependence when the intensity is proportional to q^{-3}. These small-sized microdefects can be formed upon cooling from a temperature of 950°C. It is clear that the microdefects increase in size at the expense of intrinsic point defects, which form a supersaturated solution upon cooling from the melting temperature down to 950°C. The small-sized microdefects are produced owing to the supersaturation and decomposition of the solid solution formed upon subsequent cooling.

Reasoning from the width of the rocking curves, after heat treatment no. 3, the dislocation density is constant over the entire cross-section of the sample and does not considerably differ from the dislocation density in the samples after heat treatment no. 1. An additional homogenizing annealing of wafers results in a more uniform distribution of microdefects in their number (close diffuse X-ray scattering intensities for different sample regions) and size (a smooth dependence of Jq^{-3} on q for different regions). Curve *2* in Fig. 1b is typical of different sample regions. Judging from the decrease in the diffuse X-ray scattering intensity, the number of microdefects after this heat treatment is less than that after the homogenizing annealing of the ingot. Since the intensity distribution curves exhibit pronounced inflections at $q_z > 0$ and $q_z < 0$ and, then, flatten out, it can be argued that the sample predominantly involves relatively large-sized microdefects. Evidently, at a somewhat larger dislocation density (compared to the preceding cases), an additional annealing of wafers leads to the formation of relatively large-sized (in comparison with heat treatment no. 1) vacancy and interstitial microdefects as a result of interaction with the environment.

In order to evaluate the temperature of the large-sized microdefect formation, we performed the high-temperature annealing followed by quenching (heat treatment no. 4). A decrease in the diffuse X-ray scattering intensity at small q_z (Fig. 1c, curve *1*), specifically at $q_z > 0$, indicates the dissolution of the largest-sized microdefects. As is clearly seen from comparison with the results obtained after heat treatments nos. 1, 2, and 4, a decrease in the diffuse X-ray scattering intensity and the absence of inflections in the curves near the point $q_z = 0$ are associated with the dissolution of large-sized microdefects. Away from the point $q_z = 0$, the diffuse X-ray scattering intensity increases and is comparable to that observed after heat treatment no. 1. This means that the number of small-sized defects of both types changes only slightly. The dissolution of large-sized microdefects can be caused by both a change in the concentration of intrinsic point defects due to the interaction of the surface layer with the tube atmosphere and an increase in the equilibrium concentration of intrinsic point defects, which brings about the dissolution of microdefects formed at $T < 1150°C$.

The largest lattice spacing ($a = 0.565374$ nm) is observed in the sample after heat treatment no. 4. Consequently, the number of As interstitial atoms in this sample is larger by approximately $1 \times 10^{18}\ cm^{-3}$ than that in the sample after heat treatment no. 1. It is evident that the large-sized and, especially, small-sized micro-

defects dissolve upon heating before the quenching. The presence of small-sized microdefects in the sample after the quenching implies that they are formed even upon rapid cooling.

A combination of dissolving and homogenizing annealings (heat treatment no. 5) shows that the additional annealing at 950°C after the quenching does not substantially affects the scattering pattern at small q_z (Fig. 1c, curve *2*). Near $q_z = 0$, the diffuse X-ray scattering intensity is close to that observed for the sample after heat treatment no. 4. Therefore, the number of large-sized microdefects does not increase significantly. This means that the large-sized microdefects in the grown crystal are not formed during the annealing at 950°C. These microdefects are formed at temperatures in the range 950–1150°C upon cooling of the grown crystal under conditions of supersaturation arising between the melting temperature and the temperature of their nucleation when the nuclei are absent. Upon annealing of the quenched crystal, the microdefects are formed under other conditions. First, it is possible that the excess of arsenic owing to its loss upon quenching is less than that upon crystallization. Second, the size of microdefects increases at the expense of dissolving the microdefects formed at temperatures below 950°C, which leads to a decrease in the diffuse X-ray scattering intensity at larger q as compared to the quenched crystal.

The diffuse X-ray scattering intensity across the q_z section is less for the region with the maximum density of dislocations, which are induced upon quenching and, according to the metallographic data, are rather uniformly distributed over the bulk. This structure contains a very small number of intrinsic point defects, and it is clear that prerequisites to the microdefect formation are absent.

CONCLUSION

The standard heat treatments carried out for the relieve elastic stresses and an increase in the homogeneity of wafers have a pronounced effect on microdefects formed in the crystal. Upon annealing, the behavior of microdefects in the ingots and wafers is quite different.

The long-term annealing brings about an increase in the sizes of large microdefects but does not suppress the formation of small-sized microdefects, which precipitate at $T < 950$°C upon cooling from T_{an}. The number of small-sized microdefects substantially depends on the density of dislocations, which serve as sinks for intrinsic point defects.

ACKNOWLEDGMENTS

This work was supported by the Russian Foundation for Basic Research, project no. 99-02-16517.

REFERENCES

1. D. Rumsby, I. Grant, M. R. Brozel, *et al.*, in *Semi-Insulating III–V Materials* (Shiva, Nantwich, 1984), pp. 118–121.
2. D. J. Stirland, in *Proceedings of the International Conference on Science and Technology of Defect Control in Semiconductors, Yokogama, 1989*, pp. 783–794.
3. M. Mori, G. Kano, T. Inone, *et al.*, in *Proceedings of the Sixth Conference on Semi-Insulating III–V Materials, Toronto, 1990*, pp. 315–318.
4. M. S. Abrahams and C. J. Buiocchi, J. Appl. Phys. **36**, 2855 (1965).
5. W. L. Bond, Acta Crystallogr. **13**, 814 (1960).
6. L. A. Charniy, K. D. Scherbachev, and V. T. Bublik, Phys. Status Solidi A **128**, 303 (1991).
7. K. D. Shcherbachev, V. T. Bublik, and O. É. Daricheva, Kristallografiya **40**, 868 (1995) [Crystallogr. Rep. **40**, 803 (1995)].
8. P. Ehrhart and R. S. Averback, Philos. Mag. A **60**, 283 (1989).
9. H. Trinkaus, Phys. Status Solidi B **51**, 307 (1972).
10. S. O'Hara, M. A. G. Halliwell, and J. B. Childs, J. Appl. Crystallogr., No. 5, 401 (1972).
11. A. G. Cullis, P. D. Augustus, and D. J. Stirland, J. Appl. Phys. **51**, 2556 (1980).
12. N. A. Anastas'eva, V. T. Bublik, V. B. Osvenskiĭ, *et al.*, Vysokochist. Veshchestva, No. 5, 62 (1989).
13. S. A. Laptev, V. T. Bublik, V. B. Osvenskiĭ, *et al.*, Kristallografiya **35**, 465 (1990) [Sov. Phys. Crystallogr. **35**, 561 (1990)].
14. V. T. Bublik and M. G. Mil'vidskiĭ, Materialoved., No. 1, 21 (1997).
15. A. N. Morozov, V. T. Bublik, and O. Yu. Morozova, Cryst. Res. Technol. **21**, 859 (1986).
16. S. S. Shifrin, A. V. Markov, M. G. Mil'vidskiĭ, and V. B. Osvenskiĭ, Izv. Akad. Nauk SSSR, Ser. Fiz. **47**, 295 (1983).

Translated by O. Borovik-Romanova

Crystallography Reports, Vol. 45, No. 5, 2000, pp. 827–832. Translated from Kristallografiya, Vol. 45, No. 5, 2000, pp. 899–904.

Coherent and Incoherent Reflection and Transmission of Light in Anisotropic Layer Structures

O. V. Ivanov and D. I. Sementsov

Ul'yanovsk State University, Ul'yanovsk, 432700 Russia

Received August 18, 1998

Abstract—Reflection and transmission of light in anisotropic planar structures consisting of layers coherently and incoherently interacting with light have been considered. The reflection and transmission matrices for multilayered structures are obtained for the general case of an arbitrary incidence angle. The optical characteristics of the structure are studied as functions of its parameters for the particular case of a magneto-gyrotropic film on the substrate. *© 2000 MAIK "Nauka/Interperiodica".*

INTRODUCTION

Today, the structures consisting of arbitrary-type layers characterized by anisotropy of various types are widely used in manufacturing of optical devices. These structures can consist either of thin surface layers of constant thickness not exceeding the coherence length of the light wave (the so-called coherent layers) or layers whose thickness at each point either randomly varies from a certain average value or exceeds the coherence length of the light wave (the so-called incoherent layers). In the former case, the light coherently interacts with the layer with the amplitudes of the multiply reflected waves from the layer interfaces being summed up. In the latter case, the multiply reflected waves are incoherent because of the varying phase difference (in time or in the transition from one point to another therefore, to find the "resultant" field, the wave intensities are summed up.

Today, the methods for analyzing the light propagation in the structures consisting of coherent layers are well developed. The optical properties of such structures are studied both experimentally and theoretically [1–3]. Lately, ever growing interest is given to the optical properties of structures with incoherent layers [4, 5]. Usually, the layer structures consist of both coherent and incoherent layers of both types [6]. In [7], the Mueller matrices are constructed for the structure consisting of thin and thick isotropic layers. The effect of multiple light reflection in a thick incoherent isotropic substrate on the reflection coefficient of a thin coherent layer deposited onto the substrate was studied in [6, 8]. The situation where the structure contains also anisotropic layers [9] is more complicated. An example is a thick quartz plate [10].

Below, we described the determination of the reflection and transmission coefficients of the anisotropic layer structure with the layers, coherently or incoherently interacting with light based on the four-component coherence vector and the transformation matrices [11]. As an example, we consider the determination of the angular dependences of the intensity and polarization characteristics of reflected and transmitted waves for a thin magneto-gyrotropic film applied into a thick nonmagnetic substrate.

COHERENT LAYER STRUCTURE

In order to determine the optical characteristics of a structure consisting of the layers of both types, first consider the layer not disturbing the coherence of the transmitted light. Then, we include this layer as a subsystem into the incoherent structure.

Let a plane monochromatic wave be incident at a certain angle from medium *A* onto the structure consisting of two plane layered subsystems *1* and *2*, separated by anisotropic layer *B* and propagating in medium *C* (Fig. 1). Let us assume that the reflection and the transmission 2×2 matrices be known for each given subsystem: $\hat{\rho}_j'$ and $\hat{\tau}_j'$ ($j = 1, 2$) are the reflection and the transmission (in the forward direction) matrices for subsystems *1* and *2*, $\hat{\rho}_j''$ and $\hat{\tau}_j''$ are similar matrices for the reverse direction; and $\hat{\tau}_B'$ and $\hat{\tau}_B''$ are the transmission matrices for the separating layer *B* in the direct and the reverse directions. Hereafter, the matrices of the dimension 2×2 are marked with the sign "^." The $\hat{\rho}_j$ and $\hat{\tau}_j$ matrices relate the tangential (x and y) components of the transmitted (t) and reflected (r) wave amplitudes with the corresponding amplitudes of the

1063-7745/00/4505-0827$20.00 © 2000 MAIK "Nauka/Interperiodica"

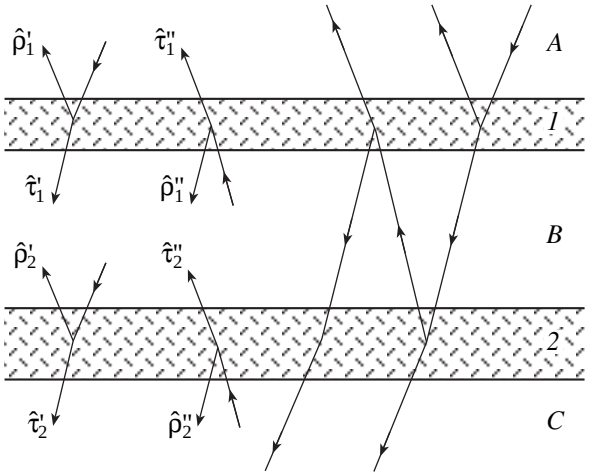

Fig. 1. Wave propagation in a planar layer structure.

incident wave (i) at the interfaces between the layers:

$$\begin{pmatrix} E_x^{(r)} \\ E_y^{(r)} \end{pmatrix} = \begin{pmatrix} \rho_{xx} & \rho_{xy} \\ \rho_{yx} & \rho_{yy} \end{pmatrix} \begin{pmatrix} E_x^{(i)} \\ E_y^{(i)} \end{pmatrix},$$
$$\begin{pmatrix} E_x^{(t)} \\ E_y^{(t)} \end{pmatrix} = \begin{pmatrix} \tau_{xx} & \tau_{xy} \\ \tau_{yx} & \tau_{yy} \end{pmatrix} \begin{pmatrix} E_x^{(i)} \\ E_y^{(i)} \end{pmatrix}. \quad (1)$$

The matrices $\hat{\tau}_B$ take into account the changes in both polarization and the phase of the light wave propagating in the layer.

Now, construct the reflection $\hat{\rho}$ and transmission $\hat{\tau}$ matrices for the system by summing up the amplitudes of all the waves formed due to multiple reflections by subsystems *1* and *2*. The first subsystem divides the incident wave into the reflected wave and the wave transmitted and propagating in a separating anisotropic layer *B*. The transmitted wave is transformed in the layer *B* and can be considered as incident for the second layer subsystem, where, again, it is divided into the wave transmitted in the forward direction and the wave reflected backward into the layer *B*. This process of wave division within the layer is repeated infinitely.

Let $\mathbf{E}_0 = (E_x, E_y)$ be the tangential component of the vector amplitude of the wave incident from the medium *A* onto subsystem *1*. As a result of the superposition of all the reflected and transmitted waves, we obtain the waves whose tangential electric-field components can be represented as:

$$\mathbf{E}^{(r)} = \left[\hat{\rho}_1' + \hat{\tau}_1''\hat{\tau}_B''\hat{\rho}_2' \sum_{m=0}^{\infty} (\hat{\tau}_B'\hat{\rho}_1''\hat{\tau}_B''\hat{\rho}_2')^m \hat{\tau}_B'\hat{\tau}_1'\right]\mathbf{E}_0,$$
$$\mathbf{E}^{(t)} = \left[\hat{\tau}_2' \sum_{m=0}^{\infty} (\hat{\tau}_B'\hat{\rho}_1''\hat{\tau}_B''\hat{\rho}_2')^m \hat{\tau}_B'\hat{\tau}_1'\right]\mathbf{E}_0. \quad (2)$$

Performing summation in (2) with due regard for (1), we obtain 2×2 reflection and transmission matrices for the normal incidence of the wave travelling in the forward direction onto the layer structure:

$$\hat{\rho}' = \hat{\rho}_1' + \hat{\tau}_1''\hat{\tau}_B''\hat{\rho}_2'(\hat{I} - \hat{\tau}_B'\hat{\rho}_1''\hat{\tau}_B''\hat{\rho}_2')^{-1}\hat{\tau}_B'\hat{\tau}_1',$$
$$\hat{\tau}' = \hat{\tau}_2'(\hat{I} - \hat{\tau}_B'\hat{\rho}_1''\hat{\tau}_B''\hat{\rho}_2')^{-1}\hat{\tau}_B'\hat{\tau}_1', \quad (3)$$

where $\hat{I}$ is the unit matrix. Similar calculations for the reflection and the transmission matrices for a wave propagating in the backward direction (the wave is incident from the medium *C* onto subsystem *2*) we obtain

$$\hat{\rho}'' = \hat{\rho}_2'' + \hat{\tau}_2'\hat{\tau}_B'\hat{\rho}_1''(\hat{I} - \hat{\tau}_B''\hat{\rho}_2'\hat{\tau}_B'\hat{\rho}_1'')^{-1}\hat{\tau}_B''\hat{\tau}_2'',$$
$$\hat{\tau}'' = \hat{\tau}_1''(\hat{I} - \hat{\tau}_B''\hat{\rho}_2'\hat{\tau}_B'\hat{\rho}_1'')^{-1}\hat{\tau}_B''\hat{\tau}_2''. \quad (4)$$

Comparing the corresponding matrices for the direct (3) and backward (4) directions of the wave propagation, we see that the matrices $\hat{\rho}''$ and $\hat{\tau}''$ can be obtained from the matrices $\hat{\rho}'$ and $\hat{\tau}'$ by simultaneous change of the indices "′" to "″" by "1" to "2."

Consider an example of the application of the above expressions. Let an isotropic dielectric layer of thickness d_B characterized by the refractive index n_B be adjacent to two isotropic media with refractive indices n_A and n_C. Now, let a linearly polarized plane wave be incident from the first medium *A* onto the layer at an angle θ_A. It is assumed that the layer interacts with the wave coherently. The roles of the first and the second subsystems are played by two planar interfaces of the dielectric. Then the 2×2 reflection and transmission matrices introduced above and related to the interface and the layer *B* are of the diagonal form:

$$\hat{\rho}_j' = -\hat{\rho}_j'' = \begin{pmatrix} r_{jx} & 0 \\ 0 & r_{jy} \end{pmatrix}, \quad \hat{\tau}_j' = \begin{pmatrix} t_{jx} & 0 \\ 0 & t_{jy} \end{pmatrix},$$
$$\hat{\tau}_j'' = \gamma_j \begin{pmatrix} c_j t_{jx} & 0 \\ 0 & c_j^{-1} t_{jy} \end{pmatrix}, \quad \hat{\tau}_B' = \hat{\tau}_B'' = \hat{I}\exp(i\beta), \quad (5)$$

where $j = 1, 2$ is the number of the interface between the layer *B* and the media *A* and *C*, $\beta = k_0 d_B n_B \cos\theta_B$, and k_0 is the wavevector in vacuum. The following notation is used:

$$\gamma_1 = \frac{n_B}{n_A}, \quad \gamma_2 = \frac{n_C}{n_B}, \quad c_1 = \frac{\cos\theta_A}{\cos\theta_B}, \quad c_2 = \frac{\cos\theta_B}{\cos\theta_C}.$$

The diagonal elements of matrices (5) correspond to the *p*- and *s*-polarized waves and are the well-known Fresnel reflection, $r_{j\alpha}$, and transmission, $t_{j\alpha}$, coefficients, where $\alpha = x, y$ [12]. Formulas (3) and the law of

energy conservation law $\rho'_{\alpha\alpha}\rho''_{\alpha\alpha} + \tau'_{\alpha\alpha}\tau''_{\alpha\alpha} = 1$ yield the well-known Airy formulas for the reflection and transmission coefficients of an isotropic dielectric layer:

$$r_\alpha = \frac{r_{1\alpha} + r_{2\alpha}\exp(i\beta)}{1 + r_{1\alpha}r_{2\alpha}\exp(2i\beta)},$$
$$t_\alpha = \frac{t_{1\alpha}t_{2\alpha}\exp(i\beta)}{1 + r_{1\alpha}r_{2\alpha}\exp(2i\beta)}. \quad (6)$$

For a multilayer structure, both reflection and transmission matrices can be obtained by the sequential use of (3) and (4). Determining the corresponding matrices of the ever growing subsystem by the recurrence formulas, one should perform the above procedure beginning from homogeneous layers and finishing with the structure as a whole.

INCOHERENT LAYER STRUCTURE

We have already mentioned that multilayer structures consisting of layers, whose thickness either considerably varies over the sample surface illuminated with a light beam or exceeds the coherence length of the propagating light, are widely used in practice. In such structures, the completely polarized coherent radiation is transformed into partly polarized spatially incoherent radiation. The determination of the parameters of such a radiation requires a special consideration.

Consider reflection and transmission of light in the structure similar to that treated in the previous Section with the only difference—now the separating layer *B* is incoherent. To analyze the field state in the reflected and the transmitted waves, we use the approach suggested in [11]. The field is described in terms of the coherence vector **Y**, whereas its transformation, by the corresponding matrix. The four components of the coherence vector are determined by the products of the corresponding electric-field components averaged over the beam cross section (if the layer has an irregular thickness) or over time (if the layer thickness exceeds the coherence length):

$$\mathbf{Y} = \begin{pmatrix} Y_{xx} \\ Y_{xy} \\ Y_{yx} \\ Y_{yy} \end{pmatrix} = \begin{pmatrix} \langle E_x E_x^* \rangle \\ \langle E_x E_y^* \rangle \\ \langle E_y E_x^* \rangle \\ \langle E_y E_y^* \rangle \end{pmatrix}. \quad (7)$$

The transformation of the coherence vector in reflection or transmission of a light wave in a coherent or incoherent optical system is determined by the 4×4 matrices:

$$\mathbf{Y}^{(r,t)} = M^{(r,t)}\mathbf{Y}^{(i)}. \quad (8)$$

For a coherent optical system, these matrices can be determined from the 2×2 reflection and transmission matrices. Let the elements of the latter be known (in the general case, they are denoted as $a_{\alpha\beta}$, where $\alpha, \beta = x, y$). Then, substituting the components of the transformed field $\mathbf{E}^{(r,t)} = \hat{a}\,\mathbf{E}^{(i)}$ into (8), we arrive at the corresponding transformation matrix for the coherence vector:

$$M(a) = \frac{1}{2}\begin{pmatrix} a_{xx}a_{xx}^* & a_{xx}a_{xy}^* & a_{xy}a_{xx}^* & a_{xy}a_{xy}^* \\ a_{xx}a_{yx}^* & a_{xx}a_{yy}^* & a_{xy}a_{yx}^* & a_{xy}a_{yy}^* \\ a_{yx}a_{xx}^* & a_{yx}a_{xy}^* & a_{yy}a_{xx}^* & a_{yy}a_{xy}^* \\ a_{yx}a_{yx}^* & a_{yx}a_{yy}^* & a_{yy}a_{yx}^* & a_{yy}a_{yy}^* \end{pmatrix}. \quad (9)$$

To construct the matrices of transformation of the coherence vector during wave reflection and its transmission by a the structure consisting of the two subsystems separated by an anisotropic incoherent layer, we have to substitute matrices of reflection and transmission of coherent and completely polarized radiation in (3) the 2×2 by the 4×4 corresponding matrices. As a result, we obtain the reflection and transmission matrices of the system as a whole for the direct direction of the propagation of the incident wave:

$$R' = R'_1 + T''_1 T''_B R'_2 (I - T'_B R''_1 T''_B R'_2)^{-1} T'_B T'_1,$$
$$T' = T'_2 (I - T'_B R''_1 T''_B R'_2)^{-1} T'_B T'_1, \quad (10)$$

where notation is the same as in Sec. 1.

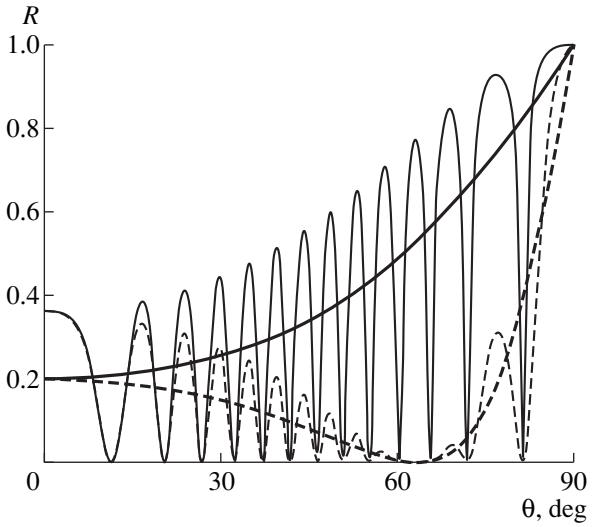

Fig. 2. Intensities of *p*- and *s*-polarized reflected waves (solid and dashed curves, respectively) as functions of the angle of incidence onto incoherent (bold curves) and coherent (of thickness $d_f = 150/k_0$, fine curves) layers with the dielectric constant $\varepsilon_f = 4$.

Using matrices (10), we can determine the optical characteristics of the reflected and the transmitted waves in the case where the *p*- and *s*-polarized waves are incident onto the anisotropic coherent structure enclosed between two isotropic layers. Let M be the matrix describing the transformation of the wave interacting with the structure, i.e., one of the 4×4 R' or T' matrices. By analogy with (7), we can introduce coherence vectors expressed in terms of the E_p and E_s field components:

$$\mathbf{G} = \begin{pmatrix} G_{pp} \\ G_{ps} \\ G_{sp} \\ G_{ss} \end{pmatrix} = \begin{pmatrix} \langle E_p E_p^* \rangle \\ \langle E_p E_s^* \rangle \\ \langle E_s E_p^* \rangle \\ \langle E_s E_s^* \rangle \end{pmatrix} = \begin{pmatrix} Y_{xx}/\cos^2\theta_j \\ Y_{xy}/\cos\theta_j \\ Y_{yx}/\cos\theta_j \\ Y_{yy} \end{pmatrix}, \quad (11)$$

where $j = A, C$ is medium index and the account is made of the fact that $E_x = E_p \cos\theta_j$ and $E_y = E_s$. For the incident *p*- and *s*-polarized waves, $\mathbf{Y}_x^{(0)} = (\cos^2\theta_A, 0, 0, 0)$ and $\mathbf{Y}_y^{(0)} = (0, 0, 0, 1)$, the corresponding vectors $\mathbf{G}$ at the exit $\mathbf{Y}_{x,y} = M\mathbf{Y}_{x,y}^{(0)}$ have the form:

$$\mathbf{G}_p = \cos^2\theta_A \begin{pmatrix} M_{11}/\cos^2\theta_j \\ M_{21}/\cos\theta_j \\ M_{31}/\cos\theta_j \\ M_{41} \end{pmatrix}, \quad \mathbf{G}_s = \begin{pmatrix} M_{14}/\cos^2\theta_j \\ M_{24}/\cos\theta_j \\ M_{34}/\cos\theta_j \\ M_{44} \end{pmatrix}, \quad (12)$$

where for the reflected wave, $j = A$ and for the transmitted one, $j = C$. Upon resolving the field in the reluctant wave with an intensity $G_{pp} + G_{ss}$ into independent polarized and nonpolarized parts, it is possible to represent the degree of polarization as

$$P = \left(1 - 4\frac{G_{pp}G_{ss} - G_{ps}G_{sp}}{(G_{pp} + G_{ss})^2}\right)^{1/2}. \quad (13)$$

The shape and the orientation of the polarization ellipse to the polarized part of the radiation are determined by the ellipticity angle χ and the rotation angle ψ of the polarization [11]:

$$\tan 2\chi = i(G_{sp} - G_{ps})/\sqrt{(G_{pp} - G_{ss})^2 + (G_{ps} + G_{sp})^2}, \quad \tan 2\psi = (G_{ps} + G_{sp})/(G_{pp} - G_{ss}). \quad (14)$$

As an example, consider reflection and transmission of light in dielectric layer similar to that discussed in Sec. 1, but with the only difference that in the isotropic dielectric layer is incoherent. Substituting (5) into (9) and then into (10), we obtain the 4×4 matrices of reflection and transmission in the layer, which, if the layer is isotropic, are diagonal and has the following elements:

$$R = \begin{pmatrix} R_{xx} & 0 & 0 & 0 \\ 0 & R_{xy} & 0 & 0 \\ 0 & 0 & R_{yx} & 0 \\ 0 & 0 & 0 & R_{yy} \end{pmatrix}, \quad T = \begin{pmatrix} T_{xx} & 0 & 0 & 0 \\ 0 & T_{xy} & 0 & 0 \\ 0 & 0 & T_{yx} & 0 \\ 0 & 0 & 0 & T_{yy} \end{pmatrix},$$

$$R_{\alpha\beta} = \frac{r_{1\alpha} + r_{1\beta} + (1 - r_{1\alpha}^2 - r_{1\beta}^2) r_{2\alpha} r_{2\beta}}{1 - r_{1\alpha} r_{1\beta} r_{2\alpha} r_{2\beta}}, \quad (15)$$

$$T_{\alpha\beta} = \frac{t_{1\alpha} t_{1\beta} t_{2\alpha} t_{2\beta}}{1 - r_{1\alpha} r_{1\beta} r_{2\alpha} r_{2\beta}},$$

where $\alpha, \beta = x, y$. The diagonal elements R_{xx}, R_{yy}, and T_{xx}, T_{yy} describe the reflectance and the transmittance for the *p*- and *s*-polarized waves, respectively.

Figure 2 shows the angular dependences of the intensities of the *p*- and *s*-polarized waves reflected from coherent ($k_0 d = 150$, dashed lines) and incoherent (solid lines) dielectric layers in vacuum ($\varepsilon_B = 4$, $\varepsilon_1 = \varepsilon_2 = 1$). It is seen that the curves for the incoherent layer are, in fact, a certain averaged curve for the fast-oscillating curves of the coherent layer. The point is that a small change in the incidence angle for a thick layer leads to substantial, variations of the path of a beam in the layer comparable to the wavelength and, in the coherent case, to pronounced oscillations of the reflection coefficient. In the incoherent case, there is no phase correlation for the waves reflected from different surfaces and, thus, no wave interference can occur. Thus, the wave intensities are summed up and slightly depend on the incidence angle.

MAGNETO-GYROTROPIC FILM ON SUBSTRATE

To illustrate the use of the above formalism, consider the widespread layer structure consisting of a thin anisotropic film on the thick isotropic dielectric substrate. Let the film be a magneto-gyrotropic layer whose magnetization vector is perpendicular to the interfaces. We assume the diagonal components ε_f of the film of the thickness d_f be equal to that of the substrate ε_s of the thickness d_s and that the reflection from the fil–substrate interface be negligible. The rotation of the polarization plane during the light propagation in the film is given by the angle $\varphi = \varphi_f d_f$, where φ_f is the specific Faraday rotation. Neglecting the interface magneto-gyrotropic phenomena at the interface (which

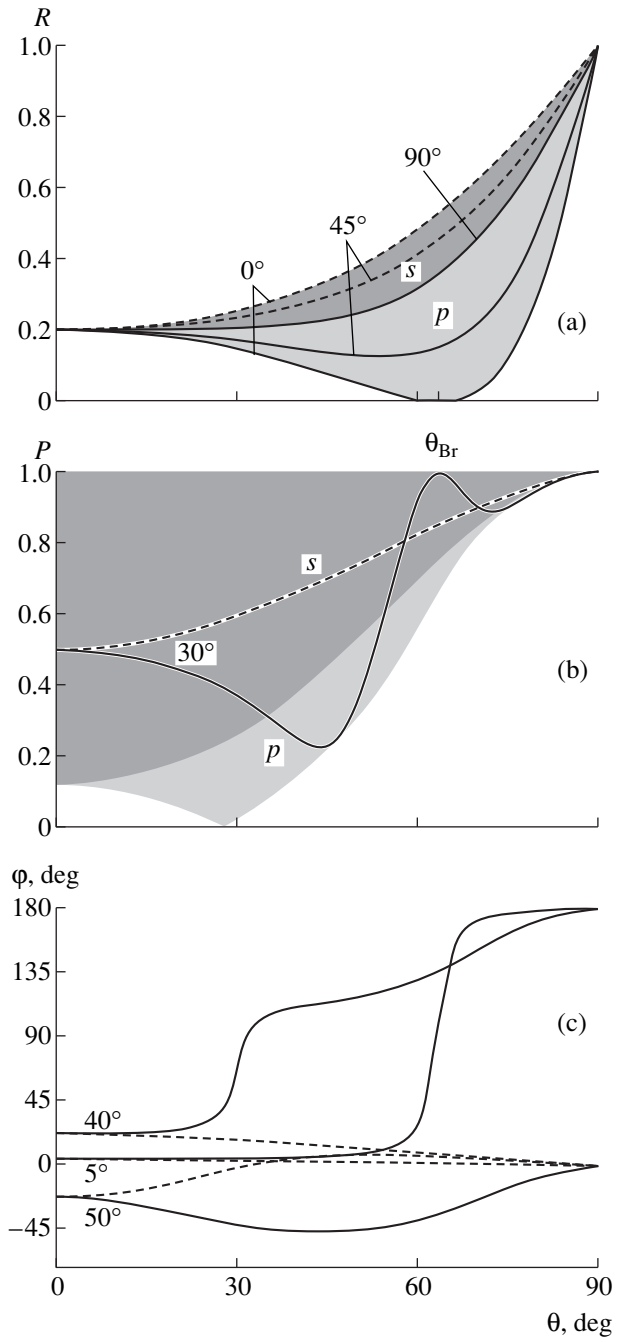

Fig. 3. (a) Intensity R, (b) degree of polarization P, and (c) the rotation angle of the polarization plane, φ, of the wave reflected from magneto-gyrotropic structure as functions of the angle of incidence of the *p*- and *s*-polarized waves (solid and dashed curves, respectively) at several values of the parameter φ.

are of the order of φ_f/k_0), we obtain that the reflection and transmission matrices at the film–substrate and film–air interfaces ($\hat{\rho}_i'$, $\hat{\rho}_i''$, $\hat{\tau}_i'$, $\hat{\tau}_i''$, and $i = 1, 2$) are specified by (5), whereas the transmission matrices of the combined structure consisting of a gyrotropic layer and the substrate have the form:

$$\hat{\tau}_f' = \hat{\tau}_f'' = \begin{pmatrix} \cos\varphi & \sin\varphi\cos\theta_f \\ -\sin\varphi/\cos\theta_f & \cos\varphi \end{pmatrix} \exp(i\beta), \quad (16)$$

where $\beta = k_0(d_s + d_f)\sqrt{\varepsilon_f}\cos\theta_f$. Substituting (5) and (16) into (9) and then into (10), we obtain the reflection and the transmission matrices that transform the coherence vectors of the incident wave.

Using the matrices obtained, we can numerically analyze the structure characteristics. Let the diagonal elements of dielectric-constant tensor of a magneto-gyrotropic film and the nonmagnetic substrate be $\varepsilon_f = \varepsilon_s = 4$. This corresponds to the parameters of the epitaxial garnet-ferrite films grown on substrates gadolinium–gallium garnet (GGG) substrate.

The analysis shows all the optical characteristics of the transmitted and the reflected waves are periodic with the period π of the Faraday rotation angle φ. The intensity and the degree of polarization are the even functions of the angle φ, while the polarization rotation is its odd function. The ellipticity angles of both reflected and transmitted waves equal zero.

Figure 3 shows the dependences of (Fig. 3a) the reflected-wave intensity R, (Fig. 3b) its polarization degree P, and (Fig. 3c) the angle φ of rotation of the polarization plane on the incidence angle θ for the *p*- and *s*-polarized waves (solid and dotted curves, respectively) at different values of the angle φ of Faraday rotation. For arbitrary φ values, the curves lie within the shaded regions for the *p*- and *s*-polarized waves. It is seen that for the reflected waves at $\varphi = 90°$, $R_p = R_s$ and $P = 1$ and $\varphi = 0°$. If a wave is incident at the Brewster angle ($\theta = \theta_{Br}$), then $P = 1$. For the curves $\varphi(\theta)$, corresponding to $\varphi \simeq 0°$, the angle φ exhibits a 180° jump. There exist such θ and φ ($\theta = 41.2°$ and $\varphi = 28°$) values, that $P = 0$, and $\varphi(\theta)$ undergoes a jump by 90°.

The intensity of the transmitted wave can be found from the law of energy conservation, $T = 1 - R$. The analysis shows that the degree of transmitted-wave polarization is not lower than 0.9.

The above consideration showed an essential difference between propagation of light in the coherent and incoherent anisotropic structures. Thus, considering various optic problems in layer media, one has necessarily take into account incoherent transmission and reflection.

REFERENCES

1. P. Yeh, *Optical Waves in Layered Media* (Wiley, New York, 1988).
2. V. M. Maevskiĭ, Fiz. Met. Metalloved. **59**, 213 (1985).

3. V. A. Shamburov and E. A. Evdishchenko, Kristallografiya **36** (4), 847 (1991) [Sov. Phys. Crystallogr. **36** (4), 473 (1991)].
4. A. V. Belinskiĭ, Usp. Fiz. Nauk **165**, 691 (1995) [Phys. Usp. **38**, 653 (1995)].
5. E. N. Grossman and D. G. McDonald, Opt. Eng. **34**, 1289 (1995).
6. C. L. Mitsas and D. J. Siapkas, Appl. Opt. **34**, 1678 (1995).
7. I. M. Minkov, Opt. Spektrosk. **66**, 231 (1989) [Opt. Spectrosc. **66**, 134 (1989)].
8. P. V. Adamson, Opt. Spektrosk. **80**, 512 (1996) [Opt. Spectrosc. **80**, 459 (1996)].
9. V. D. Tron'ko and T. E. Dovgalenko, Opt. Spektrosk. **34**, 1157 (1973).
10. S. V. Rykhlitskiĭ, K. K. Svitashev, V. K. Sokolov, and T. Kh. Khasanov, Opt. Spektrosk. **63**, 1092 (1987) [Opt. Spectrosc. **63**, 643 (1987)].
11. E. L. O'Neil, *Introduction to Statistical Optics* (Addison-Wesley, Reading, Mass., 1963; Mir, Moscow, 1968).
12. M. Born and E. Wolf, *Principles of Optics*, 4th ed. (Pergamon Press, Oxford, 1969; Nauka, Moscow, 1973).

Translated by A. Zolot'ko

Crystallography Reports, Vol. 45, No. 5, 2000, pp. 833–838. Translated from Kristallografiya, Vol. 45, No. 5, 2000, pp. 905–910.

Absolute Piezo-Optic Constants of Rochelle Salt Crystals

V. I. Stadnik

Lviv National University, Lviv, Ukraine

Received January 22, 1997; in final form, December 14, 1999

Abstract—The effect of uniaxial mechanical pressures applied along the main crystallophysical axes and the corresponding bisector directions on the birefringence of Rochelle salt crystals has been studied. The temperature (77–300 K) and spectral (300–700 nm) curves of the combined, π_{im}^0, and absolute, π_{im}, piezo-optic constants of crystals are calculated. It is found that the disperse π_{im} curves are intersected in the vicinity of the inversion of the birefringence sign, which indicates a higher symmetry of the piezo-optic constant tensor. The temperature dependences of the absolute piezo-optic constants show no clearly pronounced anomalies in the vicinity of the phase transitions in the Rochelle salt crystals. © *2000 MAIK "Nauka/Interperiodica".*

Elastooptic properties of Rochelle salt have been repeatedly studied. Pockels was the first to study the photoelastic properties of Rochelle salt [1], but he determined only the order of magnitude of three (π_{44}, π_{55}, and π_{66}) of the total twelve piezo-optic constants. Narasimhamurty determined the full matrix of absolute piezo-optic constants (orthorhombic system) at T = 27°C for the yellow sodium line by the method of localized interference fringes [2].

The temperature variations of the combined piezo-optic constants determined by the method of halfwave stresses of Rochelle salt crystals were studied in detail in [3, 4]. No clearly pronounced anomalies in the π_{im}^0 curves were observed either at the points of the upper (T_{C1} = 24.5°C) or the lower (T_{C2} = –18°C) phase transitions. At the lower Curie point, only an insignificant kink in the temperature dependence of the piezoelectric constants was observed, whereas the jump in the π_{im}^0 at the upper Curie point was insignificant and was comparable with the experimental accuracy.

Other π_{im}^0 coefficients measured by the Senarmont or the photographic method showed no temperature anomalies at all.

It was established that the π_{im}^0 coefficients of Rochelle salt crystals are mainly determined by the true piezo-optic contribution and show no clearly pronounced jumplike anomalies. Thus, one can state the high acoustooptic quality of Rochelle salt crystals is preserved over the wide temperature range including the critical phase-transition points.

The combined piezoelectric constants were measured mainly at the wavelength of λ = 633 nm; the corresponding temperature dependences were obtained only for several constants (in the range 320–200 K). Moreover, there are no data on the spectral and temperature dependences of the absolute piezo-optic constants.

The present study is aimed to investigate the effect of uniaxial mechanical stresses applied along the main crystallophysical *X*, *Y*, and *Z* axes and the corresponding bisector directions on the temperature and the spectral dependences of birefringence and determine the temperature (77–300 K) and spectral (300–700 nm) dependences of the absolute piezo-optic constants of Rochelle salt crystals.

The effect of uniaxial pressure on the temperature and spectral variations in birefringence was established from the changes of the interference patterns recorded on a DFS-8 spectrograph providing the spatial resolution of the extrema of various orders. Since the refractive index n_i and the thickness d are temperature dependent, the change in the temperature results in the displacement of the interference extrema and the birefringence Δn_i is determined by the expression

$$\Delta n_i(\lambda, T) = k(T)\lambda/d(T). \quad (1)$$

The compression of the specimen at a fixed temperature results in the shift of the interference fringes in the focal plane of the spectrograph. The temperature variations of birefringence under the fixed pressure (or the baric variations Δn_i at the constant temperature) are determined by the expressions

$$\begin{aligned} \Delta n_i(\lambda, T)|_G &= k(T)\lambda/d_i(T, G), \\ \Delta n_i(\lambda, G)|_T &= k(G)\lambda/d_i(T, G). \end{aligned} \quad (2)$$

In the present studies, such measurements were performed up to pressures of $G \sim 200$ bar.

Figure 1 shows the baric dependences of birefringence Δn_i of Rochelle salt crystals at λ = 500 nm and room temperature. The uniaxial pressures G_m ($m = X, Y$, and Z) in Δn_z result in the variations in Δn_i, which are of different nature and have different values. Thus, under

1063-7745/00/4505-0833$20.00 © 2000 MAIK "Nauka/Interperiodica"

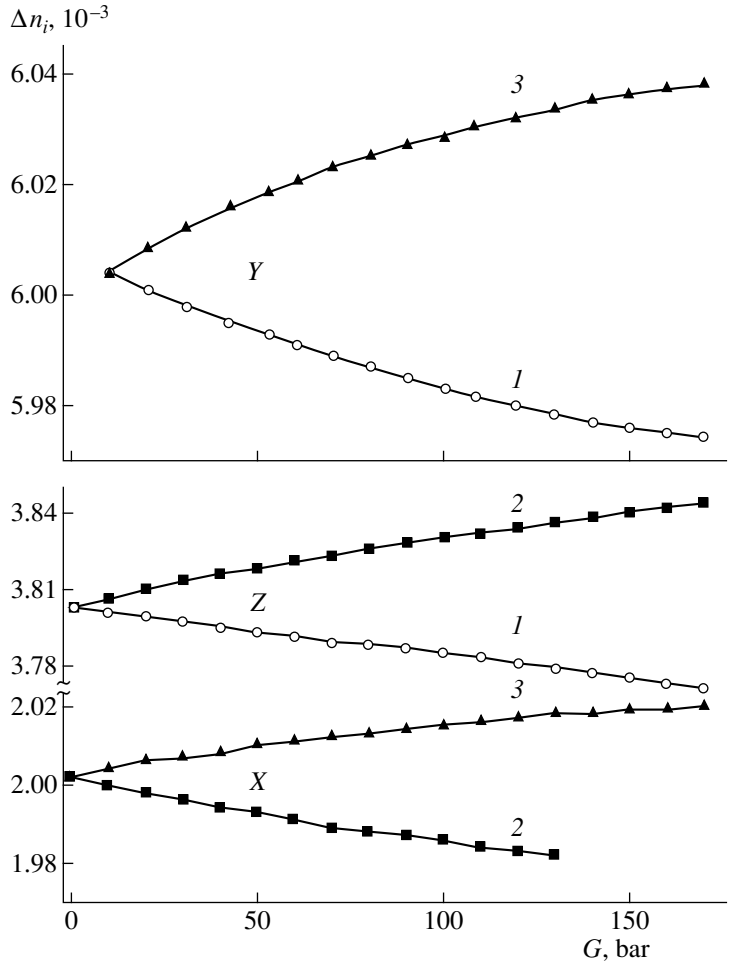

Fig. 1. Baric dependences of birefringence Δn_i of Rochelle salt crystals at λ = 500 nm and T = 298 K. Pressures: (*1*) G_X, (*2*) G_Y, and (*3*) G_Z.

a pressure of G_Y = 150 bar, birefringence Δn_i increases by a value of 4.1×10^{-5} and under a pressure of G_X = 150 bar, it decreases by 3.9×10^{-5}. It was established that with a decrease of the wavelength, the baric sensitivity of Δn_i increases.

As is well known, the birefringence changes its sign along the *X* axis (the bisector direction in the acute angle formed by the optical axes) of a Rochelle salt crystal. It was established that the temperature–spectral diagram of the inversion of the birefringence sign covers the temperature range 4.2–330 K and the spectrum range 455–280 nm [5]. The uniaxial pressures G_Y and G_Z produce a similar effect on the birefringence value: at G_z = 150 bar, $\delta\Delta n_x = 2.2 \times 10^{-5}$ and at G_Y = 150 bar, $\delta\Delta n_x = -2.9 \times 10^{-5}$. In an unstressed Rochelle salt crystal at room temperature, the inversion of the birefringence sign (Δn_x = 0) can take place only at the wavelength of λ = 285 nm. The pressure applied along G_Z shifts the point of the sign inversion to the short-wavelength range (Δn_x = 0 at λ = 270 nm) and the pressure applied along G_Y, to the long wavelength (Δn_x = 0 at λ = 308 nm). In the spectral range of sign inversion a considerable increase of the baric sensitivity of Δn_x was revealed, which would be considered in more detail below: at G_Z = 150 bar, $\delta\Delta n_x = 6.9 \times 10^{-5}$ and at G_Y = 150 bar, $\delta\Delta n_x = -6.5 \times 10^{-5}$ at λ = 300 nm and T = 294 K.

The difference in combined piezo-optic constants was calculated by the formula

$$\pi^0_{im} = 2G\Delta n_i/G_m - 2\Delta n_i s_{im}, \qquad (3)$$

where $\delta\Delta n_i$ is the variation in birefringence induced by the light propagating along the *i*-axis, G_m is the mechanical pressure applied along the *m*-axis, *i* and *m* are the crystallophysical axes, and s_{im} are the elastic-compliance coefficients. The second term in formula (3) describes the contribution provided by the pressure-induced changes in the specimen dimensions along the direction of light propagation. In our calculations, we used the s_{im} values from [6]. It should be remembered that π_{im} and s_{im} are the fourth-rank tensors, so that the *i* and *m* subscripts take the values 11, 22, 33, 23, 32, 13, 31, 21, and 12.

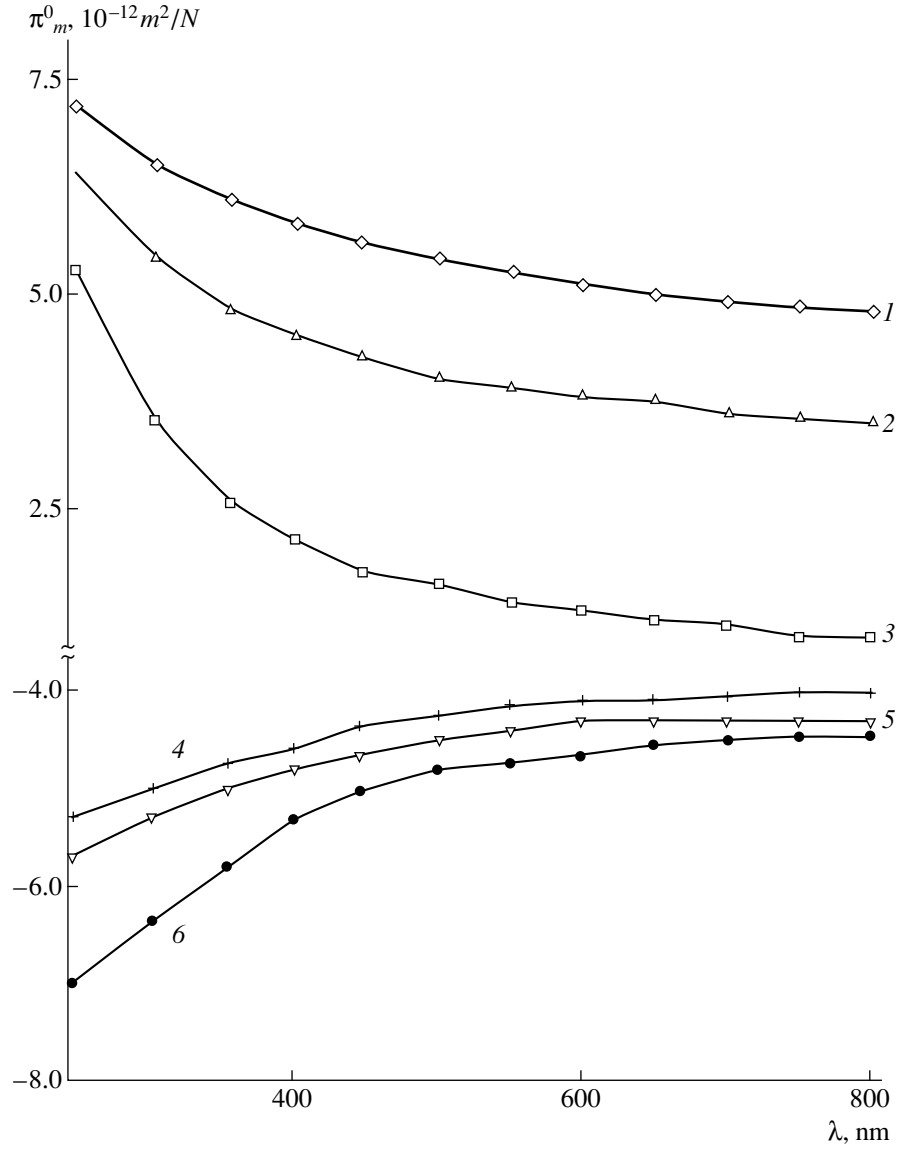

Fig. 2. Dispersion of combined piezo-optic constants of Rochelle salt crystals at T = 298 K: (*1*) π^0_{32}; (*2*) π^0_{23}; (*3*) π^0_{13}; (*4*) π^0_{21}; (*5*) π^0_{31}; and (*6*) π^0_{12}.

The dispersion dependences of π^0_{im} at room temperature are shown in Fig. 2. The sign of π^0_{im} is taken to be positive if birefringence Δn_i increases under the effect of the pressure G_m. As is seen from Fig. 2, the coefficients π^0_{32}, π^0_{23}, and π^0_{13} are positive, whereas the coefficients π^0_{12}, π^0_{31}, and π^0_{21} are negative. With a decrease of the wavelength, the absolute values of π^0_{im} also vary; in other words, there is a clearly pronounced dispersion of piezo-optic constants. This dispersion seems to be caused by the fact that, in the vicinity of the fundamental absorption edge (for the Rochelle salt crystals at room temperature it is located at λ = 247 nm), the absorption edge shifts under the effect of uniaxial pressure, thus giving rise to considerable dispersion in π^0_{im}.

The dispersion is especially pronounced for the piezo-optic constants π^0_{13} and π^0_{12}: $d\pi^0_{13}/d\lambda = -3.3 \times 10^{-2}$ B nm^{-1} and $d\pi^0_{12}/d\lambda = 1.5 \times 10^{-2}$ B nm^{-1}. The piezo-optic constants π^0_{12} and π^0_{13} correspond to the change in birefringence Δn_x under the effect of uniaxial pressures G_Y and G_Z. Since, the sign inversion of birefringence is observed in Rochelle salt crystals along the X-direction, a considerable increase in π^0_{12} and π^0_{13} in this spectral range can indicate a considerable increase of sensitivity of the sign inversion to uniaxial pressures.

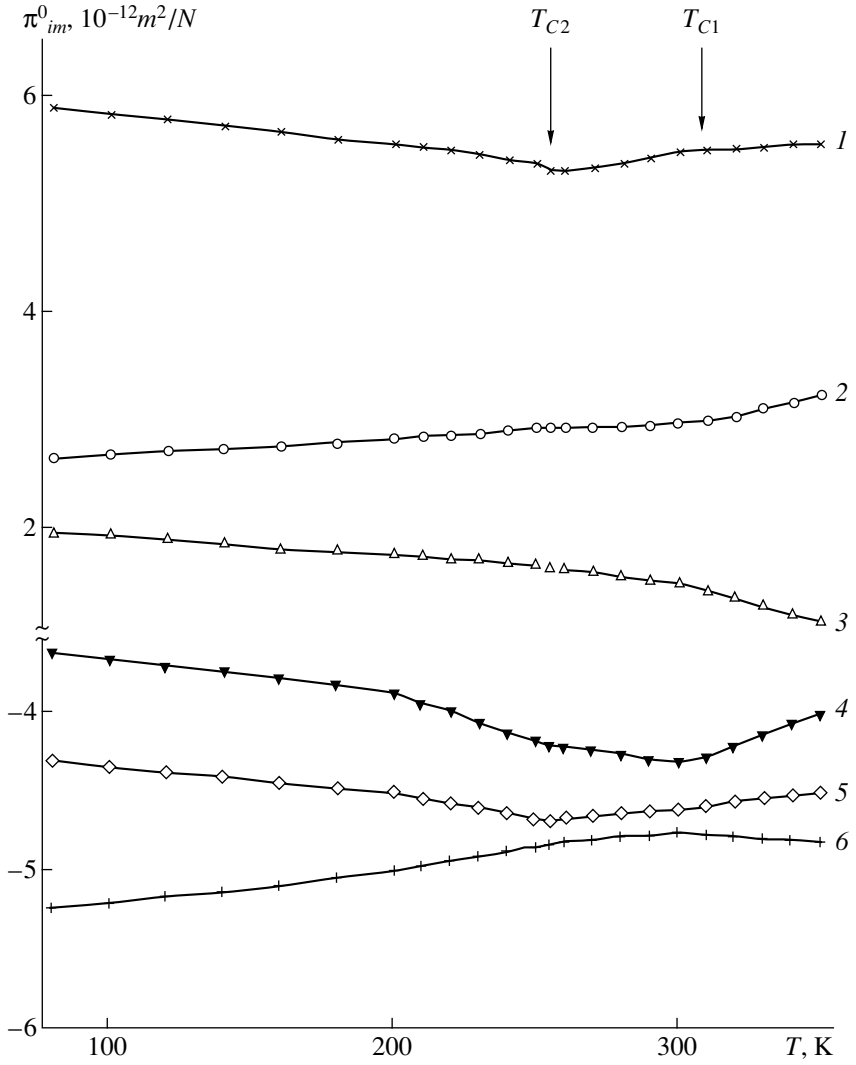

Fig. 3. Temperature dependence of combined piezo-optic constants for Rochelle salt crystals at λ = 500 nm: (*1*) π^0_{32}; (*2*) π^0_{23}; (*3*) π^0_{13}; (*4*) π^0_{21}; (*5*) π^0_{31}; and (*6*) π^0_{12}.

The temperature dependences of the π^0_{im} coefficients in Rochelle salt crystals are shown in Fig. 3. All the constants measured in the range of the phase transition show some slight anomalies (the changes in the curve slopes). The sign inversion is observed only for π^0_{32} at 255 K: the derivatives are $d\pi^0_{31}/dT = 0.005$ B K^{-1} at 280 K and $d\pi^0_{31}/dT = -0.003$ B K^{-1} at 200 K.

Since in the paraphase ($T < 255$ K and $T > 297.5$ K), the crystal structure is described by the point group 222, we calculated the spectral and temperature dependences of absolute piezo-optic constants for Rochelle salt crystals using the temperature and spectral dependence of the combined piezo-optic constants of Rochelle salt crystals and the well-known expressions for the birefringence of orthorhombic crystals (the transitional Pockels method [1]) and solving the system of nine equations of the type

$$\begin{aligned} \pi^0_{31} &= 1/2(n_3^3\pi_{11} - n_2^3\pi_{21}), \\ \pi^0_{32} &= 1/2(n_2^3\pi_{22} - n_1^3\pi_{12}). \end{aligned} \quad (4)$$

The above equations contain nine unknowns π_{im}, where n_1, n_2, and n_3 are the absolute refractive indices at the given light wavelength and the temperature [7].

Figure 4 shows the dispersion dependences of the absolute piezo-optic constants π_{im} of Rochelle salt crystals. It is seen that piezo-optic constants are characterized by normal dispersion and are equal to $d\pi_{im}/d\lambda$ = 3.3, 7.5, and 6.0 at *im* = 11, 21, 31 (which corresponds to the pressure G_X); 40, 2.8, and 3.2 at *im* = 12, 22, 32 (which corresponds to G_Y); and 3.7, 0.9, and 1.5 for *im* = 13, 23, 33 (which corresponds to G_Z).

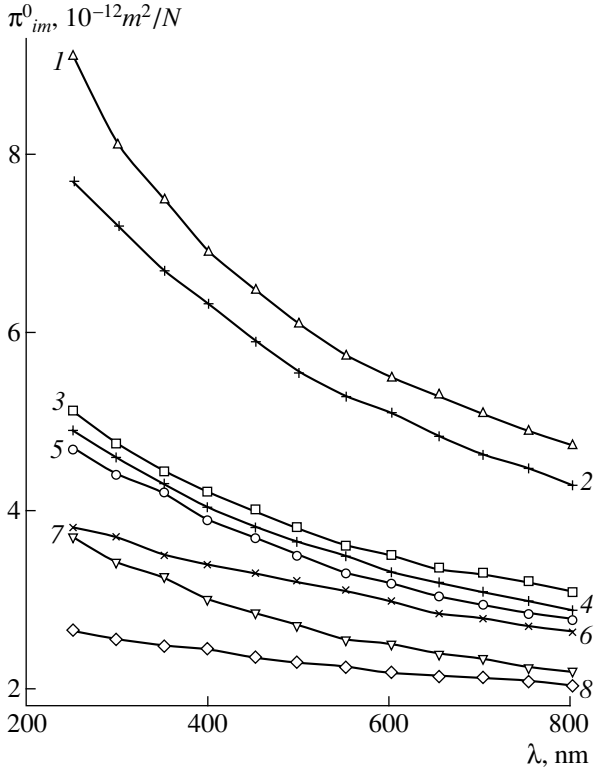

Fig. 4. Dispersion of absolute piezo-optic constants of Rochelle salt crystals at $T = 298$ K: (*1*) π_{21}, (*2*) π_{31}, (*3*) π_{12}, (*4*) π_{11}, (*5*) π_{13}, (*6*) π_{32}, (*7*) π_{22}, and (*8*) π_{23}.

There is one interesting detail. The extrapolation of the π_{23} and π_{33} and also π_{32} and π_{22} curves toward short wavelengths results in their mutual intersection, i.e., their equal values in the vicinity of ~280 nm, which corresponds to the spectral position of the point of inversion of the birefringence sign at room temperature. The piezo-optic constants π_{23} and π_{33} are responsible for the change in the refractive indices n_y and n_z under the effect of pressure G_Z, and, in turn, determine the birefringence Δn_x along the direction of its sign inversion. In a similar way, the piezo-optic constants π_{23} and π_{32} determine the change in n_y and n_z under the effect of G_Y. In other words, in the vicinity of birefringence-sign inversion the symmetry of the tensor of piezo-optic constants increases. A similar effect was observed earlier for a $LiKSO_4$ crystal [8].

Figure 5 shows the temperature dependence of the absolute piezo-optic constants of Rochelle salt crystals at the wavelength $\lambda = 500$ nm. For the upper phase transition, no anomaly in $\pi_{im}(T)$ was observed, whereas at the lower phase transition, the feebly marked anomalies were recorded. On the whole, π_{im} are only slightly temperature-dependent, with the exception of π_{21} and π_{31}.

The absence of clearly pronounced anomalies in $\pi_{im}(T)$ for the Rochelle salt crystals follows from the relationships describing the anomalies in piezo-optic

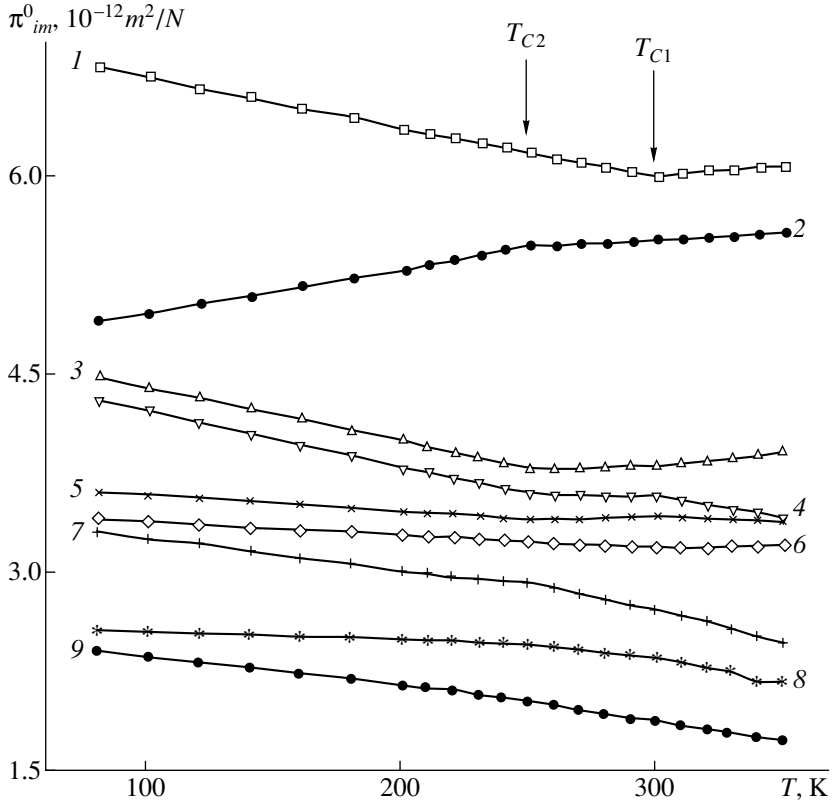

Fig. 5. Temperature dependence of absolute piezo-optic constants for Rochelle salt crystals at $\lambda = 500$ nm: (*1*) π_{21}, (*2*) π_{31}, (*3*) π_{12}, (*4*) π_{11}, (*5*) π_{13}, (*6*) π_{32}, (*7*) π_{22}, (*8*) π_{23}, and (*9*) π_{33}.

constants, i.e.,

$$\delta\pi_{im} = -2/n_i^3 \delta n_i^{cn}/G_m = -2/n_i^3 dT_C/dG_m dn_i^{cn}/dT. \quad (5)$$

The coefficients dT_C/dG_m characterizing the displacement of the phase transition point under the effect of pressure are ~0.005 K bar^{-1}. Spontaneous polarization and spontaneous electrooptic effect, which determine the dn_i^{cn}/dT value in the phase transition, are also rather weak. Therefore $\delta\pi_{im}$ has a low value, being of the order of magnitude of π_{im} or being comparable with the accuracy of π_{im} measurement. Thus, the temperature dependences of the coefficient π_{im} for Rochelle salt crystals are caused mainly by true piezo-optic contribution and, therefore, have no clearly pronounced jumpvise anomalies.

Thus, it has been established that birefringence in Rochelle salt crystals is rather sensitive to uniaxial pressures applied along the main crystallophysical axes and is less sensitive to pressures applied along the corresponding bisector directions. The calculated spectral dependences of the combined and absolute piezo-optic constants of Rochelle salt crystals show considerable dispersion in the ultraviolet spectrum range, which is explained by the effect of uniaxial pressures on the position of the fundamental absorption edge. The intersection of the dispersion curves π_{23} and π_{33} and also of π_{22} and π_{32} in the range of inversion of the birefringence sign indicates an increase of the symmetry of the fourth-rank tensor of piezo-optic constants in the vicinity of the isotropic point. The temperature dependences of the absolute piezo-optic constants show no pronounced anomalies in the vicinity of phase transitions in Rochelle salt crystals, which confirms the fact that the temperature dependences of the coefficients π_{im} are provided mainly by the true piezo-optic contribution.

ACKNOWLEDGMENTS

The authors are grateful to N. A. Romanyuk for valuable discussions.

REFERENCES

1. T. Narasimhamurty, *Photoelastic and Electro-Optic Properties of Crystals* (Plenum, New York, 1981; Mir, Moscow, 1984).
2. T. Narasimhamurty, Phys. Rev. **186**, 945 (1969).
3. N. A. Romanyuk and B. G. Mytsyk, Fiz. Élektron. (Lviv) **42**, 66 (1982).
4. B. G. Mytsyk, *Optics of Anisotropic Media* (Moscow, Nauka, 1988), p. 99.
5. N. A. Romanyuk, V. M. Gaba, and A. M. Kostetskiĭ, Opt. Spektrosk. **54**, 186 (1983) [Opt. Spectrosc. **54**, 106 (1983)].
6. I. S. Zheludev, *Physics of Crystalline Dielectrics* (Nauka, Moscow, 1968).
7. N. A. Romanyuk, V. M. Gaba, and A. M. Kostetskiĭ, Kristallografiya **25** (5), 1076 (1980) [Sov. Phys. Crystallogr. **25** (5), 618 (1980)].
8. N. A. Romanyuk and V. I. Stadnik, Ukr. Fiz. Zh. (Russ. Ed.) **41**, 232 (1996).

Translated by L. Man

Crystallography Reports, Vol. 45, No. 5, 2000, pp. 839–841. Translated from Kristallografiya, Vol. 45, No. 5, 2000, pp. 911–914.

PHYSICAL PROPERTIES OF CRYSTALS

Pseudosymmetry and Some Characteristics of Pyroelectric Properties of Crystals

V. A. Ivanov, M. A. Faddeev, and E. V. Chuprunov

Nizhni Novgorod State University, Nizhni Novgorod, 603600 Russia

Received August 18, 1998; in final form, March 10, 1999

Abstract—The relation between pseudosymmetry characteristics of the atomic structure and the values of the pyroelectric coefficients of model and real pyroelectric crystals has been studied. It is established that the electron-density projection onto the polar axis of crystals with the highest values of pyroelectric coefficients possesses the property of pseudosymmetry, i.e., that the considerable part of the electron density is invariant with respect to an additional center of symmetry. *© 2000 MAIK "Nauka/Interperiodica".*

One of the most important and complicated problems of crystals physics is the establishment of the relationship between the atomic structure of crystals and their physical properties. Considerable mathematical difficulties encountered in the analytical and numerical solutions of quantum-mechanical equations describing the motion of constituent atoms are well known and there is no hope for rigorous and complete solution of this problem in the near future. Therefore, it is of great interest to establish more or less general factors and specific features of the crystal structure that can affect physical properties of crystals.

As a rule, the structure determination of crystals by X-ray diffraction method reduces to establishment of atomic coordinates and parameters of atomic thermal vibrations. The geometric feature common to all the crystals is their symmetry, which also determines the possible spectrum of the physical properties of a crystal independently of its chemical composition. In the search for geometric factors, which can influence the physical properties of crystals, it is the most expedient to analyze the fine characteristics of the crystal symmetry and, in particular, possible presence of pseudosymmetry, i.e., to establish whether a considerable part of the electron density is invariant with respect to a certain spatial or noncrystallographic supergroup of symmetry for the crystal structure as a whole [1]. In pseudosymmetric crystals, the structural features manifest themselves as symmetric ones, which allows one to apply the group-theoretical and crystallophysical methods for the analysis of these structural features and their effect on the physical properties of the crystal.

Consider the effect of pseudosymmetric features of the atomic structure on the pyroelectric coefficients of crystals. Let a model pyroelectric crystal described by the sp. gr. G to be related to one of two classes C_n or C_{nv} and contain k symmetrically related molecules in the unit cell of the volume V. We assume that the symmetry of each molecule is described by the point group R isomorphic either to C_n or to C_{nv}. In this case, the dipole moment of each molecule is parallel to its symmetry axis, whereas the dipole moment of the unit cell is parallel to the polar (symmetry) axis of the crystal and is equal to $d = k\mu\cos\theta$, where μ is the dipole moment of the molecule parallel to its symmetry axis and θ is the angle formed by the polar axis of the crystal and the symmetry axis of the molecule. Crystal polarization is described as $P = d/V$, and the only nonzero component of the vector γ_3 of the pyroelectric coefficient of the crystal can be written in the form

$$\gamma_3 = dP_3/dT = (1/V)k\cos\theta(\partial\mu/\partial T)_{v,\theta} + (1/V)k\mu\sin\theta(\partial\theta/\partial T)_{v,\mu} + (1/V^2)k\mu\cos\theta(\partial V/\partial T)_{\mu,\theta}. \quad (1)$$

We assume that the change in the orientation of the dipole moment of the molecule with the change in the temperature would provide a considerably larger contribution to the pyroelectric coefficient than the change in the dipole-moment modulus. Then, the first term in (1) can be neglected, and formula (1) takes the form

$$\gamma_3 = (1/V)k\mu\sin\theta(\partial\theta/\partial T)_{v,\mu} + P\alpha^{\mu,\theta}, \quad (2)$$

where $\alpha^{\mu,\theta} = (1/V)(dV/dT)_{\mu,\theta}$ is the coefficient of thermal deformation at the constant μ and θ values.

If $\theta = 0°$, only the change in the dipole moment of the unit cell caused by thermal deformation of the crystal can give the contribution to the pyroelectric effect, whereas at $\theta = 90°$, the contribution of the "true" part of the pyroelectric effect is maximal.

Now, determine the conditions that should be satisfied by the atomic structure to provide the maximum values of $|\gamma_3|$. It is seen from (2) that both terms should have the same signs. Then, the maximum value of $|\gamma_3|$ is attained at $\theta = 90°$, i.e., in the case, where the symmetry

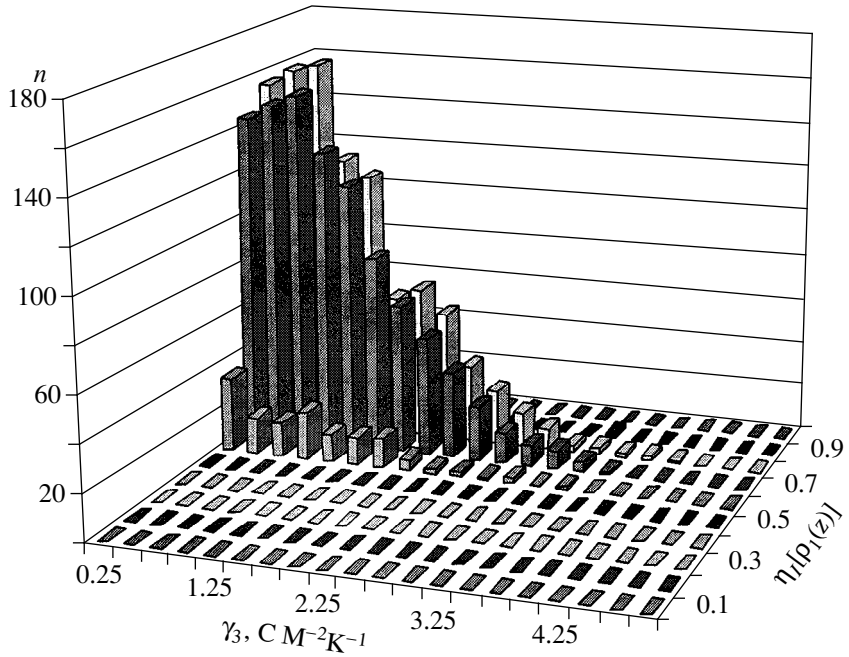

Fig. 1. Numbers n of the model crystals–pyroelectrics with 81 atoms in the unit cell (sp. gr. $P3$) for different values of the pyroelectric coefficient γ_3 and the centrosymmetricity degree η_I.

axes of the molecules are normal to the symmetry axis of the crystal.

It should be noted that the normal orientation of the symmetry axes of the molecules in the unit cell with respect to the symmetry axis of the crystal does not signifies that the crystal structure as a whole is necessarily invariant with respect to the nonpolar space group obtained by the multiplication of the group G and the symmetry groups of the molecules in accordance with any rule known in the group theory. In the general case, the symmetry axes of the molecules can be oriented arbitrarily with respect to the unit translations of the crystal lattice. In particular, if a direction in the lattice coincides with an appropriate rational direction in the crystal space, the electron-density function (or its considerable part) is invariant with respect to the nonpolar space group obtained by multiplication of the groups G and R [2]. However, in the general case, it is impossible to construct such a space group and, therefore, such structures should be described in terms of the generalized symmetry group.

Let us construct a one-dimensional projection of the electron-density function onto the polar axis of the crystal (the Z-axis)

$$\rho_1(z) = \int_0^1\int_0^1 \rho(x, y, z)dxdy. \qquad (3)$$

The invariance of each crystal molecule with respect to the symmetry axis normal to the polar axis of the crystal signifies that the function $\rho_1(z)$ is invariant with respect to the one-dimensional space group G^1. In this case, the symmetry axes of the group R of the molecule projected onto the Z-axis are mapped onto the centers of inversion in the one-dimensional space group G^1. Thus, the maximum value of the pyroelectric coefficient for the crystals under consideration is most probably attained if a considerable part of the one-dimensional projection of the electron-density function of the crystal is centrosymmetric.

Quantitatively, the degree of invariance of the function $\rho_1(z)$ with respect to the centrosymmetric group G^1

Maximum values of pyroelectric coefficients γ_3 and the corresponding centrosymmetricity degrees $\eta_I[\rho_1(z)]$ of the electron-density projection onto the polar axis for different numbers of atoms in the symmetrically independent part of the unit cell and the order of the symmetry axis obtained in computer simulation

	Order of the symmetry axis	Number of atoms		
		8	27	64
γ_3, C M^{-2} K^{-1}	2	1.00–1.25	2.50–2.75	3.25–3.50
	3	1.75–2.00	3.50–3.75	4.50–4.75
	4	2.25–3.00	3.75–4.00	4.75–5.00
	6	3.00–3.50	5.50–6.00	7.50–8.00
$\eta_I[\rho_1(z)]$	2, 3, 4, 6	0.6–0.7	0.7–0.8	0.8–0.9

can be evaluated if we introduce the following functional [3]:

$$\eta_I[\rho_1(z)] = \int_0^1 \rho_1(z)\rho_1(-z + 2u_3)dx_3 / \int_0^1 \rho_1^2(z)dx_3, \quad (4)$$

where u_3 is the coordinate of the point with respect to which the centrosymmetricity degree of the function is calculated. The value of $\max \eta_I[\rho_1(z)]$ for all the points from the interval $0 \le u_3 \le 1$ can be considered as the centrosymmetricity degree of the function $\rho_1(z)$. Functional (4) equals unity, if the function $\rho_1(z)$ is fully invariant with respect to the center of inversion located at the point with the coordinate u_3. If $\eta_I[\rho_1(z)] = 0$, the one-dimensional projection of the electron density onto the polar axis is absolutely noncentrosymmetric and the crystal is "absolutely polar."

The relationship between the pyroelectric coefficients and pseudosymmetry of the one-dimensional projection of the electron-density function onto the polar axis of the crystal can be illustrated by a computer model and some real crystals–pyroelectrics. We consider the model molecular crystals–pyroelectrics described by the space groups $P2$, $P3$, $P4$, and $P6$ with different numbers of molecules per unit cell. The atomic coordinates were generated by an arbitrary method with due regard for all the realistic interatomic distances. The crystal was assumed to consist of only positive or negative ions, with the total charge per unit cell being zero.

Crystal heating is simulated by rotating molecules for certain small angles. The change in the dipole moment of the unit cell is used to calculate the pyroelectric coefficient γ_3. We also calculated the centrosymmetricity degree of the function $\rho_1(z)$, i.e., the value of $\eta_I[\rho_1(z)]$, by formula (4). This procedure was repeated for 3000 initial pseudorandom atomic configurations in the unit cell. As a result, the distribution of γ_3 is formed at the values of the initial dipole moment calculated for each pseudorandom set of atoms in the unit cell.

As an example, Fig. 1 shows the diagram obtained for a model dielectric crystal with 81 atoms in the unit cell described by the sp. gr. $P3$. The γ_3 and η_I values are plotted along two horizontal axes. The third axis shows the number of modeled structures whose pyroelectric coefficients and the $\eta_I[\rho_1(z)]$ values are within the intervals indicated in Fig. 1. It is seen that all the crystals–pyroelectrics exist in the domain where the value of η_I exceeds 0.5, whereas the maximum number of the crystals exist in the domain where $\eta_I > 0.7$.

The calculations performed also show that γ_3 increases with the number of atoms in the unit cell, which is explained by the linear dependence of γ_3 on the modulus of the dipole moment of a molecule (2). An increase of γ_3 with an increase of the rotation-axis order

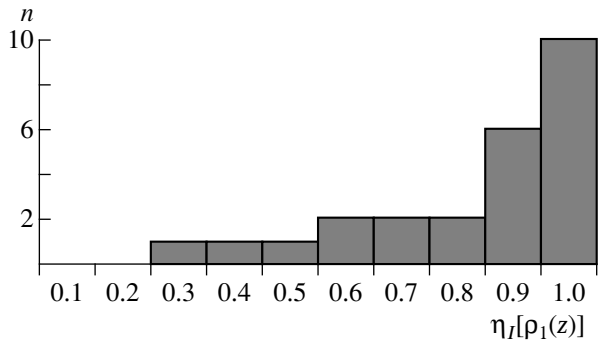

Fig. 2. Number n of the crystals–pyroelectrics for various centrosymmetricity degrees η_I on the one-dimensional projection of the electron-density function onto the polar axis.

is explained by an increase in the number of molecules k in the unit cell (2). Table shows the maximum γ_3 values and the corresponding η_I values for various numbers of atoms in the unit cell and the different orders of the symmetry axis.

A similar diagram can also be constructed for real crystals. According to the known data, the centrosymmetricity degree was calculated by formula (4) for 25 crystals–pyroelectrics (tourmaline, the ferroelectric phases of barium and lead titanates, 1,3-nitrobenzene, lithium niobate and tantalate, and $Cs_3Hg_3I_8$, Pb_3GeO_5, $Li_2B_4O_7$, Na_2GeO_3, $Cs_2S_2O_6$, $LiKSO_4$, $LiCsO_4 \cdot 3H_2O$, $C_6H_4(OH)_2$, $Na(H_3O) \cdot (I(OH)_2O_3)$, KIO_2F_2, Te_2O_5, α-$LiIO_3$, $NaNO_2$, $(NH_4)HSeO_4$, CdS, CdSe, ZnO, ZnS, and BeO. Figure 2 shows the diagram where the centrosymmetricity degree is plotted along the abscissa and the numbers of crystals from the above list are plotted along the ordinate for which the value of the function η_I lies within the above range. It is seen that the the centrosymmetricity degree of the considerable number of the crystals ranges within 0.90–1.0, thus indicating that high values of the pyroelectric coefficient are most probable for pronouncedly pseudocentrosymmetric crystals.

REFERENCES

1. B. K. Vaĭnshteĭn, *Crystallography and Crystal Chemistry* (Nauka, Moscow, 1986), p. 10.
2. A. V. Shubnikov amd V. A. Koptsik, *Symmetry in Science and Art* (Nauka, Moscow, 1972; Plenum, New York, 1974).
3. E. V. Chuprunov, E. A. Soldatov, and T. N. Tarkhova, Kristallografiya **33** (3), 759 (1988) [Sov. Phys. Crystallogr. **33** (3), 446 (1988)].

Translated by L. Man

Crystallography Reports, Vol. 45, No. 5, 2000, pp. 842–847. Translated from Kristallografiya, Vol. 45, No. 5, 2000, pp. 915–920.

SURFACE

Study of Surface and Interface Roughnesses in Porous Silicon by High-Resolution X-ray Methods

A. A. Lomov*, V. A. Bushuev, and V. A. Karavanskiĭ*****

** Shubnikov Institute of Crystallography, Russian Academy of Sciences, Leninskiĭ pr. 59, Moscow, 117333 Russia*

*** Moscow State University, Vorob'evy gory, Moscow, 119899 Moscow*

**** Institute of General Physics, Russian Academy of Sciences, ul. Vavilova 38, Moscow, 117942 Russia*

Received September 7, 1998

Abstract—The methods of triple-crystal X-ray diffractometry and the total external X-ray reflection are used to study porous silicon films on a *p*-type single crystal Si(111) substrate. For the first time, an increase of the pseudopeak intensity was experimentally observed for thick porous films. The following film characteristics are determined: thickness (1.8 μm), strain (3.8×10^{-3}), porosity (70%), pore size (~5 nm), roughness height of the surface (~3 nm) and the film–substrate interface (~7 nm), and correlation length (~7–10 nm). It is shown that the main contribution to the pseudopeak intensity for thin films on single crystal substrates comes from angular broadening of the incident beam formed by the exit slit of a monochromator of a finite width. It is shown that the method is very sensitive to density inhomogeneity in subsurface crystal layers. © *2000 MAIK "Nauka/Interperiodica".*

INTRODUCTION

In recent decades, the study of solid surfaces is of high priority in both fundamental and applied physics. Topology of a real surface and its roughness play an important part in stochastic processes of crystal growth and surface phase transitions. Even roughness with the heights ranging within 0.1–0.3 nm can be essential. One of the major problems still unsolved is the complete characterization of a solid surface.

The state of a surface undergoing macro- and microdistortions substantially influences various physical properties. The existence of microroughness at the nanostructure boundaries is an important factor in designing various devices based on quantum processes. Roughness deteriorates the reflection coefficient of various optical elements and plays the destructive role in X-ray telescopes, zone plates, mirrors used in the experiments with synchrotron radiation, etc. Therefore, the development of the methods for studying subsurface-layer roughness are of great importance, especially of such methods as profiling [1], electron microscopy [2], interference [3], atomic force microscopy [4] and various X-ray [5–7] techniques.

At present, the most advanced method for studying microroughness of subsurface layers and boundaries is total external reflection (TER) of X-rays [5]. However, similar to all the other methods, it has its limitations. Another widely used method is triple-crystal X-ray diffractometry (TCD) [6, 7], which provides important information on such surface-roughness parameters as root-mean square height σ and the correlation length l_c [8]. The TCD method allows one to single out and record, with a high angular resolution, the component that comes into the total scattering because of electron-density inhomogeneity on the sample surface and its interfaces—the so-called pseudopeak. Since the TCD method is used at incidence angles of the order of tens of degrees, the requirements to the sample dimensions and the location depth of the layer studied are not very severe.

However, up to now, no analysis of the TCD pseudopeak has been performed for characterization of the surface and subsurface layers of the crystals, which can be partly explained by the absence of appropriate objects. In recent years, ever growing attention is attracted to porous-silicon films [9–16]. The morphology, thickness, porosity, and the pore dimension of these films depend on the substrate type and the conditions of anodic etching of films. The surface area of pores in porous silicon nanostructures amounts to 200–600 m^2/cm^3 and is characterized by high photo and electroluminescence yields. These films are widely used in various optoelectronic devices. The mechanism of porous-structure formation has not been quite understood as yet. Therefore, the structural studies of porous silicon films can provide new important information.

The present article is aimed to study *p*-type porous silicon films by the X-ray diffraction and reflectometry methods. The emphasis is made on the analysis of pseudopeak intensity obtained by the TCD method and its application to small-scale roughness of single crystal surface and transient layers for determining the structural parameters of porous films on single-crystal

1063-7745/00/4505-0842$20.00

substrates. The data on the height and correlation length of microroughness obtained by X-ray diffraction method are compared with analogous data obtained by the method of total external reflection (TER). The results are confirmed by of computer simulation.

EXPERIMENTAL

We studied standard *p*-type (111)-oriented single crystal substrates with conductivity $\rho \approx 4$–$6\ \Omega$ cm. The 10- to 2000-nm-thick porous silicon films were obtained by the standard method—several-minute anodic oxidation with a 1- to 100-mA current in an electrolyte consisting of the mixture of ethyl alcohol and fluoric acid.

X-ray studies were performed by the method of total external reflection in the $\theta/2\theta$ scanning mode [6] and by the TCD method in the θ scanning mode [6] at the fixed angular deviations α of the sample from the exact Bragg angle θ_B. X-ray Cu$K_{\alpha 1}$ was collimated with the aid of a slit silicon monochromator with triple (111) reflection. The TER and TCD curves from porous silicon films and their substrates were recorded. In the TER experiments, the dimensions of the exit slit of the monochromator was 40 μm in the horizontal plane and 2 mm in the vertical one. The angular width of the slit placed in front of a detector was 200″. The intensity of the primary beam was $I_0 = 9 \times 10^4$ pulse/s. In the TCD experiments, the dimension of the exit slit of the monochromator block was 300 μm × 2 mm, $I_0 = 8.25 \times 10^5$ pulse/s. The TER and TCD curves were recorded at an angular steps of 10″ and 1″, respectively.

RESULTS AND DISCUSSION

Figure 1 shows the experimentally recorded and theoretically calculated $I(\theta)$ TER curves for the initial substrate and the sample coated with a *p*-type porous silicon with the layer thickness $t = 2000$ nm as functions of the rotation angle of the specimen. A high narrow peak at $\theta = 0°$ is obtained by recording half of an incident X-ray beam propagating along the sample surface lying on the goniometer axis. A further intensity increase is provided by a larger surface region $l = a/\sin\theta$ illuminated with the X-ray beam, where a is the slit width at the exit from the monochromator block. Polarizability of the silicon surface is $\chi_0 = (-15.15 + i0.36) \times 10^{-6}$, the critical TER angle is $\theta_c = |\chi_{0r}|^{1/2} = 13.38'$, which is quite consistent with the experimental value 13.4' obtained from the intensity data of the specular reflection at the half-height of the TER curve and from the angular position of the maximum of the $I(\theta)$ derivative with respect to the angle.

The jump in the measured TER intensity for porous silicon at $\theta = 6.67'$ (curve *3* in Fig. 1) is explained by a reduction of the critical TER angle from the film, θ_{PS}, caused by a decrease in its X-ray optical density. Since $\theta_{PS} = \theta_c(1 - P)^{1/2}$, where P is the porosity degree (i.e., the ratio of the total pore volume to the total film volume), one can estimate film porosity as $P \approx 75\%$.

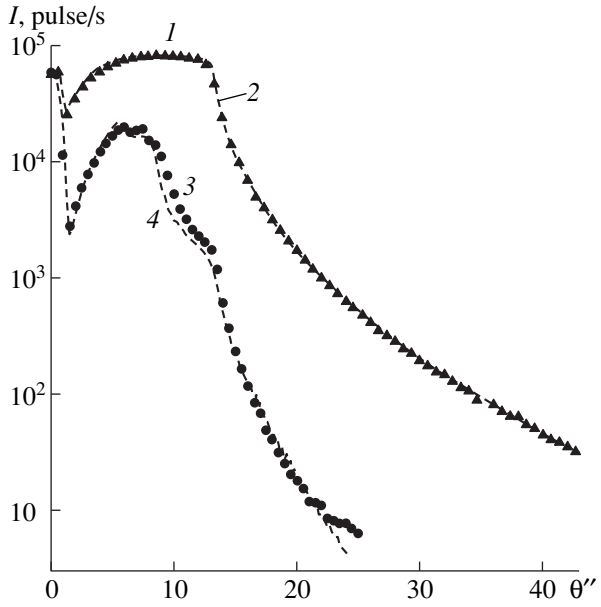

Fig. 1. Experimental (dotted lines *1*, *3*) and theoretical (dashed lines *2*, *4*) TER curves from (*1*, *2*) the substrate and (*3*, *4*) porous silicon.

A more accurate processing of the theoretically calculated TER curves was performed by varying the film thickness t, porosity P, and mean square heights of the roughness, σ_1 and σ_2, on the film surface and at the film–substrate interface, respectively. We minimized the functions of the type $\Sigma_i|I_{obs}(\theta_i) - I_{calc}(\theta_i)|/I_{obs}(\theta_i)$, which is the sum of the relative differences between the theoretical and the experimental intensities at all the points of the TER curves. In our case, the choice of this functional proved to be more advantageous than that provided by the least square procedure, because the main information on the roughness heights is contained in the tails of the specular-reflection curves whose intensities are lower (by two to four orders of magnitude) than those in the angular range $\theta \le \theta_c$. In the range of small angles and high intensities, the detailed analysis of the surface illumination effect is hindered by the necessity to take into account the intensity distribution over the cross section of the incident beam.

It was obtained that substrate roughness is $\sigma_1 = 0.76 \pm 0.03$ and $\sigma_1 = 0.79 \pm 0.03$ nm (in the case of the use of the static Debye–Waller factor [5] and the theory [17], respectively; for details, see [18]). The best agreement with the experiment was attained under the assumption on the formation of a thin ($t \approx 2 \pm 0.4$ nm) oxide layer (this assumption is consistent with numerous known data [7]), with the roughness heights σ_1 and σ_2 on the surface of this oxide layer and at the film-substrate interface being the same.

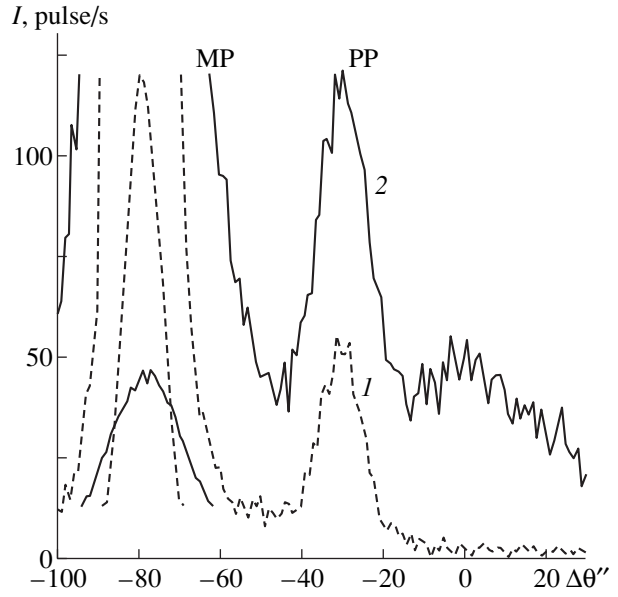

Fig. 2. Triple-crystal diffractometry (TCD) curves from (*1*) the substrate and (*2*) porous silicon. The angle of sample deviation from the exact Bragg angle, $\alpha = 30''$, the asymmetry coefficient of reflection 1.6 (the slope angle of the reflecting planes to the crystal surface $\psi = 3.5°$).

Processing the experimental data recorded for a sample coated with a porous silicon film yielded the following results: film thickness $t = 1800 \pm 100$ nm, porosity $P = 70 \pm 5\%$, and roughness heights $\sigma_1 = 3.1 \pm 0.5$ and $\sigma_2 = 7 \pm 1$ nm. It should be emphasized that, similar to [12, 15 16], the film thickness had slightly lower values than that predicted from the etching conditions, whereas porosity was slightly higher than its predicted value. It is well known that the film coating on the substrate surface gives rise to thickness oscillations of the specular reflection intensity. This was experimentally observed for 70–150 nm-thick porous silicon films in [15]. In our case, the film was rather thick and, what is more important, the roughness degree at the film–substrate interface was quite pronounced, which prevented the formation of short-period intensity oscillations on the reflection curves.

An increase of the measured intensity *3* in comparison with the intensity of the specular-reflection curve *4* in the range of the grazing angles $\theta \geq 25'$ is explained by diffuse scattering from the surface and inhomogeneities in the bulk of the porous structure. The absence of the satisfactory theory of diffuse scattering for such complicated objects as porous silicon does not allow to attain the desirable accuracy of curve processing in the large-angle range.

The roughness of the film–substrate interface $\sigma_2 \approx 7$ nm can be interpreted as the formation of a certain transient layer of thickness $l_t \approx \sigma_2$. Earlier [12], it was established from the data of double-crystal diffraction reflection and reflectometry for porous p^+- and *p*-type films having various thicknesses and porosities that $l_t \approx$ 17–22 nm (under the assumption of the existence of a homogeneous layer with the Debye–Waller factor $\exp(-W) \approx 0.85$); some other authors indicate the values $l_t \approx 15$ nm [14], 10–15 nm [15], and 10–25 nm [16] under the assumption on the existence of a linear transient layer. The analysis of these data shows that the thickness of the transient layer in the *p*-type films is less (by a factor of 1.5–2.0) than for the p^+-type films, with the thicknesses and porosity of these films being almost the same.

Film morphology depends on the type of the substrate. According to the transmission electron microscopy (TEM) data [19], the pores in the porous *p*-type silicon are randomly distributed spherical regions with a diameter of $D \approx 5$ nm, whereas the pores in the films of the p^+-type are cylindrical formations of a larger diameter (~12 nm) and are normal to the (100) surface. In this connection, the roughness observed in our case indicates the presence of spherical pores of the diameter $D \sim$ 5–7 nm in the vicinity of the interfaces and in the film bulk.

The diffraction reflection curve from a porous silicon sample consists of the Bragg maximum due to the substrate and a broad "hump" in the small-angle range. The spacing between these peaks (~200″) allows the evaluation of the average strain $\Delta d/d$ in the film along the surface normal as $\sim 3.8 \times 10^{-3}$. Broadening of the diffraction maximum or the main peaks on the TCD curves allows one to estimate sample bending. The bending radius is $R \approx l/\omega$, where $l = a/\sin\theta_B$ is the length of the illuminated region on the sample surface, $\omega \approx 13''$ is the broadening of the diffraction maximum, and $\theta_B = 14.22°$, whence it follows that $R \approx 18.6$ m. These data are very consistent with the results obtained for a porous *p*-type silicon crystal with $P = 56\%$ and $t = 20$ μm [10].

Figure 2 shows the TCD curves for our samples. It was possible to record the so-called main peak (MP) if the crystal–analyzer was rotated for an angle $\Delta\theta = (1 + b)\alpha$, where *b* is the coefficient of reflection asymmetry. It is seen that despite the use of a cut-channel slit monochromator, the TCD curves also show the well pronounced pseudopeak (PP) with the maximum at $\Delta\theta = \alpha$. It should be noted that the pseudopeak intensity for porous silicon is more than twice higher than that of the pseudopeak from the substrate, with the experimental conditions being the same. Obviously, the presence of the pseudopeak on the TCD curves is provided by small-angle scattering of the incident X-ray beam and the "redistribution" of some radiation intensity to the low-intensity wings of the angular intensity curve.

The above effect is caused by the following. The estimates made within the theory of a multicrystal spectrometer [20] show that the pseudopeak intensity should be negligible in both cases. Indeed, the pseudopeak intensity is proportional to the intensity at the tail

of the angular radiation distribution $R_1^n(\alpha)$ formed by a monochromator:

$$I_{PP}(\alpha) = I_0 A^{-1} G(\alpha) \int_{-\infty}^{\infty} R_2(\alpha') R_3^m(\alpha' + 2\alpha - \Delta\theta) d\alpha', \quad (1)$$

where

$$G(\alpha) = R_1^n(\alpha), \quad A = \int_{-\infty}^{\infty} G(\alpha) d\alpha.$$

Here R_1, R_2, and R_3 are the coefficients of single-diffraction reflection from a monochromator, a sample, and an analyzer, respectively, and n and m are the numbers of reflections in the monochromator and the analyzer blocks, respectively.

If the deviation from the exact Bragg angle in the samples $|\alpha| \gg \Delta\alpha_B$ (where $\Delta\alpha_B$ is the halfwidth of the peak at the half-height of the diffraction reflection curve), the intensity of single reflection decreases by the law $R_1(\alpha) \approx (\Delta\alpha_B/2\alpha)^2$. Then, at $n \geq 2$, the pseudopeak value R_1^n should be less, by several orders of magnitude, than the value of the main peak $R_2(\alpha)$. If, e.g., $\alpha = 30''$, $\Delta\alpha_B = 3.5''$ [Si(111), CuK_α radiation] and $n = 3$, then $I_{MP} = 3.4 \times 10^{-3}$, and $I_{PP}/I_{MP} \approx 1.2 \times 10^{-5}$. However, experiments show [6, 20] that this ratio can attain a value of several percent even if $n = 3$ or 5. For curves *1* and *2* in Fig. 2, the I_{PP}/I_{MP} ratio is about 5 and 11%, respectively. It was assumed [6] that for perfect samples, this effect is caused by imperfection of a crystal–monochromator.

In [8], a model was suggested according to which the formation of the pseudopeak on TCD curves was explained by small-angle diffuse scattering of the incident beam due to small-scale roughness of the sample surface and the corresponding angular spread of the beam upon its passage through the rough interface. In this case, the pseudopeak intensity is determined by the convolution of the angular distribution of the incident beam $R_1^n(\alpha)$ with the Fourier-components $g(\alpha)$ of the correlation function of the roughness heights. Refining the relationships given in [7, 8], one can show that the function $G(\alpha)$ in (1) for the Gaussian distribution of the roughness heights should be substituted by $G(\alpha) = [R_1^n(\alpha) + G_\sigma(\alpha)]\exp(-W)$, where

$$G_\sigma(\alpha) = 2\pi^{-1/2}(\Delta\alpha_B/\Delta\alpha_c) W \exp[-(\alpha/\Delta\alpha_c)^2]. \quad (2)$$

Here, $W = (\pi\chi_{0r}\sigma/\lambda\gamma_0)^2$ is the exponent of the Debye–Waller factor, χ_{0r} is the real part of the zeroth Fourier component of the sample polarizability, σ is the root-mean square roughness height of the sample surface, $\gamma_0 = \sin\theta_B$, and $\Delta\alpha_c = \lambda/\pi\gamma_0 l_c$ is the halfwidth of the function $g(\alpha)$, i.e., the halfwidth of the angular spectrum diffuse scattering from the roughness, and l_c is the correlation length of the roughness heights.

If $|\alpha| \leq \Delta\alpha_c$, the absolute intensity of pseudopeak (2) only slightly varies with the change in the deviation from the exact Bragg angle, α. The typical l_c values range within ~10–100 nm. If, e.g., $l_c = 100$ nm, then $\Delta\alpha_c \approx 410''$, and even at $\sigma = 10$ nm, the value of G_σ is 1.5×10^{-6}, which is less by three orders of magnitude than the intensity of the main peak. The physical nature of such weak scattering from roughness is associated with the very low polarizability $\chi_{0r} \sim 10^{-5}$. Thus, the formation of the pseudopeak on the TCD curves cannot be caused by the roughness of the sample surface (at least for the roughness heights $\sigma \ll \Lambda$, where Λ is the extinction length of the substrate).

However, there is one more cause of incident-beam spreading—broadening of the angular distribution of the wave intensity during the passage of the wave through the exit slit of a monochromator of a finite width. One can show that at $n \geq 2$ and $|\alpha| \gg \Delta\alpha_B$ in (1), we have $G(\alpha) = G_S(\alpha)$, where

$$G_S(\alpha) = \int_{-\infty}^{\infty} R_1^n(\alpha') S(\alpha - \alpha') d\alpha', \quad (3)$$

$$S(\alpha) = (\Delta\alpha_S/\pi^2\alpha^2)\sin^2(\pi\alpha/\Delta\alpha_S).$$

Here $\Delta\alpha_S = \lambda/a$ is the angular halfwidth of the transmission by a slit of width a. The function $G_S(\alpha)$ in (3) has the halfwidth $\Delta\alpha_B$ and decreases as $1/\alpha^2$, i.e., considerably slower than the intensity of the angular distribution $R_1^n(\alpha)$ for the multiplicity of reflection in the monochromator block equal to $n \geq 2$.

Figure 3 shows the angular distributions $R_1^3(\alpha)$ of the radiation incident onto the monochromator slit, the apparatus function of the slit $S(\alpha)$, and the result of the convolution $G_S(\alpha)$ (3). As earlier, let $\alpha = 30''$. Then, for the given width $a = 300$ μm, the angular halfwidth is $\Delta\alpha_S = 0.1''$, and the function $G_S(\alpha) = B\Delta\alpha_B\Delta\alpha_S/\alpha^2 \approx 1.4 \times 10^{-4}$, which is about 4% of the main-peak intensity and is close to the intensity ratio of the peaks at the curve *1* in Fig. 2. Here B is the coefficient determined by the numerical integration in (3) (in our case, $B = 0.36$). Since $G_S(\alpha) \sim 1/a$, then with a decrease of the slit width, the intensity of the pseudopeak should also increase, which was experimentally confirmed at $a = 100$ and 200 μm.

Figure 4 shows the experimentally measured intensities of pseudopeaks as functions of the angle of the sample rotation α. The curves for the substrate were calculated by formulas (1)–(3) at $a = 300$ μm. The roughness heights and the correlation lengths vary over wide ranges, $\sigma_1 \sim 1$–100 and $l_c \sim 10$–1000 nm, but this almost does not affect the behavior of dashed curve *1*. These facts confirm the conclusion that the pseudopeak

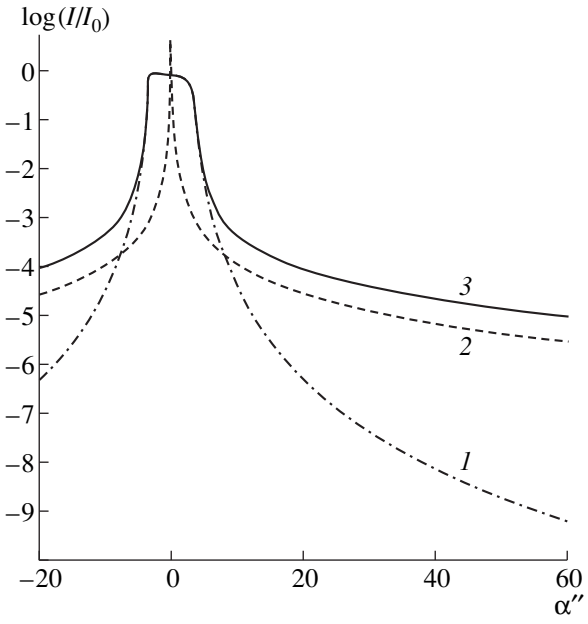

Fig. 3. (*1*) Angular distribution $R_1^3(\alpha)$ of the radiation incident onto the monochromator slit, (*2*) the apparatus function of the slit $S(\alpha)$, and (*3*) the angular distribution of the radiation $G_S(\alpha)$ incident onto the sample. The wavelength of the radiation 0.154 nm, the slit width 300 μm.

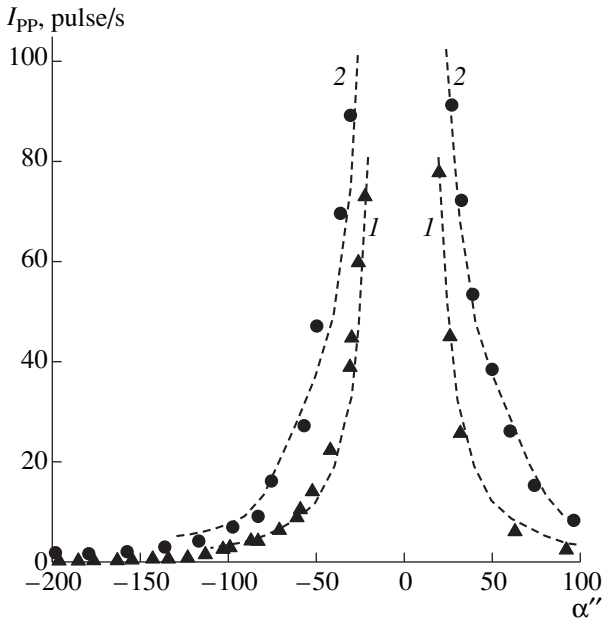

Fig. 4. Experimental (dotted lines) and calculated (dashed lines) angular dependences of the pseudopeak intensities on the TCD curves of the (*1*) substrate and (*2*) porous silicon.

is formed mainly due to the broadening of the spectrum of the incident radiation beam during its passage through a slit of finite dimensions.

An increase of the pseudopeak intensity for porous silicon under the same experimental conditions indicates that, in addition to the effect of the slit, some contribution to the intensity also comes from small-angle scattering of radiation from inhomogeneities in the bulk of the porous film. We used this fact for the characterization of a porous silicon film. When calculating curve *2* in Fig. 4, we assumed that diffuse X-ray scattering occurs from randomly distributed pores. It is also usually assumed that the correlation length, $l_c = 10$ nm, is comparable with the pore diameter, $D \approx \sigma_2 \approx 5$–8 nm. Then, one has to calculate the number of pores along the beam path and to take into account their contribution to the function $G_\sigma(\alpha)$ in (2). With this aim, one has to multiply the function in (2) by $N \approx (Pt/D) + 1$, which is equivalent to the introduction of an effective roughness height, $\sigma_e = \sigma N^{1/2}$. To some extent, this situation is analogous to the problem of diffuse scattering of X-rays by interface roughness in a multilayer structure under the assumption that the roughness profiles at different interfaces show no correlation [21].

Thus, for the first time, we confirmed the effect of porosity in the subsurface region of a single-crystal substrate on the intensity of the pseudopeak in triple-crystal X-ray diffractometry. It is also shown how one can use this effect for the analysis of porous nanostructures. On an example of the 1800 nm-thick *p*-type porous silicon film ($P \approx 70\%$), we manage to extract the information on pore dimensions and their correlation length. The pore dimensions (~5–6 nm) are in good accord with those obtained by the method of total external reflection. The obvious advantage of the TCD method in comparison with the TER method is its possible use for local surface studies of samples. Thus, using the TER method at the slit width $a = 40$ μm and the grazing angle $\theta \sim 15'$, we obtained the illuminated region with $l \approx 10$ mm comparable with the length of the porous film used in our experiment, whereas using the TCD method (even at $a = 300$ μm), the illuminated region length was only $l \approx 1.2$ mm, which is almost ten times less. Moreover, a deeper penetration of the radiation characteristic of the TCD method allows the study of 10 μm-thick and even thicker films. The computer simulation of the effect of the exit slit of the collimator onto the pseudopeak intensity for the TCD method showed that the use of the slit considerably limits the method sensitivity in the studies of thin films with nanometer-large inhomogeneities.

ACKNOWLEDGMENTS

This study was supported by the Ministry of Science and Technologies of the Russian Federation, the subprograms *Promising Technologies and Devices for Micro- and Nanoelectronics,* project no. 02.04.116.58.3.2, and *Physics of Solid Nanostructures,* project no. 97-1073.

The authors are grateful to R. M. Imamov for his interest in their study and useful discussions.

REFERENCES

1. A. Franks, in *Low Energy X-ray Diagnostics*, Ed. by D. T. Attwood and B. L. Henke (American Institute of Physics, New York, 1981), AIP Conf. Proc. **75**, 179 (1981).
2. K. A. Valiev, L. V. Velikov, V. V. Protopopov, *et al.*, Kristallografiya **40** (2), 358 (1995) [Crystallogr. Rep. **40** (2), 324 (1995)].
3. P. S. Young, Proc. SPIE **184**, 131 (1979).
4. G. Binning and H. Rohrer, Physica B (Amsterdam) **127**, 37 (1984).
5. A. Michette, *Optical Systems for Soft X-rays* (Plenum, New York, 1986; Mir, Moscow, 1989).
6. A. Iida and K. Dohra, Phys. Status Solidi A **51**, 533 (1979).
7. A. M. Afanas'ev, P. A. Aleksandrov, and R. M. Imamov, *X-ray Diffraction Diagnostics of Submicron Layers* (Nauka, Moscow, 1989).
8. A. P. Aleksandrov, A. M. Afanas'ev, and M. K. Melkonyan, Kristallografiya **26** (6), 1275 (1981) [Sov. Phys. Crystallogr. **26** (6), 725 (1981)].
9. K. Barla, R. Herino, G. Bomchil, *et al.*, J. Cryst. Growth **68**, 727 (1984).
10. D. Bellet, G. Dolino, M. Ligeon, *et al.*, J. Appl. Phys. **71**, 145 (1992).
11. D. Bellet, S. Billat, G. Dolino, *et al.*, Solid State Commun. **86**, 51 (1993).
12. A. A. Lomov, D. Bellet, and G. Dolino, Phys. Status Solidi B **190**, 219 (1995).
13. D. Bellet and G. Dolino, Thin Solid Films **276**, 1 (1996).
14. D. Buttard, D. Bellet, and T. Baumbach, Thin Solid Films **276**, 69 (1996).
15. D. Buttard, G. Dolino, D. Bellet, and T. Baumbach, Mater. Res. Soc. Symp. Proc. **452**, 437 (1997).
16. D. Buttard, D. Bellet, G. Dolino, and T. Baumbach, J. Appl. Phys. **83**, 5814 (1998).
17. L. Nevot and P. Croce, Rev. Phys. Appl. **15**, 761 (1980).
18. D. K. G. De Boer, Phys. Rev. B **49**, 5817 (1994).
19. M. I. J. Beale, N. G. Chew, M. J. Uren, *et al.*, Appl. Phys. Lett. **46**, 86 (1985).
20. P. Zaumseil and U. Winter, Phys. Status Solidi A **70**, 497 (1982).
21. V. A. Bushuev and V. V. Kozak, Kristallografiya **42**, 809 (1997) [Crystallogr. Rep. **42**, 742 (1997)].

Translated by L. Man

Crystallography Reports, Vol. 45, No. 5, 2000, pp. 848–852. Translated from Kristallografiya, Vol. 45, No. 5, 2000, pp. 921–925.

The Catalytic Effect of Impurity. The Effect of Benzene, Acetone, Organic Acids, Iron, and Chromium on Growth of KH_2PO_4 and $C_8H_5O_4K$ Crystals

T. M. Okhrimenko, E. P. Efremova, and V. A. Kuznetsov

Shubnikov Institute of Crystallography, Russian Academy of Sciences, Leninskiĭ pr. 59, Moscow, 117333 Russia

Received June 29, 1998; in final form, November 30, 1999

Abstract—The effect of benzene, acetone, acetic, formic, and oxalic acids, iron, and chromium on the growth kinetics of KH_2PO_4 and $C_8H_5O_4K$ crystal faces has been studied. It is found that low concentrations of organic impurities increase growth rates of some crystal faces (the so-called catalytic effect of impurity). This effect is rather weak in the case of organic acids, however, it is clearly seen in the presence of inorganic impurity (Fe^{3+}). The analysis of two models of growth (dislocation-free and $B + S$) under the assumption that the main cause of the catalytic effect is a decrease in the step energy showed that the calculated and experimental data are consistent only under certain assumptions that should be additionally verified both theoretically and experimentally.

INTRODUCTION

Earlier [1–4] it was shown that the introduction of trace amounts of various organic impurities increases the growth rates of KH_2PO_4 (KDP) and $C_8H_5O_4K$ (KAP) crystals. This effect is of universal nature and can be caused by a decrease of free surface energy of steps because of adsorption of impurity molecules on growing crystal faces [4] (the so-called catalytic effect of impurities).

This work continued our earlier study of the effect of impurities on the growth kinetics of KDP and KAP crystals. We studied the effect of benzene, acetone, and organic acids on the growth of KDP and KAP crystals and compared the experimental results with the theoretical predictions. According to [5], organic acids are not easily adsorbed on hydrated crystal faces, therefore, the study of their influence on the growth kinetics can provide additional information on the mechanism of the catalytic effect of impurities. The use of Fe^{3+} and Cr^{3+} impurities were chosen because the earlier observations showed a slight increase of the tangential growth rate of the KAP growth layers at very low Cr^{3+} concentrations [6] and a distinct maximum in the concentration dependence of growth rate R of the (101) face of KDP also at very low Fe^{3+} concentration [7]. Unlike the experiment conducted under static conditions [7], we performed the experiments on single-crystal seeds in the kinetic growth mode by the method described in [3]. The crystallization temperature was about 50°C in all the experiments, performed for 24 h. In all the figures, each point corresponds to three-to-five independent measurements.

EXPERIMENTAL RESULTS

Organic impurities. Figures 1–4 show growth rates of KDP and KAP faces as functions of impurity concentration.[1] It is seen that all the impurities increase the growth rates of crystal faces in narrow ranges of impurity concentrations. In KDP crystals, the effect is observed only for the pyramidal {101} faces, whereas the growth rate of the prismatic faces monotonically decrease with an impurity concentration. Similar to [3, 4], for KAP crystals, the most pronounced catalytic effect is observed on the $\{11\bar{1}\}$ faces (more active in terms of adsorbing ability [8]).

The catalytic effect produced by organic acids has some specific features (Figs. 2–4). First, an increase in the growth rates of faces caused by organic acids is rather weakly marked, although still considerably exceeds the experiment error. Earlier [4], a similar result was observed for acetic acid impurity, CH_3COOH, and was interpreted as an indirect evidence for weak adsorption of impurity molecules on hydrated crystal faces. Second, the use of oxalic acid $H_2C_2O_4$ changes the shape of the curve $R(C_i)$. Figures 2–4 show that with an increase of the $H_2C_2O_4$ concentration, the $R(C_i)$ curves measured for the (101) face of KDP crystals and the (010) and $(11\bar{1})$ faces of KAP crystals and then increase up to the attainment of the values equal to or slightly lower than initial ones. A further increase in

[1] Impurity concentration was determined as a number of moles of addition to the number of moles of solution in percent at constant supersaturations σ.

1063-7745/00/4505-0848$20.00 © 2000 MAIK "Nauka/Interperiodica"

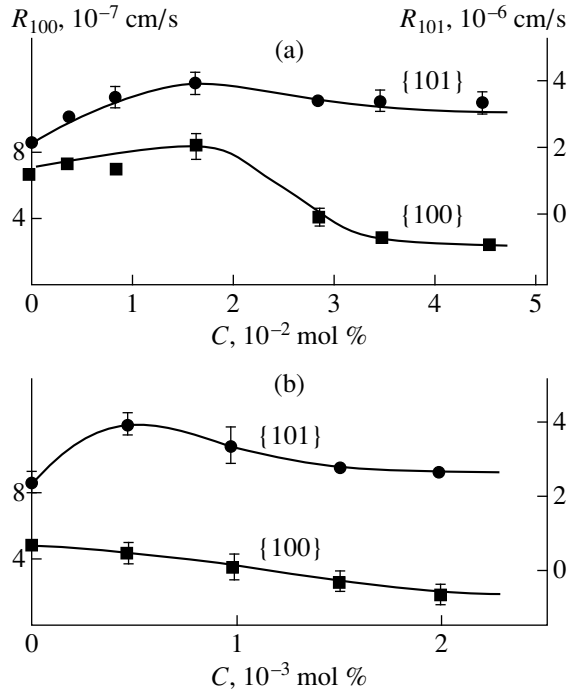

Fig. 1. Effect of (a) acetone and (b) benzene on the growth rates of the faces of a KDP crystal. T_g = 50°C, σ = 0.021.

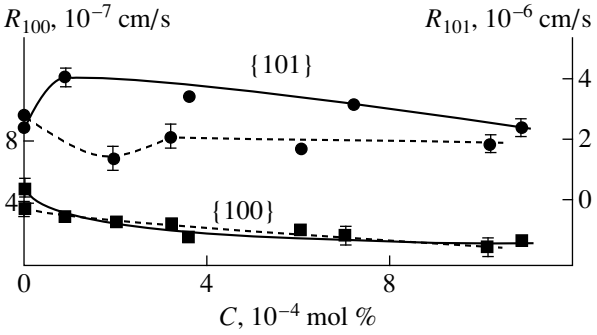

Fig. 2. Effect of formic (solid lines) and oxalic (dashed lines) acids on the growth rates of crystal faces of KDP crystals. T_g = 50°C, σ = 0.021.

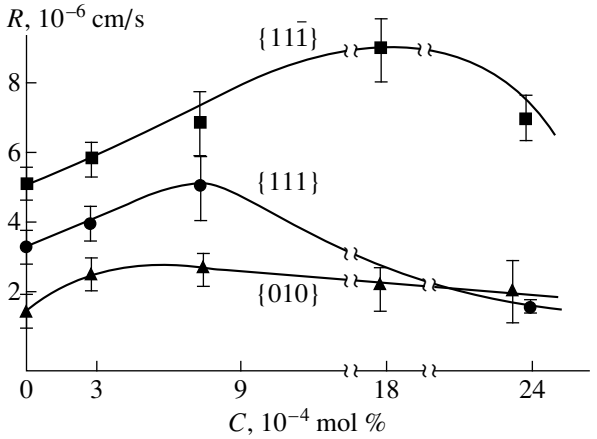

Fig. 3. Effect of formic acid on the growth rates of crystal faces of KAP crystals. T_g = 43°C, σ = 0.029.

impurity concentration results decrease the growth rate again (Fig. 4). As far as we know, such an unusual behavior of $R(C_i)$ was never observed earlier. Unfortunately, no unique interpretation of these data is given. Using the analogy with chemisorbtion of CH_3COOH [9], we can assume that such an unusual behavior is caused by the specific character of the surface carboxylation during $H_2C_2O_4$ chemisorption.

Inorganic Fe^{3+}, Cr^{3+} impurities. Figures 5–7 show the dependences of the growth rates of KDP and KAP faces on the concentration of Fe^{3+} and Cr^{3+}. Growth solutions were prepared by adding the drops of the preliminarily prepared 10^{-2} mol % $FeCl_3$ or $CrCl_3$ aqueous solutions to saturated KDP (KAP) solutions then stirred for 24 h in the presence of the KDP (KAP) solid phase.

Unlike all the other data, the data shown in Fig. 5 were obtained on a growth unit equipped with a special stirrer so that stirring of the solution was less intense. The crystals grew under both diffusion and kinetic control. As is seen from Fig. 5, under these conditions Fe^{3+} impurity, even relatively high $FeCl_3$ concentrations (0.02 mol %) provided an increase of the growth rate of the pinacoidal {010} faces in KAP crystals.

Figures 6 and 7 show the growth rates of the {101} and {100} faces of a KDP crystal as functions of Fe^{3+} and Cr^{3+} concentrations under various supersaturations. In all the cases, an increase of the impurity concentration reduces the growth rate of the {100} faces. This leads to crystal tapering, the well-known effect for KDP crystals and caused by impurity adsorption [10]. The growth rate of the {101} faces depends on the impurity concentration in a more complicated manner. At the supersaturation σ = 0.063, the $R(C_i)$ curve has a distinct maximum in the range of low Fe^{3+} concentrations. For Cr^{3+} impurity, the maximum of the $R(C_i)$ curve is weakly marked (almost comparable with the experiment error), however the curve run is noticeably different from the curves at lower supersaturations (Fig. 7). No data could be obtained for σ > 0.063

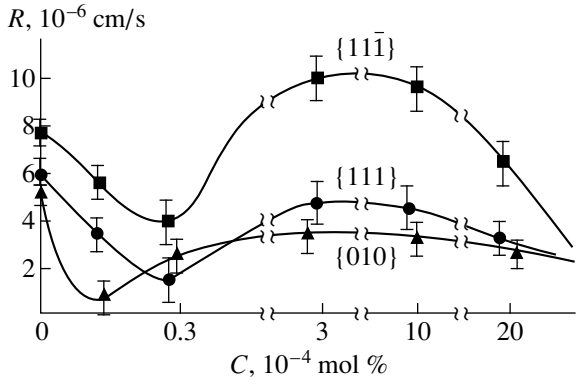

Fig. 4. Effect of oxalic acid on the growth rates of crystal faces of KAP crystals. T_g = 43°C, σ = 0.029.

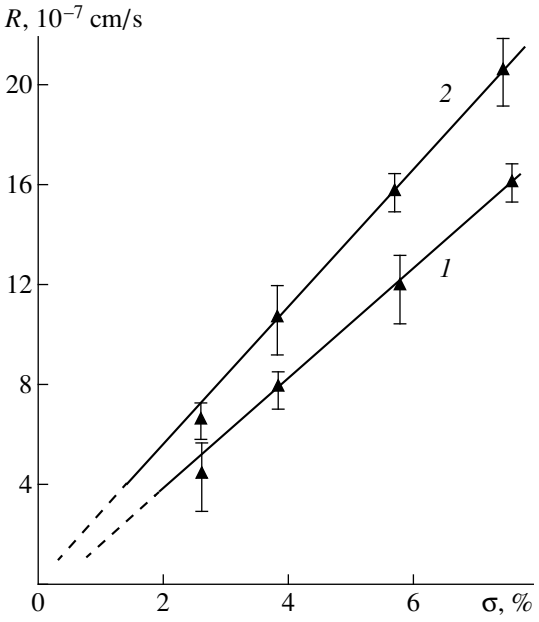

Fig. 5. Growth rate of the (010) face of a KAP crystal as function of supersaturation in the (*1*) nominally pure and (*2*) Fe^{3+}-containing solution. T_g = 43°C.

because of intense spontaneous crystallization which hinders growth-rate measurements for the seed crystal. It should be emphosized that Fig. 7 shows the R_{101} values averaged over 3–5 experiments performed under the same supersaturation and on the same seed crystal. We paid attention to the fact that the maximum increase in R_{101} at σ = 0.063 (in comparison with the control solution) was always observed in the first experiment of each run. In all the following R_{101} experiments, the growth rate of the {101} faces at the same σ and $C_{Cr^{3+}}$ concentrations regularly decreased. Therefore, the use of the data of the first experiments of each run provides the better record of the maximum of the R ($C_{Cr^{3+}}$) curves at σ = 0.063. This observation shows more intense KDP solutions with aging of Cr^{3+} which affects the growth kinetics.

RESULTS AND DISCUSSION

The data obtained confirm once again that an impurity-induced increase in the growth rates of crystal faces is a universal effect exhibited by various crystal line materials doped with impurities of various chemical nature. It also takes place due to the incorporation of inorganic ions into the crystal matrix (Fe^{3+} ions in KDP [11]). A relatively weak effect of organic acids only slightly adsorbed on hydrated crystal faces is an additional fact showing that the catalytic effect of impurities is associated with their absorption and a decrease in the step energy [4]. To confirm this opinion, we made an attempt to theoretically estimate an increase in the growth rates of faces under the assumption that the growth proceeds either by the dislocation mechanism or by the birth-and-spread ($B + S$) mechanism [12] with active two-dimensional nucleation at any site of the crystal face.

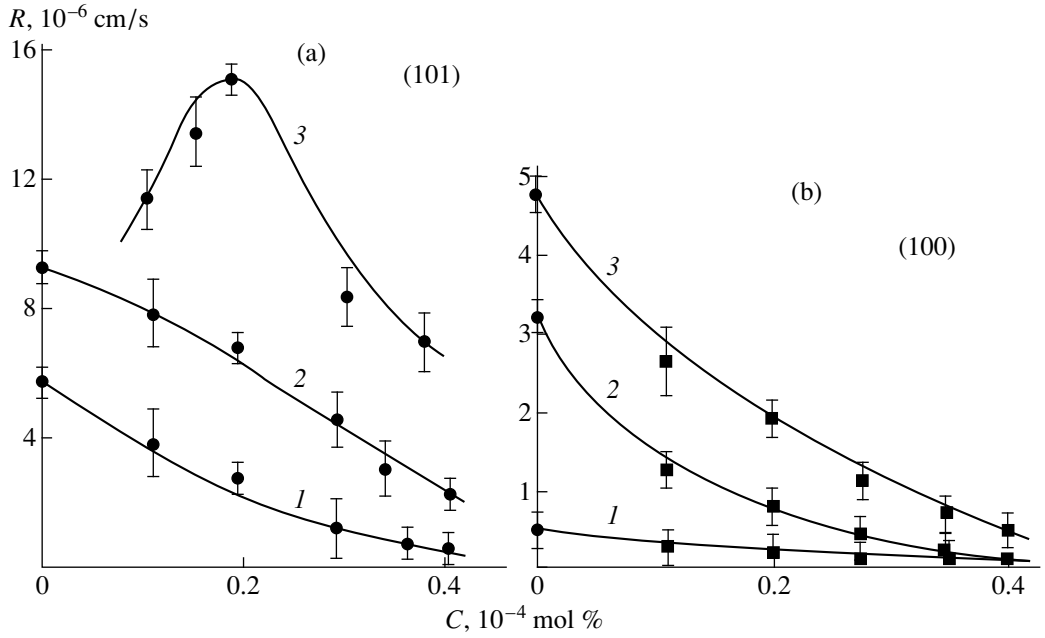

Fig. 6. Growth rate of the (a) (101) and (b) (100) faces of a KDP crystal as functions of Fe^{3+}-concentration in the solution at various supersaturations: σ = (*1*) 0.02, (*2*) 0.042, and (*3*) 0.063. T_g = 50.5°C.

In the former case, it is convenient to use for the analysis the following formula for the growth rate of faces [13]:

$$R = mh\omega C_e \beta kT\sigma^2/(19\omega\gamma + 2LkT\sigma), \quad (1)$$

where ω is the specific volume per growth unit in the crystal, h is the step height, mh is the magnitude of the Burgers vector of a dislocation or a bunch of dislocations, $2L$ is the perimeter of the dislocation source of steps, β is the kinetic coefficient of a step, γ is the surface step energy, C_e is the equilibrium concentration of the growth substance in the solution, k is the Boltzmann constant, and T is temperature.

As is shown in [14], in the presence of ethylene glycol can reduce the energy γ by 20–25% (in some other experiments, not more than by 10%). At the same time, the kinetic coefficient of the step increases by 10–15%. Then, as follows from equation (1), the growth rate R can increase by not more than 30–40%. However, the growth rate of faces R, for KDP and KAP crystals increased by 3–3.5 times higher [2, 4]. Such an increase in R cannot be explained within the classical dislocation mechanism.

A somewhat better agreement between the theoretical estimates and experimental data is obtained under the assumption of the $B + S$ growth mechanism with nucleation on the terraces and at a certain choice of the initial γ values. The growth rate of the face is given by the equation [12]

$$R = A\sigma^{5/6}\exp[-\pi(\gamma/kT)^2/3\sigma], \quad (2)$$

where A is a certain constant with all the other quantities having the same meaning as in equation (1).

The scatter in γ values ranges from ~4 to 20 erg/cm^2 [15–17]. Therefore, we calculated a possible increase in ΔR for two γ values, 20 and 5 erg/cm^2, under the assumption that impurities decrease the surface energy γ by 20 or 10%. The growth temperature was taken to be 300 K. The calculations showed that an increase in the growth rate ΔR at $\sigma = 0.03$ and $\gamma = 20$ erg/cm^2 was too high—by a factor of e_{72} and e_{38} with a decrease in γ by 20 and 10%, respectively. At higher supersaturations ($\sigma = 0.1$), the catalytic effect of impurities is much weaker (the growth rate increases by a factor of e_{22} at $\gamma = 20$ erg/cm^2). In this case, the calculated increase of growth rate becomes comparable with the experimentally observed data only at low initial surface energy, $\gamma = 5$ erg/cm^2 as well. In this case, R can increase by factors of $e^{1.16}$ and $e^{0.59}$ with a decrease of γ by 20 and 10%, respectively.

Thus, the calculations show that, first, the catalytic effect of impurities should be more pronounced at lower supersaturations. Second, the impurity-induced increase in ΔR measured at $\sigma = 0.03$–0.1 becomes comparable with the calculated value only at a relatively low surface energy, $\gamma = 5$ erg/cm^2. The values of surface energy indicated in recent publications (e.g., [17]) ranging within 15–20 erg/cm^2 would lead to an unrealistic increase of the growth rate R.

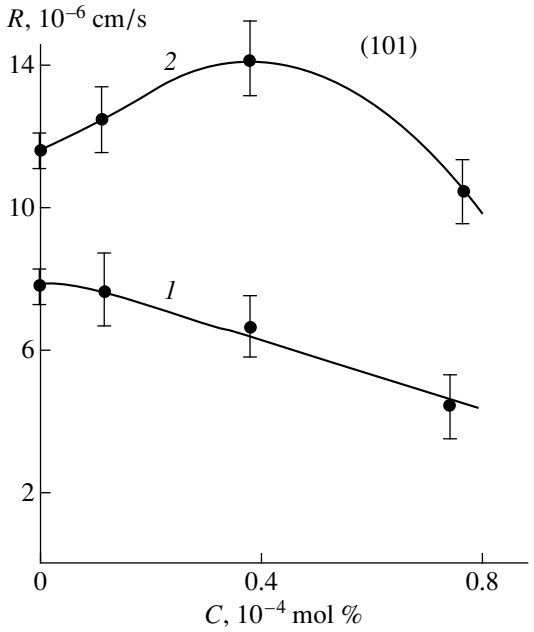

Fig. 7. Growth rate of the (101) face of a KDP crystal as a function of Cr^{3+} concentration at two supersaturations σ: (*1*) 0.042 and (*2*) 0.063. $T_g = 50.5$°C.

Thus, the assumption that a decrease γ in surface energy in the presence of impurities provides the appearance of the catalytic effect is justified only under two other assumptions:

(1) Even at low supersaturations of $\sigma = 0.03$–0.1, the two-dimensional nucleation ($B + S$ mechanism) makes a considerable contribution to the growth kinetics.

(2) The surface step energy is low, i.e., less than <10 erg/cm^2.

The above assumptions are justified by experimentally observed nucleation on the faces of KDP crystals at $\sigma \sim 10\%$ [18]. Estimates made in [17] show that, at $\sigma \geq 5\%$, the contribution of two-dimensional nucleation can be comparable with the contribution of the dislocation-assisted mechanism (the Burton–Cabrera–Frank mechanism). Nevertheless, the above assumptions require further theoretical and experimental justification. The fact of the absence of the catalytic effect of Fe^{3+} at low supersaturations $\sigma < 0.063$ is still unclear: the calculations predict more a pronounced effect with a decrease in σ. Thus, the mechanism of the catalytic effect of impurities needs the further studies. As an alternative interpretation, one can assume that this effect is associated with an increased roughness of the crystal because of a decrease in the entropy factor $\alpha = \xi\gamma/kT$ (ξ is the surface anisotropy factor) [19]. The estimates made in [20] show that for KDP crystals in the nominally pure solution $\alpha = 3.3$–3.6. A decrease in γ by 10–20% reduces α to ~3 (or even more), which

corresponds to a very rough surface. As a consequence, the direct incorporation of growth species into crystal faces (the normal growth rate) gives a larger contribution to the growth kinetics, and the face growth rate increases.

CONCLUSION

Our experimental data confirm the universal character of the catalytic effect of impurities. This effect is shown to occur also in the presence of inorganic impurities. However, the mechanism of this effect is still unclear and requires further theoretical and experimental studies. It is probable that an important part is also played by an increase of the surface roughness and the more pronounced contribution of the direct incorporation of growth species into the faces.

ACKNOWLEDGMENTS

The authors are grateful to M. Rak and T. G. Lalaeva for useful discussions and for their help in writing the manuscript.

This work was supported by the Russian Foundation for Basic Research, project no. 96-03-34141.

REFERENCES

1. T. M. Okhrimenko, S. T. Kozhoeva, V. A. Kuznetsov, *et al.*, Kristallografiya **34** (6), 1554 (1989) [Sov. Phys. Crystallogr. **34** (6), 929 (1989)].
2. M. L. Barsukova, V. A. Kuznetsov, T. M. Okhrimenko, *et al.*, Kristallografiya **37** (4), 1003 (1992) [Sov. Phys. Crystallogr. **37** (4), 533 (1992)].
3. T. M. Okhrimenko, S. T. Kozhoeva, V. A. Kuznetsov, *et al.*, Kristallografiya **37** (5), 1309 (1992) [Sov. Phys. Crystallogr. **37** (5), 705 (1992)].
4. V. A. Kuznetsov, T. M. Okhrimenko, and Kh. S. Bagdasarov, Kristallografiya **41** (3), 557 (1996) [Crystallogr. Rep. **41** (3), 527 (1996)].
5. I. A. Polunina and S. S. Mikhaĭlova, Izv. Akad. Nauk SSSR, Ser. Khim., No. 1, 200 (1992).
6. M. H. J. Hottenhuis and C. B. Lucasius, J. Cryst. Growth **91**, 623 (1988).
7. I. Owczarek and K. Sangwal, J. Cryst. Growth **102**, 574 (1990).
8. T. A. Eremina, N. G. Furmanova, L. G. Malakhova, *et al.*, Kristallografiya **38** (4), 236 (1993) [Crystallogr. Rep. **38** (4), 554 (1993)].
9. A. A. Isirikyan, S. S. Mikhaĭlova, I. A. Polunina, *et al.*, Izv. Akad. Nauk SSSR, Ser. Khim., No. 1, 20 (1983).
10. I. Owczarek and K. Sangwal, J. Cryst. Growth **99**, 827 (1990).
11. T. A. Eremina, V. A. Kuznetsov, T. M. Okhrimenko, *et al.*, Kristallografiya **41** (4), 717 (1996) [Crystallogr. Rep. **41** (4), 680 (1996)].
12. R. Y. Davey, in *Industrial Crystallization* (Elsevier, Amsterdam, 1978), p. 169.
13. I. L. Smol'skiĭ, A. I. Malkin, and A. A. Chernov, Kristallografiya **31** (4), 769 (1986) [Sov. Phys. Crystallogr. **31** (4), 454 (1986)].
14. S. P. Kuz'min, V. A. Kuznetsov, T. M. Okhrimenko, *et al.*, Kristallografiya **39** (5), 914 (1994) [Crystallogr. Rep. **39** (5), 834 (1994)].
15. P. Bennema, J. Boon, C. van Leeumen, and G. Gilmer, Krist. Tech. **27**, 659 (1973).
16. A. A. Chernov, I. L. Smol'skiĭ, V. F. Parvov, *et al.*, Kristallografiya **25** (4), 821 (1980) [Sov. Phys. Crystallogr. **25** (4), 469 (1980)].
17. A. A. Chernov, L. N. Rashkovich, I. L. Smol'skiĭ, *et al.*, Crystal Growth, Nauka, Moscow **15**, 43 (1986).
18. J. J. De Yoreo, T. A. Land, and B. Dair, Phys. Rev. Lett. **73**, 838 (1994).
19. J. R. Bourne and R. J. Davey, J. Cryst. Growth **36**, 278 (1976).
20. S. Veintemillas-Verdaguer, R. Rodríguez-Clemente, and K. Sangwal, J. Cryst. Growth **83**, 367 (1987).

Translated by A. Mel'nikova

Crystallography Reports, Vol. 45, No. 5, 2000, pp. 853–856. Translated from Kristallografiya, Vol. 45, No. 5, 2000, pp. 926–929.

CRYSTAL GROWTH

Synthesis and Magnetic Properties of Copper Metaborate Single Crystals, CuB_2O_4

G. A. Petrakovskiĭ, K. A. Sablina, D. A. Velikanov, A. M. Vorotynov, N. V. Volkov, and A. F. Bovina

Kirenskiĭ Institute of Physics, Siberian Division, Russian Academy of Sciences, Krasnoyarsk, 660036 Russia

e-mail gap@cc.krascience.rssi.ru

Received November 23, 1998

Abstract—Large high-quality single crystals of copper metaborate are grown on the basis of the phase diagram of the ternary Li_2O–CuO–B_2O_3 system. Bright blue crystals with a volume of about 1 cm^3 were grown by the method of spontaneous crystallization while slowly cooling the melt. The magnetic susceptibility and electron spin resonance were measured. It is shown that the effective magnetic moment of a Cu^{2+} ion is equal to 1.6 μ_B and the *g*-factor, to 2.170 and 2.133 for the magnetic field oriented parallel and perpendicular to the fourfold axis, respectively. At 21 and 10 K, sharp anomalies of magnetic susceptibility are observed. © *2000 MAIK "Nauka/Interperiodica".*

INTRODUCTION

In the past decade, copper oxide-containing compounds have attracted much attention because of their high-temperature superconducting properties. Moreover, they also characterized by various magnetic properties at low temperatures. The spin-Peierls and Haldane systems are typical examples of materials possessing such properties.

We had the aim to grow large CuB_2O_4 crystals and study their magnetic properties.

SYNTHESIS OF THE CRYSTALS

The first physicochemical study of the binary CuO–B_2O_3 system was reported in [1]. It was established that the system consists of two congruently melting compounds—CuB_2O_4 and $Cu_3B_2O_6$. These compounds were also found in the phase diagram of the ternary Li_2O–CuO–B_2O_3 system [2]. Later, the regions of existence of various phases and glass formation in the ternary CuO–PbO–B_2O_3 and CuO–Bi_2O_3–B_2O_3 systems were phases [3, 4] and the CuB_2O_4 and $Cu_3B_2O_6$ compounds were established. The crystal structure of CuB_2O_4 was studied in [5]. Using these data, we tried to determine the most appropriate method of growing the CuB_2O_4 single crystals. Our attempt to grow the CuB_2O_4 crystals on the basis of the phase diagram for the binary system [2] failed. The existence ranges (both with respect to temperature and concentration) CuB_2O_4 within the ternary LiO_2–CuO–B_2O_3 system [2] were much larger, and, therefore we used this system (Fig. 1) as the basis for growing CuB_2O_4 crystals. The crystallization field of copper metaborate is indicated by number 11.

The CuO, B_2O_3 and Li_2CO_3 components ground in a ball mill were mixed in the ratio of 25 : 60 : 15 (mol %), stirred, and placed into a 50-cm^3-large platinum crucible without preliminary fusing. The preliminary studies showed that the composition of this charge was optimal for growing large high-quality crystals. The crucible with the charge was placed into a furnace with SiC heaters and was slowly heated up to the temperature 800°C, then the temperature was quickly increased up to 1020°C. Upon two-hour annealing at this temperature, the melt was cooled to 800°C at a rate of 1°C/h.

Then, the crystals were extracted from the crucible, and were washed with boiling 20% aqueous solution of nitric acid. The transparent bright blue crystals were well faceted. The largest crystals had the dimensions $2 \times 1 \times 0.5$ cm^3. The unit cell parameters of ground crystals determined by the X-ray powder diffraction method were close to those indicated in [5] for CuB_2O_4.

The symmetry of tetragonal copper metaborate crystals is described by the sp. gr. $I\bar{4}2d$. The unit cell contains 12 formula units. The unite-cell parameters are equal to: a = 11.484 Å, c = 5.62 Å. The calculated density equals 4.022 g/cm^3. The electrical resistivity at 300 K is about 10° Ω cm [3]. According to [2], CuB_2O_4 undergoes a structural phase transition at 1000°C. Copper ions occupy two different positions in the unit cell: four Cu(1) ions are located in squares of oxygen ions, whereas, eight Cu(2) ions are located in a strongly distorted oxygen octahedra (Fig. 2).

1063-7745/00/4505-0853$20.00 © 2000 MAIK "Nauka/Interperiodica"

MAGNETIC PROPERTIES

The magnetic susceptibility of a CuB_2O_4 single crystal is measured by SQUID-magnetometer in 50 and 330 Oe magnetic fields in the temperature range 4.2–200 K. Above 25 K, the temperature dependence of the magnetic susceptibility for the field oriented along the *c*-axis is shown in Fig. 3. This curve follows the Curie–Weiss law with the paramagnetic Néel temperature $\theta = -5$ K and effective magnetic moment $\mu_{eff} = 1.6\mu_B$.

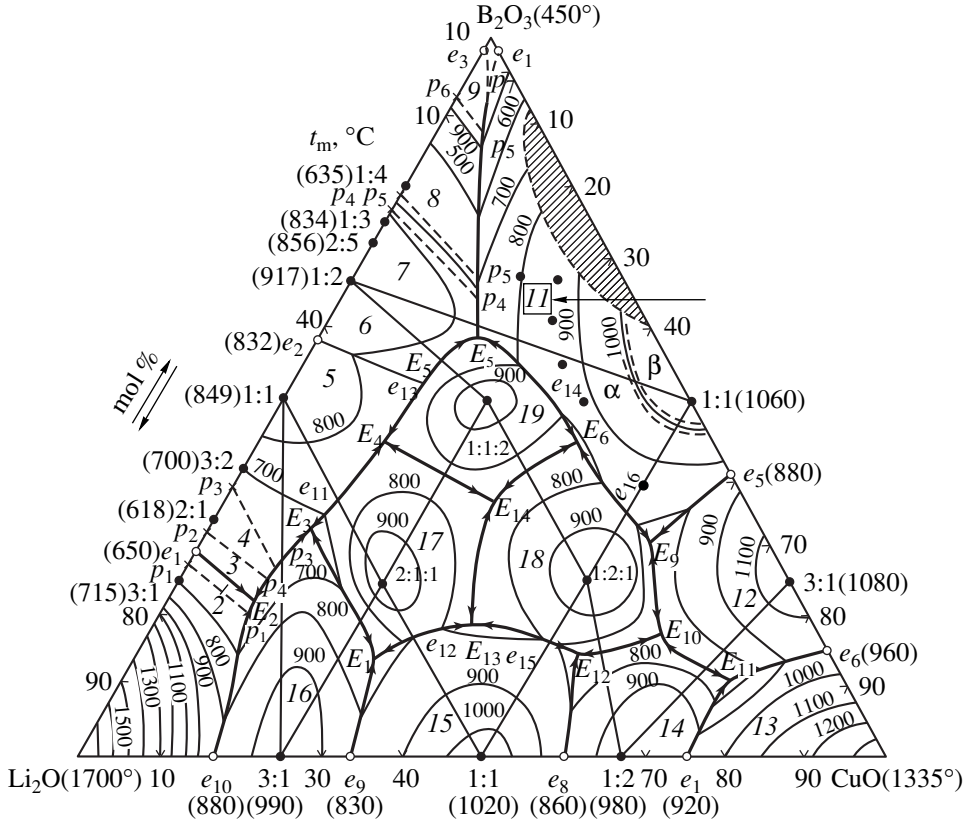

Fig. 1. Projection of the liquidus surface and the triangulation of the ternary Li_2O-CuO–B_2O_3 system [2]. The arrow shows the region of existence (11) of CuB_2O_4.

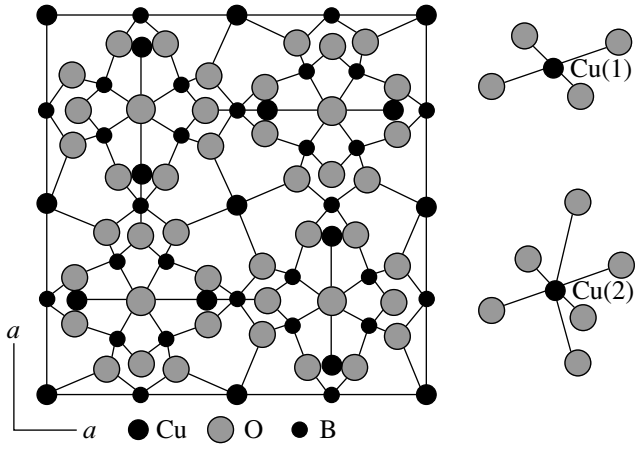

Fig. 2. CuB_2O_4 crystal structure [5].

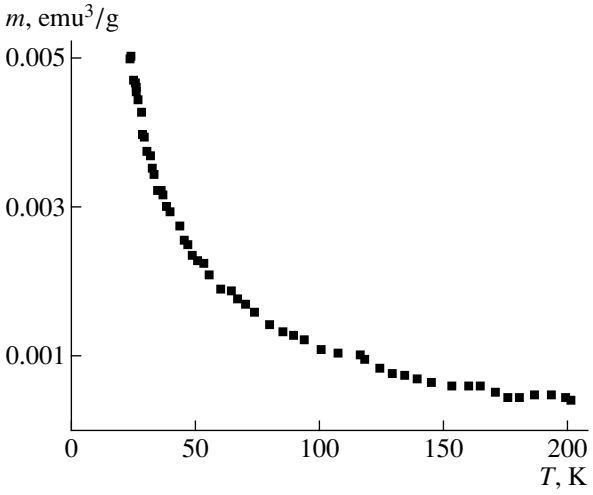

Fig. 3. Temperature dependence of the magnetic susceptibility of a CuB_2O_4 crystal in the 50 Oe-field applied along the *c*-axis.

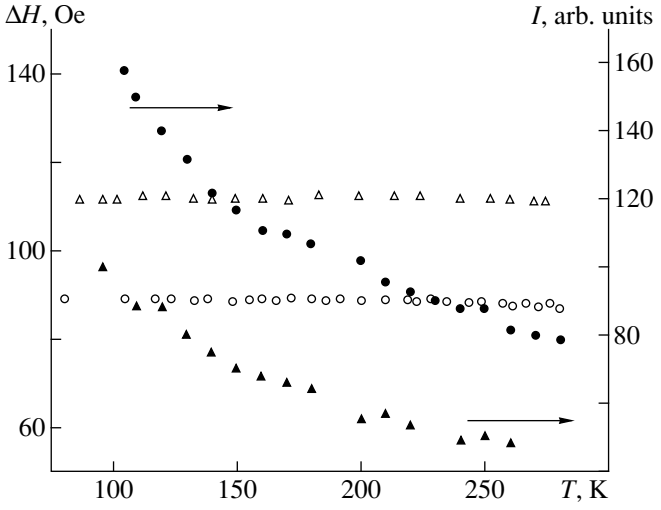

Fig. 4. Temperature dependence of the ESR linewidth ΔH (open triangles and circles) and the intensity I for a CuB_2O_4 single crystal (filled triangles and circles) for the field orientations $H \parallel c$ (open triangles) and $H \perp c$ (open circles).

Sharp anomalies in susceptibility occur at the temperatures 21 and 10 K: the susceptibility has a jump at 21 K and first increases with a further lowering of the temperature, and then abruptly decreases by about an order of magnitude at ~10 K. The measurements in the 330 Oe field show the same qualitative results.

The electron spin resonance (ESR) was measured at a frequency of 9.4 GHz in the temperature range 80–300 K and at a frequency of 10 GHz at a helium temperature. The results are shown in Figs. 4, 5. The ESR spectrum consists of a single Lorentzian line. The angular variations of the line width and the g-factor at room temperature are characteristic of a Cu^{2+} ion in a tetragonal crystal. The line width and the value of the g-factor for the field orientation parallel and perpendicular to the fourfold axis are equal to $\Delta H(\parallel) = 112$ Oe, $\Delta H(\perp) = 87$ Oe, $g(\parallel) = 2.170$, $g(\perp) = 2.133$, respectively.

The anomalies in the ESR parameters are observed below 30 K. They correlate with the temperatures of the anomalies in the magnetic susceptibility. The ESR intensity in the region of 10–20 K strongly depends on the magnetic-field orientation with respect to the crystal axes. The highest intensity is observed in the field oneuted parallel to the basal plane. The ESR signal is absent for a crystal magnetized along the fourfold axis. The resonance field in the tetragonal plane normal to the fourfold axis gradually decreases from 3560 Oe at 21 K to 2740 Oe at 10 K. At the temperatures below 10 K, the EPR signal is observed at any orientation of the field.

SUMMARY

The optimum concentration and the temperature conditions of CuB_2O_4 crystallization were determined from the analysis of the phase diagram of the ternary Li_2O–CuO–B_2O_3 system. High-quality CuB_2O_4 crystals about 1 cm^3 in size were grown for the first time.

The magnetic susceptibility and ESR measurements showed that the magnetic properties of the crystals grown are determined mainly by Cu^{2+} ions. The preliminary analysis showed that the crystals underwent magnetic phase transitions at 21 and 10 K. The further magnetic and structural studies necessary for identification

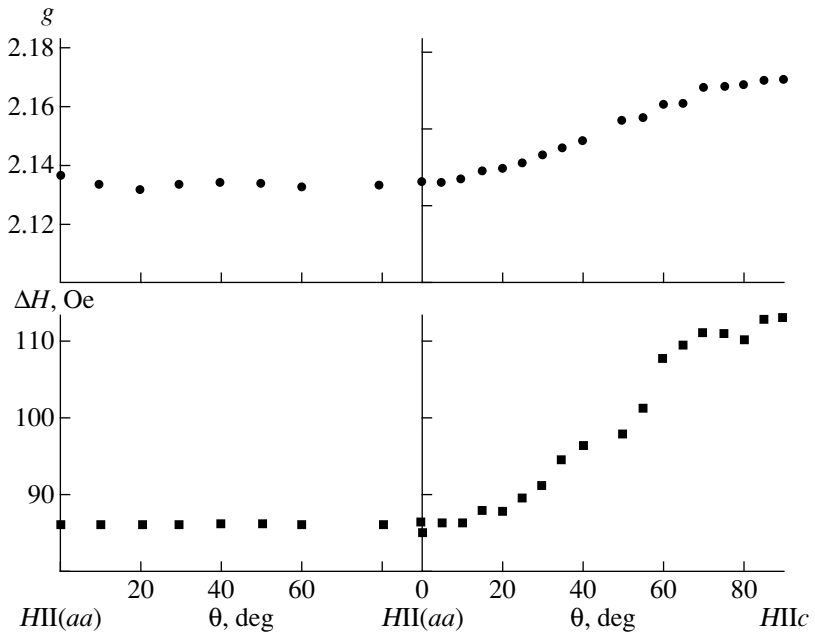

Fig. 5. Angular variations of the g-factor and the ESR linewidth for a CuB_2O_4 single crystal at room temperature.

of the magnetic state of CuB_2O_4 crystals at the temperatures below 21 K are in progress.

ACKNOWLEDGMENTS

This study was supported by the Krasnoyarsk Regional Science Foundation, project no 7F0195.

REFERENCES

1. C. E. Weir and R. A. Schroeder, J. Res. Natl. Bur. Stand., Sect. A **68**, 465 (1964).
2. G. K. Abdullaev, P. F. Rza-Zade, and Kh. S. Mamedov, Zh. Neorg. Khim. **27**, 1837 (1982).
3. M. I. Zarganova, N. M. Mustafaev, S. A. Mekhtieva, and N. S. Shuster, Izv. Akad. Nauk, Neorg. Mater. **33**, 1235 (1997).
4. M. I. Zargarova, N. M. Mustafaev, and N. S. Shuster, Izv. Akad. Nauk, Neorg. Mater. **32**, 74 (1996).
5. M. Martínez-Ripoll, S. Martínez-Carrera, and S. García-Blanco, Acta Crystallogr., Sect. B: Struct. Crystallogr. Cryst. Chem. **27**, 677 (1971).

Translated by A. Zalesskiĭ

Crystallography Reports, Vol. 45, No. 5, 2000, pp. 857–861. Translated from Kristallografiya, Vol. 45, No. 5, 2000, pp. 930–934.

CRYSTAL GROWTH

Study of Synthetic Hydroxyapatite by the Method of High-Resolution Transmission Electron Microscopy: Morphology and Growth Direction

E. I. Suvorova*, L. E. Polyak*, V. F. Komarov, and I. V. Melikhov****

** Shubnikov Institute of Crystallography, Russian Academy of Sciences, Leninskiĭ pr. 59, Moscow, 117333 Russia*
e-mail: suvorova@ns.crys.ras.ru

*** Chemistry Department, Moscow State University, Vorob'evy gory, Moscow, 119899 Russia*

Received July 23, 1998; in final form, April 29, 1999

Abstract—Hydroxyapatite crystals grown from aqueous solutions have been studied by the methods of high-resolution electron microscopy and transmission electron diffraction. Processing of the experimental electron micrographs with the use of the Digital Micrograph program and the study of the corresponding Fourier transforms showed that the submicron microcrystals grow mainly along the [0001] direction. The (0001) and the $(01\bar{1}0)$ planes are perpendicular and parallel to the long edge of the crystals, respectively. The good accord between the experimental electron-microscopy images and the electron microscopy images calculated by the EMS program was attained only for crystals with the thicknesses ranging from one to five lattice periods. This allows us to state that hydroxyapatite grows from aqueous solutions in the form of very thin (with the thickness of the order of several lattice parameters) platelike crystals. *© 2000 MAIK "Nauka/Interperiodica".*

INTRODUCTION

Synthetic hydroxyapatite (HAP), biologically resembling bone tissue and inert to the ambient media, is usually used as biological implants [1]. The directional synthesis of hydroxyapatite with the necessary optimum parameters for biomineralization (particle size and morphology, real and ideal structure) requires the corresponding conditions such as temperature, concentration of the initial reagents and rate of their mixing, supersaturation, and a certain pH value in the crystallization system. Varying these conditions, one can change not only the crystal morphology, but also the phase composition of the system as a whole, which usually results in the formation of mixtures of various calcium phosphates [2].

Hexagonal hydroxyapatite is described by the chemical formula $Ca_{10}(PO_4)_6(OH)_2$ and has the unit cell parameters $a = 0.9421$ and $c = 0.688$ nm, sp. gr. $P6_3/m$ [3]. Deposition during mass crystallization from aqueous solution yields individual elongated platelet-like crystals of submicron dimensions and their agglomerates [2].

The present article is devoted to the study of morphology and the real structure of hydroxyapatite crystals obtained by mass crystallization from aqueous solution by the methods of high-resolution electron microscopy (HREM) and transmission electron diffraction.

INITIAL MATERIALS AND METHODS OF THEIR STUDIES

Hydroxyapatite crystals were grown from an aqueous solution prepared from 100 ml of 0.018 M calcium hydroxide ($Ca(OH)_2$) solution and 10 ml of 0.108 N phosphoric acid (H_3PO_4) solution added within 3 min under constant stirring at a temperature of 20°C (upon mixing, but prior crystal deposition, pH of the solution was equal to 8.0). The concentrations of the components in the initial solutions corresponded to the stoichiometric hydroxyapatite composition. In synthesis, only extra-pure grade reagents were used.

The hydroxyapatite powders thus obtained were studied by the HREM method without any preliminary treatment. The crystals were sufficiently thin and transparent for an electron beam. The dried HAP powder on a carbon substrates and a copper grid was studied in a Philips EM 430ST microscope under an accelerated voltage of 300 kV. The HREM images usually had the magnification of 550 000×. The analysis of about 1000 experimental micrographs, including the determination of the orientations of individual crystals and grains in the agglomerates, was performed with the use the computer program Digital Micrograph. The theoretical HREM images were calculated using the EMS program [4] for crystals of various thicknesses and at various defocusing values.

1063-7745/00/4505-0857$20.00 © 2000 MAIK "Nauka/Interperiodica"

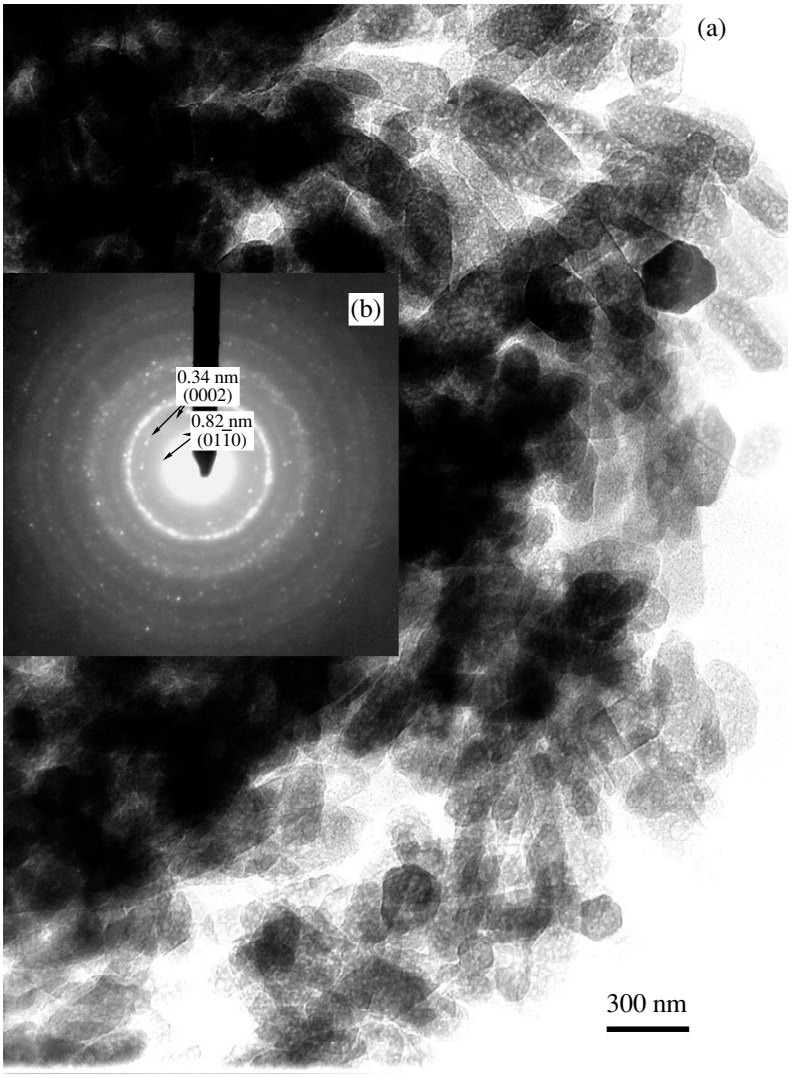

Fig. 1. (a) Agglomerate of hydroxyapatite crystals and (b) the corresponding electron diffraction pattern.

RESULTS

The specimens of dried hydroxyapatite powder consisted of agglomerates of thin platelike crystals (Fig. 1a) and gave the conventional powder-type diffraction pattern (Fig. 1b) with the 0002 reflections and very weak $01\bar{1}0$ reflections with the interplanar spacing of 0.82 nm close to the spot of the primary beam. This spacing is characteristic of hydroxyapatite and distinguishes it from other calcium phosphates. The most intense and broad ring is formed by several reflections, namely, $01\bar{1}2$, $12\bar{3}0$, $12\bar{3}1$, $11\bar{2}2$, and $02\bar{2}2$, with the interplanar spacings ranging within 0.317–0.263 nm. The agglomerates were differently oriented on the substrates with respect to an electron beam and were located at different heights with respect to the substrate surface. Therefore, high-resolution images were obtained either from small number of individual crystallites or from crystallites forming agglomerates and located normally to the electron beam. The attempts to attain high resolution were associated with the fact that the agglomerates were charged by an electron beam and started moving, the crystallites were heated by the beam, which resulted in their bending and fast change of their orientations with respect to the incident beam. In order to minimize these effects and to avoid possible radiation damage of the crystals, we used the minimum possible beam intensity, although even this precaution did not fully eliminate the above effects.

One of the most serious problems was the establishment of the crystallite thickness. Knowing the thickness of natural crystals, we could make certain conclusions about the mechanism of their growth. We used the HREM images to determine the preferential direction of hydroxyapatite growth. The theoretical simulation of images allowed us to estimate possible thickness of the crystals. Modeling by the EMS program was per-

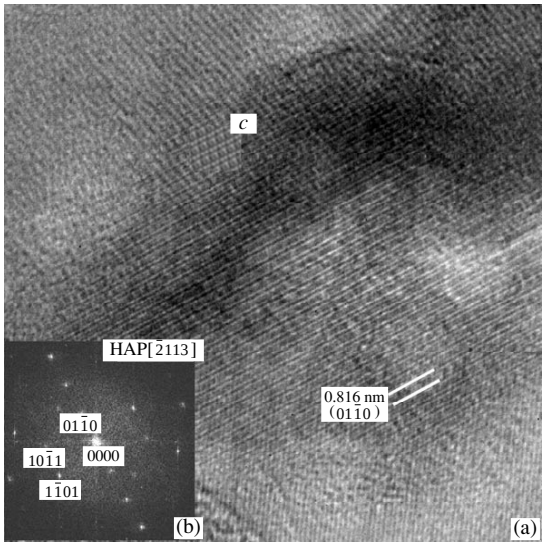

Fig. 2. (a) Experimental HREM images with the zone axis close to the [$\bar{2}$113] direction, (b) the corresponding Fourier transform with the zone axis close to [$\bar{2}$113] obtained from this image, and (inset *c*) the corresponding theoretical images with the same zone axis simulated for the defocusing value of 48 nm and the crystal thickness of 1.2 nm.

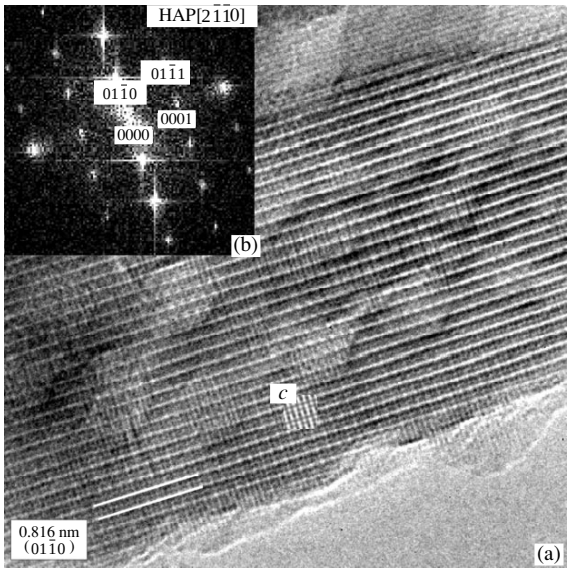

Fig. 3. (a) Experimental HREM image obtained with the zone axis close to the [2$\bar{1}\bar{1}$0] direction. The (01$\bar{1}$0) planes with the interplanar spacing 0.816 nm are parallel and the (0001) planes with the interplanar spacing 0.69 nm are normal to the crystal edge, (b) the corresponding Fourier transform with the zone axis close to [2$\bar{1}\bar{1}$0] obtained from the image in (a), and (inset *c*) the theoretical image with the same zone axis simulated for the defocusing value of 64 nm and the crystal thickness of 0.9 nm.

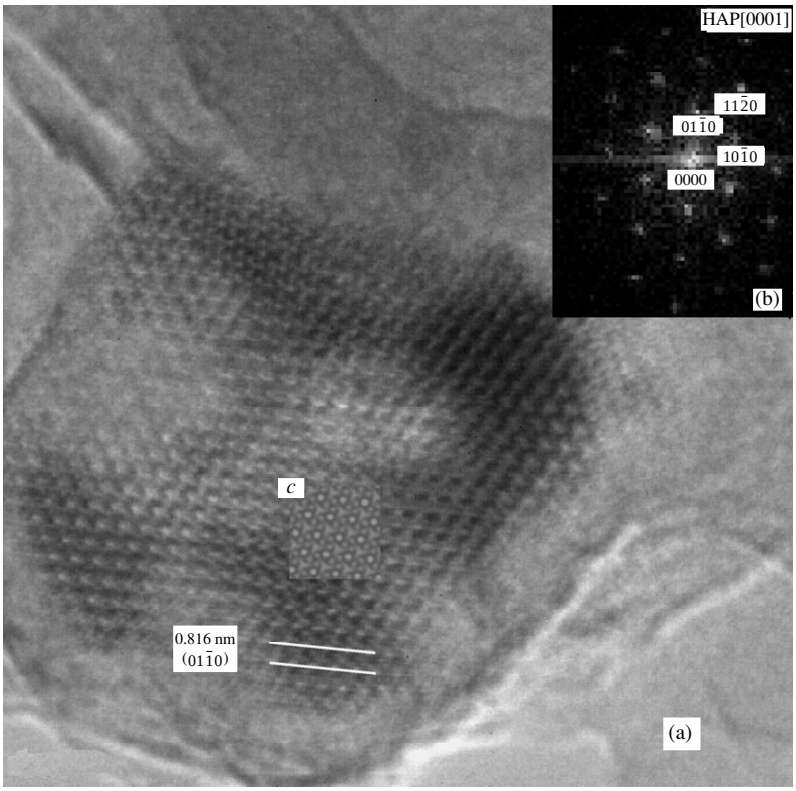

Fig. 4. (a) Experimental HREM image obtained from the crystal with the zone axis close to the [0001] direction, (b) the corresponding Fourier transform with the zone axis [0001], and (inset *c*) the theoretical image with the same zone axis simulated for the defocusing value of 50 nm and the crystal thickness of 0.7 nm.

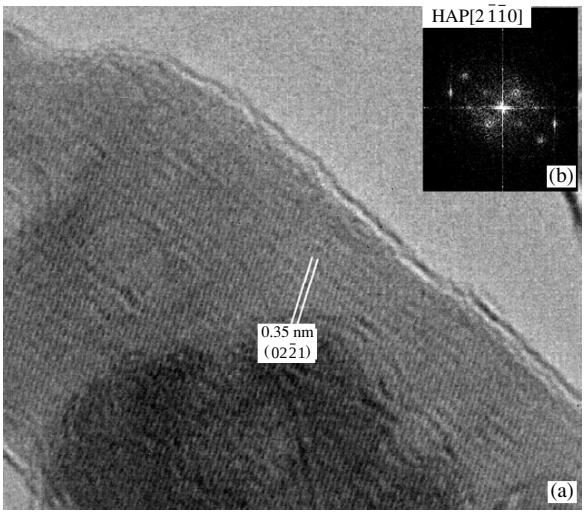

Fig. 5. (a) Experimental HREM image with one visible system of $(02\bar{2}1)$ planes with the interplanar spacing 0.35 nm, (b) the corresponding Fourier transform with two bright reflections from the $(02\bar{2}1)$ planes. The remaining weak reflections yield the $[2\bar{1}\,\bar{1}0]$ orientation.

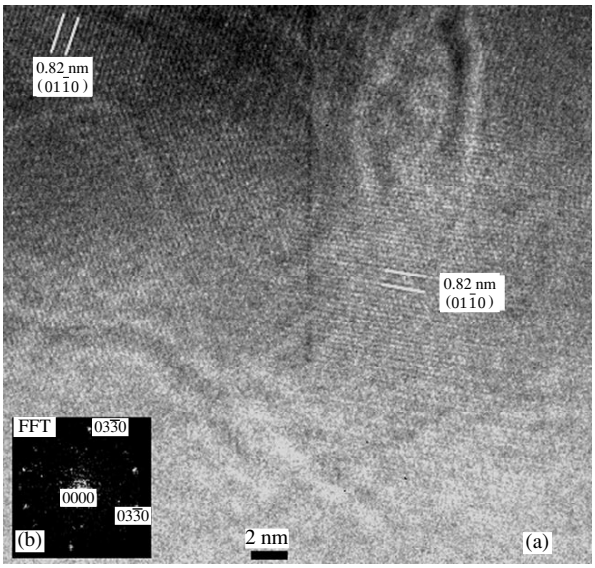

Fig. 6. (a) HREM image of polycrystal hydroxyapatite particle and (b) the corresponding Fourier transform. Only two grains are seen in the vicinity of $(01\bar{1}0)$ plane.

formed within the thickness range from one up to ten unit-cell parameters (i.e., within 0.68–9.0 nm for crystals of various orientations) and the defocusing value within the range from –100 to 100 nm. The satisfactory agreement between the theoretical and experimental HREM images at reasonable defocusing values (close to the Scherzer defocusing, i.e., about 50 nm) was attained for thicknesses ranging from one to five unit-cell parameters (0.68–5.0 nm).[1]

Figure 2a shows the high-resolution electron micrograph obtained from one of the crystallites. The $[\bar{2}113]$ crystal orientation was determined from the Fourier transform shown in Fig. 2b, the theoretical image (inset *c*) obtained for the defocusing value of 48 nm at the crystal thickness of 1.2 nm coincided with the experimental HREM image. Another orientation of the HREM image, $[\bar{2}\,\bar{1}10]$, and the corresponding Fourier transform are shown in Figs. 3a and 3b. The theoretical image (Fig. 3a, inset *c*) was modeled at the defocusing value of 64 nm and the crystal thickness of 0.9 nm. The HREM image (Fig. 3a) shows the crystal edge and the parallel $(01\bar{1}0)$ and the perpendicular (0001) planes. The formation of the forbidden 0001 maximum on the Fourier transform (Fig. 3b) can be explained by several causes, one of which is a the small thickness of the crystal. Comparing the HREM images in Figs. 2 and 3 obtained at different zone axes, we determined the exact crystal orientation with respect to the preferable growth direction. Hexagonal hydroxyapatite crystals had the shape of platelets elongated in the direction of the maximum growth rate—[0001].

The hydroxyapatite crystals with the zone axis [0001] are formed less often. In Fig. 1a, these crystals have the shape of hexagonal platelets. Figures 4a and 4b show the experimental HREM images and the corresponding Fourier transforms obtained normally to the [0001] direction. The theoretical image in inset *c* (Fig. 4a, inset *2*) was simulated at the defocusing value of 50 nm and the crystal thickness of 0.7 nm.

Figure 5a shows the crystal images in which only one system of planes is seen. On the corresponding Fourier transform (Fig. 5b), these are the brightest reflections from the $(02\bar{2}1)$ planes. However, the weak reflections on this Fourier transform provide the establishment of the orientation close to $[\bar{2}\,\bar{1}10]$ (cf. with Fig. 3b) with the (0001) planes being normal to the crystal edge, which confirms once again the preferable crystal growth along the [0001] direction.

The change of the contrast on the experimental HREM images (especially clearly seen in Fig. 3a) is caused by the beam-induced structural changes in the crystals. With an increase of the irradiation time or the beam intensity, we observed the formation of light rounded domains and, somewhat later, specimen amorphization (which was seen from the change in the initial diffraction pattern sometimes obtained from rather large crystals).

We grew both hydroxyapatite single crystals and finely granular polycrystals (Fig. 6), with the former

[1] In the EMS program used for simulation of HREM images, the positive values correspond to defocusing [4].

being always prevailed. The analysis of HREM micrographs from these crystals showed that they grew mainly along the *c*-axis. Another type of crystals (less often encountered) had the shape of almost hexagonal platelets with the [0001] orientation. The length and the width of hydroxyapatite crystals were within the range whose lower limit could be determined by the HREM method—it was equal to several nanometers. The upper limit ranged from several nanometers up to several tenths of a micrometer. The crystal thickness varied from one to several unit-cell parameters.

Thus, hydroxyapatite crystals were grown from aqueous solutions. Studying them by the method of high-resolution electron microscopy leads to the following conclusions. The crystals usually grow along the [0001] direction, with the $(01\bar{1}0)$ planes being parallel to the crystal edge. Another type of crystal morphology is [0001]-oriented hexagonal platelets.

The satisfactory agreement between the experimental and simulated HREM images was obtained for crystals whose thickness varied from 1 to 5 lattice parameters, which indicated the formation of very thin (of several lattice parameters) platelets of hydroxyapatite crystals in the solution.

ACKNOWLEDGMENTS

The authors are grateful to V. V. Klechkovskaya for valuable remarks and V. E. Bozhevol'nov for his help in crystal synthesis. Electron microscopy studies were performed at the Center of Electron Microscopy Studies of the Polytechnical University of Lausanne (CIME–EPFL), Switzerland and was supported by the Swiss company Oerlikon Contraves AG (Zürich). The hydroxyapatite crystals were grown at the Chemistry Department of Moscow State University. The study was also supported by the Russian Foundation for Basic Research, project no. 97-03-32976.

REFERENCES

1. M. Gregoire, I. Orly, and J. Menanteau, J. Biomed. Mater. Res. **24**, 165 (1990).
2. E. I. Suvorova, F. Christensson, H. E. Lundager Madsen, and A. A. Chernov, J. Cryst. Growth **186**, 262 (1998).
3. M. I. Kay, R. A. Young, and A. S. Posner, Nature **204**, 1050 (1964).
4. P. A. Stadelmann, Ultramicroscopy **21**, 131 (1987).

Translated by L. Man

Crystallography Reports, Vol. 45, No. 5, 2000, pp. 862–870. Translated from Kristallografiya, Vol. 45, No. 5, 2000, pp. 935–943.

CRYSTAL GROWTH

Convection in Melts and Impurity Distribution in Semiconductor Crystals

P. K. Volkov, B. G. Zakharov, and Yu. A. Serebryakov

Space Materials Research Center, Shubnikov Institute of Crystallography, Russian Academy of Sciences, ul. Akademicheskaya 2, Kaluga, Moscow oblast, 248640 Russia

e-mail: volkov@academ.kaluga.su

Received April 8, 1998; in final form, October 13, 1998

Abstract—Impurity distributions in semiconductor melts and crystals grown from these melts are experimentally and numerically studied on an example of Ga-doped Ge crystals. It is shown that inhomogeneous dopant distribution is observed in the form of striations and is caused by the convective flows in the melt and their nonstationary rearrangement in the vicinity of the crystallization front. The character of heat and mass transfer under the microgravity conditions is predicted. The necessity of precision experiments under terrestrial and, especially, space conditions is emphasized. © *2000 MAIK "Nauka/Interperiodica".*

INTRODUCTION

Convective processes occurring during growth of single crystals play a dual role. First, intense convective motion provides the formation of melts with uniformly distributed impurities. Second, nonstationary convection occurring in the vicinity of the crystallization front during melt crystallization provides impurity ordering along streamlines. Elements of this order are introduced into a growing crystal in the form of striations, which can be recorded because of the local changes in resistivity and, metallographically, as the variations in the crystal structure and properties. Thus, the convective processes occurring in the melt are responsible for the impurity distribution both in the melt and in the crystal grown from this melt.

The above stated is confirmed by the estimates of the heat- and mass-transfer coefficients made in mechanics of continuous media. Thus, the Schmidt number (the diffusion Prandtl number) in semiconductor melts exceeds ten, and, therefore, the convective component becomes more important than the diffusion one in the equation of impurity transfer. The heat transfer processes in semiconductor melts are of the diffusion nature. Melts show considerable heat conductivity. The corresponding Prandtl number for melts is rather low (of the order of 0.01), which indicates that the convective component in the heat transfer equation is unimportant.

The above conclusions on the nature of heat and mass transfer made on the basis of the Prandtl and Schmidt numbers are of the qualitative character. A more accurate estimation requires the knowledge of the coefficients in the transfer equations. The transition to dimensionless quantities results in the appearance of an additional coefficients before the Prandtl and the Schmidt numbers.

Below, the effect of convection on heat and mass transfer in melts caused by the varying external conditions is evaluated from the solution of the system of Oberbeck–Boussinesq equations. The convective processes in melts are calculated theoretically and compared with the results of the Ge(Ga) crystallization by the Bridgman method with heating from above performed under the terrestrial conditions. The effect of convection on crystallization under the microgravitation conditions is also estimated.

MATHEMATICAL MODEL

To describe the processes taking place in melts, we used the system of Oberbeck–Boussinesq equations [1, 2]. Consider a cylindrical domain bounded by a cylindrical solid surface and filled with a melt (Fig. 1). The upper surface is free; the lower solid surface is characterized by the melting-point temperature.

We consider an axisymmetric heating from the side surface of the cylinder and from above. Then, the free surface is characterized by a radial temperature drop. In this case, the characteristic flow velocity and the flow pattern in the melt cannot be determined *a priori*. Therefore, the introduction into consideration of any external velocity has no sense. It is more expedient to use a quantity determined by the input parameters of the medium. It is expedient to use an analogous scale as a characteristic linear dimension. Let ρ_0, σ_0, and g be the characteristic values of the density, surface tension, and free fall acceleration. In our consideration, we use the following characteristic quantities: the capillary Laplace constant for the dimension L and the velocity U:

$$\delta_\sigma = (\sigma_0/g\rho_0)^{1/2} = L$$

and

$$U = (\sigma_0 g/\rho_0)^{1/4}.$$

1063-7745/00/4505-0862$20.00

Using L and U from [3] ($t = (L/U)t' = (\delta_\sigma/g)^{1/2}t'$), we arrive at the following motion equations and the boundary conditions in the dimensionless form (the primes are omitted):

$$\frac{\partial V}{\partial t} + \mathbf{V}\nabla\mathbf{V} = -\nabla P - (1 - \mathrm{Gr}\theta)n_z + \mathrm{Re}_g^{-1}\nabla^2\mathbf{V}, \quad (1)$$

$$\mathrm{div}\mathbf{V} = 0,$$

$$\frac{\partial \theta}{\partial t} + \mathbf{V}\nabla\theta = \frac{1}{\mathrm{Re}_g\mathrm{Pr}}\nabla^2\theta, \quad (2)$$

$$\frac{\partial C}{\partial t} + \mathbf{V}\nabla C = \frac{1}{\mathrm{Re}_g\mathrm{Sc}}\nabla^2 C, \quad (3)$$

$$P - \frac{2}{\mathrm{Re}_g}\mathbf{n}\cdot D\cdot\mathbf{n} = H + P_a, \quad (4)$$

$$2\boldsymbol{\tau}\cdot D\cdot\mathbf{n} = -\mathrm{Re}_g\mathrm{Mn}\nabla_\Gamma\theta, \quad (5)$$

where t is the time, $\mathbf{V}$ is the velocity vector, P is pressure, θ is the temperature, C is the impurity concentration, $\mathrm{Gr} = \beta\Delta\theta$ the Boussinesq number, $\mathrm{Re}_g = \left(\frac{\sigma_0^3\rho_0}{g\mu^4}\right)^{1/4}$ is an analogue of the Reynolds number, $\mathrm{Pr} = \nu/k_T$, $\mathrm{Sc} = \nu/k_C$ are the Prandtl and Schmidt numbers, respectively, $\mathrm{Mn} = k_\sigma\Delta\theta$ is the analogue of the Marangoni number, μ, ν, β, k_T, k_C, and $\Delta\theta$ are the coefficients of the dynamic and kinematic viscosity, temperature expansion, thermal diffusivity, diffusion, and temperature drop, respectively, $\mathbf{n}_z$ is the unit vector directed opposite to the force of gravity, $\boldsymbol{\tau}$ and $\mathbf{n}$ are the tangential and normal vectors on the free surface, D is the tensor of the deformation rates, H is the surface curvature, P_a = const is the pressure on the free surface Γ, $\nabla_\Gamma\theta$ is the temperature gradient along the free surface Γ (we use $\sigma = \sigma_0(1 - k_\sigma(\theta - \theta_0))$).

Of all the set of the boundary conditions, we only wrote here the dynamic conditions on the free surface, (4) and (5), because they can provide the motion from the free surface into the melt [3]. The solid walls are at rest and, therefore, the sticking conditions at the walls are fulfilled. We assume that all the other boundary conditions are also known.

Thus, the transition to dimensionless variables in the motion equations under the given boundary conditions results in the following minimum set of parameters [4]: Re_g, Gr, Pr, Sc, Mn, and P_a, which characterize the geometry of the domain under consideration or the boundary conditions not indicated above. As a result, the total number of the parameters increases by the number of the independent parameters. It should be indicated that for the given choice of L and U, the well-known Froud and Weber numbers are identically equal to unities. Therefore, the quantity g enters only Re_g, which allows one to predict the processes that can occur under microgravity.

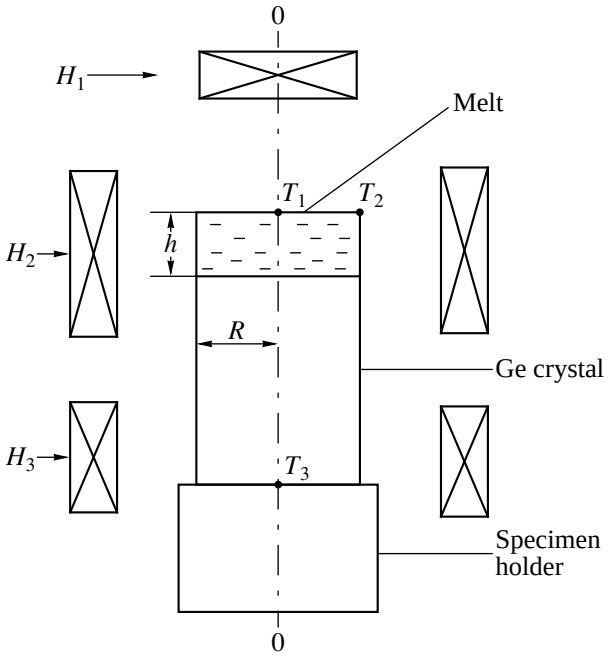

Fig. 1. Schematic of the experiment.

ANALYSIS OF DIMENSIONLESS NUMBERS

The parameter Re_g is determined in terms of the physical constants of the medium and g. For metal melts under earth conditions we have: $\mathrm{Re}_g \sim 4.5 \times 10^3$ [for Hg, Ge, and Ga melts]. This signifies that if a steady-state motion in the melt arises (e.g. due to thermocapillary or natural convection), a boundary layer of thickness $\delta \sim \mathrm{Re}_g^{-1/2}$ (or, in the dimensional form $\delta_p \sim 0.015\delta_\sigma$) is formed in the vicinity of the solid surface.

The parameter Gr is responsible for the changes associated with the variations in the liquid density. At the temperature drops of the order of 1°C, this parameter is rather small and comparable with the coefficient before the senior derivative in (1). However, its effect on the melt flow is quite considerable, because Gr determines the effect of the mass force in the whole volume. Outside the boundary layer, the term with Gr can exceed the value of the diffusion term.

The Prandtl number Pr is responsible for the character of heat distribution. In semiconductor melts, $\mathrm{Pr} \approx 0.05$. With due regard for the denominator, the coefficient before the senior derivative in (2) for the Hg, Ge, and Ga fluids is of the order of 0.1, which signifies that heat transfer has a noticeable convective component.

The Schmidt number Sc in metal melts is of the order of about ten, which shows the convective nature

of the dopant transfer. With due regard for the denominator in (3), the convective transfer becomes prevalent.

The effect of the parameter Mn is analogous to the effect of the Marangoni number. It is responsible for the motion arising on the free surface due to the change in the surface tension. In (5), Mn ≈ 350 at the temperature drop along the surface equal to 1°C, and, therefore, the effect of the parameter Mn on the hydrodynamics in the melt is essential [2].

The above estimates for media with high values of the parameter Re_g allow one to draw certain conclusions about the hydrodynamics and heat and mass transfer in the fluid. It should be emphasized that these conclusions were made in terms of the physical parameters of the fluid and the acceleration of gravity. The geometrical and other parameters can only either intensify or decrease heat and mass transfer.

The form of equations (1)–(5) allows the qualitative estimates of the hydrodynamic processes and heat and mass transfer caused by a decrease in g, which models the conditions of a space flight. Under the conditions of a free flight aboard the space station, the microaccelerations are usually on the order of 10^{-4}–10^{-5} of the acceleration of gravity, $g_0 = 9.8$ m/s^2 [5]. The values of Gr, Pr, Sc, and Mn in (1)–(5) remain constant (it is assumed that the physical characteristics, the equation of state, and the temperature behavior of σ are independent of g). The value of Re_g increases by more than an order of magnitude (~10^5). The coefficients before the senior derivative in equations of heat and mass transfer decrease by more than an order of magnitude. This signifies that under the microgravitation conditions, the inertial properties of a fluid become more pronounced, and the contribution from the convective component to heat and mass transfer increases. The influence of the Marangoni convection also becomes more pronounced.

APPROXIMATION OF A PLANAR FREE BOUNDARY

In the problems of natural convection in semiconductor melts and other low-viscosity fluids, the free surface is usually assumed to be planar [2]. In this case, condition (4) (used for the determination of the free surface [6]) is assumed to be valid. Thus, the degree of fulfillment of condition (4) is the criterion for using the approximation of the planar surface. It follows from (4) that at high Re_g values, the term including viscosity is small (Hg and semiconductor melts where $Re_g > 10^3$, whereas the situation $Re_g \longrightarrow \infty$ corresponds to the model of an ideal fluid). Therefore, in the absence of external perturbations of the free surface, in addition to the regions close to the vertical boundaries with the characteristic formation of a meniscus, the approximation of a planar surface is also fulfilled sufficiently well for any P_a.

OPEN TOP FREE SURFACE

Consider a liquid cylinder of height h and a radius R, which is limited by solid walls and by the solid bottom. The planar upper boundary is free. The computer simulation of the processes in the melt with the calculation of the equations of motion and heat transfer was performed using the COMGA package of programs [7]. The height h varied from 38 to 1.5 mm at R = 11 mm. The physical parameters of the medium corresponded to those of the Ga-doped Ge melt. The vertical temperature drop along the axis between the free surface and the cylinder bottom (at the crystallization temperature of Ge) was constant and had the value of 150°C. The temperature at the edge of the free surface was higher by one degree centigrade than the temperature along the axis. The vertical temperature profile at the side walls was set to be linear.

The dopant distribution was calculated for the stationary flow field under the conditions of the absence of flow at the side boundaries. For definiteness, the concentration on the upper and lower boundaries was taken to be constant (1 and 1.087, respectively). At the initial moment, the concentration distribution in the melt was set to be uniform (equal to unity). We solved the problem of the dopant distribution from the lower melt boundary to its free surface. The effect of convection on the dopant distribution along the concentration isolines was studied.

The boundary conditions corresponded to the conditions of the experiments on Ge(Ga) crystallization on a Zona 03 setup. A melted sample was kept under stationary conditions for several hours to attain the steady-state convection mode. The method used for calculation of the steady-state flow patterns corresponded to the initial convection in the melt. Since the crystallization rate was low, the hydrodynamics in the melt was determined mainly by the steady-state flow pattern and those variations in the vicinity of the crystallization front which could arise with a decrease of the melt height. We should like to emphasize the importance of establishing the rules governing the flow patterns at various melt heights.

Figure 2 shows the isolines of the flow pattern at various melt heights. Because of the Marangoni thermocapillary convection, the surface layer of the fluid on the free surface moves from the edge to the axis. As a result, a system of toroidal vortices is formed at the free surface and propagates downward with a decreasing intensity. At large heights of the melt, the lower region has an almost unperturbed state (Figs. 2a, 2b). With a decrease of the melt height, the flow pattern in the upper part is preserved, and only the lower part of the melt is changed.

With a decrease of the melt height, the melt velocity in the vicinity of the lower boundary, i.e., the crystallization surface, also increases. In this case, the flow direction along the lower boundary is periodically changed with disappearance of each vortex.

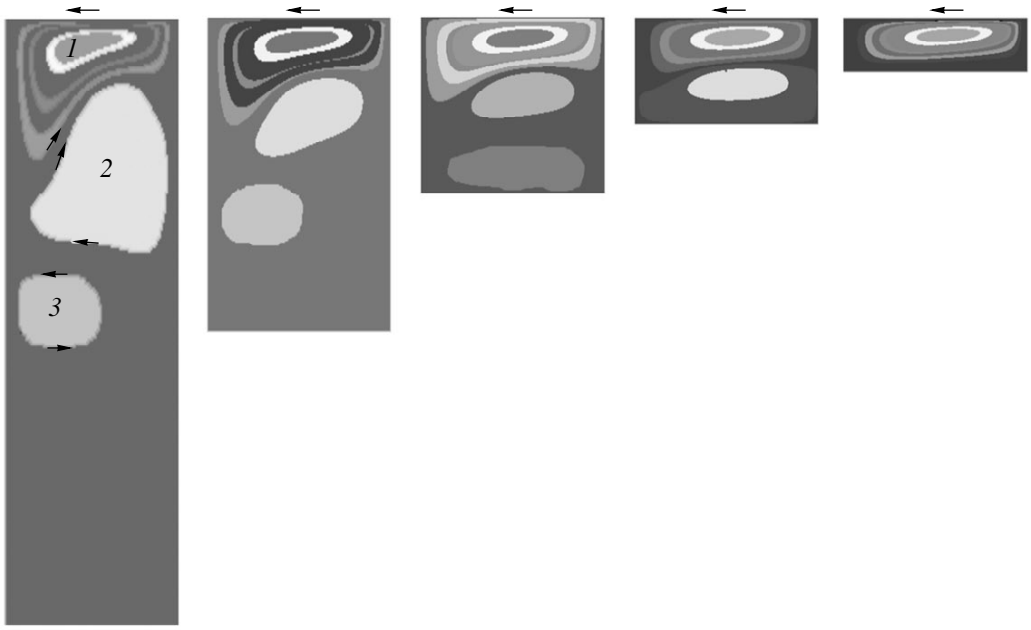

Fig. 2. Flow patterns at various heights of the melt column h: (a) 38, (b) 18, (c) 10, (d) 6, and (e) 3 mm; (a) $\psi_1 = 0.0163$, $\psi_2 = -0.00224$, $\psi_3 = 0.00007$; (b) $\psi_1 = 0.0158$, $\psi_2 = -0.00323$, $\psi_3 = 0.00003$; (c) $\psi_1 = 0.0154$, $\psi_2 = -0.004$, $\psi_3 = 0.00001$; (d) $\psi_1 = 0.0147$, $\psi_2 = -0.0042$; (e) $\psi_1 = 0.0123$ where ψ_1, ψ_2, and ψ_3 are the extreme values of the stream function characterizing the intensity (the absolute value) and the direction of rotation (the sign minus for vortex *2* indicates the reverse of the flow with respect to the flow for vortices *1* and *3*).

The same structure of the upper vortex for all the melt heights allowed us to estimate the melt velocity from the maximum absolute value of the stream function. For the data presented in Fig. 2, the melt velocity on the surface is of the order of 0.7 cm/s, which signifies that the Reynolds number along the radius is $\mathrm{Re} \approx 570$, which, in turn, evidences the developed melt flow in the subsurface layer. The Grashoff number calculated from the vertical temperature drop and the Marangoni number calculated from the radial temperature drop are equal to 10^5 and 10^3, respectively.

The temperature distribution has the layer character. In the sections h = const, the temperature can either decrease or increase, depending on the direction of the fluid motion—from the cold or from the hot edge. The temperature drop at the height of 2 mm from the crystallization surface is about 0.001°C and increases with the melt height attaining a value of 43°C at h = 6 mm. The maximum temperature drop is observed for the section of the most intense vortex. Thus, the maximum deviation from the linear temperature distribution along the vertical direction (characteristic of the diffusion-type temperature distribution) is observed in the region of the most intense vortex.

The dopant distribution shows the pronounced dependence on convection (Fig. 3). At large melt heights, the isolines in the vicinity of the lower surface indicate that the concentration distribution obeys almost a linear law along the vertical. At the melt heights less than 16 mm, the dopant has the radial distribution, which proves the existence of a considerable convective component.

The radial drop in concentration at a height of 2 mm from the lower surface in the layers with the thickness exceeding 18 mm amounts to 0.0002. At smaller distances from the free surface, it can attain the value of 0.02 and even higher. The average concentration values in the section are far from the linear law observed along the height. Thus, the diffusion nature of dopant transfer in the vicinity of the lower surface is rather conventional—it can exist only at large melt heights and very feeble laminar flows in the boundary layer.

One has to also indicate the nonmonotonic concentration distribution in the layers lying at different heights. The behavior of concentration is similar to the behavior of temperature. In the region of feeble lower flows, concentration usually decreases in the direction from the axis to the wall, which is explained by the existence of a stagnation zone in the lower right-hand "corner," caused by dopant transfer due to diffusion.

CLOSED UPPER FREE SURFACE

Figure 4 shows the melt flow for the closed upper surface, where the sticking conditions are set at the same temperature drop. Thus, the existence of the natural convection in this case results in the formation of a complicated pattern of the melt flow. The flow intensity (with respect to the stream function) is four times lower in the region of the upper vortex and even much lower

Fig. 3. Distribution of the dopant concentration in the melt corresponding to the velocity field shown in Fig. 2 at various heights of the melt column *h*: (a) 38, (b) 18, (c) 10, (d) 6, and (e) 3 mm.

in the remaining part of the melt, with the temperature fields being almost the same. The radial distribution of the concentration is visually noticeable at the melt height equal to 0.5.

RESULTS AND DISCUSSION

The above data show that the processes occurring in the melts are very complicated. The existence of the radial temperature drop at the upper boundary provides the development of multivortex convective motion in the melt. The substitution of the boundary conditions corresponding to the free surface by the sticking conditions changes the flow intensity alone but does not change the flow pattern. The flow caused by natural convection is the most intense in the upper part of the melt characterized by the maximum radial temperature drop.

With a decrease of the melt height, the number of vortices at different heights and their intensities are changed. This signifies that crystallization in the vicinity of the solid–liquid interface (crystallization front) results in rather intense dopant motion along various directions. The changes in the flow pattern give rise to nonstationary dopant redistribution in the melt and, thus, also in a growing crystal. Therefore, the dopant distributions at various crystal heights are also different. Proceeding from our calculations, the concentration variations within 1% occur at a depth of 15–

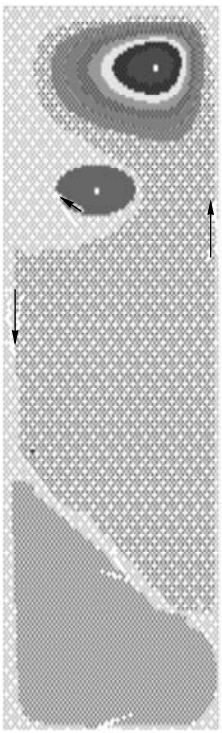

Fig. 4. Flow pattern in the melt with the closed upper boundary (h = 38 mm). The extremum values of the stream function in the vortex regions of the melt are $\psi_1 = 0.00392$, $\psi_2 = -0.00008$, and $\psi_3 = 0.00000$.

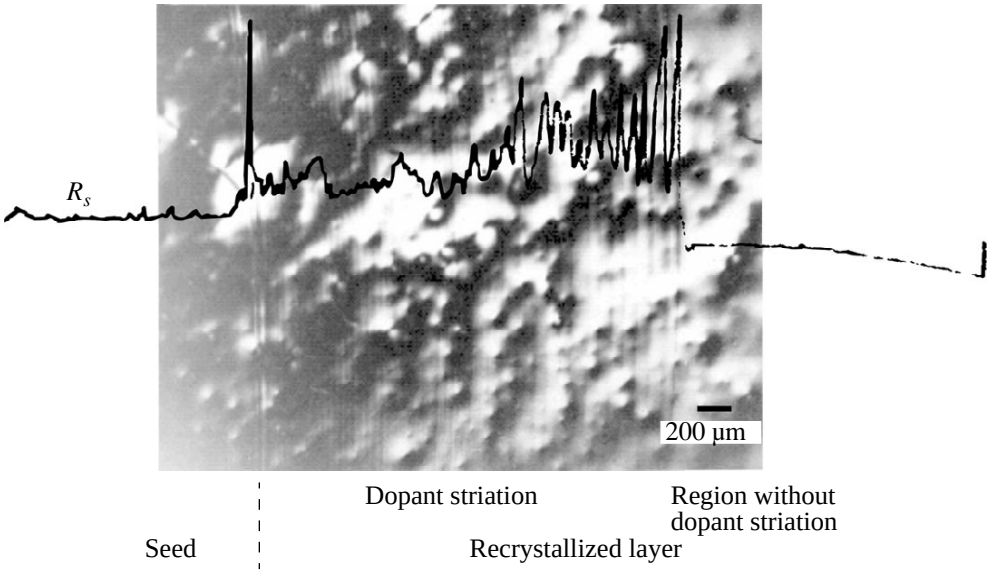

Fig. 5. Dopant distribution in the crystal at the open upper surface and the initial height of the melt column h = 6 mm for various flow patterns. Micrograph of the longitudinal (110) cut of a Ge(Ga) crystal and the distribution of the spreading resistivity R_S.

16 mm, with the convection rate attaining the values of about 0.0001 cm/s. (This estimate of the effect of the convection level on the dopant distribution coincides with the estimated concentration Pecklet number, which exceeds unity.) Thus, at the cylinder radius of the order of 10–15 mm and the temperature drop on the free surface of 1°C, the effect of the Marangoni convection on the dopant distribution in the crystal is noticeable at the melt heights $h < 18$ mm. If $h < 10$ mm, the vortices in the vicinity of the surface are more intense, and therefore, the dopant distribution in the crystal is less uniform.

Another important conclusion made from the shape of the liquid–solid interface is as follows. At large initial melt thicknesses, the melt has four main regions. These are the regions with vortices propagating downward from the free surface with decreasing intensities, whereas the remaining region is characterized by a weak melt motion on its bottom. At the initial stage of crystallization, the effect of hydrodynamics on the shape of the crystallization front (solid–liquid interface) is minimal, and the crystallization front should be planar. Then, the small temperature variations in the regions with vortices and the change in heat transfer can change the profile of the crystallization front.

The formation of the vortex region with the closed equal streamlines results, in turn, in the formation of regions having different local average dopant concentration levels, which change due to diffusion and variations in the flow pattern at the crystallization front. Then the dopant distribution in the crystal should form the regions with different average dopant concentrations along the crystal depth.

The existence of the solid surface at the upper part of the melt hinders the flow in the melt. Then, the corresponding characteristic features in the melt and the crystal are formed at smaller distances from the upper boundary.

EXPERIMENTAL

The experiments on crystallization of semiconductor crystals from melts were aimed to grow single crystal semiconductors with perfect structure and homogeneous microstructure. The existence of microinhomogeneities in the dopant distribution is essentially dependent on convection intensity [8]. The effect of the convection level in the melt is reduced by its heating from above and the directional (upward) crystallization. Taking into account that dopant transfer is of the convective nature, this method seems to be quite justified.

The experiments were performed on a Zone 03 setup. The schematic of the experiment is shown in Fig. 1. Heaters H_1, H_2, and H_3 create the thermal conditions necessary for obtaining a melt column of the height h on the upper surface of a single crystal placed into a graphite container. The melt height in the experiments is attained by an appropriate choice of the temperature at the upper, T_1, and lower, T_3, ends of the single crystal and by the appropriate positioning of the crystal with respect to heaters. The directional crystallization is provided by the upward motion of the heaters with respect to the melt or by a decrease of the heater temperature according to a linear law.

The Ga-doped (up to a level of 5×10^{18} cm^{-3}) Czochralski grown <111> Ge single crystals were used for recrystallization. The prepared cylindrical samples were 22.5 mm in diameter and 35 mm in length. The melt height varied from 1 to 24 mm. Depending on the

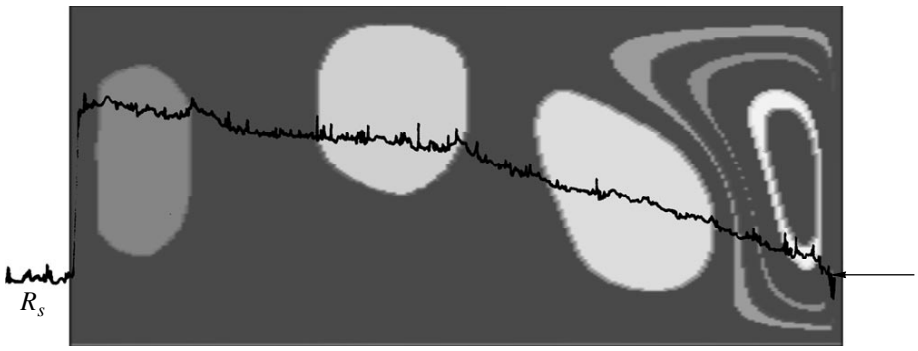

Fig. 6. The calculated flow pattern for the initial height of the melt column h = 22 mm and the experimentally measured spreading resistivity curve, R_s, in a Ge(Ga) crystal.

melt height h, the vertical temperature gradients ranged within $\Delta T/h$ = 20–150 deg/cm, the radial temperature drop on the free surface of the melt was ΔT_r = 3–5°C.

The recrystallized samples were cut along the growth direction into 1.5 mm-thick (110)-oriented plates. In order to remove the disturbed layers, the plate surfaces were subjected to special treatment with the subsequent chemical–mechanical polishing.

The layer dopant distribution in the crystals, the crystallization-front shape and the dislocation distribution and density were studied by the metallographic methods. The resistivity was measured by the standard four-probe method. The specific features of dopant (charge carrier) micro- and macrodistribution were studied by the method of spreading resistivity. The measurements were performed during gliding of the measuring-probe over the sample. The probe diameter at the site of the probe location on the sample was 10 μm.

The samples recrystallized from the melt layers of various thicknesses had the single crystal structure. The dislocation densities in the initial and the recrystallized single crystals were of the same order of magnitude and, on the average, ranged within 10^2–10^3 cm^{-2}. The structure of the recrystallized layer differed from the initial single crystal structure by the pronounced striation.

OPEN UPPER BOUNDARY

The dopant distribution manifested itself in striation of samples recrystallized at $h \approx 6$ mm (Fig. 5, a high crystallization rate, the heater temperatures was decreased by the linear law at a rate of 20°C/min). One can clearly see three regions in the samples. Two striated regions spaced by different distances—$d \approx$ (40–50) μm for the first one (located for about 1.5 mm from the seed) and $d \geq 100$ μm in the second region (located at about 2.5 mm from the free melt boundary). The third region showed no striation at all. These features were confirmed by measurements of the spreading resistivity R_s. In the second region, the variation in R_s coincides with the striation period. The striation pattern and the R_s distribution agree with the calculated flow patterns in the melt and the concept of the convective dopant transfer (Figs. 2d, 2e and 3d, 3e).

At considerable melt heights, the spreading resistivity also corresponds to the experimental flow patterns. Figure 6 was obtained at a low crystallization rate and the heaters moving with a velocity 2.73 mm/h for the melt height h = 22 mm. The arrow indicates the distance at which the measurements were made. The plot of R_s has the characteristic features caused by the flow pattern in the melt. The regions with the constant level of the average concentration are separated by the regions with the drastic concentration variations, which can be interpreted by changes of the vortex structures in the vicinity of the crystallization front. Striation at high melt heights is usually observed at a distance of 17–18 mm and disappear at a distance of 2–3 mm from the upper edge. In this case, the striation patterns are different. There are also small regions with feebly marked striation.

CLOSED MELT SURFACE

If the melt surface is completely closed by a graphite plate, the striation in the recrystallized samples is observed at smaller distances from the crystal top than in the case of an open surface (Fig. 7) even if the setup is inclined with respect to the vertical direction. In some experiments, the surface was closed only partly, so that the part of the meniscus close to the wall was open. In these cases, some diffuse stria were formed at the depths of the order of 7–11 mm; they disappeared at a distances of 3–4 mm from the upper edge.

The crystallization front was concave to the crystal at the initial growth moment and large melt heights. However, at the melt height of 9 to 11 mm, the front shape changed and became convex to the melt.

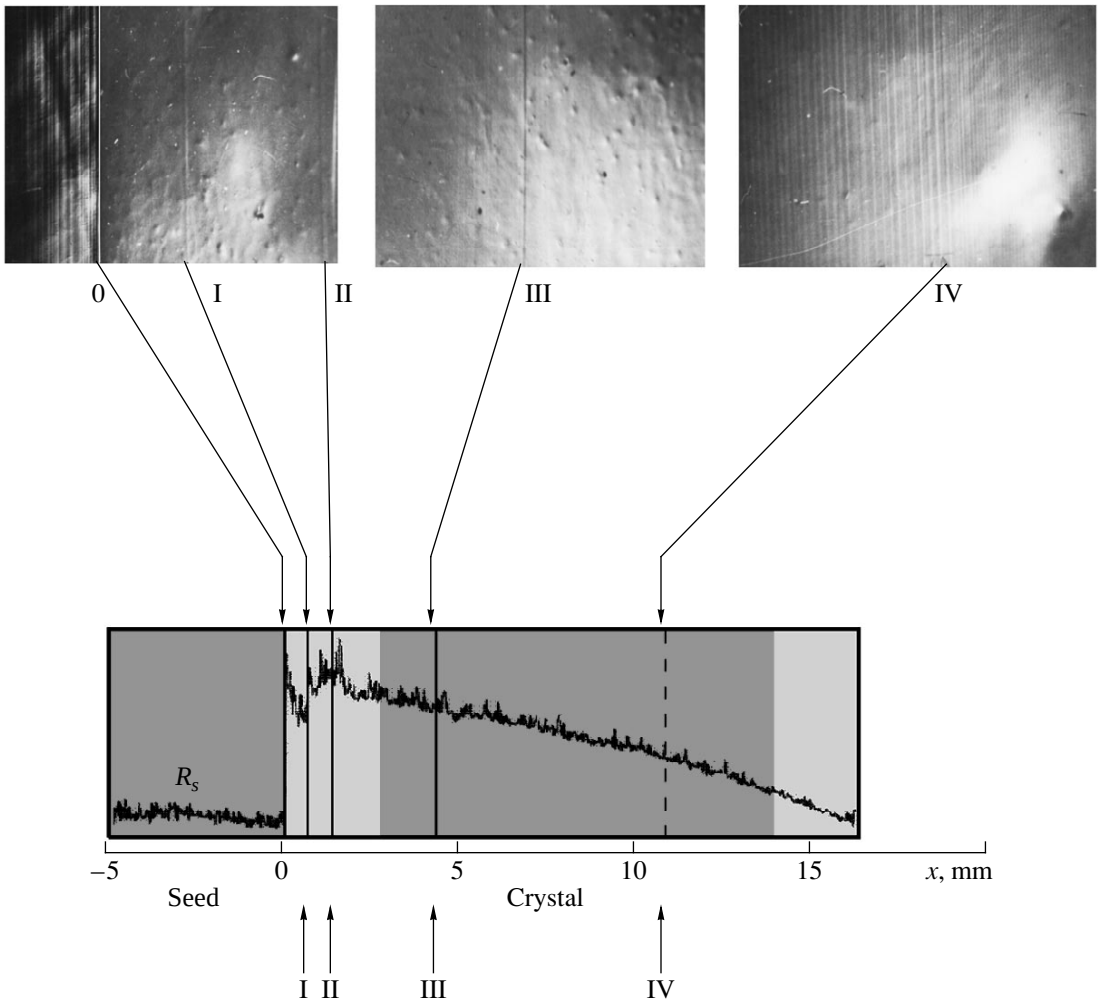

Fig. 7. The structure of microinhomogeneities and the spreading resistivity curve, R_s, for a Ge(Ga) crystal. (The melt surface is covered with a graphite plate); I, III, and IV have striation formed under the pulse action (t = 1 s), II is striation obtained at 5° setup deviation from the vertical position. The dark region on the lower scheme is the striation region, the light region has no striation at all.

CONCLUSIONS

The calculated data provide almost complete information about the flow pattern and the temperature and dopant distribution in the melt for steady-state modes. These results can be used to predict the processes of nonstationary crystallization occurring at high and low crystallization rates. In the former case, the crystallization rate should be so high that the boundary layer at the solid–liquid interface had not enough time to form. The dopant concentrations in the crystal and in the melt are almost the same, i.e., their distribution coefficients are k = 1. Figure 5 is typical for this situation. In the latter case, the crystallization rate should be considerably less than the rate of the boundary-layer development. Thus, one has to take into account the concentration boundary layer and the corresponding displacement of the dopant from the crystallization front. The characteristic distribution of the spreading resistivity is shown in Figs. 6 and 7. In both cases, the determining factor for the dopant distribution is the steady-state velocity field and the flow pattern. The comparison of the calculated and the experimental data shows a good correspondence between the velocity fields and the characteristic features of the spreading-resistivity distribution.

The calculations and the experiments performed show that weak convective motion caused by the thermocapillary or the natural convection gives rise to striation in crystals only if the convection intensity exceeds a certain value. The critical value of the convection rate can be estimated from the concentration Pecklet number (equal to unity). The periodic alternation of the groups of stria is associated with the nonstationary changes in the flows and the direction of the melt motion in the vicinity of the crystallization front.

The absence of striation at the final stage of the crystallization is explained by two factors—either a high growth rate at this moment (a small vertical temperature drop) or the disappearance or considerable decrease of the convection source in the melt (a radial temperature drop). More precise information can be

obtained from a more detailed study of the effects of the radial and the vertical temperature drop on the processes occurring during melt crystallization.

The study of heat and mass transfer under terrestrial and space conditions indicates the necessity of performing more accurate experiments (especially under microgravity conditions) with the aim of determining the threshold of the steady-state flow in the boundary layer under the effect of various external mechanical factors. The experiments show that various mechanical factors can give rise to formation of well-pronounced striation in the crystal regions either having no striation or with already existing regular striation.

REFERENCES

1. D. Joseph, *Stability of Fluid Motions* (Springer-Verlag, Heidelberg, 1976; Mir, Moscow, 1981).
2. V. I. Polezhaev, M. S. Bello, N. A. Verezub, *et al.*, *Mathematical Simulation of Convective Heat and Mass Transfer Based on the Navier–Stokes Equations* (Nauka, Moscow, 1987).
3. G. K. Batchelor, *An Introduction to Fluid Dynamics* (Cambridge University Press, Cambridge, 1967; Mir, Moscow, 1973).
4. L. I. Sedov, *A Course in Continuum Mechanics* (Nauka, Moscow, 1970; Wolters-Noordhoff, Groningen, 1971–1972).
5. S. D. Grishin, V. B. Dubovskiĭ, S. S. Obydennikov, and V. V. Savichev, *Technological Experiments under Microgravity* (Ural'skiĭ Nauchn. Tsentr, Sverdlovsk, 1983), p. 6.
6. C. I. Christov and P. K. Volkov, J. Fluid Mech. **158**, 341 (1985).
7. N. K. Ermakov, S. A. Nikitin, and V. I. Polezhaev, Izv. Ross. Akad. Nauk, Mekh. Zhidk. Gaza, No. 3, 21 (1997).
8. G. Muller, *Crystal Growth from the Melt* (Springer-Verlag, Berlin, 1988; Mir, Moscow, 1991).

Translated by L. Man

Crystallography Reports, Vol. 45, No. 5, 2000, pp. 871–886. Translated from Kristallografiya, Vol. 45, No. 5, 2000, pp. 944–960.

In memory of Professor V.V. Titov

Effect of Various External Factors and Pretransitional Phenomena on Structural Transformations in Cholesteric Liquid Crystals

G. S. Chilaya

Institute of Cybernetics, Academy of Sciences of Georgia, Sandro Euli 5, Tbilisi, 380086 Georgia

Received June 9, 1998; in final form, June 6, 1999

Abstract—The publications on low-molecular thermotropic liquid crystals with cholesteric structures have been reviewed. The effect of an applied electric field on cholesteric structures is studied. Bistability of the cholesteric–nematic transition, electric field-induced color textures of cholesteric mixtures, and electro-optics of amorphous cholesteric structures are considered as well as pretransitional (blue and TGB) phases, discotic cholesterics, PDLC films, flexoelectric electro-optics, and photostimulated switching in cholesterics. © *2000 MAIK "Nauka/Interperiodica".*

CONTENTS

INTRODUCTION

As is well known, supramolecular periodic helical structure of cholesteric liquid crystals (CLC) is highly sensitive to the various external factors [1]. Recently, a large number of articles on the studies of cholesteric liquid crystals have been published. This is associated, first and foremost, with the preparation of polymer dispersed liquid-crystal (PDLC) films [2], and the studies of both pretransitional frustrated phases (twist grain boundary [3] and blue [4] phases, TGB and BP) and new electrooptical effects [5] including flexoelectric ones [6].

According to the commonly accepted classification, there are two classes of liquid crystals (LCs)—nematic and smectic liquid crystals. Nematic liquid crystals (NLCs) or simply nematics are characterized by orientational order, whereas smectic liquid crystals (SLCs) or simply smectics are characterized not only by the orientational order, but also by a layer packing. Smectics possess polymorphism. The simplest smectics are *A* and *C* smectics. In type-*A* smectics (S_A), the "long" axes of the molecules are oriented normally to the smectic layers. In type-*C* smectics, the long axes of the molecules are tilted to such layers. In fact, *A*-smectics are not as simple as they seem at first glance. Thus, liquid crystal phases of some compounds and mixtures whose structures are formed by polar or sterically asymmetric molecules can have dimers, frustrated structures, reentrant phases, etc. [7–10]. As is shown below, the existence of these complicated structures can result in the formation of pretransitional phases in liquid crystal systems including chiral ones.

In nematic and smectic *C*-type liquid crystals with chiral molecules and in mixtures of nonchiral nematics and *C*-smectics with chiral molecules, the helical structures are formed, i.e., the so-called chiral nematics (cholesterics) or chiral *C**-smectics with the spatially modulated period *P* (where *P* is the helix pitch). The helix pitch can vary from several microns to several hundreds of microns in various chiral systems.

At large values of the helix pitch, $P \gg \lambda$ (where λ is the wavelength of visible light), the light propagating parallel to the optical axis can be considered as the superposition of two eigenwaves with electric vectors

1063-7745/00/4505-0871$20.00

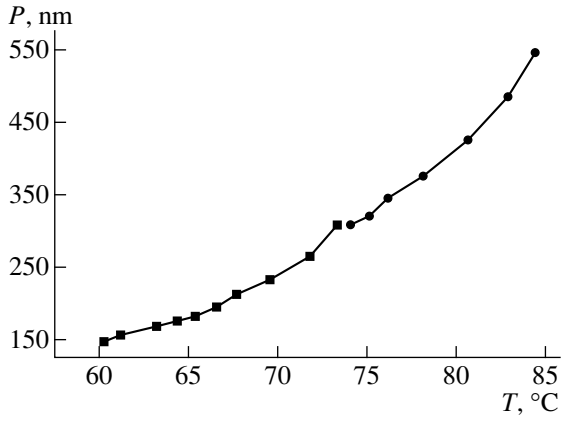

Fig. 1. Temperature dependence of the helix pitch in chiral smectic *C** liquid crystal. The mixture of 4,4'-diheptylazoxybenzene (50 wt %) + optically active 2,5-di-[4-(2-chloropentanoyloxy) phenyl]-pyrimidine [15].

parallel and normal to the local optical axis (director). This case was first considered by Mauguin [11]. A similar configuration is also formed as a result of mechanical twist of nematics and is used in conventional twisted liquid-crystal cells [12] operating in the waveguide mode (twist is followed by the formation of polarized modes).

If the wavelength of the visible light, λ, is comparable with *P*, the chiral liquid crystal provides optical diffraction satisfying the Bragg condition

$$m\lambda_0 = 2Rn\cos\varphi, \quad (1)$$

where *m* is the diffraction order, *n* is the refractive index of the medium, *R* is the period, and φ is the angle of light incidence. Measuring λ_0, one can determine the helix pitch *P*, which equals *R* for smectics and 2*R* for cholesterics.

Since in cholesterics the period corresponds to a half-pitch and in chiral smectics, to an integer number of pitches, then, at the oblique light incidence with respect to the helix axis, the measurements in chiral smectics can be made at the wavelengths twice shorter than for cholesterics [13]. Assuming that in CLCs (where $n = 1.5$), the light absorption occurs up to the wavelength of $\lambda = 300$ nm, it becomes clear that in CLCs, the helix pitch *P* less than 200 nm cannot be determined. For chiral smectics *C**, the minimum measurable pitch *P* is 100 nm. Here, the angle of light incidence is ignored, because it gives only insignificant correction at φ close to zero. Recently, even a lower value of a helix pitch (of the order of $P \approx 145$ nm) was measured for a chiral smectic *C** (Fig. 1) [14, 15].

1. CHOLESTERICS IN ELECTRIC FIELDS

Depending on the surface treatment (the boundary conditions), the helix pitch *P*, the ratio of the cell thickness *d* to *P* (the *d*/*P* ratio), the value and the sign of dielectric anisotropy, $\Delta\varepsilon$, the amplitude and frequency of an applied electric field, various electrooptic effects can be observed in cholesterics. To a large extent, all these effects are determined by the changes in the cholesteric texture. There are three main types of cholesteric textures—planar (Grandjean, *Gj*), fingerprint and focal conic (*F*) textures. In addition, there also exist the so-called superstructures [16, 17, 18] and amorphous cholesteric textures [19] (some of these textures are shown in Fig. 2).

In cholesteric liquid crystals with $\Delta\varepsilon < 0$, the memory effect of the dynamic light scattering was observed [20], i.e., the application of a low-frequency electric field provided the formation of a scattering texture, which did not disappear upon field switching-off. The texture formed can be "erased" only by applying a high-frequency electric field. The assumption that this effect is associated with the transformation of the focal conic texture into planar one was first made in [21]. Later, it was experimentally shown that the frequency of the "erasing field" is inversely proportional to the time of dielectric relaxation [22].

For chiral liquid crystals with $\Delta\varepsilon > 0$ and the initial fingerprint texture, the application of a more intense electric field results in helix unwinding. At a certain voltage V_{sw}, the helix completely untwisted, and the texture transformed into a homeotropic nematic. In other words, a cholesteric–nematic transition takes place. This theoretically predicted effect [23, 24] was confirmed experimentally in [25, 26]. In this case,

$$V_{sw} = \frac{\pi^2 d}{P}\left(\frac{4\pi K_{22}}{\Delta\varepsilon}\right)^{1/2}, \quad (2)$$

where K_{22} is the torsion elasticity modulus.

If the initial texture in a CLC is planar and an electric field is applied parallel to the helix axis, the situation becomes more complicated. In this case, the conical—helical perturbation results in helix tilt and formation of various regular domain structures. Depending on *d*, *P*, frequency of an applied electric field, and the boundary conditions, various effects are observed, which are differently interpreted. Thus, it was shown [27–29], that if $P \approx \lambda$, the maximum of the selective light reflection in an electric field is shifted toward short wavelengths (the so-called blue shift). It was assumed that the helix deformation gives rise to its "compression" and, thus, the shift of λ_0 toward short wavelengths [30]. However, it was shown [24] that this shift is caused by the texture destruction, rather than by helix compression. In [31], it was shown that the formation of a helix-pitch gradient in CLCs can also give rise to the blue shift. In all the discussed cases, an increase of the voltage applied to the CLC results in the texture transformation, first, into focal conic, and, then, into homeotropic. The detailed study of the planar texture of a cholesteric with the helix pitch $P > 5$ μm in an electric field was performed in [32, 33].

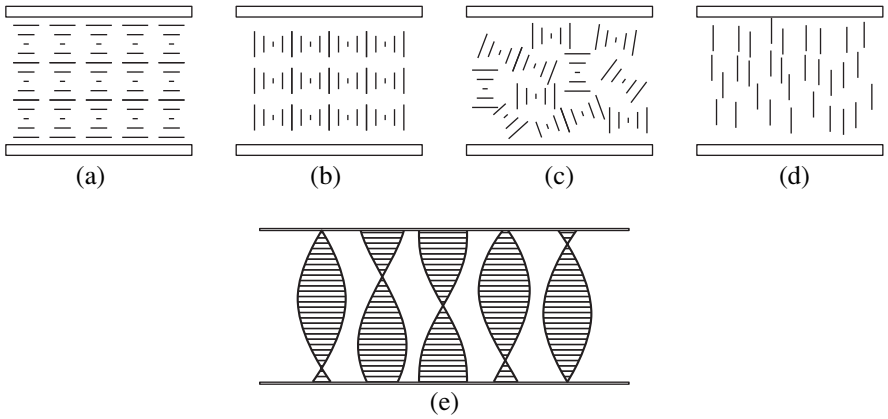

Fig. 2. Schematic depiction of various cholesteric textures: (a) planar, (b) fingerprint, (c) focal conic, (d) homeotropic, and (e) amorphous cholesteric.

1.1 Temperature Dependence of Helix Pitch in Cholesteric Liquid Crystals

As is seen from formula (2), the value of V_{sw} depends on the temperature-dependent quantities P_0, $\Delta\varepsilon$, and K_{22}. Therefore, it is rather difficult to prepare the so-called induced chiral mixtures with the temperature-independent threshold of the cholesteric–nematic transition. Thus, one has to prepare systems with the preset $\partial P/\partial T$ values. It was shown [34, 35] that at low negative $\partial P/\partial T$ values, V_{sw} becomes almost temperature-independent.

Five variants for thermal stabilization of the threshold of the cholesteric–nematic phase transition [36] for the mixtures with various temperature characteristics of the components were proposed in [36]. In [37], three-component mixtures of induced chiral systems were used. Two chiral compounds were added to a nematic of which one induced a cholesteric with a temperature-independent helix pitch, whereas the other, induced a cholesteric with the temperature-dependent inversion of the helix sign. The $P(T)$ characteristics of such mixtures at various concentrations of chiral additives are shown in Fig. 3. The upper part of Fig. 3a shows the dependence of reciprocal helix pitch for the two-component mixture of NLC + 1 wt % of the chiral substance whose formula is given in Fig. 3b. The change of the temperature of this mixture results in the change of the helix sign. The lower part of Fig. 3a shows the same dependence for the cases, where the mixture NLC + 1 wt % of the chiral substance with the temperature-independent helix pitch described by the formula in Fig. 3c was added to the chiral substance with the formula indicated in Fig. 3b at concentrations varying from 0 to 5 wt %. This tree-component mixture provides the smooth control of the $\partial P/\partial T$ value (Fig. 3a). The observed temperature dependence of the helix pitch of the cholesteric mixture [38] shows the wide possibilities for control of the parameter $\partial P/\partial T$. Figure 4 shows that for some CLCs, the whole visible-light spectrum can be observed within the temperature range equal to 0.02°C. We should like to also mention here the recent studies of the temperature dependence of the helix pitch in CLCs [39, 40].

1.2 Bistability of Cholesteric–Nematic Transition

All the effects indicated above were studied mainly in cholesterics with planar textures. However, it was

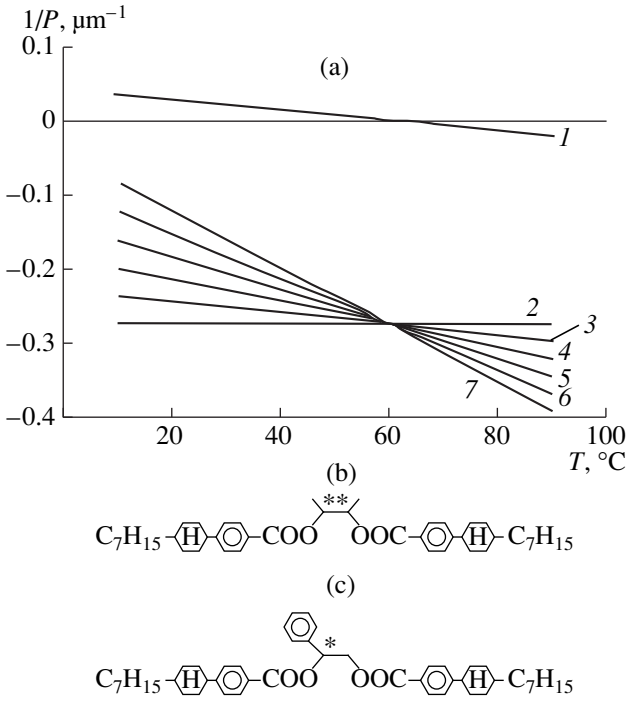

Fig. 3. (a) Temperature dependences of the reciprocal helix pitch (1/*P*) for the mixture of the RO–TN 404 (Hoffmann–La Roche) nematic liquid crystals existing over a wide temperature range and the optically active additives (b) and (c) at various concentrations. (*1*) NLC + (b) (1 wt %); (*2–7*) NLC + (c) at concentrations (*2*) 0, (*3*) 1, (*4*) 2, (*5*) 3, (*6*) 4, and (*7*) 5 wt %. Asterisk indicates the presence of chiral center in the molecules [37].

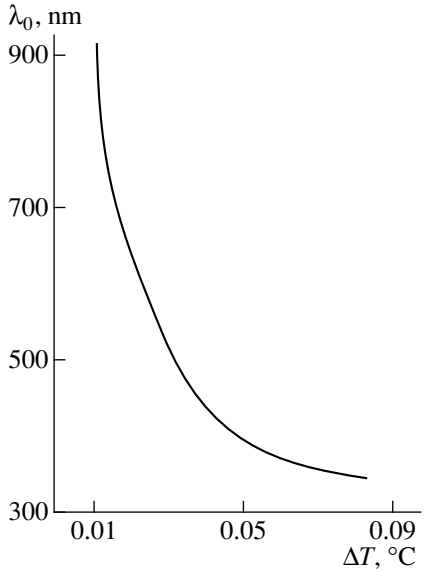

Fig. 4. Temperature dependence of the wavelength of the selective-reflection maxima for the mixture 4-*n*-hexyloxyphenyl 4-*n*'-octyloxybenzoate (HOPOOB) (72 wt %) + tigogenin caprate (TC) (28 wt %). The first point of the temperature interval $T = 0.01$°C corresponds to the temperature of 69.5°C [38].

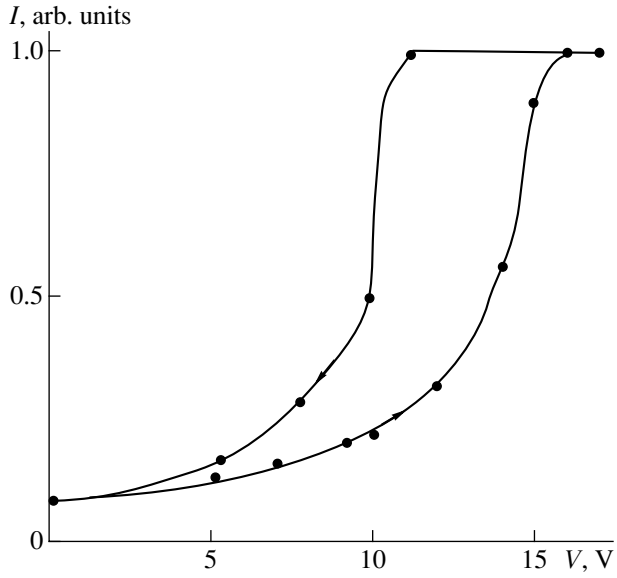

Fig. 5. Intensity (*I*) of light transmitted by the cell as a function of an applied voltage (*V*). The mixture *n*-butyl-*n*'-methoxyazoxybenzene (83.3 wt %) + *p*'-cyanophenyl *p*-butylbenzoate (14.7 wt %) + cholesteryl caprate (2 wt %) . T = 50°C, $d = 10$ μm, $P = 9$ μm [42, 43].

shown that if the molecules of a cholesteric are oriented normally to the surface, the dependence of the light intensity *I* on the applied voltage has a hysteresis, or, in other words, the system possesses bistability [41]. In [42], electrooptics of cholesterics was studied and it was shown that, under certain conditions, the formation of hysteresis is independent of the preliminary treatment of the cell-substrate surfaces. The cholesteric–nematic transition was studied at various *d*/*P* ratios (varying both because of the changes in the cell thickness and the mixture composition). If the helix pitch of a cholesteric is comparable with the cell thickness ($d \sim P$), the hysteresis is formed irrespectively of the preliminary treatment of the cell substrates (Fig. 5). Depending on the treatment of the substrate surfaces, the helix pitch *P*, the *d*/*P* ratio, and the mode of an applied electric field, the textures in cholesterics can undergo various transformations [17, 42, 43]. Under a certain value of the *d*/*P* ratio, a dye-doped cholesteric with a large helix pitch ($P \gg \lambda$) can possess tristability [44].

Bistability of a cholesteric–nematic transition in cholesterics with the homeotropic surface orientation of the molecules in the cells observed in [41] is also of a certain practical interest, because this effect can be used in the systems for displaying information. It should be indicated that formula (2) was derived for infinitely thick samples without any boundary conditions. The cholesteric–nematic transition in CLC samples of various thicknesses was studied in [45, 46]. With due regard for the surface influence, a special constant taking into account the free energy per unit surface, F_s, was introduced, and the empiric formula for V_{sw} was written in the form

$$V_{sw} = \left[\frac{8\pi^2 d^2 K_{22}}{P_0^2 \Delta\varepsilon} - \frac{8F_s d}{\Delta\varepsilon}\right]^{1/2}, \qquad (3)$$

where P_0 is the true (undistorted) value of the helix pitch. It was established [47–49] that the cohesion energy has a considerable effect on V_{sw}. In [50, 51], it was suggested to use the nematic–cholesteric transition in projection displays.

Bistability of a cholesteric–nematic transition in CLC mixtures placed into cells with the substrates preliminarily coated with polyimide films was considered in [52]. The cell surfaces were either not subjected to any preliminary treatment at all or were rubbed along a certain direction with a controlled strength. Figure 6 shows the dependence of the intensity of light transmission by a CLC layer on the applied voltage. At a certain voltage, the initial focal conic (*F*) texture was transformed into homeotropic (*H*). With a decrease of the voltage, the texture was transformed into metastable (*H*'). It is stated [52], that the texture observed can also be considered as a hometropic nematic, however, it is also assumed that the LC molecules in the central part of the sample are slightly tilted. With a further increase of the electric-field amplitude, this texture is transformed into a focal conic one, *F*. The experiment showed that the hysteresis width (the parameter Δ) depends on the preliminary treatment of the surfaces of cell substrates. The value of Δ was determined as the

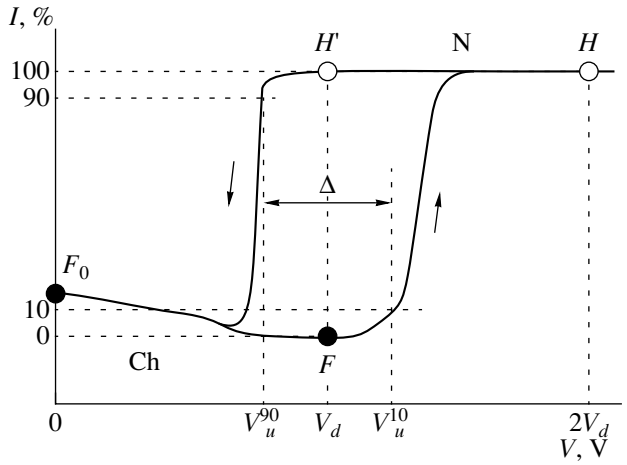

Fig. 6. Illustrating the variation in light transmission under the effect of an applied electric field and the determination of the hysteresis width [52].

difference between the positions V_U^{10} (10%-transmission) and V_U^{90} (90% transmission). The controlling voltage V_d lies between the V_U^{10} and V_U^{90} values. The maximum Δ value was obtained in a cell with glass substrates without any preliminary treatment.

The recent result [53, 54] shows that, under certain conditions, some other effects can also be observed in cholesterics.

1.3 Color Textures of Electric-Field-Induced Cholesteric Mixtures

Two-component chiral mixtures placed between two glass plates whose surfaces were preliminarily treated in different ways were studied in [53, 54]. These were samples with indium-tin oxide (ITO) electrodes or samples with additional polyimide layers or layers obliquely deposited onto SiO_x layers. The CLC mixtures with a helix pitch varying from 0.4 to 15 μm were used and the cells with the thicknesses ranging from 0.8 to 15 μm were studied in constant, alternate, or pulsed electric fields. With an increase of an electric field intensity, the textures in cholesterics changed in the following sequence: planar–quasiplanar–focal conic–homeotropic. As has already been indicated, the observed blue shift toward the blue in the planar–quasiplanar texture transition was interpreted somewhat ambiguously [28–31]. The results obtained in [53] led to new conclusions about the nature of this effect. Figure 7a shows the behavior of the reflection spectrum in various electric fields. It was discovered that the effect is more pronounced and stable if the initial value of the helix pitch in the CLC mixture is comparable with the wavelength of the shortwave range of the light spectrum. Interesting results were also obtained for the nematic matrix of the substance with the changing sign of dielectric anisotropy $\Delta\varepsilon$ under the effect of an applied low-frequency electric field. The optically active additive was a two-component mixture of cholesteric derivatives. At low frequencies, this mixture had the positive sign of $\Delta\varepsilon$, whereas at frequencies exceeding 1 kHz, the negative one. The reflection spectra obtained from such a mixture in applied low- and high-frequency electric fields are shown in Fig. 7b. In low-frequency electric fields, the initial P_0 value is shifted to shorter wavelengths (P_L) (quasiplanar texture), whereas in high-frequency electric fields, to P_H. The fact that $P_H > P_0$ seems to be associated with the tilt of the helix axis. In a low-frequency electric field, the tilt of the helix axis is accompanied by an increase of the helix pitch (the effect of unwinding). In a high-frequency electric field, an increase of the helix pitch P_H

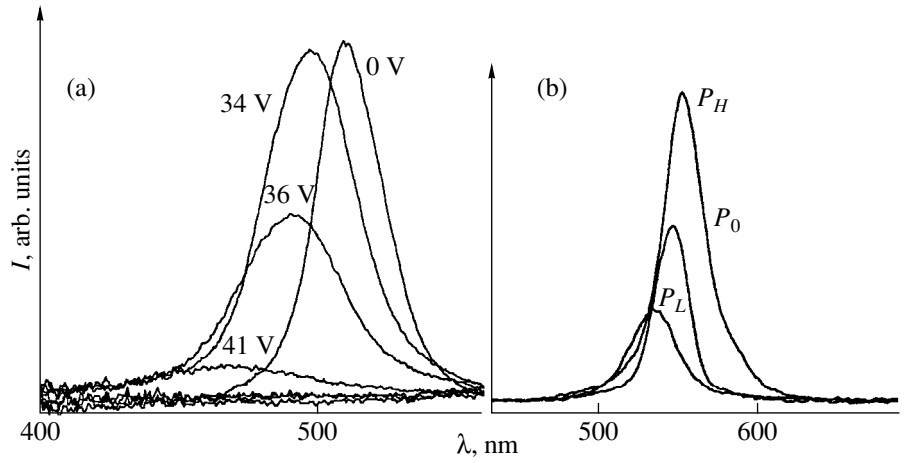

Fig. 7. Reflection spectra for (a) the mixture ZLI-6023/S811 (Merck, $\Delta\varepsilon > 0$); $d = 10$ μm, electric fields with unipolar pulses and a frequency of 350 Hz and (b) the mixture VGU 6 (Vilnius State University) + cholesteryl oleate + cholesteryl caprate; $d = 5$ μm. High- and low-frequency electric fields were alternatively applied. Peak notation: (P_0) in the zero field, (P_L) in the field with $f =$ 200 Hz, $V = 80$ V, (P_H) in the field with $f = 115$ kHz, $V = 150$ V [53].

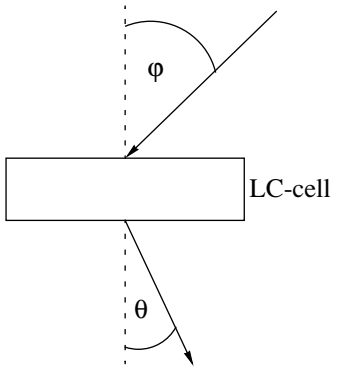

Fig. 8. Schematic of the experiments on light scattering; φ is the angle of incidence, θ is the angle of observation.

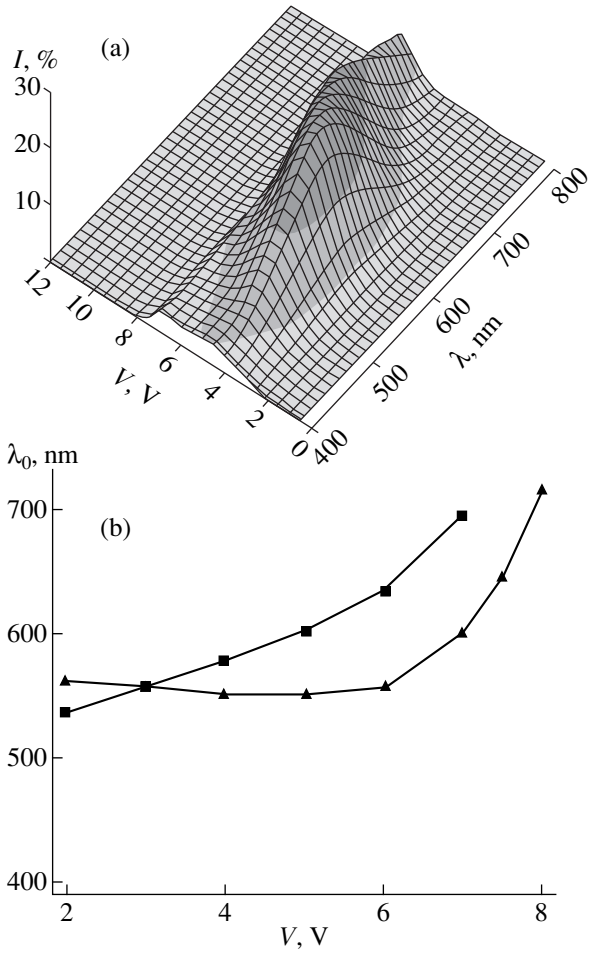

Fig. 9. (a) Spectral dependence of the scattered intensity as a function of the applied voltage. The E7(BDH)/S811 mixture, φ = 40°, θ = 20°, P = 1.1 μm and (b) the maximum wavelength λ_0 as a function of on applied varying frequency; φ = 40°, θ = 20°, P = 1.1 μm, d = 2 μm; ▲ the E7/S811 mixture; ■ PDLC film with E7/S811 [54].

results, first, in the restoration of the planar texture with an increased helix, but then the pitch decreases to its initial value, P_0. Thus, the quasiplanar texture of a cholesteric is characterized by a tilt and a slight unwinding of the helix. In the actual fact, the angle of electric field-induced tilt of the helix axis of the planar texture exceeds the angle that can be measured from the blue shift.

Cholesteric liquid crystal mixtures with positive dielectric anisotropy and the helix pitch $P \geq 0.8$ μm were studied in [54]. The wavelength of selective reflection lies in the visible spectrum range and, as the reflection studies showed, a cholesteric liquid layer with the planar texture was transparent. However, the application of the voltage corresponding to V_{sw} and its subsequent decrease resulted in the formation of color cholesteric textures. The schematic of this experiment is shown in Fig. 8. Figure 9a shows the spectral dependence of the transmitted light intensity (I) as a function of the voltage (V) applied to the cell and recorded during a decrease of the field amplitude. Figure 9b shows the analogous dependence for the maximum wavelength λ_0. It should be emphasized that the effect of coloring observed in the CLC textures is independent of the boundary conditions. The dependence $\lambda_0/(V)$ observed with a decrease of V seems to be associated with the helix twist, i.e., its return to the initial state with P_0. Another remarkable dependence is that of λ_0 on the angle of observation ϑ (Fig. 10). In CLC cells with planar or quasiplanar textures, $d\lambda_0/d\theta < 0$. However, Fig. 10 shows the dependence $d\lambda_0/d\vartheta > 0$ characteristic of diffraction gratings. Similar characteristics of $\lambda_0(\vartheta)$ were also observed for PDLC films. The initial textures and the $\lambda_0/(V)$ dependences for these films are somewhat different (Fig. 10).

The diffraction grating controlled by an electric field can also be used for changing the direction of a laser beam. The angle of the incidence of a He–Ne laser beam (λ = 632 nm) φ = 45° can be changed by an applied electric field up to a value of 30° [54].

The CLC texture with the above characteristics was denoted as a new texture. Obviously, this new texture is not focal conic. Most probably, it is oriented in a certain specific way (fingerprint texture), which is confirmed by the recent results obtained on similar CLCs in the form of cholesteric gels [55]. This texture is referred to as FC_{CHKS} (Chilaya, Hauck, Koswig, Sikharulidze focalconic texture) and has the characteristics indicated in [54]. Kitzerow [55] studied in detail the angular dependences of the wavelengths of diffracted light and showed that they can be interpreted within the theory of Bragg scattering from the spatial periodic CLC structures. Moreover, he also showed that, while applying short electric pulses, it is possible to switch a CLC textures into the states with a transparent planar (Gj) and colored (FC_{CHKS}) textures. In [56], the switching from the color Gj state into the scattering focal conic FC state was studied. In the latter case, the helix pitch is somewhat smaller, and, therefore, the relaxation time is longer.

1.4 Electro-optics of Amorphous Cholesteric Structures

According to [57], cholesteric liquid crystals in the vicinity of λ_0 are optically active because they show no linear birefringence. In this case, the angle of polarization-plane rotation for light propagating along the optical axis of a CLC depends on *P*, the cell thickness *d*, and the local birefringence $\Delta n = n_e - n_o$ as follows:

$$\Phi = 2\pi(d/P)\left(\frac{n_e^2 - n_o^2}{n_e^2 + n_o^2}\right)^2 \frac{1}{8(\lambda')^2}\frac{1}{1-(\lambda')^2}, \qquad (4)$$

where $\lambda' = \lambda/\lambda_0$.

It was suggested [58] to use an optically active CLC structure for studying the cholesteric–nematic transition. The experiments are performed in the polarized light (crossed polaroids). Then, with an increase of the applied voltage up to V_{sw}, the CLC texture transformed from the optically active planar to homeotropic nematic. The rotation angle of the polarization plane of the incident light is independent of the mutual arrangement of the polarizer and the cell, which is very important in the CLC studies in the Mauguin mode [11]. The glass substrates of the cells coated with transparent electrodes and polyimide films were not preliminarily treated to avoid possible inducing of surface orientation of CLC molecules. As a result, the amorphous cholesteric texture was formed (Fig. 2) with randomly arranged CLC molecules on the substrate surfaces. In the sample bulk, each of these molecules is rotated (by the same angle) from the lower surface of the cell substrate to the upper one. In other words, we obtain a planar texture with random orientation of the molecules along the surfaces of the cell substrates. The term "amorphous" was first applied to the "twist structure" in [59]. It should be emphasized that, in practice, the amorphous cholesteric structure was first used in a photoconductor–liquid crystal image transducer [60].

If a cholesteric structure operates in an optically active mode, the helix pitch of a CLC should necessarily correspond to the wavelength of the visible spectrum range. In practice, one has to use CLCs with large *P*. In order to avoid noncontrollable deformations of the helix pitch in this case (which can give rise to the formation of the so-called superstructures [2, 3]), one has carefully control the *d*/*P* ratio.

The ellipticity of the light transmitted by the cell with a CLC at different *P*, *d*, and Δn values was studied in detail in [61]. It was shown experimentally that, if the conditions $\lambda \geq \Delta n \times P/2$ are met, the transmitted light with the wavelength λ is circularly polarized.

According to [19, 62], the amorphous cholesteric structure possesses the following electrooptical characteristics: the switching-on time decreases with an applied voltage and can attain a value of 0.1 ms; the switching-off time ranges within 5–10 ms. The characteristics of this structure vary over the wide angular range, and therefore, the requirements set to the preliminary treatment of the substrate surfaces of the cell and the cell location between the polaroids are less severe. Figure 11 shows the intensity of the transmitted light as

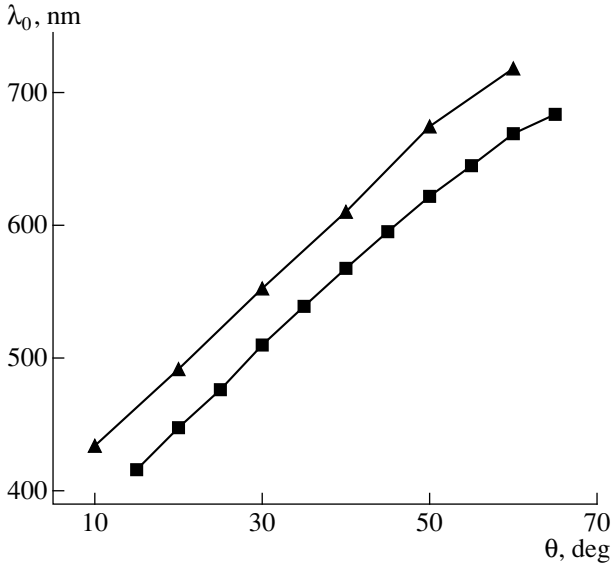

Fig. 10. Dependence of λ_0 on angle θ ($\varphi = 40°$; ▲: ZLI 6023 (Merck) + S811, $P = 0.8$ μm, $d = 5$ μm, $V = 16$ V (pulsed); ■ PDLC film with RO–TN-403 (Hoffmann–La Roche) + S811, $P = 0.8$ μm, $d = 5$ μm, $V = 10$ V (alternating voltage) [54].

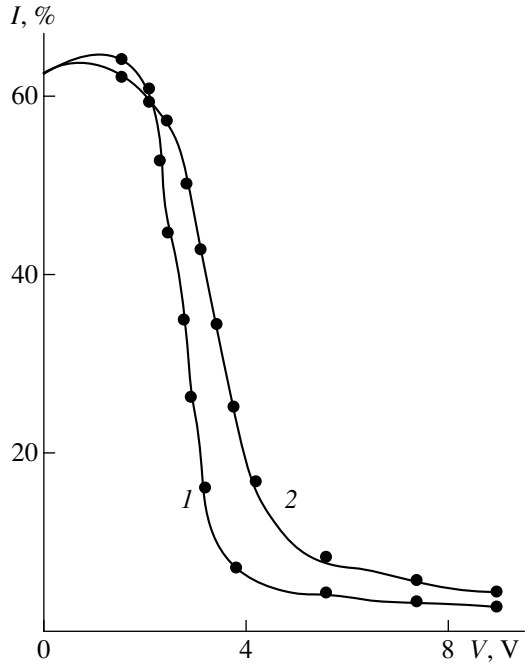

Fig. 11. Intensity of transmitted light as a function of applied voltage *V* for several mixtures: (*1*) ZLI 1132 (Merck) + TC with $P = 5.6$ μm $d = 3.7$ μm; ZLI 1132 ($\Delta n = 0.1396$, $\Delta\varepsilon = 13.13$); (*2*) ZLI1695 (Merck) + TC with $P = 5.6$ μm, $d = 4.14$ μm [19, 62]; ZLI 1695 ($\Delta n = 0.0625$, $\Delta\varepsilon = 4.8$).

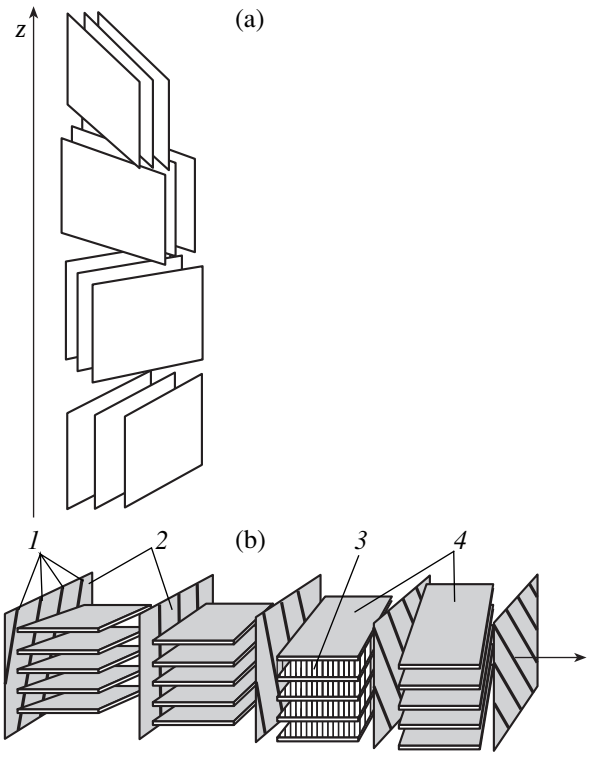

Fig. 12. (a) Model of a chiral smectic *A* phase; (b) the same phase but with various defects including twisted grain boundaries (the so-called TGB phase) [3, 65]. (*1*) Screw dislocations, (*2*) twist grain boundaries, (*3*) molecules, (*4*) smectic grains.

a function of the applied voltage for two cholesteric mixtures obtained in crossed polaroids.

In [63], PDLC films with the above structure were obtained. In comparison with the conventional PDLC films, the films in [63] showed a lower contrast and the considerably improved angular characteristics.

2. PRETRANSITIONAL PHENOMENA IN CHOLESTERICS: TGB AND BLUE PHASES

Transition of cholesterics to isotropic and smectic phases are accompanied by formation of specific structures. These are frustrated TGB and blue phases formed in the phase transitions via formation of systems of exotic complex defects. Recently, these structures are in the focus of attention of both theoreticians and experimentalists.

2.1 TGB Phases

De Gennes theoretically studied the experimentally observed unwinding of a cholesteric helix in the vicinity of the cholesteric–smectic *A* transition and came to the conclusion that it is analogous to the metal–superconductor transition [64]. This analogy provided the prediction of the TGB phase formed between the cholesteric and the smectic *A* phases [3]. The transient TGB phase is interpreted as an analogue of the Abrikosov vortex lattice in superconductors, a cholesteric is considered as a conventional metal, a smectic *A* is treated as a Meisner phase, and chirality plays the part of an external magnetic field. It was shown [65] that the formation of a chiral smectic *A** phase can also be described in terms of "epitaxial dislocations" and grain-boundary energy. The chiral smectic *A** phase consists of twisted smectic blocks (grains). The block rotations are provided by the existence of a periodic network of dislocations leading to the formation of a network of screw dislocations. The blocks consisting of smectic layers are rotated by a certain small angle with respect to one another, thus forming a helical structure similar to cholesteric one. In this model, dislocations are distributed more or less uniformly, whereas the smectic blocks located along the *z*-axis are spaced by distances much smaller than the helix pitch *P* [65]. The model of a TGB phase is shown in Fig. 12.

The consideration of the intersection points of the cholesteric and smectic *A* and *C** phases (the tricritical *N*AC** points) on various phase diagrams of chiral substances allowed us to predict the formation of other TGB phases, namely, TGB *C* and TGB *C** [66, 67]. It was shown [68] that the TGB structure can form in nonchiral liquid crystals, which is associated with the effect of cell substrates. All the phases predicted theoretically were observed experimentally [69–77]; in [78], a reentrant TGB phase was observed; in [79], a pressure-induced TGB phase; in [80, 81], a TGB phase in LC with the columnar structure of molecules was observed. The transitions from the TGB *A** and TGB *C** phases to the smectic *A** and *C** phases in electric fields were observed in [82, 83].

Recently, studying the three-component mixture of two nematics and an optically active nonmesomorphic additive, we have discovered a new phase with unusual optical properties between the cholesteric and the smectic *A* phases [84]. The transmission of the nonpolarized light in this phase decreased from 50 to 20% (Fig. 13). The calorimetric and the X-ray diffraction studies showed that this new phase is not cholesteric. It was identified with a TGB *A*-phase [85]. Later, a similar phase was also observed in the two-component mixture of NLC and an optically active nonmesomorphic additive [86]. It should be indicated that the TGB phase in the induced systems with nonliquid crystal chiral substances was first observed in [84–86]. The characteristics of such TGB phases somewhat differ from those of the TGB phases observed earlier, namely, they have no filament texture, the helix pitch is comparable with *P* of the cholesteric phase, and the phases are insensitive to an electric field. At the same time, these TB phases show anomalous selective light reflection, which cannot be interpreted in terms of the known theoretical concepts.

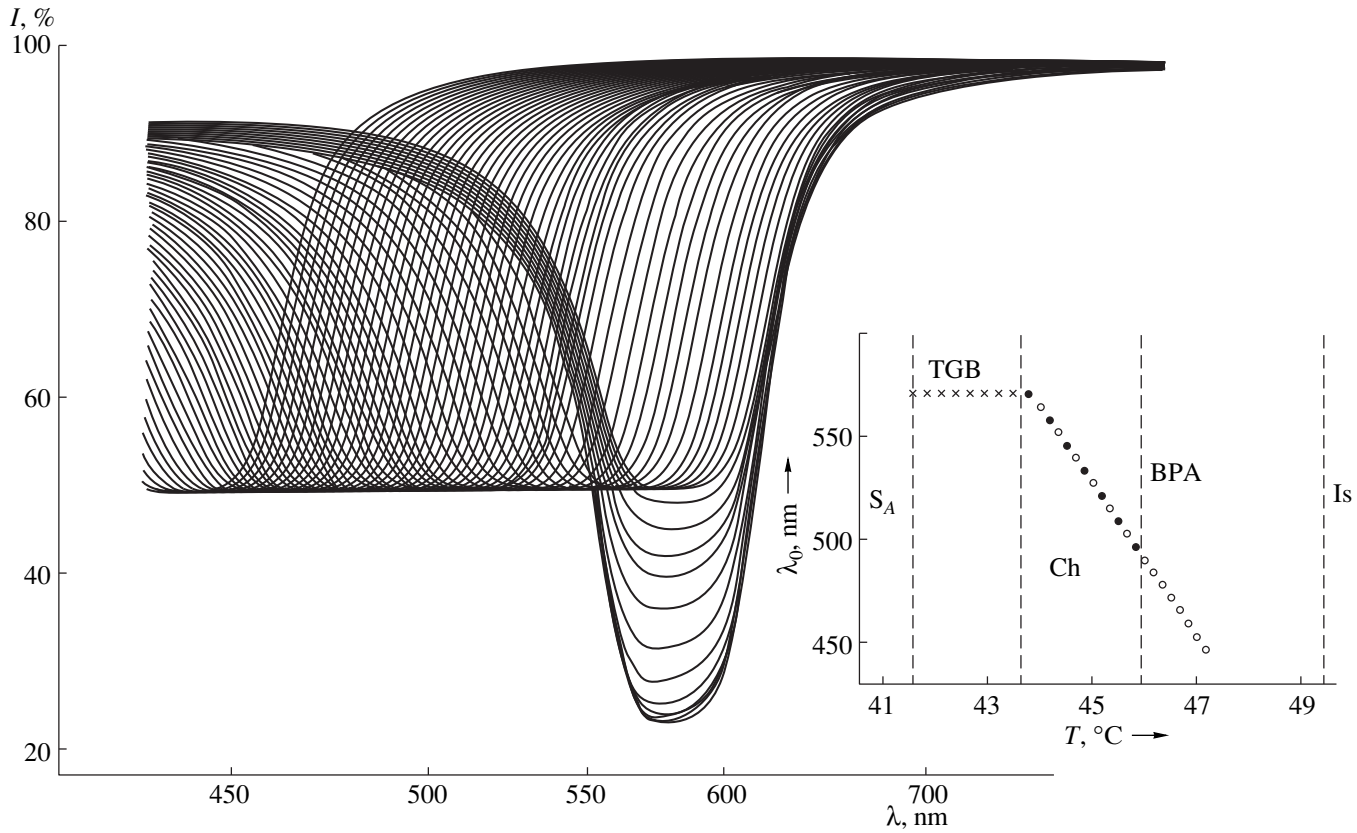

Fig. 13. Transmission spectrum of the mixture: [80 wt % 4-octyloxy-4'-cyanobiphenyl (8CB) + 20 wt % 4-*n*-hexyloxyphenyl *n*'-octyloxybenzoate (HOPOOB)] (82 wt %) + TC (18 wt %) obtained during lowering of the temperature of the cholesteric and TGB phases. In the inset: the schematic phase diagram and the dependence of the wavelengths of the transmission minima (λ_0) for the same mixture. Open circles correspond to cholesteric heating, filled ones, to cholesteric cooling. Vertical dashed lines indicate the ranges of phase existence during cooling [84, 86].

2.2 Blue Phases

Blue phases (BPs) are observed in chiral liquid crystals usually characterized by small helix pitch in the transitions from the cholesteric (Ch) to the isotropic (Is) phases. Blue phases show polymorphism: with an increase of the temperature (and also with an increase of chirality), three thermodynamically stable blue phases appear in the following sequence: BP I, BP II, and BP III [4]. The experimental studies of the spectral characteristics of Bragg scattering provided the establishment of their structures of these phases. The phase BP I has a body-centered cubic structure, the phase BP II, primitive cubic structure, and the phase BP III has a disordered (amorphous) structure. The Bragg diffraction for this phase is observed over a wide angular range, and therefore, this phase is structurally disordered and often referred to as the "fog phase."

Brazovskiĭ, Dmitriev, and Filev [87–89] showed that the decisive role in the formation of blue phases is played by the short-range order in the arrangement of molecules, i.e., the organization of the molecular groups at relatively small distances comparable with the correlation radius ξ. Because of the specific characteristics of the cholesteric–isotropic phase transition, it can happen that in the vicinity of T_c, the correlation radius ξ exceeds P. The theoretical calculations and their comparison with the experimental data showed that, in this case, the so-called double twist cylinders (vortex modes) form a primitive cubic lattice (Fig. 14). In the case of body-centered lattice, whose unit cell is shown in Fig. 15, another structure is formed [90–92].

Considering various systems possessing blue phases, different molecular structures, different num-

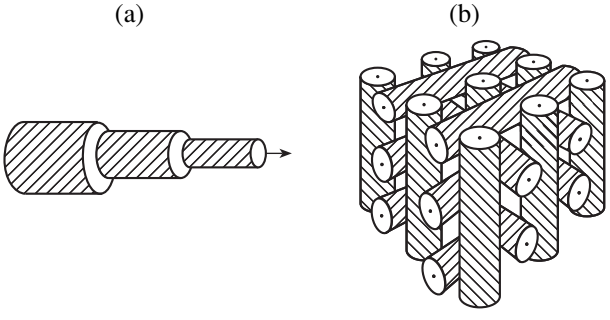

Fig. 14. (a) Model of double-twist cylinders and director orientation describing the cylinder configuration; (b) cubic structure with the sp. gr. O^2 [91].

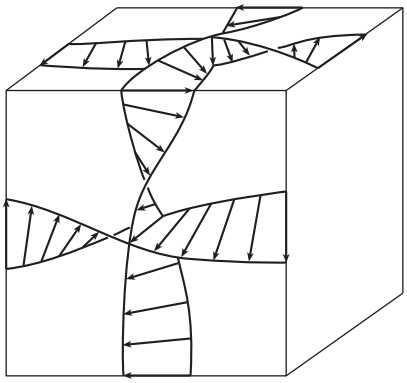

Fig. 15. Model of the double helix of the blue phase described by the sp. gr. O^5 [92].

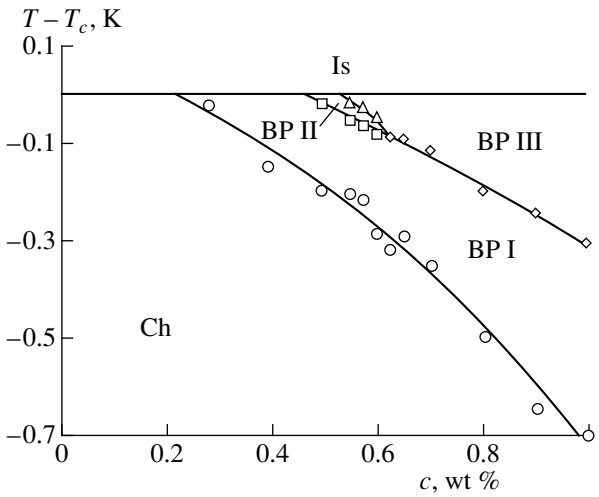

Fig. 16. Universal phase diagram for blue phases as a function of mixture chirality [93].

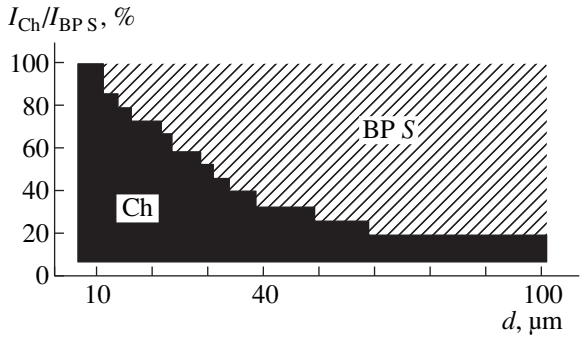

Fig. 17. The ratio of the relative Bragg intensities, of a cholesteric and BP S, $I_{ch}/I_{BP\,S}$, as functions of cell thickness [95].

bers of chiral centers, and different phase-transitions temperatures, Bowling, Collings, Booth, and Goodby [93] came to the conclusion on the existence of a certain universal phase diagram (Fig. 16). However, because of a great variety of systems possessing blue phases with very complicated structures, the above universal phase diagrams can be constructed only in some cases. On the other hand, the universal nature is inherent not only in phase diagrams (this aspect would be considered in more detail later).

Usually, the wavelength λ_0 of the Bragg reflection in BP I and BP II is either independent of the temperature growth or decreases with it. Recently, the positive temperature dependence of λ_0 was observed for BP I [94, 95]. A similar temperature dependence was also revealed for the new phase formed in supercooled BP I [96–98] or the so-called supercooled phase (BP S) [97, 98]. Also, it was also shown that an important role in the formation of the BP S phase is played by smectic fluctuations [97] and the conditions existing on the surface [95]. In the majority of cases, the cholesteric and BP S phases coexist. The measurements showed that the ratio of the intensities transmitted by the cholesteric and the BP S phases are thickness-dependent. Assuming that this ratio correlates with the relative amount of each phase in the sample, one can construct the dependence of this ratio on d (Fig. 17).

An unusual phase diagram (the sequence of the formation of blue phases) was observed in induced chiral systems. With an increase of the chiral-component concentration in the mixture, both prior to the appearance and upon the disappearance of BP I, the formation of blue phases with amorphous structures similar to that of BP III were observed [95]. In other words, with an increase of the chiral-component concentration and the temperature, the phases are formed in the following sequences: cholesteric phase—BP A_1—isotropic phase; cholesteric phase—BP I—isotropic phase; cholesteric phase—BP A_2—isotropic phase (Fig. 18a). The amorphous blue phase, BP A, forming prior to the formation of BP I and BP II at high concentrations of the chiral-component was observed in [86, 99]. This is illustrated by Fig. 18b [86]. The study of this phase leads to the assumption that the BP A phase is, in fact, a partly formed BP I phase. The effect of the chirality and other factors on the characteristics of blue phases was studied in [99]. The following characteristic features are caused by an increase of chirality: the formation of BP A and the reentrant BP II phase and disappearance of the BP II phase. The data on the formation of the latter phase are consistent with data [93], indicating that the BP II phase is less stable than other blue phases.

The application of an electric field gives rise to various effects in blue phases. It distorts their structures and shifts λ_0, induces birefringence and provides the formation of new phases, and, in some cases, also causes hydrodynamic instability [100]. The application of an electric fields to blue phases allows one to study the corresponding structures. Thus, the experimental studies of BP III in electric fields showed that this phase should have a primitive cubic structure [101]. The effect of an electric field on BP S was studied in [99, 102, 103].

The direct transition to the blue phase (in the absence of the cholesteric phase) was observed in the smectic *A* [104] and TGB *A* [105] phases. The temperature range of existence of blue phases correlates with the system chirality [106].

Of great importance are the studies of the optical activity of the isotropic phase in the vicinity of the transition from the blue phase to the isotropic one [107–109]. In this case, one observes fluctuations, which increase with an increase of chirality and essentially affect the nature of the phase transition. The measurements of the optical activity provide an important information on the orientational order in the isotropic liquid. Generally speaking, liquid crystals are unique physical objects that can be considered quantitatively within the framework of the Landau theory of phase transitions [110].

3. PDLC FILMS, DISCOTICS, FLEXOELECTRICITY, AND PHOTOSTIMULATED SWITCHING IN CHOLESTERICS

3.1 PDLC Films

Cholesterics dispersed in polymers are most often used as thermometers and other devices visualizing thermal fields [111]. In fact, the first practical application of liquid crystals was associated with the thermochromic properties of cholesterics [112]. Cholesteric films used in thermal indicators were obtained by the method of microcapsulation with the use of water-soluble substances such as gelatin, starch paste, polyvinyl alcohol, etc. However, cholestery esters used in the early studies proved to be unstable, and therefore, were substituted by chemically stable nonsteoid chiral and chirally-induced nematics. The latter are mixtures of nematics and optically active mesogenic or nonmesogenic additives [113–116]. Recently, in order to obtain a stable emulsion by the method of microcapsulation, the conventional emulsifier (hydrochloric acid added to the dispersion system liquid crystal–aqueous solution of polyvinyl alcohol) was substituted by sodium oleate [117].

The use of liquid crystals dispersed in polymers in electrooptical elements opened new vistas in the practical applications of liquid crystals [118, 119]. These systems, usually referred to as PDLC films, were first suggested for nematics. Microcapsulation is attained either during capsulation of a liquid crystal from the emulsion in the liquid or during precipitation (phase separation) of the LC phase from the polymer (the liquid–liquid separation, which reduces to the separation of the film-forming material from the solution, i.e., emulsification with the subsequent solidification). The phase separation can be a result of cooling of the LC solution and a thermoplastic polymer (the so-called thermally-induced phase separation, TIPS) or a result of evaporation of the solvent containing dissolved LC and a polymer (the so-called solvent-induced phase separation, SIPS), or else a result of polymerization of monomeric components of the LC–monomer solution (the so-called polymerization-induced phase separation, PIPS) [120].

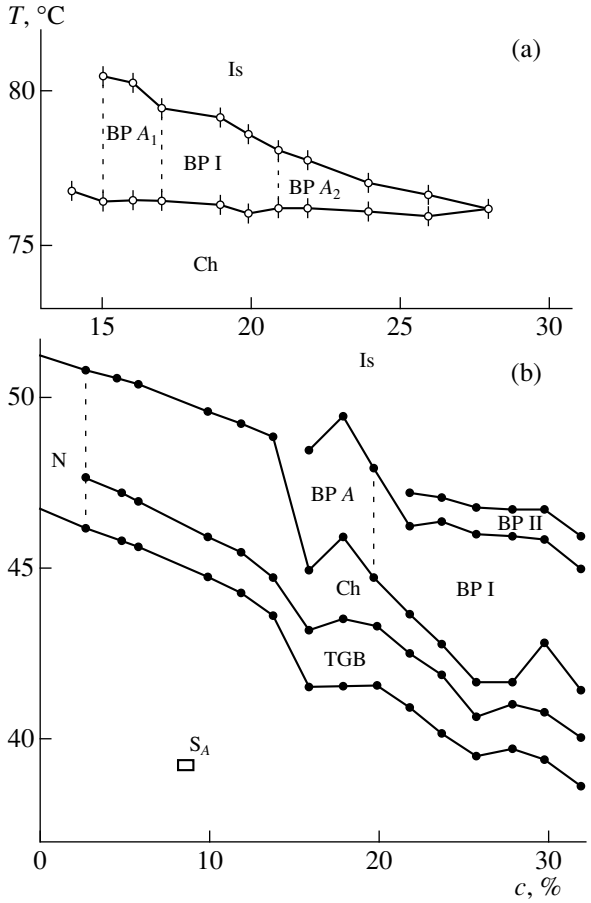

Fig. 18. Phase diagrams $T(c)$ (where c is the concentration of the chiral components) determined in the cooling mode for (a) the mixture of chiral di-2-methylheptyl 4-4'-tetraphenyldicarboxylate mixed with HOPOOB [95]; (b) the mixture of the composition indicated in Fig. 13 [86].

A color reflecting display based on cholesteric PDLC film prepared by the method of thermally-induced phase separation was proposed in [121]. In this case, a cholesteric liquid crystal with the negative dielectric anisotropy and the helix pitch comparable with the light wavelength in the visible spectrum range was used. The switching of a nonreflecting cholesteric liquid crystal to the reflecting color state was attained by the application of an electric field. Later, such films were also obtained by the polymerization-induced phase separation method, which considerably simplified the technology of film preparation and reduced the switching time [122].

In PDLC films used earlier, liquid crystals did not exceed 50 wt % of the total mixture. The films obtained at low polymer concentrations (1 to 5 wt %) showed quite unusual properties [123, 124, 56]. The helix pitch

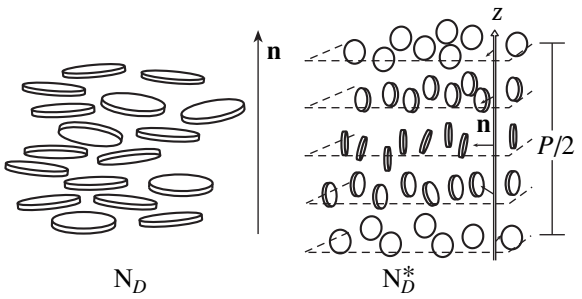

Fig. 19. Models of disklike nematic (N_D) and disklike cholesteric (N_D^*) liquid crystal phases.

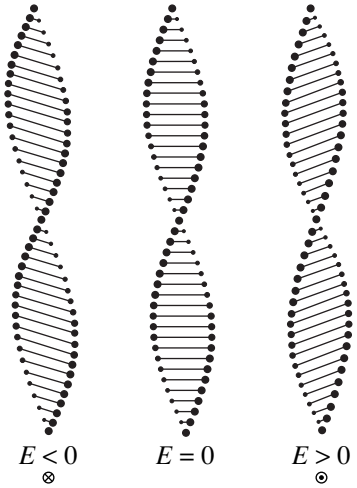

Fig. 20. Rotations of the optical axis of a cholesteric induced by an electric field applied normally to the figure plane [138].

of cholesterics used in these films was about 250–500 nm, i.e., showed the selective reflection in the visible spectrum range. Small amount of a polymer stabilized the planar and focal conic textures, so that these films can be referred to as polymer-stabilized cholesteric textures LCD (PSCT–LCD) or the LC–gel systems. Because of their high electrooptical characteristics, PSCT–LCD systems are rather promising for various practical applications.

The PDLC films [54] and the cholesteric–gel systems [55] with FC_{CHKS} textures and PDLC films with amorphous cholesteric textures [63] were considered in Sect. 1.

3.2 Discotic Cholesterics

Up to now, we have considered LC phases formed by rodlike molecules usually called calamitic phases. Liquid-crystal phases can also be formed by molecules having some other characteristic shapes. In 1977, Chandrasekhar discovered that LC phases can be formed by disklike molecules. The corresponding phases received the name of discotics [125]. Figure 19 schematically depicts a discotic nematic (N_D) and a discotic cholesteric (N_D^*). The N_D phase possesses negative optical and diamagnetic anisotropies. The sign of the dielectric anisotropy can be both positive and negative depending on the molecule structure. Discotic liquid crystals, especially in the hexagonal phase (D_h), possess rather high photoconductivity [126–128]. Recently, an optically controllable electrooptical effect was discovered in a discotic nematic [129]. Discotic cholesterics are formed in materials consisting of chiral disklike molecules [130, 131] and in the mixtures of N_D with optically active additives [132–134]. Both pure and induced N_D^* phases with small helix pitch and temperature-dependent inversion of the pitch sign were observed in [135, 136]. It was shown that along with the N_D^* phase, blue phases also formed.

3.3 Flexoelectric Electro-optics of Cholesterics

It is well known that nematic LCs are nonpolar. However, Meyer showed [137] that splay or bend deformation of nematics formed by molecules of certain shapes gives rise to electric polarization. This phenomenon received the name of the flexoelectric effect. Flexoelectric electro-optics of cholesterics was first observed in [6]. If the helix axis of a cholesteric with a small pitch is located in the plane of the cell substrate, whereas an electric field is applied normally to the helix axis, the helix is deformed. This reduces the free energy of the system. It is seen from Fig. 20 that an applied electric field provides the rotation of the optical axis, which depends on the polarity of the applied electric field. The rotation angle linearly depends on the field amplitude [138]. The medium in which the interaction with an applied electric field takes place provides the appearance of a linear electrooptical effect. The theoretical consideration of the dynamics of the flexoelectric effect is given in [139, 140]. It is shown that the theory is in good accord with the experiment. In [18, 141], a cholesteric with temperature-dependent inversion of the helix-pitch sign was considered, i.e., the use was made of a substance with the minimum dielectric anisotropy $\Delta\varepsilon$. This allowed the optimization of electrooptical parameters, the response time (~100 μs), the modulation depth (100%), etc.

3.4 Photostimulated Switching in Cholesterics

Light-induced orientational transformations were studied in various liquid crystals, however, many aspects of the physicochemical mechanism of photoinduced switching still received no unique interpretation [142]. Here, of special interest are cholesterics, because it is hardly possible to find another object so sensitive

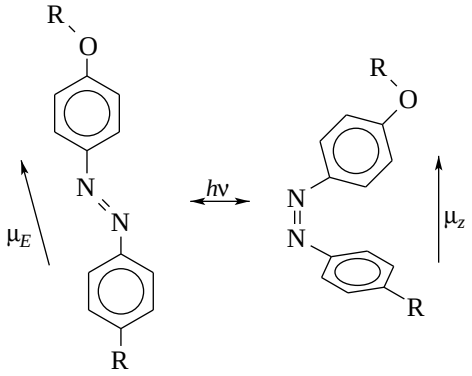

Fig. 21. Scheme of photoisomerization of azobenzene derivatives.

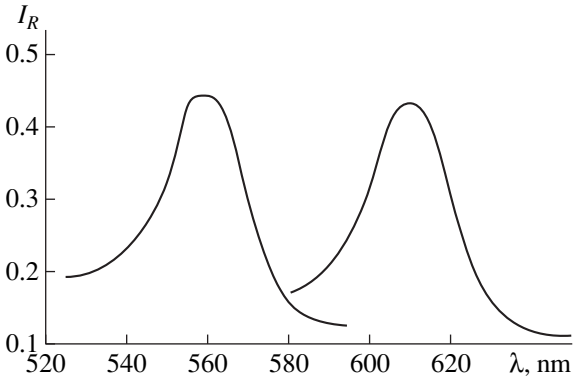

Fig. 22. Transmission spectra of an oriented cholesteric mixture of cholesteryl chloride (35 wt %) and cholesteryl nonanoate (65 wt %) containing azobenzene of a concentration of 0.35 *M*. The first spectrum with the maximum at λ_0 = 610 nm corresponds to the mixture with pure *cis*-azobenzene as solute; the left spectrum with the maximum at λ_0 = 560 nm was observed upon irradiation of this sample at 420 nm for 3 min [149].

to small variations in the molecular structure as the macromolecular parameter (helix pitch) in cholesterics [1].

The effect of the light field is studied in both absorbing and nonabsorbing chiral liquid crystal systems, in strong and weak fields, with liquid crystals having oriented or nonoriented directors, with and without mirrors, with or without the resonance or nonresonance effect of the Kerr or the non-Kerr type.

Photoinduced "tuning" of the Bragg peak was successfully used in absorbing cholesterics for observation of intrinsic bistability (without the use of mirrors) and optical switching [143, 144]. The dynamic response in cholesteric liquid crystals doped with dies with the absorption wavelength close to the wavelength of the selective-reflection maximum was studied in [145]. The use of picosecond laser pulses maximum provided the observation of switching times of the order of several subnanonseconds. The resonance nonlinearity in cholesteric liquid crystals was analyzed in [146]. It was shown that at certain incident-light intensities, the optical bistability and both dynamic and constant holographic gratings can be observed. The layers of nonabsorbing cholesteric liquid crystals can be used as mirrors for a pulsed solid-state laser in optical resonators [147, 148].

Of great importance are liquid crystal systems with conformationally active molecules (i.e., molecules providing *trans–cis* (E–Z) isomerization (Fig. 21), which are used to design the devices for optical recording of information). Under the effect of the light radiation, the geometric shape, and the value of the dipole moment, and the direction of the excitation moment of dye molecules are changed. In 1971, Sackmann discovered the reversible change of the color of a cholesteric with the aid of photochemical isomerization of the azobenzene dissolved in the cholesteric (Fig. 22) [149]. Optically-active menthone-derivative additives providing the *trans–cis*-isomerization under the UV irradiation were also used in induced chiral systems [150, 151]. In these studies, the effect of the long wavelength shift of the selective light-reflection maximum in these systems irradiated with a He–Cd laser was observed. The periodic structures were formed in induced chiral systems during their interaction with light [152]. Similar structures were also revealed in induced chiral systems with conformationally inactive components.

The theoretical aspects of the light-field effect on the helix pitch in cholesteric liquid crystals are considered in [153–158].

CONCLUSION

Thus, we have considered the effect of various external factors on the parameters of low-molecular thermotropic cholesteric liquid crystals. The results obtained are of both scientific and practical interest. In addition to the reviewed publications, there are numerous studies of the effect of magnetic and acoustic fields and pressure on cholesteric liquid crystals. Very interesting results were also obtained for polymer liquid crystals and cholesteric lyotropic liquid crystals.

ACKNOWLEDGMENTS

The author is grateful to S. P. Chumakova for valuable remarks and help in the preparation of this manuscript for publication.

REFERENCES

1. G. S. Chilaya and L. N. Lisetski, Mol. Cryst. Liq. Cryst. **140**, 243 (1986).
2. H.-S. Kitzerow, in *Liquid Crystal Complex Geometry*, Ed. by G. P. Crawford and S. Zumer (Taylor and Erancis, London, 1996), p. 187.
3. S. R. Renn and T. C. Lubensky, Phys. Rev. A **38** (4), 2132 (1988).

4. V. A. Belyakov and V. E. Dmitrienko, Usp. Fiz. Nauk **146** (3), 369 (1985) [Sov. Phys. Usp. **28**, 535 (1985)].
5. G. Chilaya, in *Abstracts of European Conference on Liquid Crystals, Zakopane, Poland, 1997*, p. 23.
6. J. S. Patel and R. Meyer, Phys. Rev. Lett. **58** (15), 1538 (1987).
7. J. Prost, Adv. Phys. **33**, 16 (1984).
8. S. A. Pikin, in *Incommensurate Phases in Dielectrics 2*, Ed. by R. Blinc and A. P. Levanyuk (Elsevier, Amsterdam, 1986), Chap. 21, p. 319.
9. B. I. Ostrovski, Liq. Cryst. **14**, 131 (1993).
10. R. Dabrowski and K. Czuprynski, in *Modern Topics in Liquid Crystal*, Ed. by A. Buka (World Scientific, Singapore, 1993), p. 125.
11. C. Mauguin, Bull. Soc. Fr. Mineral. Crystallogr. **34**, 71 (1911).
12. M. Schadt and W. Helfrich, Appl. Phys. Lett. **18** (4), 127 (1971).
13. G. S. Chilaya and V. G. Chigrinov, Usp. Fiz. Nauk **163** (10), 1 (1993) [Phys. Usp. **36**, 909 (1993)].
14. G. Sh. Petriashvili, M. N. Aronishidze, A. A. Khatiashvili, *et al.*, Kristallografiya **42** (3), 499 (1997) [Crystallogr. Rep. **42**, 452 (1997)].
15. G. Pertiashvili, G. Chilaya, A. Chanishvili, *et al.*, in *Abstracts of the VI International Conference on Ferroelectric LC, Brest, France, 1997*, p. 342.
16. M. T. Press and A. T. Arrot, J. Phys. (Paris) **37**, 387 (1976).
17. G. S. Chilaya, S. N. Aronishidze, K. D. Vinokur, *et al.*, Acta Phys. Pol. A **54** (5), 651 (1978).
18. P. Rudquist, M. Buivydas, L. Komitov, and S. T. Lagerwall, J. Appl. Phys. **76** (12), 7778 (1994).
19. G. Chilaya, A. Chanishvili, and D. Sikharulidze, in *Liquid Crystals: Materials Science and Applications*, Ed. by J. Zmija *et al.*, Proc. SPIE **2372**, 96 (1995).
20. G. Heilmeier and J. Goldmacher, Proc. IEEE **57**, 34 (1969).
21. W. Haas, J. Adams, and G. Dir, Chem. Phys. Lett. **14** (1), 95 (1972).
22. G. S. Chilaya, V. T. Lazareva, and L. M. Blinov, Kristallografiya **18** (1), 203 (1973) [Sov. Phys. Crystallogr. **18**, 127 (1973)].
23. P. G. De Gennes, Solid State Commun. **6**, 163 (1968).
24. R. B. Meyer, Appl. Phys. Lett. **12** (9), 281 (1968).
25. J. J. Wysocki, J. Adams, and W. Haas, Phys. Rev. Lett. **20** (19), 1024 (1968).
26. F. J. Kahn, Phys. Rev. Lett. **24** (5), 209 (1970).
27. W. Harper, *Liquid Crystals* (Gordon and Breach, New York, 1967).
28. N. Oron and M. M. Labes, Appl. Phys. Lett. **21**, 243 (1972).
29. H. Baessler, T. M. Laronge, and M. M. Labes, J. Chem. Phys. **51**, 3213 (1969).
30. C. J. Gerritsma and P. van Zanten, Mol. Cryst. Liq. Cryst. **15**, 257 (1971).
31. I. Fedak, R. D. Pringle, and G. H. Curtis, Mol. Cryst. Liq. Cryst. Lett. **64**, 69 (1980).
32. V. G. Chigrinov, V. V. Belyaev, S. V. Belyaev, and M. F. Grebenkin, Zh. Éksp. Teor. Fiz. **77** (5), 2081 (1979) [Sov. Phys. JETP **50**, 994 (1979)].
33. G. Hauck and H. D. Koswig, in *Selected Topics in Liquid Crystals Research*, Ed. by H. D. Koswig (Akademie-Verlag, Berlin, 1990), p. 115.
34. A. Gobl-Wunsch, G. Heppke, and F. Oestreicher, J. Phys. (Paris) **40**, 773 (1979).
35. P. Gerber, Phys. Lett. **78**, 285 (1980).
36. G. Chilaya, Z. Elashvili, D. Sikharulidze, *et al.*, Mol. Cryst. Liq. Cryst. **209**, 93 (1991).
37. G. Heppke, D. Lotsch, F. Oestreicher, Arbeitstagung Flüssigkristalle, Freiburg, 19–21 March, 1986, S. 1.
38. G. Sh. Petriashvili, Z. M. Élashvili, S. P. Tavzarashvili, and K. G. Tevdorashvili, Kristallografiya **41** (3), 548 (1996) [Crystallogr. Rep. **41**, 519 (1996)].
39. G. Chilaya, F. Oestreicher, and G. Scherowsky, Mol. Mater. **9**, 261 (1998).
40. H. Zink and V. A. Belyakov, Zh. Éksp. Teor. Fiz. **112** (2), 524 (1997) [JETP **85**, 285 (1997)].
41. W. Greubel, Appl. Phys. Lett. **25** (1), 5 (1974).
42. G. S. Chilaya, S. N. Aronishidze, K. D. Vinokur, and M. I. Brodzeli, Available from VINITI No. 1874-76 (Moscow, 1976).
43. G. S. Chilaya, in *Physical Properties and Applications of Liquid Crystals with Induced Helical Structure* (Metsniereba, Tbilisi, 1985).
44. C. G. Lin-Hendel, Appl. Phys. Lett. **38** (8), 615 (1981).
45. P. R. Gerber, Z. Naturforsch. A **36**, 718 (1981).
46. H. A. van Sprang and van de Venne, J. Appl. Phys. **57** (2), 175 (1985).
47. J. C. Lee, D. W. Allender, and V. D. Neff, Mol. Cryst. Liq. Cryst. **210**, 11 (1992).
48. J. C. Lee and D. W. Allender, Jpn. J. Appl. Phys. **33** (3A), 1407 (1994).
49. A. Mochizuki and S. Kobayashi, Mol. Cryst. Liq. Cryst. **225**, 89 (1993).
50. Y. Koike, A. Mochizuki, and K. Yoshikawa, Displays, No. 4, 93 (1989).
51. Y. Yabe, H. Saito, T. Yoshihara, *et al.*, J. Soc. Inf. Disp. **1** (4), 411 (1993).
52. Y. Yabe and D.-S. Seo, Liq. Cryst. **17**, 847 (1994).
53. G. Chilaya, G. Hauck, H. D. Koswig, *et al.*, Cryst. Res. Technol. **32** (3), 401 (1997).
54. G. Chilaya, G. Hauck, H. D. G. Koswig, and D. Sikharulidze, J. Appl. Phys. **80** (3), 1907 (1996).
55. H.-S. Kitzerow, Jpn. J. Appl. Phys. **36** (3B), L349 (1997).
56. D. K. Yang, J. W. Doane, Z. Yaniv, and J. Glasser, Appl. Phys. Lett. **64** (15), 1905 (1994).
57. H. De Vries, Acta Crystallogr. **4**, 219 (1951).
58. A. Chanishvili, G. Chilaya, and D. Sikharulidze, Mol. Cryst. Liq. Cryst. **207**, 53 (1991).
59. Y. Toko, T. Sugiyama, K. Katoh, *et al.*, J. Appl. Phys. **74** (3), 2071 (1993).
60. K. D. Vinokur, D. G. Sikharulidze, G. S. Chilaya, and Z. M. Élashvili, in *Liquid Crystals with Helicoidal Structure and Their Use in Systems for Information Display* (Metsniereba, Tbilisi, 1988).

61. A. Chanishvili, G. Chilaya, and D. Sikharulidze, Appl. Opt. **33** (16), 3482 (1994).
62. A. Chanishvili, D. Sikharulidze, G. Chilaya, and G. Petriaschvili, Mol. Mater. **8**, 295 (1997).
63. U. Behrens, H.-S. Kitzerow, and G. Chilaya, Liq. Cryst. **17** (4), 597 (1994).
64. P. G. de Gennes, Solid State Commun. **10**, 753 (1972).
65. S. A. Pikin, Mol. Cryst. Liq. Cryst. **215**, 73 (1992).
66. S. R. Renn and T. C. Lubensky, Mol. Cryst. Liq. Cryst. **209**, 349 (1991).
67. S. R. Renn, Phys. Rev. A **45** (2), 953 (1992).
68. J. S. Patel, Phys. Rev. E **49** (5), 3594 (1994).
69. J. W. Goodby, M. A. Waugh, S. M. Stein, *et al.*, J. Am. Chem. Soc. **111**, 8119 (1989).
70. O. D. Lavrentovich, Yu. A. Nastishin, V. I. Kulishov, *et al.*, Europhys. Lett. **13** (4), 313 (1990).
71. G. Srajer, R. Pindak, M. A. Waugh, *et al.*, Phys. Rev. Lett. **64** (13), 1545 (1990).
72. H. T. Nguyen, A. Bouchta, L. Navailes, *et al.*, J. Phys. II (France) **2**, 1889 (1992).
73. A. Bouchta, H. T. Nguyen, M. F. Achard, *et al.*, Liq. Cryst. **12** (4), 575 (1992).
74. L. Navailes, P. Barois, and H. T. Nguyen, Phys. Rev. Lett. **71** (4), 545 (1993).
75. A. Bouchta, H. T. Nguyen, L. Navailes, *et al.*, J. Mater. Chem. **5**, 2079 (1995).
76. H. T. Nguyen, A. Babeau, J. C. Rouillon, *et al.*, Ferroelectrics **179**, 33 (1996).
77. W. Kuczynski and H. Stegemeyer, Mol. Cryst. Liq. Cryst. **260**, 377 (1995).
78. V. Vill, H.-W. Tunger, and D. Peters, Liq. Cryst. **20** (5), 547 (1996).
79. S. K. Prasad, G. G. Nair, S. Chandrasekhar, and J. W. Goodby, Mol. Cryst. Liq. Cryst. **260**, 387 (1995).
80. Y. Galerne, J. Phys. II (France) **4**, 1699 (1994).
81. A. C. Ribeiro, A. Dreyer, L. Oswald, *et al.*, J. Phys. II (France) **4**, 407 (1994).
82. R. Shao, J. Pang, N. A. Clark, *et al.*, Ferroelectrics **147**, 255 (1993).
83. H.-S. Kitzerow, A. J. Slaney, and J. W. Goodby, Ferroelectrics **179**, 61 (1996).
84. G. Chilaya, A. Chanishvili, G. Petriashvili, and D. Sikharulidze, Mol. Cryst. Liq. Cryst. **261**, 233 (1995).
85. A. Chanishvili, G. Chilaya, M. Neundorf, *et al.*, Cryst. Res. Technol. **31** (5), 679 (1996).
86. G. Chilaya, G. Petriashvili, A. Chanishvili, and D. Sikharulidze, Mol. Mater. **8**, 245 (1997).
87. S. A. Brazovskiĭ, Zh. Éksp. Teor. Fiz. **68**, 175 (1975) [Sov. Phys. JETP **41**, 85 (1975)].
88. S. A. Brazovskiĭ and S. G. Dmitriev, Zh. Éksp. Teor. Fiz. **69**, 979 (1975) [Sov. Phys. JETP **42**, 497 (1975)].
89. S. A. Brazovskiĭ and V. M. Filev, Zh. Éksp. Teor. Fiz. **75**, 1140 (1978) [Sov. Phys. JETP **48**, 573 (1978)].
90. R. M. Hornreich and S. Shtrikman, Phys. Rev. A **28**, 1791 (1983).
91. H. Grebel, R. M. Hornreich, and S. Shtrikman, Phys. Rev. A **28**, 1114 (1983).
92. S. Meiboom, M. Sammon, and W. F. Brinkman, Phys. Rev. A **27**, 438 (1983).
93. M. B. Bowling, P. J. Collings, Ch. J. Booth, and J. W. Goodby, Phys. Rev. E **48** (5), 4113 (1993).
94. G. Heppke, H. S. Kitzerow, D. Lotzsch, and Ch. Papenfuss, Liq. Cryst. **8**, 408 (1990).
95. G. Chilaya and G. Petriashvili, Mol. Mater. **2**, 195 (1993).
96. G. Sh. Petriashvili and G. S. Chilaya, Kristallografiya **36** (5), 1325 (1991) [Sov. Phys. Crystallogr. **36**, 752 (1991)].
97. E. Demikhov and H. Stegemeyer, Liq. Cryst. **10** (6), 869 (1991).
98. H. Zink and W. Van Dael, Liq. Cryst. **14** (3), 603 (1993).
99. G. Petriashvili, D. Sikharulidze, A. Chanishvili, and G. Chilaya, Kristallografiya **44** (5), 908 (1999) [Crystallogr. Rep. **44**, 847 (1999)].
100. H.-S. Kitzerow, Mol. Cryst. Liq. Cryst. **202**, 51 (1991).
101. V. K. Dolganov, Zh. Éksp. Teor. Fiz. **108** (2), 593 (1995) [JETP **81**, 320 (1995)].
102. G. Chilaya and G. Petriashvili, Mol. Mater. **2**, 239 (1993).
103. H. Stegemeyer, M. Schumacher, and E. Demikhov, Liq. Cryst. **15** (6), 933 (1993).
104. H. Onusseit and H. Stegemeyer, Z. Naturforsch. A **39**, 658 (1984).
105. M. H. Li, H. T. Nguyen, and S. Sigoud, Liq. Cryst. **20** (3), 361 (1996).
106. R. J. Miller and H. F. Gleeson, Liq. Cryst. **14** (6), 2001 (1993).
107. B. D. Yanoff, A. A. Ruether, and P. J. Collings, Liq. Cryst. **14** (6), 1793 (1993).
108. E. Demikhov and H. Stegemeyer, Liq. Cryst. **14** (6), 1801 (1993).
109. Z. Kutnjak, C. W. Garland, C. G. Schatz, *et al.*, Phys. Rev. E **53** (5), 4955 (1996).
110. V. E. Dmitrienko, Liq. Cryst. **5** (3), 847 (1989).
111. G. M. Zharkova and A. S. Sonin, in *Liquid Crystal Composites* (Nauka, Novosibirsk, 1994), p. 214.
112. J. Fergason, Sci. Am. **211**, 77 (1964).
113. G. Chilaya, Rev. Phys. Appl. **16** (5), 193 (1981).
114. G. S. Chilaya and L. N. Lisetskiĭ, Usp. Fiz. Nauk **134** (1), 279 (1981) [Sov. Phys. Usp. **24**, 496 (1981)].
115. G. Solladie and R. G. Zimmermann, Angew. Chem. **96**, 335 (1985).
116. G. S. Chilaya and V. G. Chigrinov, Kristallografiya **33** (1), 260 (1988).
117. K. G. Dzhaparidze, Z. M. Élashvili, G. Sh. Chelidze, *et al.*, Kristallografiya **42** (2), 340 (1997) [Crystallogr. Rep. **42**, 300 (1997)].
118. J. L. Fergason, US Patent No. 4 435 047 (1984).
119. J. W. Doane, N. A. Vaz, B.-G. Wu, and S. Zumer, Appl. Phys. Lett. **48**, 269 (1986).
120. H.-S. Kitzerow, Liq. Cryst. **16**, 1 (1994).
121. P. P. Crooker and D. K. Yang, Appl. Phys. Lett. **57**, 2529 (1990).
122. H.-S. Kitzerow and P. P. Crooker, J. Phys. II (France) **3**, 719 (1993).

123. J. L. West, R. B. Akins, J. Francl, and J. W. Doane, Appl. Phys. Lett. **63** (11), 1471 (1993).
124. D. K. Yang, J. L. West, L.-C. Chien, and J. W. Doane, J. Appl. Phys. **76** (2), 1331 (1994).
125. S. Chandrasekhar and G. S. Ranganath, Rep. Prog. Phys. **53**, 57 (1990).
126. F. Closs, K. Siemensmeyer, Th. Frey, and D. Funhoff, Liq. Cryst. **14**, 629 (1993).
127. D. Adam, F. Closs, T. Frey, *et al.*, Phys. Rev. Lett. **70**, 457 (1993).
128. N. Boden, R. J. Bushby, J. Clements, *et al.*, Phys. Rev. B **52**, 13274 (1995).
129. D. Sikharulidze, G. Chilaya, K. Praefcke, and D. Blunk, Liq. Cryst. **23** (3), 439 (1997).
130. I. Cho and Y. Lim, Mol. Cryst. Liq. Cryst. **154**, 9 (1988).
131. J. Malthete, C. Destrade, N. H. Tink, and J. Jacquesp, Mol. Cryst. Liq. Cryst. Lett. **64**, 233 (1981).
132. C. Destrade, N. H. Tinh, J. Malthete, and J. Jacque, Phys. Lett. A **79**, 189 (1980).
133. N. Usoltseva, K. Praefcke, D. Singer, and B. B. Gundogan, Liq. Cryst. **16** (1), 617 (1994).
134. K. Praefcke, D. Singer, and A. Eckert, Liq. Cryst. **16** (1), 53 (1994).
135. M. Langner, K. Praefcke, D. Kruerke, and G. Heppke, J. Mater. Chem. **5** (4), 693 (1995).
136. Ch. J. Booth, D. Kruerke, and G. Heppke, J. Mater. Chem. **6** (6), 927 (1996).
137. R. Meyer, Phys. Rev. Lett. **22**, 918 (1969).
138. J. S. Patel and S.-D. Lee, J. Appl. Phys. **66** (4), 1879 (1989).
139. S.-D. Lee, J. S. Patel, and R. Meyer, J. Appl. Phys. **67** (3), 1293 (1990).
140. S.-D. Lee, J. S. Patel, and R. Meyer, Mol. Cryst. Liq. Cryst. **209**, 79 (1991).
141. L. Komitov, S. T. Lagerwall, B. Stebler, and A. Strigazzi, J. Appl. Phys. **76** (6), 3762 (1994).
142. L. M. Blinov, J. Nonlinear Opt. Phys. Mater. **5** (2), 165 (1996).
143. R. B. Alaverdyan, S. M. Arakelyan, and Yu. S. Chilingaryan, Pis'ma Zh. Éksp. Teor. Fiz. **42** (9), 366 (1985) [JETP Lett. **42**, 451 (1985)].
144. L. I. Zagaĭnova, G. V. Klimusheva, I. P. Kryzhanovskiĭ, and N. V. Kukhtarev, Pis'ma Zh. Éksp. Teor. Fiz. **42** (9), 353 (1985) [JETP Lett. **42**, 435 (1985)].
145. H. J. Eichler, D. Grebe, R. Macdonald, *et al.*, Opt. Mater. **2**, 201 (1993).
146. A. G. Iljin, G. V. Klimusheva, and L. I. Zagainova, Mol. Mater. **5**, 25 (1995).
147. D. Grebe, R. Macdonald, and H. J. Eichler, Mol. Cryst. Liq. Cryst. **282**, 309 (1996).
148. S. G. Lukishova, S. V. Belyaev, K. S. Lebedev, *et al.*, Mol. Cryst. Liq. Cryst. **303**, 79 (1997).
149. E. Sakman, J. Am. Chem. Soc. **93**, 7088 (1971).
150. V. Vinogradov, A. Khizhnyak, L. Kutulya, *et al.*, Mol. Cryst. Liq. Cryst. **192**, 273 (1990).
151. S. N. Yarmolenko, L. A. Kutulya, V. V. Vashchenko, and L. V. Chepeleva, Liq. Cryst. **16**, 877 (1994).
152. V. F. Kitaeva and A. S. Zolot'ko, Mol. Cryst. Liq. Cryst. Sci. Technol., Sect. B: Nonlinear Opt. **2**, 261 (1992).
153. S. G. Dmitriev, Zh. Éksp. Teor. Fiz. **65**, 2466 (1973) [Sov. Phys. JETP **38**, 1231 (1974)].
154. H. G. Winful, Phys. Rev. Lett. **49** (16), 1179 (1982).
155. J.-C. Lee, A. Schmid, and S. D. Jacobs, Mol. Cryst. Liq. Cryst. **166**, 253 (1989).
156. N. V. Tabiryan and B. Ya. Zel'dovich, Mol. Cryst. Liq. Cryst. **69**, 19 (1981).
157. B. Ya. Zel'dovich and N. V. Tabiryan, Zh. Éksp. Teor. Fiz. **82** (1), 167 (1982) [Sov. Phys. JETP **55**, 99 (1982)].
158. N. V. Tabiryan, A. V. Sukhov, and B. Ya. Zel'dovich, Mol. Cryst. Liq. Cryst. **136**, 1 (1986).

Translated by L. Man